DEEP NIR IMAGING OF GALAXY CLUSTERS IN THE VELA SUPERCLUSTER

PhD thesis

by

Narges Hatamkhani

Submitted in total fulfilment of the academic requirements
for the degree of Doctor of Philosophy
Department of Astronomy

University of Cape Town

February 2022

University of Cape Town

The copyright of this thesis vests in the author. No quotation from it or information derived from it is to be published without full acknowledgement of the source. The thesis is to be used for private study or non-commercial research purposes only.

Published by the University of Cape Town (UCT) in terms of the non-exclusive license granted to UCT by the author.

University of Cape Town

Supervisor
Prof. R.C. Kraan-Korteweg

Co-Supervisor
Assoc. Prof. S.-L. Blyth

Plagiarism Declaration

I, Narges Hatamkhani, know the meaning of plagiarism and declare that all of the work in the document, save for that which is properly acknowledged, is my own.

Abstract

Gravitational forces of large galaxy overdensities can perturb the smooth motions expected from the expanding universe, causing peculiar motions. The observed Cosmic Microwave Background (CMB) dipole is the result of the Local Group's peculiar motion, the direction and amplitude of which are still not fully resolved. The newly discovered Vela Supercluster (VSCL, $\ell = 272.^{\circ}5 \pm 20^{\circ}, b = 0^{\circ} \pm 10^{\circ}$), an extended structure behind the Zone of Avoidance (ZoA) at $cz \sim 18000\,\mathrm{km\ s^{-1}}$, may be a not insignificant contributor to the residual bulk flow that arises beyond $cz \sim 16000\,\mathrm{km\ s^{-1}}$. Knowledge of the structure and richness of galaxy clusters within the VSCL will enable us to assess the morphology and mass of this partially obscured supercluster. Compared to the shorter optical wavelengths, near-infrared (NIR) observations are less affected by dust obscuration in the ZoA and therewith offer a better tool to probe galaxy clusters in the VSCL, and get a better understanding of this extended supercluster.

A series of deep NIR observations of prospective clusters identified in the VSCL were conducted in the J, H and K_s bands with the InfraRed Survey Facility (IRSF) telescope. For 6 (VC02, VC04, VC05, VC08, VC10 and VC11) out of 20 potential clusters a complete set of science quality images were obtained (out to $\sim 70\%$ of the Abell radius) and were fully reduced. I identified galaxy candidates in each cluster using the SOURCE EXTRACTOR software, validated them through visual inspection of the RGB composite images and created a catalogue of galaxies with their astrometric and photometric parameters using the IRSF pipeline. There are a total number of 1715 identified galaxies distributed over the six clusters, of which only $\sim 15\%$ were previously known. Investigating the effect of foreground extinction in the region of the observed clusters shows that, the VC02 cluster has the highest foreground extinction while VC04 and VC05 have the lowest ($\langle A_{Ks} \rangle = 0.^{\mathrm{m}}10$, $\langle A_{Ks} \rangle = 0.^{\mathrm{m}}07$ and $\langle A_{Ks} \rangle = 0.^{\mathrm{m}}06$ respectively). I show that the effect of extinction on the isophotal magnitudes is small compared to the foreground extinction and additional extinction-correction is not required. The extinction-corrected completeness magnitude limit for this survey is $M^o_{Ks} < -21.^{\mathrm{m}}5$ which is $\sim 2.^{\mathrm{m}}0$ deeper than 2MASX. The six observed clusters were analysed in detail out to the clustercentric completeness radius of $r_c < 1.5$ Mpc and $M^o_{Ks} < -21.^{\mathrm{m}}5$.

Comparison of the iso-density contour maps and radial density profiles of the VSCL clusters with K_s-band data of well-known clusters (Coma, Norma, 3C129 and Virgo), finds VC04 to be a regular and massive cluster comparable to Coma and Norma (although its velocity dispersion seems rather low for a rich cluster); it is the richest of the six. H I analysis (using MeerKAT-16 data) shows that the spiral galaxies in VC04 are severely H I deficient which is consistent with its richness. VC02 and VC05 are found to be relatively rich clusters while VC08 is rather poor. VC10 has a filament-like structure and is not a cluster. VC11 is an intermediate cluster which contains two major subclusters. It appears that many of the VSCL clusters (VC02, VC04, VC05 and VC11) are not relaxed yet and are still evolving.

The K_s-band Luminosity Function (LF) was derived for the VSCL clusters up to $M^o_{Ks} < -21\overset{\mathrm{m}}{.}5$ ($\sim 2\overset{\mathrm{m}}{.}5$ deeper than M^*). I demonstrate that the Red-Sequence (RS) method is a reliable method to measure the LFs of the clusters and then compute the K_s-band LFs of the Coma, Norma and Virgo clusters using the RS method to compare to the LFs of the VSCL clusters. The comparisons show that M^* derived for the LF of VC04 ($M^* = -24\overset{\mathrm{m}}{.}70 \pm 0.42$) agrees well with those of other local clusters. The bright end of the VC04 LF is compatible with that of massive clusters that are dominated by early-type galaxies such as Norma, while the slope ($\alpha = -0.89 \pm 0.13$) is shallower compared to those of younger clusters.

The analysis of this to date small sample of the VSCL clusters (6 out of at least 20) shows that the VSCL contains potentially many more rich clusters indicative of it being a rich supercluster.

Acknowledgements

My PhD has been an incredible adventure and quite an experience. I have grown in ways that I could not have even thought of before. My journey would have not been possible without all the people who supervised, helped, supported and inspired me.

Renée, I can not thank you enough for giving me this fantastic opportunity. I am so grateful to have had you as my supervisor. Thank you for showing me the mysterious universe behind our Galaxy and sharing your immense scientific knowledge with me. Thank you for your detailed input and feedback on my work throughout my PhD. You have been always there to teach, guide and support me.

Sarah my kind co-supervisor, I highly appreciate all the input you have had in my work and your tips on programming. It has been always easy to talk to you and your words always gave me strength.

A very special thanks to Ros who has helped me extensively in learning about SALT and writing the SALT proposal. Your work has been of immense help to me. Thank you Ros for your patience, for listening to and encouraging me.

Many thanks to Tom Jarrett who gave me valuable guidance on how to address the issues in working with pipelines.

I have always enjoyed observing and spending time in Sutherland but my first observing experience with Khaled was outstanding. Thank you Khaled, for teaching me how to observe and for your further assistance on how to start my project and answering my questions.

I would like to thank the IRSF team for the allocation of observing time and Japanese collaborators, T. Nagayama, K. Morihana, Y. Nakajima, N. Tetsuya for assisting with the IRSF observations and software.

My sincere thanks go to UCT, whose Science Faculty supported me through one of the bursaries that fall under their UCT-SKA scholarship programme, without which I could not have started my PhD. This work was furthermore based upon research supported by the South African Research Chairs Initiative of the Department of Science and Technology and the National Research Foundation through my supervisor Prof. Renée C. Kraan-Korteweg as the Chairholder of the SARAO SARChI grant on Extragalactic Multiwavelength Astronomy.

A big thank you to the HOD of the department of Astronomy; Patrick, and the admins Roz and Carol.

Many thanks to the anonymous referees for the many helpful suggestions that improved this thesis.

My special thanks to my dear friends Julia and Mpati, who have been always available to help in any matter, work-related or not. I always enjoy our lovely conversations and hope we will have more in future.

I would like to specially thank Iniyan. Thank you for your wisdom and your deep insight on life that has helped me to grow and broaden my views. Thank you for your

support through hardships.

Nikki, I am so grateful to have had a very special friend since I came to South Africa. I could have not done this if I did not have you by my side, thank you.

I have had the good fortune to have known and made many more great friendships. Thank you Moses, Kosma, Rajin, Diksha, Thuso, Millie, Nikhita, Brad, Chanelle and Krishna for having filled my life with joy. To the UCT crew including those who have left; Khine, Liz, Sam, Tshia, Lennart, Trystan, Munira, Miriam, Naomi, Brenda and Sambatra. My non-Astronomy friends who supported me wholeheartedly; Razieh, Mahmood, Fatima and Sakina.

To my dearest friend back home in Iran, Leila. No words can express my gratitude to you for what you have done for me was extraordinary. Thank you for always being there for me.

My family has provided unwavering support and encouragement throughout this journey. My dearest mother, Nasrin, my kindest brothers, Reza, Amir and Omid, and my beautiful sister-in-law, Mina, who I can not even begin to say what they mean to me and how much I love them.

This work is in remembrance of my beloved father who always made me feel the most precious girl in the world, but left me too soon.

Contents

1 Introduction **2**
- 1.1 Cosmic web . . . 3
- 1.2 Superclusters . . . 3
  - 1.2.1 Supercluster detection methods . . . 4
  - 1.2.2 Properties of superclusters . . . 5
- 1.3 Dynamics of the local universe . . . 7
- 1.4 The Vela Supercluster behind the Milky Way . . . 8
  - 1.4.1 The ZoA . . . 8
  - 1.4.2 Discovery of the Vela Supercluster . . . 10
  - 1.4.3 Morphology of the Vela Supercluster . . . 11
  - 1.4.4 The Vela supercluster and bulk flows . . . 12
  - 1.4.5 Galaxy clusters within the VSCL . . . 12
- 1.5 Galaxy clusters . . . 12
  - 1.5.1 Properties of Galaxy Clusters . . . 12
  - 1.5.2 The Morphology-Density relation . . . 15
  - 1.5.3 Red-Sequence . . . 16
  - 1.5.4 The Luminosity Function . . . 16
  - 1.5.5 X-ray observations in the ZoA . . . 20
- 1.6 This thesis . . . 22
  - 1.6.1 NIR study of the VSCL clusters . . . 22
  - 1.6.2 Thesis outline . . . 23

2 NIR Observation and Data Reduction **24**
- 2.1 Sample selection . . . 25
- 2.2 The NIR observations with the IRSF . . . 27
  - 2.2.1 Imaging Method . . . 28
  - 2.2.2 IRSF Observations . . . 29
- 2.3 Preliminary Data Reduction with the SIRIUS Pipeline . . . 33
  - 2.3.1 Image Calibration . . . 35
  - 2.3.2 Photometric Properties of the Images . . . 37
- 2.4 Galaxy Identification . . . 38
  - 2.4.1 Visual Inspection of Galaxies in a Sample of Fields . . . 38
  - 2.4.2 Using Source Extractor to identify galaxy candidates . . . 40
- 2.5 Summary . . . 45

3 Galaxy Photometry **46**
- 3.1 The IRSF pipeline . . . 46
  - 3.1.1 Galaxy verification . . . 46

3.1.2 Star subtraction . . . 47
3.1.3 Galaxy photometry . . . 49
3.2 NIR extended source catalogue . . . 52
3.2.1 Catalogue parameters . . . 52
3.3 Quality control of galaxy parameters . . . 53
3.3.1 Internal consistency . . . 56
3.3.2 External consistency . . . 57
3.4 Extinction effects . . . 63
3.4.1 Foreground extinction . . . 63
3.4.2 Extinction effect on the properties of galaxies . . . 64
3.4.3 Extinction-Corrected NIR colours . . . 69
3.4.4 k-Correction . . . 70
3.5 Completeness limit . . . 72
3.6 Summary . . . 77

4 Analysis of the VSCL Galaxy Clusters 78
4.1 Comparison clusters . . . 78
4.1.1 Structure and Richness . . . 80
4.2 The VSCL galaxy clusters . . . 84
4.2.1 Galaxy cluster VC04 . . . 84
4.2.2 Other VSCL clusters . . . 91
4.2.3 Discussion on the VSCL clusters . . . 92
4.3 HI content of the rich cluster VC04 . . . 95
4.4 Summary . . . 100

5 The Luminosity Function of Galaxy Clusters 102
5.1 Introduction . . . 102
5.2 Derivation of the luminosity function . . . 103
5.2.1 Statistical field correction method . . . 103
5.2.2 Spectroscopic membership method . . . 103
5.2.3 The Red-Sequence method . . . 105
5.3 The NIR LFs of Norma, Coma and Virgo . . . 105
5.3.1 Identifying the RS galaxies . . . 106
5.3.2 The Norma cluster luminosity function . . . 108
5.3.3 The Coma and Virgo luminosity functions . . . 112
5.4 The VC04 LF . . . 114
5.5 Discussion . . . 117
5.5.1 Comparison with the Coma, Norma and Virgo LFs . . . 119
5.5.2 Comparison with previous NIR LFs . . . 119
5.5.3 Environmental effects . . . 120
5.6 The LFs of other VSCL clusters . . . 120
5.7 Summary . . . 125

6 Summary and future work 126
6.1 Thesis main features . . . 126
6.2 Future work . . . 127

A Galaxy catalogues of the VSCL clusters 160

B Plots of the six observed VSCL clusters **197**
B.1 The VC02 cluster 197
B.2 The VC04 cluster 200
B.3 The VC05 cluster 203
B.4 The VC08 cluster 207
B.5 The VC10 cluster 210
B.6 The VC11 cluster 213

List of Figures

1.1 The spatial distribution of 100,000 galaxies derived from 2dF galaxy survey, revealing the large-scale structures and voids in the local universe. Image credit: M. Colless (ANU) and the 2dF Galaxy Redshift Survey (http://magnum.anu.edu.au/\protect\unhbox\voidb@x\protect\penalty\@M\{}TDFgg/). 4

1.2 Model of large-scale structure in the local Universe assuming a ΛCDM cosmology. Superclusters (bright red knots) and long filaments with high galaxy concentration are shown in red. Galactic voids outlined by low concentration of galaxies are shown in blue. Image credit: Chris Power, Swinburne University (https://astronomy.swin.edu.au/cosmos/l/Large-scale+Structure). 5

1.3 An all-sky projection of the Galactic reddening, $E(B-V)$, map. The values for $E(B-V)$ are shown on a logarithmic scale from $0\overset{m}{.}004$ to $6\overset{m}{.}3$. The yellow/red area on the map indicates the highest value of extinction in the ZoA. Image credit: LAMBDA data products. 8

1.4 Aitoff projection of the 2MASS PSC in Galactic coordinates. The map is colour-coded based on the stellar number density in the foreground. Image credit: https://old.ipac.caltech.edu/2mass/releases/allsky/doc/sec4_5c.html 9

1.5 The location of the Vela and Shapley superclusters in Galactic coordinates. The figure is made based on the Photometric Redshift data from Bilicki et al. (2014) and the All-Sky Panorama image of the Milky Way (Mellinger, 2009). The yellow and green dots are close to the Vela supercluster distance and the orange ones are more distant. Image credit: Tom Jarrett (UCT). . 10

1.6 Wedge diagrams of the Vela overdensity out to $cz \lesssim 32000$ km s^{-1}, above the GP, $0° < b < +10°$ (left) and below the GP, $-10° < b < 0°$ (right). The main wall can be traced above and below the GP at ~ 18000 km s^{-1} while the second wall at ~ 22000 km s^{-1}, only below the GP seems to be converging the main wall. The red dots depict the galaxies in the potential clusters. 11

1.7 The luminosity function for various morphological types of galaxies in field (top) and in the Virgo cluster (bottom). The luminosity function of all galaxies with different morphological types is the combination of the luminosity functions of each type of galaxies. Taken from Binggeli et al. (1988) 18

1.8 K-band isophotal luminosity function for 1345 2MASX galaxies with $K \leq 10\overset{m}{.}0$ and $V_{gsr} \leq 3000$ km s^{-1}. The sample was segregated by visible morphology. Image credit: Devereux et al. (2009). 19

1.9 The Galactic hydrogen column density contours at $|b| < 40°$ in units of 10^{20} cm^{-2} (Dickey and Lockman, 1990). Dashed lines indicate the ZoA at $|b| < 20°$. Taken from Ebeling et al. (2002) 21
1.10 Average extinction values at different Galactic latitudes in ZoA in different wavebands. The optical extinction is determined based on the 100 μm maps Schlegel et al. (1998). The dashed curves from top to bottom display the extinction values at X-ray wavelengths which are determined with the assumption of a Bremsstrahlung spectrum for intra-cluster gas at $kT = 2, 6,$ and 10 keV respectively, at $z = 0.1$. The extinction in the K band is much lower compared to the optical V band. The figure is taken from Ebeling et al. (2002). 22

2.1 Redshift cones for the VSCL survey out to $cz \leqslant 32000$ km s^{-1}. The primary wall can be traced at 18000 km s^{-1} above and below the GP (see panels on the right), while the second wall is visible only below the GP. The red dots mark potential galaxy clusters. Image credit: Kraan-Korteweg et al. (2017) 25
2.2 The figure is taken from (Kraan-Korteweg et al., 2017). Left panel: Galaxy redshift distribution within the VSCL region. Galaxies in this figure are colour-coded based on their redshifts. cyan: $v < 8000$; green: $8000 < v < 16000$; red: $16000 < v < 20000$; magenta $20000 < v < 24000$; blue: $24000 < v < 32000$ km s^{-1}. Contours indicate extinctions of $A_K = 0\overset{m}{.}3$ (solid) and $0\overset{m}{.}18$ (dotted). The black arrows point at the galaxy clusters that are studied in this work. Right panel: the redshift cones out to $cz \leqslant 32000$ km s^{-1} above and below the GP. The positions of the investigated galaxy clusters in this work are shown in black circles. 26
2.3 False colour RGB images of four galaxies observed with both 2MASS (top row) and IRSF/SIRIUS (bottom row). J, H and K_s bands correspond to Blue, Green and Red colours respectively in the RGB images. The scale of images is $90'' \times 90''$. 28
2.4 A sample of the observed mosaic consists of 32 slightly overlapping fields for each cluster. In the notation $\pm a \pm b$, a and b are the numerical offsets in the horizontal and vertical directions respectively from the cluster center, used to identify a field within the mosaic. 29
2.5 The dithering pattern of the SIRIUS camera. Each field is observed with 25 dithered frames of 24 s exposures each. The figure is taken from Riad (2010). 31
2.6 Master flat-fields for the J, H and K_s bands for the 2015 and 2017 observing runs. 32
2.7 Master flat-fields for the J, H and K_s bands for the 2018/19 observing run. 32
2.8 Dark frames for the J, H and K_s bands for the 2015 and 2017 observing runs. 33
2.9 Dark frames for the J, H and K_s bands for the 2018/19 observing run. . . 33
2.10 The IRSF/SIRIUS (Yasushi Nakajima; private communications) and 2MASS transmission curves for the J, H, K_s bands. 36
2.11 The distribution of the seeing (left) and magnitude zero-points (right) of the final 263 survey images that were accepted for photometry in J, H, K_s bands. 38

2.12 Comparison of the mean magnitude zero-points in the J, H and K_s bands for this survey to those of the same telescope and imaging set-up. The cyan dots show mean ZPs of the VSCL survey, while blue, green and red dots illustrate Cluver (2008); Riad (2010) and Williams (2011) values respectively. 39
2.13 Colour-colour (top panel) and colour-radius (bottom panel) diagrams of 68 galaxy candidates in nine fields of VC08. 40

3.1 An example of how `findgal` highlights and displays potential candidates in a field. Light blue circles indicate the galaxy candidates. The dark blue ellipses are drawn based on the first estimation of the minor and major axes by the user. The size of this postage stamp is $\sim 2\farcm4 \times 1\farcm3$. 47
3.2 The postage stamps of three galaxy candidates in the VC08 cluster at $\langle v \rangle \sim 17316$ km s^{-1} in the K_s band, before (left) and after (right) star-subtraction. The size of the cutouts is 200×200 pixels which translate to $90'' \times 90''$ given the resolution of the IRSF of $0\farcs45$ pix^{-1}. 49
3.3 A sample of the surface brightness profiles of the galaxy ZOA085847.908-580615.22 in J, H, K_s bands. The top panels show the surface brightness, μ, as a function of the major axis a. The solid lines represent the fitted Sérsic profiles and the top left corner gives the parameters obtained by fitting. A gray-scale postage stamp of the galaxy is displayed at the top right corner of each subplot with the geometric parameters of the ellipse underneath. The vertical dashed lines show the isophotal radii where the surface brightness (μ) drops to 1σ of the sky background (shown by the horizontal lines). The bottom panel depicts the fitting residuals (mag arcsec^{-2} versus arcsec). In the J and H-band surface brightness profiles of this galaxy only an exponential profile is fitted to the outer disk. If the double Sérsic profile is fitted the difference between the magnitude at the maximum radius and the limit $r = \infty$ will be more than one magnitude 51
3.4 Consistency of the coordinate positions of the objects that were observed more than once in the mosaic of the clusters in the VSCL clusters. 55
3.5 Comparison of the K_{s20} fiducial magnitudes in the J, H, K_s bands for double-observed galaxies in VC04. The dotted line indicates the mean value of Δm and the dashed lines indicate the 1σ dispersion around the mean. The mean and standard deviation are given in the top left corner of each plot. 58
3.6 Astrometric comparison of the matched pairs between the clusters in the VSCL and 2MASX. 59
3.7 Comparison of the $7''$ aperture J, H, K_S magnitudes between IRSF/SIRIUS (VC04) and 2MASX. The dotted line indicates the mean value of Δm and the dashed lines indicate the 1σ dispersion around the mean. The error bars show the combination of the IRSF and 2MASX magnitude errors. The mean and standard deviation are given in the top left corner of each plot. 61

3.8 Comparison of the K_{s20} fiducial magnitudes in the J, H, K_s bands between IRSF/SIRIUS (VC04) and 2MASX. The dotted line indicates the mean value of Δm and the dashed lines indicate the 1σ dispersion around the mean. The error bars show the combination of the IRSF and 2MASX magnitude errors. The mean and standard deviation are given in the top left corner of each plot. 62
3.9 Histograms of galaxy candidate number counts in VC02, VC04, VC05, VC08, VC10 and VC11 per square degree as a function of Galactic extinction A_J, A_H and A_{K_s}. 66
3.10 The reddening maps of the region around the VSCL clusters. The green circles are the galaxy candidates in the galaxy clusters and the contours show the K_s-band extinction levels, with red indicating $A_{Ks} = 0\overset{\mathrm{m}}{.}07$, yellow $A_{Ks} = 0\overset{\mathrm{m}}{.}08$, blue $A_{Ks} = 0\overset{\mathrm{m}}{.}09$, cyan $A_{Ks} = 0\overset{\mathrm{m}}{.}10$, black $A_{Ks} = 0\overset{\mathrm{m}}{.}11$, white $A_{Ks} = 0\overset{\mathrm{m}}{.}12$, orange $A_{Ks} = 0\overset{\mathrm{m}}{.}13$, magenta $A_{Ks} = 0\overset{\mathrm{m}}{.}14$. The black boxes indicate the outlines of the observed mosaic in each cluster. The galaxies outside of the boxes are located in the extra fields that were observed to compensate for the Infrared detector problem of the IRSF telescope. The colourbar shows the reddening map values as grey-scale. 67
3.11 Extinction-corrected colour-colour diagrams of galaxy candidates with $r > 2''$ in VC04. 70
3.12 The plot of colour versus redshift of 2236 selected galaxies from the ZoA master list. The selected galaxies are restricted to the Galactic longitude range of $255° < \ell < 285°$ and the latitude range of $|b| < 10°$. The left panel shows the $(J - K_s)$ colour of the galaxies as a function of redshift, the middle panel the extinction-corrected colour $(J - K_s)$, and the right panel the extinction and k-corrected colour of galaxies. The dashed line shows the mean $(J - K_s)$ colour of nearby early-type galaxies (Jarrett, 2000) 71
3.13 The change in the mean value of $(J - K_s)$ colour as a function of redshift for S0 and Sc type galaxies (reddening curve). 71
3.14 The colour-magnitude diagram ($(J-K_s)$ versus K_s). From left to right the plots are observed, extinction-correction and extinction plus k-correction. The dashed lines indicate the mean NIR isophotal colour $(J - K_s)$=$0\overset{\mathrm{m}}{.}92$ for nearby early-type galaxies (Jarrett, 2000). 72
3.15 Isophotal magnitude vs central surface brightness of candidate galaxies in VC04 in three J, H and K_s bands. The fitted relation is shown by the solid black line, with the thin gray lines representing a deviation of 3σ on either side. The completeness magnitude is indicated by the solid thick blue line. 73
3.16 Distributions of the logarithm of the cumulative galaxy count, $\log(\mathrm{N})_{\mathrm{cum}}$, as a function of observed $K_s = 20$ fiducial isophotal magnitudes in J, H and K_s bands in VC04. The black dashed lines show the completeness magnitude limits in each band at the knee of the distributions. The red dashed line is plotted to show the deviation point from the ascending trend. 76

4.1 Left: the iso-density contour maps of the Coma, Norma, 3C129 and Virgo clusters out to $r_c = 1.5\,\mathrm{Mpc}$ and the extinction-corrected magnitude completeness limit of $M^o_{Ks} = -21\overset{\mathrm{m}}{.}5$. The galaxies are shown as black dots and the centres of clusters as red stars. The red and magenta circles represent the r_{200} and r_c respectively. Right: the radial density profile of the clusters. 82

4.2 Left: the Iso-density contour map of the Norma cluster out to $r \sim 0.5\,\mathrm{Mpc}$. The galaxies are shown as black dots and the centre of cluster as a red star. The red and magenta circles represent the r_{200} and r_c respectively. Right: the radial density profile of the Norma cluster out to $r \sim 0.5\,\mathrm{Mpc}$. 83
4.3 The VC04 mosaic. The identified galaxies are shown as black dots. The two hatched fields are the ones that are not of good quality. The two blue fields indicate the extra observed fields to compensate for the blank quarter in K_s band caused by the infrared detector problem of the IRSF telescope. 85
4.4 Top: VC04 histograms of isophotal magnitudes at $K_s = 20\overset{\mathrm{m}}{.}0$ in J, H and K_s bands. The dashed histograms show the observed magnitudes and the hatched ones are extinction-corrected. The dashed lines are the completeness magnitude limits in each band. Bottom: Histograms of central surface brightnesses of VC04 galaxies in J, H and K_s bands. The dividing values of central surface brightnesses between elliptical and spiral galaxies, derived by Jarrett et al. (2003), in each band are shown by the dashed lines. 86
4.5 The on-sky distribution of galaxies with $K_s^o < 15\overset{\mathrm{m}}{.}5$ and $r > 2''$ in VC04. The IRSF galaxies are shown with filled green circles. Galaxies that have counterpart in 2MASX are encircled in blue. The red star shows the centre of cluster and the big green circle is the Abell radius. 87
4.6 Left: the velocity histogram of VC04 for 89 galaxies with spectroscopic redshifts. Right: Distribution of the extinction-corrected K_s magnitudes for 416 identified galaxies in VC04. The 89 galaxies with redshift data are shown as black hatched areas. The red areas mark foreground and background galaxies ($v < 16000$ km s^{-1} and $v > 20000$ km s^{-1} respectively). 88
4.7 Left: the radial density profile, N/Mpc^2, out to $r < 2$ Mpc. The total number density of galaxies is shown in blue histogram and the completeness-limited sample ($K^0_{slim} < 15\overset{\mathrm{m}}{.}5$) in pink. Right: iso-density map of VC04 for $r < 2$ Mpc. Galaxies are shown as black dots and the centre of cluster as red star. The red and magenta circles represent the r_{200} and r_c respectively. The three brightest galaxies are shown as red, magenta and yellow dots. . . 89
4.8 Left: the iso-density contour map of VC04 to the same density level as the comparison clusters. The galaxies are shown as black dots and the red and magenta circles demonstrate the r_{200} and r_c radii respectively. Right: the iso-density map of the Coma cluster. 90
4.9 The iso-density contour map of the VSCL clusters to the same density level as the comparison clusters out to $r_c = 1.5\,\mathrm{Mpc}$, complete to $K^0_{slim} < -21\overset{\mathrm{m}}{.}5$. The galaxies are shown as black dots and the red and magenta circles demonstrate the r_{200} and r_c radii respectively. 93
4.10 The iso-density contour maps of the Coma, Norma, 3C129 and Virgo clusters out to $r_c = 1.5\,\mathrm{Mpc}$ and complete to $M^0_{Ks} \sim -21\overset{\mathrm{m}}{.}5$. The galaxies are shown as black dots. The red and magenta circles represent the r_{200} and r_c respectively. 94
4.11 The velocity (left) and magnitude (right) histograms of galaxies with redshifts. The 45 spirals are marked in cyan. 96
4.12 $\log(\mathrm{M_{HI}})$ vs $\log(L_K)$ for the HIZOA sample of 326 galaxies. The fitted line on galaxies with $\log(L_K) > 9.92\,\mathrm{L_\odot}$ and $W_{50} > 200$ km s^{-1} is shown as a red line. The dashed line $\log(L_K) = 9.92\,\mathrm{L_\odot}$ is the completeness limit of this study. 98

4.13 The estimated M_{HI} of 45 spirals, using the scaling relation L_K-M_{HI}. 98
4.14 Left: the derived W_{50} of 45 spiral galaxies in VC04 using the TF relation. Right: The estimated upper limit of M_{HI} of the spirals. 99
4.15 The estimated H I deficiency as a function of distance from the centre of VC04 for the 45 spiral galaxies and the three 2MASX galaxies that were detected with MeerKAT. 100

5.1 The RS of the Coma, Norma and Virgo clusters performed on galaxies within a clustercentric distance of $r_c = 1.5$. Galaxies with $M^0_{K_s} < -21\overset{m}{.}5$ are shown as filled blue circles and galaxies with $M^0_{K_s} > -21\overset{m}{.}5$ as open circles. The RS galaxies are displayed as red filled circles and the black line corresponds to the RS fit. 107
5.2 The LF of the Norma cluster in the K_s-band, using Skelton et al. (2009) data, determined from the spectroscopic membership method out to $r = 0.5$ Mpc. The best fit is shown with the red line and the gray area shows the 3σ uncertainty of the fit. Left: $-26\overset{m}{.}0 < M_{Ks} < -19\overset{m}{.}5$. Right: excluding the first bin (the two cD galaxies) $-25\overset{m}{.}5 < M_{Ks} < -19\overset{m}{.}5$. 108
5.3 The number counts of galaxies in the Norma cluster in half-magnitude bins out to the completeness limit $M_{Ks} = -21\overset{m}{.}5$ and $r_c = 1.5$ Mpc. Cluster members are shaded in black. Galaxies with no spectroscopic information are unshaded. The spectroscopically confirmed foreground and background galaxies are shown with the red shading. 110
5.4 The LF of the Norma cluster in the K_s-band out to $r < 0.5$ Mpc, excluding the two cD galaxies (the first bin). Left: using Skelton et al. (2009) data, determined from the spectroscopic membership method for $-25\overset{m}{.}5 < M_{Ks} < -21\overset{m}{.}5$. Right: using 2MASX data, determined from the RS method for $-26\overset{m}{.}0 < M_{Ks} < -21\overset{m}{.}5$. The best fit is shown with the red line and the gray area shows the 3σ uncertainty of the fit. 111
5.5 The LFs of the Norma cluster in the K_s-band out to $r_c < 1.5$ Mpc. The left panel shows the LFs derived from the spectroscopic method and the right panel derived from the RS method. In both panels the top and bottom plots show the LFs with and without the two cD galaxies respectively. The best fit is shown with the red line and the gray area shows the 3σ uncertainty of the fit. 111
5.6 The LF of the Coma cluster in the K_s-band using the RS method. (a): out to $r < 0.5$ Mpc, excluding the two cD galaxies (the first bin), $-25\overset{m}{.}0 < M_{Ks} < -21\overset{m}{.}5$. (b): out to $r_c < 1.5$ Mpc, $-26\overset{m}{.}5 < M_{Ks} < -21\overset{m}{.}5$. (c): out to $r_c < 1.5$ Mpc, excluding the two cD galaxies (the first bin), $-26\overset{m}{.}0 < M_{Ks} < -21\overset{m}{.}5$. The best fit is shown with the red line and the gray area shows the 3σ uncertainty of the fit. 113
5.7 The LF of the Virgo cluster in the K_s-band using the RS method. (a): $r < 0.5$ Mpc, $-26\overset{m}{.}0 < M_{Ks} < -21\overset{m}{.}5$. (b): $r_c < 1.5$ Mpc, $-26\overset{m}{.}0 < M_{Ks} < -21\overset{m}{.}5$. (c): $r_c < 1.5$ Mpc, $-25\overset{m}{.}5 < M_{Ks} < -21\overset{m}{.}5$. The best fit is shown with the red line and the gray area shows the 3σ uncertainty of the fit. . . 115

5.8 Left: the RS of the VC04 cluster performed on galaxies within a clustercentric distance of $r_c = 1.5$. Galaxies with $M^0_{K_s} < -21\overset{\text{m}}{.}5$ are shown as filled blue circles and galaxies $M^0_{K_s} > -21\overset{\text{m}}{.}5$ as open circles. The RS galaxies are displayed as red circles and the RS fit is shown as black line. Right: the iso-density contour map of VC04 complete to $M^0_{Ks} = -21\overset{\text{m}}{.}5$. The galaxies are shown as black dots and the RS galaxies as yellow dots. The red and magenta circles represent the $r = 0.5$ Mpc and $r_c = 1.5$ Mpc respectively. 117

5.9 The LF of the VC04 cluster in the K_s-band using the RS method. (a): $r < 0.5\,$Mpc, $-25\overset{\text{m}}{.}0 < M_{Ks} < -21\overset{\text{m}}{.}5$. (b): $r_c < 1.5\,$Mpc, $-25\overset{\text{m}}{.}5 < M_{Ks} < -21\overset{\text{m}}{.}5$. (c): $r_c < 1.5\,$Mpc, $-25\overset{\text{m}}{.}0 < M_{Ks} < -21\overset{\text{m}}{.}5$. The best fit is shown with the red line and the gray area shows the 3σ uncertainty of the fit. . . 118

5.10 The RS of the VSCL cluster performed on galaxies within a clustercentric radii of $r_c < 1.5$ for VC02, VC04, VC08 and $r < 0.5$ for VC05, VC11a and VC11b. Galaxies with $M^0_{K_s} < -21\overset{\text{m}}{.}5$ are shown as filled blue circles and galaxies $M^0_{K_s} > -21\overset{\text{m}}{.}5$ as open circles. The RS galaxies are displayed as red circles and the RS fit is shown as black line. 121

5.11 The iso-density contour maps of the VC02, VC05, VC08 and VC11 clusters out to $r_c = 1.5\,$Mpc and $M^0_{Ks} < -21\overset{\text{m}}{.}5$. The galaxies are shown as black dots and the RS galaxies as yellow dots. The red and magenta circles represent the $r = 0.5$ Mpc and $r_c = 1.5$ Mpc respectively. 122

5.12 Top panel: the K_s-band LFs of VC05, VC11a and VC11b, using the RS method out to $r < 0.5\,$Mpc for $-25\overset{\text{m}}{.}0 < M_{Ks} < -21\overset{\text{m}}{.}5$. bottom panel: the K_s-band LFs of VC02 and VC08, using the RS method out to $r_c < 1.5\,$Mpc. VC02 for $-26\overset{\text{m}}{.}0 < M_{Ks} < -21\overset{\text{m}}{.}5$ and VC08 for $-25\overset{\text{m}}{.}0 < M_{Ks} < -21\overset{\text{m}}{.}5$. The best fit is shown with the red line and the gray area shows the 3σ uncertainty of the fit. 124

B.1.1 Top: VC02 histograms of isophotal magnitudes at $K_s = 20\overset{\text{m}}{.}0$ in J, H and K_s bands. The dashed histograms show the observed magnitudes and the hatched ones are the extinction-corrected. The dashed lines are the completeness magnitude limits in each band. Bottom: Histograms of central surface brightness of VC02 galaxies in J, H and K_s bands. The dividing values of central surface brightnesses between elliptical and spiral galaxies in each band are shown by the dashed lines. 197

B.1.2 The on-sky distribution of galaxies with $K^o_s < 15\overset{\text{m}}{.}5$ and $r > 2''$ in VC02. The IRSF galaxies are shown with filled green circles. Galaxies that have counterpart in 2MASX are encircled in blue. 198

B.1.3 Left: the velocity histogram of the VC02 cluster. Right: the distribution of the extinction-corrected K_s magnitude for identified galaxies in VC02 with $r > 2''$. The galaxies with redshift data are shown as black hatched areas. The red areas mark foreground and background galaxies (10 with $v < 17000$ km s^{-1} and 16 with $v > 21000$ km s^{-1} respectively). 198

B.1.4Left: the radial density profile, N/Mpc^2, out to $r < 2$ Mpc. The total number density of galaxies is shown in blue histogram and the completeness-limited sample ($K^0_{slim} < 15\overset{\text{m}}{.}5$) in pink. Right: iso-density map of VC02 for $r < 2$ Mpc. Galaxies are shown as black dots and the centre of cluster as red star. The red and magenta circles represent the r_{200} and r_c respectively. The three brightest galaxies are shown as red, magenta and yellow dots. . . 199
B.1.5The distribution of the extinction-corrected absolute magnitude $M^o_{K_s}$ up to $M^o_{Ks} < -21\overset{\text{m}}{.}5$ and $r_c < 1.5$ Mpc for identified galaxies in VC02. The hatched areas shows the identified Red-Sequence galaxies in VC02. 199
B.2.1Top: VC04 histograms of isophotal magnitudes at $K_s = 20\overset{\text{m}}{.}0$ in J, H and K_s bands. The dashed histograms show the observed magnitudes and the hatched ones are the extinction-corrected. The dashed lines are the completeness magnitude limits in each band. Bottom: Histograms of central surface brightness of VC04 galaxies in J, H and K_s bands. The dividing values of central surface brightnesses between elliptical and spiral galaxies in each band are shown by the dashed lines. 200
B.2.2The on-sky distribution of galaxies with $K^o_s < 15\overset{\text{m}}{.}5$ and $r > 2''$ in VC04. The IRSF galaxies are shown with filled green circles. Galaxies that have counterpart in 2MASX are encircled in blue. 201
B.2.3Left: the velocity histogram of VC04. Right: the distribution of the extinction-corrected K_s magnitude for 416 identified galaxies in VC04. The 89 galaxies with redshift data are shown as black hatched areas. The red areas mark foreground and background galaxies ($v < 16000$ km s^{-1} and $v > 20000$ km s^{-1} respectively). 201
B.2.4Left: the radial density profile, N/Mpc^2, out to $r < 2$ Mpc. The total number density of galaxies is shown in blue histogram and the completeness-limited sample ($K^0_{slim} < 15\overset{\text{m}}{.}5$) in pink. Right: iso-density map of VC04 for $r < 2$ Mpc. Galaxies are shown as black dots and the centre of cluster as red star. The red and magenta circles represent the r_{200} and r_c respectively. The three brightest galaxies are shown as red, magenta and yellow dots. . . 202
B.2.5The distribution of the extinction-corrected absolute magnitude up to $M^o_{Ks} < -21\overset{\text{m}}{.}5$ and $r_c < 1.5$ Mpc for identified galaxies in VC04. The hatched areas shows the identified Red-Sequence galaxies in VC04. 202
B.3.1Top: VC05 histograms of isophotal magnitudes at $K_s = 20\overset{\text{m}}{.}0$ in J, H and K_s bands. The dashed histograms show the observed magnitudes and the hatched ones are the extinction-corrected. The dashed lines are the completeness magnitude limits in each band. Bottom: Histograms of central surface brightness of VC05 galaxies in J, H and K_s bands. The dividing values of central surface brightnesses between elliptical and spiral galaxies in each band are shown by the dashed lines. 203
B.3.2The on-sky distribution of galaxies with $K^o_s < 15\overset{\text{m}}{.}5$ and $r > 2''$ in VC04. The IRSF galaxies are shown with filled green circles. Galaxies that have counterpart in 2MASX are encircled in blue. 204
B.3.3Left: the velocity histogram of the VC05 cluster. Right: the distribution of the extinction-corrected K_s magnitude for identified galaxies in VC05 with $r > 2''$. The galaxies with redshift data are shown as black hatched areas. The red areas mark foreground galaxies (22 with $v < 19000$ km s^{-1}). 204

B.3.4Left: the radial density profile, N/Mpc^2, out to $r < 2$ Mpc. The total number density of galaxies is shown in blue histogram and the completeness-limited sample ($K^0_{slim} < 15\overset{\text{m}}{.}5$) in pink. Right: iso-density map of VC05 for $r < 2$ Mpc. Galaxies are shown as black dots and the centre of cluster as red star. The red circle represents the r_c. The three brightest galaxies are shown as red, magenta and yellow dots. 205
B.3.5The radial density profile, N/Mpc^2 (left) and iso-density contour map of VC05 out to $r < 2$ Mpc (right), using the adjusted centre. 205
B.3.6The distribution of the extinction-corrected absolute magnitude up to $M^o_{Ks} < -21\overset{\text{m}}{.}5$ and $r_c < 0.5$ Mpc (around the adjusted centre) for identified galaxies in VC05. The hatched areas shows the identified Red-Sequence galaxies in VC05. 206
B.4.1Top: VC08 histograms of isophotal magnitudes at $K_s = 20\overset{\text{m}}{.}0$ in J, H and K_s bands. The dashed histograms show the observed magnitudes and the hatched ones are the extinction-corrected. The dashed lines are the completeness magnitude limits in each band. Bottom: Histograms of central surface brightness of VC08 galaxies in J, H and K_s bands. The dividing values of central surface brightnesses between elliptical and spiral galaxies in each band are shown by the dashed lines. 207
B.4.2The on-sky distribution of galaxies with $K^o_s < 15\overset{\text{m}}{.}5$ and $r > 2''$ in VC04. The IRSF galaxies are shown with filled green circles. Galaxies that have counterpart in 2MASX are encircled in blue. 208
B.4.3Left: the velocity histogram of the VC08 cluster. Right: the distribution of the extinction-corrected K_s magnitude for identified galaxies in VC08 with $r > 2''$. The galaxies with redshift data are shown as black hatched areas. The red areas mark background galaxies (2 with $v > 19000$ km s^{-1}). 208
B.4.4Left: the radial density profile, N/Mpc^2, out to $r < 2$ Mpc. The total number density of galaxies is shown in blue histogram and the completeness-limited sample ($K^0_{slim} < 15\overset{\text{m}}{.}1$) in pink. Right: iso-density map of VC08 for $r < 2$ Mpc. Galaxies are shown as black dots and the centre of cluster as red star. The red and magenta circles represent the r_{200} and r_c respectively. The three brightest galaxies are shown as red, magenta and yellow dots. . . 209
B.4.5The distribution of the extinction-corrected absolute magnitude up to $M^o_{Ks} < -21\overset{\text{m}}{.}5$ and $r_c < 1.5$ Mpc for identified galaxies in VC08. The hatched areas shows the identified Red-Sequence galaxies in VC08. 209
B.5.1Top: VC10 histograms of isophotal magnitudes at $K_s = 20\overset{\text{m}}{.}0$ in J, H and K_s bands. The dashed histograms show the observed magnitudes and the hatched ones are the extinction-corrected. The dashed lines are the completeness magnitude limits in each band. Bottom: Histograms of central surface brightness of VC10 galaxies in J, H and K_s bands. The dividing values of central surface brightnesses between elliptical and spiral galaxies in each band are shown by the dashed lines. 210
B.5.2The on-sky distribution of galaxies with $K^o_s < 15\overset{\text{m}}{.}5$ and $r > 2''$ in VC04. The IRSF galaxies are shown with filled green circles. Galaxies that have counterpart in 2MASX are encircled in blue. 211

B.5.3Left: the velocity histogram of the VC10 cluster. Right: the distribution of the extinction-corrected K_s magnitude for identified galaxies in VC10 with $r > 2''$. The galaxies with redshift data are shown as black hatched areas. The red areas mark background galaxies (2 with $v > 20000$ km s^{-1}). 211
B.5.4Left: the radial density profile, N/Mpc^2, out to $r < 2$ Mpc. The total number density of galaxies is shown in blue histogram and the completeness-limited sample ($K^0_{slim} < 15\overset{\text{m}}{.}5$) in pink. Right: iso-density map of VC10 for $r < 2$ Mpc. Galaxies are shown as black dots and the centre of cluster as red star. The red and magenta circles represent the r_{200} and r_c respectively. The three brightest galaxies are shown as red, magenta and yellow dots. . . 212
B.6.1Top: VC11 histograms of isophotal magnitudes at $K_s = 20\overset{\text{m}}{.}0$ in J, H and K_s bands. The dashed histograms show the observed magnitudes and the hatched ones are the extinction-corrected. The dashed lines are the completeness magnitude limits in each band. Bottom: Histograms of central surface brightness of VC11 galaxies in J, H and K_s bands. The dividing values of central surface brightnesses between elliptical and spiral galaxies in each band are shown by the dashed lines. 213
B.6.2The on-sky distribution of galaxies with $K^o_s < 15\overset{\text{m}}{.}5$ and $r > 2''$ in VC04. The IRSF galaxies are shown with filled green circles. Galaxies that have counterpart in 2MASX are encircled in blue. 214
B.6.3Left: the velocity histogram of the VC11. Right: the distribution of the extinction-corrected K_s magnitude for identified galaxies in VC11 with $r > 2''$. The galaxies with redshift data are shown as black hatched areas. The red areas mark foreground and background galaxies (1 with $v < 16000$ km s^{-1} and 1 with $v > 20000$ km s^{-1} respectively). 214
B.6.4Left: the radial density profile, N/Mpc^2, out to $r < 2$ Mpc. The total number density of galaxies is shown in blue histogram and the completeness-limited sample ($K^0_{slim} < 15\overset{\text{m}}{.}5$) in pink. Right: iso-density map of VC11 for $r < 2$ Mpc. Galaxies are shown as black dots and the centre of cluster as red star. The red and magenta circles represent the r_{200} and r_c respectively. The three brightest galaxies are shown as red, magenta and yellow dots. . . 215
B.6.5The radial density profile, N/Mpc^2 (left) and iso-density contour map of VC11a out to $r < 2$ Mpc (right), using the centre of left clump. 215
B.6.6The radial density profile, N/Mpc^2 (left) and iso-density contour map of VC11b out to $r < 2$ Mpc (right), using the centre of right clump. 216
B.6.7The distribution of the extinction-corrected absolute magnitude up to $M^o_{Ks} < -21\overset{\text{m}}{.}5$ and $r_c < 0.5$ Mpc (around the adjusted centres) for identified galaxies in VC11a and VC11b (left and right panel respectively). The hatched areas shows the identified Red-Sequence galaxies in VC11a. 216

List of Tables

1.1 2MASS stellar density metric . . . 9
1.2 Abell richness classification. . . . 13
1.3 Properties of the various morphological classification schemes of clusters. The table is adapted from Abell (1975) and Bahcall (1977). . . . 15

2.1 Properties of the six galaxy clusters within the VSCL selected for a NIR study (based on the Kraan-Korteweg et al. (2017) redshift catalogue). . . . 27
2.2 Comparison between the IRSF and 2MASS surveys characteristics. . . . 28
2.3 IRSF observations and observers. Observers: Ahmed Elagali (AE), Khaled Said (KS), Narges Hatamkhani (NH) . . . 30
2.4 Mean magnitude zero-point ($\langle ZP \rangle$) and average seeing with their respective standard deviations (σ) for all 263 images. . . . 37
2.5 Source Extractor parameters . . . 44

3.1 The VC08 IRSF pipeline output sample catalogue. The dashes indicate that the pipeline could not fit a total magnitude. . . . 54
3.2 The total number of identified galaxies (N) and the number of their 2MASX counterparts (N_{2MASX}) in each cluster. . . . 56
3.3 $\langle \Delta RA \rangle$ and $\langle \Delta Dec \rangle$ with their respective standard deviation (σ) for the matched pairs in NWS and the VSCL clusters. . . . 56
3.4 The values of the mean magnitude difference and the standard deviation of one clusters in this survey (VC04 with 249 matched pairs) and the NWS (1061 matched pair) (Riad, 2010). . . . 57
3.5 $\langle \Delta RA \rangle$ and $\langle \Delta Dec \rangle$ with their respective standard deviations (σ) for the matched pairs in VC02, VC04, VC05, VC08, VC10, VC11 and NWS respectively. . . . 60
3.6 Comparison of the 2MASX and IRSF/SIRIUS 7″ and K_{s20} fiducial isophotal magnitudes for 82 matched pairs in VC04. . . . 60
3.7 Comparison of the IRSF/SIRIUS K_{s20} fiducial isophotal magnitude offsets with other surveys in J, H and K_s bands. . . . 63
3.8 The mean, minimum and maximum values of A_J, A_H and A_{K_s} for the galaxies within the VSCL clusters. . . . 65
3.9 The mean values of Δm_{iso} for early-type (E/S0) galaxies over the regions of the six VSCL clusters. . . . 69
3.10 Comparison of the completeness limits of VSCL clusters to other NIR surveys performed by IRSF/SIRIUS camera. . . . 75
3.11 Comparing the completeness limits of the VSCL clusters using two methods of derivation. . . . 75

4.1 Properties of four comparison clusters, Coma, Norma, 3C129 and Virgo. All the references are given in the text. $\langle A_{Ks} \rangle$ indicates the mean foreground extinction in each cluster. 80
4.2 Photometric parameters of the VC04 galaxies. 85
4.3 Parameters of the six VSCL clusters. 91

5.1 Table of NIR luminosity functions parameters of the Coma and Norma clusters. The Norma cluster has two entries in the first and second row of the table which represent the parameters of the Norma LF with and without the first bin (containing the central cD galaxies) respectively. . . . 106
5.2 The total and spectroscopic number counts in K_s-band magnitude intervals in the Norma cluster out to $r_c < 1.5\,\mathrm{Mpc}$. $N_p(m)$ is the number of galaxies in a given (magnitude) interval. $N_s(m)$ is the total number of galaxies with spectroscopic data, in a given range of apparent magnitude. $N_m(m)$ is the number of cluster members as a function of magnitude. $f(m)$ is the fraction of galaxies in each magnitude bin that satisfies the membership criterion (Skelton et al., 2009). 109
5.3 The K_s-band luminosity function parameters of Norma, Coma and Virgo. . 116
5.4 The K_s-band luminosity function parameters of VC04. 117
5.5 Table of previous NIR luminosity functions parameters of clusters. 119
5.6 RS properties of the VSCL clusters. RS fit relation is defined as $(J-K)^o = (\alpha)K^o + \beta$. N_{RS} is the number of identified RS galaxies. 122
5.7 The K_s-band luminosity function parameters of the VC02, VC04, VC05, VC08 and VC11 clusters, using the RS method. 123
5.8 The K_s-band Luminosity Function parameters of VC02, VC05, VC08, VC11a and VC11b for a fixed $M^* = -24\overset{\mathrm{m}}{.}70$, using the RS method. 123

A.0.1VC02 catalogue of galaxies 161
A.0.2VC04 catalogue of galaxies 167
A.0.3VC05 catalogue of galaxies 175
A.0.4VC08 catalogue of galaxies 181
A.0.5VC10 catalogue of galaxies 186
A.0.6VC11 catalogue of galaxies 191

B.1.1Photometric parameters of the VC02 galaxies. 198
B.2.1Photometric parameters of the VC04 galaxies. 200
B.3.1Photometric parameters of the VC05 galaxies. 203
B.4.1Photometric parameters of the VC08 galaxies. 207
B.5.1Photometric parameters of the VC10 galaxies. 210
B.6.1Photometric parameters of the VC11 galaxies. 213

همتم بدرقه راه کن ای طایر قدس

که دراز است ره مقصد و من نو سفرم

حافظ

Chapter 1

Introduction

The largest overdensities in the universe, superclusters and clusters of galaxies, are distributed along filaments and walls with voids in between (Shapley, 1930; Joeveer and Einasto, 1978; Davis et al., 1982; de Lapparent et al., 1986). This structure of the universe is called the 'cosmic web'. The inhomogeneous distribution of matter introduces an asymmetric gravitational force on the galaxies and gives rise to deviations from the smooth motions expected from the expansion of the universe (Hubble flow), known as 'peculiar motions'. The observed dipole in the Cosmic Microwave Background (CMB) is the result of the peculiar motion of the Local Group (LG) (e.g. Fixsen et al., 1996). Despite long-term efforts by various authors (e.g. Erdoğdu et al., 2006; Lavaux et al., 2010; Hoffman et al., 2015; Springob et al., 2016), the direction and amplitude of the LG peculiar velocity and derived mass density distributions still show discrepancies. The 6dF peculiar velocity survey detected positive radial peculiar velocities based on near 9000 galaxies in the southern hemisphere, suggestive of large mass overdensities at distances beyond a volume $cz < 16000\,\mathrm{km\,s^{-1}}$, directed toward the Vela constellation, close to or in the Zone of Avoidance (ZoA) (Springob et al., 2014, 2016; Staveley-Smith et al., 2016). Therefore, mapping the large-scale structure behind the Milky Way could play an important role in reconciling the discrepancies in the local bulk flow.

The Vela supercluster (VSCL), located at a distance of $\sim 260\,h_{70}^{-1}$ Mpc in the ZoA was recently discovered by Kraan-Korteweg et al. (2017) as a result of a long-term program to map the large-scale structure behind the Milky Way. The high stellar density and the extinction caused by the interstellar dust of the Milky Way affects the visibility of the VSCL (e.g. Kraan-Korteweg and Lahav, 2000). Compared to the shorter optical wavelength, observing at the Near-InfraRed (NIR) is less affected by dust obscuration and offers a better tool to probe the ZoA and large-scale structures like the VSCL. We have undertaken a deep NIR (JHK_s) imaging campaign of prospective clusters identified in the VSCL to determine the structures, density profiles and luminosity functions of these clusters. This will allow a better understanding of the morphology, richness and mass of this partially obscured supercluster which, despite its redshift distance of $cz \sim 18000\,\mathrm{km\,s^{-1}}$, may add an appreciable contribution to the residual bulk flow generated at distances beyond $\sim 16000\,\mathrm{km\,s^{-1}}$.

To set the background for such an analysis, which forms the bulk of this thesis, this introductory chapter presents an overview of the theoretical background of superclusters, clusters of galaxies and the ZoA, and discusses what is known so far about the VSCL and its constituent galaxy clusters. In Sect. 1.1 superclusters and their properties are described. Dynamics of the nearby universe are presented in Sect. 1.3. In Sect. 1.4 the

ZoA, the VSCL and its properties are explained. Section 1.5 describes galaxy clusters and their properties. Finally, in Sect. 1.6 motivations to perform a NIR study on the clusters in the VSCL are presented.

1.1 Cosmic web

According to our latest understandings, the universe can be well-described by a physical model called ΛCDM (see e.g. Carroll, 2001; Peebles and Ratra, 2003). In the ΛCDM model, which is also called the standard model of Big Bang cosmology, the universe can be described by; first, Λ which represents the dark energy, second, the proposed Cold Dark Matter (CDM) and third, the baryonic matter. The ΛCDM model provides a good description of the observed cosmic structure. The large-scale structure of the universe can be classified into four components; voids, sheets, filaments and knots. This structure is called the cosmic web (Bond et al., 1996), since it resembles a web-like network. In the ΛCDM the cosmic web have originated from the small-density fluctuations in the early universe and evolved by merging and accumulation of smaller-scale structures into larger structures under the current ΛCDM cosmological model (White and Rees, 1978; Einasto et al., 1980).

1.2 Superclusters

Superclusters are defined as collections of galaxy clusters and groups above a specified spatial overdensity (Bahcall, 1988; Einasto et al., 2011b,c). The spatial distribution of matter in the universe is not homogeneous, as extended surveys such as the Two-Degree Field Galaxy Redshift Survey (Fig. 1.1) (2dFGRS, Colless et al., 2001), the Sloan Digital Sky Survey (SDSS, York et al., 2000), the Galaxy And Mass Assembly survey (GAMA, Driver et al., 2009), the Dark Energy Survey (DES, Dark Energy Survey Collaboration et al., 2016), and the VIMOS Public Extragalactic Redshift Survey (VIPERS, Scodeggio et al., 2018) have shown. Superclusters contribute to the largest density enhancements in the cosmic web. These clusters and groups (known as knots in the cosmic web) are usually interacting and merging. Filaments connect these clusters, and voids separate them (Jõeveer et al., 1978; Einasto et al., 1980; Kofman and Shandarin, 1988). Figure 1.2 displays a snapshot of large-scale structure in the local universe as evolved from a ΛCDM cosmology. Superclusters (bright red knots) and long filaments indicate where the concentration of galaxies is high. Galactic voids (blue) are the areas with low concentration of galaxies.

The first supercluster was identified by de Vaucouleurs (1953, 1958) from the large-scale distribution of galaxies in the nearby universe. It is known as the Local supercluster with the Virgo cluster at its centre. Superclusters can range from lower-mass systems such as the Hercules supercluster (Abell, 1961) consisting of three clusters, to very large and massive systems such as the Shapley supercluster, which is a massive concentration of clusters and groups (9 Abell clusters and 2 poor clusters) spanning over 100 Mpc (Raychaudhury, 1989; Bardelli et al., 2000; Proust et al., 2006; Merluzzi et al., 2016; Haines et al., 2018). Also, our Milky Way, located at the outskirts of the Local supercluster, forms part of the entity defined as *Laniakea* which spans $\sim$ 160 Mpc across (Tully et al., 2014). At the gravitational centre of Laniakea lies a massive concentration of mass, called *The Great Attractor*. At higher redshifts Lietzen et al. (2016) discovered a massive wall-like

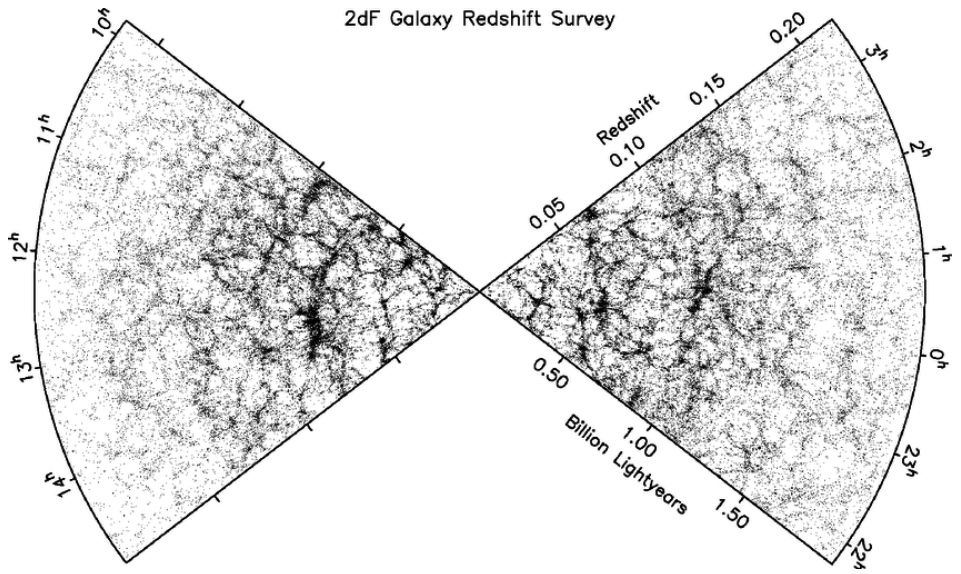

Figure 1.1: The spatial distribution of 100,000 galaxies derived from 2dF galaxy survey, revealing the large-scale structures and voids in the local universe. Image credit: M. Colless (ANU) and the 2dF Galaxy Redshift Survey (http://magnum.anu.edu.au/~TDFgg/).

structured supercluster complex in the SDSS-BSS survey at redshift 0.47 called the BOSS Great Wall (BGW), which spans $\sim$ 250 Mpc across.

While superclusters are not virialized[1] on the largest scales, they contain high-density regions at their centres consisting of very massive galaxy clusters (Jõeveer et al., 1978). These large overdensities are either in the process of collapsing or will collapse in the future (Reisenegger et al., 2000; Proust et al., 2006; Pearson et al., 2014; Gramann et al., 2015; Einasto et al., 2016). Therefore, these supercluster cores form ideal laboratories to study the effects of large scale structure on the formation, evolution and properties of the constituent galaxy clusters and groups (Plionis, 2004; Wolf et al., 2005; Haines et al., 2006; Einasto et al., 2007c; Porter et al., 2008; Fleenor and Johnston-Hollitt, 2010; Tempel et al., 2011; Einasto et al., 2011d; Merluzzi et al., 2015). In addition, superclusters at higher redshifts are used to probe both baryonic and dark matter in the universe (Génova-Santos et al., 2005; Heymans et al., 2008; Buote et al., 2009; Schirmer et al., 2011; Finney et al., 2018), and to examine cosmological models (Wray et al., 2006; Einasto et al., 2011b; Lim and Lee, 2014).

1.2.1 Supercluster detection methods

One method of identifying superclusters is by applying the friends-of-friends (FOF) algorithm, with a certain linking length that will connect nearby groups and clusters together. Various all-sky catalogues of superclusters have been compiled using the FOF algorithm (e.g. Einasto et al., 1994; Chow-Martínez et al., 2014) from the galaxy clusters information in Abell (1958) and Abell et al. (1989).

A second method to locate superclusters is called the luminosity-density field which searches for high density regions over a certain threshold in the cosmic web. This method was developed after deeper galaxy redshift surveys became available (e.g. using the 2dF-GRS by Einasto et al. (2007b), and the SDSS by Costa-Duarte et al. (2011); Luparello

[1]When a system is virialized the merging process and the collapse of matter have finished and its formation process is done.

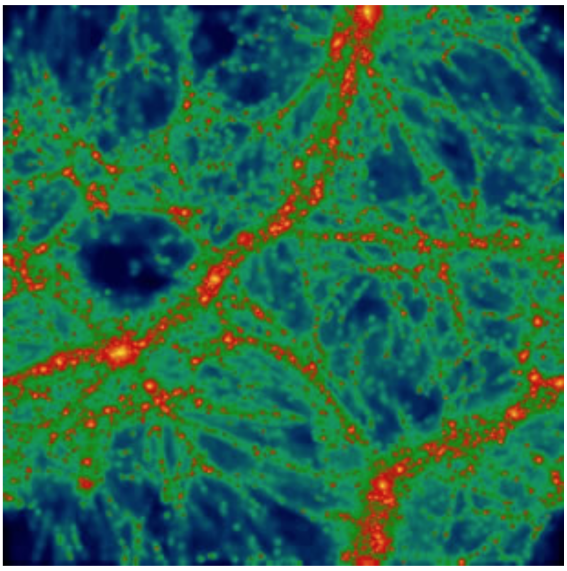

Figure 1.2: Model of large-scale structure in the local Universe assuming a ΛCDM cosmology. Superclusters (bright red knots) and long filaments with high galaxy concentration are shown in red. Galactic voids outlined by low concentration of galaxies are shown in blue. Image credit: Chris Power, Swinburne University (https://astronomy.swin.edu.au/cosmos/l/Large-scale+Structure).

et al. (2011); Liivamägi et al. (2012)). This method uses the weighted luminosity of galaxies to measure the density field on a grid of a selected distance. A detailed description of the luminosity-density field method is provided in Liivamägi et al. (2012).

1.2.2 Properties of superclusters

In this section I will summarize some of the typical properties of superclusters.

Mutiplicity

Superclusters can be divided into four richness classes using the multiplicity parameter (i.e. the number of constituent galaxy clusters); poor (< 3 clusters), medium rich ($3-9$ clusters), rich ($10-19$ clusters) and extremely rich (> 20 clusters) (Wray et al., 2006; Einasto et al., 2007a). The Virgo and Coma superclusters are examples of poor superclusters, Perseus-Pisces is a medium rich supercluster, Horologium-Reticulum and Leo-Sextans are rich superclusters and Shapley is classified as an extremely rich supercluster.

Maximal, minimal and effective diameters

The maximal diameter is the length of the diagonal of the rectangular box which circumscribes a supercluster. The minimal diameter is the shortest distance between two edges of the rectangular box; and the effective diameter is the diameter of a sphere with the same volume as the volume of a supercluster.

Luminosity and shape

The luminosity of a supercluster is directly proportional to its richness and ranges from $10^{11}\,L_\odot$ to $10^{14}\,L_\odot$. Einasto et al. (2007a) shows that the larger the size of the three

diameters, the richer the supercluster and the higher its total luminosity. However this dependence is stronger for the minimal and maximal diameters than it is for the effective diameter. This is due to the differences in shape and compactness of superclusters with varying luminosities. The minimal and maximal diameters increase faster with the luminosity of superclusters than the effective diameter. Poor superclusters are smaller in size compared to the luminous rich superclusters that have more filament-like structures (Einasto et al., 2011b,c; Costa-Duarte et al., 2011).

Morphology of superclusters

The morphology of a supercluster can reveal differences in its evolutionary processes (Aragón-Calvo et al., 2010; Einasto et al., 2011b). In-depth information of supercluster morphology can throw light on the interaction between the environment and galaxies. The morphology of superclusters can also be used to compare simulations with observations of superclusters (Kolokotronis et al., 2002; Einasto et al., 2007a) and to differentiate between plausible cosmological models (Kolokotronis et al., 2002; Costa-Duarte et al., 2011; Shim and Lee, 2013).

The Minkowski functionals and shapefinders method is used to study the general morphology of the large scale structures (Sathyaprakash et al., 1998; Basilakos, 2003; Sheth et al., 2003; Shandarin et al., 2004; Einasto et al., 2007d) and superclusters (Basilakos, 2003; Costa-Duarte et al., 2011; Einasto et al., 2011b, 2012a, 2017; Bag and Liivamägi, 2021). In this method a given surface is characterized by four Minkowski functionals ($V_0 - V_3$), the volume (V), the surface area (S), the integrated mean curvature (C) and the integrated Gaussian curvature or Euler characteristic (χ). The fourth Minkowski functional delineates the inner structure of a supercluster, the higher it is, the clumpier the morphology of a supercluster is (for a detailed description of the Minkowski functionals see Einasto et al. (2007b, 2011b) and references therein). The dimensionless shapefinders, which can be computed by implementing the first three Minkowski functionals, are used to determine the morphology of superclusters. The shapefinders, K_1, K_2 and the ratio K_1/K_2, describe the planarity, filamentarity, and the shape parameter of a supercluster respectively (for more details see Einasto et al. (2007d, 2011c)).

Applying Minkowski functionals and shapefinders method, the overall shape of superclusters can be divided into two categories: more and less elongated superclusters. More elongated superclusters are more luminous, more massive, have larger diameters and consist of a complex (filament-like) inner or fine structure (Einasto et al., 2011b), whereas less elongated superclusters tend to have a planar structure (Einasto et al., 2011b; Costa-Duarte et al., 2011). Several studies such as Kolokotronis et al. (2002); Basilakos (2003); Einasto et al. (2007a); Costa-Duarte et al. (2011); Einasto et al. (2011b); Luparello et al. (2011) have shown that more elongated superclusters are the more dominant type of supercluster.

Poor (less elongated) superclusters are reasonably symmetrical while rich (more elongated) superclusters are asymmetric and filament-like (Einasto et al., 1997). Rich superclusters possess highly-dense cores (Einasto et al., 2007c), with higher numbers of rich and X-ray clusters (Einasto et al., 2001; Luparello et al., 2011) that could be merging (Bardelli et al., 2000; Rose et al., 2002). The structure of superclusters from poorest to richest can be described with four main morphological types based on their morphological information and appearance: spiders, multispiders, filaments, and multibranching filaments (Einasto et al., 2011b). A typical poor supercluster like the Local Supercluster has a spider-like morphology: a system of multiple filaments spreading from a high-density

core (a rich cluster) (Einasto et al., 2007d). The supercluster SCl 094 (the Corona Borealis supercluster) has a multispider morphology, where lower-density filaments connect several high-density clumps. The morphology of SCl 001 corresponds to a filament with clusters located along its length. The extremely rich supercluster. SCl 061, in the Sloan Great Wall resembles a multibranching filament (Einasto et al., 2011d; Luparello et al., 2011). Einasto et al. (2014) shows that filament-like superclusters host a larger fraction of early-type galaxies in their galaxy groups and clusters than spider-like superclusters.

Superclusters are the largest mass agglomerations that have impact on the surrounding structures. In the next section, I will describe the effect of overdense regions in our local universe.

1.3 Dynamics of the local universe

The large-scale overdense regions (galaxy clusters and superclusters) in our cosmic neighbourhood (the local universe) are great gravitational attractors and perturb the local Hubble flow, causing peculiar motions. The best example for such a motion is the observed Cosmic Microwave Background (CMB) dipole. The CMB dipole is explained as the peculiar motion of the Local Group (LG) with respect to the rest frame of the total mass within our observable universe ($\sim 622\,\mathrm{km\ s^{-1}}$; Fixsen et al., 1996). The first clues of dipole anisotropy was discovered by Conklin (1969) and Henry (1971) and a more conclusive determination was made by Smoot et al. (1977). These studies have led to attempts to map the 3-D velocity field in the local universe (e.g., Aaronson et al., 1982; Lynden-Bell et al., 1988; Shaya et al., 1995; Willick et al., 1997; Springob et al., 2007; Tully et al., 2008; Courtois et al., 2012; Hoffman et al., 2017; Graziani et al., 2019). The study of the local velocity field is important for two reasons: (1) to investigate the mass distribution in our nearby universe in order to determine the source of the CMB dipole and (2) to probe the matter density fluctuations and test the accuracy of cosmological models and measure cosmological parameters.

Several studies have been carried out to determine the amplitude and direction of the LG peculiar velocity and of local bulk flows (e.g., Erdoğdu et al., 2006; Kocevski and Ebeling, 2006; Watkins et al., 2009; Lavaux et al., 2010; Bilicki et al., 2011; Branchini et al., 2012; Hoffman et al., 2015; Springob et al., 2016; Rameez et al., 2018; Lilow and Nusser, 2021). However the results of these studies are not fully consistent. Less than 80% of the velocity measured from the CMB dipole can be explained by the gravitational attraction of the nearby massive structures such as the Great Attractor and the Shapley supercluster (e.g., Lavaux et al., 2010; Colin et al., 2011; Feindt et al., 2013). Recent peculiar velocity surveys such as 6dFGS and 2MTF detected a residual bulk flow arising from the direction of the Vela constellation close to or in the ZoA at reshifts beyond $cz \sim 16000$ km s^{-1} (Springob et al., 2014, 2016; Scrimgeour et al., 2016), where several studies suggest a significant mass overdensity (Hudson et al., 2004; Feldman et al., 2010; Nusser and Davis, 2011; Carrick et al., 2015; Hoffman et al., 2015). Previous all-sky galaxy surveys either have excluded areas at $|b| < 10°$ or mapped it with low sensitivity beyond a volume $cz \sim 16000$ km s^{-1} (e.g. Hudson and Lynden-Bell, 1991; Jones et al., 2009; Huchra et al., 2012; Tully et al., 2016).

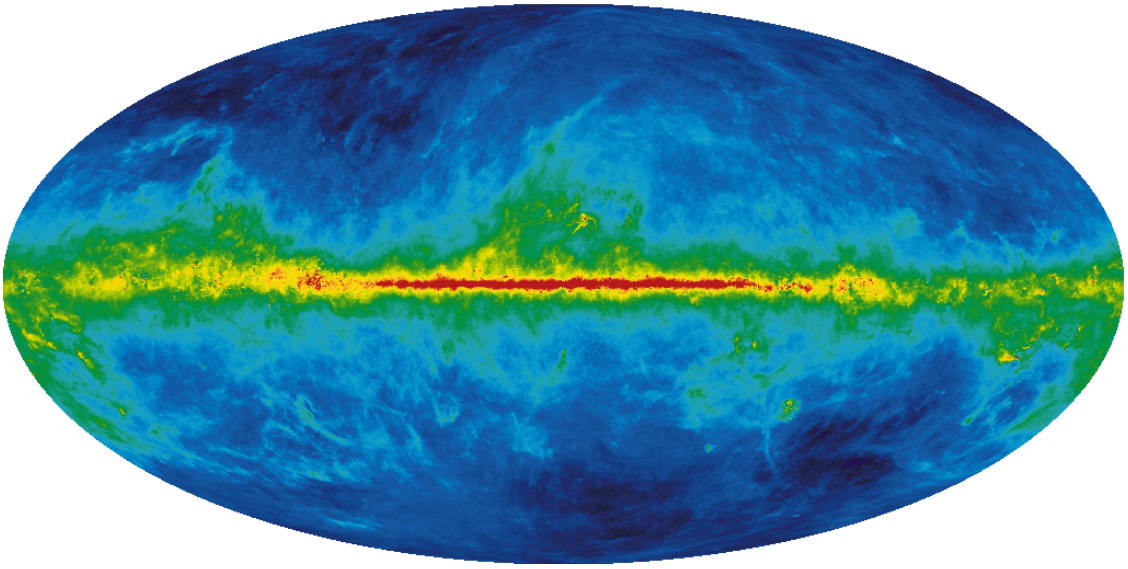

Figure 1.3: An all-sky projection of the Galactic reddening, $E(B-V)$, map. The values for $E(B-V)$ are shown on a logarithmic scale from $0\overset{m}{.}004$ to $6\overset{m}{.}3$. The yellow/red area on the map indicates the highest value of extinction in the ZoA. Image credit: LAMBDA data products.

1.4 The Vela Supercluster behind the Milky Way

1.4.1 The ZoA

The region of sky that is obscured by the Milky way is called the ZoA. Proctor (1878) called the ZoA the 'Zone of few Nebulae' when he mapped the distribution of nebulae in the General Catalogue of Nebulae (Herschel, 1864). The ZoA obscuration is due to the thick layers of dust and high stellar density towards the Galactic Plane (GP) which makes the identification of extragalactic objects increasingly difficult at low Galactic latitudes (Kraan-Korteweg and Lahav, 2000). Shapley (1961) was the first to define the ZoA quantitatively as the region with 'the isopleth of five galaxies or less per square degree from the Lick and Harvard surveys'. Areas further away from the GP have a mean of 54 galaxies per square degree (Shane and Wirtanen, 1967).

Galactic Extinction

The light from the Galactic objects in the ZoA is strongly absorbed and scattered by the dust in the Milky Way making them appear redder than they really are. The Galactic interstellar extinction depends on the wavelength of the observation and the relative size of the dust grains. Extinction is more prominent towards shorter wavelengths. For instance, the extinction (in term of magnitude) in the Near-Infrared (NIR) J (1.26 μm), H (1.63 μm) and K_s (2.14 μm) bands (A_J, A_H and A_{Ks}) is 21%, 13% and 9% of the extinction in the B (0.44 μm) band (A_B) (Cardelli et al., 1989). The general extinction law to deredden IR-UV spectrophotometric data is given by:

$$\frac{A_V}{E(B-V)} = R_V, \tag{1.1}$$

where A_V is the extinction in optical V band and $E(B-V)$ is the colour-reddening.

Figure 1.3 shows the map of Galactic reddening, $E(B-V)$, in magnitudes, as derived from dust maps in Schlegel et al. (1998). This image is taken from the Legacy Archive

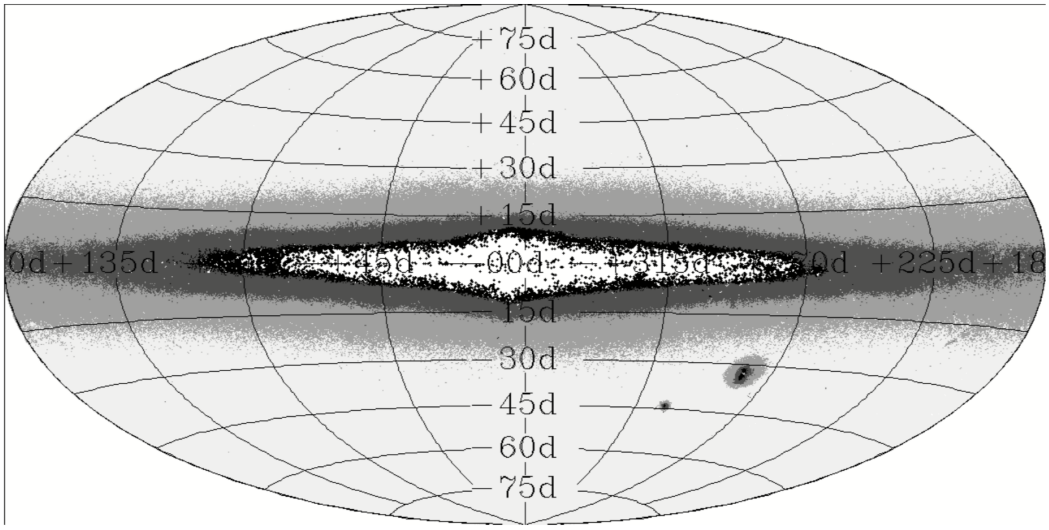

Figure 1.4: Aitoff projection of the 2MASS PSC in Galactic coordinates. The map is colour-coded based on the stellar number density in the foreground. Image credit: https://old.ipac.caltech.edu/2mass/releases/allsky/doc/sec4_5c.html

Table 1.1: 2MASS stellar density metric

$\log(N_{(K_s<14)}/\deg^2)$	$\lvert b\rvert$	colour code
$0.0 - 3.2$	$\sim 25° - 90°$	light gray
$3.2 - 3.6$	$\sim 10° - 25°$	gray
$3.6 - 4.0$	$\sim 5° - 10°$	dark gray
$4.0 - 4.5$	$\sim 0° - 5°$	black
> 4.5	$\sim 0° - 5°$	white

for Microwave Background Data Analysis (LAMBDA) data products[2]. The values for $E(B-V)$ in Fig. 1.3 on a logarithmic scale are from $0\overset{m}{.}004$ to $6\overset{m}{.}3$. The yellow/red area on the map indicates the highest value of extinction in the ZoA. The VSCL lies where the shown colour of reddening in Fig. 1.3 varies from green to red (see Fig. 1.5). Therefore the extinction effect can not be neglected even in K_s band.

Stellar Density

High stellar density is another source of confusion that makes detecting galaxies difficult in the ZoA. The sky background noise also increases as the stellar density rises, therefore, identifying faint galaxies and performing precise photometry in the ZoA is not straightforward.

Figure 1.4 displays the The Two Micron All-Sky Survey (2MASS) stellar density metric, $\log(N_{(K_s<14)}/\deg^2)$, as projected on Galactic coordinates. $\log(N_{(K_s<14)}/\deg^2)$ is the number of stars with $K_s < 14\overset{m}{.}0$ from the 2MASS Point Source Catalog (2MPSC; Skrutskie et al., 2006). The key to the grey-scale plot is shown in Table 1.1. The map and table are taken from the 2MASS Extended Source Catalog, "Algorithms, Analysis and

[2]https://lambda.gsfc.nasa.gov/product/foreground/f_images.cfm

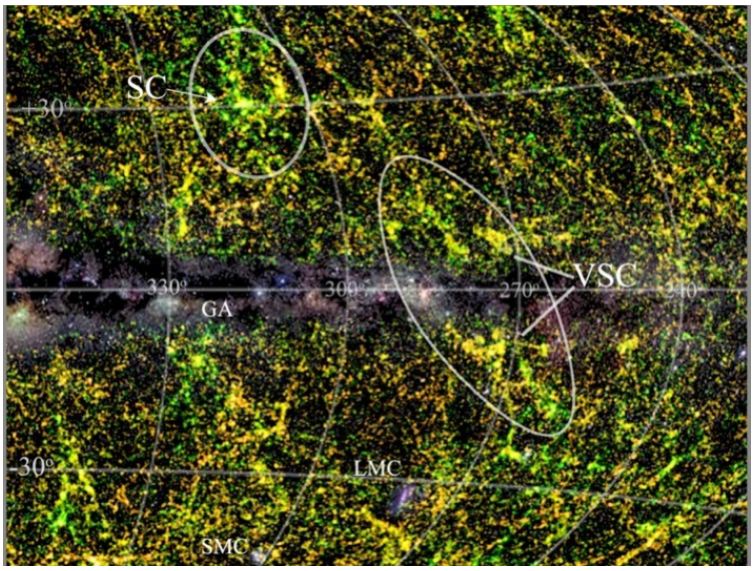

Figure 1.5: The location of the Vela and Shapley superclusters in Galactic coordinates. The figure is made based on the Photometric Redshift data from Bilicki et al. (2014) and the All-Sky Panorama image of the Milky Way (Mellinger, 2009). The yellow and green dots are close to the Vela supercluster distance and the orange ones are more distant. Image credit: Tom Jarrett (UCT).

Results web-page[3]", (2MASX; Jarrett et al., 2000b). Both Fig. 1.4 and Table 1.1 indicate high stellar density towards the GP and the Galactic bulge. The VSCL lies where the the stellar density metric ($\log(N_{(K_s<14)}/\mathrm{deg}^2)$ is shown with dark gray, black and white in Fig. 1.4 (see Fig. 1.5) and therefore, high stellar density needs to be taken into account when deriving the photometry of objects.

1.4.2 Discovery of the Vela Supercluster

A prolonged program by Kraan-Korteweg et al. (2017), designed to map the large-scale structure behind the ZoA, led to the discovery of an extended supercluster centred on the Vela region ($\ell = 272.^{\circ}5 \pm 20^{\circ}, b = 0^{\circ} \pm 10^{\circ}$). The VSCL location on the sky is shown in Fig. 1.5.

From redshift surveys of optical (Kraan-Korteweg and Lahav, 2000; Kraan-Korteweg, 2000a) and near-infrared (2MASS, Jarrett et al., 2000b) galaxies in the ZoA region around Vela ($245^{\circ} \lesssim \ell \lesssim 295^{\circ}$ and $|b| \lesssim 10^{\circ}$), over 4000 new redshifts were obtained mainly using AAOmega+2dF on the 4-m Australian Telescope in addition to the 11-m Southern African Large Telescope (SALT), which were primarily used to observe the dense cores of potential galaxy clusters in the VSCL (Kraan-Korteweg et al., 2015, 2017). The distribution of the redshifts is shown in Fig. 2 of Kraan-Korteweg et al. (2017). The peak of the redshift histogram is centred at $17000 - 19000\,\mathrm{km\,s^{-1}}$, its full extent ranging from $15000 - 23000$ km s^{-1}. The extended redshift range is consistent with the definition of a typical supercluster (Einasto et al., 2014). Galaxies with redshifts within the VSCL range are distributed both above and below the GP, implying continuity of the Vela overdensity across the GP. As such this overdensity extends over at least $25^{\circ} \times 20^{\circ}$ on the sky respectively $\sim 115 \times 90\,h_{70}^{-1}$ Mpc at the distance of the VSCL. The inner part of the VSCL is fully obscured by the thick dust layers close to the GP, given that the redshift

[3]https://old.ipac.caltech.edu/2mass/releases/allsky/doc/sec4_5c.html

sample is highly incomplete in areas of $|b| \lesssim 5°$.

Through an independent assessment of mass overdensities and reconstruction of the velocity field in the Vela region, Sorce et al. (2017) indicated the core of the VSCL deep in the ZOA. More recently Courtois et al. (2019) analysed the VSCL theoretically based on the peculiar velocities in this region using the *CosmicFlows* − 3 catalogue[4] (Tully et al., 2016) and compared it with the redshift study in Kraan-Korteweg et al. (2017). Their result indicates a mass concentration located at $(\ell, b, cz) = (269°, -9°, 19900\,\mathrm{km\,s^{-1}})$. This centre is only $\sim 10°$ away from what is found by Kraan-Korteweg et al. (2017) and the redshift is in good agreement taking into account the second higher-redshift wall of the VSCL.

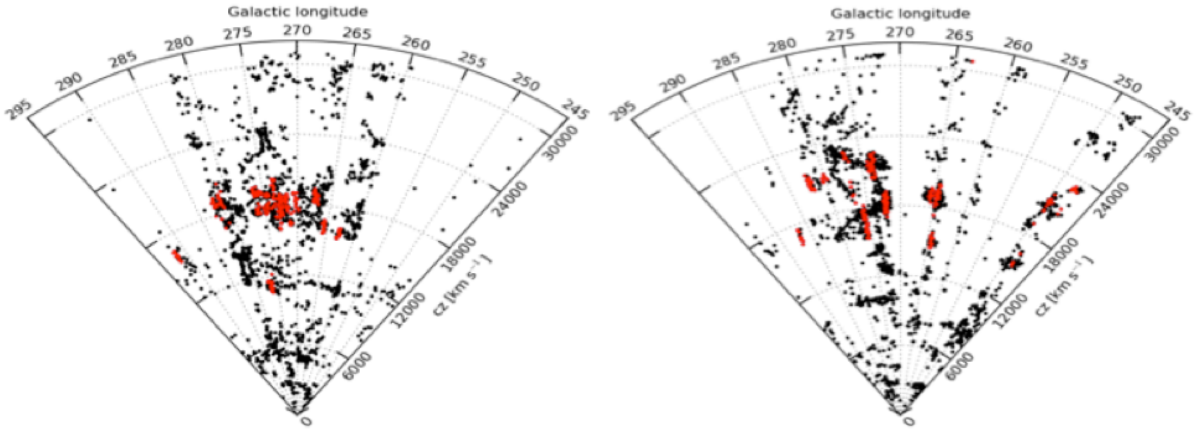

Figure 1.6: Wedge diagrams of the Vela overdensity out to $cz \lesssim 32000$ km s^{-1}, above the GP, $0° < b < +10°$ (left) and below the GP, $-10° < b < 0°$ (right). The main wall can be traced above and below the GP at ~ 18000 km s^{-1} while the second wall at ~ 22000 km s^{-1}, only below the GP seems to be converging the main wall. The red dots depict the galaxies in the potential clusters.

1.4.3 Morphology of the Vela Supercluster

Analysis of the spectroscopic data indicates that the VSCL has an elongated and wall-like structure which is a typical morphology of a rich supercluster (Einasto et al., 2011b). Wedge diagrams of the Vela overdensity above and below the GP indicate that the VSCL consists of two walls (Fig. 1.6). The first wall is at $\sim 18000\,\mathrm{km\,s^{-1}}$, both below and above the GP, while the second one is at $\sim 22000\,\mathrm{km\,s^{-1}}$, only below the GP, and seems to be joining the main wall. The study of the structure of the VSCL at lower Galactic latitude, based on photometric redshift data from Bilicki et al. (2014), suggests that the two walls below the GP merge into one structure above the GP. The merger point is located behind the thickest dust layers of the GP. This multi-branching structure of filaments and walls is another indication consistent with that of a massive and rich supercluster (Einasto et al., 2011b).

Blind H I surveys are the only tools that can explore the large-scale structure behind the deepest parts of the ZoA through H I emission of galaxies. Therefore, H I observations have been planned and started with the MeerKAT telescope (Jonas and MeerKAT Team, 2016). The pilot project with MeerKAT-16 in 2018 mapped the main VSCL wall, part of which lies one the clusters that has been also observed in NIR (this project), VC04. More

[4]The *CosmicFlows* − 3 catalogue is currently the largest compilation of accurate galaxy distances independent of redshift.

recent surveys such as the Galactic Plane Survey (GPS using MeerKAT-64, 2018-2019) and other MeerKAT-64 observations in 2021 (PI, S. Rajohnson) have been started to unveil the hidden core of the VSCL. These projects will cover $\sim 20°$-wide strip across the ZoA for $|b| \lesssim 7°$.

1.4.4 The Vela supercluster and bulk flows

An assessment of the galaxy counts in a limited Vela survey region where 2MASX is complete ($260° < \ell < 285°$ and $6° < |b| < 10°$), performed by Kraan-Korteweg et al. (2017) in a redshift shell centred at the mean distance of the VSCL, revealed a significant overdensity in counts compared to the 2MASX galaxy sample. The current Vela dataset is too sparse to yield a precise quantification of the VSCL contribution to the LG peculiar velocity. However, a preliminary analysis based on linear perturbation theory gives $v_{LG} \simeq 50\,\mathrm{km\,s^{-1}}$ (Kraan-Korteweg et al., 2017), while the contribution of the Shapley supercluster (SSC) is estimated to be $v_{LG} \simeq 55\,\mathrm{km\,s^{-1}}$ (Loeb and Narayan, 2008) or $v_{LG} \simeq 90\,\mathrm{km\,s^{-1}}$ (Lavaux and Hudson, 2011), depending on the method of its derivation. It shows that the impact of the VSCL on the local bulk flow is likely to be comparable to that of the SSC, which would reduce the discrepancies in the derivation of the LG peculiar motion relative to the CMB.

1.4.5 Galaxy clusters within the VSCL

One of the properties of the massive superclusters is the large number of their galaxy clusters. In spite of the sparse sampling of the redshift data, Kraan-Korteweg et al. (2017) identified 20 potential galaxy clusters with velocity dispersions $\sigma_v > 400\,\mathrm{km\,s^{-1}}$ in the Vela overdensity, in addition to the two CIZA X-ray clusters at the outer edges of the Vela survey (CIZA J0812.5-5714 and CIZA J0820.9-5704; Kocevski and Ebeling, 2006). Two of the newly identified potential clusters have X-ray counterparts in ROSAT, that were not uncovered in CIZA (the ROSAT cluster survey in the ZoA Ebeling et al., 2005) (see Kraan-Korteweg et al., 2017). Together with the CIZA clusters, this number would classify the VSCL as a rich supercluster (Einasto et al., 2007a).

It is therefore our goal to get a better understanding of the structure and richness of the galaxy clusters in the VSCL, to provide a better insight into the supercluster as a whole, and potentially about its influence on the observed residual bulk flow.

1.5 Galaxy clusters

The first systematic catalogue of 2712 galaxy clusters was presented by Abell (1958) based on optical searches of photographic plates. Abell et al. (1989) extended the Abell catalogue to the southern sky leading a total number of 4073 clusters.

1.5.1 Properties of Galaxy Clusters

Richness

The richness of a cluster is a statistical measure of the population or the number of galaxies belonging to that cluster (i.e. cluster members), which has been proven difficult to determine rigorously due to the presence of background galaxies. Abell (1958) classified

galaxy clusters into six 'richness groups', where richness, N_R is determined as the number of galaxies in the magnitude range of m_3 and $m_3 + 2$ that lie within one Abell radius. The Abell radius is a measure of the radius of a galaxy cluster and is given by:

$$R_A = 1.7/z \quad \text{arcmin} \tag{1.2}$$

where z is the redshift of the cluster (Bahcall, 1977). m_3 is the magnitude of the third brightest galaxy in the cluster. The Abell richness groups (R) are shown in Table 1.2.

Table 1.2: Abell richness classification.

R	0	1	2	3	4	5
N_R	30-49	50-79	80-129	130-199	200-299	≥ 300

The richness and mass of a cluster are correlated (Carlberg et al., 1996). The first attempts to describe the mass-richness calibration quantitatively, was performed by Koester et al. (2007); Rozo et al. (2008) and references therein, in their work on maxBCG catalogue. However this quantification will not be very accurate as long as the richnesses have not been fully calibrated.

The number of red galaxies within r_{200} of a cluster (n_{200}) is a more reliable proxy for mass with a known and small scatter up to $z = 0.55$ when the passive evolution of red galaxies are accounted for (Andreon, 2016, and references therein). r_{200} is a radius at which the average interior density of the cluster is 200 times the critical density of the universe. r_{200} contains the major fraction of the virialized mass of the cluster. It is generally considered as a reliable proxy for the virial radius. Following Carlberg et al. (1997), r_{200} is derived using:

$$r_{200} = 2.47 \frac{\sigma_v}{1000\,\mathrm{km\,s^{-1}}} \frac{1}{\sqrt{\Omega_\Lambda + \Omega_0(1+z)^3}} h_{70}^{-1}\,\mathrm{Mpc}, \tag{1.3}$$

where σ_v is the velocity dispersion of the cluster and z is the redshift of the cluster.

An insignificant scatter (0.02 dex) between an accurately measured number of red galaxies in a cluster and its mass has been found in the relation (Andreon, 2016):

$$\log M_{200} = 14.86 \pm 0.03 + (1.30 \pm 0.10)(\log n_{200} - 2.0), \tag{1.4}$$

where $n_{200} = n(< r_{200})$. This richness-based mass estimate is independent of dynamical or hydrostatic equilibrium state of the cluster.

Velocity Dispersion

The velocity dispersion of a galaxy cluster is the statistical dispersion of radial velocities about the mean velocity of the member galaxies of that cluster. To precisely estimate the velocity dispersion in a cluster, some corrections must be taken into account, such as foreground and background contamination, the presence of substructure in the cluster and the intrinsic velocities of the galaxies.

Rich clusters typically have a radial velocity dispersion (line-of-sight) range of $\sigma_r \sim 400 - 1400\,\mathrm{km\,s^{-1}}$ (Struble and Rood, 1991), e.g. the rich Coma cluster at heliocentric velocity of $v_{hel} = 6942\,\mathrm{km\,s^{-1}}$ has a velocity dispersion of $\sigma = 1034\,\mathrm{km\,s^{-1}}$ (Wegner et al., 1999).

Virial Mass

The virial theorem applies to systems that are self-gravitating and contain bodies of equal masses. Assuming that a cluster is a spherical, isolated and non-rotating system, the virial mass of a cluster is obtained as (e.g. Limber and Mathews 1960; Heisler et al. 1985; Merritt 1988):

$$M_V = \frac{3\pi}{G}\sigma_P^2 R_{PH}, \tag{1.5}$$

where σ_P is the projected (line-of-sight) velocity dispersion and R_{PH} is the projected harmonic mean radius given by

$$\sigma_P = \sqrt{\frac{\sum_i v_{rf,i}^2}{N-1}}, \tag{1.6}$$

$$R_{PH} = \frac{N(N-1)}{2\sum_{i>j} R_{ij}^{-1}}, \tag{1.7}$$

where N denotes the number of galaxies, v_{rf} the rest-frame line-of-sight velocity relative to the center of the cluster, and R_{ij} the projected separation between galaxy pairs.

However, a caveat to using this method is that it can lead to a large estimate of the dark matter content. If subclustering is not correctly taken into account, it also introduces uncertainties into the determination of the cluster mass.

Structure & Morphology

In the ΛCDM model of cosmology, galaxy clusters are formed in a hierarchical manner via accretion of matter from their nearby large-scale structure or merging with smaller-scale structures (Dressler and Shectman, 1988; Colberg et al., 1999; Moore et al., 1999b; Evrard et al., 2002; Ouchi et al., 2005; Springel et al., 2005; Muldrew et al., 2015). Optical and X-ray data have shown that the presence of substructure in clusters is a sign of either starting the process of dynamical relaxation in them or infalling additional clumps into already virialized clusters (Mohr et al., 1996; Girardi et al., 1997; Jones and Forman, 1999; Schuecker et al., 2001; Burgett et al., 2004).

Analysing the existence of structures in galaxy clusters either through dynamical analyses (e.g. Solanes et al., 1999; Oegerle and Hill, 2001; Aguerri and Sánchez-Janssen, 2010; Einasto et al., 2012b; Lourenço et al., 2020; Healy et al., 2021c), lensing analysis (e.g. Dahle et al., 2002; Smith et al., 2005; Martinet et al., 2016), X-ray observations (e.g. Mohr et al., 1995; Schuecker et al., 2001; Jeltema et al., 2005; Santos et al., 2008; Böhringer et al., 2010; Chon et al., 2012; Mann and Ebeling, 2012) or optical observations (e.g. Flin and Krywult, 2006; Ramella et al., 2007; Einasto et al., 2012b; Foëx et al., 2013), have revealed the presence of substructure in a high fraction of clusters (30% - 70%). This also applies to clusters at low redshifts which indicates that many clusters still continue to form or significantly reshape and have not yet reached dynamical equilibrium.

Galaxy clusters can be roughly characterized in a one-dimensional sequence that runs from regular to irregular clusters (Abell, 1965, 1975). The properties of different morphological classes are summarized in Table 1.3, which is adapted from Abell (1975) and Bahcall (1977).

As shown in Table 1.3, regular clusters have high central galaxy densities and are symmetric in shape, whereas irregular clusters are not highly concentrated or symmetric and often show substructures. This suggests that regular clusters are dynamically more

Table 1.3: Properties of the various morphological classification schemes of clusters. The table is adapted from Abell (1975) and Bahcall (1977).

Property	Regular	Intermediate	Irregular
Zwicky[1] Type	Compact	Medium-Compact	Open
Bautz-Morgan[2] Type	I,I-II,II	II,II-III	II-III,III
Rood-Sastry[3] Type	cD, B[6], L[7], C[8]	L, C, F[9]	F, I[10]
Galactic Content	Elliptical-rich	Spiral-poor	Spiral-rich
E:S0:Sp	3:4:2	1:4:2	1:2:3
Morgan[4] Type	ii	i-ii	i
Oemler[5] Type	cD, Spiral-poor	Spiral-poor	Spiral-rich
Symmetry	Spherical	Intermediate	Irregular
Central Concentration	High	Moderate	Low
Richness	Rich	Rich-Moderate	Rich-Poor
X-ray Luminosity $(2-10$ keV)	High	Intermediate	Low
Examples	Abell 401, Coma	Abell 194	Virgo, Abell 1228

[1] Zwicky et al. (1961, 1968) [2] Bautz and Morgan (1970) [3] Rood and Sastry (1971)
[4] Morgan (1961) [5] Oemler (1974)
[6] Binary [7] Line [8] Core [9] Flat [10] Irregular

relaxed and evolved than irregular clusters. Table 1.3 also indicates a correlation between the galaxy content and the types of clusters (see Sect. 1.5.2). The morphology of a cluster and its richness are not necessarily connected; regular clusters are always rich while irregular clusters may or may not be rich.

1.5.2 The Morphology-Density relation

The correlation between the different morphological types of galaxies and their habitats, known as the morphology-density relation, has been known for decades (Smith, 1935; Zwicky, 1942; Dressler, 1980). This relation indicates that dense environments (e.g., cores of galaxy clusters) are mainly populated by elliptical and S0 galaxies, and low-density environments (e.g., outer regions of clusters and the field) by late-type galaxies (Dressler, 1980; Vogt et al., 2004). Studies of the morphology-density relation have shown that the morphology of a galaxy and its star formation history are strongly correlated (Larson et al., 1980; Strateva et al., 2001; Lee et al., 2013) and most of the galaxies in clusters are quiescent. This implies that in high density environments, star formation is inhibited.

Dressler (1980) found a correlation between the morphology of galaxies and density in 55 nearby galaxy clusters regardless of their types. Later Dressler et al. (1997) probed the morphology-density relation in 10 high-redshift clusters at $z \sim 0.5$ and found it to be robust in high elliptical-concentrated (regular) clusters but not in irregular clusters. The morphology-density relation in groups of galaxies was investigated by Postman and Geller (1984) using the data from the Center for Astrophysics (CfA) Redshift Survey (Huchra et al., 1983). Their results were consistent with Dressler (1980). Recently Sazonova et al. (2020) studied the morphology-density relation in 4 galaxy clusters at $1 < z < 2$ and established its existence as far back as $z = 1.75$.

Multiple physical mechanisms have been suggested to be responsible for the star formation quenching and transformation from late-type to early-type galaxies in cosmic dense regions such as clusters, which could be the origin of the morphology-density relation. These mechanisms include:

- Ram-pressure stripping of gas; a process in which the interaction of gas with the intra-cluster medium causes its removal from the disk of galaxies (e.g., Gunn and Gott, 1972; Farouki and Shapiro, 1980; Fujita and Nagashima, 1999; Quilis et al., 2000; Healy et al., 2021b).
- Galaxy harassment; high-speed galaxy encounters transform spiral galaxies to dwarf ellipticals in clusters (e.g., Moore et al., 1996, 1999a; Bialas et al., 2015).
- Cluster tidal forces; gravitational effects that change the morphology of galaxies and their masses as they come close to central regions of clusters (e.g., Byrd and Valtonen, 1990; Valluri, 1993; Fujita, 1998; Łokas, 2020).
- Interaction or merging of galaxies (e.e., Icke, 1985; Lavery and Henry, 1988; Mamon, 1992; Makino and Hut, 1997; Bekki, 1998).
- Galaxy Strangulation; the cluster environment removes or consumes the gas in galaxies (e.g., Larson et al., 1980; Bekki et al., 2002).

1.5.3 Red-Sequence

The RS is a reliable method to detect galaxy clusters that uses photometric data of galaxies. The RS method is built based on the fact that the cores of almost all types of galaxy clusters are dominated by early-type galaxies. The colour of early-type galaxies becomes bluer as they become fainter, and they are the reddest normal galaxies at any given redshift (known as colour-magnitude relation, Baum, 1959; de Vaucouleurs, 1961; Visvanathan and Sandage, 1977). Therefore, the early-type galaxies, that are likely to be cluster members, follow a strong relation in the Colour-Magnitude Diagrams (CMD) called the RS. Yee et al. (1999) showed that the RS method is a powerful tool for cluster-finding and photometric redshift estimation in the optical waveband by identifying early-type galaxies and knowing that the 4000 Å break is the signature that can be used to determine photometric redshift. The RS appears to be universal and is observed even in the most distant studied clusters (e.g. Bower et al., 1992; Stanford et al., 1995, 1998; Blakeslee et al., 2003; López-Cruz et al., 2004a; Holden et al., 2004; Mei et al., 2006a,b; Papovich et al., 2010). The origin of RS is interpreted as a metallicity effect. The supernovae driven winds eject the mass in low-mass galaxies more efficiently than high-mass ones due to the shallower potential well of low-mass galaxies (e.g., Kodama and Arimoto (1997)). Therefore massive metal-abundant galaxies appear redder than less massive equivalents.

1.5.4 The Luminosity Function

The luminosity function (LF) is a probability distribution, representing the number density of galaxies in different luminosity bins within a particular environment. There is a distinction between the LF of galaxy clusters and field galaxies because of the different galaxy population in different environments. The LF of galaxies provides a fundamental tool for observational cosmology, and a test of models for the formation, evolution and

assembly of galaxies (e.g. Benson et al., 2003; Henriques et al., 2015; Rodrigues et al., 2017; Mitchell et al., 2018). The study of the LFs of clusters and their comparison with field LFs could provide information on the formation of clusters and how the environment affects the properties of galaxies in them. Furthermore, comparing the nearby field and cluster LFs with those in higher redshifts can be used to probe the galaxy evolution.

The shape of the luminosity function

Study of the galaxy LF was initiated by Hubble (1936) and has continued to the present day. Hubble (1936) believed that the LF of galaxies was approximately Gaussian with a small dispersion of ~ 0.8 mag. Later Zwicky (1942, 1957, 1964) reported that the LF was exponentially increasing toward the faint end. It is known now that the LF shape of a sample of galaxies depends on the details of the mix of morphological types that are included (e.g. Holmberg, 1969; Christensen, 1975; Tammann and Kraan, 1978; Sandage et al., 1985; Jerjen and Tammann, 1997). Hubble's sample was magnitude-limited and giant elliptical dominated, whereas Zwicky's sample was volume-limited and consisted of faint late-type and irregular galaxies.

The question was then centred on the possible universality of the general LF or whether the environment affects the shape of the LF. The difference between the shapes of cluster and field LFs can be explained as a result of the morphology-density relation of galaxies (Dressler, 1980). High-density enivronments such as clusters are populated by early-type galaxies, whereas low-density regions such as field are dominated by late-type galaxies. Consequently, the overall LF of a cluster depends on the morphological composition of its constituent galaxies and the type of the cluster. Binggeli et al. (1988) showed that the overall LF of galaxy clusters is a combination (sum) of different populations: a Gaussian function for ellipticals and early spirals, and exponential with different slopes for dwarf gas-rich galaxies like irregulars or dwarf ellipticals (see Fig. 1.7). Dwarf ellipticals are morphologically different from elliptical galaxies (Wirth and Gallagher, 1984; Sandage and Binggeli, 1984). Ellipticals are compact with high surface brightness and their luminosity decreases as the compactness increases (Kormendy, 1980, 1985). Dwarf ellipticals on the other hand are diffuse and have low surface brightness and their luminosity decreases as they become more diffuse (Baade, 1944; Caldwell, 1983; Binggeli et al., 1984; Bothun et al., 1986; Caldwell and Bothun, 1987). As seen in Fig. 1.7, dwarf ellipticals are prominent in clusters and dwarf irregulars in the field. Thompson and Gregory (1980) suggested that the different values of Schechter parameters in different clusters are due to the relative number of galaxies of various morphological types and Jerjen and Tammann (1997) confirmed this claim by showing that the LF of each morphological type of galaxies in the Centaurus cluster has the same shape as those in the Virgo and Fornax clusters, while their total LFs vary in shape.

Binggeli et al. (1988) proposed that the LF of each morphological type (LFT) could be universal. This suggestion was supported by different authors (e.g. Andreon et al., 1997; Jerjen and Tammann, 1997; Andreon, 1998). They compared LFTs derived in different environments and found that the shape of the LF of galaxy types of Es, S0s, Ss seems to be independent of the environmental density. However, other authors (e.g. Bromley et al., 1998; Marinoni et al., 1999; Cuesta-Bolao and Serna, 2003) found that the LFTs significantly differ between environments of different densities. They proposed that, in general the LF should be stated as a combination of both density and morphology.

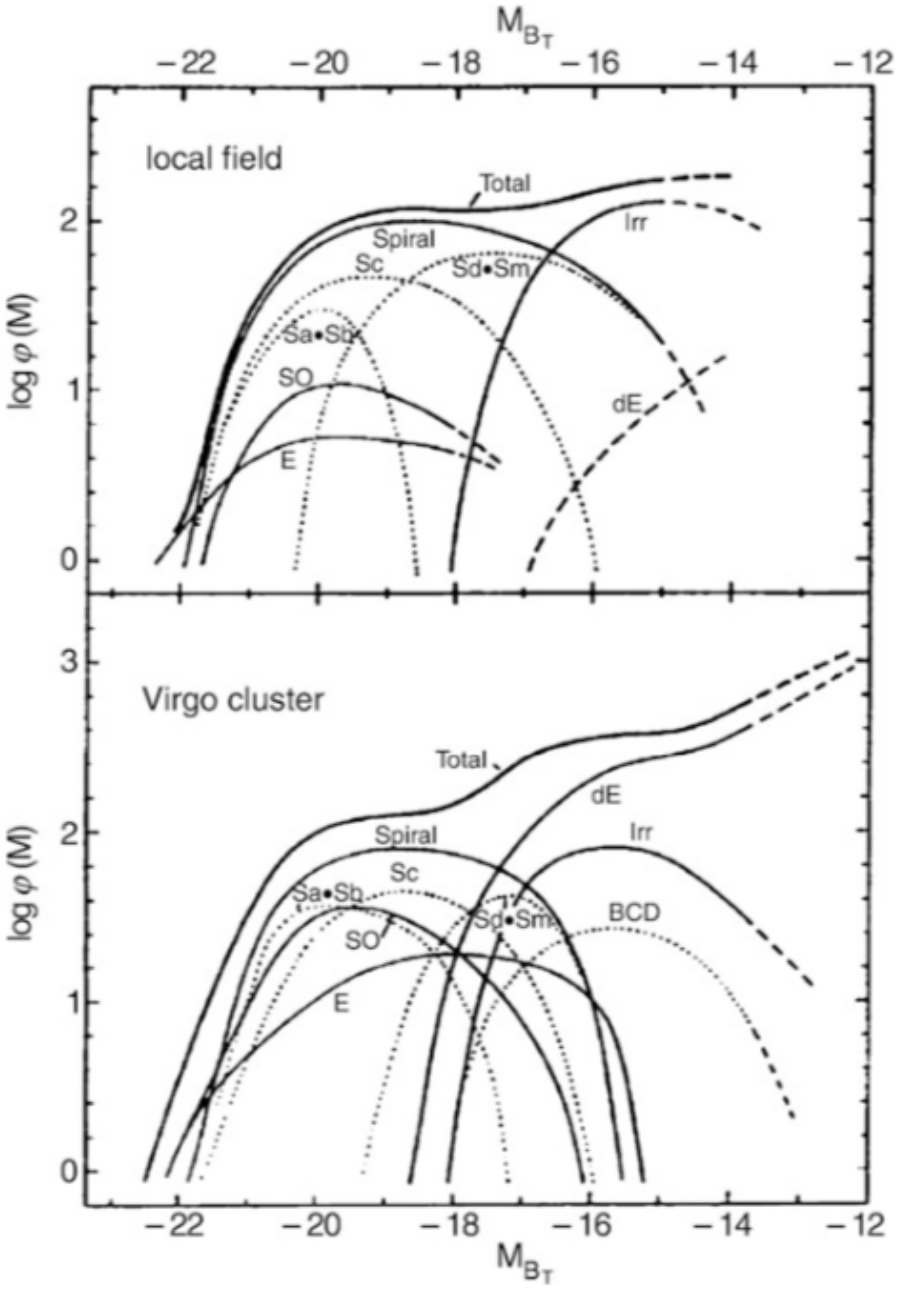

Figure 1.7: The luminosity function for various morphological types of galaxies in field (top) and in the Virgo cluster (bottom). The luminosity function of all galaxies with different morphological types is the combination of the luminosity functions of each type of galaxies. Taken from Binggeli et al. (1988)

.

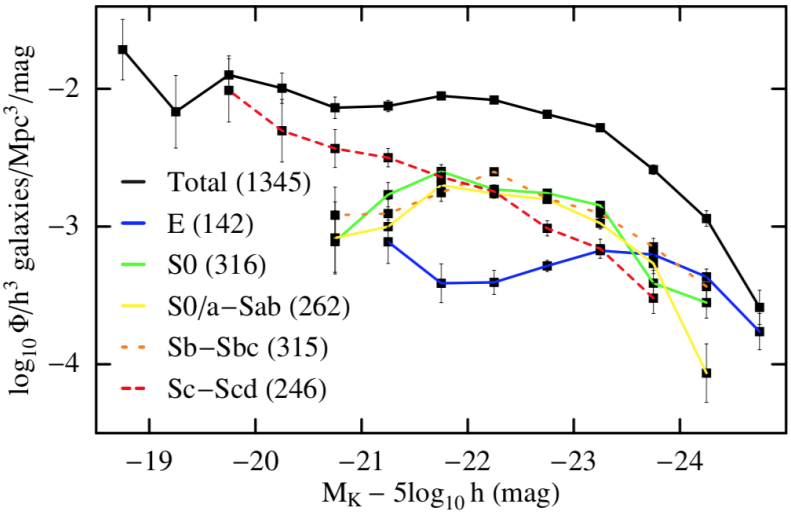

Figure 1.8: K-band isophotal luminosity function for 1345 2MASX galaxies with $K \leq 10^{\rm m}.0$ and $V_{gsr} \leq 3000\,{\rm km\ s^{-1}}$. The sample was segregated by visible morphology. Image credit: Devereux et al. (2009).

The Schechter function

Abell (1975) was the first to investigate the LF of clusters and determine the characteristics of the "general" LF integrated over all morphological types. In 1976, an analytic approximation to the LFs of galaxies was suggested by Paul Schechter (Schechter, 1976). The Schechter function in terms of luminosity has the form

$$\phi(L)dL = \frac{\phi^*}{L^*}\left(\frac{L}{L^*}\right)^{\alpha} e^{-\left(\frac{L}{L^*}\right)} dL, \tag{1.8}$$

where $\phi(L)dL$ is the number of galaxies per unit volume in the luminosity interval from L to $L + dL$. The ϕ^* denotes number per unit volume, L^* is the "characteristic luminosity", at which a rapid change in the slope of the LF is observed, and α is a dimensionless parameter that gives the faint end slope of the LF. In terms of absolute magnitude, equation 1.8 has the form

$$\phi(M)dM = \phi^* 10^{0.4(\alpha+1)(M^*-M)} e^{-10^{0.4(M^*-M)}} dM, \tag{1.9}$$

which indicates a double exponential profile.

Luminosity function in K_s band

LFs derived at different wavelengths are sensitive to different galaxy evolution mechanisms, which result in the visible morphology of galaxies seen today. In this thesis galaxy clusters are studied in the NIR (J, H and K_s bands) where the impact of extinction is much weaker at infrared wavelengths than in the optical ones. Moreover, the infrared K-band is sensitive to the underlying old stellar mass function and less sensitive to the star formation effects in galaxies than the optical wavelengths, as such K-band LFs differ from optical ones. K-band LFs can be used to determine the dynamical mass of a cluster and be compared with that predicted from theoretical models (Devereux et al., 1987; Gavazzi et al., 1996; Bell and de Jong, 2001; Bell et al., 2003). Also, the small effect of

k-correction, the process of converting the apparent magnitude of any astronomical object to an equivalent measurement in its rest-frame, on the NIR wavelengths and its minor dependence on galaxy types make the NIR LFs effective for comparisons and evolutionary studies over a range of redshifts.

A detailed study of the K_s-band LF was done by Kochanek et al. (2001) and Bell et al. (2003) based on categorising the galaxies into two broad types: early and late-type. Both groups selected their galaxies from 2MASS (Skrutskie et al., 2006) and used K_s-band magnitudes measured within the 20 mag arcsec^{-2} elliptical isophote (K_{s20}). Their results were consistent and show that the early- and late-type K_s-band LFs can be well-defined by a Schechter function. The shapes of the LFs are essentially identical with a slight difference in M^* and ϕ^* (Bell et al. (2003), Fig. 9). This was rather surprising given the known dependence of the LF on the morphology of galaxies in the optical.

Devereux et al. (2009) performed a more detailed study on the dependence of K_s-band LF on the morphological types of galaxies. Their sample consisted of galaxies that were identified using HYPERLEDA[5] (Paturel et al., 2003). These galaxies have very reliable and finely divided morphological information. In order to use the K_s-band magnitudes of galaxies, Devereux et al. (2009) identified their 2MASS counterparts in the Extended Source Catalogue (XSC, Jarrett et al., 2000b). Their volume-limited sample comprised 1604 galaxies with $K_{s20} \leq 10\overset{\text{m}}{.}0$, $V_{gsr} \leq 3000$ km s^{-1} (Galactic standard-of-rest velocity) and Galactic latitude $|b| > 10°$. LFs derived in Devereux et al. (2009) are shown in Fig. 1.8.

Figure 1.8 indicates that the K-band LFs also depend significantly on morphological type and that no individual type resembles the overall shape of the total LF. Elliptical galaxies are the main component of the LF at the bright end, whereas late-type (Sc - Scd) spirals take over the LF at the faint end. Between the two extremes lie the lenticular galaxies and the bulge-dominated spirals (S0/a − Sbc).

The total LF in Fig. 1.8 shows a dip starting from $M_K - 5\,log\,h_{70} \sim -21\overset{\text{m}}{.}0$ where the space density of elliptical and bulgy spiral galaxies (E, S0, Sa, Sb) is decreasing and late-type spirals start taking over. The dip is at the intersection of two curves, a Gaussian for bulge dominated galaxies and a power-law for late-type spirals. This dip has also been observed in other NIR LFs of clusters (e.g. Merluzzi et al., 2010) and also at optical wavelengths. For example, Mobasher et al. (2003) found a dip at $B \sim -18\overset{\text{m}}{.}0$ where the transition between giants and dwarf galaxies occurs. I will show later in the thesis that the NIR researched clusters data are complete to $M_{Ks} - 5\,\log\,h_{70} = -21\overset{\text{m}}{.}5$ despite their large distances ($v \sim 18000$ km s^{-1}) and that the determined LFs of the VSCL clusters in this project, will be measuring mainly bright bulgy galaxies, and will not be sensitive to the dwarf population.

1.5.5 X-ray observations in the ZoA

All rich clusters of galaxies have X-ray luminosities from $10^{42} - 10^{45}$ ergs sec^{-1} (in the $0.5 - 4.5$ keV band) due to thermal Bremsstrahlung radiation from their hot intracluster gas at temperatures from $10^7 - 10^8$ K (Jones and Forman, 1984; Sarazin, 1986; Edge et al., 1990; Edge and Stewart, 1991; Henry and Arnaud, 1991; Henry et al., 1992; David et al., 1993; Burg et al., 1994).

If a cluster has a central X-ray dominant galaxy, its X-ray emission tends to peak at

[5]A web-based interface that provides access to the Principal Galaxy Catalogue: http://leda.univ-lyon1.fr

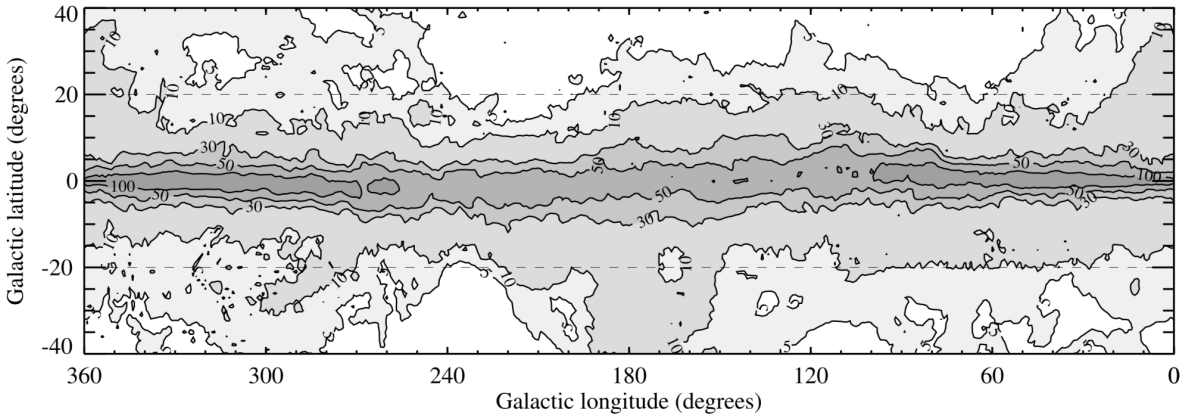

Figure 1.9: The Galactic hydrogen column density contours at $|b| < 40°$ in units of 10^{20} cm^{-2} (Dickey and Lockman, 1990). Dashed lines indicate the ZoA at $|b| < 20°$. Taken from Ebeling et al. (2002)

.

the position of such a galaxy. Forman and Jones (1982) classified clusters based on the presence of a massive galaxy into X-ray dominant (XD) and non-X-ray dominant (nXD) clusters. The need for this classification arises from the presence of the dominant galaxy in both regular dynamically evolved, and irregular dynamically young clusters which gives a second dimension to the cluster classification system (see Table 3 in Forman and Jones (1982)). There are regular clusters such as Coma and irregular ones such as A1362 that do not contain an X-ray dominant galaxy, whereas clusters like Perseus (regular) and Virgo (irregular) contain an X-ray dominant galaxy.

X-ray observations are an optimal tool for identifying extragalactic objects (galaxies and rich galaxy clusters) at low Galactic latitudes in the ZoA. For example, four out of the seven most X-ray luminous clusters at $z < 0.2$ (the Perseus, Ophiuchus, Triangulum Australis, and PKS 07491 clusters, all with $L_X > 10^{45}\,\mathrm{erg\,s^{-1}}$) are located at $|b| < 20°$ (Edge and Stewart, 1991), in the ZoA. The ROSAT All Sky Survey (RASS) has observed rich clusters out to redshifts of $z \sim 0.4$ (e.g. Ebeling et al., 1996, 1998, 2000), and is complete to $|b| > 20°$. However, the CIZA project by Ebeling et al. (2005) extended the RASS survey to the ZoA and could find galaxy clusters out to lower latitudes of $|b| > 5°$.

X-ray emission is hardly obscured by dust in the ZoA compared to the optical wavelengths. However, the foreground gas or the equivalent hydrogen column density, n_H, is the limiting factor particularly for the soft X-ray emission (0.1-2.4 keV). Figure 1.9 shows the contours of the Galactic n_H column density at $|b| < 40°$ and how n_H increases towards the GP.

Figure 1.10 shows the mean value of extinction due to dust in different wavebands as a function of Galactic latitude. This figure indicates that at $|b| < 5°$ optical wavelengths are highly affected by the dust extinction. The hard X-ray emission ($2 - 10$ keV) is not hampered by the extinction and the softer emission of X-ray (0.1-2.4 keV), in which the RASS has imaged the whole sky, is only moderately affected by it. However, as stated earlier the foreground gas in the ZoA will affect the detection of galaxy clusters in the soft X-ray wavelengths.

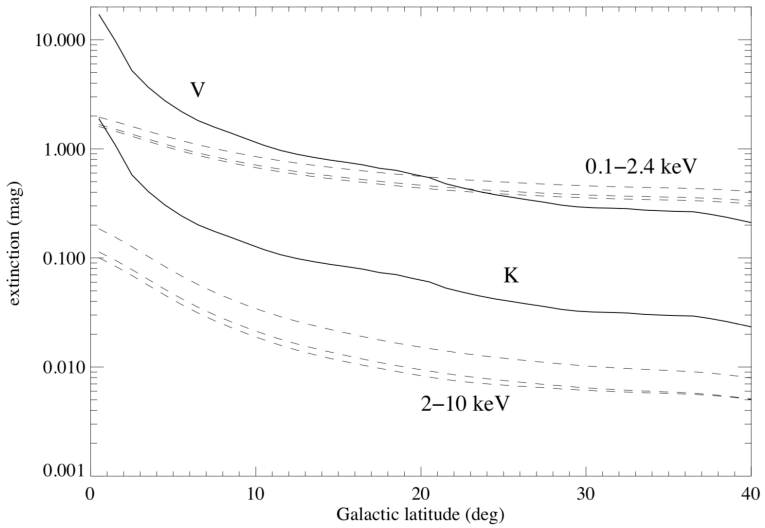

Figure 1.10: Average extinction values at different Galactic latitudes in ZoA in different wavebands. The optical extinction is determined based on the 100 μm maps Schlegel et al. (1998). The dashed curves from top to bottom display the extinction values at X-ray wavelengths which are determined with the assumption of a Bremsstrahlung spectrum for intra-cluster gas at $kT = 2, 6$, and 10 keV respectively, at $z = 0.1$. The extinction in the K band is much lower compared to the optical V band. The figure is taken from Ebeling et al. (2002).

1.6 This thesis

1.6.1 NIR study of the VSCL clusters

In Sect. 1.4.2 the VSCL and its potential clusters were described. To get a better understanding of the morphology of the VSCL, its mass and potential effect on the local bulk flows, a deeper investigation on the richness and structure of its constituent galaxy clusters is needed. The redshift survey sample that was used to map the VSCL was sparse and consisted of optical galaxies (e.g., Kraan-Korteweg, 2000a) and 2MASX galaxies (Jarrett et al., 2000b). The optical sample is complete to $M_B - 5 \log h_{70} \lesssim -19\overset{\text{m}}{.}5$ to $-21\overset{\text{m}}{.}5$ depending on the foreground extinction, and the 2MASX sample is complete to $M_{Ks} - 5 \log h_{70} \lesssim -23\overset{\text{m}}{.}5$ at the distance of the VSCL ($\sim 260\ h_{70}^{-1}$ Mpc). This only probes slightly deeper than the knee of the LF of galaxies (e.g., $M_{Ks} - 5 \log h_{70} = -24\overset{\text{m}}{.}2$, Kochanek et al., 2001), and is not sufficient to yield a conclusion about the richness (through the luminosity function). Also, a more complete sample will help to study the structure of these galaxy overdensities more inclusively (through the iso-density contour maps). We therefore, conducted a series of deep NIR observations of the VSCL galaxy clusters in the J, H and K_s bands with the InfraRed Survey Facility (IRSF) telescope.

Near-Infrared observations ($0.9 - 5.0\,\mu$m) are very efficient in detecting structures obscured by the dust layers of the Milky Way, where optical cluster catalogues (Abell, 1958; Abell et al., 1989) become increasingly incomplete (e.g. van Haarlem et al., 1997, and references therein), while the K-band extinction is much lower compared to the optical (see Fig. 1.10). NIR surveys are particularly useful to detect early-type galaxies, since they are dominated by the old stellar component (e.g., Silva et al., 2008; Cesetti et al., 2009). Therefore NIR studies are good tracers of galaxy groups and clusters (the morphology-density relation). Although 21-cm emission from neutral hydrogen gas, H I, and mid/far infrared have longer wavelengths than NIR and can penetrate more effectively through

the dust layers, they are biased towards star forming spiral galaxies. X-ray surveys (as discussed before) are sensitive to rich galaxy clusters and are thus not useful to map the galaxy distribution in all type of clusters objectively. It should be also noted that a large fraction of blue and low surface brightness spiral galaxies are detectable in NIR (see e.g., Said et al., 2016a). For instance, a large nearby edge-on spiral galaxy, with an extension of $5'$ in K_s band, was discovered by 2MASS (Hurt et al., 1999) in the ZoA at (ℓ, b) = ($236\overset{\circ}{.}8, -1\overset{\circ}{.}8$). Not surprisingly, this galaxy with extinction of $A_B = 6\overset{\mathrm{m}}{.}6$ had not been detected in the optical (Saito et al., 1991).

The SIRIUS camera on the IRSF telescope has been used in various NIR surveys such as Woudt et al. (2005); Nagayama et al. (2006); Cluver (2008); Riad (2010); Kraan-Korteweg et al. (2011) and proven to probe $\sim 2\overset{\mathrm{m}}{.}0$ deeper than 2MASX in K_s band (e.g., Riad, 2010). Since it is sensitive to both elliptical and bulgy spiral galaxies, it is ideal for an in-depth study of the VSCL clusters and by extension the VSCL itself. Also the NIR results can be compared to those of other wavelengths such as X-ray and H I observations to learn more about the galaxy clusters located in the ZoA.

1.6.2 Thesis outline

The structure of this thesis is as follows. Chapter 2 describes the sample selection, the NIR observations conducted with the IRSF telescope and the preliminary data reduction using SIRIUS pipeline. It ends with explaining the identification of the galaxy candidates in the reduced images based on a combination of the Source Extractor automatic detection algorithm and visual inspection. Chapter 3 starts with describing the IRSF pipeline, extraction of the photometric parameters of galaxies in the observed VSCL clusters and checking their internal and external consistency. After assessing the effect of extinction and k-correction on the photometric parameters of galaxies, the NIR extended source catalogue with the derived parameters is represented, as well as a derivation of the completeness magnitude limit of all of the clusters. Chapter 4 is then dedicated to the analysis of the VSCL galaxy clusters. I first describe a sample of well-known clusters and their K-band properties to compare with the VSCL clusters, and then investigate the richness and structure of VSCL clusters through their radial density profiles and iso-density contour maps and relate those results to the comparison clusters. A brief H I analysis of VC04, the most prominent cluster in the VSCL is presented in this chapter. Chapter 5 is dedicated to the derivation of the LFs of the VSCL clusters. I first present two methods to compute the LF, i.e. the spectroscopic membership and RS methods, and prove the reliability of the RS method by performing them on the comparison clusters and comparing the results. The RS method is then used to derive the LFs of the observed VSCL clusters and a detailed discussion of the VC04 LF is presented in this chapter.

Chapter 2

NIR Observation and Data Reduction

The discovery of the Vela Supercluster (VSCL) behind the Zone of Avoidance (ZoA) is reported in Kraan-Korteweg et al. (2017): over 4000 new spectroscopic galaxy redshifts obtained with the 3.9m Anglo-Australian Telescope (AAT) show a significant overdensity at $\sim 18000\,\mathrm{km\ s^{-1}}$ and $\sim 22000\,\mathrm{km\ s^{-1}}$, on either side of the Galactic Plane (GP), including cores of galaxy clusters observed with the Southern African Large Telescope (SALT). The galaxy sample consisted of a combination of galaxies from deep optical galaxy surveys (Kraan-Korteweg and Lahav, 2000; Kraan-Korteweg, 2000a) and galaxies in the 2MASX catalogue (Jarrett et al., 2000b). The redshift overdensity is extended, elongated and has a wall-like structure (Fig. 2.1). The suspected crossing of the two walls above and below the GP is hidden in the most obscured part of the ZoA. This was indirectly confirmed from theoretical reconstructions of the velocity field from the *Cosmicflows* -3 catalogue of peculiar velocities (Courtois et al., 2019). All of the above are in agreement with the definition of a supercluster (Einasto et al., 2011a). Using the redshift information, Kraan-Korteweg et al. (2017) identified 20 potential galaxy clusters/groups in the Vela ZoA area ($\ell = 272\overset{\circ}{.}5 \pm 20^\circ, b = 0^\circ \pm 10^\circ$), with velocity dispersions $\sigma_v > 400\,\mathrm{km\ s^{-1}}$ (including 2 CIZA X-ray clusters; Kocevski and Ebeling, 2006) .

The VSCL is located at a distance of $\sim 260\,h_{70}^{-1}$ Mpc in the ZoA and hence is subject to a high level of extinction due to interstellar dust, and star-crowding because of the high stellar density of the Milky Way (e.g. Kraan-Korteweg, 2000b). Therefore, to estimate the richness of the VSCL and study its contribution to the bulk flow, deep observations of its potential clusters can pave the way toward a better understanding of the properties of the supercluster, its state of evolution and overall mass density. This also provides an indication of the richness of the supercluster itself, since the higher the number of clusters in a supercluster, the richer it is (Einasto et al., 2007a). The Near-InfraRed (NIR) wavelength is well-suited to probe the ZoA since it is less affected by the dust obscuration of the Milky way than the shorter optical waveband. Also, galaxy clusters are dominated by early-type galaxies (i.e. the morphology-density relation (Dressler, 1980)) which appear red due to their old stellar populations. Therefore, I used NIR observations to study to the clusters in the VSCL.

In this chapter I describe the NIR imaging observations of a sample of potential clusters in the VSCL , obtained with the Infrared Survey Facility (IRSF) telescope in Sutherland, and the process of reducing the obtained data. Section 2.1 presents the candidate clusters that were chosen for NIR observations. The telescope and the details of the observations are explained in Section 2.2. Section 2.3 describes the preliminary data reduction using

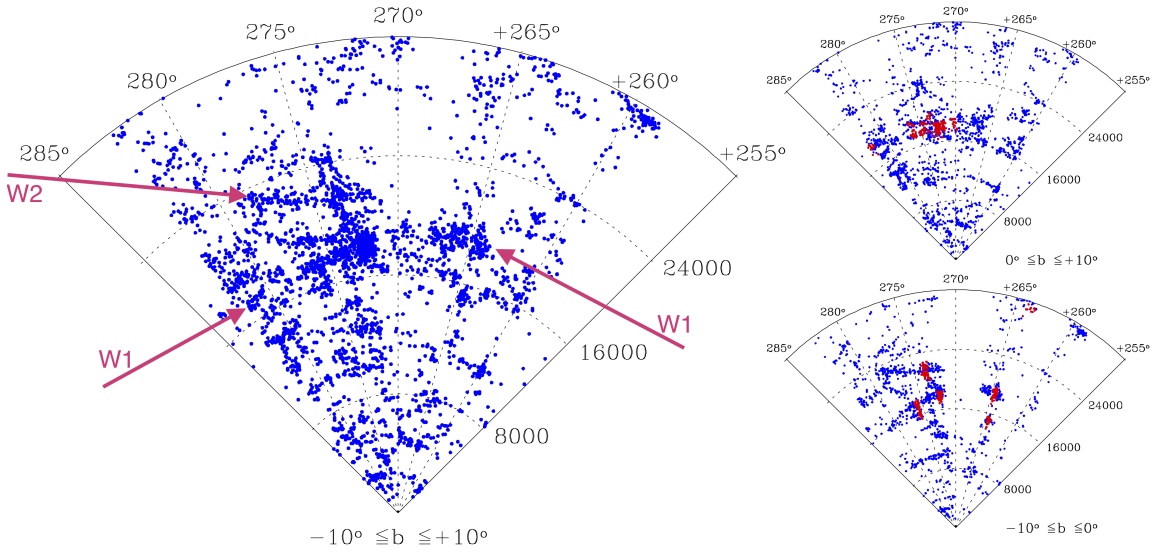

Figure 2.1: Redshift cones for the VSCL survey out to $cz \leqslant 32000$ km s^{-1}. The primary wall can be traced at 18000 km s^{-1} above and below the GP (see panels on the right), while the second wall is visible only below the GP. The red dots mark potential galaxy clusters. Image credit: Kraan-Korteweg et al. (2017)

the SIRIUS[1] pipeline and Section 2.4 explains the method of identifying galaxy candidates in the reduced images based on a combination of the Source Extractor automatic detection algorithm and visual inspection.

2.1 Sample selection

The 20 potential clusters in the VSCL were identified by analysing the velocity dispersions, distributions of the redshifts of galaxies and the steepness of the extinction-corrected K_s-band luminosity functions (magnitude distribution) (Kraan-Korteweg et al., 2017).

Figure 2.2 (adapted from Kraan-Korteweg et al. (2017)) depicts the positions of the 20 galaxy clusters/groups identified in the VSCL region with velocity dispersion $\sigma_v >$ 400 km s^{-1}. The left panel shows the redshift distribution of known galaxies in Galactic coordinates, where redshifts of galaxies are colour-coded and contours indicate extinctions of $A_K = 0\overset{\text{m}}{.}3$ (solid) and $0\overset{\text{m}}{.}18$ (dotted). In this figure galaxies with a redshift within the VCSL redshift range $16000 < cz < 24000$ km s^{-1} (red and magenta dots), show a clear prominence. The potential galaxy clusters or groups are embedded in this overdensity of galaxies at the distance of the VSCL. Note that there is no redshift information within the extinction contours ($|b| \lesssim 5°$) given that the galaxy sample is highly incomplete at these low latitudes. The right panel diagrams display the redshift cones out to $cz \leqslant$ 32000 km s^{-1} above ($0 \leq b \leq 10°$; top panel) and below ($-10 \leq b \leq 0°$; bottom panel) the GP, where red dots are galaxies belonging to the potential galaxy clusters. The positions of VC02, VC04, VC05, VC08, VC10, VC11, the galaxy clusters that are studied in this thesis, are indicated by black arrows.

Given the distance of the VSCL ($\sim 260\, h_{70}^{-1}$ Mpc), the depth of the optical sample is limited to an absolute magnitude of $M_B^0 \lesssim -19\overset{\text{m}}{.}5$ to $-21\overset{\text{m}}{.}5$ depending on the varying foreground extinction, and $M_K^0 \approx -23\overset{\text{m}}{.}5$ for 2MASX galaxies. This probes the clusters

[1]https://sourceforge.net/projects/irsfsoftware/.

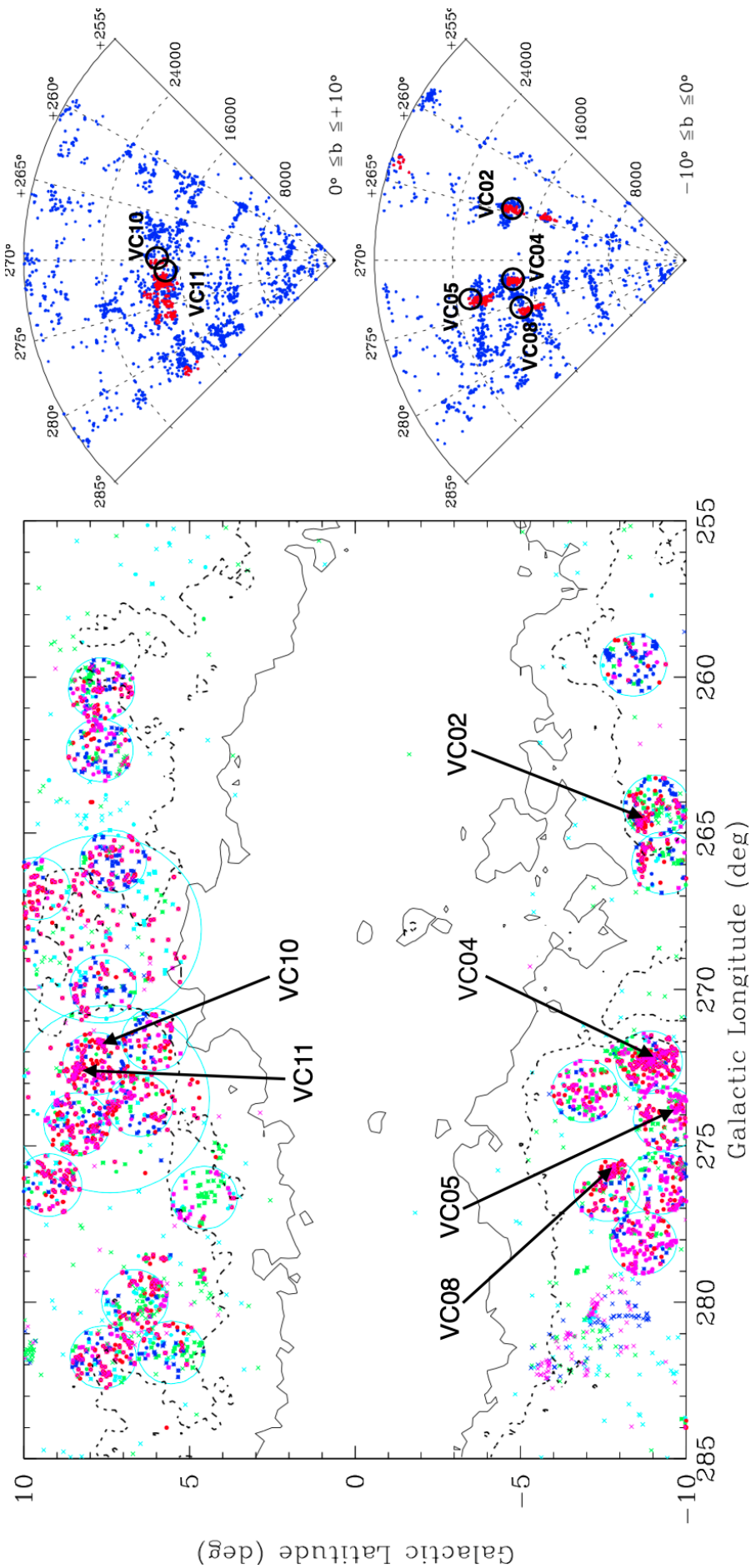

Figure 2.2: The figure is taken from (Kraan-Korteweg et al., 2017). Left panel: Galaxy redshift distribution within the VSCL region. Galaxies in this figure are colour-coded based on their redshifts. cyan: $v < 8000$; green: $8000 < v < 16000$; red: $16000 < v < 20000$; magenta $20000 < v < 24000$; blue: $24000 < v < 32000$ km s^{-1}. Contours indicate extinctions of $A_K = 0\overset{m}{.}3$ (solid) and $0\overset{m}{.}18$ (dotted). The black arrows point at the galaxy clusters that are studied in this work. Right panel: the redshift cones out to $cz \leqslant 32000$ km s^{-1} above and below the GP. The positions of the investigated galaxy clusters in this work are shown in black circles.

only marginally below M^*, and is insufficient to study these clusters comprehensively and hence draw conclusions about the richness of the clusters. Therefore, given that NIR wavelengths can penetrate effectively through the dust in the ZoA, a series of deep NIR observations were conducted with the InfraRed Survey Facility (IRSF) telescope. Clusters with more than 25 galaxies and $\sigma_v > 400$ km s^{-1} (based on the preliminary analysis by Kraan-Korteweg et al., 2017), were considered strong candidates for the NIR observations and are expected to provide the most information on the richness and the structure of the VSCL.

The main focus of this work consists of a deep NIR imaging survey of six cluster candidates over $\sim 2/3$ of their Abell radii. Some properties of the galaxy clusters are given in Table 2.1.

Table 2.1: Properties of the six galaxy clusters within the VSCL selected for a NIR study (based on the Kraan-Korteweg et al. (2017) redshift catalogue).

Name	Center (α, δ) (deg)	Center (ℓ, b) (deg)	v km s^{-1}	σ km s^{-1}	N*
VC02	122.69, −49.39	264.67, −8.60	18985	659	82
VC04	129.14, −55.81	272.27, −8.96	18196	455	89
VC05	129.78, −57.47	273.84, −9.65	21275	469	52
VC08	134.54, −57.75	275.65, −7.83	17316	355	38
VC10	147.38, −43.84	271.67, +7.71	18173	428	29
VC11	149.00, −43.89	272.62, +8.41	17919	633	67

* Number of galaxies with redshift

2.2 The NIR observations with the IRSF

The VSCL imaging data were obtained with the IRSF, a 1.4m Alt-Azimuth Cassegrain telescope built by a Japanese company which is located at the South African Astronomical Observatory (SAAO) site in Sutherland. It is equipped with the Simultaneous 3-colour Infrared Imager for Unbiased Surveys (SIRIUS) camera in the three J, H and K_s bandpasses. SIRIUS utilizes three 1024×1024 pixel HgCdTe Astronomical Wide Area Infrared Imager (HAWAII) arrays, with a gain of 5.5 e^-/ADU (Analog-to-Digital Unit) and a readout-noise of 30 e^-. The read system of SIRIUS HAWAII arrays includes MACS2 (Nakaya and Sato, 1998), Messia IV (Sekiguchi et al., 1998) and the data acquisition computer (Nagayama et al., 2003, and references therein). The field-of-view of the camera is $7\farcm7 \times 7\farcm7$ with a resolution of $0\farcs45$ pix^{-1}. An exposure time of 900 seconds results in the limiting magnitudes of the SIRIUS camera for point sources to be $J = 19\fm0$, $H = 18\fm5$ and $K_s = 17\fm0$ (S/N = 10 σ) (Nagashima et al., 1999; Nagayama et al., 2003; Nagayama, 2012).

The excellent angular resolution of the IRSF, $0\farcs45$, compared to 2MASS, $2\farcs0$, makes it a suitable instrument for surveys of regions with high stellar density. It improves the processes of galaxy identification and star-subtraction due to the better deblending between stars and galaxies, resulting in more reliable photometry for the galaxies. A comparison between IRSF (Nagayama et al., 2003) and 2MASS (Skrutskie et al., 2006),

Table 2.2: Comparison between the IRSF and 2MASS surveys characteristics.

Telescope/ Survey	Diameter (m)	Field-of-View (arcmin)	Filters*	Resolution (arcsec/pix)	Imaging Exposure Time (s)
SIRIUS/VSCL	1.4	7.7×7.7	J, H, K_s	0.45	600
2MASS	1.3	8.5×8.5	J, H, K_s	2.0	7.8

* The filters are not exactly the same between the IRSF and 2MASS surveys (see Fig. 2.10 for more details).

is given in Table 2.2. Figure 2.3 shows four galaxies in the VSCL that were observed with the IRSF/SIRIUS (bottom row) and also as part of the 2MASS survey (top row). It demonstrates the improved quality of IRSF/SIRIUS over the whole-sky photometry of 2MASS.

Figure 2.3: False colour RGB images of four galaxies observed with both 2MASS (top row) and IRSF/SIRIUS (bottom row). J, H and K_s bands correspond to Blue, Green and Red colours respectively in the RGB images. The scale of images is $90'' \times 90''$.

2.2.1 Imaging Method

At the VSCL distance of ∼18000 km s^{-1}, the Abell radius (R_A) corresponds to 28.′6 which translates to 2.1 h_{70}^{-1} Mpc. Given the IRSF Field-of-View (FoV) of 7.′7 versus the Abell radius of 28.′6, a mosaic of 32 fields was defined to provide good coverage of the cluster cores ($r \lesssim 0.7R_A$). Each cluster consists of 4 rows of 6 slightly overlapping fields with an additional row of 4 fields at the top and bottom, thus bringing the total number of observed fields to 32 (see Figure 2.4). The strips of constant Right Ascension (RA) are separated from the adjacent strips by 7.′2 in RA and 7.′2 in Declination (DEC) resulting in an overlap of 0.′5 between any two neighbouring fields in RA and DEC. Using this method of observing, each cluster mosaic covers almost 80% of the Abell radius and therefore, the completeness radius of this survey varies from $1.5 - 1.8$ Mpc depending on the distance of the observed cluster.

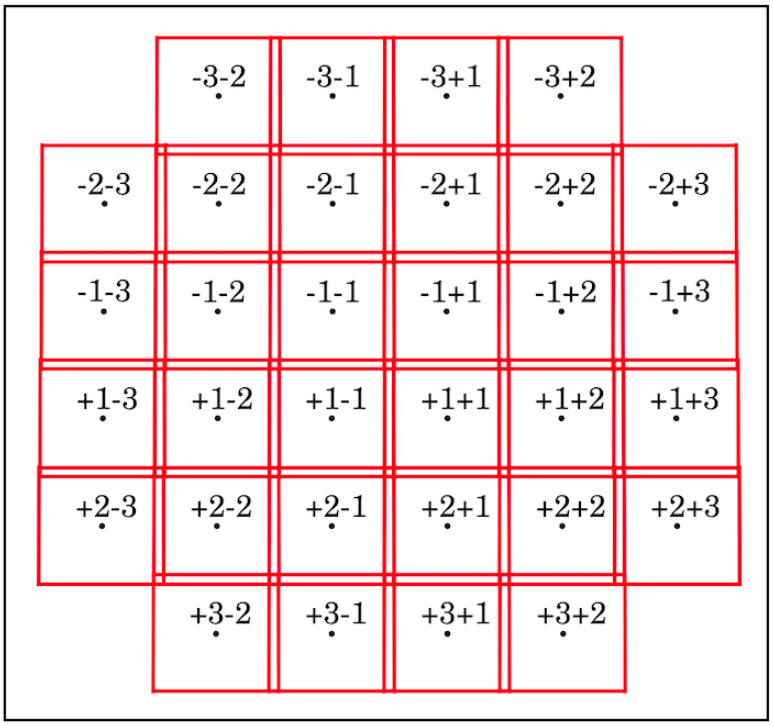

Figure 2.4: A sample of the observed mosaic consists of 32 slightly overlapping fields for each cluster. In the notation $\pm a \pm b$, a and b are the numerical offsets in the horizontal and vertical directions respectively from the cluster center, used to identify a field within the mosaic.

2.2.2 IRSF Observations

The observations of the galaxy clusters in the VSCL were started in 2015 by A. Elagali and K. Said. They observed 8 galaxy clusters and 2 galaxy groups in February, March and April 2015. Due to bad weather and a telescope readout issue, more than 60% of the 268 observed fields were not of science quality. The remaining fields therefore, covered the 8 clusters only partially. A follow-up observing run was performed in April 2017 for two weeks. K. Said and I re-observed the gaps and unsatisfactory fields of the 6 high priority clusters. Because of bad weather during the 2017 observing run, almost 40% of the 150 obtained fields had poor seeing (FWHM$>2\farcs2$) and were not suitable for scientific analysis, and a third observing run of two weeks was conducted in December 2018 and January 2019. During this run I re-observed all remaining unsatisfactory fields of the 6 clusters. During the 2018/2019 observing run, the lower right quadrant of the K_s band was deteriorated and found to be unusable in the SIRIUS camera system (see e.g. Fig. 2.6). To cover the blank quadrant, the observations were set up so that there was a 50% overlap between neighbouring fields in the horizontal direction. And although the number of independent fields that required observing was 82, a total of 164 images had to be observed. A summary of all the observing runs is given in Table 2.3.

Out of 9 galaxy clusters observed with the IRSF telescope, the 6 clusters labelled as VC02, VC04, VC05, VC08, VC10 and VC11 have complete and high-quality imaging data that allow in-depth studies for richness and structure.

The observation procedure detailed below follows the standard IRSF observing procedure outlined in Riad (2010) and in the SIRIUS pipeline manual[2], and were adapted to

[2]https://sourceforge.net/projects/irsfsoftware/files/

Table 2.3: IRSF observations and observers. Observers: Ahmed Elagali (AE), Khaled Said (KS), Narges Hatamkhani (NH)

Year	Month(s) (weeks)	Observed Clusters	Observed Fields	Observer(s)
2015	Feb-Apr (3 weeks)	VC02	29	AE/KS
		VC04	28	
		VC05	32	
		VC06	22	
		VC07	32	
		VC08	32	
		VC10	32	
		VC11	32	
		VG01	16	
		VG17	11	
2017	Apr (2 weeks)	VC02	22	NH/KS
		VC04	32	
		VC05	32	
		VC06	19	
		VC07	7	
		VC12	23	
2018/2019	Dec-Jan (2 weeks)	VC02	14	NH
		VC04	30	
		VC05	21	
		VC06	5	
		VC10	2	
		VC11	10	

specifics of my observations.

Exposure Time

At NIR wavelengths, exposure times greater than 1 minute result in the sky brightness and other bright sources saturating the images, while short exposures of $\lesssim 1$ minute result in low signal-to-noise ratio (S/N) which will make the detection of faint galaxies difficult. Taking multiple (N) short exposures and co-adding them ensures that the noise is lowered by $\sqrt{N}$.

Each image was observed for 25 successive frames of 24s (600s in total) and as a result this study has $\sim 2\overset{\text{m}}{.}0$ limiting magnitude deeper than 2 MASX survey (Jarrett et al., 2000a). Observing for longer than 10 minutes in the densely populated ZoA results in increased sky background noise due to NIR emission from the old stellar population in the Galaxy and will impact the reliability of photometry (Riad, 2010). This approach was used in various studies of galaxy clusters and large-scale structures in the ZoA such as Nagayama et al. (2004); Woudt et al. (2005); Nagayama et al. (2006); Cluver (2008); Skelton et al. (2009); Riad (2010); Williams (2011); Said et al. (2016a).

Dithering

Dithering is the process of observing the same area of the sky using different regions of the detector, by pointing the telescope with a small spatial offset compared to the size of the detector during observations. Stacking and median-combining the dithered frames removes the bad pixels. Figure 2.5, shows the dithering pattern used by the SIRIUS camera: a 5×5 grid with a spacing of 15″. These dithered frames are called `self` frames in the SIRIUS pipeline. Frame 1 is centered at the field center. Due to a bug in the pattern controller software, frame 11 is offset from its expected position but this does not affect the final image since the SIRIUS pipeline is aware of the relative centers of each frame and aligns them appropriately. As a result of dithering, the size of the final image is increased to $\sim 8\overset{\prime}{.}6 \times 8\overset{\prime}{.}6$, though only the central region of $7\overset{\prime}{.}7 \times 7\overset{\prime}{.}7$ has the appropriate S/N.

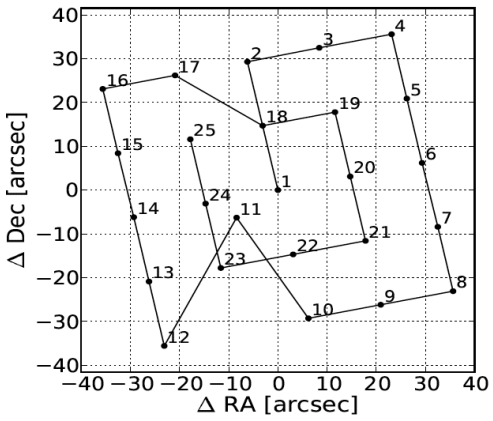

Figure 2.5: The dithering pattern of the SIRIUS camera. Each field is observed with 25 dithered frames of 24 s exposures each. The figure is taken from Riad (2010).

Dithering is also used to measure the sky background and subtraction from the science images. Since the positions of bad pixels and other detector artefacts are fixed relative to

the detector, stacking the dithered frames instead of aligning them as stated above, and median-combining them, will remove the astronomical sources that are smaller than the offset length (which move relative to the detector) while retaining the structure of the sky, with possibly some residuals left by large scale diffuse structures. This technique serves as a reasonable substitute to alternating observations of empty regions of the sky with the science targets, which takes twice the time to observe, not to mention the difficulty of finding empty areas of sky to observe in the ZoA.

Flat-Fields

The detector response to the light varies from pixel to pixel depending on its quantum efficiency. This results in measuring different values for the flux of the same region of the sky by different parts of the detector and must be corrected. This correction is done by the process of `flat-fielding`. The flat-field is the response of the detector to uniform light. The sky is a good source of uniform light during twilight. Typically 100 flat-fields of 5 second exposure each were taken on each night of observation. These were then fed into the SIRIUS pipeline which makes a master flat-field by computing the median of the normalized flat-fields and uses it to correct all the raw data collected during the observing run. The master flat-fields for the 2015 and the 2017 observing runs are shown in Figure 2.6. Sadly the K_s band detector deteriorated at the end of 2018 making one quarter of the images unusable. An example of a master flat-field from the 2019 observing run, is shown in Figure 2.7.

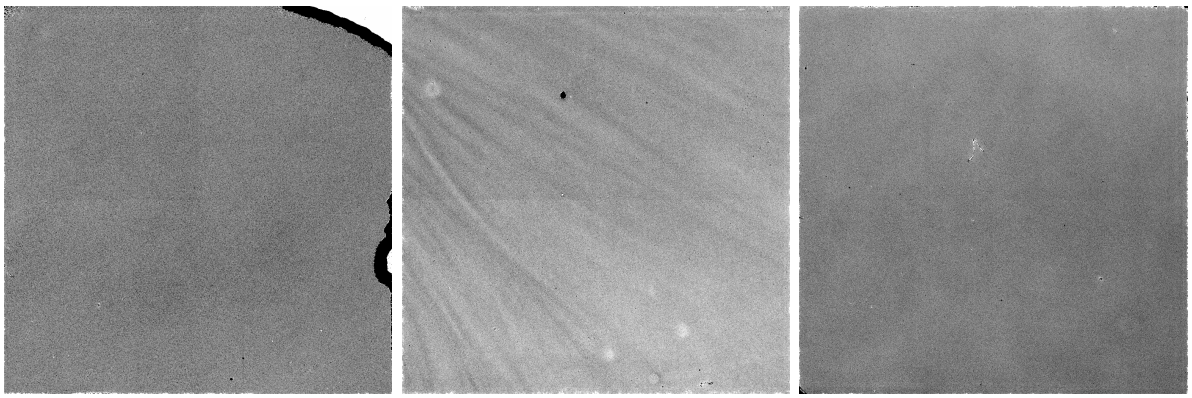

Figure 2.6: Master flat-fields for the J, H and K_s bands for the 2015 and 2017 observing runs.

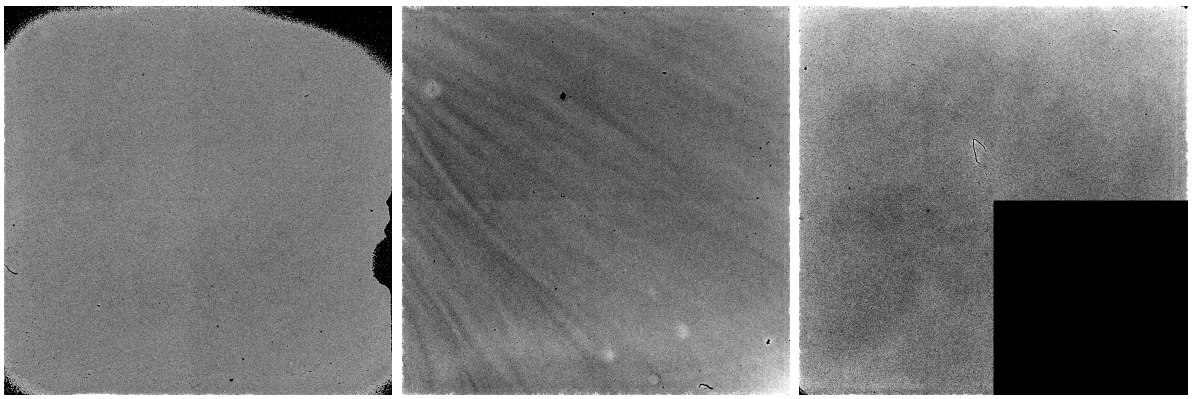

Figure 2.7: Master flat-fields for the J, H and K_s bands for the 2018/19 observing run.

Dark Frames

During long exposure observations a significant amount of charge can accumulate on the infrared detectors due to thermal excitation and generate noisy pixels. This effect can be seen even when the telescope shutter is closed and must be subtracted from the final images. To correct for this, observations were performed with the shutter closed to obtain so-called *dark frames*. Ten dark frames with 24 second exposure and 10 more with 5 second exposure were taken every night. Dark frames with 24 s exposure were averaged and subtracted from the `self`(i) frames, while the 5 s exposures were used to correct the flat-field frames. The dark frames corresponding to the 2015 and 2017 observations are shown in Fig. 2.8, while those pertaining to the 2019 observing run, in which the dark frame for the K_s band has an unusable quadrant are shown in Fig. 2.9.

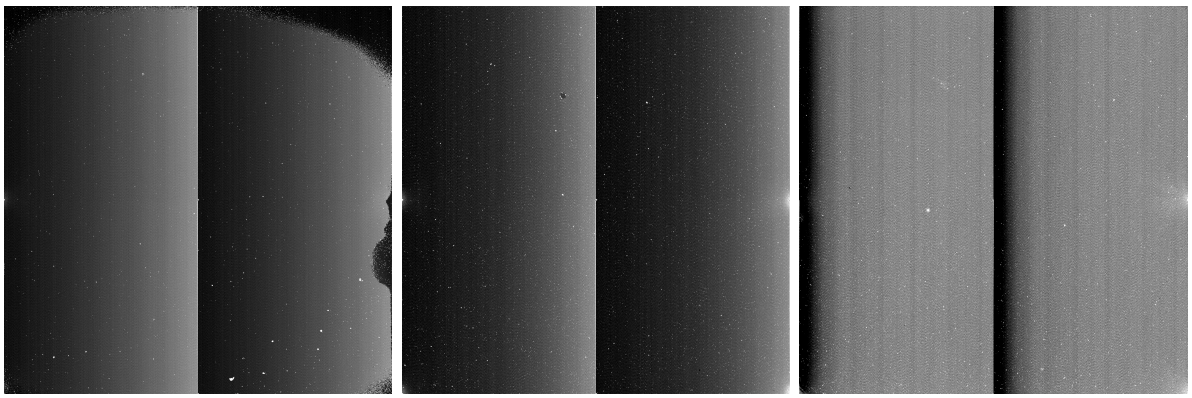

Figure 2.8: Dark frames for the J, H and K_s bands for the 2015 and 2017 observing runs.

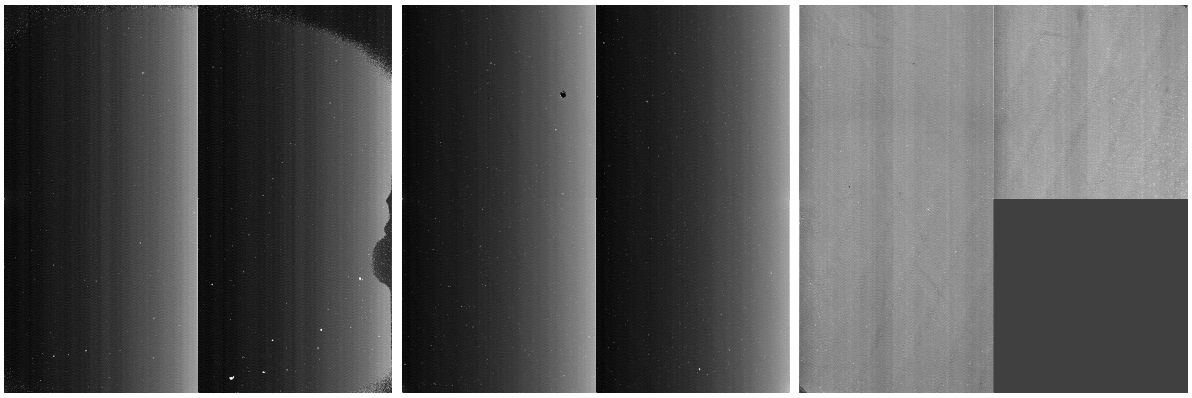

Figure 2.9: Dark frames for the J, H and K_s bands for the 2018/19 observing run.

2.3 Preliminary Data Reduction with the SIRIUS Pipeline

The SIRIUS pipeline, developed and maintained by Yasushi Nakajima, was used to perform a preliminary data reduction on all the raw frames obtained with the SIRIUS camera. The pipeline uses `pipeneolist` tasks in IRAF[3] (Image Reduction and Analysis Facility) to create the ASCII files containing the statistics and then runs the `pipeneo` task to reduce the raw data. The image processing consists of the four steps listed below:

[3]iraf.noao.edu.

- Dark frame subtraction
- Flat-fielding
- Sky determination and sky subtraction
- Combining the corrected frames into a single frame

Dark Frame Subtraction

The 10 dark frames of 24 s exposure that were taken during each night of observation are median-combined to make a single dark frame, which is subtracted from each dithered frame (i.e. `self`(i) frame) to create a new frame $\texttt{self}_{\rm d}(i)$. This process is repeated for the 5 s exposure frames, and the median dark frame obtained is then used to correct for the flat fields.

Flat-Fielding

The SIRIUS pipeline uses the task `autotwflat` to create a master flat field. It first generates separate flat fields for each night from pairs of brighter and fainter twilight sky frames. The pairs with the median of the pixel values less than 6000 ADUs ($\approx 30\%$ of the saturation level), are selected so that the difference of the background level is more than 2000 ADUs. The differential images created from each pair is normalised by the median of the pixel values. The normalised frames from all nights are median-combined and produce a master flat field which is called `twilight`. The frames $\texttt{self}_{\rm d}(i)$ are divided by the `twilight` frame to correct for the response of the detector. The new frames are called $\texttt{self}_{\rm d}{}^{\rm f}(i)$.

The pixel-to-pixel efficiency of the detector does not vary remarkably over a month. This variation is even small over a time scale of a year.

Sky determination and subtraction

The atmospheric emission as well as the dust or dirt in the telescope optical system can give rise to patterns on the observed frames. The J band is usually free of the sky patterns. The H band suffers significantly from the OH emission in the atmosphere. In the K_s band, the radiation of hot dust on the detector window creates patterns on the observed frames. To obtain science quality images and extract reliable photometry of the sources, these patterns should be removed from each frame. Moreover, the detector readout system divides the frames vertically in the middle, creating another pattern on the frames. The `pipeneo` task eliminates these artefacts by determining the sky and subtracting it.

The first step for sky determination is to ensure that all the frames have the same median flux value. This is obtained by scaling each dither frame, $\texttt{self}_{\rm d}{}^{\rm f}(i)$, to have the same median flux as the first dither frame in each field.

$$\texttt{self}_{\rm d}{}^{\rm f'}(i) = \texttt{self}_{\rm d}{}^{\rm f}(i) + (<\texttt{self}_{\rm d}{}^{\rm f}(1)> - <\texttt{self}_{\rm d}{}^{\rm f}(i)>)$$

In the second step the $\texttt{self}_{\rm d}{}^{\rm f'}(i)$ frames are median-combined without aligning. This ensures that no astronomical source imprints on the sky pattern, since the dithering

makes the sources move around the detector and their median flux is zero in the median-combined frames. The new frames which are called *sky* frames, are divided by the flat fields to correct for pixel-to-pixel variation of the detector.

In the last step the flat-field-corrected sky frame is subtracted from all frames in a dithering pattern and the median value of the sky background is added back to get a constant sky background value in each frame.

$$\texttt{SELF}(i) = \texttt{self}_{\rm d}{}^{\rm f'}(i) \texttt{ - sky + <sky>}$$

Dither Combination

The SIRIUS pipeline aligns and median-combines the SELF(i) dithered frames to create the final image. This alignment is done by running the `daofind` and `phot` IRAF tasks on the dithered images. A list of stars with fluxes of 10σ greater than the sky background and a magnitude error of $\epsilon \leq 0\overset{\rm m}{.}1$ is created for each of the dithered images. The stars are selected from the central region of the images where S/N is high. After aligning, the frames are average-combined resulting in the final image with a gain enhanced by the factor of N (the number of frames in the dither pattern), and a reduced noise by a factor of $1/\sqrt{N}$.

2.3.1 Image Calibration

The final images from the SIRIUS pipeline are still not quite ready for photometry. The image coordinates must first be transformed into the World Coordinate System (WCS), and the instrumental magnitudes must be converted to calibrated apparent magnitudes in a standard system, i.e. the *astrometric* calibration, and the *photometric* calibration. The 2MASS Point Source Catalogue (2MPSC, Skrutskie et al., 2006), which contains 470 million stars and matches the three filters used in our survey, is used as a standard system for both calibration procedures.

Astrometric Calibration

The SIRIUS pipeline converts the image coordinates to WCS and embeds it into the headers of the FITS images. The script was developed by Noriyuki Matsunaga and implements the Optimistic Pattern Matching (OPM) algorithm proposed by Tabur (2007). The OPM algorithm works as follows:

First a list of the 50 brightest detected stars (DoPHOT; Schechter et al. (1993)) is created for each image. Then, the header information from the FITS images is used to create a second list of the 50 brightest stars out of the 2MPSC catalogue (Cutri et al., 2003). 2MPSC contains over 470 million sources. This all-sky survey is more than 99% complete to $J < 15\overset{\rm m}{.}8$, $H < 15\overset{\rm m}{.}1$ and $K_s < 14\overset{\rm m}{.}3$. For all combinations of three stars in the two lists, triangles are produced, with each triangle parametrized by two numbers (x_t, y_t). x_t is the dot product of the two longest sides of the triangle while y_t is the ratio of the longest to the shortest side. In this triangle space, the triangular combination of two closely located stars with a third one occurs far less frequently than the triangular combination in which all three sources lie close to each other. Hence, any match found in this region is assumed to be a good match and limiting the matching process to these regions reduces the computational time considerably.

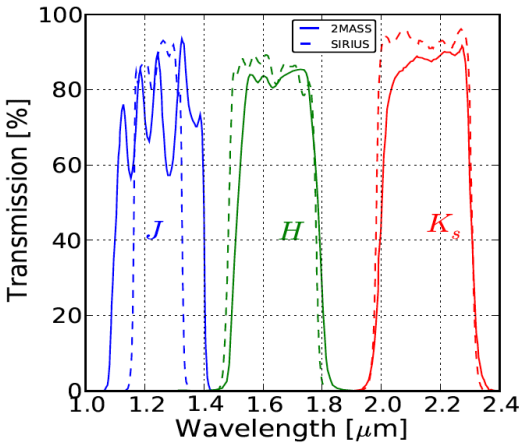

Figure 2.10: The IRSF/SIRIUS (Yasushi Nakajima; private communications) and 2MASS transmission curves for the J, H, K_s bands.

After verifying the goodness of each match, the astrometric transformation is performed using the IRAF task `ccmap`. The astrometric transformation between the image physical coordinates, and the calibration catalogue WCS, is done by solving the equations:

$$\begin{aligned} X &= C_0 x + C_1 y + C_2 \\ Y &= C_3 x + C_4 y + C_5, \end{aligned} \tag{2.1}$$

where (x, y) are the objects physical coordinates, (X, Y) are the WSC (J2000) of the matched pair and C_i are the transformation coefficients. To check the accuracy of the astrometric calibration a comparison between the matched pairs of galaxies in the VSCL clusters and 2MASX is presented in Section 3.3.2.

Photometric Calibration

Ideally, photometric calibration is performed using observations of a set of standard stars (e.g. Carter and Meadows, 1995; Persson et al., 1998) interspersed with observations of target sources. But this method is time-consuming. An alternative is to use the 2MPSC as a standard catalogue. This method is especially suitable in this work since the star-crowding is high in the ZoA. The transmission properties of the filters differ between 2MASS [4] and SIRIUS (see Fig. 2.10). The 2MPSC magnitudes are therefore, converted to the SIRIUS filter magnitude system using the equations provided by Yasushi Nakajima (private communications):

$$\begin{aligned} J_{\rm SIRIUS} &= J_{\rm 2MASS} + (-0.045 \pm 0.008)(J-H)_{\rm 2MASS} + (-0.001 \pm 0.008) \\ H_{\rm SIRIUS} &= H_{\rm 2MASS} + (0.027 \pm 0.007)(J-H)_{\rm 2MASS} + (-0.009 \pm 0.008) \\ K_{s_{\rm SIRIUS}} &= K_{s_{\rm 2MASS}} + (0.015 \pm 0.008)(J-K_s)_{\rm 2MASS} + (-0.001 \pm 0.008). \end{aligned} \tag{2.2}$$

The standard magnitudes, m_λ, can be obtained from the instrumental magnitudes, m^i_λ, which vary between instruments and depend on the photometric conditions, using

[4] Explanatory Supplement to the 2MASS Second Incremental Data Release available at http://www.ipac.caltech.edu/2mass/releases/second/doc/explsup.html.

the equation

$$\begin{aligned} m_\lambda &= ZP_\lambda + m^i_\lambda + c_1 \times X + c_2 \times m_{\rm col}\,, \\ \text{where} \quad m^i_\lambda &= -2.5 \log\left(\frac{F_\lambda}{t_{\rm exp}}\right). \end{aligned} \tag{2.3}$$

ZP_λ is the zero-point magnitude in a given waveband, c_1 is the airmass extinction coefficient, X is the airmass, c_2 is the colour coefficient, $m_{\rm col}$ is a colour term, $t_{\rm exp}$ is the exposure time per image and F_λ is the background-subtracted flux of a source in a given waveband. Equation 2.3 is not dependent on colour, based on what the foregoing observations with IRSF/SIRIUS have shown and therefore c_2 was set to zero (Parick Woudt; private communication). From Equation 2.3 one obtains:

$$m^{\rm SIRIUS}_\lambda = ZP'_\lambda + m^i_\lambda \tag{2.4}$$

where $m^{\rm SIRIUS}_\lambda$ is the SIRIUS magnitude and the zero-point $ZP'_\lambda = ZP_\lambda + c_1 \times X$.

To derive the zero-point magnitude, the magnitudes of the cross-matched stars between IRSF and 2MAPSC in each field were obtained. Then using the IRAF task `phot`, the magnitudes of these point sources were determined with IRSF applying a circular aperture large enough to capture the total flux of the stars. The zero point was then calculated for each matched pair of stars using Equation 2.4. The median values of the zero points in each image after determination, was written to the fits headers. The distribution of the zero-point magnitudes over the various observing runs are presented in the next section.

2.3.2 Photometric Properties of the Images

To ensure that all the images were observed under photometric conditions, their seeing values and magnitude zero-points (ZPs) in the three observing periods were assessed. Images with seeing of FWHM$\geq$ 2.″3 (5.11 pixels) in the first two observing runs were marked and re-observed in the 2018/2019 observing run. During the third observing run, images that were still of unsatisfactory quality were re-observed under photometric conditions. In total there are 263 images distributed over 6 mosaics in this survey.

The distribution of the seeing and ZP values are shown in Fig. 2.11 and the values of the average seeing and the mean ZP with their respective standard deviations (σ) are given in Table 2.4. The images that are being used in the further data analysis process are restricted to have ZPs that lie within a value of $\langle ZP \rangle \pm 2\sigma$ and a seeing of FWHM$<$ 2.″3. The J and H bands are more sensitive to the photometric conditions compared to the K_s band and hence a slight shift towards the right is seen in the seeing histogram (left panel of Fig. 2.11).

Table 2.4: Mean magnitude zero-point ($\langle ZP \rangle$) and average seeing with their respective standard deviations (σ) for all 263 images.

Band	$\langle ZP \rangle$ (mag)	σ (mag)	Seeing (arcsec)	σ (arcsec)
J	20.604	0.185	1.55	0.316
H	20.773	0.172	1.46	0.302
K_s	19.967	0.167	1.37	0.265

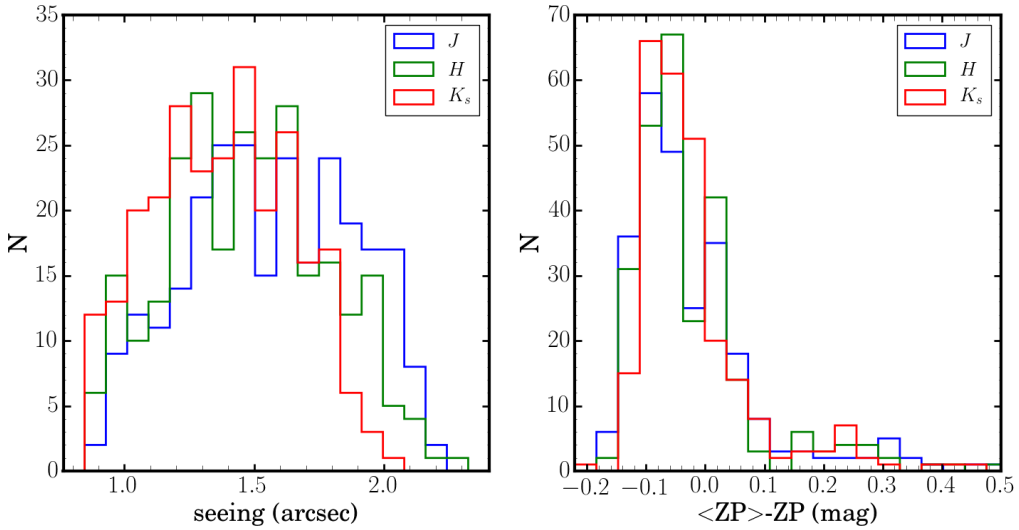

Figure 2.11: The distribution of the seeing (left) and magnitude zero-points (right) of the final 263 survey images that were accepted for photometry in J, H, K_s bands.

A comparison between the mean ZPs of this survey (the VSCL survey) and the previous surveys in which the IRSF telescope had been used in the ZoA with the same imaging set-up (Cluver, 2008; Riad, 2010; Williams, 2011) is shown in Fig. 2.12. The ZPs of the VSCL survey (cyan symbols) are brighter compared to the earlier surveys. The variation of the reflective quality of the telescope mirror is presumably the reason for this difference. A detailed analysis of the time variation of the ZP and its correlation with the reflective quality of the telescope mirror is given in Riad (2010).

2.4 Galaxy Identification

After the preliminary data reduction using the SIRIUS pipeline, the images were ready for extraction of sources to create a catalogue of galaxies with their photometric parameters.

Various software packages such as FOCAS (Jarvis and Tyson, 1981), COSMOS (Beard et al., 1990) and Source Extractor (Bertin and Arnouts, 1996), have been developed to automate the process of identifying galaxies, stars or other astronomical objects. The source identification routines in these algorithms perform well at high Galactic latitudes, however their performance does deteriorate towards sources in crowded fields and foreground extinction, such as near the GP in the ZoA (Beard et al., 1990). However, manual source identification is time consuming and can have observer-dependant biases, i.e. the number of identified galaxies can vary from one person to another. I therefore opted for a combination of automatic and manual galaxy identification, by using Source Extractor to identify the potential sources, then visually inspected and verified each identified source using the RGB images in a pipeline specifically developed for analysing IRSF data (hereafter the IRSF pipeline, Williams, 2011), before starting the photometry analysis.

2.4.1 Visual Inspection of Galaxies in a Sample of Fields

Before utilizing any software to identify galaxies, I first familiarised myself with how obscured galaxies in the ZoA can look on the IRSF images. I therefore, started processing a

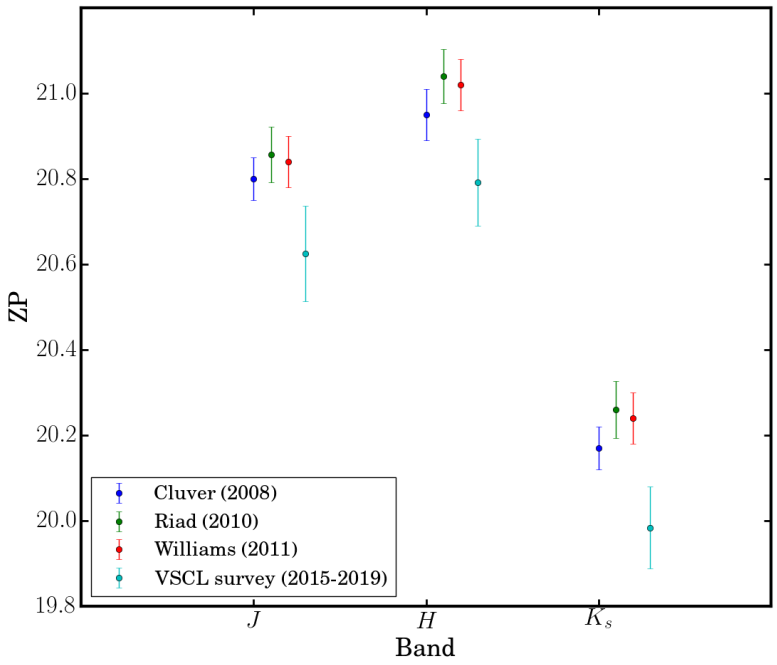

Figure 2.12: Comparison of the mean magnitude zero-points in the J, H and K_s bands for this survey to those of the same telescope and imaging set-up. The cyan dots show mean ZPs of the VSCL survey, while blue, green and red dots illustrate Cluver (2008); Riad (2010) and Williams (2011) values respectively.

sample of nine fields pertaining to the potential cluster VC08. This data sample underwent a preliminary reduction using the SIRIUS pipeline as described in Sect. 2.3.

Since galaxies are naturally extended and their colours are redder than the foreground stars or other astronomical sources, identifying them in RGB composite images is feasible. To produce the RGB images, the three bands J, H and K_s are written into the Blue, Green and Red channels respectively of an image in application SAOImage `DS9`[5]. I visually identified reddish extended and slightly fuzzy objects as potential galaxy candidates from the RGB composite images of nine sample fields in VC08, and found 68 galaxy candidates in this way. In a second step the IRSF pipeline (discussed in details in Sect. 3.1) was run on these candidates to derive their photometric parameters such as the isophotal J, H and K_s magnitudes.

To differentiate between true galaxies and other extended Galactic objects or blended stars, I ran, in addition to the visual inspection of these objects, various diagnostics. In Fig. 2.13 I plotted for instance the extinction-corrected colour-colour and colour versus radius diagrams[6] in the top and bottom panel respectively for 68 visually identified galaxies in the nine fields. The dashed lines in the diagrams show the mean NIR isophotal colours determined by Jarrett (2000), $(J-H)$=$0\overset{\text{m}}{.}64$, $(H-K_s)$=$0\overset{\text{m}}{.}28$ and $(J-K_s)$=$0\overset{\text{m}}{.}92$ for nearby (low redshift) early-type galaxies[7]. The candidate galaxies with $r \geqslant 2''$ are

[5]http://ds9.si.edu/site/Home.html

[6]The dust of the Milky way causes the objects to appear fainter. This effect was corrected for the magnitudes of objects and then the colours were measured. More detailed discussion on the effect of the extinction on magnitudes and NIR colours is given in Sect. 3.4.

[7]I use NIR colours of S0 galaxies in this work, since clusters mostly contain early-type galaxies particularly in their central regions.

shown in red. The isophotal radius, r, is the radius of the isophote at surface brightness 20 mag arcsec^{-2}. The cut-off radius was selected after analysing the colour-radius diagrams which showed a clear gap around $r = 2''$: the colours of extended objects with $r < 2''$ are extremely blue. It was verified in the colour-colour diagrams that objects with $r < 2''$ are mostly quite offset from the mean values (where the dashed lines cross) and their blue colours which indicate that they are either stars or other Galactic objects but not galaxies.

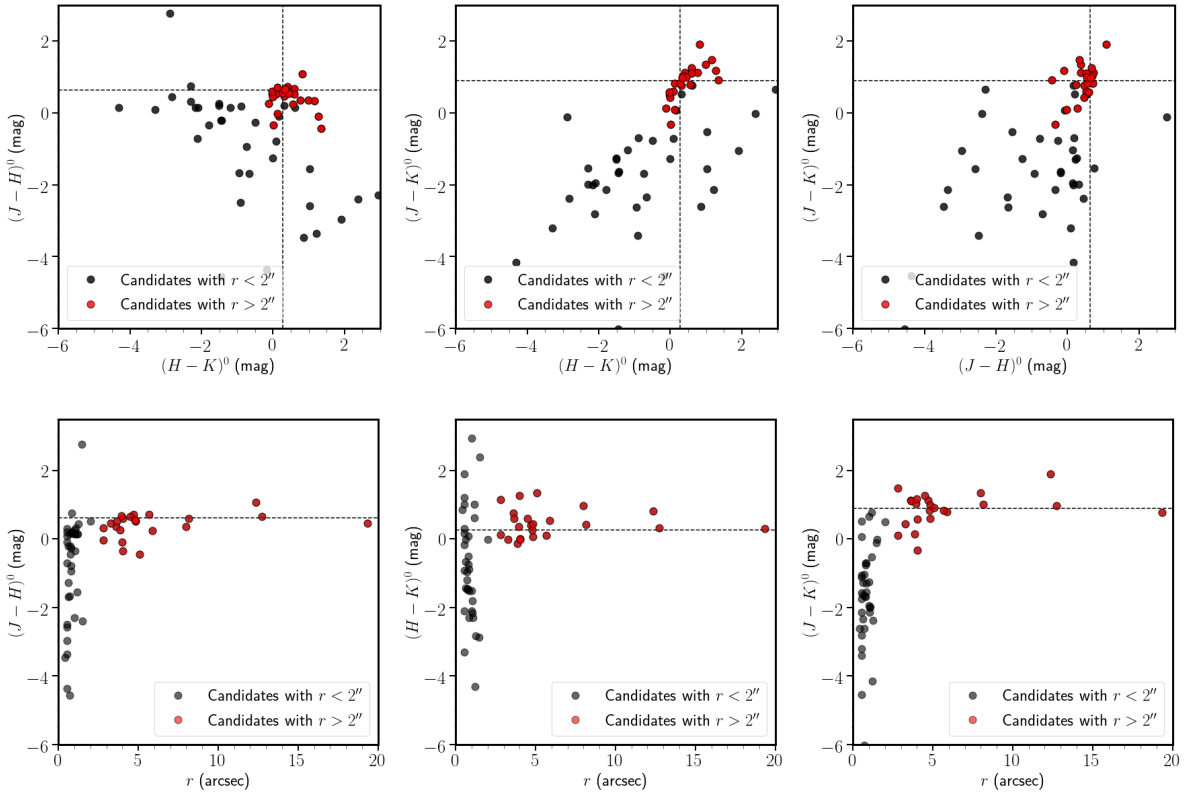

Figure 2.13: Colour-colour (top panel) and colour-radius (bottom panel) diagrams of 68 galaxy candidates in nine fields of VC08.

Based on this analysis, objects with a radius $r \geqslant 2''.0$ were classified as potential galaxies contrary to the others which either are extended Galactic objects or blended stars. This classification reduced the sample of reliable galaxy candidates suitable for scientific analysis considerably.

2.4.2 Using Source Extractor to identify galaxy candidates

Henceforth, the process of identifying galaxy candidates for the six VSCL clusters was done using Source Extractor (Bertin and Arnouts, 1996). Source Extractor is a tool that performs automatic source identification. Although it is particularly oriented towards the reduction of large scale galaxy-survey data (located generally at latitudes far from the Milky Way), it performs reasonably well on moderately crowded star fields (Bertin and Arnouts, 1996). The various sub-processes of Source Extractor are controlled by different sets of parameters, which can be defined in a configuration file by the user.

The Source Extractor image analysis steps are explained in detail in Bertin and Arnouts (1996) and are summarized below:

- Background and rms determination
- Background subtraction
- Filter application to smooth over local variations due to bright objects in the image
- Object detection as a number of connected pixels above a specified threshold
- Close object deblending
- Performing photometry
- Star/Galaxy classification
- Catalogue creation of geometric and photometric calibration

Of these steps, the most relevant to the purposes of the VSCL survey are star/galaxy classification and photometry. These are explained further.

Star/Galaxy Classification

Source Extractor uses a Neural Network (NN) to classify the extracted objects either as stars or extended sources. The NN yields an index, CLASS-STAR, that indicates the stellarity-index. CLASS-STAR ranges from 0 for galaxies to 1 for point sources; with a likelihood of being one or the other as follows:

- CLASS-STAR≤ 0.35 (galaxies),
- $0.35 <$ CLASS-STAR < 0.8 (stars or galaxies),
- CLASS-STAR ≥ 0.8 (stars).

The Source Extractor classification has been shown to be reliable by testing it on simulated and real images (Bertin and Arnouts, 1996). In my analyses, I use only those sources for which the stellarity-index (CLASS-STAR) is less than 0.35 i.e. classified as galaxies. Examples of galaxies identified using Source Extractor can be found in Sect. 3.1.1.

Photometry

Source Extractor can derive four types of photometry – isophotal, corrected isophotal, aperture and Kron photometry. The isophotal area of the object is the pixel area above the detected threshold. The isophotal flux is the flux enclosed within the isophotal area after sky subtraction. This flux is converted to magnitudes using the effective gain and the zero-point magnitude. The gain is calculated as follows:

$$\mathrm{gain_{eff}} = 2 \times N \times \mathrm{gain_{det}}/3 \tag{2.5}$$

where N is the number of frames in a median-combined image.

The zero-point magnitude for a median-combined image is determined using:

$$\mathrm{mag_{ZP}} = \mathrm{ZP} + 2.5 \log(\text{average exposure time}) \tag{2.6}$$

The Source Extractor output catalogue has a parameter, `flag`, which indicates the reliability of the photometry. In the final extracted output catalogue of Source Extractor, a number is assigned to each source. This number is the combination of one or more of the following flags:
"0": reliable photometry
"1": photometry may be affected by the neighbouring objects
"2": object was originally blended with another object
"4": at least one pixel of the object is saturated (or very close to being saturated)
"8": object is too close to the boundary of an image
"16": object's isophotal aperture is incomplete or corrupted
"32": object's isophotal aperture is incomplete or corrupted
"64": a memory overflow happened during deblending
"128": a memory overflow happened during extraction.

In subsequent steps only those galaxy candidates for which the photometry is reliable (flag = "0", "1", "2") are considered.

Based on the output parameters of Source Extractor in the three J, H and K_s bands, I prepared a list of the sources that were common and had reliable photometry in all three bands (the number of sources were not the same in all three bands). Even after using CLASS-STAR and flags to clean the final output of the galaxy candidates, the visual inspection process uncovered quite a few spurious detections that needed to be removed. One method to identify false detections is based on NIR colours. The NIR colours are derived from the isophotal magnitudes[8] and were utilized to finalize the galaxy catalogue list. Objects with colours far from the mean NIR galaxy colours, $(J-H)$=$0\overset{\text{m}}{.}64$, $(H-K_s)$=$0\overset{\text{m}}{.}28$ and $(J-K_s)$=$0\overset{\text{m}}{.}92$ (Jarrett, 2000), were removed in addition to all objects with $r < 2''$.

Optimising Source Extractor Parameters

The Source Extractor configuration file must be adjusted to the characteristics of the imaged fields. The parameters of the configuration file can be defined by the user. Since the VSCL survey is carried out in the ZoA, the high stellar density makes it quite hard for Source Extractor to deblend adjacent stars and other Galactic objects and the configuration parameters needed to be optimised for work in the ZoA.

There are a few parameters in Source Extractor related to detection of galaxies in crowded fields. These are:

- DETECT_MINAREA
- DETECT_THRESH
- DEBLEND_NTHRESH
- DEBLEND_MINCONT

The parameters were optimized based on deep visual galaxy identification pursued on the sample of nine fields (Sect. 2.4.1). The parameters were chosen empirically and iterated on to result in a catalogue that included the objects that were visually confirmed

[8]Note that the isophotal magnitudes derived by Source Extractor were in agreement with 2MASX isophotal magnitudes.

as galaxies. While minimizing the number of false positives, the Source Extractor galaxy output list objects were all visually inspected. Here I briefly describe these parameters and the selected values:

DETECT_MINAREA
This parameter sets the minimum number of neighbouring pixels to initiate a detection in Source Extractor. The flux of these pixels must be over the DETECT_THRESH. The value of 10 pixels worked reasonably well on images of the VSCL survey.

DETECT_THRESH
Every object must have a threshold value above the local background to be detected. After multiple tests, the value 1.5 was selected for this parameter which is given in units of the standard deviation of the background (σ). This value was optimised to not miss out on any faint or low surface brightness galaxy.

DEBLEND_NTHRESH

This parameter is the number of sub-thresholds between the selected threshold and the maximum count in the object. It changes the aperture shape and orientation: at higher values a larger aperture is fitted and therefore more blended objects can be detected. Source Extractor only accepts the powers of 2 for DEBLEND_NTHRESH. The default value is 32 and it worked effectively on the images of the VSCL survey.

DEBLEND_MINCONT
Source Extractor is able to use the count values of an object and break it up into smaller or larger fractions. For example if a small galaxy is very close to a bright star, DEBLEND_MINCONT provides a minimum flux ratio for which the galaxy can be detected successfully. The smaller value for DEBLEND_MINCONT results in the detection of even the faintest local peaks as an object. The value of 0.001 was chosen for the VSCL survey.

The background grid size was selected as BACK_SIZE=64 pixels. This is not too small for the flux of the extended objects to be absorbed by the background nor too large to not be able to reconstruct the small scale variations of the background. A sample configuration file with optimized parameters values for all 263 fields in the VSCL survey is provided in Table 2.5. These values were rechecked and verified for the observed fields in this work.

Source Extractor Output

Source Extractor generates a catalogue of geometric and photometric parameters of the extracted sources. Some of these parameters that are either used in cleaning the list of galaxy candidates or in preparation of the input tables to feed into the IRSF pipeline (Section 3.1) are listed below.

- ALPHA_SKY: Right Ascension
- DELTA_SKY: Declination
- MAG_ISO: Isophotal magnitude

Table 2.5: Source Extractor parameters

Parameter	Value	Description
DETECT_MINAREA	10	minimum number of pixels above threshold
DETECT_THRESH	1.5	<sigmas> or <threshold>, <ZP> in mag arcsec^{-2}
ANALYSIS_THRESH	1.5	<sigmas> or <threshold>, <ZP> in mag arcsec^{-2}
FILTER	Y	apply filter for detection (Y or N)?
FILTER_NAME	default.conv	name of the file containing the filter
DEBLEND_NTHRESH	32	Number of deblending sub-thresholds
DEBLEND_MINCONT	0.001	Minimum contrast parameter for deblending
CLEAN	Y	Clean spurious detections? (Y or N)?
CLEAN_PARAM	1.0	Cleaning efficiency
MASK_TYPE	CORRECT	Type of detection MASKing: can be NONE, BLANK or CORRECT
PHOT_APERTURES	5	MAG_APER aperture diameter(s) in pixels
PHOT_AUTOPARAMS	2.5, 3.5	MAG_AUTO parameters: <Kron_fact>, <min_radius>
PHOT_PETROPARAMS	2.0, 3.5	MAG_PETRO parameters: <Petrosian_fact>, <min_radius>
SATUR_LEVEL	50000.0	level (in ADUs) at which arises saturation
MAG_ZEROPOINT	zero-point	magnitude zero-point
GAIN	91.66	detector gain in e-/ADU
GAIN_KEY	GAIN	keyword for detector gain in e-/ADU
PIXEL_SCALE	0.45	size of pixel in arcsec (0=use FITS WCS info)
SEEING_FWHM	seeing	stellar FWHM in arcsec
STARNNW_NAME	default.nnw	Neural-Network_Weight table filename
BACK_SIZE	64	Background mesh: <size> or <width>, <height>
BACK_FILTERSIZE	3	Background filter: <size> or <width>, <height>
BACKPHOTO_TYPE	GLOBAL	can be GLOBAL or LOCAL

- MAGERR_ISO: RMS error for isophotal magnitude
- KRON_RADIUS: Kron radius in units of A or B
- A_IMAGE: Profile RMS along major axis
- B_IMAGE: Profile RMS along minor axis
- THETA_IMAGE: Position angle
- FLAGS: Extraction flags
- CLASS_STAR: S/G classifier output

Two sets of input tables from the Source Extractor output need to be provided to run the first and second part of the IRSF pipeline. The first one contains the RA and Dec of the galaxy candidates. The second one consists of RA, Dec, major and minor axes and the position angle of the galaxy candidates. The major and minor axes are derived using:

$$\begin{aligned} a &= \text{KRON_RADIUS} \times \text{A_IMAGE}, \\ b &= \text{KRON_RADIUS} \times \text{B_IMAGE}. \end{aligned} \tag{2.7}$$

2.5 Summary

To learn more about the VSCL, a series of deep NIR observations of its constituent galaxy clusters were conducted using the IRSF telescope during three observing runs (2015-2019). Each cluster was observed in a mosaic of 32 fields centred on prospective VSCL clusters. Six of the observed clusters have a full set of science quality images with mean seeing values of FWHM=$1\farcs55$, $1\farcs46$ and $1\farcs37$ in the J, H and K_s bands respectively. I reduced the images using the SIRIUS pipeline and performed astrometric and photometric calibration. Analysis of visually identified galaxy candidates in a sample of fields based on colours showed that any object with $r < 2''$ is increasingly likely to be a star or other Galactic objects and not a galaxy. The Source Extractor software (an automatic detection algorithm) was used for galaxy identification. The Source Extractor parameters were optimised to apply on the fields in the ZoA with high stellar density. The galaxy candidates identified by Source Extractor were validated through visual inspection of the RGB composite images to make sure that no obvious galaxy was missed, while minimizing the number of false positives. Any object that seemed to be extended but was not likely a galaxy based on colour or size or morphology was discarded.

The photometry on the acquired galaxy catalogue using the IRSF pipeline will be explained in detail in the next chapter.

Chapter 3

Galaxy Photometry

The previous chapter described how Source Extractor was used to identify galaxies in the NIR imaged VSCL clusters. This chapter focuses on the derivation of the photometric parameters of galaxy candidates and data quality assessment of the parameters.

Section 3.1 starts with a description the IRSF pipeline which consists of: interactive manual galaxy verification, star subtraction and extraction of the photometric parameters such as isophotal and total magnitudes. In Sect. 3.3, the internal and external consistency of the photometric parameters is examined. The astrometric and photometric parameters of the galaxies that were observed more than once in the overlapping areas were used to check the internal consistency. Counterpart galaxies in 2MASX were used for an external consistency verification. The derived offsets of parameters were also compared to those of other surveys that used the same telescope and observation set-up, such as Riad (2010). In Sect. 3.2 the NIR extended source catalogue with the derived parameters is described and a sample catalogue is presented for one of the clusters (VC08). The effect of extinction on the photometric parameters and applied extinction corrections are explained in Sect. 3.4. In the final section the completeness magnitude limit for the NIR cluster galaxies is derived. This magnitude limit is essential to the subsequent derivation and analysis of the properties of the galaxy clusters.

3.1 The IRSF pipeline

3.1.1 Galaxy verification

Section 2.4 described the identification process of galaxies from the extended source list created with Source Extractor followed by a visual inspection to distinguish galaxies from blended stars or other Galactic objects. This was based on my experience from the analysis of nine fields using the first part of the IRSF pipeline (see Sect. 2.4.1).

The script `findgal` used in the first part of the pipeline was developed by Wendy Williams (Williams, 2011). It uses `pyDS9`[1] that interfaces with the astronomical imaging and data visualization application SAOImage `DS9`[2]. It displays the RGB composite images with the interactive `DS9` interface with which the user can mark the approximate centers of the galaxies and specify their major and minor axes. This information is recorded in the form of a table and is subsequently used in the pipeline that performs the star subtraction and photometry. Figure 3.1 shows an example of objects found by Source Extractor and

[1] http://hea-www.harvard.edu/RD/pyds9/.
[2] http://ds9.si.edu/site/Home.html.

displayed by DS9 using the script findgal. I used findgal to display all the fields of the six fully imaged clusters to select all objects that clearly are galaxies. These sources were then saved for processing through the rest of the IRSF photometry pipeline.

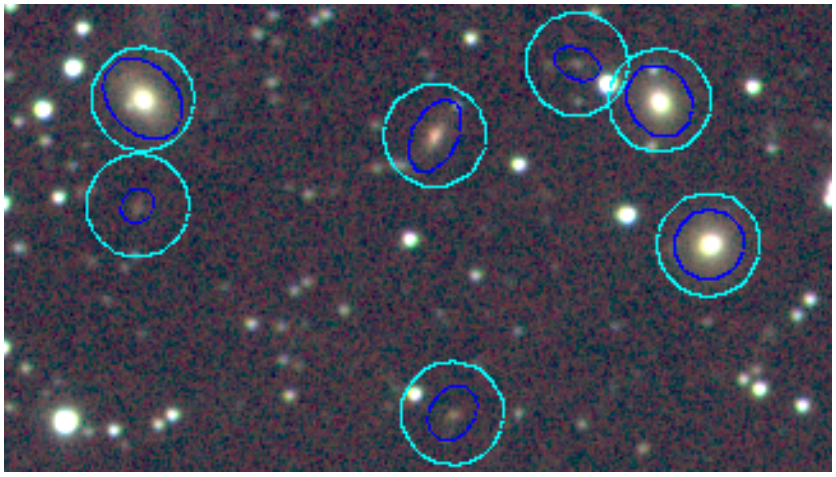

Figure 3.1: An example of how findgal highlights and displays potential candidates in a field. Light blue circles indicate the galaxy candidates. The dark blue ellipses are drawn based on the first estimation of the minor and major axes by the user. The size of this postage stamp is $\sim 2\farcs4 \times 1\farcs3$.

3.1.2 Star subtraction

In the regions close to the GP ($|b| \leq 10°$), increased stellar density results in higher contamination from neighbouring or overlapping stars (Jarrett et al., 2000b). This has two consequences for galaxy photometry: isolating the flux of a galaxy becomes more difficult due to the light from nearby or overlapping sources. Moreover, the flux from unresolved stars in crowded fields causes an increase in the noise amplitude of the background sky (or background surface brightness). This makes the galaxies appear smaller than their actual sizes since the outer regions of the Low Surface Brightness (LSB) galaxies fade into the background sky, and complicates the detection of LSB galaxies overall.

The second part of the pipeline removes the stars around the detected galaxies via Point-Spread-Function (PSF) fitting. It first determines an average PSF for point sources in the field which is used to remove the stars in a box around each detected galaxy. The PSF-fitting routine was developed by Takahiro Nagayama (private communication) and Riad (2010) using the DAOPHOT package in IRAF, and was modified by Williams (2011) to run in PyRAF[3]. The star-subtraction pipeline script performs the following steps:

- Creation of a PSF : The PSF is specific to each optical instrument. In the case of IRSF, the PSF has a symmetric Gaussian profile. This shape is sensitive to atmospheric turbulence (characterized by seeing). Saturated stars also cause the shape of the PSF to deviate from the ideal. To mitigate this effect, an average PSF can be created by selecting a number of stars distributed all over the image, using the following algorithm:

  1. A maximum of 50 unsaturated and isolated stars are selected over the whole image.

[3]http://www.stsci.edu/institute/software_hardware/pyraf

2. With this set of stars, an initial PSF is created and used to subtract all the stars in the image except the PSF model stars.
3. A new PSF is modeled based on the set of selected stars. This process reduces any contamination from nearby stars and creates an improved PSF.
4. This improved PSF is used to again remove stars from the original image and hence only the selected stars are left in the image. The set of selected stars are once again modeled to create the final PSF, which is then used in star subtraction.

- STAR SUBTRACTION AROUND EACH GALAXY : This script removes the stars around each galaxy without altering the galaxy light profile. The user is able to verify whether the identified source is a star or a galaxy, and remove false detections or add unidentified sources. The steps of star subtraction are listed below:

  1. In each image the sky background and the root mean square (rms), σ, is determined using the `imstatistics` task in IRAF with 30 iterations and 3σ clipping.
  2. The galaxy is modeled using the `ellipse` and `bmodel` tasks and subtracted using the `imarith` task.
  3. The bright stars are detected in the galaxy-subtracted image and removed. Source Extractor is used to detect all the sources above 3σ of the background. PSF photometry and removal of these sources is done by the `phot` and `allstar` tasks in the DAOPHOT package of IRAF. A file is created by `allstar` containing the details of the subtracted stars.
  4. The previous procedure is repeated to detect and remove faint stars, with the threshold parameter of Source Extractor chosen to be 1.8σ of the sky background and another list of subtracted stars is created and appended to the original list. All these stars are removed from the original image.
  5. Any flaw in the PSF-fitting results in residuals in the image, which are then removed.
  6. Steps 2 to 5 are repeated four times. Each iteration improves the PSF model leading to a more accurate galaxy photometry.

- POSTAGE STAMP CREATION : A three colour postage stamp image of each galaxy before and after removing the stars is created during star subtraction. The RGB images are produced using the `make_rgb_image` routine in `APLpy`[4].

Figure 3.2 shows the cutouts of three galaxy candidates in VC08 before and after star-subtraction. As shown by Nagayama et al. (2004), the photometry of galaxies after star-subtraction in star-crowded regions has a systematic difference of $\Delta m = 0\overset{\mathrm{m}}{.}04 \pm 0\overset{\mathrm{m}}{.}2$ compared to their original photometry (if they were not located in star-crowded regions). The difference is well within the standard deviation of the derived magnitudes in the VSCL survey. This means that the star-subtraction process works satisfactorily in performing photometry on galaxies.

[4]https://aplpy.github.io/.

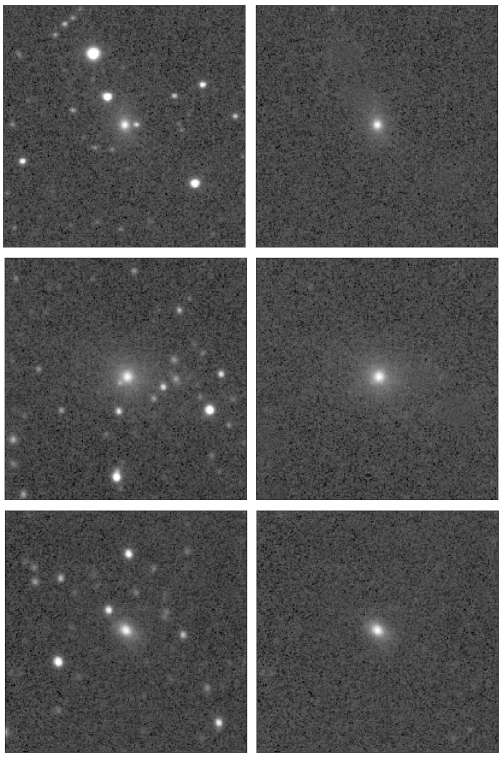

Figure 3.2: The postage stamps of three galaxy candidates in the VC08 cluster at $\langle v \rangle \sim 17316$ km s^{-1} in the K_s band, before (left) and after (right) star-subtraction. The size of the cutouts is 200×200 pixels which translate to $90'' \times 90''$ given the resolution of the IRSF of $0\farcs45$ pix^{-1}.

3.1.3 Galaxy photometry

The third part of the pipeline extracts astrometric, geometric and photometric parameters of the galaxies. The various derived parameters are explained below.

Astrometric Parameters

- **Source Position:** To find the centre of the source, first the $J + H + K_s$ 'super co-add' images are made. The central positions are determined from the intensity-weighted centroid using the following equations:

$$\begin{aligned} X = \bar{x} &= \frac{\sum_i I_i x_i}{\sum_i I_i} \\ Y = \bar{y} &= \frac{\sum_i I_i y_i}{\sum_i I_i} \end{aligned} \tag{3.1}$$

  where I_i is the intensity at source pixel (x_i, y_i).

Geometric Parameters

- **Ellipticity and Position angle:** The task `ellipse` in IRAF is used to determine the ellipticity ($\epsilon = 1 - b/a$) and position angle (ϕ, measured counterclockwise from +Y), for a fixed (X, Y) coordinate. The output table from `ellipse` contains 40 or more columns with parameters for each fitted isophote, one row per isophote. The intensity counts contained within the fitted isophotes, the position angle, ellipticity and the corresponding errors are among the output parameters of the table. Each

isophote is fitted at a pre-defined, fixed semi-major axis length. The first elliptical isophote is based on an estimate using the approximate values of the center coordinates (X,Y), ellipticity and position angle of the galaxy. This reduces the two-dimensional image into a one-dimensional intensity distribution as a function of position angle.

The ellipticity and position angle are measured in the outer parts of the disk, where they are usually stable. The average value of the ellipticity and position angle is determined between the 1σ and 2σ isophotes, where σ is the sky rms. The ellipse parameters are determined for each J, H, K_s band individually.

PHOTOMETRIC PARAMETERS

- **Radial Surface Brightness Profile:** The astrometric and geometric parameters obtained above are used to compute the one-dimensional radial surface brightness profiles (SBP) of the galaxy candidates using the IRAF task `ellipse`. The pipeline then uses the double Sérsic function to simultaneously fit an inner bulge and an outer disk to the galaxies with $n=4$ and $n_2=1$ respectively in the following equation:

$$\mu(a) = -2.5\,log\,(10^{-0.4(\mu_0+1.086(\frac{a}{r_h})^n)} + 10^{-0.4(\mu_{02}+1.086(\frac{a}{r_{h_2}})^{n_2})}), \tag{3.2}$$

In terms of intensity, this equation becomes

$$I(a) = I_0 \exp\left(\frac{a}{r_h}\right)^n + I_{02} \exp\left(\frac{a}{r_{h_2}}\right)^{n_2}, \tag{3.3}$$

where I_0 is the intensity at centre and the parameter n is the "Sérsic index" and constrains the degree of curvature of the profile. Number 2 in μ_{02}, I_{02} and $\left(\frac{a}{r_{h_2}}\right)^{n_2}$ indicates the parameters in the second Sérsic function. After fitting the double Sérsic profile on the radial profiles of galaxies in each J, H, K_s bands, the pipeline measures the difference between the magnitude at the maximum radius and the limit $r = \infty$ for each galaxy. If $\Delta m > 1$ mag, the pipeline only fits an exponential profile on the outer disk of the galaxy. Figure 3.3 shows the SBP derived by IRSF pipeline for one galaxy in VC08 in the J, H and K_s bands. The SBPs are used to determine the morphology of the galaxies by means of the Sérsic index and to derive the total and isophotal magnitudes of the galaxies.

- **Total Magnitudes:** An accurate estimation of the remaining undetected flux below the sky background noise can be obtained by extrapolating the double Sérsic function, following Kirby et al. (2008). The difference between the magnitude at the maximum radius and the limit $r = \infty$ for each galaxy is derived by:

$$\Delta m = -2.5 \log\left(\frac{I_{\rm missing}}{I_{\rm total}}\right) \tag{3.4}$$

where

$$\begin{aligned} I_{\rm missing} &= \int_0^{a_{\rm tot}} 2\pi(1-\epsilon) I(a)\, a\, {\rm da} \\ &= \int_0^{a_{tot}} 2\pi(1-\epsilon)\left[I_0 \exp\left(\frac{a}{r_h}\right)^n + I_{02} \exp\left(\frac{a}{r_{h_2}}\right)^{n_2}\right] a\, {\rm da} \\ &= 2\pi(1-\epsilon)\left\{\frac{I_0 r_h^2}{n}\Gamma\left[\frac{2}{n}, \left(\frac{r_{\rm tot}}{r_h}\right)^n\right] + \frac{I_{02} r_{h_2}^2}{n_2}\Gamma\left[\frac{2}{n_2}, \left(\frac{r_{\rm tot}}{r_{h_2}}\right)^{n_2}\right]\right\} \end{aligned} \tag{3.5}$$

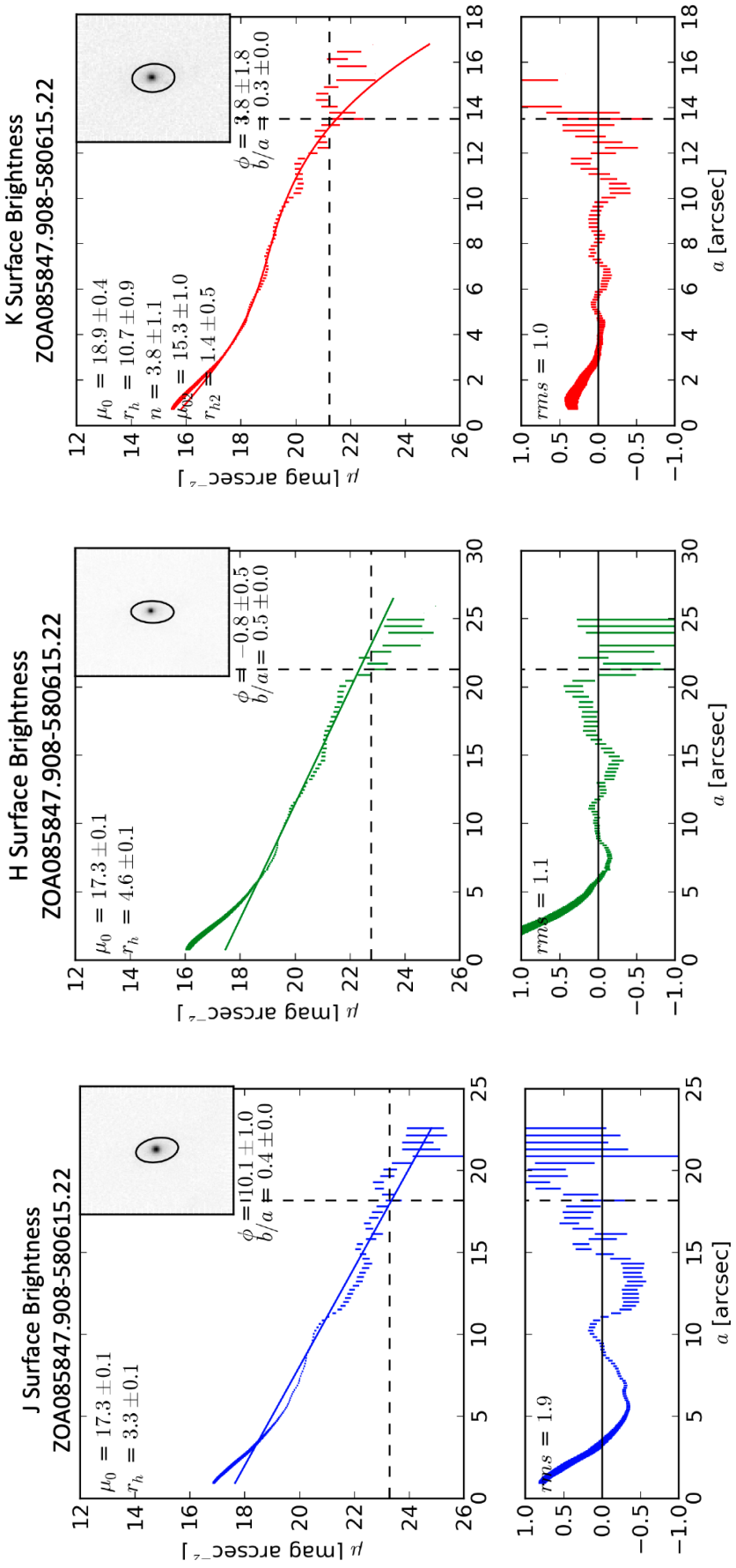

Figure 3.3: A sample of the surface brightness profiles of the galaxy ZOA085847.908-580615.22 in J, H, K_s bands. The top panels show the surface brightness, μ, as a function of the major axis a. The solid lines represent the fitted Sérsic profiles and the top left corner gives the parameters obtained by fitting. A gray-scale postage stamp of the galaxy is displayed at the top right corner of each subplot with the geometric parameters of the ellipse underneath. The vertical dashed lines show the isophotal radii where the surface brightness (μ) drops to 1σ of the sky background (shown by the horizontal lines). The bottom panel depicts the fitting residuals (mag arcsec^{-2} versus arcsec). In the J and H-band surface brightness profiles of this galaxy only an exponential profile is fitted to the outer disk. If the double Sérsic profile is fitted the difference between the magnitude at the maximum radius and the limit $r = \infty$ will be more than one magnitude

and

$$\begin{aligned} I_{\rm total} &= \int_0^\infty 2\pi(1-\epsilon) I(a) a \, {\rm da} \\ &= \int_0^\infty 2\pi(1-\epsilon) \left[I_0 \exp\left(\frac{a}{r_h}\right)^n + I_{02} \exp\left(\frac{a}{r_{h_2}}\right)^{n_2} \right] a \, {\rm da} \\ &= 2\pi(1-\epsilon) \left\{ \frac{I_0 r_h^2}{n} \Gamma\left[\frac{2}{n}\right] + \frac{I_{02} r_{h_2}^2}{n_2} \Gamma\left[\frac{2}{n_2}\right] \right\} \end{aligned} \tag{3.6}$$

where $\Gamma[\alpha, x]$ is the incomplete gamma function and a_{tot} is the radius at which surface brightness drops to 1σ of the sky background. The magnitude contained within this radius is called the observed total magnitude, m_{obs}. The total magnitude is then determined as

$$m_{\rm tot} = m_{\rm obs} - \Delta m \quad . \tag{3.7}$$

- **Isophotal Magnitudes:** The isophotal magnitude, m_μ, is measured within a given radius or aperture, using the `ellipse` task. The isophotal radius, r_μ, is the radius of the isophote at surface brightness μ. Both m_μ and r_μ are determined at the points $\mu = 20$ mag arcsec^{-2}, $\mu = 21$ mag arcsec^{-2} and $\mu = 22$ mag arcsec^{-2} in the surface brightness profile.

- **Photometric Errors:** The accuracy of the photometry strongly depends on the sky background determination, the photometric calibration and the S/N inside the aperture. The flux error within a given aperture, σ_F, is given by

$$\sigma_F = \sqrt{F + N\sigma_{\rm rms}^2}\,, \tag{3.8}$$

where F is the flux within the aperture, N is the pixel counts inside this aperture and $\sigma_{\rm rms}$ is the sky background rms. The error arising from the ellipse fitting procedure is negligible compared to the aforementioned errors.

3.2 NIR extended source catalogue

The following steps were performed to arrive at a catalogue of galaxies in the VSCL clusters. After running Source Extractor with optimised parameters (as described in Sect. 2.4.2), I used 0.35 < CLASS_STAR < 0.8 (Sect. 2.4.2) to identify extended sources as galaxies. I then examined the extracted sources by eye in the composite RGB images to minimise the number of spurious detections and make sure that no obvious galaxy was missed. I also prepared the required tables of center coordinates of the galaxy candidates, along with their major and minor axes from the Source Extractor output catalogue to feed into the IRSF pipeline (Sect. 3.1). By running the IRSF pipeline on the galaxy candidates, a catalogue of their astrometric, geometric and photometric parameters was created.

3.2.1 Catalogue parameters

The output catalogue from the IRSF pipeline contains 125 parameters for each galaxy which are listed in Williams (2011). Here I describe the NIR parameters that are the most relevant for the subsequent analysis. As an example I present a sample output page of the catalogue for the cluster VC08 in Table 3.1.

- **1** - `Designation:` Unique identifier [ZOAhhmmss.sss±ddmmss.ss].
- **6, 7** - `l, b:` Galactic coordinates [deg].
- **8, 9** - `j_ell, j_ell_sig:` J-band ellipticity ($\epsilon = 1 - b/a$) and error.
- **10, 11** - `j_phi, j_phi_sig:` J-band position angle (East of North) and error [deg].
- **47** - `r_k20fe:` K_{s20} fiducial isophotal radius [arcsec].
- **48, 49** - `j_m_k20fe, j_msig_k20fe:` J-band K_{s20} fiducial isophotal magnitude and error [mag].
- **50, 51** - `h_m_k20fe, h_msig_k20fe:` H-band K_{s20} fiducial isophotal magnitude and error [mag].
- **52, 53** - `k_m_k20fe, k_msig_k20fe:` K_s-band K_{s20} fiducial isophotal magnitude and error [mag].
- **61** - `j_m_ext:` J-band extrapolated total magnitude [mag].
- **62** - `h_m_ext:` H-band extrapolated total magnitude [mag].
- **63** - `k_m_ext:` K_s-band extrapolated total magnitude [mag].
- **64** - `j_msig_ext:` J-band extrapolated total magnitude error [mag].
- **65** - `h_msig_ext:` H-band extrapolated total magnitude error [mag].
- **66** - `k_msig_ext:` K_s-band extrapolated total magnitude error [mag].
- **100-102** - `j_sb_core, h_sb_core, K_sb_core:` J, H and K_s central surface brightness [mag arcsec^{-2}], defined as $\mu_\lambda = m_\lambda(3'') + log(3.0^2 \times \pi)$.
- **124** - `ebv:` Galactic reddening along the line of sight (Schlegel et al., 1998) [mag].

Table 3.2 lists the total number of identified galaxies and the number of their 2MASX counterparts in each cluster. The full catalogue of galaxies for all of the six VSCL clusters is provided in Appendix A.

3.3 Quality control of galaxy parameters

In this section the accuracy of astrometric and photometric parameters is examined. This process is performed for all clusters in this survey.

Table 3.1: The VC08 IRSF pipeline output sample catalogue. The dashes indicate that the pipeline could not fit a total magnitude.

Designation	ℓ (deg)	b (deg)	e_J	ϕ_J (deg)	r_{k20fe} (arcsec)	J_{k20fe} (mag)	H_{k20fe} (mag)	Ks_{k20fe} (mag)	J_{tot} (mag)	H_{tot} (mag)	Ks_{tot} (mag)	μ_J	μ_H (mag arcsec^{-2})	μ_{Ks}	$E(B-V)$ (mag)
$ZOA085648.318-575226.01$	275.628	−8.047	0.14	50.74	2.84	17.13 ± 0.07	16.66 ± 0.08	15.87 ± 0.10	16.58 ± 0.20	15.74 ± 0.29	15.80 ± 0.10	20.68	20.03	19.02	0.218
$ZOA085707.906-574718.60$	275.590	−7.959	0.23	28.81	6.35	15.35 ± 0.03	14.71 ± 0.03	14.23 ± 0.04	–	14.34 ± 0.07	13.35 ± 0.18	18.77	18.11	17.63	0.218
$ZOA085636.836-574745.78$	275.552	−8.017	0.29	−45.14	11.33	13.45 ± 0.02	12.69 ± 0.02	12.31 ± 0.03	13.18 ± 0.11	–	11.57 ± 0.20	17.50	16.76	16.38	0.218
$ZOA085700.212-574832.51$	275.595	−7.985	0.11	−39.62	2.88	17.51 ± 0.09	16.51 ± 0.07	15.59 ± 0.07	–	–	14.74 ± 0.25	20.34	19.47	18.91	0.218
$ZOA085646.873-574902.59$	275.583	−8.013	0.30	82.70	4.22	16.55 ± 0.06	15.75 ± 0.05	15.33 ± 0.07	15.60 ± 0.40	14.53 ± 0.36	–	19.57	18.96	18.47	0.218
$ZOA085656.746-575026.96$	275.615	−8.012	0.16	40.71	6.71	14.34 ± 0.03	13.60 ± 0.02	13.22 ± 0.03	13.61 ± 0.24	13.20 ± 0.09	12.91 ± 0.06	17.95	17.21	16.83	0.218
$ZOA085640.877-574550.96$	275.533	−7.990	0.12	57.58	3.67	15.33 ± 0.03	14.55 ± 0.03	14.00 ± 0.03	15.02 ± 0.09	13.24 ± 0.39	11.86 ± 0.68	18.63	17.90	17.36	0.218
$ZOA085647.800-574524.99$	275.537	−7.973	0.21	−4.19	4.84	15.33 ± 0.04	14.56 ± 0.03	14.19 ± 0.04	–	14.03 ± 0.12	–	18.69	17.92	17.55	0.218
$ZOA085633.644-574928.12$	275.569	−8.041	0.10	−85.66	3.89	17.04 ± 0.08	16.14 ± 0.06	15.27 ± 0.07	13.39 ± 1.28	14.46 ± 0.55	–	20.16	19.30	18.50	0.218
$ZOA085651.875-575753.11$	275.704	−8.099	0.38	31.61	3.38	16.59 ± 0.05	15.95 ± 0.04	15.83 ± 0.08	–	15.68 ± 0.04	–	19.64	19.09	19.20	0.235
$ZOA085638.371-580142.02$	275.734	−8.163	0.05	−32.06	2.92	16.19 ± 0.04	15.46 ± 0.03	14.84 ± 0.04	–	14.59 ± 0.27	14.43 ± 0.09	19.38	18.75	18.10	0.238
$ZOA085643.022-580324.85$	275.763	−8.173	0.35	−1.65	2.10	17.50 ± 0.08	16.60 ± 0.06	16.13 ± 0.10	–	–	–	20.38	19.70	19.56	0.238
$ZOA085710.532-580408.06$	275.811	−8.135	0.34	48.53	9.97	13.27 ± 0.02	12.49 ± 0.02	12.13 ± 0.02	–	11.94 ± 0.16	12.00 ± 0.03	16.98	16.20	15.82	0.238
$ZOA085629.176-580505.56$	275.765	−8.215	0.08	−70.08	2.92	17.21 ± 0.07	16.38 ± 0.06	15.66 ± 0.08	–	–	15.34 ± 0.09	20.18	19.47	18.81	0.238
$ZOA085703.083-580611.25$	275.827	−8.169	0.26	11.66	2.01	18.09 ± 0.13	17.17 ± 0.09	16.11 ± 0.10	–	–	15.90 ± 0.11	21.39	20.31	20.42	0.238
$ZOA085705.491-580146.31$	275.774	−8.118	0.09	76.54	2.51	17.79 ± 0.10	16.67 ± 0.06	16.12 ± 0.09	–	–	–	20.55	19.85	19.52	0.238
$ZOA085834.283-572605.83$	275.443	−7.584	0.22	50.20	3.07	16.72 ± 0.05	15.83 ± 0.04	15.30 ± 0.06	–	14.69 ± 0.33	14.96 ± 0.08	19.82	19.02	18.49	0.215
$ZOA085811.545-572607.43$	275.410	−7.623	0.13	46.94	4.06	16.07 ± 0.05	15.26 ± 0.04	14.62 ± 0.05	–	–	13.94 ± 0.15	19.26	18.55	17.90	0.215
$ZOA085812.792-572637.97$	275.418	−7.627	0.28	−75.44	4.67	15.52 ± 0.04	14.71 ± 0.03	14.42 ± 0.05	15.37 ± 0.07	–	13.28 ± 0.31	18.91	18.12	17.77	0.215
$ZOA085830.956-572352.63$	275.409	−7.566	0.17	−64.48	3.72	17.32 ± 0.10	16.37 ± 0.07	15.44 ± 0.08	–	–	–	20.47	19.49	18.79	0.215
$ZOA085857.503-572746.54$	275.498	−7.562	0.06	−66.49	4.11	16.37 ± 0.05	15.63 ± 0.04	15.49 ± 0.09	14.94 ± 0.39	14.62 ± 0.15	13.01 ± 0.62	19.36	18.63	18.55	0.215
$ZOA085814.502-572651.08$	275.424	−7.626	0.68	77.28	2.59	17.83 ± 0.11	16.77 ± 0.07	16.05 ± 0.09	–	–	12.58 ± 0.98	21.20	19.72	19.03	0.215
$ZOA085813.602-572701.32$	275.424	−7.629	0.25	24.06	2.25	18.06 ± 0.12	17.04 ± 0.08	16.31 ± 0.11	–	–	16.12 ± 0.12	20.84	20.07	19.61	0.215
$ZOA085809.682-572911.78$	275.447	−7.659	0.12	36.69	3.42	17.05 ± 0.10	16.38 ± 0.08	15.66 ± 0.11	16.28 ± 0.32	–	11.31 ± 1.20	19.86	19.34	18.57	0.215
$ZOA085821.261-573250.20$	275.510	−7.679	0.21	−8.35	2.43	17.06 ± 0.06	16.16 ± 0.04	15.65 ± 0.07	11.16 ± 1.90	–	14.14 ± 0.34	20.05	19.18	18.61	0.209
$ZOA085831.042-573712.41$	275.581	−7.709	0.22	−31.29	2.97	16.72 ± 0.05	16.03 ± 0.04	15.37 ± 0.06	-11.48 ± 8.94	–	–	19.81	19.22	18.46	0.209
$ZOA085816.493-573225.22$	275.498	−7.682	0.67	−0.16	7.30	15.51 ± 0.04	14.66 ± 0.03	14.19 ± 0.04	15.15 ± 0.11	13.82 ± 0.24	13.16 ± 0.31	18.96	18.14	17.66	0.209
$ZOA085818.652-573146.87$	275.493	−7.672	0.19	45.90	2.90	16.68 ± 0.06	15.85 ± 0.04	15.23 ± 0.06	–	15.12 ± 0.21	14.49 ± 0.20	19.97	19.07	18.41	0.209
$ZOA085821.087-573256.46$	275.511	−7.680	0.05	−49.88	4.25	17.71 ± 0.10	17.01 ± 0.08	16.23 ± 0.12	–	–	15.49 ± 0.19	20.49	19.79	19.18	0.209
$ZOA085815.583-574502.92$	275.659	−7.820	0.45	33.42	6.82	14.49 ± 0.03	13.79 ± 0.02	13.38 ± 0.03	12.97 ± 0.47	12.42 ± 0.38	12.97 ± 0.04	17.96	17.26	16.87	0.216
$ZOA085902.891-574009.90$	275.665	−7.687	0.25	53.21	3.56	15.89 ± 0.04	15.14 ± 0.03	14.80 ± 0.05	–	13.31 ± 0.52	11.01 ± 1.07	19.21	18.38	17.99	0.216
$ZOA085824.933-574134.48$	275.628	−7.766	0.52	−72.60	5.50	15.10 ± 0.03	14.40 ± 0.03	13.94 ± 0.03	14.74 ± 0.13	13.86 ± 0.16	13.73 ± 0.04	18.56	17.87	17.41	0.216
$ZOA085842.568-574132.50$	275.653	−7.736	0.22	−66.53	8.02	13.90 ± 0.02	13.15 ± 0.02	12.81 ± 0.03	13.24 ± 0.22	–	12.43 ± 0.10	17.57	16.82	16.46	0.216
$ZOA085838.007-574201.32$	275.653	−7.749	0.08	−17.91	2.65	15.63 ± 0.03	15.01 ± 0.03	14.70 ± 0.04	–	14.78 ± 0.05	–	19.01	18.35	18.26	0.216
$ZOA085836.000-574252.69$	275.661	−7.762	0.22	19.23	3.03	16.78 ± 0.05	15.90 ± 0.04	15.16 ± 0.05	–	–	14.83 ± 0.09	19.95	19.12	18.39	0.216
$ZOA085852.452-574311.59$	275.689	−7.737	0.38	33.74	4.04	16.64 ± 0.05	16.02 ± 0.04	15.26 ± 0.06	–	15.79 ± 0.08	14.98 ± 0.08	20.17	19.43	18.77	0.216
$ZOA085900.120-574320.52$	275.702	−7.726	0.40	78.68	3.12	16.55 ± 0.05	15.81 ± 0.04	15.35 ± 0.06	16.20 ± 0.10	–	15.13 ± 0.08	19.70	19.03	18.62	0.216
$ZOA085821.509-574424.85$	275.659	−7.803	0.47	06.72	7.13	15.02 ± 0.03	14.27 ± 0.03	13.90 ± 0.03	14.78 ± 0.08	13.65 ± 0.17	13.70 ± 0.05	18.48	17.74	17.43	0.216
$ZOA085829.346-574338.82$	275.661	−7.781	0.04	−46.23	2.15	16.26 ± 0.04	15.61 ± 0.03	15.42 ± 0.05	–	–	15.38 ± 0.05	19.50	18.87	18.74	0.216
$ZOA085851.330-575226.84$	275.806	−7.839	0.28	−41.01	7.50	13.90 ± 0.02	13.15 ± 0.02	12.77 ± 0.03	13.31 ± 0.20	12.89 ± 0.07	12.34 ± 0.11	17.50	16.74	16.38	0.235
$ZOA085826.056-574700.67$	275.699	−7.823	0.32	−52.72	2.12	17.80 ± 0.08	16.99 ± 0.06	16.30 ± 0.09	–	–	16.14 ± 0.10	20.74	20.07	19.99	0.235

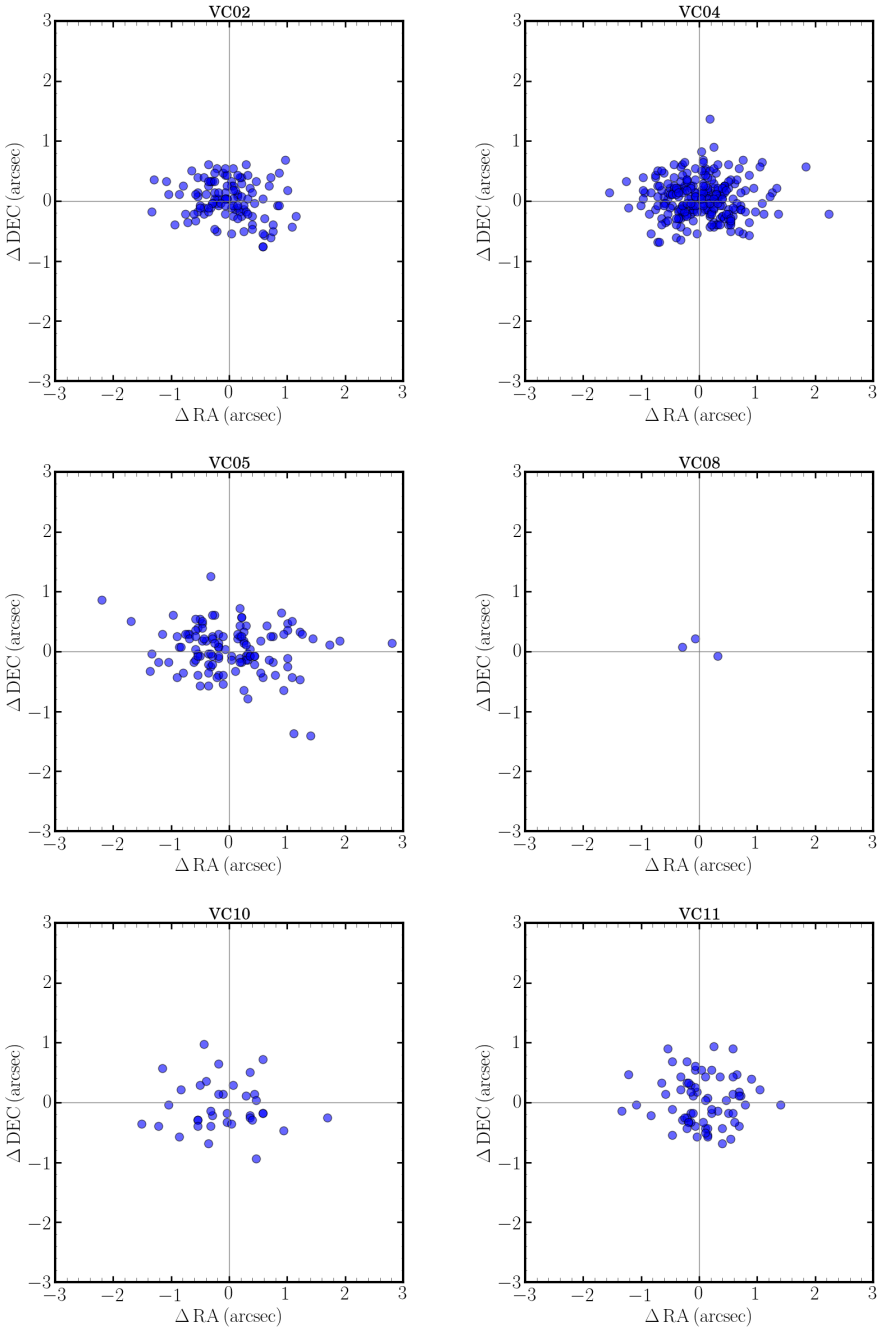

Figure 3.4: Consistency of the coordinate positions of the objects that were observed more than once in the mosaic of the clusters in the VSCL clusters.

Table 3.2: The total number of identified galaxies (N) and the number of their 2MASX counterparts (N_{2MASX}) in each cluster.

Cluster	N	N_{2MASX}
VC02	290	43
VC04	416	82
VC05	279	35
VC08	217	31
VC10	232	29
VC11	281	48

3.3.1 Internal consistency

As seen in Fig. 2.4, galaxies close to the border or a corner of an image can be identified up to three images within the mosaic of a cluster (Section 2.2.1). The overlap regions are used to check the consistency of geometric and photometric parameters.

Figure 3.4 shows the offsets of ΔRA and ΔDec for galaxies that were observed more than once in mosaics of any of the six observed clusters (VC02, VC04, VC05, VC08, VC10 and VC11). Table 3.3 compares the mean values of ΔRA and ΔDec and their standard deviations for the six observed VSCL clusters with those of the Norma Wall Survey (NWS; Riad, 2010). The values of ΔRA and ΔDec in each cluster are insignificant and the small offset is likely due to the differences in the quality of images (e.g. different seeing). The positional offsets are on average slightly larger than the results from the analysis of the NWS data (e.g. VC04 with $\langle\Delta\text{RA}\rangle = 0.031$ compared to NWS with $\langle\Delta\text{RA}\rangle = 0.009$). However, they are consistent when the uncertainties are considered. There is no systematic shift seen in the position of galaxies in each cluster.

Table 3.3: $\langle\Delta\text{RA}\rangle$ and $\langle\Delta\text{Dec}\rangle$ with their respective standard deviation (σ) for the matched pairs in NWS and the VSCL clusters.

Survey	$\langle\Delta\text{RA}\rangle$ (arcsec)	σ (arcsec)	$\langle\Delta\text{Dec}\rangle$ (arcsec)	σ (arcsec)	no. of samples
VC02	−0.011	0.492	0.023	0.316	124
VC04	0.031	0.537	0.046	0.318	249
VC05	0.021	0.754	0.039	0.395	121
VC08	−0.011	0.253	0.071	0.117	4
VC10	−0.106	0.649	−0.063	0.410	43
VC11	0.060	0.507	0.028	0.404	78
NWS	0.009	0.202	0.003	0.202	1061

To check the consistency of the photometric parameters, I compared the K_{s20} fiducial isophotal magnitudes for each galaxy observed in two different fields by computing:

$$\Delta m = m_{\text{field}} - m_{\text{neighbouring field}}. \tag{3.9}$$

The result of the magnitude comparison is shown in Fig. 3.5, for only the VC04 cluster. This is the richest cluster with numerous galaxies that were observed more than once in the overlapping fields. The results are typical of what has been found in the other observed clusters as well. The values of the mean magnitude difference and the standard deviation are displayed at the top left corner of each plot in Fig. 3.5 ($\langle \Delta J \rangle = 0.014 \pm 0.169$, $\langle \Delta H \rangle = 0.007 \pm 0.181$ and $\langle \Delta K_s \rangle = 0.025 \pm 0.180$). The mean magnitude difference and standard deviation are consistent between the two fields and no systematic difference is seen in photometry over the region. The values of the mean magnitude difference and the standard deviation of VC04 and the NWS (Riad, 2010) are given in Table 3.4. The offsets in VC04 are within 1σ of those of the NWS ($\langle \Delta J \rangle = 0.012 \pm 0.161$, $\langle \Delta H \rangle = 0.003 \pm 0.156$ and $\langle \Delta K_s \rangle = 0.006 \pm 0.143$).

Note that the standard deviation values in both positions and magnitudes are the highest because they are derived for the galaxies located at the outskirts of the images.

Table 3.4: The values of the mean magnitude difference and the standard deviation of one clusters in this survey (VC04 with 249 matched pairs) and the NWS (1061 matched pair) (Riad, 2010).

Band	$\langle \Delta m \rangle$ VC04 (mag)	σ VC04 (mag)	$\langle \Delta m \rangle$ NWS (mag)	σ NWS (mag)
J	0.014	0.169	0.012	0.161
H	0.007	0.181	0.003	0.156
K_s	0.025	0.180	0.006	0.143

3.3.2 External consistency

Astrometric parameters

For the comparison of the parameters I searched for counterparts in the 2MASX catalogue (Jarrett et al., 2000a). Any two candidates in the catalogues (the VSCL clusters and 2MASX) that lie within a distance of $r \leq 2\farcs0$ from each other were assumed to be counterparts.

The astrometric comparison was done by computing the offsets ΔRA and ΔDEC for each matched pair. The result is shown in Fig. 3.6. The determination of the positions are not derived in exactly the same manner. 2MASX uses the pixel with the peak J-band flux as the centre of a galaxy to perform photometry while our method is based on the centroid of the co-added image. As shown in Fig. 3.6, the positions of the VSCL galaxies are consistent with 2MASX and no overall offsets are seen in any direction. The $\langle \Delta \mathrm{RA} \rangle$ and $\langle \Delta \mathrm{Dec} \rangle$ offsets with their dispersions are given in Table 3.5. The 2MASX coordinates were found to have a rms uncertainty of $\sim 0\farcs5$ (Jarrett et al., 2000b) which is compatible with what is found for the VSCL clusters, despite the differences in the determination methods and other survey characteristics such as the pixel size and seeing of the observed images. The offsets were also compared to those of Riad (2010) for the Norma wall, since it was done with the same telescope and instrument and observation set up. The values

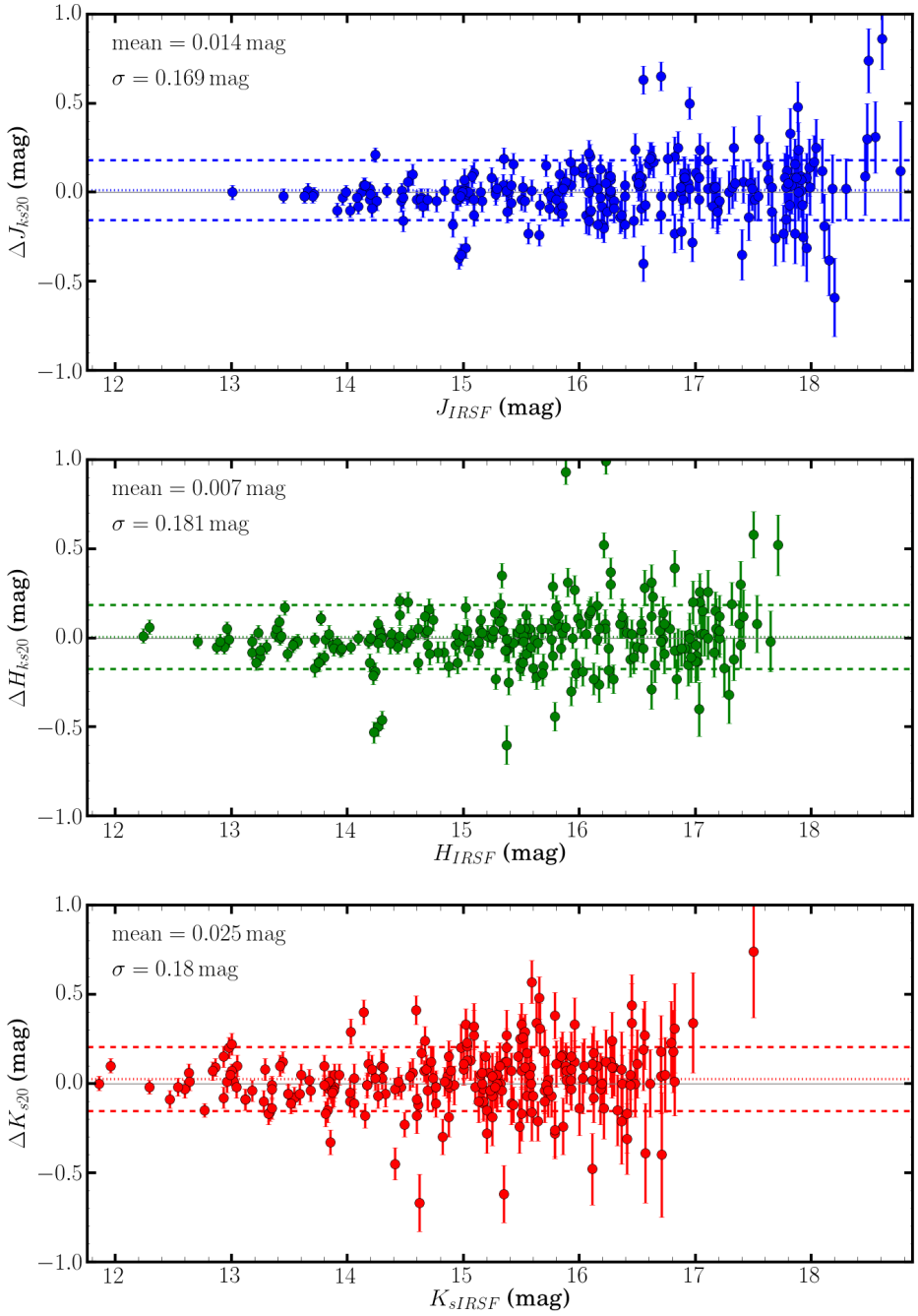

Figure 3.5: Comparison of the K_{s20} fiducial magnitudes in the J, H, K_s bands for double-observed galaxies in VC04. The dotted line indicates the mean value of Δm and the dashed lines indicate the 1σ dispersion around the mean. The mean and standard deviation are given in the top left corner of each plot.

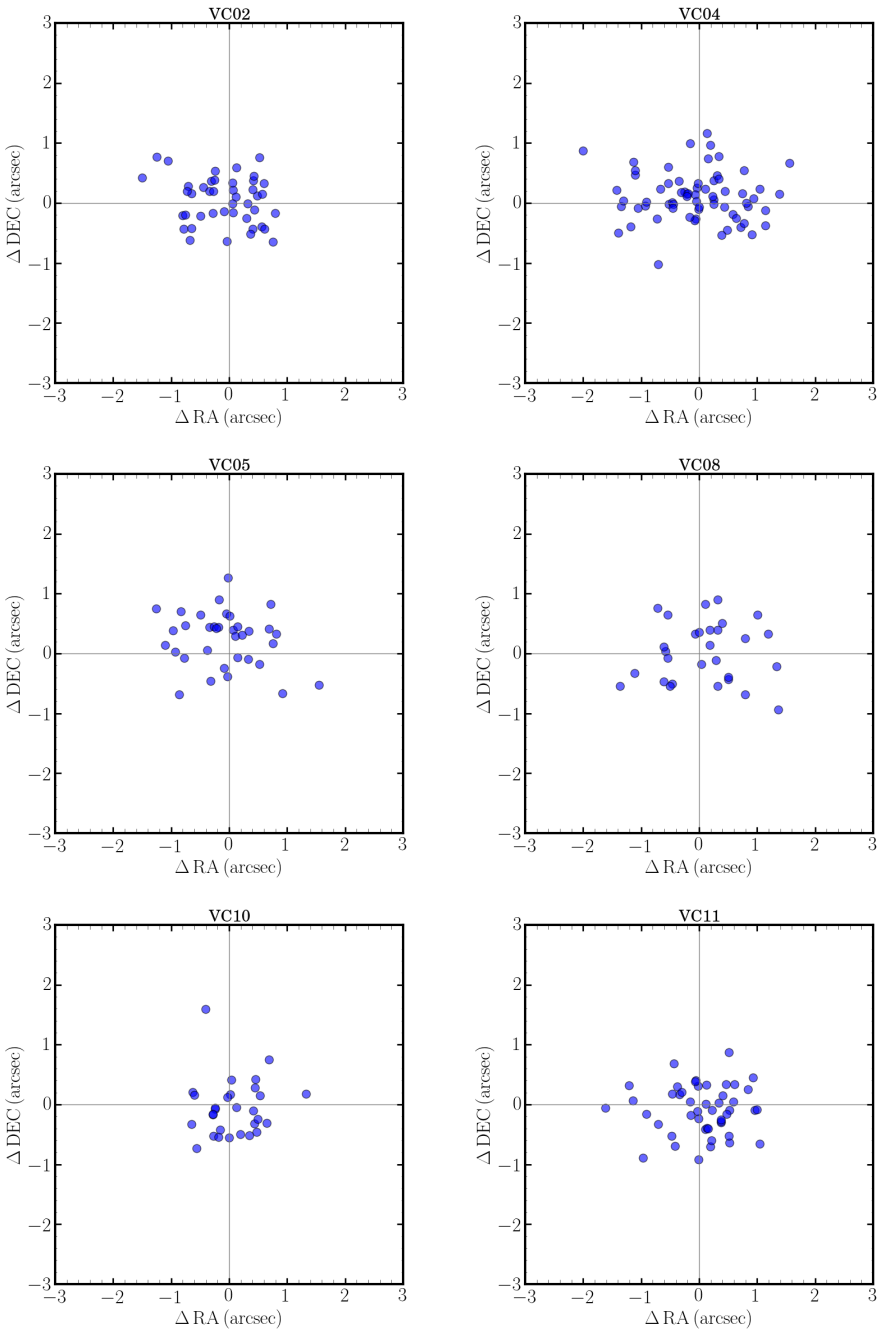

Figure 3.6: Astrometric comparison of the matched pairs between the clusters in the VSCL and 2MASX.

for the NWS for 237 matched galaxies are listed in Table 3.5, and are in agreement with those obtained for the VSCL and 2MASX galaxies.

Table 3.5: $\langle\Delta\text{RA}\rangle$ and $\langle\Delta\text{Dec}\rangle$ with their respective standard deviations (σ) for the matched pairs in VC02, VC04, VC05, VC08, VC10, VC11 and NWS respectively.

Survey	$\langle\Delta\text{RA}\rangle$ (arcsec)	σ (arcsec)	$\langle\Delta\text{Dec}\rangle$ (arcsec)	σ (arcsec)	no. of samples
VC02	−0.089	0.570	0.045	0.383	43
VC04	−0.055	0.749	0.122	0.502	82
VC05	−0.078	0.628	0.245	0.451	35
VC08	0.086	0.695	0.023	0.495	31
VC10	0.071	0.464	−0.047	0.468	29
VC11	0.048	0.592	−0.083	0.402	48
NWS	−0.010	0.420	0.110	0.390	237

Photometric Parameters

Table 3.6: Comparison of the 2MASX and IRSF/SIRIUS 7″ and K_{s20} fiducial isophotal magnitudes for 82 matched pairs in VC04.

Band	7″ aperture Δm (mag)	K_{s20} fiducial Δm (mag)
J	0.064 ± 0.168	0.118 ± 0.177
H	0.035 ± 0.123	0.064 ± 0.167
K_s	0.053 ± 0.148	0.091 ± 0.196

To verify the accuracy of the IRSF/SIRIUS magnitude system, I computed the difference between the IRSF/SIRIUS and 2MASX K_{s20} fiducial isophotal and 7″ aperture magnitudes of the 68 cross-identified galaxies in the VC04 cluster, in the J, H and K_s bands using the metric:

$$\Delta m = m_{IRSF} - m_{2MASS}. \tag{3.10}$$

A positive value of Δm would indicate that the magnitudes of the IRSF/SIRIUS system are fainter.

Before performing the photometric comparison and calculating the magnitude differences, 2MASX magnitudes were converted to the SIRIUS filter magnitude system using Equation 2.2. The comparison of the 7″ aperture and K_{s20} fiducial isophotal magnitudes in the three J, H and K_s bands are shown in Figs. 3.7 and 3.8. The dotted line indicates the mean value of Δm and the dashed lines show the 1σ dispersion around the mean. The error bars show the combination of the IRSF and 2MASX magnitude errors. Table 3.6 lists the offset values with their standard deviations for both 7″ aperture and K_{s20} fiducial

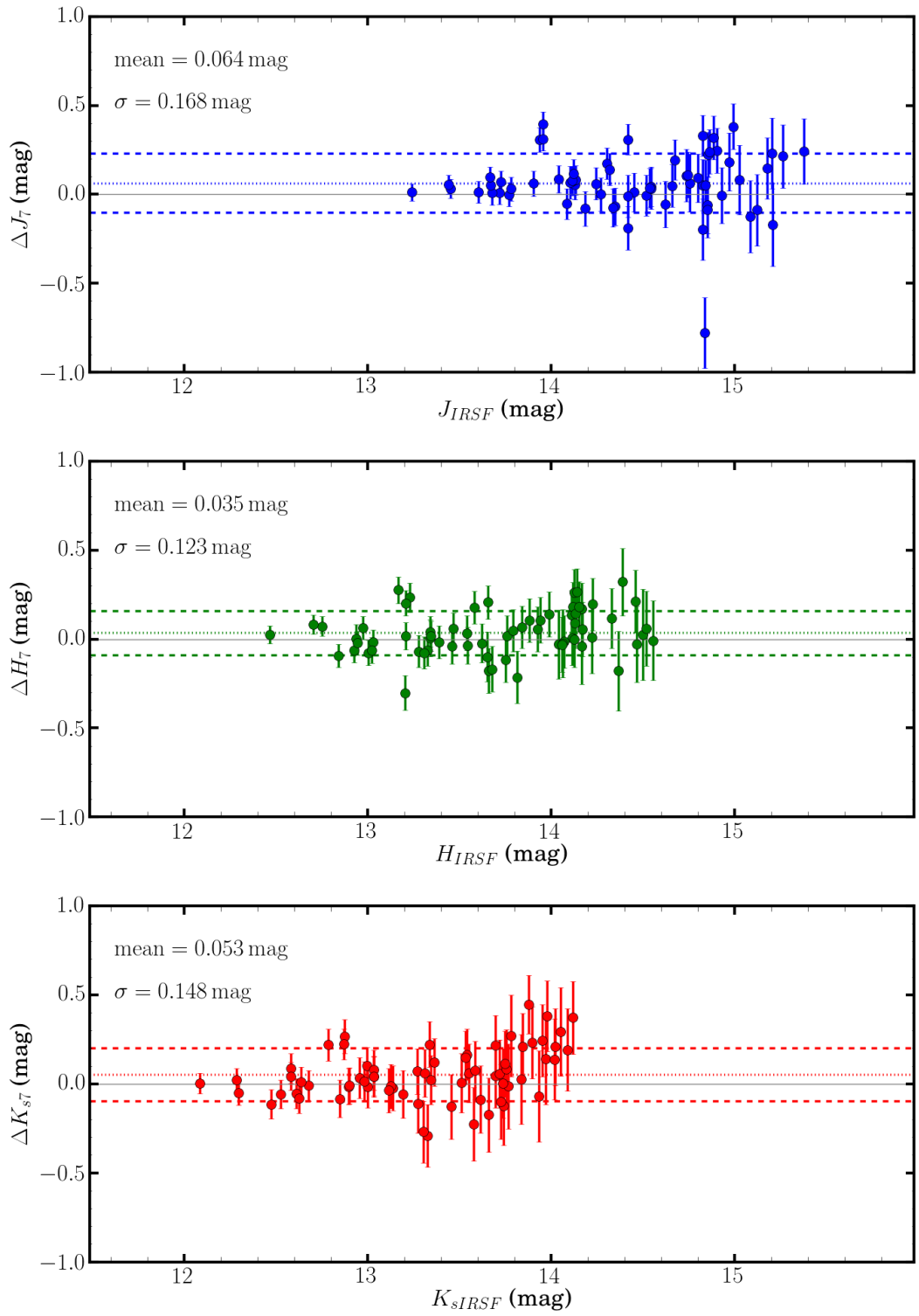

Figure 3.7: Comparison of the 7″ aperture J, H, K_S magnitudes between IRSF/SIRIUS (VC04) and 2MASX. The dotted line indicates the mean value of Δm and the dashed lines indicate the 1σ dispersion around the mean. The error bars show the combination of the IRSF and 2MASX magnitude errors. The mean and standard deviation are given in the top left corner of each plot.

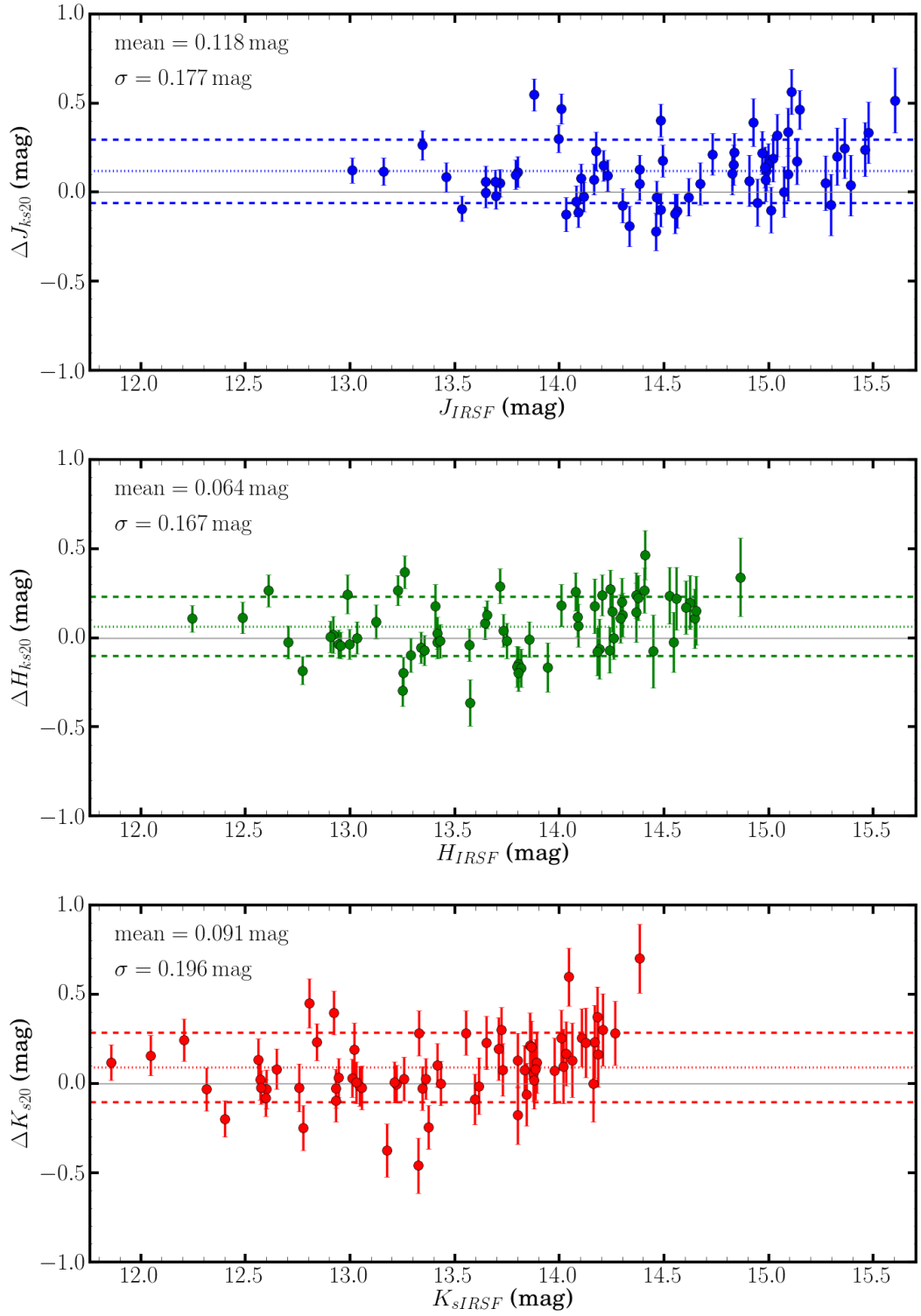

Figure 3.8: Comparison of the K_{s20} fiducial magnitudes in the J, H, K_s bands between IRSF/SIRIUS (VC04) and 2MASX. The dotted line indicates the mean value of Δm and the dashed lines indicate the 1σ dispersion around the mean. The error bars show the combination of the IRSF and 2MASX magnitude errors. The mean and standard deviation are given in the top left corner of each plot.

Table 3.7: Comparison of the IRSF/SIRIUS K_{s20} fiducial isophotal magnitude offsets with other surveys in J, H and K_s bands.

Band	Δm_{K20} (mag) VC04	Δm_{K20} (mag) Williams (2011)	Δm_{K20} (mag) Riad (2010)	Δm_{K20} (mag) Cluver (2008)
J	0.118 ± 0.177	-0.070 ± 0.190	-0.029 ± 0.098	-0.070 ± 0.110
H	0.064 ± 0.167	-0.030 ± 0.170	0.051 ± 0.101	0.030 ± 0.120
K_s	0.091 ± 0.196	-0.030 ± 0.180	0.045 ± 0.095	0.020 ± 0.070

isophotal magnitudes. The offsets and dispersions of the 7″ aperture magnitudes are, as expected, smaller compared to the values for the K_{s20} fiducial isophotal magnitudes.

Table 3.7 lists the offsets and dispersions of the K_{s20} fiducial isophotal magnitudes to compare them with other surveys pursued with IRSF/SIRIUS that used the same imaging set up (Williams, 2011; Riad, 2010; Cluver, 2008). The VC04 offsets are within 1σ of the findings of the other surveys. The increase in Δm at the faint end, particularly for the K_{s20} fiducial isophotal magnitudes, could be due to the increase in 2MASX errors for the low surface brightness galaxies (due to losing their flux at their outer areas) and also the lower spatial resolution of 2MASX which could result in not resolving the stars that are superimposed on galaxies (although star-subtraction was a part of the 2MASX photometry of galaxies) and hence resulting in brighter magnitudes.

3.4 Extinction effects

3.4.1 Foreground extinction

The light of the extended objects in the ZoA is strongly absorbed by the dust of the Milky Way. The Galactic interstellar extinction depends on the wavelength of the light and the relative size of the dust grains. Extinction decreases toward longer wavelength, therefore, objects seen through a dust layer appear redder because more of the blue light is absorbed.

The general extinction law to deredden IR-UV spectrophotometric data is given by:

$$\frac{A_V}{E(B-V)} = R_V, \tag{3.11}$$

where A_V is the extinction in optical V band and $E(B-V)$ is the colour-reddening. According to Cardelli et al. (1989) this ratio has an average value of $R_V = 3.1$ toward the Galactic diffuse interstellar medium (ISM) line of sight. R_V can decrease to $R_V \sim 2$ along diffuse sightlines (Fitzpatrick, 1999; Wang et al., 2017) or increase to $R_V \sim 6$ towards dense molecular clouds (Fitzpatrick, 1999; Mathis, 1990).

The value of colour-reddening can be derived from the Schlegel et al. (1998) dust maps in which they presented a full-sky 100 μm map that can be converted to a map proportional to dust column density. A detailed follow-up analysis of dust reddening was carried on by Schlafly et al. (2010) using the colours of stars in the Sloan Digital Sky Survey (SDSS). It was found that Schlegel et al. (1998) overestimated reddening by about 14% in $(B-V)$ and this is therefore seen in all colours. Consequently a factor

of 0.86 must be applied to the Schlegel et al. (1998) extinction maps for recalibration. This overestimation was proven to be even higher at low Galactic latitudes, $|b| < 5°$. For example Nagayama et al. (2004) determined the total foreground extinction by measuring the colour excess for giant stars around the radio galaxy PKS 1343-601 and found the extinction to be overestimated by 33% when extrapolating Schlegel maps to their survey region. Numerous other studies such as Arce and Goodman (1999); Dutra et al. (2002); van Driel et al. (2009); Schröder et al. (2007) confirm the overestimate of $f = 0.86$ for latitudes of $|b| < 5°$. In this work we adopt the Schlegel et al. (1998) $E(B-V)$ values corrected by a factor of 0.86.

Using the Cardelli et al. (1989) parametrisation, the extinctions in J, H, K_s and B bands are:

$$\begin{aligned} A_J &= 0.863E(B-V), \\ A_H &= 0.570E(B-V), \\ A_{K_s} &= 0.368E(B-V), \\ A_B &= 4.315E(B-V). \end{aligned} \tag{3.12}$$

The extinction in the NIR, J, H and K_s bands are clearly lower than in optical B band, one of the reasons why the NIR is suitable to work in the ZoA. Equation 3.13 is employed to derive the extinction-corrected magnitudes using:

$$m_\lambda^0 = m_\lambda - A_\lambda, \tag{3.13}$$

where m_λ^0 is the extinction-corrected magnitude in each wavelength and A_λ is the extinction in that wavelength.

The mean, minimum and maximum values of extinction derived at the position of the detected galaxies in the clusters of the VSCL region are listed in Table 3.8. The distributions of the number of galaxies as a function of A_J, A_H and A_{K_s} in each cluster are shown in Fig. 3.9. Figure 3.9 also show that the galaxy candidates in clusters, VC04 and VC05, are on average located in a less extincted area compared to the other galaxy clusters.

In Fig. 3.10 the galaxy distributions of the six analysed clusters are plotted on the extracts of the Schlegel et al. (1998) extinction maps[5]. The green open circles represent the positions of the candidate galaxies and the contours show the extinction levels in the K_s band (A_{K_s}). These figures indicate that amongst these six clusters VC02 is located in the highest extinction area ($\langle A_{K_s} \rangle = 0.106 \pm 0.010$), and VC04 and VC05 have the lowest foreground extinction ($\langle A_{K_s} \rangle = 0.071 \pm 0.006$ and $\langle A_{K_s} \rangle = 0.063 \pm 0.005$ respectively). The foreground extinction in the regions of VC08, VC10 and VC11 is roughly in the same range ($\langle A_{K_s} \rangle = 0.084 \pm 0.006$, $\langle A_{K_s} \rangle = 0.080 \pm 0.005$ and $\langle A_{K_s} \rangle = 0.086 \pm 0.018$ respectively). Also there are more patches of higher extinction in VC02 than the other clusters. The final analysis will be based on the extinction-corrected magnitudes.

3.4.2 Extinction effect on the properties of galaxies

Galaxies appear fainter and redder due to foreground extinction. In addition Galactic extinction results in galaxies appearing smaller than they really are. The low surface brightness outer parts will disappear as the extinction increases. This therefore, prevents the detection of fainter outer parts of the galaxies and they seem to have smaller radii.

[5]Downloaded from https://irsa.ipac.caltech.edu/applications/DUST/

Table 3.8: The mean, minimum and maximum values of A_J, A_H and A_{K_s} for the galaxies within the VSCL clusters.

Extinction		A_J (mag)	A_H (mag)	A_{K_s} (mag)
VC02	mean	0.249 ± 0.024	0.164 ± 0.016	0.106 ± 0.010
	min	0.191	0.126	0.081
	max	0.310	0.204	0.132
VC04	mean	0.166 ± 0.015	0.110 ± 0.010	0.071 ± 0.006
	min	0.147	0.097	0.062
	max	0.204	0.135	0.087
VC05	mean	0.147 ± 0.011	0.097 ± 0.007	0.063 ± 0.005
	min	0.125	0.083	0.053
	max	0.185	0.122	0.079
VC08	mean	0.197 ± 0.014	0.130 ± 0.009	0.084 ± 0.006
	min	0.180	0.119	0.076
	max	0.226	0.149	0.096
VC10	mean	0.188 ± 0.013	0.124 ± 0.008	0.080 ± 0.005
	min	0.170	0.112	0.072
	max	0.235	0.155	0.100
VC11	mean	0.201 ± 0.041	0.132 ± 0.027	0.086 ± 0.018
	min	0.141	0.093	0.060
	max	0.302	0.200	0.129

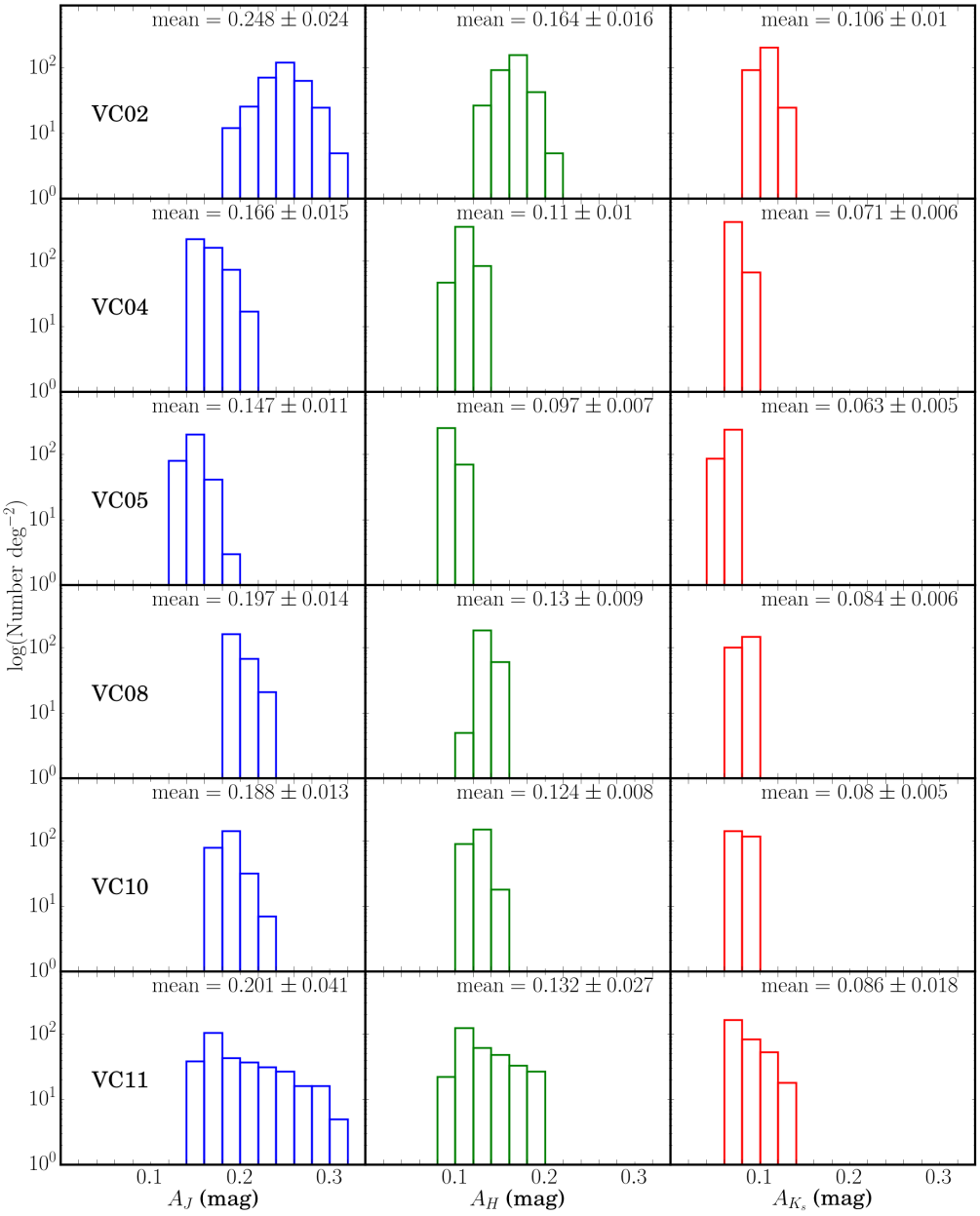

Figure 3.9: Histograms of galaxy candidate number counts in VC02, VC04, VC05, VC08, VC10 and VC11 per square degree as a function of Galactic extinction A_J, A_H and A_{K_s}.

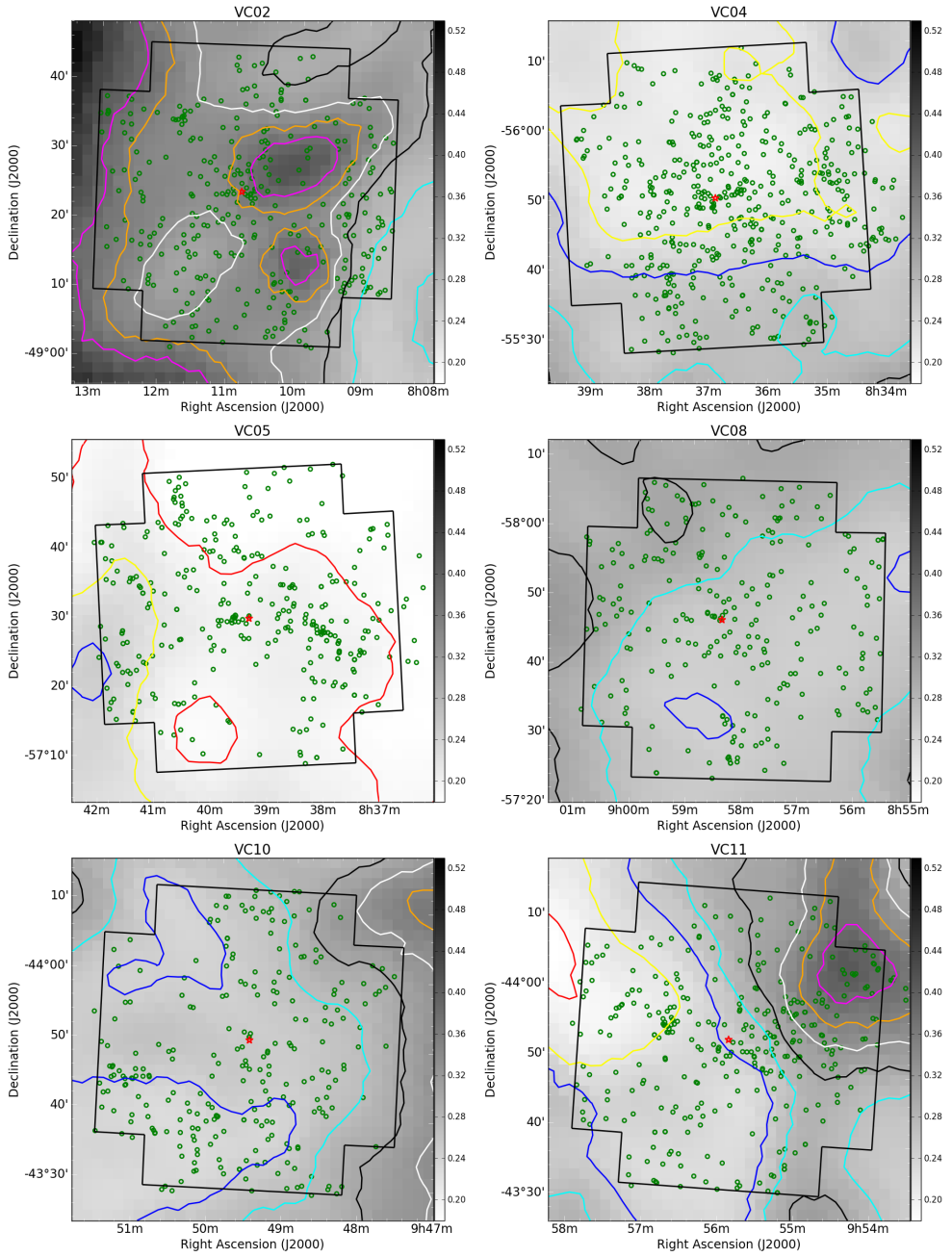

Figure 3.10: The reddening maps of the region around the VSCL clusters. The green circles are the galaxy candidates in the galaxy clusters and the contours show the K_s-band extinction levels, with red indicating $A_{Ks} = 0\overset{m}{.}07$, yellow $A_{Ks} = 0\overset{m}{.}08$, blue $A_{Ks} = 0\overset{m}{.}09$, cyan $A_{Ks} = 0\overset{m}{.}10$, black $A_{Ks} = 0\overset{m}{.}11$, white $A_{Ks} = 0\overset{m}{.}12$, orange $A_{Ks} = 0\overset{m}{.}13$, magenta $A_{Ks} = 0\overset{m}{.}14$. The black boxes indicate the outlines of the observed mosaic in each cluster. The galaxies outside of the boxes are located in the extra fields that were observed to compensate for the Infrared detector problem of the IRSF telescope. The colourbar shows the reddening map values as grey-scale.

The extinction will also affect the derivation of total magnitudes since the fainter outer parts of a galaxy cannot be fully retrieved with the extrapolation of the surface brightness profiles (Cameron, 1990; Nagayama et al., 2004; Riad et al., 2010; Said et al., 2014). The isophotal magnitudes are preferable to total magnitudes in the ZoA surveys. This was shown in Said et al. (2014) who compared the total and isophotal magnitudes of a sample of 2MASX ZoA galaxies with much deeper IRSF photometry. The observational setup was the same as this survey, i.e. $\sim 2\overset{\text{m}}{.}0$ deeper than 2MASX. Figure 1 in Said et al. (2014) indicates that the mean offset between 2MASX and IRSF for the total magnitudes is considerable while the offset is insignificant for the isophotal magnitudes. I therefore, only use the K_{s20} fiducial isophotal magnitudes for the VSCL cluster analyses in this thesis and the effect of extinction on the isophotal magnitudes will be discussed later in this section.

I used the empirical relation that Riad et al. (2010) found to correct for the effect of extinction on the isophotal magnitudes of galaxies in the J, H and K_s bands. Riad et al. (2010) simulated extinction on 64 galaxies from the 2MASS Large Galaxy Atlas (Jarrett et al., 2003) for the extinction range of $A_{J,H,K_s} = 0\overset{\text{m}}{.}0 - 3\overset{\text{m}}{.}0$. Their galaxy sample includes all morphological types. They simulated the effect of extinction by defining limiting isophotes at different extinction levels and shifting them along the light profiles of galaxies, to measure the loss of the size and flux at each level. They defined $f(R)$ and Δm_{iso} as:

$$\begin{aligned} f(R) &= \frac{R^{\circ}}{R}, \\ \Delta m_{iso} &= m_{iso} - m^{\circ}_{iso}, \end{aligned}$$

where m°_{iso}, m_{iso}, R° and R are the intrinsic and absorbed magnitudes and radii respectively. This follows the formalism of Cameron (1990) for the empirical relations which are given by:

$$f(R) = 10^{a\cdot(A_\lambda)^b}, \tag{3.14}$$

$$\Delta m_{iso} = F\cdot(A_\lambda)^v, \tag{3.15}$$

where F, v, a, b are the fitting parameters, and A_λ the extinction. To incorporate the central surface brightness (μ_c) into the corrections, Riad et al. (2010) rewrote equations 3.14 and 3.15 as

$$f(R,\mu_c) = 10^{a(\mu_c)\cdot(A_\lambda)^{b(\mu_c)}}, \tag{3.16}$$

$$\Delta m_{iso}(\mu_c) = F(\mu_c)\cdot(A_\lambda)^{v(\mu_c)}, \tag{3.17}$$

with

$$\begin{aligned} a(\mu_c) &= a_\circ \exp(\mu_c\cdot a_1), \\ b(\mu_c) &= b_\circ \exp(\mu_c\cdot b_1), \\ F(\mu_c) &= F_\circ \exp(\mu_c\cdot F_1), \\ v(\mu_c) &= v_\circ \exp(\mu_c\cdot v_1). \end{aligned} \tag{3.18}$$

To use their method one only requires the information on the morphological types, early or late-type, and the central surface brightness of galaxies (μ_c). The derived values

for $a_\circ, b_\circ, F_\circ, v_\circ, a_1, b_1, F_1$, and v_1 for this method and the average magnitudes and radii corrections (Δm_{iso} and $f(R)$) at $A_{K_s} = 0\overset{m}{.}5, 1\overset{m}{.}0, 2\overset{m}{.}0$ and $3\overset{m}{.}0$ mag are also listed in Riad et al. (2010).

I implemented this method to assess the additional μ_c-optimized extinction effect on the isophotal magnitudes of early-type galaxies in the VSCL clusters (early-type galaxies are dominant in galaxy clusters). The results are shown in Table 3.9 . This table shows that the effect of the μ_c-optimized extinction on the magnitudes are significantly smaller compared to the overall foreground extinction (A_λ, see Table 3.8) and much smaller compared to the uncertainties of the isophotal magnitudes of galaxies (even for VC02 which suffers from the highest foreground extinction and largest amount of variation over the mosaic: $\langle\sigma\rangle_J = 0\overset{m}{.}054$, $\langle\sigma\rangle_H = 0\overset{m}{.}042$ and $\langle\sigma\rangle_{K_s} = 0\overset{m}{.}058$). It was therefore concluded to not correct for the additional extinction-correction. It is sufficient to apply the Schlafly et al. (2010) foreground values to the isophotal magnitudes.

Table 3.9: The mean values of Δm_{iso} for early-type (E/S0) galaxies over the regions of the six VSCL clusters.

Cluster	$\langle\Delta J_{iso}\rangle$ (mag)	$\langle\Delta H_{iso}\rangle$ (mag)	$\langle\Delta K_{iso}\rangle$ (mag)
VC02	0.040	0.048	0.006
VC04	0.021	0.028	0.003
VC05	0.018	0.025	0.002
VC08	0.028	0.036	0.004
VC10	0.027	0.036	0.003
VC11	0.028	0.036	0.004

3.4.3 Extinction-Corrected NIR colours

Using equation 3.13, the extinction-corrected NIR colours are derived as a function of $E(B-V)$:

$$\begin{aligned}(J-H)^0 &= (J-H) - 0.293E(B-V),\\ (H-K_s)^0 &= (H-K_s) - 0.202E(B-V),\\ (J-K_s)^0 &= (J-K_s) - 0.495E(B-V),\end{aligned} \tag{3.19}$$

colours can be used as a tool in NIR to distinguish galaxies from stars. Galaxies appear red on J, H, K_s composite images due to the old (red) population of stars in their bulges or cores. In addition, the extinction effect in the ZoA causes galaxies to look even redder.

Unlike the optical colours, the NIR colours hardly depend on the morphology of the galaxies (Jarrett, 2000). However, the late spirals (e.g. Sd/Sdm) are bluer compared to other spiral and elliptical galaxies. Therefore, I used extinction-corrected colour-colour diagrams to distinguish between galaxies and Galactic objects as shown in Fig. 3.11. Jarrett (2000) determined the mean NIR isophotal colours as $(J-H)=0\overset{m}{.}64$, $(H-K_s)=0\overset{m}{.}28$ and $(J-K_s)=0\overset{m}{.}92$ for nearby (low redshift) early-type and $(J-K_s) =0\overset{m}{.}99$ for late-type

spiral galaxies. In colour-colour diagrams the candidates far from the intersection of mean NIR colours are unlikely to be galaxies.

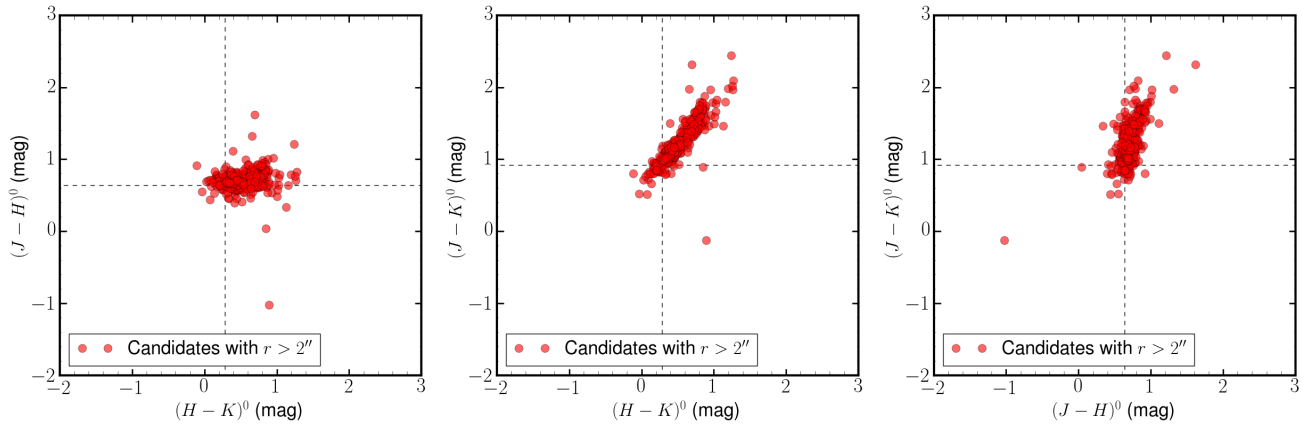

Figure 3.11: Extinction-corrected colour-colour diagrams of galaxy candidates with $r > 2''$ in VC04.

In addition, at higher redshifts the emission of galaxies shifts from H band to K_s band and as a result $(H-K_s)$ becomes redder while $(J-H)$ remains roughly constant (cosmic reddening, Jarrett, 2004). This effect is particularly obvious in the $(J-K_s)^0$ vs $(H-K_s)^0$ diagram (see the middle panel of Fig. 3.11). The reddest points in $(H-K_s)$ and $(J-K_s)$ might be AGNs which are intrinsically red in colour and affected more by dust extinction and the expansion of the universe (k-correction).

3.4.4 k-Correction

The expansion of the universe causes the rest-frame wavelength of an object to shift to longer wavelengths as a function of redshift. The apparent magnitude of any astronomical object needs to be converted to an equivalent measurement of its rest-frame by the so-called k-correction.

To assess the effect of redshifts on the magnitudes I plotted the colour-magnitude diagram, $(J-K_s)$ versus K_s, for over 2200 galaxies in the VSCL distance range, in Fig. 3.12. Glass (1999) showed that the redshift effect is the highest on $(J-K_s)$ colour compared to the two other NIR colours ($(J-H)$ and $(H-K_s)$). The effect of redshift on the mean value of $(J-K_s)$ colour of early (S0) and late (Sc) type galaxies is shown in Fig. 3.13 (the reddening curve). The data to plot this figure are obtained from Tom Jarrett (private communication). Figure 3.13 indicates the higher and redder mean value of $(J-K_s)$ colour at higher redshifts. To plot Fig. 3.12, I used the ZoA master list of optical and 2MASX galaxies[6] which contains over 35000 galaxies over the area of Galactic longitude $240^\circ < \ell < 295^\circ$ and latitude $|b| < 12^\circ$. The details of the master list are given in Kraan-Korteweg (2000b). The selected 2236 galaxies in this sample are restricted to the Galactic longitude range of $255^\circ < \ell < 285^\circ$ and the latitude range of $|b| < 10^\circ$ (the VSCL region) with reliable redshift values. The first panel of Fig. 3.12 shows an increasing trend in the colour $(J-K_s)$ as a function of redshift. In the second panel, in which the colour is corrected for the foreground extinction, although the mean value of the $(J-K_s)$ colour is reduced, the increasing trend is still visible. The third panel of

[6]Obtained from Prof. Renée Kraan-Korteweg

Fig. 3.12 shows the extinction and k-corrected colour, and as a result no rise is seen in the colour of galaxies as a function of redshift. The dashed line in Fig. 3.12 shows the mean $(J - K_s)$ colour of nearby early-type galaxies $(J - K_s) = 0\overset{\text{m}}{.}92$ (Jarrett, 2000).

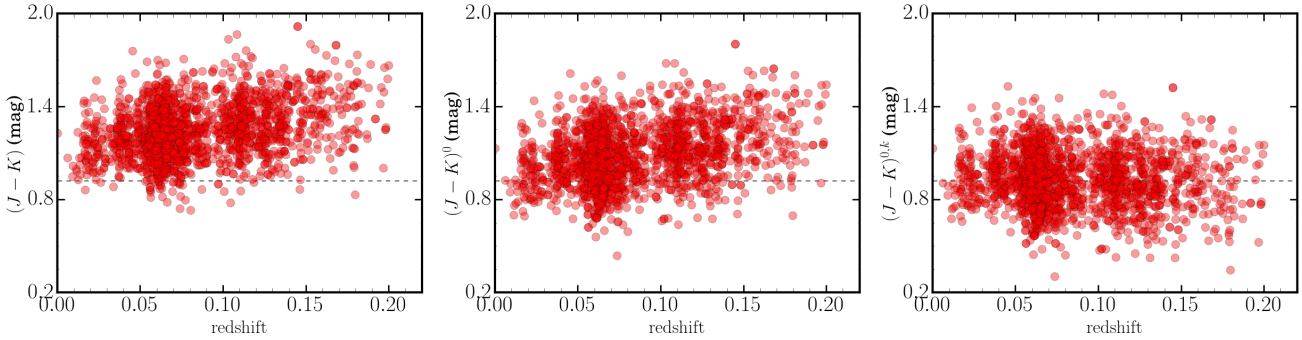

Figure 3.12: The plot of colour versus redshift of 2236 selected galaxies from the ZoA master list. The selected galaxies are restricted to the Galactic longitude range of $255° < \ell < 285°$ and the latitude range of $|b| < 10°$. The left panel shows the $(J - K_s)$ colour of the galaxies as a function of redshift, the middle panel the extinction-corrected colour $(J - K_s)$, and the right panel the extinction and k-corrected colour of galaxies. The dashed line shows the mean $(J - K_s)$ colour of nearby early-type galaxies (Jarrett, 2000)

.

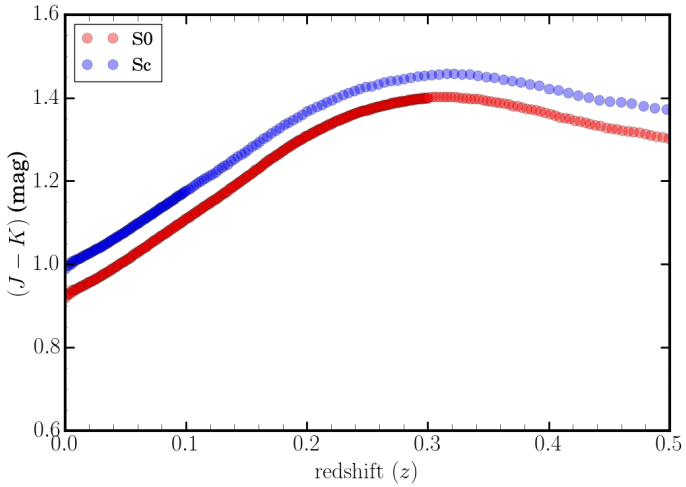

Figure 3.13: The change in the mean value of $(J - K_s)$ colour as a function of redshift for S0 and Sc type galaxies (reddening curve).

k-correction in the VSCL clusters

To implement the k-correction on NIR colours of galaxies in the VSCL clusters, I used the k-correction derived by T. Jarrett (private communication). At the distance of the VSCL, 18000 km s^{-1} (Kraan-Korteweg et al., 2017), the k-correction for $(J - K_s)$ is $\sim 0\overset{\text{m}}{.}112$ for early-type galaxies. Here, I show the effect of k-correction on the VSCL cluster VC04 only, which has the largest number of identified galaxy candidates, assuming that all galaxy candidates in VC04 lie at the VSCL distance. As before, I plotted in Fig. 3.14 the colour-magnitude diagram for VC04 potential galaxies before and after foreground

extinction-correction and extinction plus k-correction. This plot clearly reveals the offset due to redshift. The offset is small at the distance of the VSCL but not insignificant ($\Delta m = 0\overset{\mathrm{m}}{.}112$). However, after k-correction the mean $(J - K_s)$ colour value becomes closer to the mean colour of nearby early-type galaxies, $(J - K_s) = 0\overset{\mathrm{m}}{.}92$ (Jarrett, 2000). This value of $(J - K_s)$ was chosen since early type galaxies dominate the core of almost all types of galaxy clusters (morphology-density relation of galaxies (Dressler, 1980)).

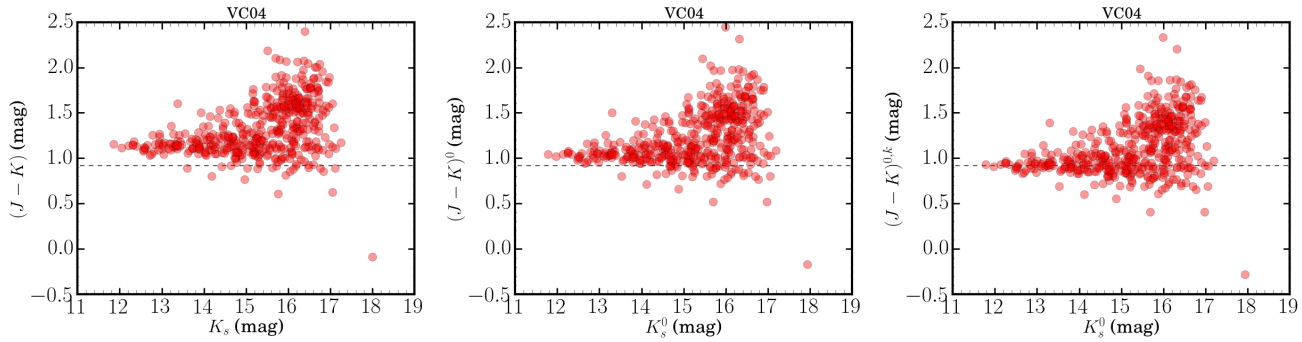

Figure 3.14: The colour-magnitude diagram ($(J - K_s)$ versus K_s). From left to right the plots are observed, extinction-correction and extinction plus k-correction. The dashed lines indicate the mean NIR isophotal colour $(J - K_s)$=$0\overset{\mathrm{m}}{.}92$ for nearby early-type galaxies (Jarrett, 2000).

It is clear from Fig. 3.14 that at the faint end there remains an increasing number of highly reddened galaxies, which mark the background galaxies in the cluster. Bulgy galaxies in clusters closely follow a relation in the colour-magnitude diagram called the red-sequence, which can be used to identify cluster galaxies (see Sect. 5.2.3).

3.5 Completeness limit

To perform scientific analysis on the cluster properties a good assessment of the magnitude completeness limits is required. To determine this I applied the procedure described in Garilli et al. (1999); Andreon et al. (2000) which was also followed by Skelton et al. (2009) in the analysis of the Norma cluster. This method is based on the assumption that galaxies will not be detected once their surface brightness falls below a certain brightness threshold. In Fig. 3.15 the relation between the extinction-corrected K_{s20} fiducial isophotal magnitude of galaxies in VC04 and their central surface brightnesses is shown in three J, H and K_s bands. To plot this figure, galaxies with $r > 2''$ are used according to the analysis of extinction-corrected colour-colour diagrams performed in section 2.4.1. Recall that all the galaxies were visually inspected to minimise the number of spurious detections. Also note that I used the mean central surface brightness within $r < 3''$ which is larger than the mean seeing of the images in J, H and K_s bands (FWHM= $1\overset{''}{.}55, 1\overset{''}{.}46$ and $1\overset{''}{.}37$ respectively) therefore, the effect of PSF-smearing is minimized and its impact on the completeness limit analysis is insignificant.

In Fig. 3.15 the identified galaxies are displayed as red circles. The thick black line (b) is the linear fit between the magnitudes and surface brightnesses of galaxies. The $\pm 3\sigma$ are shown as gray lines on either side of the linear fit. The vertical thick black line represents the surface brightness detection limit, which is roughly chosen at where the number of galaxies with faint surface brightnesses starts to decrease and where no data points are found above the fitted line (the drop-offs in the numbers can be verified in the surface

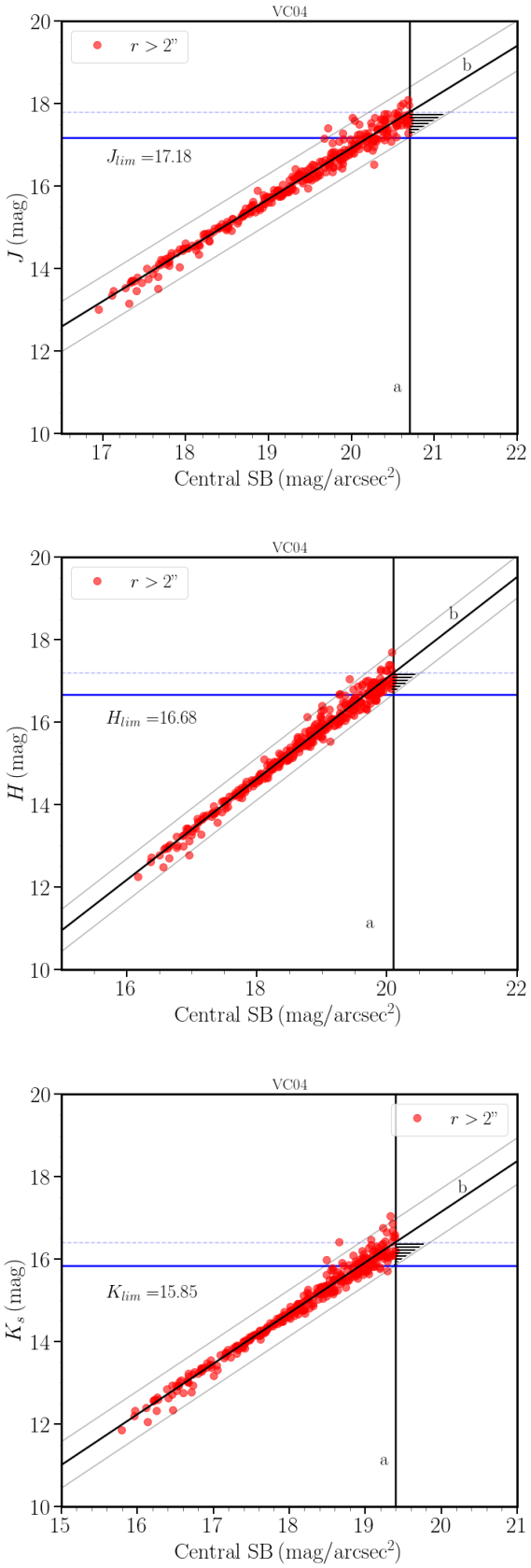

Figure 3.15: Isophotal magnitude vs central surface brightness of candidate galaxies in VC04 in three J, H and K_s bands. The fitted relation is shown by the solid black line, with the thin gray lines representing a deviation of 3σ on either side. The completeness magnitude is indicated by the solid thick blue line.

brightness histograms displayed in Chapter 4). The intersection between the detection limit and the linear fit can not be taken as the completeness limit because galaxies in the hatched area would not be detected even if they are brighter than the completeness limit. Therefore, where the surface brightness limit line (a) intersects with the -3σ of the linear fit was selected to be the completeness limit magnitude. The equations of the fitted lines, one sigma (σ) and completeness limit values for the VC04 cluster in the J, H and K_s bands are as follows:

$$y = (1.23 \pm 0.01)x - (7.85 \pm 0.20) \qquad J_{lim} = 17\overset{\text{m}}{.}18 \tag{3.20}$$

$$y = (1.22 \pm 0.01)x - (7.44 \pm 0.17) \qquad H_{lim} = 16\overset{\text{m}}{.}68 \tag{3.21}$$

$$y = (1.22 \pm 0.01)x - (7.42 \pm 0.18) \qquad K_{slim} = 15\overset{\text{m}}{.}85 \tag{3.22}$$

The extinction-corrected values of the magnitude completeness limits were determined by subtracting the maximum values of extinction on galaxies within each cluster (see Table 3.8) from the observed magnitude completeness values. It was done in the three J, H and K_s bands. The observed and extinction-corrected completeness magnitude limits for the six VSCL clusters are listed in Table 3.10. This table also contains the magnitude completeness limits of the other NIR surveys performed with the IRSF/SIRIUS camera. The 2MASS survey completeness magnitude at high Galactic latitudes ($|b| > 10°$), is limited to $K_s = 13\overset{\text{m}}{.}5$ (Skrutskie et al., 2006) which shows that the VSCL survey is $\sim 2\overset{\text{m}}{.}0$ deeper compared to the 2MASS survey. Table 3.10 shows that the observed K_s-band completeness limit in this work is consistent with the other NIR surveys using the IRSF/SIRIUS camera. Note that the survey area in Riad (2010) is located closer to the GP, where the extinction is much higher than this work.

The lowest extinction-corrected value of the K_s-band magnitude limit belongs to VC08, $K_s^o = 15\overset{\text{m}}{.}34$, which after applying the extinction and k-correction becomes $K_s^{o,k} = 15\overset{\text{m}}{.}12$. However, this value is much less than those of the other five clusters, since the images of VC08 are of slightly lower quality and had slightly higher seeing values than the other cluster images. Furthermore, VC08 is located in a region with higher stellar density which results in higher sky brightness. The lowest extinction-corrected value of the K_s-band magnitude limit for the other five clusters is $K_s^o = 15\overset{\text{m}}{.}65$, or k-corrected value of $K_s^{o,k} = 15\overset{\text{m}}{.}53$. Therefore, in this thesis, I will use $K_s^{o,k} \sim 15\overset{\text{m}}{.}5$, which at the distance of the VSCL ($v \sim 18000$ km s^{-1}) translates to $M_{Ks} = -21\overset{\text{m}}{.}5$. However, for the particular cluster VC08 analysis, the completeness magnitude limit of $K_s^{0,k} = 15\overset{\text{m}}{.}12$ will be considered as well.

To check the consistency of the results a second independent method was used to derived the completeness magnitude limits. To perform this method the distribution of the logarithm of the cumulative galaxy count, $\log(\mathrm{N})_{\mathrm{cum}}$, as a function of observed K_{s20} fiducial isophotal magnitudes was plotted (Fig. 3.16). The completeness magnitude was estimated to be the point where the galaxy counts start deviating from the ascending linear trend (the knee of the distribution) and start flattening. The values of magnitude completeness limit for the six VSCL clusters, using the two methods of derivation, are listed in Table 3.11. It shows that the cumulative method overestimated the magnitude completeness limits, compared to the first method. In this work, we use the completeness limit derived from the first method.

Table 3.10: Comparison of the completeness limits of VSCL clusters to other NIR surveys performed by IRSF/SIRIUS camera.

	J (mag)	J^0 (mag)	H (mag)	H^0 (mag)	K_s (mag)	K_s^0 (mag)
VC02 [a]	17.31	17.00	16.57	16.37	15.78	15.65
VC04 [a]	17.18	16.98	16.68	16.55	15.85	15.76
VC05 [a]	17.36	17.18	16.49	16.37	15.84	15.76
VC08 [a]	17.25	17.03	16.32	16.17	15.43	15.34
VC10 [a]	17.43	17.20	16.55	16.40	15.89	15.79
VC11 [a]	17.18	16.88	16.42	16.24	15.83	15.70
Norma wall[b]	16.60	15.60	15.80	15.30	15.40	14.80
HIZOA J0836-43 [c]	16.40	–	15.80	–	15.40	–
Norma cluster [d]	–	–	–	–	15.74	–

[a] This work.
[b] Riad (2010).
[c] Cluver (2008).
[d] Skelton et al. (2009).

Table 3.11: Comparing the completeness limits of the VSCL clusters using two methods of derivation.

	J (mag)	H (mag)	K_s (mag)
VC02 [a]	17.31	16.57	15.78
VC02 [b]	17.65	16.95	16.20
VC04 [a]	17.18	16.68	15.85
VC04 [b]	17.60	16.90	16.20
VC05 [a]	17.36	16.49	15.84
VC05 [b]	17.65	16.95	16.15
VC08 [a]	17.25	16.32	15.43
VC08 [b]	17.55	16.85	16.10
VC10 [a]	17.43	16.55	15.89
VC10 [b]	17.60	16.90	16.10
VC11 [a]	17.18	16.42	15.83
VC11 [b]	17.65	16.90	16.15

[a] The first method (SB).
[b] The second method ($\log(N)$).

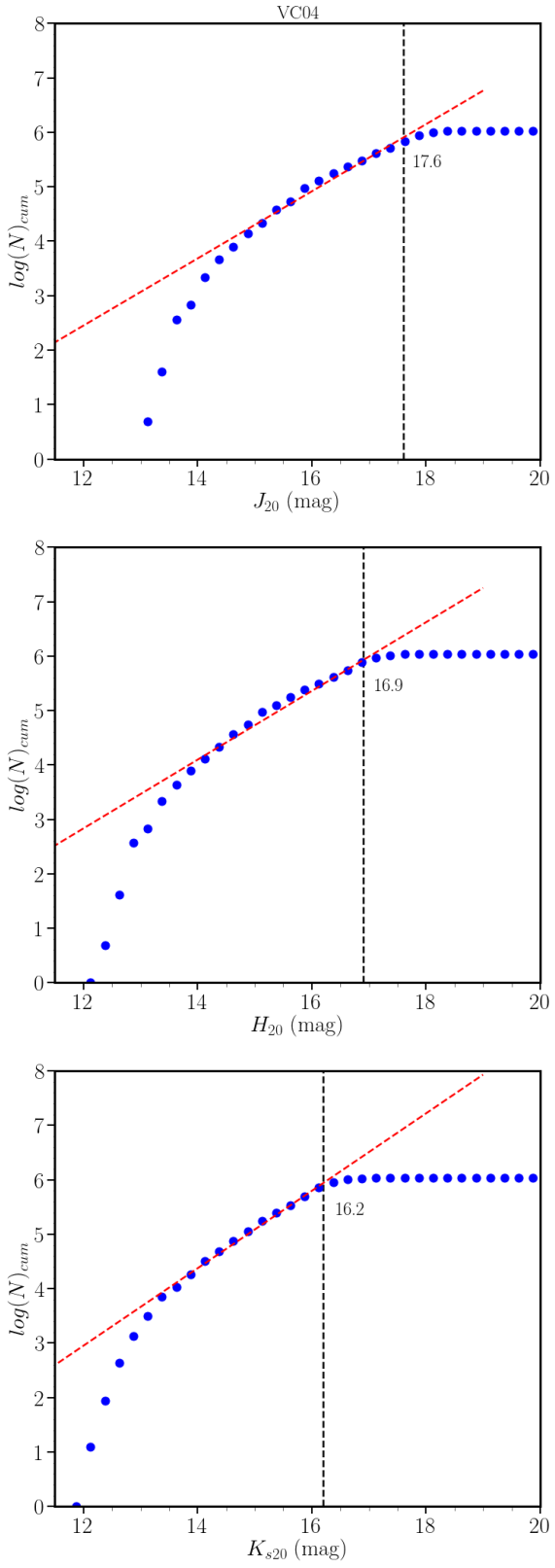

Figure 3.16: Distributions of the logarithm of the cumulative galaxy count, $\log(N)_{cum}$, as a function of observed $K_s = 20$ fiducial isophotal magnitudes in J, H and K_s bands in VC04. The black dashed lines show the completeness magnitude limits in each band at the knee of the distributions. The red dashed line is plotted to show the deviation point from the ascending trend.

3.6 Summary

In this chapter the process of creating a catalogue of galaxies with their astrometric and photometric parameters in the observed VSCL clusters using the IRSF pipeline was explained. After introducing some of the most important parameters of galaxies in the catalogue their internal and external consistency was confirmed. Next, the effect of extinction in the regions of the clusters was probed. The VC02 cluster has the highest foreground extinction while VC04 and VC05 have the lowest. The effect of extinction on the isophotal magnitudes is significantly smaller than the overall foreground extinction and it was concluded to not correct for it. In the next step, it was shown that although the effect of redshift on the galaxies at the distance of the VSCL ($z \sim 0.06$) is small, it is not insignificant and should be taken into account. Finally the completeness magnitude limit in each cluster was derived, using the surface brightness values of galaxies in each cluster, and the lowest derived value (between the six clusters) which is $K_s^{o,k} = 15\overset{\text{m}}{.}5$, was chosen to be the completeness magnitude limit of this survey. This value is extinction and k-corrected and at the distance of the VSCL translates to $M_{Ks} = -21\overset{\text{m}}{.}5$.

Knowing the reliability of the derived galaxy parameters and completeness magnitude limit of the survey, I analyse various aspects of the VSCL clusters in the next chapters.

Chapter 4

Analysis of the VSCL Galaxy Clusters

This chapter is dedicated to the analysis of the VSCL galaxy clusters based on the NIR photometry derived in the previous chapter. There are a total number of 1715 identified galaxies distributed over the six clusters. To put the results in context I will in Sect. 4.1 summarize the typical NIR characteristics of a selection of clusters with varying richnesses to compare them with the VSCL clusters. For this I selected the well-studied Coma, Norma, 3C129 and Virgo clusters. Afterwards in Sect. 4.2, I will present the catalogue statistics of the six observed clusters in the VSCL and analyse their iso-density contours and radial density profiles to determine their structures and richnesses. VC04 is one of the most prominent clusters in the VSCL. It has been observed by MeerKAT as an early Science Commissioning Project by R. Kraan-Korteweg and collaborators in 2018, which allows me an analysis of its H I content which is presented in Sect.4.3.

4.1 Comparison clusters

The four clusters Coma, Norma, 3C129 and Virgo were selected for comparison because they are all quite local ($v \lesssim 7000$ km s^{-1}) and because of their availability of NIR data to the approximate same magnitude completeness limit as the more distant VSCL clusters ($17000-22000$ km s^{-1}) explored with the IRSF and their variety in richness from a young, irregular cluster like Virgo to a virialized, very massive cluster like Coma.

The NIR data for all clusters, both the VSCL and comparison clusters, are extinction-corrected and complete to the extinction-corrected magnitude completeness limit of this work which is $M^o_{K_s} = -21\overset{\mathrm{m}}{.}5$ and the properties of these clusters are summarized in Table 4.1.

The Coma cluster

The Coma cluster, or ACO 1656 (Abell et al., 1989) at $(\ell, b) \approx (58\overset{\circ}{.}08, 87\overset{\circ}{.}95)$, heliocentric velocity $v_{hel} = 6942\,\mathrm{km\,s^{-1}}$ with a velocity dispersion $\sigma = 1034\,\mathrm{km\,s^{-1}}$ (Wegner et al., 1999), is the prototype of a rich, regular cluster, and is one of the best-studied clusters (see Pimbblet et al., 2014, and references therein), although signs of substructure are present implying that Coma is not fully relaxed (Biviano et al., 1996; Healy et al., 2021a).

The mass of Coma was first estimated by Zwicky (1933, 1937) to be $M > 5 \times 10^{14}$ M$_\odot$, using the virial theorem. Using X-ray data, Hughes (1989) determined a virial mass for Coma of $M_X \sim 1.32 \pm 0.24 \times 10^{15}\,h_{70}^{-1}$ M$_\odot$within $3.57\,h_{70}^{-1}$ Mpc. The X-ray flux of this cluster is about 3.19×10^{-10} erg s^{-1} cm^{-2} in the 0.1-2.4 keV range (Ebeling et al., 1998).

Kubo et al. (2007) presented a weak lensing analysis of the Coma cluster and derived a virial mass of $2.68^{+0.65}_{-0.56} \times 10^{15}\, h_{70}^{-1}$ $M_\odot$within a virial radius of $2.84^{+0.21}_{-0.22}\, h_{70}^{-1}$ Mpc.

The core of the Coma cluster is dominated by two cD galaxies, NGC 4874 and NGC 4889. Most of the galaxies in the central regions of Coma are ellipticals, including plenty of dwarf ellipticals. I used the 2MASX catalogue (Jarrett et al., 2000b), to extract the NIR data for Coma out to a comparable radius and magnitude completeness limit as the IRSF mosaics of the VSCL clusters sample.

The Norma cluster

The Norma cluster, or ACO 3627 (Abell et al., 1989) at $(\ell, b) \approx (325°, -7°)$, $v_{hel} = 4844\,\mathrm{km\,s^{-1}}$ and $\sigma = 925\,\mathrm{km\,s^{-1}}$ (Woudt et al., 2008), is the most massive galaxy cluster in the Great Attractor (GA) overdensity (Kraan-Korteweg et al., 1996; Woudt, 1998), with properties comparable to the Coma cluster (Woudt, 1998). The X-ray observations such as the ROentgen SATellite (ROSAT) (Boehringer et al., 1996) and ASCA (Tamura et al., 1998), also verify the massive nature of the Norma cluster. The X-ray flux of this cluster is about $2.2 \times 10^{-10}\,\mathrm{erg\ s^{-1}\ cm^{-2}}$ over 0.1-2.4 keV (Ebeling et al., 2002). This cluster shows signs of mergers making it an interesting object to study cluster mergers (Boehringer et al., 1996; Woudt et al., 2008). Boehringer et al. (1996) obtained a total virial mass of $M_V \sim 8.5 \times 10^{14}\, h_{70}^{-1}$ $M_\odot$ within viral radius of $r_v = 2.14\, h_{70}^{-1}$ Mpc. They also obtained a X-ray mass of $15.7 \times 10^{14}\, h_{70}^{-1}$ $M_\odot$ within the virial radius.

The Norma cluster contains two large cD galaxies, WKK 6312 and WKK6269. Woudt et al. (2008) showed that there is no detectable substructure in the E/S0 galaxy distribution in Norma which appears relaxed but that, the spiral/irregular population shows quite some substructure. They determined the dynamical mass of the Norma cluster within its Abell radius to be $1.04 - 1.14 \times 10^{15}\, h_{70}^{-1}$ $M_\odot$.

I used two datasets of NIR data to analyse the Norma cluster in this survey. The first set was obtained from the deep K_s band catalogue of galaxies created by Skelton et al. (2009). The observations of the Norma cluster were done using the SIRIUS camera on the IRSF telescope (same as this work, see Sect. 2.2). The Skelton et al. (2009) study only covers the central $0.8\, h_{70}^{-2}$ Mpc^2 of the Norma cluster. This catalogue consists of 390 objects, 235 of which are classified as certain galaxies and 155 as candidate galaxies. The second NIR data set was obtained from the 2MASX (Jarrett et al., 2000b) to reach out to the completeness radius of the VSCL NIR data, i.e. $0.7R_A$.

The 3C129 cluster

The 3C129 cluster is a fairly rich cluster in the Perseus-Pisces filament, located at $(\ell, b) \approx (160.52°, 0.27°)$ (Ebeling et al., 2002), $v_{hel} = 5227\,\mathrm{km\,s^{-1}}$ and $\sigma = 765\,\mathrm{km\,s^{-1}}$ (Leahy and Yin, 2000). The 3C129 cluster is obscured in optical wavelengths due to its location in the ZoA. This cluster was first spotted as an X-ray source called 4U 0446+44 with the Uhuru satellite. Its observation was followed up by ROSAT[1], the European Space Agency X-ray Observatory (EXOSAT)[2] and the Einstein[3] satellite. Ebeling et al. (2002) also detected this cluster as CIZA J0450.0+4501 with X-ray flux of $0.91 \times 10^{-10}\,\mathrm{erg\ s^{-1}\ cm^{-2}}$ in 0.1-2.4 keV and Leahy and Yin (2000) reported an X-ray mass of $\sim 3.5 \times 10^{14}\, h_{70}^{-1}\,\mathrm{M}_\odot$ for

[1]https://heasarc.gsfc.nasa.gov/docs/rosat/rosat3.html
[2]https://heasarc.gsfc.nasa.gov/docs/exosat/exosat.html
[3]https://heasarc.gsfc.nasa.gov/docs/einstein/heao2_about.html

this cluster. Pinzke et al. (2011) estimated the virial radius and mass of this cluster to be $r_{200} = 1.89\,h_{70}^{-1}$ Mpc and $M_{200} = 7.8\times10^{14}\,h_{70}^{-1}\,M_\odot$. This cluster is not dynamically relaxed (virialized) and the presence of substructure in it suggests that it may have experienced a recent merger, as reported in Leahy and Yin (2000) and Ramatsoku (2017).

The NIR data of the 3C129 cluster is obtained from a catalogue of galaxies in the J and K bands provided by Ramatsoku et al. (2020), using the UKIRT Infrared Deep Sky Survey (UKIDSS, Lawrence et al., 2007). Ramatsoku et al. (2020) studied the central area of $\sim 4^\circ \times 4^\circ$ of 3C129 and identified 261 galaxies in this region.

The Virgo cluster

The Virgo cluster is the closest galaxy cluster located at $(\ell, b) \approx (283.80^\circ, 74.43^\circ)$, $v_{hel} \approx 1050\,\mathrm{km\,s^{-1}}$ $\sigma \sim 700\,\mathrm{km\,s^{-1}}$ (Binggeli et al., 1993) and the core of the Local supercluster (de Vaucouleurs, 1961). It is an irregular and dynamically young cluster (Arnaboldi et al., 2004; Aguerri et al., 2005) with substructures around M87 (cD galaxy), M49 and M86 (de Vaucouleurs, 1961; Schindler et al., 1999; Mei et al., 2007; Kim et al., 2014; Kashibadze et al., 2020). Kashibadze et al. (2020) estimated a virial mass of $\sim (6.57 \pm 0.9) \times 10^{14}\,h_{70}^{-1}\,M_\odot$ for this cluster. The X-ray flux of Virgo is presented in Ebeling et al. (1998) to be $8.21 \times 10^{-10}\,\mathrm{erg\ s^{-1}\ cm^{-2}}$ in 0.1-2.4 keV (ROSAT band). McLaughlin (1999) determined an X-ray mass of $\sim (4.2 \pm 0.5) \times 10^{14}\,h_{70}^{-1}\,M_\odot$within a virial radius of $1.55\,h_{70}^{-1}$ Mpc.

The NIR data for the Virgo cluster used in this work were obtained from 2MASX (Jarrett et al., 2000b).

Table 4.1: Properties of four comparison clusters, Coma, Norma, 3C129 and Virgo. All the references are given in the text. $\langle A_{Ks}\rangle$ indicates the mean foreground extinction in each cluster.

Cluster	Distance h_{70}^{-1} Mpc	X-ray flux 10^{-10} ergs s^{-1} cm^{-2}	r_{virial} h_{70}^{-1} Mpc	σ_v km s^{-1}	Virial Mass $10^{15}h_{70}^{-1}\,M_\odot$	X-ray Mass $10^{15}h_{70}^{-1}\,M_\odot$	$\langle A_{Ks}\rangle$ mag
Coma	$\sim$99.1	3.20	2.84	1034	2.68	1.32	0.003
Norma	$\sim$69.2	2.20	2.14	925	0.85	1.50	0.070
3C129	$\sim$74.0	0.91	1.89	765	0.78	0.35	0.350
Virgo	$\sim$15.0	8.21	1.55	700	0.65	0.42	0.009

4.1.1 Structure and Richness

Iso-density contour maps and radial density profiles are very useful tools for examining the structure and richness of clusters. In order to compare the richness of the VSCL clusters to those of the comparison clusters, I first perform the analysis on the comparison clusters, starting with deriving the 2-D spatial distribution of galaxies for the comparison clusters.

As stated in the introduction chapter, regular clusters have high central galaxy densities and are symmetric in shape, whereas irregular clusters are not highly concentrated or symmetric and often show substructures. To perform a dynamical analysis on clusters and a more robust 3-D test such as the Dressler-Shectman δ-test for substructure (Dressler and Shectman, 1988), spectroscopic redshifts are required. For the VSCL clusters only limited spectroscopic information is available (Kraan-Korteweg, 2000a). Only 2MASX galaxies ($K^o \lesssim 13\overset{\mathrm{m}}{.}5$) in the VSCL region have spectroscopic redshifts, hence

they are $\sim 2\overset{m}{.}0$ brighter than the IRSF photometric data and such a methodology cannot be applied to the current cluster dataset.

Isodensity contour and radial density plots

To produce the isodensity contour plots, the number of galaxies per square grid of $\sim 2' \times 2'$ was determined. The grids cover the area of each cluster. To have the proper square grids, a curved surface of RA (α) and Dec (δ) must be flattened into a plane. For each galaxy, offsets with respect to the centre of the cluster were determined where

$$\begin{aligned} \Delta\delta(deg) &= (\delta_1 - \delta_c) \\ \Delta\alpha(deg) &= (\alpha_1 - \alpha_c)\ cos(\delta_1), \end{aligned} \tag{4.1}$$

and α_1 and δ_1 are the coordinates of each galaxy and α_c and δ_c are the coordinates of the centre of that cluster. This equation is valid for relatively small separations.

In the next step, $\Delta\alpha$ and $\Delta\delta$ were converted to a physical radial distance (in Mpc) with respect to the centre of each cluster. The cluster distance was based on the mean heliocentric velocity of each cluster, using a cosmological model with parameters: $H_0 = 70\,\mathrm{km\ s^{-1}\ Mpc^{-1}}, \Omega_M = 0.3$ and $\Omega_\Lambda = 0.7$. Note that the velocities are not corrected for flow fields. The number of galaxies in each grid area was converted to densities (N/deg^2), smoothed by a Gaussian filter to plot the isodensity contour maps. The magnitude completeness limit for the comparison clusters was constrained to be the same as for the six VSCL clusters: $M_{Ks} = -21\overset{m}{.}5$.

As stated in Sect. 2.2.1, the completeness radius of this survey varies from $r_c = 1.5$ Mpc to 1.8 Mpc depending on the actual distance of the cluster. For consistency the completeness radius was selected to be $r_c = 1.5$ Mpc and the cluster analyses will be performed out to this radius. The r_c covers ~ 71 % of the Abell radius. The isodensity contour maps for the four comparison clusters are displayed in the left panel of Fig. 4.1. The Norma cluster has two maps, one for the 2MASX sample out to $r_c < 1.5$ Mpc, and the second one for the deep IRSF K_s-band data Skelton et al. (2009) out to $r \lesssim 0.5$ Mpc. The IRSF isodensity map for Norma is shown in the left panel of Fig. 4.2. In the left panels of Figs. 4.1 and 4.2, the galaxies are shown as black dots and the centres of clusters as red stars. The red and magenta circles represent r_{200} and r_c respectively. r_{200} was derived for each cluster using equation 1.3.

The number densities of each cluster, shown in the colour bar of Fig. 4.1, depict that the Coma cluster is the richest cluster, followed by Norma, 3C129 and Virgo. This figure also demonstrates an elongated structure in Coma and a clear substructure in the Virgo cluster, while 3C129 shows a symmetric structure in the central region. The Norma cluster out to $r \sim 0.5$ Mpc shows a symmetric and regular structure but it is slightly elongated when its outer area is mapped.

To illustrate the degree of concentration of galaxies, I plotted the radial distribution of each cluster, with the number density (N/Mpc^2) of galaxies in bins of 0.1 Mpc. The radial density profiles of the comparison clusters out to r_c are shown in the right panels of Fig. 4.1. The red and magenta lines mark the r_{200} and r_c.

The radial density profiles of the Coma and Norma clusters show that they are highly concentrated toward the centre and have gradual and smooth distributions which are indicative of rich and massive clusters, while the Virgo cluster shows signs of an irregular cluster (Abell, 1975; Bahcall, 1977). The 3C129 cluster is not as rich as Coma and Norma but it is centrally concentrated and seems like an intermediate cluster (see Sect. 1.5.1).

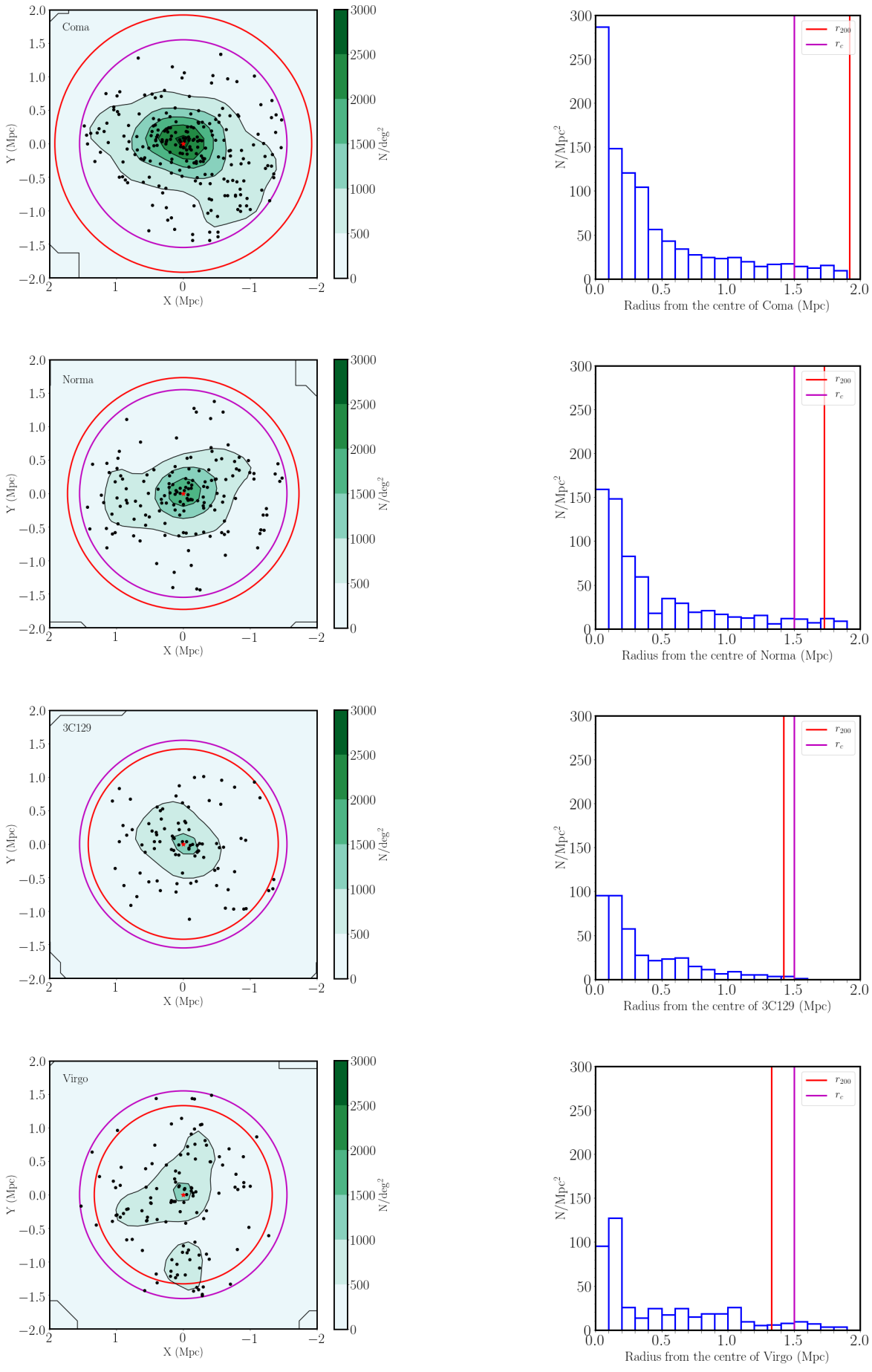

Figure 4.1: Left: the iso-density contour maps of the Coma, Norma, 3C129 and Virgo clusters out to $r_c = 1.5\,\mathrm{Mpc}$ and the extinction-corrected magnitude completeness limit of $M^o_{Ks} = -21\overset{\mathrm{m}}{.}5$. The galaxies are shown as black dots and the centres of clusters as red stars. The red and magenta circles represent the r_{200} and r_c respectively. Right: the radial density profile of the clusters.

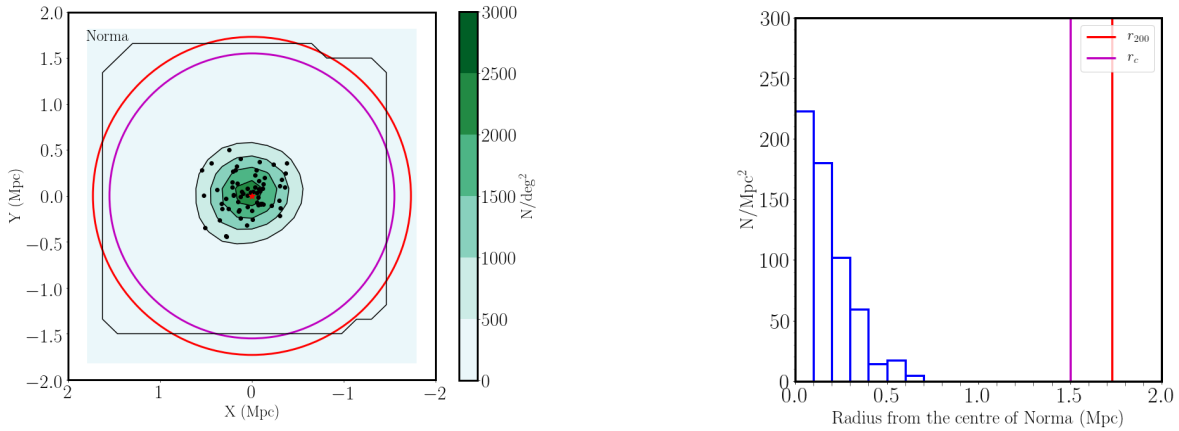

Figure 4.2: Left: the Iso-density contour map of the Norma cluster out to $r \sim 0.5$ Mpc. The galaxies are shown as black dots and the centre of cluster as a red star. The red and magenta circles represent the r_{200} and r_c respectively. Right: the radial density profile of the Norma cluster out to $r \sim 0.5$ Mpc.

The higher number density of Norma within 0.1 Mpc in the right panel of Fig 4.2 compared to Fig 4.1, shows that Skelton et al. (2009) identified more galaxies in the central regions of Norma compared to 2MASX due to the higher resolution of IRSF. The comparisons in this thesis were performed using the 2MASX galaxies in Norma, since it covers the full area out to $r_c = 1.5$ Mpc, while the IRSF covered only the inner (~ 0.5 Mpc) of the Norma cluster.

Abell richness class

The Abell richness classification is based on the number of galaxies in the magnitude range of m_3 (the third brightest galaxy in the cluster) and $m_3 + 2$ that lie within one Abell radius (described in Sect. 1.5.1). Abell (1958) carried out his work in the optical R band, in which late-type galaxies are more visible compared to the NIR (this work). However, the NIR is less affected by extinction compared to optical, therefore in the ZoA, more galaxies can be identified using NIR rather than optical bands. Moreover, the Abell catalogue is complete to $R \sim 17\overset{m}{.}5$. Using the colours $(R - K) = 2\overset{m}{.}62$ for early- and $(R - K) = 2\overset{m}{.}30$ for late-type galaxies (Huang et al., 2001), this translates to $K \sim 14\overset{m}{.}88$ for early- and $K \sim 15\overset{m}{.}20$ for late-type galaxies. Here, I only derive N_A in K_s band ($N_A(K_s)$) for the Coma, Norma, 3C129 and Virgo clusters for later comparisons with the VSCL data.

Using the 2MASX data for the Coma cluster, I derived $m_3 = 9\overset{m}{.}4$ and the number of galaxies within $m_3 < m < m_3 + 2$ and an Abell radius $\sim 2.1\ h_{70}^{-1}$ Mpc is $N_A(K_s) = 57$. Abell et al. (1989) found $N_A = 106$ and classified Coma as $R = 2$. The magnitude completeness limit of 2MASX is $K_{slim} = 13\overset{m}{.}5$ (Skrutskie et al., 2006) while Abell's catalogue is complete to $K \sim 14\overset{m}{.}88$ for early- and $K \sim 15\overset{m}{.}20$ for late-type galaxies. This could be the reason for the smaller number of galaxies found in NIR.

In Norma, $m_3 = 8\overset{m}{.}5$, based on the 2MASX data. The number of galaxies within $m_3 < m < m_3 + 2$, is $N_A(K_s) = 53$. Using optical data, Abell et al. (1989) found $N_A = 59$ and $R = 1$. Note that Norma is located in the ZoA and therefore the lower depth of 2MASX in magnitude is compensated for by the more robust NIR observations near the Galactic plane, hence the numbers are similar.

Using data in Ramatsoku (2017) for the 3C129 cluster, I found $m_3 = 9\overset{\text{m}}{.}6$. The data are complete out to $r \sim 1.5$ Mpc and the number of galaxies with $m_3 < m < m_3 + 2$ that lie within this radius is $N_A(K_s) = 39$. Note that this data are not complete out to the Abell radius.

Using the 2MASX data in Virgo, I found $m_3 = 5\overset{\text{m}}{.}9$, and the number of galaxies within the Abell radius and $m_3 < m < m_3 + 2$, is $N_A(K_s) = 37$.

4.2 The VSCL galaxy clusters

In this section I present the results of a detailed analysis performed on one of the most prominent clusters in the VSCL; VC04. I start with the NIR catalogue statistics of VC04 and the on-sky distribution of galaxies, followed by analysis of its structure and richness. This is followed by a brief presentation of the other five clusters for which the same procedure was applied, as well as a comparison between the properties of the six clusters with respect to each other and the comparison clusters. The VC04 cluster was also observed by the MeerKAT telescope (Jonas and MeerKAT Team, 2016) to search for possible galaxy detections in H I. I performed a brief H I analysis on the potential H I deficiency of the cluster which is presented in Sect. 4.3.

4.2.1 Galaxy cluster VC04

Cluster catalogue statistics

The NIR study of VC04 has uncovered 465 galaxy candidates. The full catalogue of VC04 galaxies is provided in Appendix A. The distribution of the galaxy candidates in the observed mosaic is displayed in Fig. 4.3 with black dots. The observed fields are shown in red. There are a few candidates out of the mosaic boundaries. This is due to the extra observed fields that were taken to compensate for the blank quarter in K_s band, caused by the infrared detector problem of the IRSF telescope (explained in detail in Chapter 2). To make it clear, two of these extra fields are shown in Fig. 4.3 in blue. The two hatched fields are the ones that are of low science quality and only a few galaxies were found in them.

The first step in analysing the result of the NIR study is to statistically quantify the observed parameters for the galaxies in VC04. To do this, I study the distribution of the isophotal magnitudes and the central surface brightness of the 416 identified galaxy candidates with $r > 2''$. A summary of their photometric properties is listed in Table 4.2. The isophotal magnitudes are used to perform the clusters analyses, while the surface brightness values are used to measure the μ_c-optimised extinction corrections and completeness magnitude limits (Sect. 3.5).

The top panel of Fig. 4.4 displays the distribution in J, H and K_s magnitudes determined at $K_s = 20\overset{\text{m}}{.}0$ fiducial isophotal magnitudes in J, H and K_s bands. The dashed histograms are observed values while the hatched ones are the extinction-corrected magnitudes. The dashed lines show the extinction and k-corrected completeness magnitude limits of this work, $J^o_{lim} = 16\overset{\text{m}}{.}9$, $H^o_{lim} = 16\overset{\text{m}}{.}3$ and $K^o_{slim} = 15\overset{\text{m}}{.}5$.

The central surface brightness is an important attribute since it allows us to classify galaxies into early- or late-type. Jarrett et al. (2003) analysed the correlation between the morphology and central surface brightness of galaxies using the 2MASS Large Galaxy Atlas. They found that early-type galaxies have brighter mean central surface

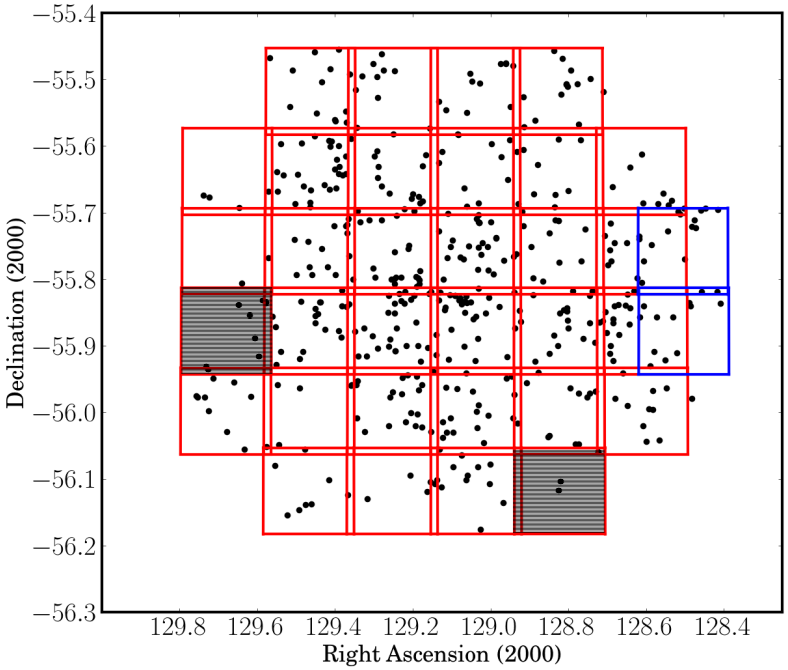

Figure 4.3: The VC04 mosaic. The identified galaxies are shown as black dots. The two hatched fields are the ones that are not of good quality. The two blue fields indicate the extra observed fields to compensate for the blank quarter in K_s band caused by the infrared detector problem of the IRSF telescope.

Table 4.2: Photometric parameters of the VC04 galaxies.

Parameter	Max	Min
J^0_{20} (mag)	18.44	12.82
H^0_{20} (mag)	17.73	12.10
K^0_{s20} (mag)	17.20	11.76
μ^0_{cJ} (mag arcsec^{-2})	21.94	15.95
μ^0_{cH} (mag arcsec^{-2})	21.01	16.04
μ^0_{cKs} (mag arcsec^{-2})	21.37	15.71

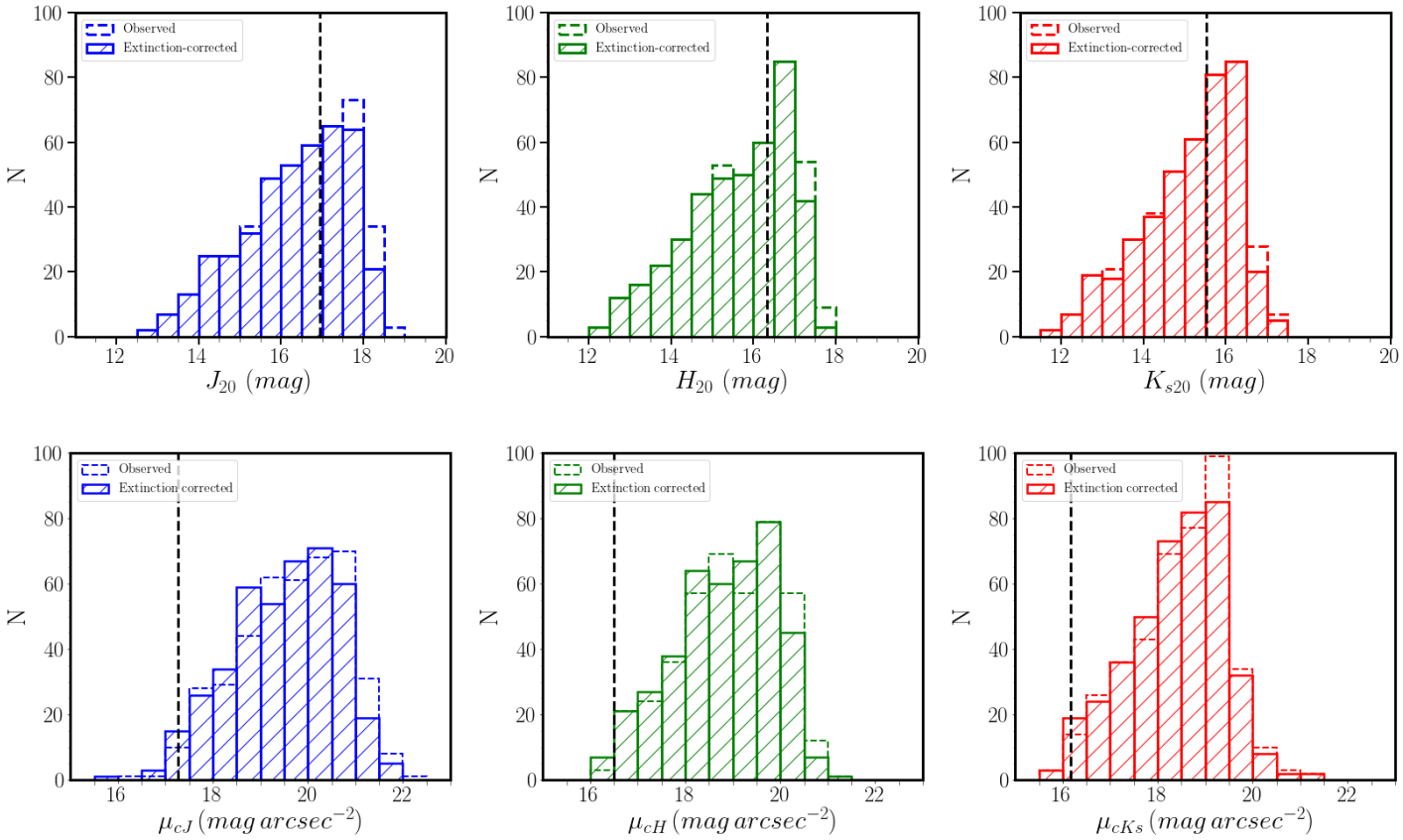

Figure 4.4: Top: VC04 histograms of isophotal magnitudes at $K_s = 20\overset{\text{m}}{.}0$ in J, H and K_s bands. The dashed histograms show the observed magnitudes and the hatched ones are extinction-corrected. The dashed lines are the completeness magnitude limits in each band. Bottom: Histograms of central surface brightnesses of VC04 galaxies in J, H and K_s bands. The dividing values of central surface brightnesses between elliptical and spiral galaxies, derived by Jarrett et al. (2003), in each band are shown by the dashed lines.

brightness compared to late-types. The surface brightness values that divides ellipticals from spiral galaxies lies at $\mu_J = 17.27$ mag arcsec^{-2}, $\mu_H = 16.49$ mag arcsec^{-2} and $\mu_{Ks} = 16.17$ mag arcsec^{-2}. The bottom panel of Fig. 4.4 displays the distribution of central surface brightness for all 416 galaxies in the J, H and K_s bands. Jarrett et al. (2003) dividing values are derived for large and bright galaxies which agrees with the galaxies detected at the large distances of the VSCL, hence Fig. 4.4 shows that our NIR work is sensitive to both early- and late-type galaxies. Note that, although the uncorrected central surface brightness values for PSF-smearing could bias morphological classification of galaxies, using the 3″ isophote to measure the central surface brightness values, minimizes this bias significantly (see section 3.5). The drop-off at the faint end of the distribution of surface brightnesses in deriving the completeness magnitude limit was discussed in Sect. 3.5.

On-sky distribution and 2MASX counterparts

In Sect. 3.5 I determined the extinction-corrected magnitude completeness limit to be $K_{slim} < 15\overset{m}{.}5$. Of the 416 galaxies in the VC04 mosaic, 225 have magnitudes brighter than the completeness limit. An on-sky distribution of the 225 galaxies is displayed in Fig. 4.5. There are 82 2MASX galaxies within the Abell radius of VC04, out of which 69 galaxies have counterparts with galaxies found in this NIR work. Of the 13 galaxies not found on the IRSF fields, 8 lie beyond the boundaries of the cluster mosaic, 3 are in the two fields that were of lower quality and 2 are not galaxies based on the inspection of the deeper, more resolved IRSF images. In Fig. 4.5, IRSF galaxies are shown with filled green circles, the ones with a blue circle have a counterpart in 2MASX. The lower number of 2MASX galaxies is due to the 2MASX completeness magnitude limit of $K_s = 13\overset{m}{.}5$ (Skrutskie et al., 2006).

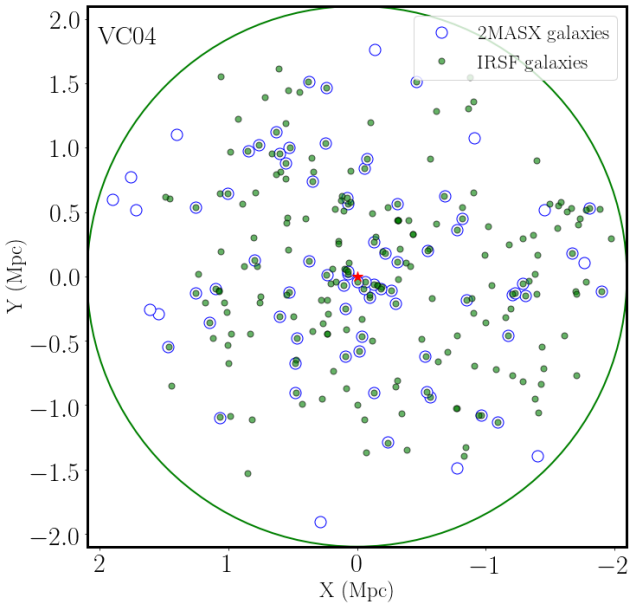

Figure 4.5: The on-sky distribution of galaxies with $K_s^o < 15\overset{m}{.}5$ and $r > 2''$ in VC04. The IRSF galaxies are shown with filled green circles. Galaxies that have counterpart in 2MASX are encircled in blue. The red star shows the centre of cluster and the big green circle is the Abell radius.

Spectroscopic information

The redshift data for all VSCL clusters observed in this work were extracted from the master list of spectroscopic data provided by R. Kraan-Korteweg (see Kraan-Korteweg, 2000a, for details). The galaxies in the master list were identified either in the optical, 2MASX or both. All galaxies with redshifts were recovered and have IRSF photometry confirming that we are sensitive to both early- and late-type galaxies. The fraction of galaxies with spectroscopic data differs for each cluster.

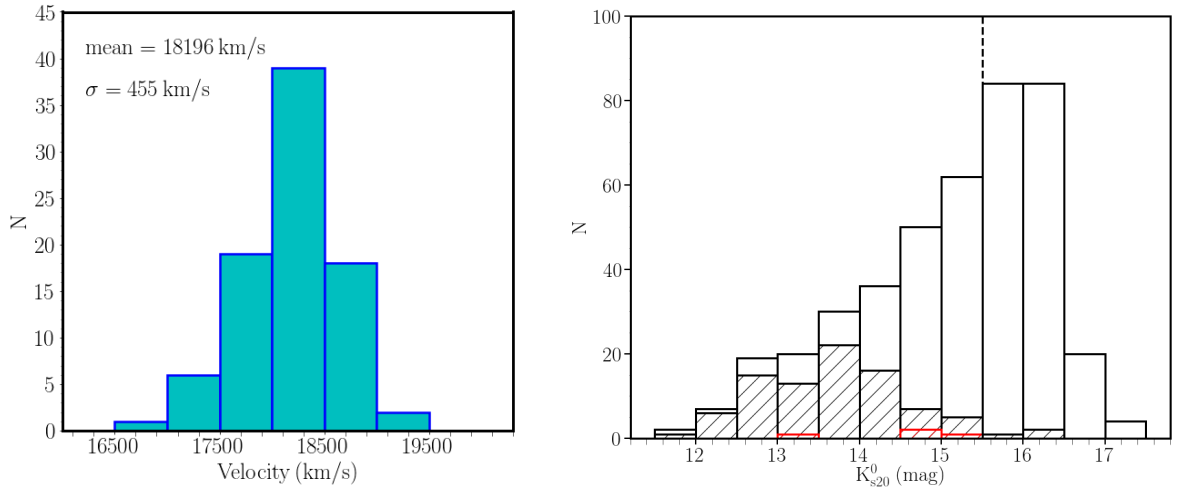

Figure 4.6: Left: the velocity histogram of VC04 for 89 galaxies with spectroscopic redshifts. Right: Distribution of the extinction-corrected K_s magnitudes for 416 identified galaxies in VC04. The 89 galaxies with redshift data are shown as black hatched areas. The red areas mark foreground and background galaxies ($v < 16000$ km s^{-1} and $v > 20000$ km s^{-1} respectively).

The velocity distribution of galaxies with available redshift data in VC04 was determined assuming a Gaussian distribution of velocities and removing foreground and background galaxies by iterating the 3σ-clipping technique (Yahil and Vidal, 1977). The result is shown in the left panel of Fig. 4.6. Based on the velocities of the cluster member galaxies, VC04 is located at a distance of $v = 18191$ km s^{-1}, very close to the main VSCL wall at $v \sim 18000$ km s^{-1}, and its velocity dispersion is $\sigma = 455$ km s^{-1}.

The distribution of the extinction-corrected K_s magnitudes for all identified galaxies in the region of VC04 is shown in the right panel of Fig. 4.6. The 89 galaxies with redshift data are shown as black hatched areas. The red areas depict the foreground and background galaxies with $v < 16000$ km s^{-1} and $v > 20000$ km s^{-1} respectively.

Structure and richness

The right panel of Fig. 4.7 displays the isodensity contour map of VC04, according to the method presented in Sect. 4.1.1. The magenta and red circles in the iso-density contour plot display r_c and r_{200}, respectively. The velocity dispersion of VC04 is $\sigma_v = 455$ km s^{-1}, and the value for r_{200} is 0.82 Mpc (see equation 1.3), while r_c was defined as the completeness radius of this work, 1.5 Mpc.

This iso-density contour map reveals VC04 to be quite regular with a high central density indicative of a rich cluster. In the central regions the distribution of galaxies is fairly spherically symmetric and the iso-density contour map does not show any elongation. There is another small peak north-west just outside r_{200}. The brightest galaxy

in VC04 resides in this overdensity which suggests the existence of a possible infalling subgroup in this cluster. More spectroscopic information is needed to prove this claim. We submitted a proposal to obtain spectroscopic redshifts of all the galaxies at the core of VC04 and many at its outskirts, using the Southern African Large Telescope (SALT). The proposal was accepted and observations were finalised towards the end of 2021. They will be analysed in 2022 and are not in the scope of this thesis.

After creating the iso-density contour plot, the centre of the cluster was adjusted based on the derived isopleths. The new coordinates of the centre are $\alpha = 129.145°$ and $\delta = -55.815°$ indicated by a red star in Fig. 4.7. The new centre coordinates are in good agreement with the coordinate derived by Böhringer (private communication) from their X-ray study ($\alpha = 129.140°$ and $\delta = -55.810°$) and the difference between the two centres is only $\sim 30\farcs34$. The X-ray data was based on ROSAT (Boehringer et al., 1996) in 0.1-2.4 keV.

The left panel of Fig. 4.7 displays the radial density profile, N/Mpc^2, out to 2 Mpc. The completeness-limited sample ($K^0_{slim} < 15\overset{\mathrm{m}}{.}5$) is shown in pink in this plot. It shows a high central density of $N \sim 160/\mathrm{Mpc}^2$, i.e. the number of galaxies within inner central radius of $r_c < 0.1$ Mpc. The radial density profile of VC04 shows a gradual and smoothly descending trend.

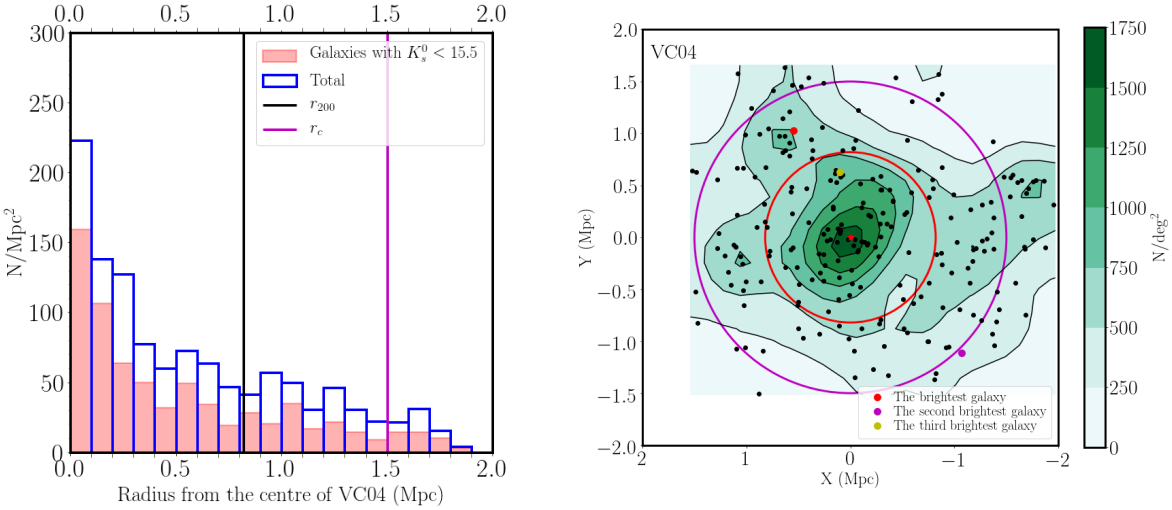

Figure 4.7: Left: the radial density profile, N/Mpc^2, out to $r < 2$ Mpc. The total number density of galaxies is shown in blue histogram and the completeness-limited sample ($K^0_{slim} < 15\overset{\mathrm{m}}{.}5$) in pink. Right: iso-density map of VC04 for $r < 2$ Mpc. Galaxies are shown as black dots and the centre of cluster as red star. The red and magenta circles represent the r_{200} and r_c respectively. The three brightest galaxies are shown as red, magenta and yellow dots.

Richness class

In VC04, the K^o_s-band magnitude of the third brightest galaxy is $m_3 = 12\overset{\mathrm{m}}{.}13$ and the number of galaxies with magnitude between m_3 and m_3+2 is $N_A(K_s) = 79$. Note that this number is determined within $r_c < 1.5$ Mpc not the full Abell radius of $R_A \sim 2.1\, h_{70}^{-1}$ Mpc. Moreover Abell richness classification is defined for the R band not the K_s band. Therefore they can not be directly compared, however, I will compare the VSCL cluster numbers to the Coma and Norma number counts in the K_s band (see Sect. 4.1.1). The Coma cluster with $N_A(K_s) = 57$ galaxies within $m_3 < m < m_3 + 2$ has Abell classification of $R = 2$

and the Norma cluster with $N_A(K_s) = 53$ has $R = 1$. The 3C129 and Virgo clusters with $N_A(K_s) = 39$ (within $r_c < 1.5$ Mpc) and $N_A(K_s) = 37$ in the K_s band do not have Abell classes but they are clearly less rich than Coma and Norma. Therefore, we consider clusters with $N_A(K_s) > 50$ and $30 < N_A(K_s) < 50$ as rich and intermediate-type clusters respectively. The comparison implies that the VC04 cluster with $N_A(K_s) = 79$ is quite a rich cluster.

A further assessment of the richness of VC04 can be done by comparing its iso-density map and radial density profile to those of the comparison clusters. To allow a fair comparison of VC04 to the comparison clusters, its iso-density contour map was determined to the same density levels as those of the Coma, Norma, 3C129 and Virgo clusters (which were determined to the same radius $r_c < 1.5$ Mpc, and completeness magnitude limit $K^0_{slim} = -21\overset{\mathrm{m}}{.}5$ as for the VSCL clusters). The VC04 cluster is shown in the left panel of Fig. 4.8, while the right panel shows the iso-density map of the Coma cluster as an example scaled to the same density level. In this figure VC04 shows high central density, but clearly is not quite as rich as Coma. However, when compared to the other comparison clusters (see the left panels of Fig. 4.1), it is clear that VC04 is very similar to Norma and is clearly richer than the 3C129 and Virgo clusters. The radial density profile of VC04 and those of the other comparison clusters which are shown in Fig. 4.7 and the right panel of Fig. 4.1, substantiate this. The central number density of VC04 ($\sim 160\ N/\mathrm{Mpc}^2$) is the same as that of the Norma cluster ($160\ N/\mathrm{Mpc}^2$), but is smaller than the central number density of Coma ($\sim 290\ N/\mathrm{Mpc}^2$) which implies that VC04 is less concentrated towards the centre and probably less evolved than the Coma cluster. The 3C129 and Virgo clusters have central number densities of ~ 100 N/Mpc^2 which are smaller than that of VC04.

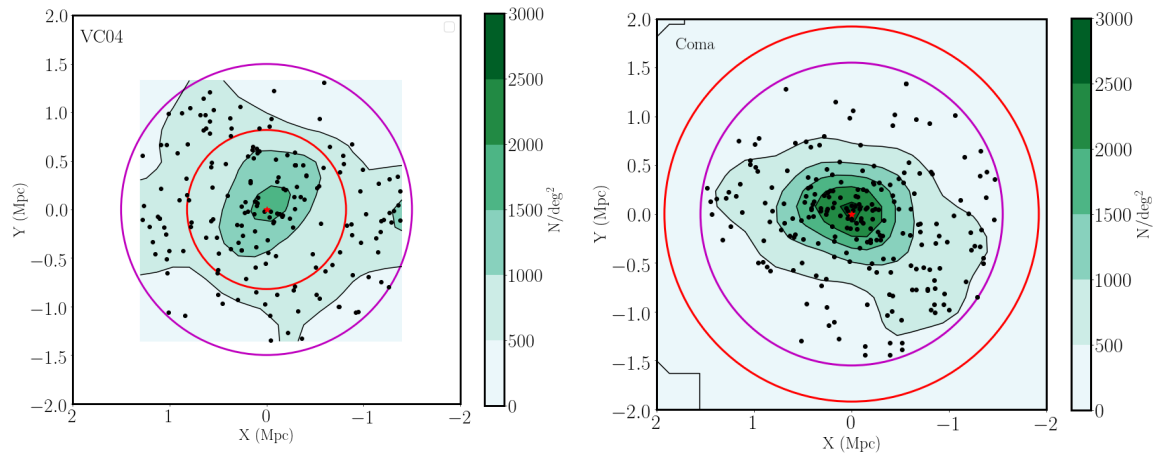

Figure 4.8: Left: the iso-density contour map of VC04 to the same density level as the comparison clusters. The galaxies are shown as black dots and the red and magenta circles demonstrate the r_{200} and r_c radii respectively. Right: the iso-density map of the Coma cluster.

It is interesting that X-ray emission does not suggest VC04 to be a rich cluster. The X-ray study of VC04 (Böhringer, private communication), using ROSAT (Boehringer et al., 1996) in 0.1-2.4 keV, revealed $L_x \sim 5 \times 10^{43}$ erg s^{-1} which would make it more like an irregular Virgo-like cluster. This might well indicate that X-ray emission (in particular in 0.1-2.4 keV) could be underestimated for clusters low in the GP. This could be due to the gas in the Milky Way (hydrogen atoms in the interstellar medium) that absorbs the X-ray emission, especially the softest X-ray emission (0.1-2.4 keV).

4.2.2 Other VSCL clusters

For the other five VSCL clusters I list their properties in Table 4.3. I followed the same steps to extract their richness and number densities as outlined for VC04 in the preceding sections. For comparison the table contains the properties of VC04 as well. The galaxy catalogues for all six VSCL clusters, listing their astrometric and photometric parameters (see Sect. 3.2) are provided in Appendix A, and the relevant plots are presented in Appendix B. A discussion of the overall richness and structure of the six VSCL clusters is presented below.

Table 4.3: Parameters of the six VSCL clusters.

	Cluster	VC02	VC04	VC05	VC08	VC10	VC11[1]a & b
1	RA (J2000)	08 10 49.20	08 36 34.80	08 37 46.80	08 58 33.60	09 49 31.92	09 55 29.28, 09 56 52.80
2	Dec (J2000)	−49 24 36	−55 48 54	−57 25 30	−57 46 12	−43 50 42	−43 52 30, −43 56 24
3	ℓ (deg)	264.690	272.268	273.685	275.699	271.673	272.532, 272.771
4	b (deg)	−8.608	−8.960	−9.776	−7.801	7.713	8.369, 8.474
5	N	290	416	279	217	232	281
6	N_c	175	225	143	127	112	128
7	$N_{\rm 2MASX}$	43	82	35	31	29	48
8	N_r	70	85	46	34	26	55
9	Redshift (km s^{-1})	18955	18196	21275	17298	18173	17889
10	σ_r (km s^{-1})	670	455	469	355	428	636
11	m (mag)	11.35	11.85	11.93	11.60	12.21	11.76
12	A_{Ks} (mag)	0.10	0.07	0.06	0.08	0.08	0.08
13	f (%)	42	38	35	27	25	44
14	r_{200} (Mpc)	1.18	0.82	0.84	0.63	0.77	1.14
15	$N_A(K_s)$	39	79	48	40	40	37
16	Density (N Mpc^{-2})	190	160	413	95	95	95, 254
17	Richness	intermediate[2]	very rich[3]	rich	poor	poor	intermediate
18	Structure	regular	regular	regular	regular	filament	irregular (two clumps)
19	X-ray	Yes[4]	Yes[5]	No	No	No	No

[1] VC11 consists of two main clumps (subclusters), VC11a and VC11b.
[2] 3C129- or Virgo-like richness.
[3] Coma- or Norma-like richness.
[4] $L_x \sim 2.6 \times 10^{43}$ erg s^{-1}, $\sim 19.50'$ offset from the centre.
[5] $L_x \sim 5 \times 10^{43}$ erg s^{-1} $\sim 30.''34$ offset from the centre.

The parameters of Table 4.3 are defined as follows:
1. Equatorial longitude (hhmmss.ss).
2. Equatorial latitude (ddmmss).
3. Galactic longitude (deg).
4. Galactic latitude (deg).
5. Total number of identified galaxies.
6. Number of identified galaxies brighter than the completeness magnitude limit ($K^o_{slim} < 15\overset{\rm m}{.}5$).
7. Number of 2MASX galaxies within the cluster region.
8. Number of galaxies with redshift, brighter than $K^o_{slim} < 15\overset{\rm m}{.}5$.
9. Mean v_{hel}.
10. Velocity dispersion.
11. Magnitude of the brightest cluster galaxy.
12. Mean value of the foreground extinction in the region of clusters.
13. Fraction of galaxies with redshift up to $K^o_{slim} < 15\overset{\rm m}{.}5$ and within $r_c < 1.5$ Mpc.
14. r_{200} (see Sect. 1.5.1).
15. Number of galaxies with $m_3 < m < m_3 + 2$ and within $r_c < 1.5$ Mpc.

16. Central number density within 0.1 Mpc.
17. Estimated richness of the cluster based on studying the velocity dispersion, iso-density maps, radial density plots and $N_A(K_s)$ of clusters and comparing them with those of the comparison clusters.
18. Structure of the clusters based on the iso-density map and the shape of the radial density profile.
19. X-ray emission in 0.1-2.4 keV, using ROSAT (Böhringer, private communication).

4.2.3 Discussion on the VSCL clusters

To compare the VSCL clusters to the Coma, Norma, 3C129 and Virgo clusters, their iso-density maps were limited to $r_c = 1.5$ Mpc and completeness magnitude limit $K^0_{slim} = -21\overset{\text{m}}{.}5$, and were scaled to the same density levels. The iso-density maps of the six VSCL clusters and comparison clusters are shown in Figs. 4.9 and 4.10 respectively. The radial profiles of the comparison clusters are shown in Fig. 4.1.

The analysis shows that VC02 appears not to be as rich as the Coma and Norma clusters but richer than Virgo or 3C129. However, foreground extinction is higher for VC02, especially in the right top quadrant, than for any of the other VSCL clusters (see Fig. 3.10). Some galaxies might be missing from this analysis due to the heavier obscuration by the dust of the Milky Way. Weak X-ray emission was found for VC02 with offset from the centre towards its north. Furthermore, there is a small clump of galaxies to the south-east of the central region which could be a small group falling into the core of VC02.

VC04 stands out as the richest cluster among the six and is comparable to the Coma and Norma clusters, although its velocity dispersion seems rather low for a rich cluster (more details in Sect. 4.2.1).

The centre of VC05 was estimated incorrectly by a previous study based on available redshift data in identifying this cluster at the time (Elagali, 2015). Using the iso-density contour map, the coordinates of the centre of VC05 were adjusted and listed in Table 4.3. Comparison of the iso-density maps indicates that VC05 is much richer than the 3C129 and Virgo clusters and could be comparable to the Norma and Coma clusters. Note that VC05 has the highest central density of all the clusters studied in VSCL. However, due to the offset the sample of galaxies in VC05 is not complete to $r_c < 1.5$ Mpc (and therefore r_c is not indicated in its figure).

Although VC08 is centrally concentrated, it is a relatively poor cluster and not as rich as the 3C129 and Virgo clusters. However, the images of VC08 are of slightly lower quality because of higher seeing values than the other cluster images. VC08 is also located in a region with higher stellar density which results in higher sky brightness.

The iso-density map of VC10 shows that it does not show a central concentration typical of clusters but rather a similar galaxy density across the observed field indicating that it is more likely some sort of filamentary / wall-like structure rather than a cluster. This is not surprising in a supercluster, since high density clusters in relatively rich superclusters are connected by lower-density filaments (Einasto et al., 2007d).

The iso-density map of VC11 depicts that the previously predicted centre is located in the middle of the two major clumps (or subclusters) in its region. The two clumps are named VC11a and VC11b and their centres are listed in Table 4.3. The radial density profiles (Figs. B.6.5 and B.6.6) show that VC11a is more centrally concentrated than VC11b. VC11 in general, has the same order of richness as the 3C129 and Virgo clusters.

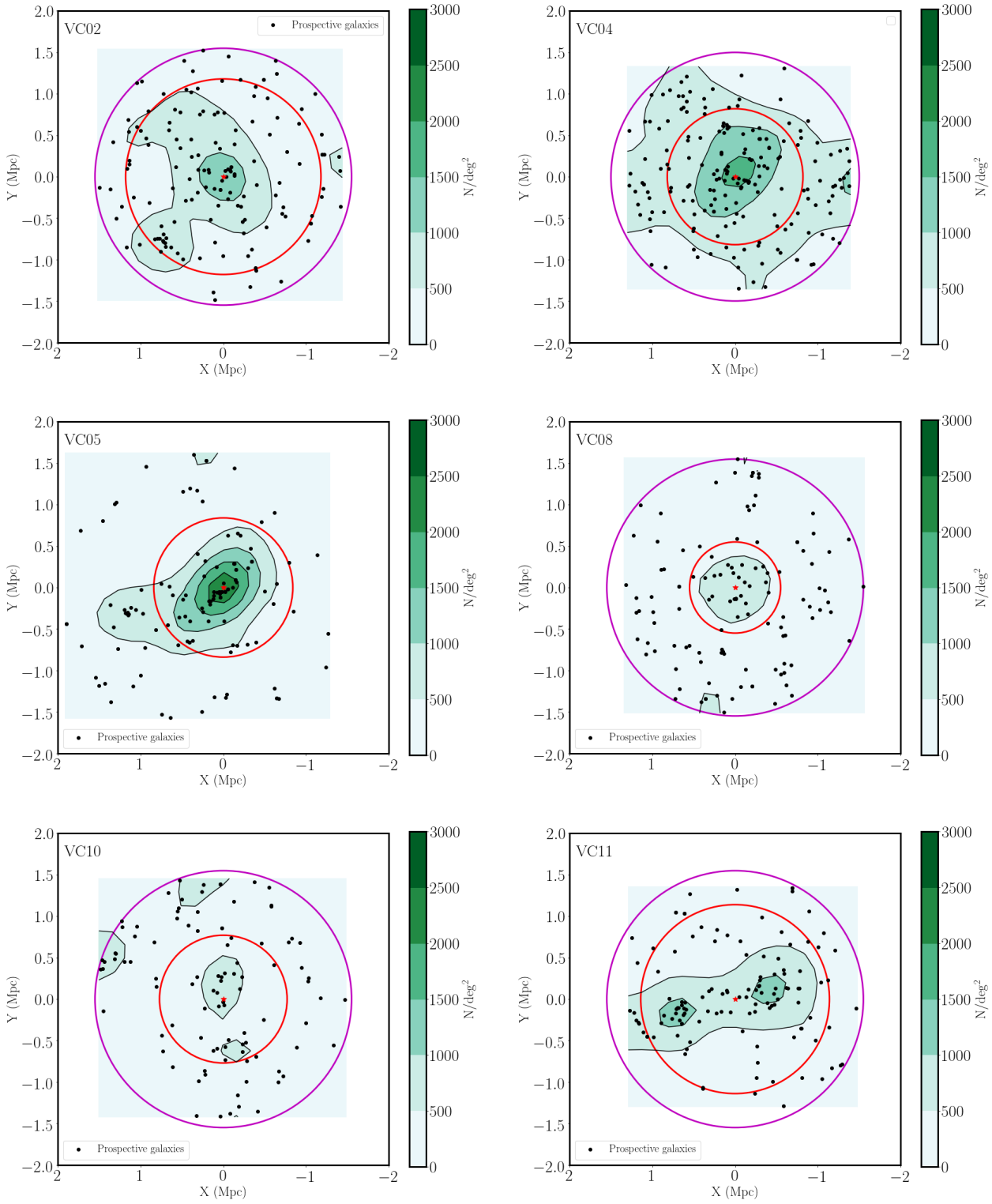

Figure 4.9: The iso-density contour map of the VSCL clusters to the same density level as the comparison clusters out to $r_c = 1.5\,\mathrm{Mpc}$, complete to $K^0_{slim} < -21\overset{\mathrm{m}}{.}5$. The galaxies are shown as black dots and the red and magenta circles demonstrate the r_{200} and r_c radii respectively.

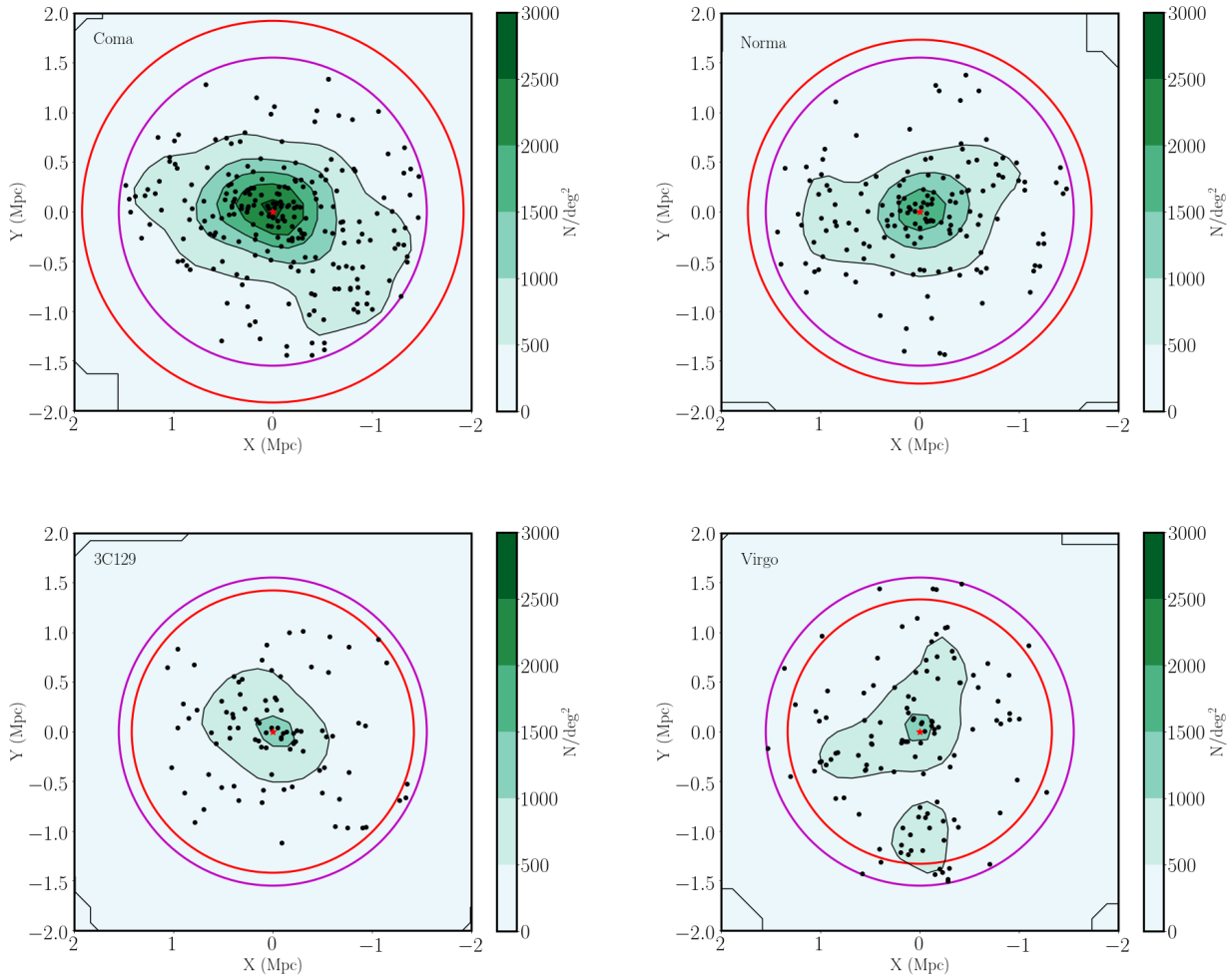

Figure 4.10: The iso-density contour maps of the Coma, Norma, 3C129 and Virgo clusters out to $r_c = 1.5\,\mathrm{Mpc}$ and complete to $M^0_{Ks} \sim -21\overset{\mathrm{m}}{.}5$. The galaxies are shown as black dots. The red and magenta circles represent the r_{200} and r_c respectively.

The two subclusters might be merging into a one rich cluster, although more spectroscopic data is needed to confirm this.

The analysis of the six clusters, based on studying their velocity dispersions, iso-density maps, radial density plots, and $N_A(K_s)$, indicates that the VSCL consists of different types of galaxy clusters from poor to rich and even lower density filament-like structure to connect the high density clusters. This is consistent with the definition of a relatively rich supercluster (Einasto et al., 2007b). From studying the iso-density maps, it appears that about half of the VSCL clusters are not relaxed and still evolving. Spectroscopic coverage to include more of the fainter cluster members is needed to perform a precise dynamical analysis on them. As stated in Chapter 2, Kraan-Korteweg et al. (2017) identified at least 20 potential clusters in the VSCL. We found that about half of our small sample of 6 clusters are rich or relatively rich, however ROSAT did either not detect X-ray emission or detected lower emission than expected. The VSCL is therefore, likely to have more rich clusters supporting the richness of this supercluster (Wray et al., 2006; Einasto et al., 2007a). Since the extinction highly affects the ROSAT X-ray band (see Sect. 1.5.5), resulting in poorer detection capability of galaxy clusters close to the GP, it would be interesting to see that what other X-ray all-sky surveys like eROSITA (extended ROentgen Survey with an Imaging Telescope Array, Predehl et al., 2021) in 0.3-8 keV band will reveal about them.

4.3 HI content of the rich cluster VC04

The VC04 cluster is the richest cluster of the sample of six VSCL clusters and could be as rich as the Norma cluster based on the analysis presented in Sect.4.2.1. Interestingly this cluster was observed as a part of the VSCL wall using the MeerKAT radio telescope during the 16-dish (MK16) Early Science programme (2018) (Jonas and MeerKAT Team, 2016). These observations allowed me to explore the gas content of VC04. The NIR observation of VC04 is complete to $M^o_{Ks} < -21\overset{\text{m}}{.}5$, therefore, sensitive to all normal spirals as the luminosity function for each galaxy type shows (see Fig. 1.8). If VC04 is a rich cluster, its spiral galaxies are expected to be H I deficient.

The morphology-density relation (Oemler, 1974; Dressler, 1980) indicates that the dense environment of galaxy clusters is dominated by elliptical and lenticular galaxies while spirals are the main inhabitant of the field. Galaxy clusters seem to suppress star formation in galaxies compared to the field (e.g., Balogh et al., 1997; Gómez et al., 2003). With regard to H I content, spiral galaxies in dense environments are likely to have less H I, on average, compared to the same type and size of field galaxies (e.g., Chamaraux et al., 1980; Solanes et al., 2001). This suggests that the gas has been stripped from the late-type galaxies and that they have been transformed to gas-poor early-type galaxies (e.g., Fasano et al., 2000; Bekki et al., 2002; Bekki and Couch, 2011). Ram-pressure stripping, a process in which the interaction of gas with the intra-cluster medium causes its removal from the disk of galaxies, is thought to be the dominant gas stripping mechanism (Gunn and Gott, 1972; Giovanelli and Haynes, 1985; Bravo-Alfaro et al., 2000; Gavazzi et al., 2006; Dénes et al., 2014; Yoon et al., 2017). There are other mechanisms that have been suggested to be responsible for removing gas in cluster galaxies such as harrassment (e.g. Moore et al., 1996), tidal interactions (e.g. Byrd and Valtonen, 1990), and strangulation (e.g. Larson et al., 1980). Solanes et al. (2001) found that H I deficiency can extend out to 2 Abell radii in galaxy clusters. The H I deficiency in galaxy clusters seems to correlate with their X-ray luminosity (Giovanelli and Haynes, 1985) and therefore, with their richness (see

Sect. 1.5.1). The H I deficiency parameter is defined as (Haynes and Giovanelli, 1984):

$$\mathrm{DEF_{HI}} = \log(\mathrm{M_{HI,exp}}) - \log(\mathrm{M_{HI,obs}}), \tag{4.2}$$

where $\mathrm{M_{HI,exp}}$ and $\mathrm{M_{HI,obs}}$ are the expected and observed H I masses respectively.

MeerKAT observations of 3 hours integration time were performed with the goal of reaching a rms of 1.2 mJy sensitivity per beam, which should result in a 5σ detection limit of $\log(\mathrm{M_{HI}}) = 9.6\,\mathrm{M_\odot}$ for a typical 200 km s^{-1} linewidth galaxy at the distance of the VSCL, $v \sim 18000$ km s^{-1}. This is deeper than the knee of the H I mass function, $\log(\mathrm{M^*_{HI}}) = 9.9\,\mathrm{M_\odot}$ (Said et al., 2019) and therefore, sensitive to the normal population of spiral galaxies. Six MeerKAT fields of ~ 1 deg^2 were observed and a total of 26 real and possible H I detections were identified within the velocity range of $16000 < v < 20000$ km s^{-1}. The list of H I detections around VC04 including their positions, velocities, H I masses and linewidths was provided by Renée Kraan-Korteweg[4]. However, these H I detections have no counterpart in the VC04 NIR catalogue. The H I detections are located beyond one Abell radius of VC04.

Galaxies with optical redshift data in VC04 were visually examined to classify their morphological type and 45 galaxies were confirmed to be spirals by eye (since I did not have access to the galaxies spectra). This classification was also validated by their central surface brightness values (as discussed in Sect. 4.2.1). Spiral galaxies are known to be rich in H I gas. The velocity and magnitude histograms of galaxies with known redshifts is shown in the left and right panels of Fig. 4.11 respectively, with the 45 spirals marked in cyan. It was found that all galaxies classified as spirals have redshifts that confirm them to be cluster members. In the following I will probe the H I content of the 45 spirals using the available information.

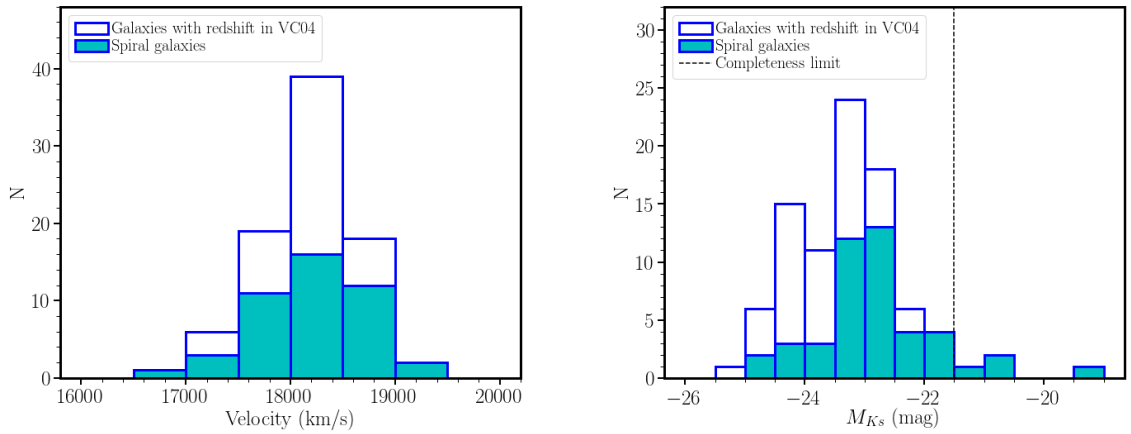

Figure 4.11: The velocity (left) and magnitude (right) histograms of galaxies with redshifts. The 45 spirals are marked in cyan.

Since none of these spiral galaxies were directly detected in H I, I first set out to estimate their expected H I masses by exploring the relation between H I mass and luminosity of galaxies in the K_s band, i.e. the H I-NIR scaling relation. The K-band luminosity is a good proxy for the stellar mass of a galaxy (Broadhurst et al., 1992; Kauffmann and Charlot, 1998), since it is hardly dependent on recent star formation nor dust extinction.

[4]Paper in preparation

I used the deep NIR catalogue of sources from the blind H I survey, the Parkes H I Zone of Avoidance HIZOA (Said et al., 2016a), and the southern ZOA galaxies 21cm H I-line catalogue in Said et al. (2016b) (HIZOA-NIR) to determine the scaling relation between the luminosity of galaxies in K_s band and their H I masses (L_K-$\mathrm{M_{HI}}$). The HIZOA sample is suitable to work with since its NIR observations were performed using the IRSF telescope with the same observation strategy as this study and its H I data were obtained from a systematic blind H I survey. Also since HIZOA is a blind survey it includes both high and low-density regions. Most of the galaxies in HIZOA are field galaxies (not H I deficient). The only overdensity in the HIZOA region is the Norma cluster. The H I content of Norma has been investigated by Schröder et al. (2009). They found no H I detections in Norma which is a sign of H I deficiency, however, the HIZOA sample (in the Norma region) only contains a very few galaxies close to the Abell radius and their effect on the derived relation is insignificant. Note that the difference between the H I flux of galaxies derived from Parkes and MeerKAT observations has been determined to be insignificant and lie well within the errors. 326 galaxies in the H I catalogue with a counterpart in the HIZOA-NIR catalogue were selected to determine the scaling relation. I determined H I masses of the 326 galaxies as:

$$\left(\frac{\mathrm{M_{HI}}}{h^{-2}M_\odot}\right) \simeq \frac{2.35\times10^5}{1+z}\left(\frac{D_L}{h^{-1}\mathrm{Mpc}}\right)^2\left(\frac{S}{\mathrm{Jy\,kms^{-1}}}\right), \tag{4.3}$$

Where S is the rest frame velocity integrated flux and D_L is the luminosity distance to the galaxy. The K band luminosity of galaxies in solar luminosities, L_K, was determined using:

$$L_K = 10^{(K_{sun}-M_K)/2.5} \tag{4.4}$$

For an assumed solar absolute magnitude of $3\overset{\mathrm{m}}{.}31$ (Colina and Bohlin, 1997), Fig. 4.12 presents $\log(\mathrm{M_{HI}})$ as a function of $\log(L_K)$ for the HIZOA sample of 326 galaxies. Using linear regression a fit was made to galaxies with $\log(L_K) > 9.92\,\mathrm{L_\odot}$ (corresponding to the completeness limit for the IRSF galaxies $M_{Ks} = -21\overset{\mathrm{m}}{.}5$), and linewidth W_{50}[5] $>$ 200 km s^{-1}, since the study of spirals in VC04 shows that almost all of them have $W_{50} >$ 200 km s^{-1} (will be discussed later in this section). The fitted line equation is:

$$\log(\mathrm{M_{HI}}) = (0.39\pm0.08)\,\log(L_K) + 5.71, \tag{4.5}$$

with a scatter of 0.8 dex around the fit.

The H I masses of the 45 spiral galaxies in VC04 were then predicted using equation 4.5, and the predicted H I masses are presented in the histogram in Fig. 4.13. Note that the scatter of the estimated H I masses is relatively high ($\sim$ 0.8) dex and the masses do not exceed $\log(\mathrm{M_{HI}}) > 10.2\,\mathrm{M_\odot}$ while the mass of a normal spiral is about $\log(\mathrm{M_{HI}}) \sim 10.5\,\mathrm{M_\odot}$. Figure 4.13 shows that all galaxies with $\log(L_K) > 9.92\,\mathrm{L_\odot}$ (corresponding to $M_{Ks} < -21\overset{\mathrm{m}}{.}5$) have H I masses above $\log(\mathrm{M_{HI}}) \gtrsim 9.6\,\mathrm{M_\odot}$ (using equation 4.5). Interestingly $\log(\mathrm{M_{HI}}) \sim 9.6\,\mathrm{M_\odot}$ is also the MeerKAT 5σ detection limit and therefore, galaxies with $\log(L_K) > 9.92\,\mathrm{L_\odot}$ should have been detected by MeerKAT. However none of these galaxies were detected which implies the depletion of gas in them.

In the next step I attempted to estimate the total H I deficiency of the spirals in VC04, using the predicted H I masses (based on the extinction-corrected isophotal magnitudes). To do this, I used an independent method, the all-sky NIR Tully-Fisher (TF) relation in

[5] W_{50} is the profile velocity widths in km s^{-1} at 50% of the peak maximum

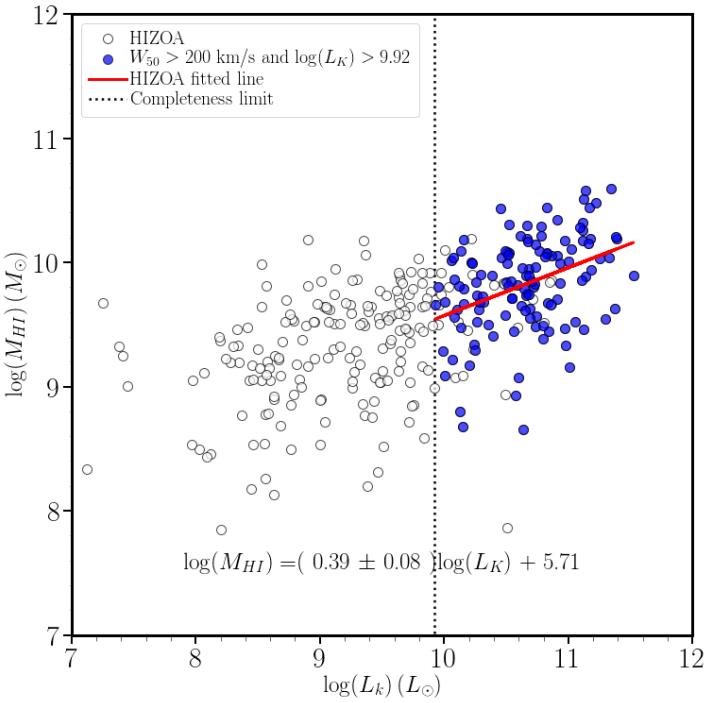

Figure 4.12: log(M_{HI}) vs log(L_K) for the HIZOA sample of 326 galaxies. The fitted line on galaxies with $\log(L_K) > 9.92\,L_\odot$ and $W_{50} > 200$ km s^{-1} is shown as a red line. The dashed line $\log(L_K) = 9.92\,L_\odot$ is the completeness limit of this study.

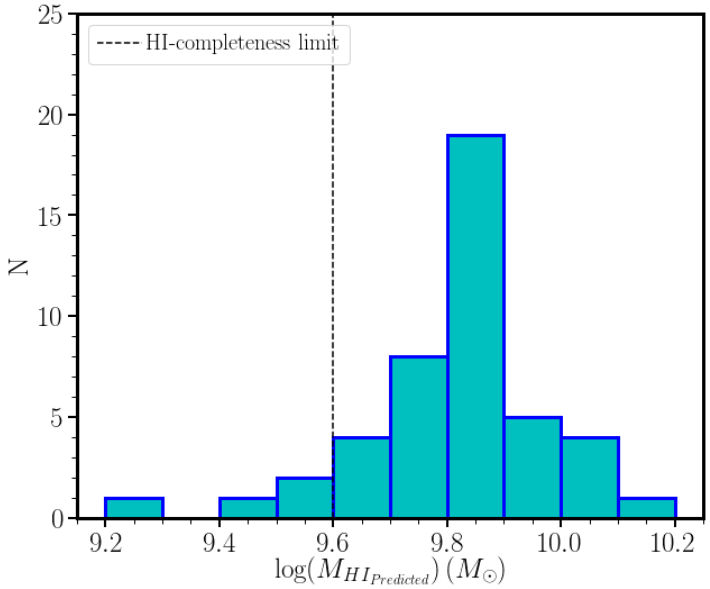

Figure 4.13: The estimated M_{HI} of 45 spirals, using the scaling relation L_K-M_{HI}.

the ZoA (Said et al., 2015), to estimate the linewidths (W_{50}) of the spirals and subsequently the H I masses that they would have for a 5σ detection. This is an upper limit for H I masses since the spirals were not detected and hence must have lower H I masses. The TF relation in K_s band is given by:

$$M_{K_s} - 5\log h \;=\; -21.861 - 10.369(\log W - 2.5). \tag{4.6}$$

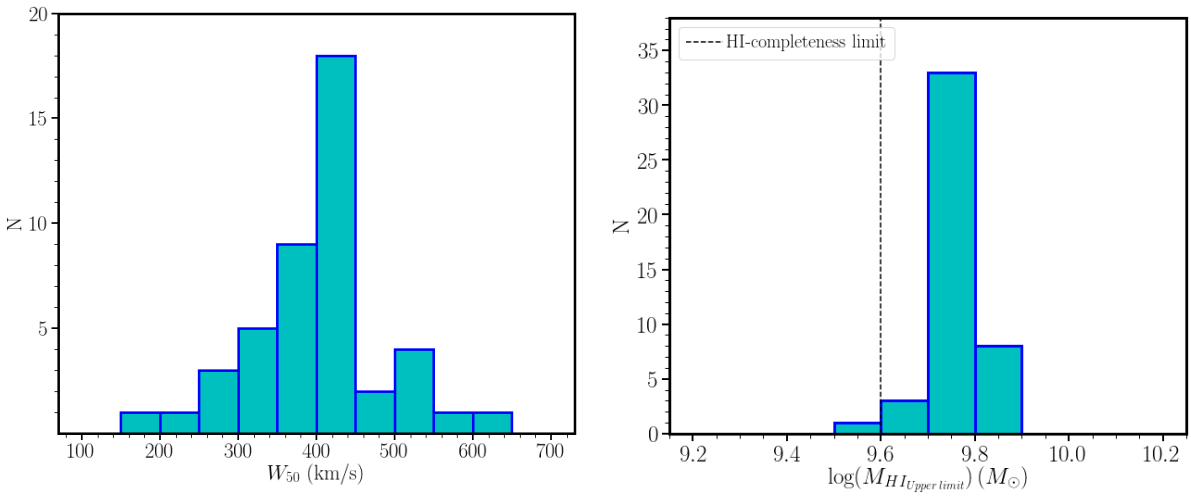

Figure 4.14: Left: the derived W_{50} of 45 spiral galaxies in VC04 using the TF relation. Right: The estimated upper limit of M_{HI} of the spirals.

The distribution of the derived W_{50} values of the sample is shown in the left panel of Fig 4.14. This confirms that all but one of the spirals must have linewidths $W_{50} > 200$ km s^{-1}. I then used these W_{50} values in equation 4.3 to estimate an upper limit for H I masses of the 45 spirals individually, using the TF relation. The distribution of the upper limit H I masses are displayed in the right panel of Fig 4.14. To determine the flux (S) of the spirals to apply in equation 4.3, I used:

$$S_{int} = (N_\sigma) \times (rms) \times (\sqrt{(W_{50} \times N_{ch})}) \tag{4.7}$$

where N_σ is 5 and the rms is 1.2 mJy per beam. N_{ch} is the channel width, which is 11 km s^{-1} per channel, for this dataset.

To estimate the H I deficiency of the 45 spirals I measured

$$\mathrm{DEF_{HI}} = \log(\mathrm{M_{HI_{Predicted}}}) - \log(\mathrm{M_{HI_{upper\ limit}}}).$$

This is a minimum value for the H I deficiency since the real H I masses are certainly lower than the $\mathrm{M_{HI_{upper\ limit}}}$. The predicted H I masses have a scatter of 0.8 dex, therefore, this measurement is only a lower limit and rough estimation of H I deficiency. The H I deficiency of the spirals as a function of their cluster-centric distances is shown in Fig. 4.15. Although it is only a rough estimation, Fig. 4.15 shows a descending trend for H I deficiency at distances above ~ 1.5 Mpc.

To explore the H I content of galaxies that were detected by MK16, I analysed the outskirts of VC04 out to 4 Mpc ($\sim 5r_{200}$) and found 3 of the H I detections at the distance $16000 < v < 20000$ km s^{-1} with counterparts in 2MASX. I estimated their expected

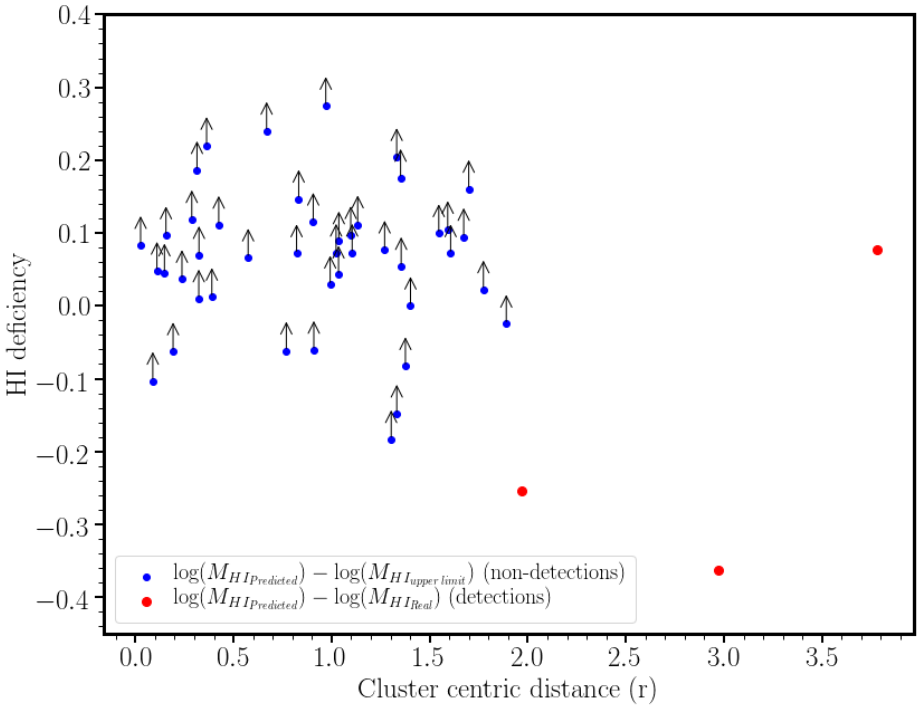

Figure 4.15: The estimated H I deficiency as a function of distance from the centre of VC04 for the 45 spiral galaxies and the three 2MASX galaxies that were detected with MeerKAT.

H I masses using equation 4.5. The real H I masses are $\log(M_{HI}) = 10.00\,M_{\odot}$, $\log(M_{HI}) = 10.22\,M_{\odot}$ and $\log(M_{HI}) = 10.33\,M_{\odot}$, and the predicted H I masses are $\log(M_{HI}) = 10.07\,M_{\odot}$, $\log(M_{HI}) = 9.96\,M_{\odot}$ and $\log(M_{HI}) = 9.96\,M_{\odot}$ respectively. To estimate the H I deficiency of the three galaxies I computed

$$DEF_{HI} = \log(M_{HI_{Predicted}}) - \log(M_{HI_{Real}}).$$

The estimated H I deficiency of the three real detections is shown by the red symbols in Fig. 4.15 as a function of distance from the centre of VC04. Figure 4.15 indicates that galaxies at the outer areas of VC04 are not as H I deficient as galaxies in its interior regions. These galaxies were indeed detected by MeerKAT.

As stated before, this NIR survey is sensitive to both elliptical and normal spiral galaxies. This can also be seen from the luminosity function of the observed VSCL clusters (will be discussed Chapter 5), which are complete to $M^0_{Ks} = -21\overset{m}{.}5$. Based on the performed analysis, the spirals in VC04 are extremely H I deficient which could be due to different gas stripping mechanisms in clusters such as ram-pressure stripping (Gunn and Gott, 1972). The H I deficiency in VC04 is another hint that VC04 is a dense and rich cluster, contradictory to what its X-ray emission suggests.

4.4 Summary

After presenting the NIR catalogue parameters of the six observed clusters, I probed their structures and estimated their richnesses using their iso-density contour maps and

radial density profiles and compared them to those of a sample of well-known clusters (Coma, Norma, 3C129 and Virgo). The analysis was performed out to the completeness magnitude and radius of this work, $M_{Ks} < -21\overset{\text{m}}{.}0$ and $r_c < 1.5$ Mpc. Rich clusters are considered comparable to the Coma or Norma clusters and intermediate clusters have similar characteristics as the 3C129 and Virgo clusters. This study shows that VC04 is the richest cluster among the six with the highest number of identified galaxies. VC05 is also a rich cluster although its data are not complete out to r_c due to the wrong estimation of its prospective centre. VC05 has the highest central density among the six clusters. VC02 is an intermediate cluster but could be a rich cluster considering that it is located in the area with the highest foreground extinction (more galaxies might have been identified if it was subjected to the same amount of extinction as the other clusters). VC08 was found to be a poor cluster. VC10 has a filament-like structure (not a cluster). VC11 consists of two subclusters and is shown to be an intermediate cluster. The two subclusters could be merging into a one rich cluster, although one needs more spectroscopic data to confirm this. Only two of these clusters has X-ray emission in ROSAT: VC04 (a Virgo-like emission) and VC02 (weak with offset from its centre). I also explored the H I content of spiral galaxies in VC04, one of the most prominent clusters in the VSCL that was observed with MeerKAT-16 as a part of the VSCL wall. The H I analysis showed that the spirals in VC04 are severely H I deficient which is another indication of it being a rich cluster.

Chapter 5

The Luminosity Function of Galaxy Clusters

5.1 Introduction

The Luminosity Function (hereafter LF) or space density of galaxies, ϕ(L) is the number density of galaxies in a given luminosity range. The LF of a population of galaxies provides us with insight into the physics of the formation and evolution of these galaxies (e.g. Henriques et al., 2015; Rodrigues et al., 2017; Mitchell et al., 2018). For instance, the impact of environment on galaxy evolution can be studied by comparing the LFs of galaxies in different environments as can be seen in Fig. 1.7, which displays the difference between the cluster and field LFs. The LFs of galaxies are also important in determining the amount of luminous matter in the universe, which is contingent on the cosmological parameters.

The shape of the K_s-band LF itself is strongly dependent on the composition of the morphological types of galaxies. There is a dip in the total K_s-band LF of galaxies which happens roughly at $M_K - 5 \log h_{70} = -21\overset{\text{m}}{.}0$. The dip is situated where the space density of elliptical and lenticular galaxies drops and late-type spirals and dwarf ellipticals take over (see Figs. 1.7 and 1.8). This NIR study is likely to undercount the number of dwarfs because the low surface brightness galaxies are difficult to detect against the bright infrared background. The completeness magnitude limit of the NIR VSCL survey is $K^0 = 15\overset{\text{m}}{.}5$ which translate to $M_{Ks} - 5 \log h_{70} = -21\overset{\text{m}}{.}5$ at the large distance of the VSCL ($cz \sim 16000$ km s^{-1}). Moreover, rich clusters are dominated by ellipticals and S0s as the morphology-density relation shows, particularly at their central regions (Dressler, 1980). The LFs of the VSCL clusters are expected to be dominated by the ellipticals and early spirals with their morphological mix of galaxies depending on the type of clusters.

The late-type spiral and irregular galaxies are the dominated population in fields. The most recent determination of K-band field LF was done by Jones et al. (2006), using the 6dFGS at $z = 0.054$ complete to $M_K \lesssim -24\overset{\text{m}}{.}0$. Their derived Schechter parameters are $M^* = -24\overset{\text{m}}{.}60 \pm 0.03$ and $\alpha = -1.16 \pm 0.04$, although their fit to the Schechter function could not reproduce the flat faint-end slope and decline at the bright end simultaneously.

In this chapter, I review three methods to derive LFs of clusters, i.e. based on statistical field correction, spectroscopic membership and the Red-Sequence (RS) methods (Sect. 5.2). In Sect. 5.3 I compute the LFs of the Norma, Coma and Virgo clusters (the properties of which are presented in Sect. 4.1) and show that the RS method is a reliable and optimised method to derive the LFs of the VSCL clusters. These three comparison

clusters are located in the local universe and have different richnesses and therefore, different galaxy populations. The 3C129 cluster dataset are not complete to $r_c = 1.5$ Mpc (the completeness radius of this study), therefore its LF was not derived. The comparison between the LFs of the comparison clusters and the VSCL clusters will further help to provide more insight on the VSCL clusters and their galaxy populations. I first derive the K_s-band LF of VC04, which is described in detail in Sect. 5.4 following by a discussion presented in Sect. 5.5. The LF parameters of the other five VSCL clusters are presented in Sect. 5.6. The histograms of absolute magnitudes of galaxies in each VSCL cluster, which were used to derive their LFs, are shown in Appendix B.

5.2 Derivation of the luminosity function

In this section I review three methods to derive the cluster LF: a statistical correction for field contamination, spectroscopic membership and Red-Sequence (hereafter RS) methods.

5.2.1 Statistical field correction method

The traditional way to compute the cluster LFs is to statistically subtract the control field counts from galaxy counts in the cluster direction in each magnitude bin. This statistical approach has been used in numerous studies (e.g. Zwicky, 1957; Oemler, 1974; Schechter, 1976; Colless, 1989; Driver et al., 1998; Yagi et al., 2002; Andreon et al., 2004; Merluzzi et al., 2010; Yamanoi et al., 2012). For this method to yield reliable results, the photometric calibration of the galaxies in the cluster and the control field must be accurate. Also the control field should not be too close to or too far from the cluster. If it is too close, its counts might be contaminated by the cluster counts and if too far, it would not take into account the field nonuniformities on the scale of the angular size of the cluster (Paolillo et al., 2001). Furthermore, the field contamination correction method could result in significant systematic errors (for a detailed discussion see e.g. Andreon et al., 2005).

There are no control field samples in the correct photometric band that are deep enough in the surroundings to correct the IRSF VSCL clusters sample. Therefore, it is not ideal to use this method to derive the LFs of the VSCL clusters.

5.2.2 Spectroscopic membership method

Biviano et al. (1995) corroborated the membership fraction obtained from the colour-magnitude plane by computing a statistical estimate of the same. A similar statistical approach was applied by Mobasher et al. (2003) on spectroscopic data and later by Skelton et al. (2009) to measure the LFs of the Coma and Norma clusters respectively. In this method, the foreground and background contamination can be determined when a large proportion of galaxies in a cluster have spectroscopic information.

Skelton et al. (2009) compared the result of this method with the statistical field correction method and showed that they are in good agreement.

Spectroscopic membership derivation

Following the formalism in Mobasher et al. (2003), the fraction of galaxies in each magnitude bin that satisfies the membership criterion is given by

$$f(m) = \frac{N_m(m)}{N_m(m) + N_{nm}(m)} = \frac{N_m(m)}{N_s(m)}, \tag{5.1}$$

where $N_s(m)$ is the total number of galaxies in the survey area with spectroscopic data in a given range of apparent magnitude; $N_m(m)$ and $N_{nm}(m)$ are the number of galaxies that are cluster members and non-members respectively as a function of magnitude. $f(m)$ gives the probability that any random galaxy drawn from the spectroscopic sample is a cluster member and $N_m(m)$ is a binomial random variable whose probability of success is given by $f(m)$ for each of the N_s trials. The error in the membership fraction is given by

$$\begin{aligned} \mathrm{var}[f(m)]^{1/2} &= \frac{\mathrm{var}[N_m(m)]^{1/2}}{N_s(m)}, \\ &= \left[\frac{f(m)(1-f(m))}{N_s(m)}\right]^{1/2}. \end{aligned} \tag{5.2}$$

Assuming that the membership fraction derived for the spectroscopic sample holds for the full photometric sample, the number of galaxies without redshift information that are cluster members can be estimated as $f(m)N_{nv}(m)$, where $N_{nv}(m)$ is the number of galaxies without redshift information, in a given range of apparent magnitude. The LF can then be computed as

$$\begin{aligned} \phi(m) &= \frac{1}{A}(N_m(m) + f(m)N_{nv}(m)) \\ &= \frac{N_p(m)}{A} f(m), \end{aligned} \tag{5.3}$$

where $N_p(m)$ is the K_s-band photometric sample size in each magnitude bin and A is the survey area. $N_p(m)$ can be charaterized by a Poisson distribution since it expresses the number of galaxies in a given (magnitude) interval. Then, the LF ($\phi(m)$) becomes a product of a Poisson random variable ($N_p(m)$) and a binomial random variable ($f(m)$), and the error in LF can be computed by adding the relative errors in $N_p(m)$ and $f(m)$ in quadrature:

$$\frac{\mathrm{var}[\phi(m)]}{\phi(m)^2} = \frac{\mathrm{var}[N_p(m)]}{N_p(m)^2} + \frac{\mathrm{var}[f(m)]}{f(m)^2}. \tag{5.4}$$

The variance of $N_p(m)$ is equal to its expectation value, while the variance of $f(m)$ is given by Equation 5.2. Substituting Equation 5.2 in Equation 5.4, we get

$$\frac{\delta\phi(m)}{\phi(m)} = \left[\frac{1}{N_p(m)} + \frac{1}{N_m(m)} - \frac{1}{N_s(m)}\right]^{1/2}. \tag{5.5}$$

If the photometric and the spectroscopic sample sizes are equal i.e. $N_p(m) = N_s(m)$, the above expression reduces to $1/\sqrt{N_m(m)}$; if all the galaxies in the spectroscopic sample are cluster members i.e. $N_m(m) = N_s(m)$, it reduces to $1/\sqrt{N_p(m)}$.

5.2.3 The Red-Sequence method

The spectroscopic membership method to derive the LF is reliable only when a high percentage of galaxies in a cluster have measured redshifts. Therefore, another method is needed when most of the galaxies in a cluster lack spectroscopic information. In this section I investigate the Red-Sequence (RS) method (described in Section 5.3.1) to measure the LFs of clusters.

The RS galaxies have been used in numerous studies to derive the LF of clusters. The LFs showed a flat faint end which some authors found to be constant with redshift in optical wavelengths (e.g. Paolillo et al., 2001; Andreon, 2006; De Propris et al., 2007, 2013), while others detected a strong decrease in the RS population at higher redshifts in the same wavelength range (e.g. Smail et al., 1998; De Lucia et al., 2004; Tanaka et al., 2005; De Lucia et al., 2007; Stott et al., 2007; Gilbank et al., 2008; Rudnick et al., 2009; Vulcani et al., 2011; Martinet et al., 2015; Zenteno et al., 2016; Martinet et al., 2017; Sarron et al., 2018).

5.3 The NIR LFs of Norma, Coma and Virgo

Before measuring the LFs for the VSCL clusters, I derive the LFs of three comparison clusters, Coma, Norma and Virgo, as a comparison sample for the more distant VSCL clusters. This has been done out to the clustercentric distances of $r < 0.5$ Mpc (the radius of the Norma IRSF K_s-band survey) and $r_c < 1.5$ Mpc, to include the outer regions of clusters, which typically contain more late-type galaxies compared to the cores which are dominated by early-type galaxies. I also investigate the consistency of the spectroscopic membership method and the RS method by using both to derive the LF, strating with the Norma cluster. This cluster has excellent spectroscopic as well as photometric data available to enable this comparison. Moreover, Norma has been observed with the same IRSF instrument and set up as the VSCL clusters. My aim is to determine how the results of the two methods compare in order to determine the reliability of the RS method in situations where spectroscopic data is not available (e.g. for the VSCL clusters). I then derive the LFs of the Coma and Virgo clusters using only the RS method for later comparisons to those of the VSCL clusters.

I use a nonlinear least-squares Marquardt-Levenberg algorithm to fit a single Schechter function to the LFs to find the characteristic magnitude, M^*, faint-end slope, α, and normalisation, ϕ^*. Clusters that contain cD galaxies appear to have steeper slope at the bright end of the LFs than clusters which do not contain them. cD galaxies cannot be fitted properly by the Schechter function and are usually excluded in deriving the LF to get a better fit. Therefore, I derive the LFs of the Norma, Coma and Virgo clusters with and without the cD galaxies.

Table 5.1 lists the previously reported Schechter parameters of the Coma and Norma NIR LFs. The Schechter parameters have not been published for the Virgo LF in the K_s-band to date. McDonald et al. (2009) plotted the LF of Virgo in H-band but they did not state any parameters for it. The list of galaxies used to compute the K_s-band LFs of these clusters were taken from the 2MASX catalogue (Jarrett et al., 2000b) and selected to go out to the same completeness magnitude limit ($M_{Ks} = -21\overset{\text{m}}{.}5$) and completeness clustercentric distance ($r_c = 1.5h_{70}^{-1}$ Mpc) of this work. The completeness radius is $\sim 71\%$ of the Abell radius.

2MASS is known to miss a considerable fraction of the flux for bright galaxies and to

Table 5.1: Table of NIR luminosity functions parameters of the Coma and Norma clusters. The Norma cluster has two entries in the first and second row of the table which represent the parameters of the Norma LF with and without the first bin (containing the central cD galaxies) respectively.

Cluster	Reference	Band	M^* (mag)	α	Area (Mpc^2)	Sample Notes
Norma	Skelton et al. (2009)	K_s	-25.39 ± 0.80	-1.26 ± 0.10	central 0.8	$-26.0 < M_{K_s} < -19.5$
Norma	Skelton et al. (2009)	K_s	-25.09 ± 1.07	-1.23 ± 0.13	central 0.8	$-25.5 < M_{K_s} < -19.5$
Coma	de Propris et al. (1998)	H	-23.82	-0.93	central 0.53	$M_H < -20.5$
Coma	de Propris et al. (1998)	K	-24.02	-0.98	central 0.53	$M_H < -20.5$
Coma	Andreon and Pelló (2000)	H	-23.86	-1.3	off-centre 0.30	$M_H < -18.0$

The M^*s have been adjusted for $H_0 = 70$ km s^{-1} Mpc^{-1}. The differences between the magnitude systems have not been taken into account, however characteristic magnitudes in H and K-bands can be converted using the colour: $H - K \sim 0\overset{m}{.}22$ (de Propris et al., 1998).

be incomplete for fainter ones (Andreon, 2002; Kirby et al., 2008). This incompleteness happens roughly below the completeness limit of the NIR VSCL survey and it will not affect our analyses out to absolute magnitude of $-21\overset{m}{.}5$. In agreement with the photometry presented in this thesis, I use the isophotal magnitude (K_{s20}) to derive the LFs for the comparison with the VSCL clusters.

Before deriving the LFs of the Norma, Coma and Virgo clusters, I first identified their RS galaxies which will be used for an independent way of measuring their LFs.

5.3.1 Identifying the RS galaxies

In the RS method, the tight relation between the colour and magnitudes in the Colour-Magnitude Diagram (CMD) of early-type galaxies (dominated population in clusters), is used to identify the cluster members. To find the RS galaxies, I performed an estimated initial fit by visual inspection in a region of the CMD containing the RS relation and only the points within $\pm 3\sigma$ of this fit were kept for the next step. Then an iterative linear regression fit of the form $J - K = \alpha K + c$ was performed on the points within 3σ of the initial fit. Galaxies within $\pm 3\sigma$ of the final fit are the RS galaxies which are used to derive the LF of the clusters. α is the slope of the red sequence. Errors are assumed to be Poissonian in this method of LF determination.

It should be noted that this CMDs are not field corrected. Stott et al. (2009) performed a statistical field correction test to a sub-sample of their low-redshift clusters and found that the slope of the field-corrected sequence varies randomly by less than 1σ than that obtained for the uncorrected sequence. The RS method can therefore, be performed on low-redshift clusters without the field correction.

Figure 5.1 shows the resulting RS galaxies in the CMD of $(J - K)$ versus M_K for the Coma, Norma and Virgo clusters. The RS is clearly visible in Fig. 5.1. At the faint end the number of galaxies however increases towards redder colours due to an increase in background contamination by background galaxies. However, the RS is visible in the CMD. Also note that galaxy clusters at different redshifts are found to have different slopes (Gladders et al., 1998; López-Cruz et al., 2004b).

The RS fits for each cluster were done for galaxies within $r_c = 1.5$ Mpc and were as follows:

For the Coma cluster, 185 RS galaxies were selected out of 227 2MASX galaxies up to $M_{Ks} < -21\overset{m}{.}5$ with the equation:

$$(J - K)^o = (-0.014 \pm 0.003)K^o + 0.644.$$

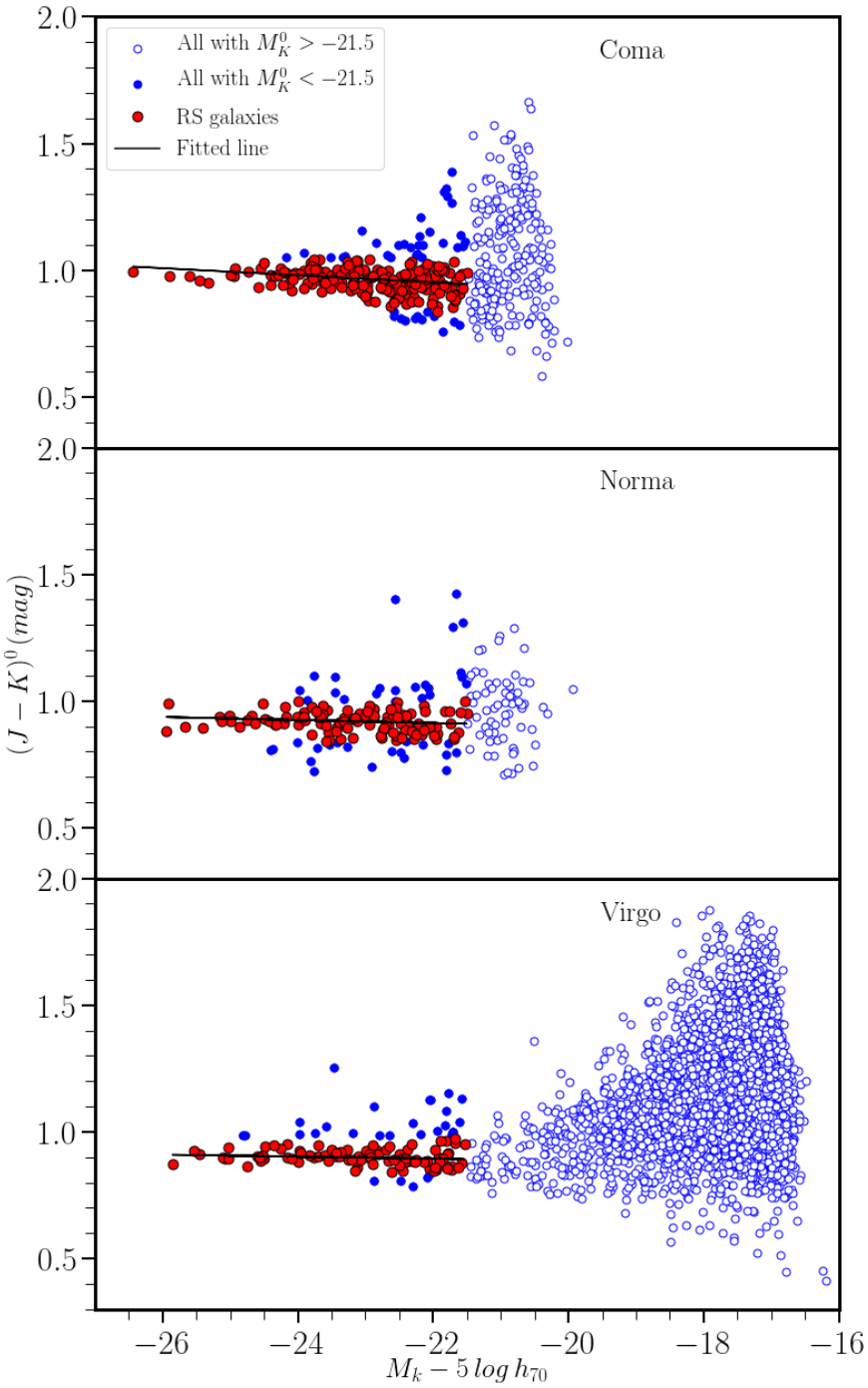

Figure 5.1: The RS of the Coma, Norma and Virgo clusters performed on galaxies within a clustercentric distance of $r_c = 1.5$. Galaxies with $M^0_{K_s} < -21\overset{\text{m}}{.}5$ are shown as filled blue circles and galaxies with $M^0_{K_s} > -21\overset{\text{m}}{.}5$ as open circles. The RS galaxies are displayed as red filled circles and the black line corresponds to the RS fit.

For the Norma cluster, 108 RS galaxies were selected out of 150 2MASX galaxies up to $M_{Ks} < -21\overset{m}{.}5$ with the equation:

$$(J-K)^o = (-0.006 \pm 0.004)K^o + 0.781.$$

For the Virgo cluster, 91 RS galaxies were selected out of 120 2MASX galaxies up to $M_{Ks} < -21\overset{m}{.}5$ with the equation:

$$(J-K)^o = (-0.004 \pm 0.003)K^o + 0.806.$$

The Coma has a slope within 1σ of what Stott et al. (2009) found for this cluster in NIR, $\alpha = -0.017 \pm 0.009$. The slope in NIR is shallower than what Gladders et al. (1998) measured for the Coma cluster in optical ($\delta(B-R)/\delta R$), $\alpha = -0.0450 \pm 0.0029$, since $J - K_s$ colour is only weakly contingent on the stellar population of galaxies. No NIR slope has been published for the Norma and Virgo clusters to date in the CMD ($(J-K)$ vs K) used in this work.

5.3.2 The Norma cluster luminosity function

I now derive the LF of the Norma cluster using two methods, the spectroscopic membership and RS. Norma is located at a mean heliocentric velocity of $v_{hel} \sim 4844 \pm 63\,\mathrm{km\,s^{-1}}$ (Woudt, 1998). Norma is a rich cluster that was observed with the same telescope, IRSF, and observation strategy as this work (Skelton et al., 2009). The completeness magnitude limit of the Norma sample is $M_{Ks} \sim -19\overset{m}{.}5$ which is deeper than that of this work ($M_{Ks} = -21\overset{m}{.}5$) due to the roughly 3 times closer distance of Norma.

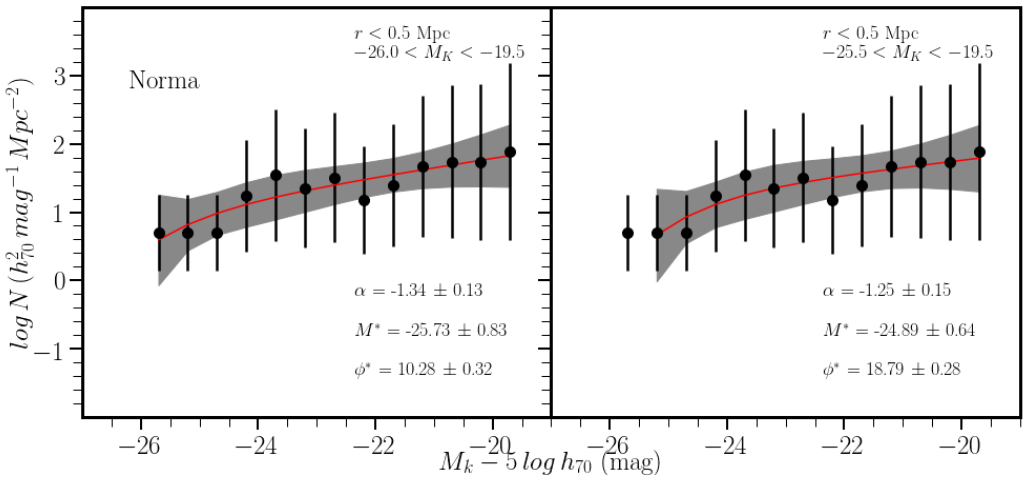

Figure 5.2: The LF of the Norma cluster in the K_s-band, using Skelton et al. (2009) data, determined from the spectroscopic membership method out to $r = 0.5$ Mpc. The best fit is shown with the red line and the gray area shows the 3σ uncertainty of the fit. Left: $-26\overset{m}{.}0 < M_{Ks} < -19\overset{m}{.}5$. Right: excluding the first bin (the two cD galaxies) $-25\overset{m}{.}5 < M_{Ks} < -19\overset{m}{.}5$.

The LF of the Norma cluster for the central area of $0.8\,\mathrm{Mpc}^2$ ($r \lesssim 0.5$ Mpc), determined from the spectroscopic membership method is reproduced in Fig. 5.2 using data[1] from

[1]The details of the sample and spectroscopic information can be found in Skelton et al. (2009).

Skelton et al. (2009). The left and right panels of Fig. 5.2 show the Norma LFs for all the bins, and apart from the first bin which contains two cD galaxies respectively. I compared the LF parameters in Fig. 5.2 (Table 5.3) with those reported in Skelton et al. (2009) (listed in Table 5.1). The derived M^* and α in this work are within 1σ of those found in Skelton et al. (2009), confirming that my fitting method to derive the LF produces accurate results.

Table 5.2: The total and spectroscopic number counts in K_s-band magnitude intervals in the Norma cluster out to $r_c < 1.5$ Mpc. $N_p(m)$ is the number of galaxies in a given (magnitude) interval. $N_s(m)$ is the total number of galaxies with spectroscopic data, in a given range of apparent magnitude. $N_m(m)$ is the number of cluster members as a function of magnitude. $f(m)$ is the fraction of galaxies in each magnitude bin that satisfies the membership criterion (Skelton et al., 2009).

K_s^0 (mag)	$N_p(m)$	$N_s(m)$	$N_m(m)$	$f(m)$
8.25	2	2	2	1.00
8.75	2	2	2	1.00
9.25	5	5	5	1.00
9.75	10	10	10	1.00
10.25	20	20	19	0.95
10.75	27	27	27	1.00
11.25	25	22	21	0.95
11.75	35	15	14	0.93
12.25	24	4	3	0.75

Since the data in Skelton et al. (2009) for the Norma cluster are only complete out to $r \lesssim 0.5$ Mpc, I independently obtained 2MASX data to compute a LF out to the completeness radius applied in this study, $r_c = 1.5$ Mpc. Also the Skelton et al. (2009) data sample only contains K_s-band magnitudes. The 2MASX data also allows a derivation of the LF for employing the RS method, i.e. for both datasets ($r_c < 1.5$ and $r < 0.5$ Mpc).

Norma has 150 galaxies within $r_c < 1.5$ Mpc with $M_{Ks} < -21\overset{\text{m}}{.}5$ ($K_s < 12\overset{\text{m}}{.}7$) in 2MASX and 107 of them have redshift information (71%). The redshift data were obtained from Woudt et al. (2008) and 2MRS (Huchra et al., 2012). Galaxies with $2000 < v < 8000$ km s^{-1} are assumed to be cluster members. There is only 1 foreground and 3 background galaxies in the Norma spectroscopic sample. The total and spectroscopic number counts in K_s-band magnitude intervals, which are used in the spectroscopic membership method to derive the Norma LF, are shown in Table 5.2 for data out to $r_c < 1.5$ Mpc. The magnitude distribution of the data is shown in Fig. 5.3.

Comparing Norma LF parameters using two methods

To compare the K_s-band LFs of the Norma cluster derived from the spectroscopic membership and RS methods, I derived the Norma LFs out to $r < 0.5$ Mpc and $r_c < 1.5$ Mpc, up to $M_{Ks} < -21\overset{\text{m}}{.}5$, using both methods. Figure 5.4 depicts the Norma LFs out to $r < 0.5$ Mpc, derived from the spectroscopic method in the left and RS method in the right panel. I used the spectroscopic method on the Skelton et al. (2009) data sample and the RS method on the 2MASX data within $r < 0.5$ Mpc, since the Skelton et al. (2009) galaxy sample does not contain the J-band (needed to perform the RS method). The Skelton et al. (2009) sample is complete to $M_{Ks} < -19\overset{\text{m}}{.}5$ with 390 galaxies. This sample has 63 galaxies up to the completeness magnitude limit of this work, $M_{Ks} < -21\overset{\text{m}}{.}5$. The

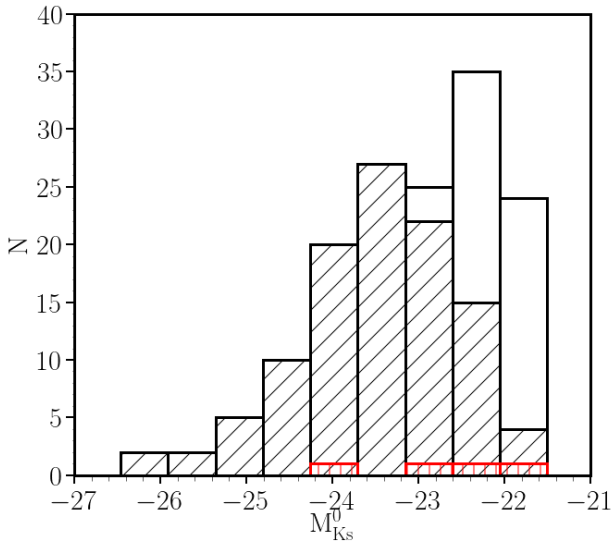

Figure 5.3: The number counts of galaxies in the Norma cluster in half-magnitude bins out to the completeness limit $M_{Ks} = -21\overset{\text{m}}{.}5$ and $r_c = 1.5\,\text{Mpc}$. Cluster members are shaded in black. Galaxies with no spectroscopic information are unshaded. The spectroscopically confirmed foreground and background galaxies are shown with the red shading.

2MASX sample has 58 galaxies within $r < 0.5$ Mpc up to $M_{Ks} < -21\overset{\text{m}}{.}5$, and 43 of them are RS galaxies. Therefore a high percentage (92%) of galaxies in Skelton et al. (2009) sample has an overlap with the 2MASX data set.

Figure 5.5 shows the Norma LFs out to $r_c < 1.5$ Mpc, derived from the spectroscopic method in the left and the RS method in the right panel using the 2MASX data. In both panels the top row (a,c) includes all magnitude bins and the bottom row (b,d) show the LFs excluding the first magnitude bin (containing the two cD galaxies). There is a dip visible in both panels of Fig. 5.4 at $M_{Ks} \sim -22\overset{\text{m}}{.}0$ which is not as apparent in the LF out to $r_c < 1.5$ Mpc in Fig. 5.5. However, a deeper dip appears to happen at $M_{Ks} \sim -21\overset{\text{m}}{.}5$ which could be the start of the dip in the LF where we observe a transition from bright elliptical and spiral galaxies to the dwarf regime (see also Fig. 1.8 in Sect. 1.5.4). Note that the number densities of galaxies in the core ($r < 0.5$ Mpc) LFs (see Fig. 5.4), are much higher than those in $r_c < 1.5$ Mpc LFs (see Fig. 5.5). The value of ϕ^* is marginally lower for the LF derived using the RS method compared to the spectroscopic membership method, due to the lower number of galaxies used in the RS method, which could be due to the fact that the RS method is a priori restricted to cluster members.

The Norma Schechter parameters extracted from the RS LF are in good agreement (within 1σ) with the ones derived from the spectroscopic membership method (see Table 5.3). Various authors have reported a flat faint end slope of RS LFs (e.g. Barkhouse et al., 2007; De Propris, 2017; Chan et al., 2019). De Propris (2017) studied the composite K-band LFs of 24 clusters at the mean redshift of $z = 0.075$, using both the redshift information and RS method. The full composite LF in their work yields $M_K^* = -24.71 \pm 0.14$ and $\alpha = -1.41 \pm 0.10$ and the RS LF yields $M_K^* = -24.34 \pm 0.15$ and $\alpha = -1.00 \pm 0.12$. The much steeper slope at the faint end is not seen for the comparison clusters in this work which is complete to $r_c < 1.5\,\text{Mpc}$ and $M_{Ks} < -21\overset{\text{m}}{.}5$. In this study I compute LFs for each individual cluster and not a composite LF.

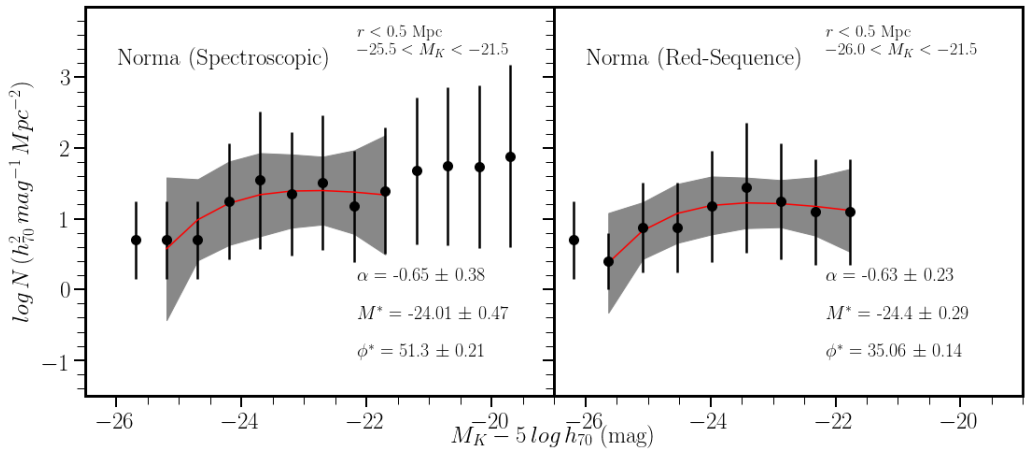

Figure 5.4: The LF of the Norma cluster in the K_s-band out to $r < 0.5$ Mpc, excluding the two cD galaxies (the first bin). Left: using Skelton et al. (2009) data, determined from the spectroscopic membership method for $-25.^{\rm m}5 < M_{Ks} < -21.^{\rm m}5$. Right: using 2MASX data, determined from the RS method for $-26.^{\rm m}0 < M_{Ks} < -21.^{\rm m}5$. The best fit is shown with the red line and the gray area shows the 3σ uncertainty of the fit.

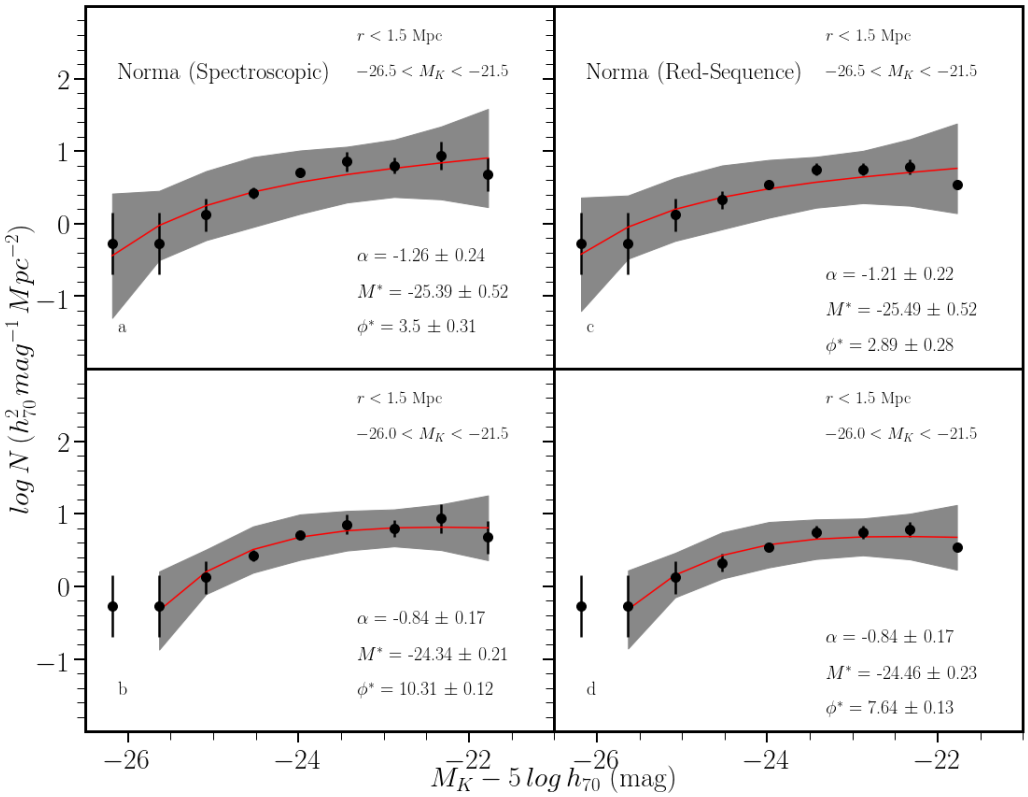

Figure 5.5: The LFs of the Norma cluster in the K_s-band out to $r_c < 1.5$ Mpc. The left panel shows the LFs derived from the spectroscopic method and the right panel derived from the RS method. In both panels the top and bottom plots show the LFs with and without the two cD galaxies respectively. The best fit is shown with the red line and the gray area shows the 3σ uncertainty of the fit.

The comparison between the spectroscopic and RS methods was done for the Coma and Virgo clusters as well and the result was consistent with what is found for the Norma cluster. The comparison confirmed that the RS method is reliable and can be used in the absence of high coverage of spectroscopic information. The redshift data for Coma was obtained from the SDSS DR16 catalogue (Ahumada et al., 2020). The redshift data for Virgo was obtained from SDSS DR16 catalogue (Ahumada et al., 2020) and 2MRS (Huchra et al., 2012). The Coma clusters dataset has 98% redshift coverage. Using this data, I investigated the redshift coverage percentage, below which the spectroscopic method becomes unreliable. The uncertainty in LF parameters becomes very high and the results are not trustworthy when the fraction of redshift data goes below 50%.

In the next section I will derive the LFs of the Coma and Virgo cluster using the RS method. This will later be used for comparison and classification of the VSCL clusters.

5.3.3 The Coma and Virgo luminosity functions

Coma

The Coma cluster, located at $v_{hel} \sim 6942\,\mathrm{km\,s^{-1}}$ (Wegner et al., 1999), is the most comprehensively studied cluster in both the optical and NIR bands. To derive the Coma LF, 108 RS galaxies were selected out of 150 2MASX galaxies that have $M_{Ks} < -21\overset{\mathrm{m}}{.}5$ within $r_c < 1.5$ Mpc, while there are 82 RS galaxies within $r < 0.5$ Mpc (see Fig. 5.1). The RS LFs of the Coma cluster in the K_s-band, complete to $M_{Ks} = -21\overset{\mathrm{m}}{.}5$ ($K_s = 13\overset{\mathrm{m}}{.}5$), are plotted in Fig. 5.6 and the Schechter parameters are listed in Table 5.3.

In Fig. 5.6, plot (a) shows the Coma LF out to $r < 0.5$ Mpc when the two cD galaxies are excluded from the sample. Plots (b) and (c) are the Coma LFs out to $r_c < 1.5$Mpc with and without the cD galaxies respectively. Similar to the Norma LFs, the dip appears at $M_{Ks} \sim -21\overset{\mathrm{m}}{.}5$.

To check the consistency of the Schechter parameters found for Coma, I compare them to those reported in previous studies. Various authors have investigated the Coma LF in NIR (e.g. de Propris et al., 1998; Andreon and Pelló, 2000). The NIR LF parameters of the Coma cluster derived in the previous papers are listed in Table 5.1. de Propris et al. (1998) computed the H-band LF of the Coma cluster for bright galaxies $M_H < -20\overset{\mathrm{m}}{.}5$ using only the cluster members and converted their derived Schechter parameters to the K-band applying a colour term $(H-K) \sim 0\overset{\mathrm{m}}{.}22$. de Propris et al. (1998) also computed the H-band LF for faint galaxies in Coma with $-21\overset{\mathrm{m}}{.}0 < M_H < -19\overset{\mathrm{m}}{.}0$ using two methods: the $B-R$ colour-magnitude relation and field correction methods. Andreon and Pelló (2000) measured the H-band LF of galaxies with $M_H < -18\overset{\mathrm{m}}{.}0$ using the field correction method.

The characteristic magnitude for the Coma cluster found by de Propris et al. (1998) in the K-band ($M^*_K = -24\overset{\mathrm{m}}{.}02$) agrees well with what Andreon and Pelló (2000) found in the H-band ($M^*_H = -23\overset{\mathrm{m}}{.}86$), taking into account the colour difference $H-K \approx 0\overset{\mathrm{m}}{.}22$ (de Propris et al., 1998). No errors for M^* and α are reported in de Propris et al. (1998). Nevertheless the 1σ error ellipse shown in their Fig. 2 indicates $1\sigma \sim 0\overset{\mathrm{m}}{.}75$ and $1\sigma \sim 0.25$ for M^* and α respectively. The confidence interval for the LF fit shown in Fig. 3 of Andreon and Pelló (2000) is even larger.

The M^* found in this work both for $r < 0.5$ and $r_c < 1.5\,\mathrm{Mpc}$ (excluding cD galaxies, $-23\overset{\mathrm{m}}{.}98$ and $-24\overset{\mathrm{m}}{.}44$) are within 1σ of those found in the de Propris et al. (1998) and Andreon and Pelló (2000) studies. The slope, α, found in this work for $r < 0.5\,\mathrm{Mpc}$

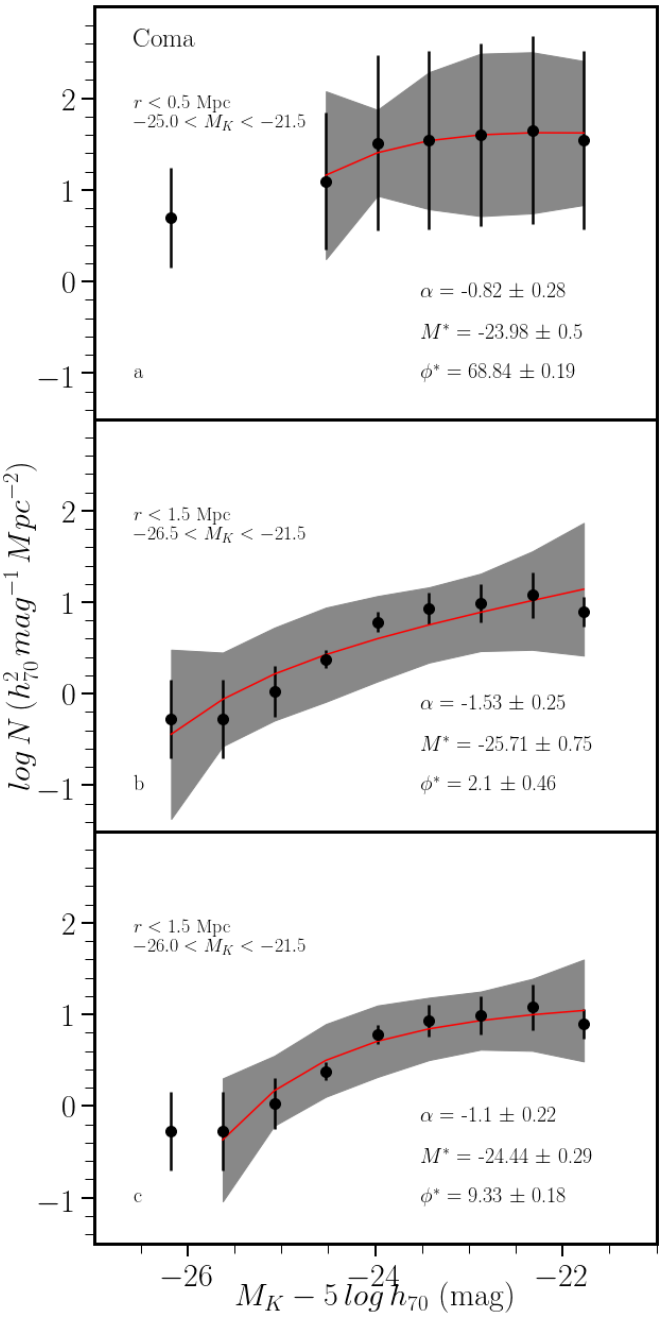

Figure 5.6: The LF of the Coma cluster in the K_s-band using the RS method. (a): out to $r < 0.5\,\mathrm{Mpc}$, excluding the two cD galaxies (the first bin), $-25\overset{\mathrm{m}}{.}0 < M_{Ks} < -21\overset{\mathrm{m}}{.}5$. (b): out to $r_c < 1.5\,\mathrm{Mpc}$, $-26\overset{\mathrm{m}}{.}5 < M_{Ks} < -21\overset{\mathrm{m}}{.}5$. (c): out to $r_c < 1.5\,\mathrm{Mpc}$, excluding the two cD galaxies (the first bin), $-26\overset{\mathrm{m}}{.}0 < M_{Ks} < -21\overset{\mathrm{m}}{.}5$. The best fit is shown with the red line and the gray area shows the 3σ uncertainty of the fit.

LF (-0.82) and $r_c < 1.5$ Mpc LF (-1.10) are within 1σ of that of de Propris et al. (1998) where the completeness magnitude limit, $M_K \sim -20\overset{m}{.}5$, is close to this work, $M_K \sim -21\overset{m}{.}5$. However, when survey is deeper, (e.g. Andreon et al. (2000)) the slope is steeper due to the inclusion of the faint dwarf population in their sample.

Virgo

The Virgo cluster, located at a mean heliocentric recession velocity of $\sim 1305\,\mathrm{km\,s^{-1}}$ (Firth et al., 2008) is the closest galaxy cluster to the Milky Way. To derive its LF, 91 RS galaxies were selected out of 120 2MASX galaxies with $M_{Ks} < -21\overset{m}{.}5$ and $r_c < 1.5$ Mpc. There are 24 RS galaxies within $r < 0.5$ Mpc (see Fig. 5.1). The LFs of the Virgo cluster in the K_s-band, complete to $M_{Ks} = -21\overset{m}{.}5$ ($K_s = 9\overset{m}{.}85$) using the RS method, are plotted in Fig. 5.7 and the resulting Schechter parameters are listed in Table 5.3. The top panel in Fig. 5.7 (a) is the Virgo LF out to $r < 0.5$ Mpc. The number of RS galaxies within $r < 0.5$ Mpc for this young irregular cluster is very low and the LF fit has large uncertainties. The Schechter parameters could not even be constrained when the first bin (the cD galaxy in Virgo) is excluded. The middle and bottom panels of Fig. 5.7 (b,c) are the Virgo LFs out to $r_c < 1.5$ Mpc with and without the first bin, respectively. There are two galaxies in the Virgo region which are located out of the clustercentric distance of $r < 0.5$ Mpc and are brighter than the cD galaxy in this cluster. The first bin in the $r_c < 1.5$ Mpc LFs contains these two galaxies and the cD galaxy. The dip that appears at $M_{Ks} = -21\overset{m}{.}5$ in the Norma and Coma cluster LFs (in previous sections) is not visible in the Virgo LFs out to $r_c < 1.5$ Mpc. This could be due to the fact that Virgo is a young and irregular cluster and contains a low fraction of early-type galaxies at its central regions and an overall high fraction of late-type galaxies. However, in the central and denser regions two dips are apparent in the $r < 0.5$ Mpc LF of Virgo at $M_{Ks} \sim -23\overset{m}{.}0$ and $M_{Ks} \sim -21\overset{m}{.}5$, where the latter marks the region where the dwarfs start to dominate and the number of giant galaxies decline. But one should note that the number of galaxies is very low in the $r < 0.5$ Mpc LF sample and the result might not be reliable.

5.4 The VC04 LF

After having derived the K_s-band LF for a set of well-known clusters, ranging from rich clusters to the younger Virgo cluster, I will now explore the LF of the VSCL clusters, after which their different parameters can be compared. I start with the derivation of the LFs of VC04, one of the most prominent clusters in the VSCL at $v_{hel} \sim 18196$ km s^{-1} with $\sigma \sim 455$ km s^{-1} (see Sect. 4.2.1 for the velocity histogram plot), for which both H I and X-ray data are also available. I will then compare the derived VC04 LF parameters to the above derived NIR LFs.

The redshift data of galaxies in the VSCL clusters were obtained from the 2MASS and optical data, using the 2dF+AAOmega spectrograph on the 3.9m AAT. The VSCL IRSF data are complete to $K_s = 15\overset{m}{.}5$ ($M_{Ks} < -21\overset{m}{.}5$), and most of the fainter galaxies ($K_s \gtrsim 13\overset{m}{.}5$, $M_{Ks} \gtrsim -23\overset{m}{.}5$) do not have redshifts. The fraction of galaxies with spectroscopic data varies in each of the observed VSCL clusters (see Table 4.3) and the redshift data coverage is too low to perform the spectroscopic membership method to derive the LFs reliably. For example, out of 231 galaxies in VC04, 190 are located within $r_c = 1.5$ Mpc and 73 of them have redshift information (38 %). Fifty galaxies are located within the central radius of $r = 0.5$ Mpc of VC04, of which 25 have spectroscopic data ($\sim 50\%$). It

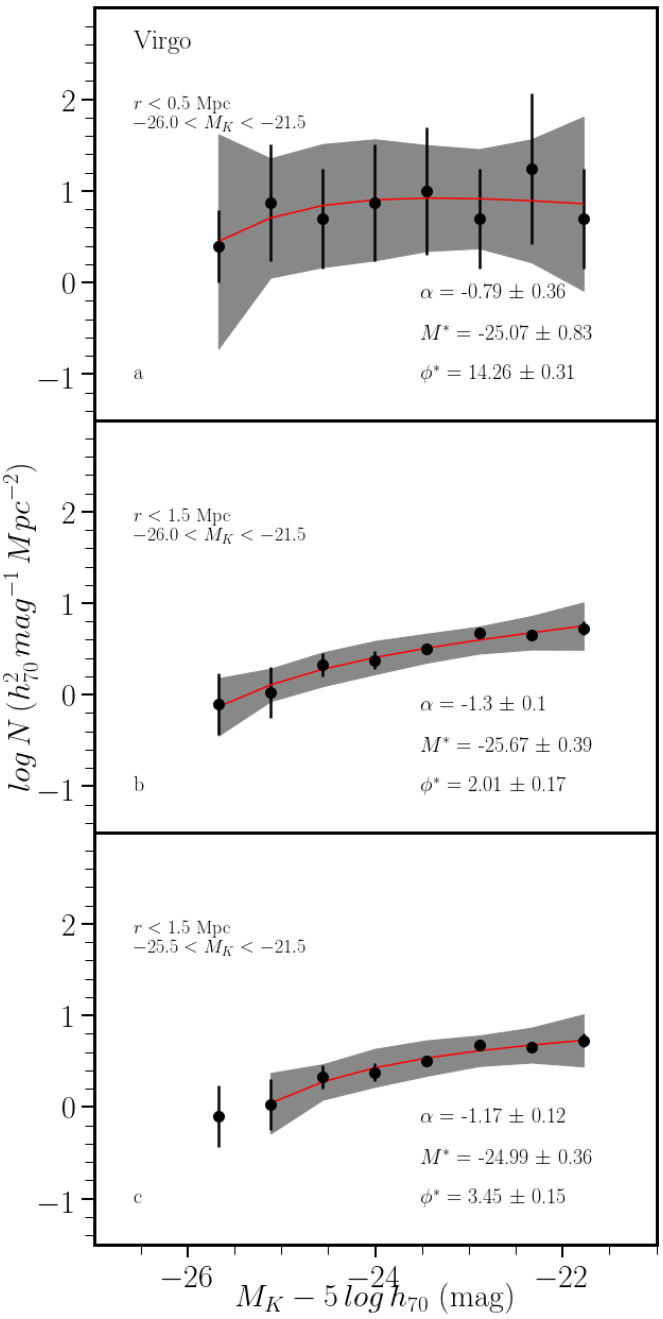

Figure 5.7: The LF of the Virgo cluster in the K_s-band using the RS method. (a): $r < 0.5\,$Mpc, $-26\overset{\text{m}}{.}0 < M_{Ks} < -21\overset{\text{m}}{.}5$. (b): $r_c < 1.5\,$Mpc, $-26\overset{\text{m}}{.}0 < M_{Ks} < -21\overset{\text{m}}{.}5$. (c): $r_c < 1.5\,$Mpc, $-25\overset{\text{m}}{.}5 < M_{Ks} < -21\overset{\text{m}}{.}5$. The best fit is shown with the red line and the gray area shows the 3σ uncertainty of the fit.

Table 5.3: The K_s-band luminosity function parameters of Norma, Coma and Virgo.

Cluster	$M^*_{Ks} - 5log\,h_{70}$ mag	α	ϕ^* $h^2_{70}\,\mathrm{Mpc}^{-2}$	r Mpc	Sample Notes	Method
Norma	-25.73 ± 0.83	-1.34 ± 0.13	10.28 ± 0.32	< 0.5	$-26\overset{\mathrm{m}}{.}0 < M_{Ks} < -19\overset{\mathrm{m}}{.}5$	SM[a]
Norma	-24.89 ± 0.64	-1.25 ± 0.15	18.79 ± 0.28	< 0.5	$-25\overset{\mathrm{m}}{.}5 < M_{Ks} < -19\overset{\mathrm{m}}{.}5$[c]	SM
Norma	-24.01 ± 0.47	-0.65 ± 0.38	51.30 ± 0.21	< 0.5	$-25\overset{\mathrm{m}}{.}5 < M_{Ks} < -21\overset{\mathrm{m}}{.}5$	SM
Norma	-24.40 ± 0.29	-0.63 ± 0.23	35.06 ± 0.14	< 0.5	$-26\overset{\mathrm{m}}{.}0 < M_{Ks} < -21\overset{\mathrm{m}}{.}5$	RS[b]
Norma	-25.39 ± 0.52	-1.26 ± 0.24	3.50 ± 0.31	< 1.5	$-26\overset{\mathrm{m}}{.}5 < M_{Ks} < -21\overset{\mathrm{m}}{.}5$	SM
Norma	-25.49 ± 0.52	-1.21 ± 0.22	2.89 ± 0.28	< 1.5	$-26\overset{\mathrm{m}}{.}5 < M_{Ks} < -21\overset{\mathrm{m}}{.}5$	RS
Norma	-24.34 ± 0.21	-0.84 ± 0.17	10.31 ± 0.12	< 1.5	$-26\overset{\mathrm{m}}{.}0 < M_{Ks} < -21\overset{\mathrm{m}}{.}5$[c]	SM
Norma	-24.46 ± 0.23	-0.84 ± 0.17	7.64 ± 0.13	< 1.5	$-26\overset{\mathrm{m}}{.}0 < M_{Ks} < -21\overset{\mathrm{m}}{.}5$[c]	RS
Coma	-23.98 ± 0.89	-0.82 ± 0.28	68.84 ± 0.19	< 0.5	$-25\overset{\mathrm{m}}{.}0 < M_{Ks} < -21\overset{\mathrm{m}}{.}5$	RS
Coma	-25.71 ± 0.75	-1.53 ± 0.25	2.1 ± 0.46	< 1.5	$-26\overset{\mathrm{m}}{.}5 < M_{Ks} < -21\overset{\mathrm{m}}{.}5$	RS
Coma	-24.44 ± 0.29	-1.10 ± 0.22	9.39 ± 0.18	< 1.5	$-26\overset{\mathrm{m}}{.}0 < M_{Ks} < -21\overset{\mathrm{m}}{.}5$[c]	RS
Virgo	-25.07 ± 0.83	-0.79 ± 0.36	14.26 ± 0.31	< 0.5	$-26\overset{\mathrm{m}}{.}0 < M_{Ks} < -21\overset{\mathrm{m}}{.}5$	RS
Virgo	-25.67 ± 0.39	-1.30 ± 0.10	2.01 ± 0.17	< 1.5	$-26\overset{\mathrm{m}}{.}0 < M_{Ks} < -21\overset{\mathrm{m}}{.}5$	RS
Virgo	-24.99 ± 0.36	-1.17 ± 0.12	3.45 ± 0.15	< 1.5	$-25\overset{\mathrm{m}}{.}5 < M_{Ks} < -21\overset{\mathrm{m}}{.}5$[c]	RS

[a] Spectroscopic Membership method.
[b] The Red-Sequence method.
[c] Excluding the first bin which contains cD galaxy or galaxies.

was for exactly this reason that I tested the validity of using the RS method to derive LFs in the previous section. Therefore, the RS method is more suitable to derive the LFs of the VSCL clusters.

Figure 5.8 shows the CMD of the VC04 cluster in the left panel and the distribution of the RS galaxies identified from it in the iso-density contour map of VC04 in the right panel. The RS fit of VC04 as determined from the galaxy sample delimited by $M^0_{Ks} < -21\overset{\mathrm{m}}{.}5$ has the relation,

$$(J - K)^o = (-0.011 \pm 0.005)K^o + 0.766.$$

The slope of the fit is within 1σ of what is found for the Coma cluster in Sect. 5.2.3. Out of 190 galaxies within $r_c = 1.5$ Mpc, 118 are identified as RS galaxies up to $M^0_{Ks} = -21\overset{\mathrm{m}}{.}5$.

Figure 5.9 shows the LFs of VC04 out to $r < 0.5$ Mpc (top panel) and $r_c < 1.5$ Mpc (middle and bottom panels) derived from the RS method complete to $M_{Ks} < -21\overset{\mathrm{m}}{.}5$. The VC04 cluster does not have a cD galaxy, and the brightest cluster member galaxy within $r_c < 1.5$ Mpc lie outside of $r < 0.5$ Mpc. Therefore, to perform a fair comparison of $r_c < 1.5$ Mpc LF of VC04 with its $r < 0.5$ Mpc LF and the LFs of the other clusters, the bottom panel (c) of Fig. 5.9 was made excluding the first bin. The LF parameters of VC04 are listed in Table 5.4.

The fact that the brightest VC04 galaxy is not at the centre but within a small density enhancement suggests that there is a possible subgroup at its outskirts (north-east, see the iso-density contour map of VC04, Fig. 5.8). VC04 is not as relaxed and virialized as the Coma and more similar to Norma clusters (the gravitational forces make the massive galaxies move toward the central regions of clusters). Also, from visual examination of the morphology of galaxies and the fraction of galaxies with emission lines in the spectroscopic data (R. C. Kraan-Korteweg, private comm.), it is likely that VC04 contains many spiral galaxies, even in the central regions (see Sect.4.3). Therefore, one could say that VC04 is

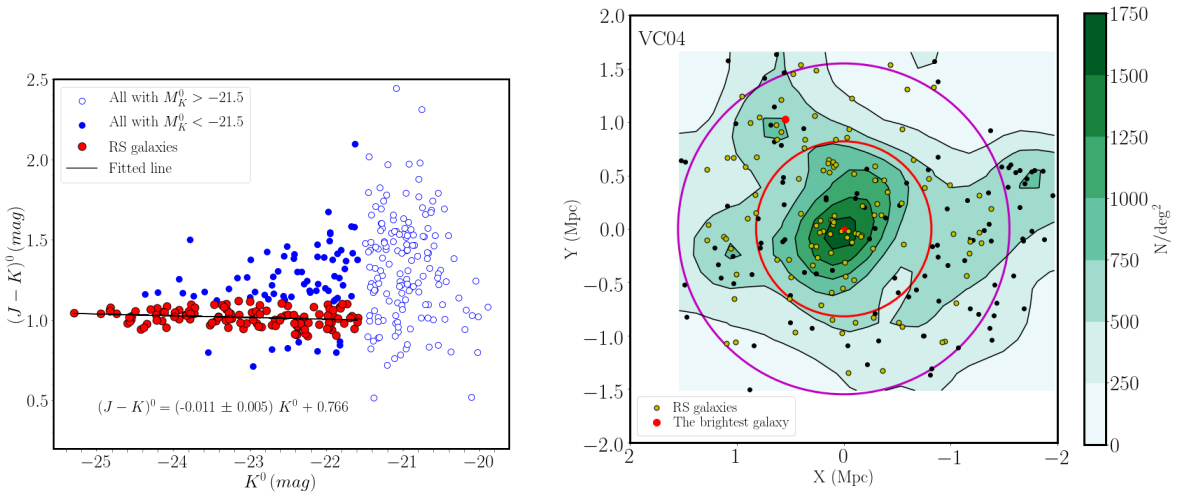

Figure 5.8: Left: the RS of the VC04 cluster performed on galaxies within a clustercentric distance of $r_c = 1.5$. Galaxies with $M^0_{K_s} < -21\overset{\text{m}}{.}5$ are shown as filled blue circles and galaxies $M^0_{K_s} > -21\overset{\text{m}}{.}5$ as open circles. The RS galaxies are displayed as red circles and the RS fit is shown as black line. Right: the iso-density contour map of VC04 complete to $M^0_{Ks} = -21\overset{\text{m}}{.}5$. The galaxies are shown as black dots and the RS galaxies as yellow dots. The red and magenta circles represent the $r = 0.5$ Mpc and $r_c = 1.5$ Mpc respectively.

a massive cluster but not yet fully evolved.

Table 5.4: The K_s-band luminosity function parameters of VC04.

Cluster	$M^*_{Ks} - 5log\,h_{70}$ mag	α	ϕ^* h^2_{70} Mpc^{-2}	r Mpc	Sample Notes	Method
VC04	-24.48 ± 0.39	-0.78 ± 0.16	30.95 ± 0.12	< 0.5	$-25\overset{\text{m}}{.}0 < M_{Ks} < -21\overset{\text{m}}{.}5$	RS[a]
VC04	-23.90 ± 0.25	-0.68 ± 0.23	12.75 ± 0.12	< 1.5	$-25\overset{\text{m}}{.}5 < M_{Ks} < -21\overset{\text{m}}{.}5$	RS
VC04	-24.70 ± 0.42	-0.89 ± 0.13	8.42 ± 0.12	< 1.5	$-25\overset{\text{m}}{.}0 < M_{Ks} < -21\overset{\text{m}}{.}5$[b]	RS

[a] The red-sequence method.
[b] Excluding the first bin.

Comparison between the LF fit parameters of VC04 shows that the slope and M^* of the $r < 0.5$ Mpc LF are within 1σ of those of $r_c < 1.5$ Mpc LF, when $-25\overset{\text{m}}{.}0 < M_{Ks} < -21\overset{\text{m}}{.}5$ (excluding the first bin). This will be further discussed in the next section.

5.5 Discussion

To compare the Schechter parameters of LFs of clusters studied in different surveys, one should note that they depend on the wavelength band, magnitude system, location and size of the area surveyed, and the depth of the survey. For example, Andreon (2001) found that the same analysis technique can yield different LF parameters in different regions of the same cluster (see Table 5.5). Therefore, useful comparisons between cluster LFs can only be made when the area and depth of the surveys are the same (Jerjen and Tammann, 1997). Also, because cD galaxies cannot be mapped properly by a Schechter function,

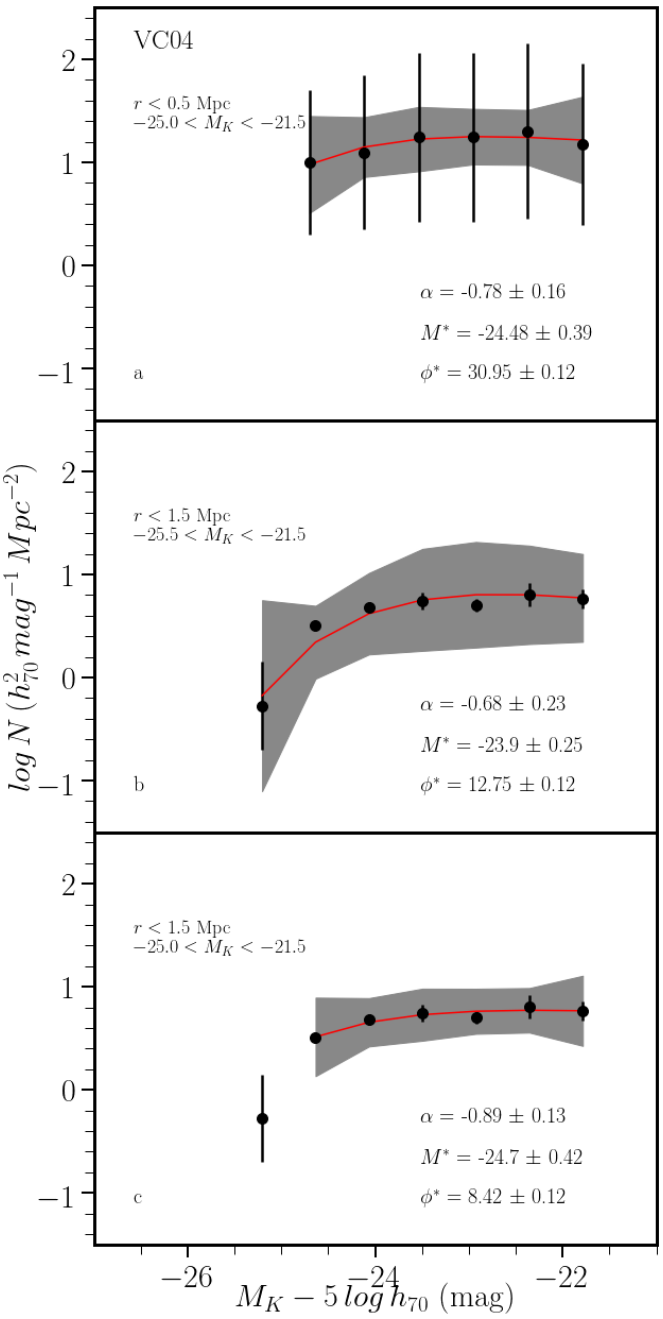

Figure 5.9: The LF of the VC04 cluster in the K_s-band using the RS method. (a): $r < 0.5\,\mathrm{Mpc}$, $-25\overset{\mathrm{m}}{.}0 < M_{Ks} < -21\overset{\mathrm{m}}{.}5$. (b): $r_c < 1.5\,\mathrm{Mpc}$, $-25\overset{\mathrm{m}}{.}5 < M_{Ks} < -21\overset{\mathrm{m}}{.}5$. (c): $r_c < 1.5\,\mathrm{Mpc}$, $-25\overset{\mathrm{m}}{.}0 < M_{Ks} < -21\overset{\mathrm{m}}{.}5$. The best fit is shown with the red line and the gray area shows the 3σ uncertainty of the fit.

Table 5.5: Table of previous NIR luminosity functions parameters of clusters.

Cluster	Reference	Band	M^* mag	α	Sample Notes
AC118	Andreon (2001)	K_s	-25.26	-1.2	1.36 Mpc^2, $M_K \lesssim -21.5$
AC118	Andreon (2001)	K_s	-23.96	-0.5	0.26 Mpc^2 Main clump
AC118	Andreon (2001)	K_s	-23.56	-0.9	0.26 Mpc^2 NW clump
93 clusters[a]	Lin et al. (2004)	K_s	$-24.34 \lesssim M^* \lesssim -24.02$	$-1.1 \lesssim \alpha \lesssim -0.84$	Composite LF, $M_K \lesssim -21.0$
5 clusters[b]	Merluzzi et al. (2010)	K_s	-24.96 ± 0.10	-1.42 ± 0.03	Composite LF, $M_K \lesssim -18.5$
24 clusters[c]	De Propris (2017)	K	-24.78 ± 0.14	-1.41 ± 0.10	Composite LF[d], $M_K \lesssim -22.5$
24 clusters	De Propris (2017)	K	-24.41 ± 0.15	-1.00 ± 0.12	Composite LF[e]

M^*s have been adjusted for $H_0 = 70$ km s^{-1} Mpc^{-1}. The difference between the magnitude systems have not been taken into account.
[a] $0.01 \lesssim z \lesssim 0.09$.
[b] Clusters in the Shapley supercluster at $z = 0.048$.
[c] Clusters are at mean redshift of $z = 0.075$.
[d] Using the spectroscopic information.
[e] The RS LFs.

it is justified to only compare the Schechter parameters of LFs when the cD galaxies are excluded. With this in mind, the LF parameters of the Coma, Norma and Virgo clusters derived in this work are summarized in Table 5.3 and the derived LF parameters of the VC04 cluster are summarized in Table 5.4. Table 5.5 lists some of the previous NIR cluster and composite LFs found. Note that the parameters α, M^* and ϕ^* are interdependent while ϕ^* (in the mentioned tables) shows how the overall galaxy density decreases when incorporating samples with increasing radii.

5.5.1 Comparison with the Coma, Norma and Virgo LFs

In Sect. 5.3, I showed that the Schechter parameters of the Norma and Coma clusters derived in this work agree well with those reported in the literature (see Table 5.1). The LF parameters out to $r_c < 1.5$ Mpc and up to $M_{Ks} < -21\overset{\text{m}}{.}5$ from the RS method are,

VC04: $M^* = -24\overset{\text{m}}{.}70 \pm 0.42$, $\alpha = -0.89 \pm 0.13$.
Norma: $M^* = -24\overset{\text{m}}{.}46 \pm 0.23$, $\alpha = -0.84 \pm 0.17$.
Coma: $M^* = -24\overset{\text{m}}{.}44 \pm 0.29$, $\alpha = -1.10 \pm 0.22$.
Virgo: $M^* = -24\overset{\text{m}}{.}99 \pm 0.36$, $\alpha = -1.17 \pm 0.12$.

The M^* of the VC04 LF lies within those of the Norma, Coma and Virgo clusters. The slope of the VC04 LF is shallower than that of the Coma and Virgo cluster, but within 1σ of the slope of the Norma LF. The Coma cluster contains substructure (see Sect. 4.1) and hence likely to have more late-type galaxies in its outer regions. The Virgo cluster is a young and intermediate cluster with many late-type galaxies and its faint-end slope is steeper than those of VC04 and Norma clusters.

5.5.2 Comparison with previous NIR LFs

Lin et al. (2004); Merluzzi et al. (2010) and De Propris (2017) computed the composite LFs of clusters at nearby redshifts as listed in Table 5.5. The M^* of VC04 LF ($M^* = -24\overset{\text{m}}{.}70 \pm 0.42$) is in good agreement with that of the previous K_s-band cluster LF studies, considering its uncertainty. Lin et al. (2004) computed a composite LF with $-24.34 \lesssim M^* \lesssim -24.02$ for 93 clusters at $0.01 \lesssim z \lesssim 0.09$. Merluzzi et al. (2010) measured $M^* = -24\overset{\text{m}}{.}96 \pm 0.10$ for composite LF of 5 clusters in the Shapley supercluster. For

24 clusters at $z = 0.075$, De Propris (2017) derived $M^* = -24\overset{m}{.}78 \pm 0.14$ using the spectroscopic information, and $M^* = -24\overset{m}{.}41 \pm 0.15$ using the RS members.

The faint end slope of VC04 LF ($\alpha = -0.89 \pm 0.13$) is in agreement with that of Lin et al. (2004) ($-1.1 \lesssim \alpha \lesssim -0.84$) and the RS composite LF of De Propris (2017) (-1.0 ± 0.12). Merluzzi et al. (2010) survey is deeper than this work and therefore, the upturn in their composite LFs, caused by the power law curve of the late-type and dwarf galaxies is the reason for their steeper faint end slope.

AC118 is a cluster at $z = 0.3$ and comparison of its LF to LFs of nearby clusters could provide information on the evolution of galaxies in clusters. Andreon (2001) found $\alpha = 1.2$ and $M^* = -25.26$ for the K_s-band LF of AC118 up to $M_K \lesssim -21\overset{m}{.}5$ (same as this work). The slope of the AC118 LF is steeper and its M^* is brighter than the VC04 LF parameters. This could be due to evolution of galaxies in clusters from intermediate redshifts to the present time. However, the main clump of AC118 has LF parameters of $\alpha = -0.5$ and $M^* = -23\overset{m}{.}96$ which agree well with those of VC04. Andreon (2001) showed that in their sample the number of bright early-type galaxies in the clump is higher (due to its denser environment) compared to the number of dwarfs (which is higher in the outer regions). It is possible that as a cluster grows by accretion of galaxies or small groups, the dwarfs break apart and become part of massive galaxies.

5.5.3 Environmental effects

Lobo et al. (1997) suggested that the faint-end slope of the LF is shallower in the central regions of a cluster where the density is higher compared to the more sparsely populated outskirts. Andreon and Pelló (2000) and Andreon (2001) found evidence for this claim for the Coma and AC118 clusters respectively. Merluzzi et al. (2010) studied the LF of clusters in the Shapley supercluster in three regions with different densities of galaxies and found that the faint-end slope increases significantly as one moves from high-density to low-density regions and the upturn in the LF for $M_K > -21\overset{m}{.}0$ becomes more apparent in low-density environments. De Propris (2017) found that M^*_K is largely unaffected by the environment but that the faint-end slope, α, increases towards lower mass clusters ($\sigma < 800$ km s^{-1}) and clusters with Bautz-Morgan type $< II$. The steeper faint-end slope in low-density regions has been observed in optical bands as well (e.g. Boué et al., 2008; McNaught-Roberts et al., 2014; Lee et al., 2016).

The faint-end slopes of VC04 for the $r < 0.5$ Mpc LF (-0.78 ± 0.16) does not vary significantly when it is measured out to the outer and lower density regions, $r_c < 1.5$ Mpc LF (-0.89 ± 0.13) and is within 1σ uncertainty. This could be because this NIR study is complete to $M_{Ks} < -21\overset{m}{.}5$ which is $M \lesssim M^* + 2.5$ and hence it is not within the dwarf regime and will not be sensitive to them. Therefore, we mainly map the Gaussian part of the LF relating to elliptical and bulgy spiral galaxies and the upturn in the faint-end slope of the cluster LF due to the contribution of late-type spirals and dwarf ellipticals is not visible in the cluster LF (see Sect. 1.5.4).

5.6 The LFs of other VSCL clusters

Having completed a detailed analysis of the VC04 K_s-band LF, I now turn to the other VSCL clusters. In this section I derive the LFs of the other four observed VSCL clusters, VC02, VC05, VC08 and VC11, using the RS method. The LF of VC10 is not computed, since it appears to be a filament-like structure and not a cluster (see Sect. 4.2.2). The

iso-density contour maps of VC02, VC05, VC08 and VC11 are shown in Fig. 5.11. The LFs of VC02 and VC08 are derived for both $r < 0.5$ Mpc and $r_c < 1.5$ Mpc. However, for VC05, I derive the LF out only to $r < 0.5$ Mpc, since the centre of VC05 had to be adjusted for the analysis of this study, and the data are not complete to $r_c = 1.5$ Mpc. Since VC11 consists of two clumps, VC11a (left) and VC11b (right), as shown in Fig. 5.11, the LFs are derived separately for each clump out to $r < 0.5$ Mpc. Figure 5.10 shows the colour-magnitude diagrams of VC02, VC04, VC05, VC08, VC11a and VC11b with their RS fit. The RS fit relation and the number of identified RS galaxies in each VSCL cluster is listed in Table 5.6. The RS members in each cluster are shown as yellow dots in Fig. 5.11.

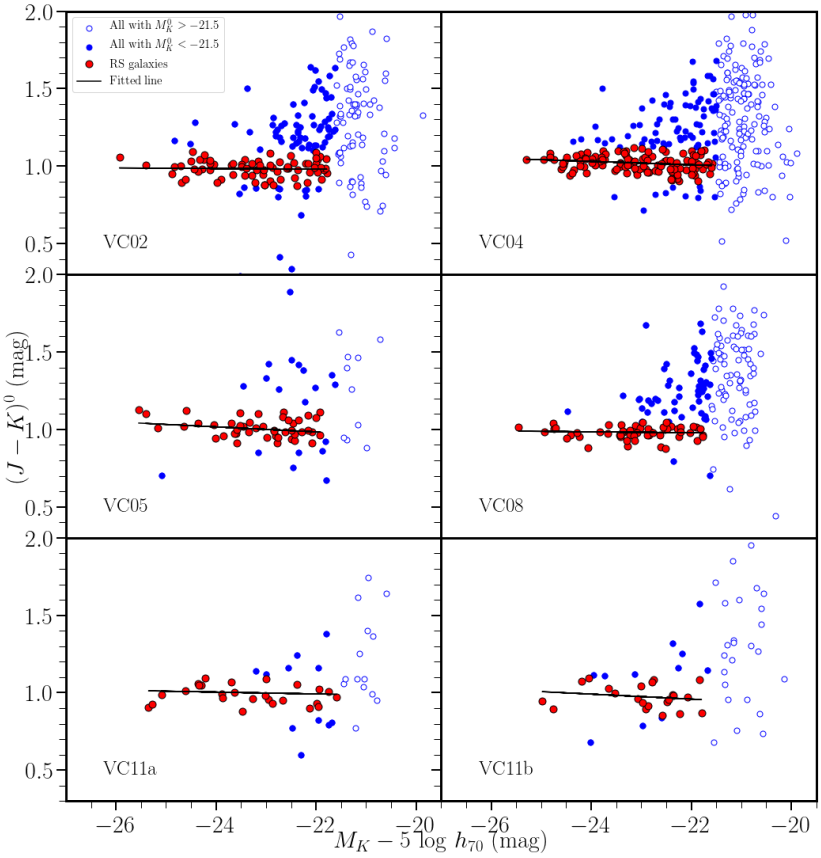

Figure 5.10: The RS of the VSCL cluster performed on galaxies within a clustercentric radii of $r_c < 1.5$ for VC02, VC04, VC08 and $r < 0.5$ for VC05, VC11a and VC11b. Galaxies with $M^0_{K_s} < -21\overset{\text{m}}{.}5$ are shown as filled blue circles and galaxies $M^0_{K_s} > -21\overset{\text{m}}{.}5$ as open circles. The RS galaxies are displayed as red circles and the RS fit is shown as black line.

The K_s-band LFs of the VC02, VC05, VC08, VC11a and VC11b are shown in Fig. 5.12 and their Schechter parameters are listed in Table 5.7. The figure and table show that the LF parameters of VC05, VC08, VC11a and VC11b have very large uncertainties, due to the low numbers of galaxies in the respective samples. Therefore, any comparison with other clusters would not be precise. Only VC02 LF for $r_c < 1.5$ Mpc has reasonable uncertainties for its parameters ($M^* = -24.39 \pm 0.22$ and $\alpha = -0.85 \pm 0.18$) and they

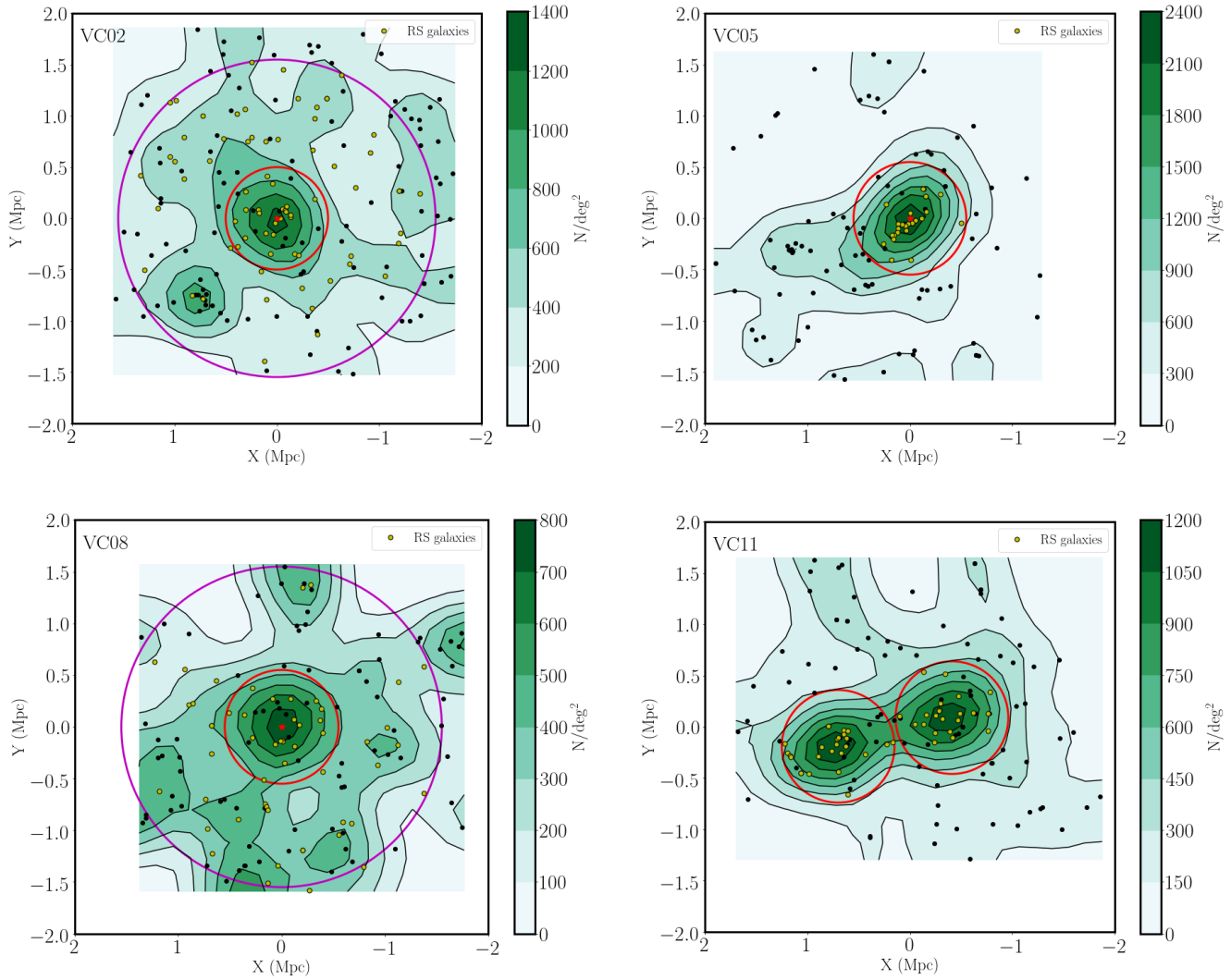

Figure 5.11: The iso-density contour maps of the VC02, VC05, VC08 and VC11 clusters out to $r_c = 1.5$ Mpc and $M^0_{Ks} < -21\overset{\text{m}}{.}5$. The galaxies are shown as black dots and the RS galaxies as yellow dots. The red and magenta circles represent the $r = 0.5$ Mpc and $r_c = 1.5$ Mpc respectively.

Table 5.6: RS properties of the VSCL clusters. RS fit relation is defined as $(J-K)^o = (\alpha)K^o + \beta$. N_{RS} is the number of identified RS galaxies.

Cluster	α	β	N_{RS} in $r_c < 1.5$ Mpc	N_{RS} in $r < 0.5$ Mpc
VC02	-0.002 ± 0.006	0.936	72	23
VC04	-0.011 ± 0.005	0.766	118	37
VC05	-0.016 ± 0.010	0.632	–	30
VC08	-0.003 ± 0.007	0.912	54	20
VC11a	-0.006 ± 0.011	0.860	–	26
VC11b	-0.016 ± 0.019	0.607	–	22

Table 5.7: The K_s-band luminosity function parameters of the VC02, VC04, VC05, VC08 and VC11 clusters, using the RS method.

Cluster	$M^*_{Ks} - 5log\,h_{70}$ mag	α	ϕ^* $h^2_{70}\,\mathrm{Mpc}^{-2}$	r Mpc	Sample Notes
VC02	-24.66 ± 1.31	-0.74 ± 0.41	18.40 ± 0.30	< 0.5	$-25\overset{\mathrm{m}}{.}0 < M_{Ks} < -21\overset{\mathrm{m}}{.}5$
VC02	-24.39 ± 0.22	-0.85 ± 0.18	5.45 ± 0.13	< 1.5	$-26\overset{\mathrm{m}}{.}0 < M_{Ks} < -21\overset{\mathrm{m}}{.}5$
VC04	-24.48 ± 0.39	-0.78 ± 0.16	30.95 ± 0.12	< 0.5	$-25\overset{\mathrm{m}}{.}0 < M_{Ks} < -21\overset{\mathrm{m}}{.}5$
VC04	-24.70 ± 0.42	-0.89 ± 0.13	8.42 ± 0.12	< 1.5	$-25\overset{\mathrm{m}}{.}0 < M_{Ks} < -21\overset{\mathrm{m}}{.}5$
VC05	-23.42 ± 0.95	-0.55 ± 0.97	29.86 ± 0.38	< 0.5	$-25\overset{\mathrm{m}}{.}0 < M_{Ks} < -21\overset{\mathrm{m}}{.}5$
VC08	-23.69 ± 0.88	-0.63 ± 0.69	20.11 ± 0.34	< 0.5	$-25\overset{\mathrm{m}}{.}0 < M_{Ks} < -21\overset{\mathrm{m}}{.}5$
VC08	-23.91 ± 0.90	-0.61 ± 0.58	5.75 ± 0.30	< 1.5	$-25\overset{\mathrm{m}}{.}0 < M_{Ks} < -21\overset{\mathrm{m}}{.}5$
VC11a	-24.08 ± 1.21	-0.55 ± 0.67	24.38 ± 0.34	< 0.5	$-25\overset{\mathrm{m}}{.}0 < M_{Ks} < -21\overset{\mathrm{m}}{.}5$
VC11b	-24.75 ± 2.36	-1.04 ± 0.73	10.89 ± 0.82	< 0.5	$-25\overset{\mathrm{m}}{.}0 < M_{Ks} < -21\overset{\mathrm{m}}{.}5$

Table 5.8: The K_s-band Luminosity Function parameters of VC02, VC05, VC08, VC11a and VC11b for a fixed $M^* = -24\overset{\mathrm{m}}{.}70$, using the RS method.

Cluster	$M^*_{Ks} - 5log\,h_{70}$ mag	α	ϕ^* $h^2_{70}\,\mathrm{Mpc}^{-2}$	r Mpc	Sample Notes
VC02	$-24\overset{\mathrm{m}}{.}70$	-1.04 ± 0.08	3.71 ± 0.05	< 1.5	$-26\overset{\mathrm{m}}{.}0 < M_{Ks} < -21\overset{\mathrm{m}}{.}5$
VC05	$-24\overset{\mathrm{m}}{.}70$	-1.19 ± 0.35	9.18 ± 0.25	< 0.5	$-25\overset{\mathrm{m}}{.}0 < M_{Ks} < -21\overset{\mathrm{m}}{.}5$
VC08	$-24\overset{\mathrm{m}}{.}70$	-0.95 ± 0.18	3.22 ± 0.13	< 1.5	$-25\overset{\mathrm{m}}{.}0 < M_{Ks} < -21\overset{\mathrm{m}}{.}5$
VC11a	$-24\overset{\mathrm{m}}{.}70$	-0.79 ± 0.20	16.98 ± 0.14	< 0.5	$-25\overset{\mathrm{m}}{.}0 < M_{Ks} < -21\overset{\mathrm{m}}{.}5$
VC11b	$-24\overset{\mathrm{m}}{.}70$	-1.02 ± 0.22	11.32 ± 0.16	< 0.5	$-25\overset{\mathrm{m}}{.}0 < M_{Ks} < -21\overset{\mathrm{m}}{.}5$

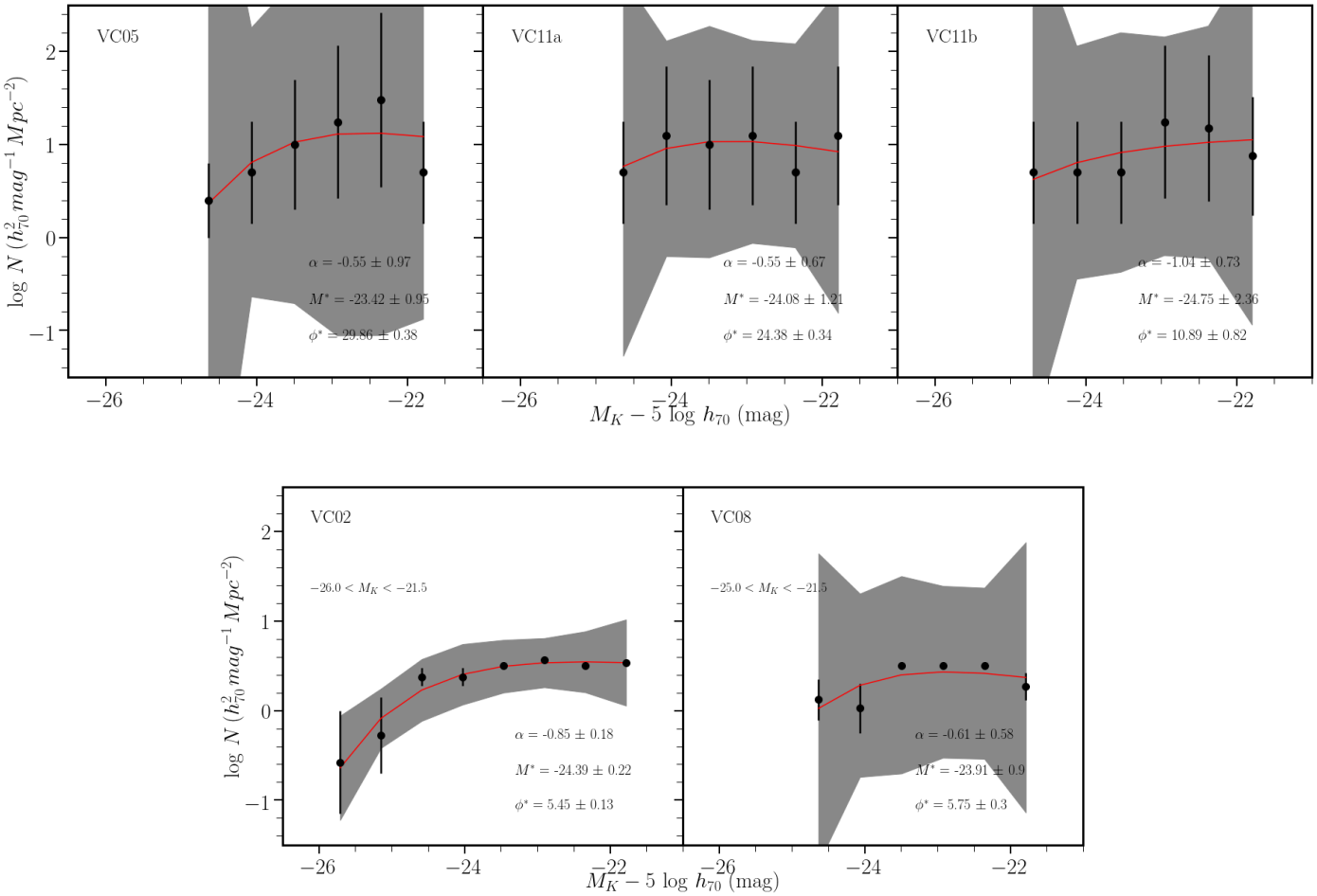

Figure 5.12: Top panel: the K_s-band LFs of VC05, VC11a and VC11b, using the RS method out to $r < 0.5\,\mathrm{Mpc}$ for $-25\overset{\mathrm{m}}{.}0 < M_{Ks} < -21\overset{\mathrm{m}}{.}5$. bottom panel: the K_s-band LFs of VC02 and VC08, using the RS method out to $r_c < 1.5\,\mathrm{Mpc}$. VC02 for $-26\overset{\mathrm{m}}{.}0 < M_{Ks} < -21\overset{\mathrm{m}}{.}5$ and VC08 for $-25\overset{\mathrm{m}}{.}0 < M_{Ks} < -21\overset{\mathrm{m}}{.}5$. The best fit is shown with the red line and the gray area shows the 3σ uncertainty of the fit.

are in good agreement with those of the VC04 cluster and therefore, consistent with the Norma cluster results (see Sect. 5.5.1).

I derive the α and ϕ^* of VC02, VC05, VC08, VC11a and VC11b for a fixed $M^* = -24\overset{m}{.}70$ which is the M^* of the VC04 cluster for $r_c < 1.5$ Mpc, and the results are listed in Table 5.8. The resulting α values for these clusters are in good agreement with what is found for VC04 considering their uncertainties ($\alpha = -0.89 \pm 0.13$). The fixed M^* causes a decrease in the ϕ^* values of VC05 and VC11a with LFs out to $r < 0.5$ Mpc. The ϕ^* value of VC11b does not vary significantly since its original fitted value, $M^* \sim -24\overset{m}{.}75$, is close to the fixed value. The ϕ^* values of VC02 and VC08 decrease only slightly for their LFs out to $r_c < 1.5$ Mpc.

5.7 Summary

In this chapter I first reviewed three methods of deriving the cluster LF and showed that the RS method is a reliable method to measure the LF, using data for the Norma cluster through comparison to the results from the spectroscopic membership method. Next, the K_s-band LFs of the five observed VSCL clusters were determined using the RS method up to the completeness magnitude limit of this survey ($M_{Ks} < -21\overset{m}{.}5$) and out to clustercentric radii of $r < 0.5$ Mpc $r_c < 1.5$ Mpc (where applicable, to explore the LFs in the high-density core as well as to regions including the outskirts of the clusters). A Schechter function was fitted to the LFs to derive their α, M^* and ϕ^*. The K_s-band LFs of the Norma, Coma and Virgo were also derived. They served as a comparison sample for the VSCL clusters.

For VC04, the most prominent cluster in the VSCL, I obtained $M^* = -24\overset{m}{.}48 \pm 0.39$, $\alpha = -0.76 \pm 0.16$, $\phi^* = 30.95 \pm 0.12$ when $r < 0.5$ Mpc, and $M^* = -24\overset{m}{.}70 \pm 0.42$, $\alpha = -0.89 \pm 0.13$, $\phi^* = 8.42 \pm 0.12$ when $r_c < 1.5$ Mpc. The M^* and α of VC04 were compared to those of the comparison clusters and previous NIR LF studies of clusters.

The VC04 LF parameters were measured up to $M_{Ks} < -21\overset{m}{.}5$ which is $\sim 2\overset{m}{.}5$ deeper than M^*. Therefore, the LF is measured for ellipticals and bulgy spirals, with Gaussian contribution in the shape of the LF and there is no upturn at the faint end of the LF because it does not reach the dwarf regime. The comparisons showed that M^* of the VC04 LF (up to $M_{Ks} < -21\overset{m}{.}5$) agrees well with those of other local clusters and appears to be unaffected whether the higher density inner region is probed or the overall LF out to larger radius. The faint end slope of the VC04 is compatible with that of massive clusters that are dominated by early-type galaxies e.g. Norma, but it is shallower than that of younger clusters e.g. Virgo. The LF parameters of VC04 were also compared to those of the AC118 cluster at $z = 0.3$ (Andreon, 2001). This comparison can give us hints on the evolution of galaxies in clusters. The VC04 LF has fainter M^* and shallower faint end slope, α, compared to those of AC118 LF. Their sample contains a larger number of dwarfs in the outer regions of the cluster. It is possible that the dwarf galaxies break apart and become a part of giant galaxies, as a cluster grows by accreting galaxies or small nearby groups.

Chapter 6

Summary and future work

6.1 Thesis main features

In this thesis I performed a systematic deep NIR imaging survey, covering $\sim$ 70% of the Abell radii of six VSCL clusters and analysed them in detail based on the obtained data. The NIR (JHK_s) observations of the VSCL clusters were conducted using the InfraRed Survey Facility (IRSF) telescope during three observing runs (2015-2019). Of the six observed clusters, four lie below the GP and two above. These six clusters have a complete set of science quality images with mean seeing values of $1\farcs55$, $1\farcs46$ and $1\farcs37$ in the J, H and K_s bands respectively. The images were reduced using the SIRIUS pipeline and galaxies were identified with Source Extractor and were visually validated through visual inspection on RGB composite images. Six catalogues were prepared containing the astrometric and photometric parameters of 1715 identified galaxies distributed over six clusters, of which only $\sim$ 15% were previously known (see Table 4.3 for details). The internal and external consistency of the parameters were confirmed to be of good quality (e.g. $\langle \Delta K_{int} \rangle = 0\fm025 \pm 0\fm180$ and $\langle \Delta K_{ext} \rangle = 0\fm091 \pm 0\fm196$ for VC04). Probing the effect of foreground extinction in the region of each cluster revealed that the VC02 cluster has the highest foreground extinction while VC04 and VC05 have the lowest ($\langle A_{Ks} \rangle = 0\fm10$, $\langle A_{Ks} \rangle = 0\fm07$ and $\langle A_{Ks} \rangle = 0\fm06$ respectively). The effect of extinction on the isophotal magnitudes is small and could be ignored (i.e. $\langle \Delta K_{iso} \rangle = 0\fm003$ for VC04). The completeness magnitude limit in each cluster was derived, using the magnitude versus central surface brightness method described by Garilli et al. (1999). The lowest derived completeness magnitude values in common to all six clusters are $J^{o,k} = 16\fm9$, $H^{o,k} = 16\fm3$ and $K_s^{o,k} = 15\fm5$ (extinction and k-corrected), and are adopted as the completeness magnitude limits for the whole imaging survey. The value in the K_s band translates to $M_{Ks} = -21\fm5$ at the distance of VSCL ($cz \sim 18000$ km s^{-1}). There are 910 cluster members brighter than the completeness magnitude limit in the 6 clusters.

The six clusters were analysed out to a completeness magnitude limit of $M_{Ks} < -21\fm5$ and a clustercentric radius of $r_c < 1.5$ Mpc. Their structures and richnesses were probed through iso-density contour maps and radial density profiles and comparing them with those of well-known clusters (Coma, Norma, 3C129 and Virgo). VC04 is the richest of the six. It is a regular and massive cluster comparable to Coma and Norma, although its velocity dispersion seems rather low for a rich cluster. VC02 and VC05 are relatively rich clusters while VC08 was found to be a poor cluster. VC05 has the highest central number density among the six clusters. The centre coordinate of VC05 was adjusted using the iso-density maps (the previous centre estimation was wrong). VC10 has a

filament-like structure and VC11 is an intermediate cluster consisting of two subclusters. The centre coordinates for both subclusters were determined. It appears that many of the VSCL clusters (VC02, VC04, VC05 and VC11) are not relaxed yet and are still evolving. The H I deficiency of spiral galaxies was explored in VC04, using MeerKAT-16 observations. Spiral galaxies in VC04 were shown to be extremely H I deficient which provides independent support for the richness of VC04. For two of the six clusters X-ray emission in the ROSAT band (0.1-2.4 keV) has been detected, a Virgo-like emission for the VC04 cluster very close to its estimated centre, and a weak X-ray emission for VC02 with an offset from its centre. The X-ray emissions are not consistent with the richnesses of VC02 and VC04 based on what was found in this project and we suspect they might have been underestimated due to obscuration by Galactic foreground gas.

Using the Red-Sequence (RS) method to determine cluster memberships the K_s-band LFs of the five observed VSCL clusters (VC10 was excluded due to its filament-like structure) were computed up to a completeness magnitude limit $M_{Ks} < -21\overset{\text{m}}{.}5$, which is $\sim 2\overset{\text{m}}{.}5$ deeper than M^*, and out to clustercentric radii of $r < 0.5$ Mpc and $r_c < 1.5$ Mpc. The RS method was shown to be reliable for computing the LF of clusters. This was confirmed for Norma, Coma and Virgo for which we derived LFs using both spectroscopic membership and RS methods to the same magnitude and radius limits as this IRSF survey and furthermore, their RS LFs served as a comparison sample for the VSCL clusters. For VC04, the most prominent cluster in the VSCL, the Schechter parameters are $M^* = -24\overset{\text{m}}{.}48 \pm 0.39$, $\alpha = -0.76 \pm 0.16$, $\phi^* = 30.95 \pm 0.12$ when $r < 0.5$ Mpc, and $M^* = -24\overset{\text{m}}{.}70 \pm 0.42$, $\alpha = -0.89 \pm 0.13$, $\phi^* = 8.42 \pm 0.12$ when $r_c < 1.5$ Mpc. The derived M^* for the VC04 LF is in good agreement with those of other local clusters and its faint end slope is compatible with that of massive clusters such as Norma but is shallower than those of younger clusters. The M^* and α of VC02 are within 1σ of the VC04 cluster parameters.

The analysis of our small sample of clusters in the VSCL (6 out of at least 20) shows that almost half of the clusters are rich or relatively rich. It shows that the VSCL has potentially many rich clusters, although the X-ray studies in $0.1 - 2.4$ keV do not imply that. The high number of massive clusters in the VSCL is an indication of its high richness (Wray et al., 2006; Einasto et al., 2007a). We also found a filament-like structure, possibly connecting the rich clusters. All of these are signatures of a rich supercluster with multi-branching structure of filaments and walls (Einasto et al., 2007b, 2011b).

6.2 Future work

In 2021 we acquired spectroscopic data with the SALT telescope. The forthcoming reduction will provide a tool to derive the VC04 LF using the spectroscopic membership method to compare with the RS method and to verify the consistency of results. The spectroscopic information will enable us to determine the morphology of galaxies and derive the LF for each morphological type and further investigate the shape of the K-band LF of galaxies in clusters based on their morphological type. Using the confirmed cluster members, the velocity dispersion of the VC04 cluster can also be revised. Moreover, the additional redshift data can be used to determine the dynamical mass of the cluster. It will also enable us to perform a dynamical analysis by carrying out a robust 3-D test such as the Dressler-Shectman δ-test (Dressler and Shectman, 1988) to investigate substructure in VC04. Having demonstrated the success of this approach, more SALT proposals will be put forward to obtain spectroscopic data for the other VSCL clusters, in particular for VC05 with the highest central density, and VC11 with its interesting subclusters, to

explore their properties in more detail. To learn more about VC05, we could re-observe it in NIR with the centre of the mosaic shifted to the location of its newly determined centre. Also in this work we managed to map 6 out of at least 20 identified potential clusters in the VSCL. The rest of these clusters still need NIR observations to be analysed in detail (similar to what has been done in this thesis). In future we can analyse the VSCL through the X-ray all-sky surveys such as eROSITA (extended ROentgen Survey with an Imaging Telescope Array, Predehl et al., 2021) in 0.3-8 keV band (less biased by the varying extinction levels across the extent of the VSCL) to identify more clusters and take this study further.

It would be interesting to see (through possible collaborations) what eROSITA will reveal about the rich VC04 cluster. It might be able to confirm that the richness of VC04 is underestimated based on its ROSAT X-ray emission. Verifying the richness of other massive VSCL clusters such as VC05 and VC02 should also become possible with exploring their eROSITA X-ray emissions.

H I surveys such as the Galactic Plane Survey (GPS, using MeerKAT-64 2018-2019) and other MeerKAT-64 observations in 2021 (PI, S. Rajohnson) are currently in progress to unveil the large-scale structure in the most opaque parts of the ZoA ($|b| \lesssim 7^\circ$) in the VSCL region (over 20°-wide strip). The H I observations should trace the walls of the VSCL. Rich galaxy clusters are expected to reside at the cross points of major walls. Further follow up NIR observations could be then performed to confirm the existence of galaxy clusters. In addition, their richnesses can be probed through searching for counterparts in X-ray (ideally eROSITA).

In this project, we showed that many of the VSCL clusters are richer than expected (see Section 6.1). With the proposed follow up projects we will try to confirm this claim. Also the presence of a large number of rich clusters implies a rich supercluster and this will support the hypothesis that the VSCL is indeed a massive and extended supercluster whose contribution to the local bulk flow could be comparable to the Shapley Supercluster.

References

Aaronson, M., Huchra, J., Mould, J., Schechter, P. L., and Tully, R. B. (1982). The velocity field in the local supercluster. *ApJ* , 258:64–76.

Abell, G. O. (1958). The Distribution of Rich Clusters of Galaxies. *ApJS* , 3:211.

Abell, G. O. (1961). Evidence regarding second-order clustering of galaxies and interactions between clusters of galaxies. *AJ* , 66:607.

Abell, G. O. (1965). Clustering of Galaxies. *ARA&A* , 3:1.

Abell, G. O. (1975). *Clusters of Galaxies*, page 601.

Abell, G. O., Corwin, Jr., H. G., and Olowin, R. P. (1989). A catalog of rich clusters of galaxies. *ApJS* , 70:1–138.

Aguerri, J. A. L., Gerhard, O. E., Arnaboldi, M., Napolitano, N. R., Castro-Rodriguez, N., and Freeman, K. C. (2005). Intracluster Stars in the Virgo Cluster Core. *AJ* , 129(6):2585–2596.

Aguerri, J. A. L. and Sánchez-Janssen, R. (2010). A study of catalogued nearby galaxy clusters in the SDSS-DR4. II. Cluster substructure. *A&A* , 521:A28.

Ahumada, R., Prieto, C. A., Almeida, A., Anders, F., Anderson, S. F., Andrews, B. H., Anguiano, B., Arcodia, R., Armengaud, E., Aubert, M., Avila, S., Avila-Reese, V., Badenes, C., Balland, C., Barger, K., Barrera-Ballesteros, J. K., Basu, S., Bautista, J., Beaton, R. L., Beers, T. C., Benavides, B. I. T., Bender, C. F., Bernardi, M., Bershady, M., Beutler, F., Bidin, C. M., Bird, J., Bizyaev, D., Blanc, G. A., Blanton, M. R., Boquien, M., Borissova, J., Bovy, J., Brandt, W. N., Brinkmann, J., Brownstein, J. R., Bundy, K., Bureau, M., Burgasser, A., Burtin, E., Cano-Díaz, M., Capasso, R., Cappellari, M., Carrera, R., Chabanier, S., Chaplin, W., Chapman, M., Cherinka, B., Chiappini, C., Doohyun Choi, P., Chojnowski, S. D., Chung, H., Clerc, N., Coffey, D., Comerford, J. M., Comparat, J., da Costa, L., Cousinou, M.-C., Covey, K., Crane, J. D., Cunha, K., Ilha, G. d. S., Dai, Y. S., Damsted, S. B., Darling, J., Davidson, James W., J., Davies, R., Dawson, K., De, N., de la Macorra, A., De Lee, N., Queiroz, A. B. d. A., Deconto Machado, A., de la Torre, S., Dell'Agli, F., du Mas des Bourboux, H., Diamond-Stanic, A. M., Dillon, S., Donor, J., Drory, N., Duckworth, C., Dwelly, T., Ebelke, G., Eftekharzadeh, S., Davis Eigenbrot, A., Elsworth, Y. P., Eracleous, M., Erfanianfar, G., Escoffier, S., Fan, X., Farr, E., Fernández-Trincado, J. G., Feuillet, D., Finoguenov, A., Fofie, P., Fraser-McKelvie, A., Frinchaboy, P. M., Fromenteau, S., Fu, H., Galbany, L., Garcia, R. A., García-Hernández, D. A., Oehmichen, L. A. G., Ge, J., Maia, M. A. G., Geisler, D., Gelfand, J., Goddy, J., Gonzalez-Perez, V., Grabowski, K., Green, P., Grier, C. J., Guo, H., Guy, J., Harding, P., Hasselquist, S., Hawken,

A. J., Hayes, C. R., Hearty, F., Hekker, S., Hogg, D. W., Holtzman, J. A., Horta, D., Hou, J., Hsieh, B.-C., Huber, D., Hunt, J. A. S., Chitham, J. I., Imig, J., Jaber, M., Angel, C. E. J., Johnson, J. A., Jones, A. M., Jönsson, H., Jullo, E., Kim, Y., Kinemuchi, K., Kirkpatrick, Charles C., I., Kite, G. W., Klaene, M., Kneib, J.-P., Kollmeier, J. A., Kong, H., Kounkel, M., Krishnarao, D., Lacerna, I., Lan, T.-W., Lane, R. R., Law, D. R., Le Goff, J.-M., Leung, H. W., Lewis, H., Li, C., Lian, J., Lin, L., Long, D., Longa-Peña, P., Lundgren, B., Lyke, B. W., Ted Mackereth, J., MacLeod, C. L., Majewski, S. R., Manchado, A., Maraston, C., Martini, P., Masseron, T., Masters, K. L., Mathur, S., McDermid, R. M., Merloni, A., Merrifield, M., Mészáros, S., Miglio, A., Minniti, D., Minsley, R., Miyaji, T., Mohammad, F. G., Mosser, B., Mueller, E.-M., Muna, D., Muñoz-Gutiérrez, A., Myers, A. D., Nadathur, S., Nair, P., Nandra, K., do Nascimento, J. C., Nevin, R. J., Newman, J. A., Nidever, D. L., Nitschelm, C., Noterdaeme, P., O'Connell, J. E., Olmstead, M. D., Oravetz, D., Oravetz, A., Osorio, Y., Pace, Z. J., Padilla, N., Palanque-Delabrouille, N., Palicio, P. A., Pan, H.-A., Pan, K., Parker, J., Paviot, R., Peirani, S., Ramírez, K. P., Penny, S., Percival, W. J., Perez-Fournon, I., Pérez-Ràfols, I., Petitjean, P., Pieri, M. M., Pinsonneault, M., Poovelil, V. J., Povick, J. T., Prakash, A., Price-Whelan, A. M., Raddick, M. J., Raichoor, A., Ray, A., Rembold, S. B., Rezaie, M., Riffel, R. A., Riffel, R., Rix, H.-W., Robin, A. C., Roman-Lopes, A., Román-Zúñiga, C., Rose, B., Ross, A. J., Rossi, G., Rowlands, K., Rubin, K. H. R., Salvato, M., Sánchez, A. G., Sánchez-Menguiano, L., Sánchez-Gallego, J. R., Sayres, C., Schaefer, A., Schiavon, R. P., Schimoia, J. S., Schlafly, E., Schlegel, D., Schneider, D. P., Schultheis, M., Schwope, A., Seo, H.-J., Serenelli, A., Shafieloo, A., Shamsi, S. J., Shao, Z., Shen, S., Shetrone, M., Shirley, R., Aguirre, V. S., Simon, J. D., Skrutskie, M. F., Slosar, A., Smethurst, R., Sobeck, J., Sodi, B. C., Souto, D., Stark, D. V., Stassun, K. G., Steinmetz, M., Stello, D., Stermer, J., Storchi-Bergmann, T., Streblyanska, A., Stringfellow, G. S., Stutz, A., Suárez, G., Sun, J., Taghizadeh-Popp, M., Talbot, M. S., Tayar, J., Thakar, A. R., Theriault, R., Thomas, D., Thomas, Z. C., Tinker, J., Tojeiro, R., Toledo, H. H., Tremonti, C. A., Troup, N. W., Tuttle, S., Unda-Sanzana, E., Valentini, M., Vargas-González, J., Vargas-Magaña, M., Vázquez-Mata, J. A., Vivek, M., Wake, D., Wang, Y., Weaver, B. A., Weijmans, A.-M., Wild, V., Wilson, J. C., Wilson, R. F., Wolthuis, N., Wood-Vasey, W. M., Yan, R., Yang, M., Yèche, C., Zamora, O., Zarrouk, P., Zasowski, G., Zhang, K., Zhao, C., Zhao, G., Zheng, Z., Zheng, Z., Zhu, G., and Zou, H. (2020). The 16th Data Release of the Sloan Digital Sky Surveys: First Release from the APOGEE-2 Southern Survey and Full Release of eBOSS Spectra. *ApJS* , 249(1):3.

Andreon, S. (1998). On the universality of the type-dependent luminosity functions. *A&A* , 336:98–102.

Andreon, S. (2001). Deep Near-Infrared Luminosity Function of a Cluster of Galaxies at Z=0.3. *ApJ* , 547(2):623–634.

Andreon, S. (2002). Dim galaxies and outer halos of galaxies missed by 2MASS? The near-infrared luminosity function and density. *A&A* , 382:495–502.

Andreon, S. (2006). The build-up of the red sequence in the galaxy cluster MS1054-0321 at z = 0.831. *MNRAS* , 369(2):969–975.

Andreon, S. (2016). Richness-based masses of rich and famous galaxy clusters. *A&A* , 587:A158.

Andreon, S., Cuillandre, J. C., and Pello, R. (2000). The Coma Cluster Luminosity Function from Ultraviolet to Near-Infrared. In *Constructing the Universe with Clusters of Galaxies*, page 4.2.2.

Andreon, S., Davoust, E., and Heim, T. (1997). The morphological segregation of galaxies in clusters. III. The distant cluster CL 0939+4713 (Abell 851). *A&A* , 323:337–348.

Andreon, S. and Pelló, R. (2000). Near-infrared luminosity function in the Coma cluster. *A&A* , 353:479–486.

Andreon, S., Punzi, G., and Grado, A. (2005). Rigorous luminosity function determination in the presence of a background: theory and application to two intermediate redshift clusters*. *MNRAS* , 360(2):727–736.

Andreon, S., Willis, J., Quintana, H., Valtchanov, I., Pierre, M., and Pacaud, F. (2004). Galaxy evolution in clusters up to z= 1.0. *MNRAS* , 353(2):353–368.

Aragón-Calvo, M. A., van de Weygaert, R., and Jones, B. J. T. (2010). Multiscale phenomenology of the cosmic web. *MNRAS* , 408(4):2163–2187.

Arce, H. G. and Goodman, A. A. (1999). Measuring Galactic Extinction: A Test. *ApJL* , 512:L135–L138.

Arnaboldi, M., Gerhard, O., Aguerri, J. A. L., Freeman, K. C., Napolitano, N. R., Okamura, S., and Yasuda, N. (2004). The Line-of-Sight Velocity Distributions of Intracluster Planetary Nebulae in the Virgo Cluster Core. *ApJL* , 614(1):L33–L36.

Baade, W. (1944). NGC 147 and NGC 185, Two New Members of the Local Group of Galaxies. *ApJ* , 100:147.

Bag, S. and Liivamägi, L. J. (2021). The shape distribution of superclusters in SDSS DR 12. *arXiv e-prints*, page arXiv:2111.10253.

Bahcall, N. A. (1977). Clusters of galaxies. *ARA&A* , 15:505–540.

Bahcall, N. A. (1988). Large-scale structure in the universe indicated by galaxy clusters. *ARA&A* , 26:631–686.

Balogh, M. L., Morris, S. L., Yee, H. K. C., Carlberg, R. G., and Ellingson, E. (1997). Star Formation in Cluster Galaxies at $0.2 < Z < 0.55$. *ApJL* , 488(2):L75–L78.

Bardelli, S., Zucca, E., Zamorani, G., Moscardini, L., and Scaramella, R. (2000). A study of the core of the Shapley Concentration - IV. Distribution of intercluster galaxies and supercluster properties*. *MNRAS* , 312(3):540–556.

Barkhouse, W. A., Yee, H. K. C., and López-Cruz, O. (2007). The Luminosity Function of Low-Redshift Abell Galaxy Clusters. *ApJ* , 671(2):1471–1496.

Basilakos, S. (2003). Shape statistics of Sloan Digital Sky Survey superclusters. *MNRAS* , 344(2):602–606.

Baum, W. A. (1959). Population Inferences from Star Counts, Surface Brightness and Colors. *PASP* , 71(419):106–117.

Bautz, L. P. and Morgan, W. W. (1970). On the Classification of the Forms of Clusters of Galaxies. *ApJL* , 162:L149.

Beard, S. M., MacGillivray, H. T., and Thanisch, P. F. (1990). The Cosmos system for crowded-field analysis of digitized photographic plate scans. *MNRAS* , 247:311–321.

Bekki, K. (1998). Unequal-Mass Galaxy Mergers and the Creation of Cluster S0 Galaxies. *ApJL* , 502(2):L133–L137.

Bekki, K. and Couch, W. J. (2011). Transformation from spirals into S0s with bulge growth in groups of galaxies. *MNRAS* , 415(2):1783–1796.

Bekki, K., Couch, W. J., and Shioya, Y. (2002). Passive Spiral Formation from Halo Gas Starvation: Gradual Transformation into S0s. *ApJ* , 577(2):651–657.

Bell, E. F. and de Jong, R. S. (2001). Stellar Mass-to-Light Ratios and the Tully-Fisher Relation. *ApJ* , 550:212–229.

Bell, E. F., McIntosh, D. H., Katz, N., and Weinberg, M. D. (2003). The Optical and Near-Infrared Properties of Galaxies. I. Luminosity and Stellar Mass Functions. *ApJS* , 149(2):289–312.

Benson, A. J., Bower, R. G., Frenk, C. S., Lacey, C. G., Baugh, C. M., and Cole, S. (2003). What Shapes the Luminosity Function of Galaxies? *ApJ* , 599(1):38–49.

Bertin, E. and Arnouts, S. (1996). SExtractor: Software for source extraction. *A&AS* , 117:393–404.

Bialas, D., Lisker, T., Olczak, C., Spurzem, R., and Kotulla, R. (2015). On the occurrence of galaxy harassment. *A&A* , 576:A103.

Bilicki, M., Chodorowski, M., Jarrett, T., and Mamon, G. A. (2011). Is the Two Micron All Sky Survey Clustering Dipole Convergent? *ApJ* , 741:31.

Bilicki, M., Jarrett, T. H., Peacock, J. A., Cluver, M. E., and Steward, L. (2014). Two Micron All Sky Survey Photometric Redshift Catalog: A Comprehensive Three-dimensional Census of the Whole Sky. *ApJS* , 210(1):9.

Binggeli, B., Popescu, C. C., and Tammann, G. A. (1993). The kinematics of the Virgo cluster revisited. *A&AS* , 98:275.

Binggeli, B., Sandage, A., and Tammann, G. A. (1988). The luminosity function of galaxies. *ARA&A* , 26:509–560.

Binggeli, B., Sandage, A., and Tarenghi, M. (1984). Studies of the Virgo Cluster. I. Photometry of 109 galaxies near the cluster center to serve as standards. *AJ* , 89:64–82.

Biviano, A., Durret, F., Gerbal, D., Le Fevre, O., Lobo, C., Mazure, A., and Slezak, E. (1995). On the galaxy luminosity function in the central regions of the Coma cluster. *A&A* , 297:610.

Biviano, A., Durret, F., Gerbal, D., Le Fevre, O., Lobo, C., Mazure, A., and Slezak, E. (1996). Unveiling hidden structures in the Coma cluster. *A&A* , 311:95–112.

Blakeslee, J. P., Franx, M., Postman, M., Rosati, P., Holden, B. P., Illingworth, G. D., Ford, H. C., Cross, N. J. G., Gronwall, C., Benítez, N., Bouwens, R. J., Broadhurst, T. J., Clampin, M., Demarco, R., Golimowski, D. A., Hartig, G. F., Infante, L., Martel, A. R., Miley, G. K., Menanteau, F., Meurer, G. R., Sirianni, M., and White, R. L. (2003). Advanced Camera for Surveys Photometry of the Cluster RDCS 1252.9-2927: The Color-Magnitude Relation at z = 1.24. *ApJL* , 596(2):L143–L146.

Boehringer, H., Neumann, D. M., Schindler, S., and Kraan-Korteweg, R. C. (1996). Abell 3627: A Nearby, X-Ray Bright, and Massive Galaxy Cluster. *ApJ* , 467:168.

Böhringer, H., Pratt, G. W., Arnaud, M., Borgani, S., Croston, J. H., Ponman, T. J., Ameglio, S., Temple, R. F., and Dolag, K. (2010). Substructure of the galaxy clusters in the REXCESS sample: observed statistics and comparison to numerical simulations. *A&A* , 514:A32.

Bond, J. R., Kofman, L., and Pogosyan, D. (1996). How filaments of galaxies are woven into the cosmic web. *Nature* , 380(6575):603–606.

Bothun, G. D., Mould, J. R., Caldwell, N., and MacGillivray, H. T. (1986). Comparative photometric parameters of dwarf irregular and elliptical galaxies in the Virgo cluster : two different classes of dwarf galaxies ? *AJ* , 92:1007–1019.

Boué, G., Adami, C., Durret, F., Mamon, G. A., and Cayatte, V. (2008). The galaxy luminosity function of the Abell 496 cluster and its spatial variations. *A&A* , 479(2):335–346.

Bower, R. G., Lucey, J. R., and Ellis, R. S. (1992). Precision photometry of early-type galaxies in the Coma and Virgo clusters : a test of the universality of the colour-magnitude relation - II. Analysis. *MNRAS* , 254:601.

Branchini, E., Davis, M., and Nusser, A. (2012). The linear velocity field of 2MASS Redshift Survey, K_s= 11.75 galaxies: constraints on β and bulk flow from the luminosity function. *MNRAS* , 424(1):472–481.

Bravo-Alfaro, H., Cayatte, V., van Gorkom, J. H., and Balkowski, C. (2000). VLA H I Imaging of the Brightest Spiral Galaxies in Coma. *AJ* , 119(2):580–592.

Broadhurst, T. J., Ellis, R. S., and Glazebrook, K. (1992). Faint galaxies: evolution and cosmological curvature. *Nature* , 355(6355):55–58.

Bromley, B. C., Press, W. H., Lin, H., and Kirshner, R. P. (1998). Spectral Classification and Luminosity Function of Galaxies in the Las Campanas Redshift Survey. *ApJ* , 505(1):25–36.

Buote, D. A., Zappacosta, L., Fang, T., Humphrey, P. J., Gastaldello, F., and Tagliaferri, G. (2009). X-Ray Absorption by WHIM in the Sculptor Wall. *ApJ* , 695(2):1351–1356.

Burg, R., Giacconi, R., Forman, W., and Jones, C. (1994). The X-Ray Luminosity Functions of Abell Clusters from the Einstein Cluster Survey. *ApJ* , 422:37.

Burgett, W. S., Vick, M. M., Davis, D. S., Colless, M., De Propris, R., Baldry, I., Baugh, C., Bland-Hawthorn, J., Bridges, T., Cannon, R., Cole, S., Collins, C., Couch, W.,

Cross, N., Dalton, G., Driver, S., Efstathiou, G., Ellis, R., Frenk, C. S., Glazebrook, K., Hawkins, E., Jackson, C., Lahav, O., Lewis, I., Lumsden, S., Maddox, S., Madgwick, D., Norberg, P., Peacock, J. A., Percival, W., Peterson, B., Sutherland, W., and Taylor, K. (2004). Substructure analysis of selected low-richness 2dFGRS clusters of galaxies. *MNRAS* , 352(2):605–654.

Byrd, G. and Valtonen, M. (1990). Tidal Generation of Active Spirals and S0 Galaxies by Rich Clusters. *ApJ* , 350:89.

Caldwell, N. (1983). Structure and stellar content of dwarf elliptical galaxies. *AJ* , 88:804–812.

Caldwell, N. and Bothun, G. D. (1987). Dwarf Elliptical Galaxies in the Fornax Cluster. II. Their Structure and Stellar Populations. *AJ* , 94:1126.

Cameron, L. M. (1990). The influence of absorption on galaxy diameters and magnitudes. *A&A* , 233:16–20.

Cardelli, J. A., Clayton, G. C., and Mathis, J. S. (1989). The relationship between infrared, optical, and ultraviolet extinction. *ApJ* , 345:245–256.

Carlberg, R. G., Yee, H. K. C., and Ellingson, E. (1997). The Average Mass and Light Profiles of Galaxy Clusters. *ApJ* , 478(2):462–475.

Carlberg, R. G., Yee, H. K. C., Ellingson, E., Abraham, R., Gravel, P., Morris, S., and Pritchet, C. J. (1996). Galaxy Cluster Virial Masses and Omega. *ApJ* , 462:32.

Carrick, J., Turnbull, S. J., Lavaux, G., and Hudson, M. J. (2015). Cosmological parameters from the comparison of peculiar velocities with predictions from the 2M++ density field. *MNRAS* , 450(1):317–332.

Carroll, S. M. (2001). The Cosmological Constant. *Living Reviews in Relativity*, 4(1):1.

Carter, B. S. and Meadows, V. S. (1995). Fainter Southern JHK Standards Suitable for Infrared Arrays. *MNRAS* , 276:734.

Cesetti, M., Ivanov, V. D., Morelli, L., Pizzella, A., Buson, L., Corsini, E. M., Dalla Bontà, E., Stiavelli, M., and Bertola, F. (2009). Early-type galaxies in the near-infrared: 1.5-2.4 μm spectroscopy. *A&A* , 497(1):41–51.

Chamaraux, P., Balkowski, C., and Gerard, E. (1980). The H I deficiency of the Virgo cluster spirals. *A&A* , 83:38–51.

Chan, J. C. C., Wilson, G., Rudnick, G., Muzzin, A., Balogh, M., Nantais, J., van der Burg, R. F. J., Cerulo, P., Biviano, A., Cooper, M. C., Demarco, R., Forrest, B., Lidman, C., Noble, A., Old, L., Pintos-Castro, I., Reeves, A. M. M., Webb, K. A., Yee, H. K. C., Abdullah, M. H., De Lucia, G., Marchesini, D., McGee, S. L., Stefanon, M., and Zaritsky, D. (2019). The Rest-frame H-band Luminosity Function of Red-sequence Galaxies in Clusters at $1.0 < z < 1.3$. *ApJ* , 880(2):119.

Chon, G., Böhringer, H., and Smith, G. P. (2012). Statistics and implications of substructure detected in a representative sample of X-ray clusters. *A&A* , 548:A59.

Chow-Martínez, M., Andernach, H., Caretta, C. A., and Trejo-Alonso, J. J. (2014). Two new catalogues of superclusters of Abell/ACO galaxy clusters out to redshift 0.15. *MNRAS* , 445(4):4073–4085.

Christensen, C. G. (1975). Luminosity function of nearby galaxies. *AJ* , 80:282.

Cluver, M. E. (2008). *The Nature and Nurture of a Starburst Supermassive Hi Galaxy: HIZOA J0836-43*. PhD thesis, University of Cape Town.

Colberg, J. M., White, S. D. M., Jenkins, A., and Pearce, F. R. (1999). Linking cluster formation to large-scale structure. *MNRAS* , 308(3):593–598.

Colin, J., Mohayaee, R., Sarkar, S., and Shafieloo, A. (2011). Probing the anisotropic local Universe and beyond with SNe Ia data. *MNRAS* , 414(1):264–271.

Colina, L. and Bohlin, R. (1997). Absolute Flux Distributions of Solar Analogs from the UV to the Near-IR. *AJ* , 113:1138–1144.

Colless, M. (1989). The dynamics of rich clusters. II. Luminosity functions. *MNRAS* , 237:799–826.

Colless, M., Dalton, G., Maddox, S., Sutherland , W., Norberg, P., Cole, S., Bland - Hawthorn, J., Bridges, T., Cannon, R., Collins, C., Couch, W., Cross, N., Deeley, K., De Propris, R., Driver, S. P., Efstathiou, G., Ellis, R. S., Frenk, C. S., Glazebrook, K., Jackson, C., Lahav, O., Lewis, I., Lumsden, S., Madgwick, D., Peacock, J. A., Peterson, B. A., Price, I., Seaborne, M., and Taylor, K. (2001). The 2dF Galaxy Redshift Survey: spectra and redshifts. *MNRAS* , 328(4):1039–1063.

Conklin, E. K. (1969). Velocity of the Earth with Respect to the Cosmic Background Radiation. *Nature* , 222(5197):971–972.

Costa-Duarte, M. V., Sodré, L., J., and Durret, F. (2011). Morphological properties of superclusters of galaxies. *MNRAS* , 411(3):1716–1726.

Courtois, H. M., Hoffman, Y., Tully, R. B., and Gottlöber, S. (2012). Three-dimensional Velocity and Density Reconstructions of the Local Universe with Cosmicflows-1. *ApJ* , 744(1):43.

Courtois, H. M., Kraan-Korteweg, R. C., Dupuy, A., Graziani, R., and Libeskind, N. I. (2019). A kinematic confirmation of the hidden Vela supercluster. *MNRAS* , 490(1):L57–L61.

Cuesta-Bolao, M. J. and Serna, A. (2003). Environmental and morphological dependence of the luminosity function of galaxies. *A&A* , 405:917–930.

Cutri, R. M., Skrutskie, M. F., van Dyk, S., Beichman, C. A., Carpenter, J. M., Chester, T., Cambresy, L., Evans, T., Fowler, J., Gizis, J., Howard, E., Huchra, J., Jarrett, T., Kopan, E. L., Kirkpatrick, J. D., Light, R. M., Marsh, K. A., McCallon, H., Schneider, S., Stiening, R., Sykes, M., Weinberg, M., Wheaton, W. A., Wheelock, S., and Zacarias, N. (2003). *2MASS All Sky Catalog of point sources.*

Dahle, H., Kaiser, N., Irgens, R. J., Lilje, P. B., and Maddox, S. J. (2002). Weak Gravitational Lensing by a Sample of X-Ray Luminous Clusters of Galaxies. I. The Data Set. *ApJS* , 139(2):313–368.

Dark Energy Survey Collaboration, Abbott, T., Abdalla, F. B., Aleksić, J., Allam, S., Amara, A., Bacon, D., Balbinot, E., Banerji, M., Bechtol, K., Benoit-Lévy, A., Bernstein, G. M., Bertin, E., Blazek, J., Bonnett, C., Bridle, S., Brooks, D., Brunner, R. J., Buckley-Geer, E., Burke, D. L., Caminha, G. B., Capozzi, D., Carlsen, J., Carnero-Rosell, A., Carollo, M., Carrasco-Kind, M., Carretero, J., Castander, F. J., Clerkin, L., Collett, T., Conselice, C., Crocce, M., Cunha, C. E., D'Andrea, C. B., da Costa, L. N., Davis, T. M., Desai, S., Diehl, H. T., Dietrich, J. P., Dodelson, S., Doel, P., Drlica-Wagner, A., Estrada, J., Etherington, J., Evrard, A. E., Fabbri, J., Finley, D. A., Flaugher, B., Foley, R. J., Fosalba, P., Frieman, J., García-Bellido, J., Gaztanaga, E., Gerdes, D. W., Giannantonio, T., Goldstein, D. A., Gruen, D., Gruendl, R. A., Guarnieri, P., Gutierrez, G., Hartley, W., Honscheid, K., Jain, B., James, D. J., Jeltema, T., Jouvel, S., Kessler, R., King, A., Kirk, D., Kron, R., Kuehn, K., Kuropatkin, N., Lahav, O., Li, T. S., Lima, M., Lin, H., Maia, M. A. G., Makler, M., Manera, M., Maraston, C., Marshall, J. L., Martini, P., McMahon, R. G., Melchior, P., Merson, A., Miller, C. J., Miquel, R., Mohr, J. J., Morice-Atkinson, X., Naidoo, K., Neilsen, E., Nichol, R. C., Nord, B., Ogando, R., Ostrovski, F., Palmese, A., Papadopoulos, A., Peiris, H. V., Peoples, J., Percival, W. J., Plazas, A. A., Reed, S. L., Refregier, A., Romer, A. K., Roodman, A., Ross, A., Rozo, E., Rykoff, E. S., Sadeh, I., Sako, M., Sánchez, C., Sanchez, E., Santiago, B., Scarpine, V., Schubnell, M., Sevilla-Noarbe, I., Sheldon, E., Smith, M., Smith, R. C., Soares-Santos, M., Sobreira, F., Soumagnac, M., Suchyta, E., Sullivan, M., Swanson, M., Tarle, G., Thaler, J., Thomas, D., Thomas, R. C., Tucker, D., Vieira, J. D., Vikram, V., Walker, A. R., Wechsler, R. H., Weller, J., Wester, W., Whiteway, L., Wilcox, H., Yanny, B., Zhang, Y., and Zuntz, J. (2016). The Dark Energy Survey: more than dark energy - an overview. *MNRAS* , 460(2):1270–1299.

David, L. P., Slyz, A., Jones, C., Forman, W., Vrtilek, S. D., and Arnaud, K. A. (1993). A Catalog of Intracluster Gas Temperatures. *ApJ* , 412:479.

Davis, M., Huchra, J., Latham, D. W., and Tonry, J. (1982). A survey of galaxy redshifts. II. The large scale space distribution. *ApJ* , 253:423–445.

de Lapparent, V., Geller, M. J., and Huchra, J. P. (1986). A Slice of the Universe. *ApJL* , 302:L1.

De Lucia, G., Poggianti, B. M., Aragón-Salamanca, A., Clowe, D., Halliday, C., Jablonka, P., Milvang-Jensen, B., Pelló, R., Poirier, S., Rudnick, G., Saglia, R., Simard, L., and White, S. D. M. (2004). The Buildup of the Red Sequence in Galaxy Clusters since z ~0.8. *ApJL* , 610(2):L77–L80.

De Lucia, G., Poggianti, B. M., Aragón-Salamanca, A., White, S. D. M., Zaritsky, D., Clowe, D., Halliday, C., Jablonka, P., von der Linden, A., Milvang-Jensen, B., Pelló, R., Rudnick, G., Saglia, R. P., and Simard, L. (2007). The build-up of the colour-magnitude relation in galaxy clusters since z ~0.8. *MNRAS* , 374(3):809–822.

De Propris, R. (2017). The K-band luminosity functions of cluster galaxies. *MNRAS* , 465(4):4035–4043.

de Propris, R., Eisenhardt, P. R., Stanford, S. A., and Dickinson, M. (1998). The Infrared Luminosity Function of Galaxies in the Coma Cluster. *ApJL* , 503(1):L45–L48.

De Propris, R., Phillipps, S., and Bremer, M. N. (2013). Deep luminosity functions and colour-magnitude relations for cluster galaxies at $0.2 < z < 0.6$. *MNRAS* , 434(4):3469–3486.

De Propris, R., Stanford, S. A., Eisenhardt, P. R., Holden, B. P., and Rosati, P. (2007). The Rest-Frame K-Band Luminosity Function of Galaxies in Clusters to $z = 1.3$. *AJ* , 133(5):2209–2215.

de Vaucouleurs, G. (1953). Evidence for a local super,galaxy. *AJ* , 58:30.

de Vaucouleurs, G. (1958). The Local Supercluster of Galaxies. *Nature* , 182(4648):1478–1480.

de Vaucouleurs, G. (1961). Structure of the Virgo Cluster of Galaxies. *ApJS* , 6:213.

Dénes, H., Kilborn, V. A., and Koribalski, B. S. (2014). New H I scaling relations to probe the H I content of galaxies via global H I-deficiency maps. *MNRAS* , 444(1):667–681.

Devereux, N., Hriljac, P., Willner, S. P., Ashby, M. L. N., and Willmer, C. N. A. (2009). The Morphological Type Dependence of K-band Luminosity Functions. In Jogee, S., Marinova, I., Hao, L., and Blanc, G. A., editors, *Galaxy Evolution: Emerging Insights and Future Challenges*, volume 419 of *Astronomical Society of the Pacific Conference Series*, page 171.

Devereux, N. A., Becklin, E. E., and Scoville, N. (1987). Infrared Characteristics of the Nuclei of Normal Galaxies. *ApJ* , 312:529.

Dickey, J. M. and Lockman, F. J. (1990). H I in the galaxy. *ARA&A* , 28:215–261.

Dressler, A. (1980). Galaxy morphology in rich clusters: implications for the formation and evolution of galaxies. *ApJ* , 236:351–365.

Dressler, A., Oemler, Augustus, J., Couch, W. J., Smail, I., Ellis, R. S., Barger, A., Butcher, H., Poggianti, B. M., and Sharples, R. M. (1997). Evolution since $z = 0.5$ of the Morphology-Density Relation for Clusters of Galaxies. *ApJ* , 490(2):577–591.

Dressler, A. and Shectman, S. A. (1988). Evidence for substructure in rich clusters of galaxies from radial-velocity measurements. *AJ* , 95:985–995.

Driver, S. P., Couch, W. J., and Phillipps, S. (1998). Luminosity distributions within rich clusters - III. A comparative study of seven Abell/ACO clusters. *MNRAS* , 301(2):369–381.

Driver, S. P., GAMA Team, Baldry, I. K., Bamford, S., Bland-Hawthorn, J., Bridges, T., Cameron, E., Conselice, C., Couch, W. J., Croom, S., Cross, N. J. G., Driver, S. P., Dunne, L., Eales, S., Edmondson, E., Ellis, S. C., Frenk, C. S., Graham, A. W., Jones, H., Hill, D., Hopkins, A., van Kampen, E., Kuijken, K., Lahav, O., Liske, J., Loveday, J., Nichol, B., Norberg, P., Oliver, S., Parkinson, H., Peacock, J. A., Phillipps, S., Popescu, C. C., Prescott, M., Proctor, R., Sharp, R., Staveley-Smith, L., Sutherland, W., Tuffs, R. J., and Warren, S. (2009). Galaxy And Mass Assembly (GAMA). In Andersen, J., Nordströara, m, B., and Bland -Hawthorn, J., editors, *The Galaxy Disk in Cosmological Context*, volume 254 of *IAU Symposium*, pages 469–474.

Dutra, C. M., Santiago, B. X., and Bica, E. (2002). Low-extinction windows in the inner Galactic Bulge. *A&A* , 381:219–226.

Ebeling, H., Edge, A. C., Allen, S. W., Crawford, C. S., Fabian, A. C., and Huchra, J. P. (2000). The ROSAT Brightest Cluster Sample - IV. The extended sample. *MNRAS* , 318(2):333–340.

Ebeling, H., Edge, A. C., Bohringer, H., Allen, S. W., Crawford, C. S., Fabian, A. C., Voges, W., and Huchra, J. P. (1998). The ROSAT Brightest Cluster Sample - I. The compilation of the sample and the cluster log N-log S distribution. *MNRAS* , 301(4):881–914.

Ebeling, H., Kocevski, D., Tully, R. B., and Mullis, C. R. (2005). CIZA: X-ray Selected Galaxy Clusters as Tracers of Large-Scale Structure and Streaming Motions behind the Galactic Plane. In Fairall, A. P. and Woudt, P. A., editors, *Nearby Large-Scale Structures and the Zone of Avoidance*, volume 329 of *Astronomical Society of the Pacific Conference Series*, page 83.

Ebeling, H., Mullis, C. R., and Tully, R. B. (2002). A Systematic X-Ray Search for Clusters of Galaxies behind the Milky Way. *ApJ* , 580:774–788.

Ebeling, H., Voges, W., Bohringer, H., Edge, A. C., Huchra, J. P., and Briel, U. G. (1996). Properties of the X-ray-brightest Abell-type clusters of galaxies (XBACs) from ROSAT All-Sky Survey data - I. The sample. *MNRAS* , 281(3):799–829.

Edge, A. C. and Stewart, G. C. (1991). EXOSAT observations of clusters of galaxies - II. X-ray to optical correlations. *MNRAS* , 252:428.

Edge, A. C., Stewart, G. C., Fabian, A. C., and Arnaud, K. A. (1990). An X-ray flux-limited sample of clusters of galaxies : evidence for evolution of the luminosity function. *MNRAS* , 245:559.

Einasto, J., Einasto, M., Saar, E., Tago, E., Liivamägi, L. J., Jõeveer, M., Suhhonenko, I., Hütsi, G., Jaaniste, J., Heinämäki, P., Müller, V., Knebe, A., and Tucker, D. (2007a). Superclusters of galaxies from the 2dF redshift survey. II. Comparison with simulations. *A&A* , 462(2):397–410.

Einasto, J., Einasto, M., Tago, E., Saar, E., Hütsi, G., Jõeveer, M., Liivamägi, L. J., Suhhonenko, I., Jaaniste, J., Heinämäki, P., Müller, V., Knebe, A., and Tucker, D. (2007b). Superclusters of galaxies from the 2dF redshift survey. I. The catalogue. *A&A* , 462(2):811–825.

Einasto, J., Joeveer, M., and Saar, E. (1980). Superclusters and galaxy formation. *Nature* , 283(5742):47–48.

Einasto, M., Einasto, J., Tago, E., Dalton, G. B., and Andernach, H. (1994). The structure of the universe traced by rich clusters of galaxies. *MNRAS* , 269:301–322.

Einasto, M., Einasto, J., Tago, E., Müller, V., and Andernach, H. (2001). Optical and X-Ray Clusters as Tracers of the Supercluster-Void Network. I. Superclusters of Abell and X-Ray Clusters. *AJ* , 122(5):2222–2242.

Einasto, M., Einasto, J., Tago, E., Saar, E., Liivamägi, L. J., Jõeveer, M., Hütsi, G., Heinämäki, P., Müller, V., and Tucker, D. (2007c). Superclusters of galaxies in the 2dF redshift survey. III. The properties of galaxies in superclusters. *A&A* , 464(3):815–826.

Einasto, M., Lietzen, H., Gramann, M., Saar, E., Tempel, E., Liivamägi, L. J., Montero-Dorta, A. D., Streblyanska, A., Maraston, C., and Rubiño-Martín, J. A. (2017). BOSS Great Wall: morphology, luminosity, and mass. *A&A* , 603:A5.

Einasto, M., Lietzen, H., Gramann, M., Tempel, E., Saar, E., Liivamägi, L. J., Heinämäki, P., Nurmi, P., and Einasto, J. (2016). Sloan Great Wall as a complex of superclusters with collapsing cores. *A&A* , 595:A70.

Einasto, M., Lietzen, H., Tempel, E., Gramann, M., Liivamägi, L. J., and Einasto, J. (2014). SDSS superclusters: morphology and galaxy content. *A&A* , 562:A87.

Einasto, M., Liivamägi, L. J., Saar, E., Einasto, J., Tempel, E., Tago, E., and Martínez, V. J. (2011a). SDSS DR7 superclusters. Principal component analysis. *A&A* , 535:A36.

Einasto, M., Liivamägi, L. J., Tago, E., Saar, E., Tempel, E., Einasto, J., Martínez, V. J., and Heinämäki, P. (2011b). SDSS DR7 superclusters. Morphology. *A&A* , 532:A5.

Einasto, M., Liivamägi, L. J., Tempel, E., Saar, E., Tago, E., Einasto, P., Enkvist, I., Einasto, J., Martínez, V. J., Heinämäki, P., and Nurmi, P. (2011c). The Sloan Great Wall. Morphology and Galaxy Content. *ApJ* , 736(1):51.

Einasto, M., Liivamägi, L. J., Tempel, E., Saar, E., Tago, E., Einasto, P., Enkvist, I., Einasto, J., Martínez, V. J., Heinämäki, P., and Nurmi, P. (2011d). The Sloan Great Wall. Morphology and Galaxy Content. *ApJ* , 736(1):51.

Einasto, M., Liivamägi, L. J., Tempel, E., Saar, E., Vennik, J., Nurmi, P., Gramann, M., Einasto, J., Tago, E., Heinämäki, P., Ahvensalmi, A., and Martínez, V. J. (2012a). Multimodality of rich clusters from the SDSS DR8 within the supercluster-void network. *A&A* , 542:A36.

Einasto, M., Saar, E., Liivamägi, L. J., Einasto, J., Tago, E., Martínez, V. J., Starck, J. L., Müller, V., Heinämäki, P., Nurmi, P., Gramann, M., and Hütsi, G. (2007d). The richest superclusters. I. Morphology. *A&A* , 476(2):697–711.

Einasto, M., Tago, E., Jaaniste, J., Einasto, J., and Andernach, H. (1997). The supercluster-void network I. The supercluster catalogue and large-scale distribution. *A&AS* , 123:119–133.

Einasto, M., Vennik, J., Nurmi, P., Tempel, E., Ahvensalmi, A., Tago, E., Liivamägi, L. J., Saar, E., Heinämäki, P., Einasto, J., and Martínez, V. J. (2012b). Multimodality in galaxy clusters from SDSS DR8: substructure and velocity distribution. *A&A* , 540:A123.

Elagali, A. (2015). The Vela Supercluster - does it provide the missing link to explain the local flow fields? Master's thesis, University of Cape Town.

Erdoğdu, P., Huchra, J. P., Lahav, O., Colless, M., Cutri, R. M., Falco, E., George, T., Jarrett, T., Jones, D. H., Kochanek, C. S., Macri, L., Mader, J., Martimbeau, N., Pahre, M., Parker, Q., Rassat, A., and Saunders, W. (2006). The dipole anisotropy of the 2 Micron All-Sky Redshift Survey. *MNRAS* , 368:1515–1526.

Evrard, A. E., MacFarland, T. J., Couchman, H. M. P., Colberg, J. M., Yoshida, N., White, S. D. M., Jenkins, A., Frenk, C. S., Pearce, F. R., Peacock, J. A., and Thomas, P. A. (2002). Galaxy Clusters in Hubble Volume Simulations: Cosmological Constraints from Sky Survey Populations. *ApJ* , 573(1):7–36.

Farouki, R. and Shapiro, S. L. (1980). Computer simulations of environmental influences on galaxy evolution in dense clusters. I - Ram-pressure stripping. *ApJ* , 241:928–945.

Fasano, G., Poggianti, B. M., Couch, W. J., Bettoni, D., Kjærgaard, P., and Moles, M. (2000). The Evolution of the Galactic Morphological Types in Clusters. *ApJ* , 542(2):673–683.

Feindt, U., Kerschhaggl, M., Kowalski, M., Aldering, G., Antilogus, P., Aragon, C., Bailey, S., Baltay, C., Bongard, S., Buton, C., Canto, A., Cellier-Holzem, F., Childress, M., Chotard, N., Copin, Y., Fakhouri, H. K., Gangler, E., Guy, J., Kim, A., Nugent, P., Nordin, J., Paech, K., Pain, R., Pecontal, E., Pereira, R., Perlmutter, S., Rabinowitz, D., Rigault, M., Runge, K., Saunders, C., Scalzo, R., Smadja, G., Tao, C., Thomas, R. C., Weaver, B. A., and Wu, C. (2013). Measuring cosmic bulk flows with Type Ia supernovae from the Nearby Supernova Factory. *A&A* , 560:A90.

Feldman, H. A., Watkins, R., and Hudson, M. J. (2010). Cosmic flows on 100 h^{-1} Mpc scales: standardized minimum variance bulk flow, shear and octupole moments. *MNRAS* , 407(4):2328–2338.

Finney, E. E., Haynes, M. P., and APPSS Team (2018). The Baryonic Tully Fisher Relation for the ALFALFA 100 Sample. In *American Astronomical Society Meeting Abstracts #231*, volume 231 of *American Astronomical Society Meeting Abstracts*, page 351.12.

Firth, P., Drinkwater, M. J., and Karick, A. M. (2008). Compact stellar systems and cluster environments. *MNRAS* , 389(4):1539–1555.

Fitzpatrick, E. L. (1999). Correcting for the Effects of Interstellar Extinction. *PASP* , 111:63–75.

Fixsen, D. J., Cheng, E. S., Gales, J. M., Mather, J. C., Shafer, R. A., and Wright, E. L. (1996). The Cosmic Microwave Background Spectrum from the Full COBE FIRAS Data Set. *ApJ* , 473:576.

Fleenor, M. C. and Johnston-Hollitt, M. (2010). Megaparsec-Scale Triggers for Star Formation: Clusters and Filaments of Galaxies in the Horologium-Reticulum Supercluster. In Smith, B., Higdon, J., Higdon, S., and Bastian, N., editors, *Galaxy Wars: Stellar Populations and Star Formation in Interacting Galaxies*, volume 423 of *Astronomical Society of the Pacific Conference Series*, page 81.

Flin, P. and Krywult, J. (2006). Substructures in Abell clusters of galaxies. *A&A* , 450(1):9–14.

Foëx, G., Motta, V., Limousin, M., Verdugo, T., More, A., Cabanac, R., Gavazzi, R., and Muñoz, R. P. (2013). SARCS strong-lensing galaxy groups. I. Optical, weak lensing, and scaling laws. *A&A* , 559:A105.

Forman, W. and Jones, C. (1982). X-ray-imaging observations of clusters of galaxies. *ARA&A* , 20:547–585.

Fujita, Y. (1998). Quantitative Estimates of Environmental Effects on the Star Formation Rate of Disk Galaxies in Clusters of Galaxies. *ApJ* , 509(2):587–594.

Fujita, Y. and Nagashima, M. (1999). Effects of Ram Pressure from the Intracluster Medium on the Star Formation Rate of Disk Galaxies in Clusters of Galaxies. *ApJ* , 516(2):619–625.

Garilli, B., Maccagni, D., and Andreon, S. (1999). Composite luminosity function of cluster galaxies. *A&A* , 342:408–416.

Gavazzi, G., O'Neil, K., Boselli, A., and van Driel, W. (2006). H I observations of galaxies. II. The Coma Supercluster. *A&A* , 449(3):929–935.

Gavazzi, G., Pierini, D., and Boselli, A. (1996). The phenomenology of disk galaxies. *A&A* , 312:397–408.

Génova-Santos, R., Rubiño-Martín, J. A., Rebolo, R., Cleary, K., Davies, R. D., Davis, R. J., Dickinson, C., Falcón, N., Grainge, K., Gutiérrez, C. M., Hobson, M. P., Jones, M. E., Kneissl, R., Lancaster, K., Padilla-Torres, C. P., Saunders, R. D. E., Scott, P. F., Taylor, A. C., and Watson, R. A. (2005). A Very Small Array search for the extended Sunyaev-Zel'dovich effect in the Corona Borealis supercluster. *MNRAS* , 363(1):79–92.

Gilbank, D. G., Yee, H. K. C., Ellingson, E., Gladders, M. D., Loh, Y. S., Barrientos, L. F., and Barkhouse, W. A. (2008). The Red-Sequence Luminosity Function in Galaxy Clusters since z ~1. *ApJ* , 673(2):742–751.

Giovanelli, R. and Haynes, M. P. (1985). Gas deficiency in cluster galaxies : a comparison of nine clusters. *ApJ* , 292:404–425.

Girardi, M., Escalera, E., Fadda, D., Giuricin, G., Mardirossian, F., and Mezzetti, M. (1997). Optical Substructures in 48 Galaxy Clusters: New Insights from a Multiscale Analysis. *ApJ* , 482(1):41–62.

Gladders, M. D., López-Cruz, O., Yee, H. K. C., and Kodama, T. (1998). The Slope of the Cluster Elliptical Red Sequence: A Probe of Cluster Evolution. *ApJ* , 501(2):571–577.

Glass, I. S. (1999). *Handbook of Infrared Astronomy.*

Gómez, P. L., Nichol, R. C., Miller, C. J., Balogh, M. L., Goto, T., Zabludoff, A. I., Romer, A. K., Bernardi, M., Sheth, R., Hopkins, A. M., Castander, F. J., Connolly, A. J., Schneider, D. P., Brinkmann, J., Lamb, D. Q., SubbaRao, M., and York, D. G. (2003). Galaxy Star Formation as a Function of Environment in the Early Data Release of the Sloan Digital Sky Survey. *ApJ* , 584(1):210–227.

Gramann, M., Einasto, M., Heinämäki, P., Teerikorpi, P., Saar, E., Nurmi, P., and Einasto, J. (2015). Characteristic density contrasts in the evolution of superclusters. The case of A2142 supercluster. *A&A* , 581:A135.

Graziani, R., Courtois, H. M., Lavaux, G., Hoffman, Y., Tully, R. B., Copin, Y., and Pomarède, D. (2019). The peculiar velocity field up to z $\sim$ 0.05 by forward-modelling Cosmicflows-3 data. *MNRAS* , 488(4):5438–5451.

Gunn, J. E. and Gott, J. Richard, I. (1972). On the Infall of Matter Into Clusters of Galaxies and Some Effects on Their Evolution. *ApJ* , 176:1.

Haines, C. P., Busarello, G., Merluzzi, P., Pimbblet, K. A., Vogt, F. P. A., Dopita, M. A., Mercurio, A., Grado, A., and Limatola, L. (2018). Shapley Supercluster Survey: mapping the filamentary network connecting the clusters. *MNRAS* , 481(1):1055–1074.

Haines, C. P., Merluzzi, P., Mercurio, A., Gargiulo, A., Krusanova, N., Busarello, G., La Barbera, F., and Capaccioli, M. (2006). Shapley Optical Survey - II. The effect of environment on the colour-magnitude relation and galaxy colours. *MNRAS* , 371(1):55–66.

Haynes, M. P. and Giovanelli, R. (1984). Neutral hydrogen in isolated galaxies. IV. Results for the Arecibo sample. *AJ* , 89:758–800.

Healy, J., Blyth, S. L., Verheijen, M. A. W., Hess, K. M., Serra, P., van der Hulst, J. M., Jarrett, T. H., Yim, K., and Józsa, G. I. G. (2021a). H I content in Coma cluster substructure. *A&A* , 650:A76.

Healy, J., Deb, T., Verheijen, M. A. W., Blyth, S. L., Serra, P., Ramatsoku, M., and Vulcani, B. (2021b). MeerKAT 21-cm H I imaging of Abell 2626 and beyond. *A&A* , 654:A173.

Healy, J., Willner, S. P., Verheijen, M. A. W., and Blyth, S. L. (2021c). A2626 and Friends: Large- and Small-scale Structure. *AJ* , 162(5):193.

Heisler, J., Tremaine, S., and Bahcall, J. N. (1985). Estimating the masses of galaxy groups: alternatives to the virial theorem. *ApJ* , 298:8–17.

Henriques, B. M. B., White, S. D. M., Thomas, P. A., Angulo, R., Guo, Q., Lemson, G., Springel, V., and Overzier, R. (2015). Galaxy formation in the Planck cosmology - I. Matching the observed evolution of star formation rates, colours and stellar masses. *MNRAS* , 451(3):2663–2680.

Henry, J. P. and Arnaud, K. A. (1991). A Measurement of the Mass Fluctuation Spectrum from the Cluster X-Ray Temperature Function. *ApJ* , 372:410.

Henry, J. P., Gioia, I. M., Maccacaro, T., Morris, S. L., Stocke, J. T., and Wolter, A. (1992). The Extended Medium Sensitivity Survey Distant Cluster Sample: X-Ray Data and Interpretation of the Luminosity Evolution. *ApJ* , 386:408.

Henry, P. S. (1971). Isotropy of the 3 K Background. *Nature* , 231(5304):516–518.

Herschel, J. F. W. (1864). A General Catalogue of Nebulae and Clusters of Stars. *Philosophical Transactions of the Royal Society of London Series I*, 154:1–137.

Heymans, C., Gray, M. E., Peng, C. Y., van Waerbeke, L., Bell, E. F., Wolf, C., Bacon, D., Balogh, M., Barazza, F. D., Barden, M., Böhm, A., Caldwell, J. A. R., Häußler, B., Jahnke, K., Jogee, S., van Kampen, E., Lane, K., McIntosh, D. H., Meisenheimer, K., Mellier, Y., Sánchez, S. F., Taylor, A. N., Wisotzki, L., and Zheng, X. (2008). The dark matter environment of the Abell 901/902 supercluster: a weak lensing analysis of the HST STAGES survey. *MNRAS* , 385(3):1431–1442.

Hoffman, Y., Courtois, H. M., and Tully, R. B. (2015). Cosmic bulk flow and the local motion from Cosmicflows-2. *MNRAS* , 449(4):4494–4505.

Hoffman, Y., Pomarède, D., Tully, R. B., and Courtois, H. M. (2017). The dipole repeller. *Nature Astronomy*, 1:0036.

Holden, B. P., Stanford, S. A., Eisenhardt, P., and Dickinson, M. (2004). Evolution in the Color-Magnitude Relation of Early-Type Galaxies in Clusters of Galaxies at z~=1. *AJ* , 127(5):2484–2510.

Holmberg, E. (1969). A study of physical groups of galaxies. *Arkiv for Astronomi*, 5:305–343.

Huang, J. S., Thompson, D., Kümmel, M. W., Meisenheimer, K., Wolf, C., Beckwith, S. V. W., Fockenbrock, R., Fried, J. W., Hippelein, H., von Kuhlmann, B., Phleps, S., Röser, H. J., and Thommes, E. (2001). The Calar Alto Deep Imaging Survey: K-band Galaxy number counts. *A&A* , 368:787–796.

Hubble, E. (1936). The Luminosity Function of Nebulae. I. The Luminosity Function of Resolved Nebulae as Indicated by Their Brightest Stars. *ApJ* , 84:158.

Huchra, J., Davis, M., Latham, D., and Tonry, J. (1983). A survey of galaxy redshifts. IV - The data. *ApJS* , 52:89–119.

Huchra, J. P., Macri, L. M., Masters, K. L., Jarrett, T. H., Berlind, P., Calkins, M., Crook, A. C., Cutri, R., Erdoğdu, P., Falco, E., George, T., Hutcheson, C. M., Lahav, O., Mader, J., Mink, J. D., Martimbeau, N., Schneider, S., Skrutskie, M., Tokarz, S., and Westover, M. (2012). The 2MASS Redshift Survey - Description and Data Release. *ApJS* , 199:26.

Hudson, M. J. and Lynden-Bell, D. (1991). Diameter functions of UGC and ESO galaxies. *MNRAS* , 252:219–228.

Hudson, M. J., Smith, R. J., Lucey, J. R., and Branchini, E. (2004). Streaming motions of galaxy clusters within 12 000 km s^{-1}- V. The peculiar velocity field. *MNRAS* , 352(1):61–75.

Hughes, J. P. (1989). The mass of the Coma Cluster - Combined X-ray and optical results. *ApJ* , 337:21–33.

Hurt, R. L., Jarrett, T., Cutri, R., Skrutskie, M., Schneider, S., and van Driel, W. (1999). Serendipitous 2MASS Discoveries in the Galactic Plane: A Galaxy and a Globular Cluster. In *American Astronomical Society Meeting Abstracts #194*, volume 194 of *American Astronomical Society Meeting Abstracts*, page 07.11.

Icke, V. (1985). Distant encounters between disk galaxies and the origin of S 0 spirals. *A&A* , 144(1):115–123.

Jõeveer, M., Einasto, J., and Tago, E. (1978). Spatial distribution of galaxies and of clusters of galaxies in the southern galactic hemisphere. *MNRAS* , 185:357–370.

Jarrett, T. (2004). Large Scale Structure in the Local Universe - The 2MASS Galaxy Catalog. *PASA* , 21(4):396–403.

Jarrett, T. H. (2000). Near-Infrared Galaxy Morphology Atlas. *PASP* , 112:1008–1080.

Jarrett, T.-H., Chester, T., Cutri, R., Schneider, S., Rosenberg, J., Huchra, J. P., and Mader, J. (2000a). 2MASS Extended Sources in the Zone of Avoidance. *AJ* , 120:298–313.

Jarrett, T. H., Chester, T., Cutri, R., Schneider, S., Skrutskie, M., and Huchra, J. P. (2000b). 2MASS Extended Source Catalog: Overview and Algorithms. *AJ* , 119:2498–2531.

Jarrett, T. H., Chester, T., Cutri, R., Schneider, S. E., and Huchra, J. P. (2003). The 2MASS Large Galaxy Atlas. *AJ* , 125:525–554.

Jarvis, J. F. and Tyson, J. A. (1981). FOCAS - Faint Object Classification and Analysis System. *AJ* , 86:476–495.

Jeltema, T. E., Canizares, C. R., Bautz, M. W., and Buote, D. A. (2005). The Evolution of Structure in X-Ray Clusters of Galaxies. *ApJ* , 624(2):606–629.

Jerjen, H. and Tammann, G. A. (1997). Studies of the Centaurus cluster. III. Luminosity functions of individual Hubble-types as compared to Virgo and Fornax. *A&A* , 321:713–723.

Joeveer, M. and Einasto, J. (1978). Has the Universe the Cell Structure? In Longair, M. S. and Einasto, J., editors, *Large Scale Structures in the Universe*, volume 79, page 241.

Jonas, J. and MeerKAT Team (2016). The MeerKAT Radio Telescope. In *MeerKAT Science: On the Pathway to the SKA*, page 1.

Jones, C. and Forman, W. (1984). The structure of clusters of galaxies observed with Einstein. *ApJ* , 276:38–55.

Jones, C. and Forman, W. (1999). Einstein Observatory Images of Clusters of Galaxies. *ApJ* , 511(1):65–83.

Jones, D. H., Peterson, B. A., Colless, M., and Saunders, W. (2006). Near-infrared and optical luminosity functions from the 6dF Galaxy Survey. *MNRAS* , 369(1):25–42.

Jones, D. H., Read, M. A., Saunders, W., Colless, M., Jarrett, T., Parker, Q. A., Fairall, A. P., Mauch, T., Sadler, E. M., Watson, F. G., Burton, D., Campbell, L. A., Cass, P., Croom, S. M., Dawe, J., Fiegert, K., Frankcombe, L., Hartley, M., Huchra, J., James, D., Kirby, E., Lahav, O., Lucey, J., Mamon, G. A., Moore, L., Peterson, B. A., Prior, S., Proust, D., Russell, K., Safouris, V., Wakamatsu, K.-I., Westra, E., and Williams, M. (2009). The 6dF Galaxy Survey: final redshift release (DR3) and southern large-scale structures. *MNRAS* , 399(2):683–698.

Kashibadze, O. G., Karachentsev, I. D., and Karachentseva, V. E. (2020). Structure and kinematics of the Virgo cluster of galaxies. *A&A* , 635:A135.

Kauffmann, G. and Charlot, S. (1998). The K-band luminosity function at z=1: a powerful constraint on galaxy formation theory. *MNRAS* , 297(1):L23–l28.

Kim, S., Rey, S.-C., Jerjen, H., Lisker, T., Sung, E.-C., Lee, Y., Chung, J., Pak, M., Yi, W., and Lee, W. (2014). The Extended Virgo Cluster Catalog. *ApJS* , 215(2):22.

Kirby, E. M., Jerjen, H., Ryder, S. D., and Driver, S. P. (2008). Deep Near-Infrared Surface Photometry of 57 Galaxies in the Local Sphere of Influence. *AJ* , 136:1866–1888.

Kocevski, D. D. and Ebeling, H. (2006). On the Origin of the Local Group's Peculiar Velocity. *ApJ* , 645(2):1043–1053.

Kochanek, C. S., Pahre, M. A., Falco, E. E., Huchra, J. P., Mader, J., Jarrett, T. H., Chester, T., Cutri, R., and Schneider, S. E. (2001). The K-Band Galaxy Luminosity Function. *ApJ* , 560:566–579.

Kodama, T. and Arimoto, N. (1997). Origin of the colour-magnitude relation of elliptical galaxies. *A&A* , 320:41–53.

Koester, B. P., McKay, T. A., Annis, J., Wechsler, R. H., Evrard, A. E., Rozo, E., Bleem, L., Sheldon, E. S., and Johnston, D. (2007). MaxBCG: A Red-Sequence Galaxy Cluster Finder. *ApJ* , 660(1):221–238.

Kofman, L. A. and Shandarin, S. F. (1988). Theory of adhesion for the large-scale structure of the Universe. *Nature* , 334(6178):129–131.

Kolokotronis, V., Basilakos, S., and Plionis, M. (2002). Supercluster properties as a cosmological probe. *MNRAS* , 331(4):1020–1026.

Kormendy, J. (1980). Photometric Studies of Galaxy Dynamics. In Crane, P. and Kjär, K., editors, *Two Dimensional Photometry*, page 191.

Kormendy, J. (1985). Families of ellipsoidal stellar systems and the formation of dwarf elliptical galaxies. *ApJ* , 295:73–79.

Kraan-Korteweg, R. C. (2000a). A catalog of galaxies behind the Southern Milky Way . I. The Hydra/Antlia extension (l~266^{o}r - 296^{o}r). *A&AS* , 141:123–140.

Kraan-Korteweg, R. C. (2000b). An Overview of Optical Galaxy Searches and their Completeness. In Kraan-Korteweg, R. C., Henning, P. A., and Andernach, H., editors, *Mapping the Hidden Universe: The Universe behind the Mily Way - The Universe in HI*, volume 218 of *Astronomical Society of the Pacific Conference Series*, page 19.

Kraan-Korteweg, R. C., Cluver, M. E., Bilicki, M., Jarrett, T. H., Colless, M., Elagali, A., Böhringer, H., and Chon, G. (2017). Discovery of a supercluster in the Zone of Avoidance in Vela. *MNRAS* , 466:L29–L33.

Kraan-Korteweg, R. C., Jarrett, T. H., Elagali, A., Cluver, M. E., Bilicki, M., and Colless, M. M. (2015). The Unveiling of the newly discovered Vela Supercluster. *SALT Science Conference 2015 (SSC2015)*, page 40.

Kraan-Korteweg, R. C. and Lahav, O. (2000). The Universe behind the Milky Way. *A&ARv* , 10:211–261.

Kraan-Korteweg, R. C., Riad, I. F., Woudt, P. A., Nagayama, T., and Wakamatsu, K. (2011). The Mass Distribution of the Great Attractor as Revealed by a Deep NIR Survey. *arXiv e-prints*, page arXiv:1107.1069.

Kraan-Korteweg, R. C., Woudt, P. A., Cayatte, V., Fairall, A. P., Balkowski, C., and Henning, P. A. (1996). A nearby massive galaxy cluster behind the Milky Way. *Nature* , 379:519–521.

Kubo, J. M., Stebbins, A., Annis, J., Dell'Antonio, I. P., Lin, H., Khiabanian, H., and Frieman, J. A. (2007). The Mass of the Coma Cluster from Weak Lensing in the Sloan Digital Sky Survey. *ApJ* , 671(2):1466–1470.

Larson, R. B., Tinsley, B. M., and Caldwell, C. N. (1980). The evolution of disk galaxies and the origin of S0 galaxies. *ApJ* , 237:692–707.

Lavaux, G. and Hudson, M. J. (2011). The 2M++ galaxy redshift catalogue. *MNRAS* , 416(4):2840–2856.

Lavaux, G., Tully, R. B., Mohayaee, R., and Colombi, S. (2010). Cosmic Flow From Two Micron All-Sky Redshift Survey: the Origin of Cosmic Microwave Background Dipole and Implications for ΛCDM Cosmology. *ApJ* , 709:483–498.

Lavery, R. J. and Henry, J. P. (1988). Evidence for Galaxy-Galaxy Interactions as an Active Agent of the "Butcher-Oemler Effect" at a Redshift of 0.2. *ApJ* , 330:596.

Lawrence, A., Warren, S. J., Almaini, O., Edge, A. C., Hambly, N. C., Jameson, R. F., Lucas, P., Casali, M., Adamson, A., Dye, S., Emerson, J. P., Foucaud, S., Hewett, P., Hirst, P., Hodgkin, S. T., Irwin, M. J., Lodieu, N., McMahon, R. G., Simpson, C., Smail, I., Mortlock, D., and Folger, M. (2007). The UKIRT Infrared Deep Sky Survey (UKIDSS). *MNRAS* , 379(4):1599–1617.

Leahy, D. A. and Yin, D. (2000). X-ray analysis of the cluster 3C 129. *MNRAS* , 313(3):617–626.

Lee, B., Giavalisco, M., Williams, C. C., Guo, Y., Lotz, J., Van der Wel, A., Ferguson, H. C., Faber, S. M., Koekemoer, A., Grogin, N., Kocevski, D., Conselice, C. J., Wuyts, S., Dekel, A., Kartaltepe, J., and Bell, E. F. (2013). CANDELS: The Correlation between Galaxy Morphology and Star Formation Activity at z ~2. *ApJ* , 774(1):47.

Lee, Y., Rey, S.-C., Hilker, M., Sheen, Y.-K., and Yi, S. K. (2016). Galaxy Luminosity Function of the Dynamically Young Abell 119 Cluster: Probing the Cluster Assembly. *ApJ* , 822(2):92.

Lietzen, H., Tempel, E., Liivamägi, L. J., Montero-Dorta, A., Einasto, M., Streblyanska, A., Maraston, C., Rubiño-Martín, J. A., and Saar, E. (2016). Discovery of a massive supercluster system at z ~0.47. *A&A* , 588:L4.

Liivamägi, L. J., Tempel, E., and Saar, E. (2012). SDSS DR7 superclusters. The catalogues. *A&A* , 539:A80.

Lilow, R. and Nusser, A. (2021). Constrained realizations of 2MRS density and peculiar velocity fields: growth rate and local flow. *MNRAS* , 507(2):1557–1581.

Lim, S. and Lee, J. (2014). An Analytic Formula for the Supercluster Mass Function. *ApJ* , 783(1):39.

Limber, D. N. and Mathews, W. G. (1960). The Dynamical Stability of Stephan's Quintet. *ApJ* , 132:286.

Lin, Y.-T., Mohr, J. J., and Stanford, S. A. (2004). K-band Properties of Galaxy Clusters and Groups: Luminosity Function, Radial Distribution and Halo Occupation Number. In *American Astronomical Society Meeting Abstracts #204*, volume 36 of *Bulletin of the American Astronomical Society*, page 731.

Lobo, C., Biviano, A., Durret, F., Gerbal, D., Le Fevre, O., Mazure, A., and Slezak, E. (1997). Environmental effects on the Coma cluster luminosity function. *A&A* , 317:385–392.

Loeb, A. and Narayan, R. (2008). Dynamical constraints on the Local Group from the CMB and 2MRS dipoles. *MNRAS* , 386:2221–2226.

Łokas, E. L. (2020). Tidal evolution of galaxies in the most massive cluster of IllustrisTNG-100. *A&A* , 638:A133.

López-Cruz, O., Barkhouse, W. A., and Yee, H. K. C. (2004a). The Color-Magnitude Effect in Early-Type Cluster Galaxies. *ApJ* , 614(2):679–691.

López-Cruz, O., Barkhouse, W. A., and Yee, H. K. C. (2004b). The Color-Magnitude Effect in Early-Type Cluster Galaxies. *ApJ* , 614(2):679–691.

Lourenço, A. C. C., Lopes, P. A. A., Laganá, T. F., Nascimento, R. S., Machado, R. E. G., Moura, M. T., Jaffé, Y. L., Ribeiro, A. L., Vulcani, B., Moretti, A., and Riguccini, L. A. (2020). The dynamical state of Abell 2399: a bullet-like cluster. *MNRAS* , 498(1):835–849.

Luparello, H., Lares, M., Lambas, D. G., and Padilla, N. (2011). Future virialized structures: an analysis of superstructures in the SDSS-DR7. *MNRAS* , 415(1):964–976.

Lynden-Bell, D., Faber, S. M., Burstein, D., Davies, R. L., Dressler, A., Terlevich, R. J., and Wegner, G. (1988). Spectroscopy and photometry of elliptical galaxies. V - Galaxy streaming toward the new supergalactic center. *ApJ* , 326:19–49.

Makino, J. and Hut, P. (1997). Merger Rate of Equal-Mass Spherical Galaxies. *ApJ* , 481(1):83–94.

Mamon, G. A. (1992). Are Cluster Ellipticals the Products of Mergers? *ApJL* , 401:L3.

Mann, A. W. and Ebeling, H. (2012). X-ray-optical classification of cluster mergers and the evolution of the cluster merger fraction. *MNRAS* , 420(3):2120–2138.

Marinoni, C., Monaco, P., Giuricin, G., and Costantini, B. (1999). The Nearby Optical Galaxy Sample: The Local Galaxy Luminosity Function. *ApJ* , 521(1):50–63.

Martinet, N., Clowe, D., Durret, F., Adami, C., Acebrón, A., Hernandez-García, L., Márquez, I., Guennou, L., Sarron, F., and Ulmer, M. (2016). Weak lensing study of 16 DAFT/FADA clusters: Substructures and filaments. *A&A* , 590:A69.

Martinet, N., Durret, F., Adami, C., and Rudnick, G. (2017). The faint end of the red sequence galaxy luminosity function: unveiling surface brightness selection effects with the CLASH clusters. *A&A* , 604:A80.

Martinet, N., Durret, F., Guennou, L., Adami, C., Biviano, A., Ulmer, M. P., Clowe, D., Halliday, C., Ilbert, O., Márquez, I., and Schirmer, M. (2015). The evolution of the cluster optical galaxy luminosity function between z = 0.4 and 0.9 in the DAFT/FADA survey. *A&A* , 575:A116.

Mathis, J. S. (1990). Interstellar dust and extinction. *ARA&A* , 28:37–70.

McDonald, M., Courteau, S., and Tully, R. B. (2009). The near-IR luminosity function and bimodal surface brightness distributions of Virgo cluster galaxies. *MNRAS* , 394(4):2022–2042.

McLaughlin, D. E. (1999). Evidence in Virgo for the Universal Dark Matter Halo. *ApJL* , 512(1):L9–L12.

McNaught-Roberts, T., Norberg, P., Baugh, C., Lacey, C., Loveday, J., Peacock, J., Baldry, I., Bland-Hawthorn, J., Brough, S., Driver, S. P., Robotham, A. S. G., and Vázquez-Mata, J. A. (2014). Galaxy And Mass Assembly (GAMA): the dependence of the galaxy luminosity function on environment, redshift and colour. *MNRAS* , 445(2):2125–2145.

Mei, S., Blakeslee, J. P., Côté, P., Tonry, J. L., West, M. J., Ferrarese, L., Jordán, A., Peng, E. W., Anthony, A., and Merritt, D. (2007). The ACS Virgo Cluster Survey. XIII. SBF Distance Catalog and the Three-dimensional Structure of the Virgo Cluster. *ApJ* , 655(1):144–162.

Mei, S., Blakeslee, J. P., Stanford, S. A., Holden, B. P., Rosati, P., Strazzullo, V., Homeier, N., Postman, M., Franx, M., Rettura, A., Ford, H., Illingworth, G. D., Ettori, S., Bouwens, R. J., Demarco, R., Martel, A. R., Clampin, M., Hartig, G. F., Eisenhardt, P., Ardila, D. R., Bartko, F., Benítez, N., Bradley, L. D., Broadhurst, T. J., Brown, R. A., Burrows, C. J., Cheng, E. S., Cross, N. J. G., Feldman, P. D., Golimowski, D. A., Goto, T., Gronwall, C., Infante, L., Kimble, R. A., Krist, J. E., Lesser, M. P., Menanteau, F., Meurer, G. R., Miley, G. K., Motta, V., Sirianni, M., Sparks, W. B., Tran, H. D., Tsvetanov, Z. I., White, R. L., and Zheng, W. (2006a). Evolution of the Color-Magnitude Relation in High-Redshift Clusters: Blue Early-Type Galaxies and Red Pairs in RDCS J0910+5422. *ApJ* , 639(1):81–94.

Mei, S., Holden, B. P., Blakeslee, J. P., Rosati, P., Postman, M., Jee, M. J., Rettura, A., Sirianni, M., Demarco, R., Ford, H. C., Franx, M., Homeier, N., and Illingworth, G. D. (2006b). Evolution of the Color-Magnitude Relation in High-Redshift Clusters: Early-Type Galaxies in the Lynx Supercluster at z ~1.26. *ApJ* , 644(2):759–768.

Mellinger, A. (2009). A Color All-Sky Panorama Image of the Milky Way. *PASP* , 121(885):1180.

Merluzzi, P., Busarello, G., Haines, C. P., Mercurio, A., Grado, A., Limatola, L., and Pimbblett, K. J. (2016). Shapley Supercluster Survey. In Napolitano, N. R., Longo, G., Marconi, M., Paolillo, M., and Iodice, E., editors, *The Universe of Digital Sky Surveys*, volume 42, page 173.

Merluzzi, P., Busarello, G., Haines, C. P., Mercurio, A., Okabe, N., Pimbblet, K. J., Dopita, M. A., Grado, A., Limatola, L., Bourdin, H., Mazzotta, P., Capaccioli, M., Napolitano, N. R., and Schipani, P. (2015). Shapley Supercluster Survey: Galaxy evolution from filaments to cluster cores. *MNRAS* , 446(1):803–822.

Merluzzi, P., Mercurio, A., Haines, C. P., Smith, R. J., Busarello, G., and Lucey, J. R. (2010). ACCESS: NIR luminosity function and stellar mass function of galaxies in the Shapley supercluster environment. *MNRAS* , 402(2):753–766.

Merritt, D. (1988). Internal dynamics of galaxy clusters. In Dickey, J. M., editor, *The Minnesota lectures on Clusters of Galaxies and Large-Scale Structure*, volume 5 of *Astronomical Society of the Pacific Conference Series*, pages 175–196.

Mitchell, P. D., Lacey, C. G., Lagos, C. D. P., Frenk, C. S., Bower, R. G., Cole, S., Helly, J. C., Schaller, M., Gonzalez-Perez, V., and Theuns, T. (2018). Comparing galaxy formation in semi-analytic models and hydrodynamical simulations. *MNRAS* , 474(1):492–521.

Mobasher, B., Colless, M., Carter, D., Poggianti, B. M., Bridges, T. J., Kranz, K., Komiyama, Y., Kashikawa, N., Yagi, M., and Okamura, S. (2003). A Photometric and Spectroscopic Study of Dwarf and Giant Galaxies in the Coma Cluster. IV. The Luminosity Function. *ApJ* , 587(2):605–618.

Mohr, J. J., Evrard, A. E., Fabricant, D. G., and Geller, M. J. (1995). Cosmological Constraints from Observed Cluster X-Ray Morphologies. *ApJ* , 447:8.

Mohr, J. J., Geller, M. J., Fabricant, D. G., Wegner, G., Thorstensen, J., and Richstone, D. O. (1996). An Optical and X-Ray Study of Abell 576, a Galaxy Cluster with a Cold Core. *ApJ* , 470:724.

Moore, B., Katz, N., Lake, G., Dressler, A., and Oemler, A. (1996). Galaxy harassment and the evolution of clusters of galaxies. *Nature* , 379(6566):613–616.

Moore, B., Lake, G., Quinn, T., and Stadel, J. (1999a). On the survival and destruction of spiral galaxies in clusters. *MNRAS* , 304(3):465–474.

Moore, B., Quinn, T., Governato, F., Stadel, J., and Lake, G. (1999b). Cold collapse and the core catastrophe. *MNRAS* , 310(4):1147–1152.

Morgan, W. W. (1961). The Classification of Clusters of Galaxies. *Proceedings of the National Academy of Science*, 47(7):905–906.

Muldrew, S. I., Hatch, N. A., and Cooke, E. A. (2015). What are protoclusters? - Defining high-redshift galaxy clusters and protoclusters. *MNRAS* , 452(3):2528–2539.

Nagashima, C., Nagayama, T., Nakajima, Y., Tamura, M., Sugitani, K., Nagata, T., Hirao, T., Nakaya, H., Yanagisawa, K., and Sato, S. (1999). Development of SIRIUS — A Simultaneous-Color InfraRed Imager for Unbiased Survey. In Nakamoto, T., editor, *Star Formation 1999*, pages 397–398.

Nagayama, T. (2012). The IRSF, a Japanese Near-Infrared Telescope in South Africa. *African Skies*, 16:98.

Nagayama, T., Nagashima, C., Nakajima, Y., Nagata, T., Sato, S., Nakaya, H., Yamamuro, T., Sugitani, K., and Tamura, M. (2003). SIRUS: a near infrared simultaneous three-band camera. In Iye, M. and Moorwood, A. F. M., editors, *Instrument Design and Performance for Optical/Infrared Ground-based Telescopes*, volume 4841 of *Proc. SPIE* , pages 459–464.

Nagayama, T., Woudt, P. A., Nagashima, C., Nakajima, Y., Kato, D., Kurita, M., Nagata, T., Nakaya, H., Tamura, M., Sugitani, K., Wakamatsu, K., and Sato, S. (2004). A deep near-infrared survey around the giant radio galaxy PKS 1343-601. *MNRAS* , 354:980–990.

Nagayama, T., Woudt, P. A., Wakamatsu, K., Nishiyama, S., Nagashima, C., Kato, D., Nagata, T., Nakaya, H., Sugitani, K., Tamura, M., and Sato, S. (2006). Near-infrared study of CIZA J1324.7-5736, the second richest cluster of galaxies in the Great Attractor. *MNRAS* , 368:534–543.

Nakaya, H. and Sato, S. (1998). Multi-array control system for a wide-wavelength observation. In Fowler, A. M., editor, *Infrared Astronomical Instrumentation*, volume 3354 of *Society of Photo-Optical Instrumentation Engineers (SPIE) Conference Series*, pages 368–372.

Nusser, A. and Davis, M. (2011). The Cosmological Bulk Flow: Consistency with ΛCDM and z ≈ 0 Constraints on σ_8 and γ. *ApJ* , 736(2):93.

Oegerle, W. R. and Hill, J. M. (2001). Dynamics of cD Clusters of Galaxies. IV. Conclusion of a Survey of 25 Abell Clusters. *AJ* , 122(6):2858–2873.

Oemler, Augustus, J. (1974). The Systematic Properties of Clusters of Galaxies. Photometry of 15 Clusters. *ApJ* , 194:1–20.

Ouchi, M., Shimasaku, K., Akiyama, M., Sekiguchi, K., Furusawa, H., Okamura, S., Kashikawa, N., Iye, M., Kodama, T., Saito, T., Sasaki, T., Simpson, C., Takata, T., Yamada, T., Yamanoi, H., Yoshida, M., and Yoshida, M. (2005). The Discovery of Primeval Large-Scale Structures with Forming Clusters at Redshift 6. *ApJL* , 620(1):L1–L4.

Paolillo, M., Andreon, S., Longo, G., Puddu, E., Gal, R. R., Scaramella, R., Djorgovski, S. G., and de Carvalho, R. (2001). Luminosity function of clusters of galaxies. *A&A* , 367:59–71.

Papovich, C., Momcheva, I., Willmer, C. N. A., Finkelstein, K. D., Finkelstein, S. L., Tran, K. V., Brodwin, M., Dunlop, J. S., Farrah, D., Khan, S. A., Lotz, J., McCarthy, P., McLure, R. J., Rieke, M., Rudnick, G., Sivanandam, S., Pacaud, F., and Pierre, M. (2010). A Spitzer-selected Galaxy Cluster at z = 1.62. *ApJ* , 716(2):1503–1513.

Paturel, G., Petit, C., Prugniel, P., Theureau, G., Rousseau, J., Brouty, M., Dubois, P., and Cambrésy, L. (2003). HYPERLEDA. I. Identification and designation of galaxies. *A&A* , 412:45–55.

Pearson, D. W., Batiste, M., and Batuski, D. J. (2014). The largest gravitationally bound structures: the Corona Borealis supercluster - mass and bound extent. *MNRAS* , 441(2):1601–1614.

Peebles, P. J. and Ratra, B. (2003). The cosmological constant and dark energy. *Reviews of Modern Physics*, 75(2):559–606.

Persson, S. E., Murphy, D. C., Krzeminski, W., Roth, M., and Rieke, M. J. (1998). A New System of Faint Near-Infrared Standard Stars. *AJ* , 116:2475–2488.

Pimbblet, K. A., Penny, S. J., and Davies, R. L. (2014). How typical is the Coma cluster? *MNRAS* , 438(4):3049–3057.

Pinzke, A., Pfrommer, C., and Bergström, L. (2011). Prospects of detecting gamma-ray emission from galaxy clusters: Cosmic rays and dark matter annihilations. *PhRvD* , 84(12):123509.

Plionis, M. (2004). The large-scale environment of groups and clusters of galaxies. In Diaferio, A., editor, *IAU Colloq. 195: Outskirts of Galaxy Clusters: Intense Life in the Suburbs*, pages 19–25.

Porter, S. C., Raychaudhury, S., Pimbblet, K. A., and Drinkwater, M. J. (2008). Star formation in galaxies falling into clusters along supercluster-scale filaments. *MNRAS* , 388(3):1152–1160.

Postman, M. and Geller, M. J. (1984). The morphology-density relation - The group connection. *ApJ* , 281:95–99.

Predehl, P., Andritschke, R., Arefiev, V., Babyshkin, V., Batanov, O., Becker, W., Böhringer, H., Bogomolov, A., Boller, T., Borm, K., Bornemann, W., Bräuninger, H., Brüggen, M., Brunner, H., Brusa, M., Bulbul, E., Buntov, M., Burwitz, V., Burkert, W., Clerc, N., Churazov, E., Coutinho, D., Dauser, T., Dennerl, K., Doroshenko, V., Eder, J., Emberger, V., Eraerds, T., Finoguenov, A., Freyberg, M., Friedrich, P., Friedrich, S., Fürmetz, M., Georgakakis, A., Gilfanov, M., Granato, S., Grossberger, C., Gueguen, A., Gureev, P., Haberl, F., Hälker, O., Hartner, G., Hasinger, G., Huber, H., Ji, L., Kienlin, A. v., Kink, W., Korotkov, F., Kreykenbohm, I., Lamer, G., Lomakin, I., Lapshov, I., Liu, T., Maitra, C., Meidinger, N., Menz, B., Merloni, A., Mernik, T., Mican, B., Mohr, J., Müller, S., Nandra, K., Nazarov, V., Pacaud, F., Pavlinsky, M., Perinati, E., Pfeffermann, E., Pietschner, D., Ramos-Ceja, M. E., Rau, A., Reiffers, J., Reiprich, T. H., Robrade, J., Salvato, M., Sanders, J., Santangelo, A., Sasaki, M., Scheuerle, H., Schmid, C., Schmitt, J., Schwope, A., Shirshakov, A., Steinmetz, M., Stewart, I., Strüder, L., Sunyaev, R., Tenzer, C., Tiedemann, L., Trümper, J., Voron, V., Weber, P., Wilms, J., and Yaroshenko, V. (2021). The eROSITA X-ray telescope on SRG. *A&A* , 647:A1.

Proctor, R. (1878). *The Universe of Stars: Presenting Researches Into and New Views Respecting the Constitution of the Heavens.* Longmans, Green, and Company.

Proust, D., Quintana, H., Carrasco, E. R., Reisenegger, A., Slezak, E., Muriel, H., Dünner, R., Sodré, L., J., Drinkwater, M. J., Parker, Q. A., and Ragone, C. J. (2006). Structure and dynamics of the Shapley Supercluster. Velocity catalogue, general morphology and mass. *Astronomy and Astrophysics*, 447(1):133–144.

Quilis, V., Moore, B., and Bower, R. (2000). Gone with the Wind: The Origin of S0 Galaxies in Clusters. *Science*, 288(5471):1617–1620.

Ramatsoku, M., Verheijen, M. A. W., Kraan-Korteweg, R. C., Jarrett, T. H., Said, K., and Schröder, A. C. (2020). A near-infrared study of the obscured 3C129 galaxy cluster. *A&A* , 644:A107.

Ramatsoku, M. A. (2017). *A Westerbork blind Hi imaging survey of the Perseus-Pisces filament in the Zone of Avoidance*. PhD thesis, University of Groningen and University of Cape Town.

Rameez, M., Mohayaee, R., Sarkar, S., and Colin, J. (2018). The dipole anisotropy of AllWISE galaxies. *MNRAS* , 477(2):1772–1781.

Ramella, M., Biviano, A., Pisani, A., Varela, J., Bettoni, D., Couch, W. J., D'Onofrio, M., Dressler, A., Fasano, G., Kjørgaard, P., Moles, M., Pignatelli, E., and Poggianti, B. M. (2007). Substructures in WINGS clusters. *A&A* , 470(1):39–51.

Raychaudhury, S. (1989). The distribution of galaxies in the direction of the 'Great Attractor'. *Nature* , 342(6247):251–255.

Reisenegger, A., Quintana, H., Carrasco, E. R., and Maze, J. (2000). The Shapley Supercluster. III. Collapse Dynamics and Mass of the Central Concentration. *AJ* , 120(2):523–532.

Riad, I. F. (2010). *A Deep Near InfraRed Survey Along The Norma Wall*. PhD thesis, University of Cape Town.

Riad, I. F., Kraan-Korteweg, R. C., and Woudt, P. A. (2010). The effect of dust extinction on the observed properties of galaxies in the near-infrared. *MNRAS* , 401:924–932.

Rodrigues, L. F. S., Vernon, I., and Bower, R. G. (2017). Constraints on galaxy formation models from the galaxy stellar mass function and its evolution. *MNRAS* , 466(2):2418–2435.

Rood, H. J. and Sastry, G. N. (1971). "Tuning Fork" Classification of Rich Clusters of Galaxies. *PASP* , 83(493):313.

Rose, J. A., Gaba, A. E., Christiansen, W. A., Davis, D. S., Caldwell, N., Hunstead, R. W., and Johnston-Hollitt, M. (2002). Multiple Merging Events in the Double Cluster A3128/A3125. *AJ* , 123(3):1216–1246.

Rozo, E., Rykoff, E. S., Koester, B. P., McKay, T., Hao, J., Evrard, A., Wechsler, R. H., Hansen, S., Sheldon, E., Johnston, D., Becker, M., Annis, J., Bleem, L., and Scranton, R. (2008). An Improved Cluster Richness Estimator. *arXiv e-prints*, page arXiv:0809.2797.

Rudnick, G., von der Linden, A., Pelló, R., Aragón-Salamanca, A., Marchesini, D., Clowe, D., De Lucia, G., Halliday, C., Jablonka, P., Milvang-Jensen, B., Poggianti, B., Saglia, R., Simard, L., White, S., and Zaritsky, D. (2009). The Rest-frame Optical Luminosity Function of Cluster Galaxies at z $<$ 0.8 and the Assembly of the Cluster Red Sequence. *ApJ* , 700(2):1559–1588.

Said, K., Kraan-Korteweg, R. C., and Jarrett, T. H. (2014). Galaxy peculiar velocities in the Zone of Avoidance. *preprint (arXiv:1410.2992)*.

Said, K., Kraan-Korteweg, R. C., and Jarrett, T. H. (2015). On how to extend the NIR Tully-Fisher relation to be truly all-sky. *MNRAS* , 447:1618–1629.

Said, K., Kraan-Korteweg, R. C., Jarrett, T. H., Staveley-Smith, L., and Williams, W. L. (2016a). NIR Tully-Fisher in the Zone of Avoidance - III. Deep NIR catalogue of the HIZOA galaxies. *MNRAS* , 462(3):3386–3400.

Said, K., Kraan-Korteweg, R. C., and Staveley-Smith, L. (2019). The H I mass function in the Parkes H I Zone of Avoidance survey. *MNRAS* , 486(2):1796–1804.

Said, K., Kraan-Korteweg, R. C., Staveley-Smith, L., Williams, W. L., Jarrett, T. H., and Springob, C. M. (2016b). NIR Tully-Fisher in the Zone of Avoidance - II. 21 cm H I-line spectra of southern ZOA galaxies. *MNRAS* , 457(3):2366–2376.

Saito, M., Ohtani, H., Baba, A., Hotta, H., Kameno, S., Kurosu, S., Nakada, K., and Takata, T. (1991). A Search for Galaxies behind the Milky Way between L = 230(deg) and 250(deg). *PASJ* , 43:449–468.

Sandage, A. and Binggeli, B. (1984). Studies of the Virgo cluster. III. A classification system and an illustrated Atlas of Virgo cluster dwarf galaxies. *AJ* , 89:919–931.

Sandage, A., Binggeli, B., and Tammann, G. A. (1985). Studies of the Virgo cluster. V. Luminosity functions of Virgo cluster galaxies. *AJ* , 90:1759–1771.

Santos, J. S., Rosati, P., Tozzi, P., Böhringer, H., Ettori, S., and Bignamini, A. (2008). Searching for cool core clusters at high redshift. *A&A* , 483(1):35–47.

Sarazin, C. L. (1986). X-ray emission from clusters of galaxies. *Reviews of Modern Physics*, 58(1):1–115.

Sarron, F., Martinet, N., Durret, F., and Adami, C. (2018). Evolution of the cluster optical galaxy luminosity function in the CFHTLS: breaking the degeneracy between mass and redshift. *A&A* , 613:A67.

Sathyaprakash, B. S., Sahni, V., and Shandarin, S. (1998). Morphology of Clusters and Superclusters in N-Body Simulations of Cosmological Gravitational Clustering. *ApJ* , 508(2):551–569.

Sazonova, E., Alatalo, K., Lotz, J., Rowlands, K., Snyder, G. F., Boone, K., Brodwin, M., Hayden, B., Lanz, L., Perlmutter, S., and Rodriguez-Gomez, V. (2020). The Morphology-Density Relationship in $1 < z < 2$ Clusters. *ApJ* , 899(1):85.

Schechter, P. (1976). An analytic expression for the luminosity function for galaxies. *ApJ* , 203:297–306.

Schechter, P. L., Mateo, M., and Saha, A. (1993). DOPHOT, a CCD photometry program: Description and tests. *PASP* , 105:1342–1353.

Schindler, S., Binggeli, B., and Böhringer, H. (1999). Morphology of the Virgo cluster: Gas versus galaxies. *A&A* , 343:420–438.

Schirmer, M., Hildebrandt, H., Kuijken, K., and Erben, T. (2011). Mass, light and colour of the cosmic web in the supercluster SCL2243-0935 (z = 0.447). *A&A* , 532:A57.

Schlafly, E. F., Finkbeiner, D. P., Schlegel, D. J., Jurić, M., Ivezić, Ž., Gibson, R. R., Knapp, G. R., and Weaver, B. A. (2010). The Blue Tip of the Stellar Locus: Measuring Reddening with the Sloan Digital Sky Survey. *ApJ* , 725(1):1175–1191.

Schlegel, D. J., Finkbeiner, D. P., and Davis, M. (1998). Maps of Dust Infrared Emission for Use in Estimation of Reddening and Cosmic Microwave Background Radiation Foregrounds. *ApJ* , 500:525.

Schröder, A. C., Kraan-Korteweg, R. C., and Henning, P. A. (2009). Parkes H I observations of galaxies behind the southern Milky Way. II. The Crux and Great Attractor regions. *A&A* , 505:1049–1074.

Schröder, A. C., Mamon, G. A., Kraan-Korteweg, R. C., and Woudt, P. A. (2007). The highly obscured region around <ASTROBJ>PKS 1343 - 601</ASTROBJ>. I. Galactic interstellar extinctions using DENIS galaxy colours. *A&A* , 466:481–499.

Schuecker, P., Böhringer, H., Reiprich, T. H., and Feretti, L. (2001). A systematic study of X-ray substructure of galaxy clusters detected in the ROSAT All-Sky Survey. *A&A* , 378:408–427.

Scodeggio, M., Guzzo, L., Garilli, B., Granett, B. R., Bolzonella, M., de la Torre, S., Abbas, U., Adami, C., Arnouts, S., Bottini, D., Cappi, A., Coupon, J., Cucciati, O., Davidzon, I., Franzetti, P., Fritz, A., Iovino, A., Krywult, J., Le Brun, V., Le Fèvre, O., Maccagni, D., Małek, K., Marchetti, A., Marulli, F., Polletta, M., Pollo, A., Tasca, L. A. M., Tojeiro, R., Vergani, D., Zanichelli, A., Bel, J., Branchini, E., De Lucia, G., Ilbert, O., McCracken, H. J., Moutard, T., Peacock, J. A., Zamorani, G., Burden, A., Fumana, M., Jullo, E., Marinoni, C., Mellier, Y., Moscardini, L., and Percival, W. J. (2018). The VIMOS Public Extragalactic Redshift Survey (VIPERS). Full spectroscopic data and auxiliary information release (PDR-2). *A&A* , 609:A84.

Scrimgeour, M. I., Davis, T. M., Blake, C., Staveley-Smith, L., Magoulas, C., Springob, C. M., Beutler, F., Colless, M., Johnson, A., Jones, D. H., Koda, J., Lucey, J. R., Ma, Y.-Z., Mould, J., and Poole, G. B. (2016). The 6dF Galaxy Survey: bulk flows on 50-70 h^{-1} Mpc scales. *MNRAS* , 455(1):386–401.

Sekiguchi, M., Nakaya, H., Kataza, H., and Miyazaki, S. (1998). High-Speed Data Acquisition System Messia for SUBARU. *Experimental Astronomy*, 8(1):51–58.

Shandarin, S. F., Sheth, J. V., and Sahni, V. (2004). Morphology of the supercluster-void network in ΛCDM cosmology. *MNRAS* , 353(1):162–178.

Shane, C. and Wirtanen, C. (1967). *The distribution of galaxies*. University of California publications. Publications of the Lick Observatory; vol. XXII, pt. 1.

Shapley, H. (1930). Note on a Remote Cloud of Galaxies in Centaurus. *Harvard College Observatory Bulletin*, 874:9–12.

Shapley, H. (1961). *Galaxies*.

Shaya, E. J., Peebles, P. J. E., and Tully, R. B. (1995). Action Principle Solutions for Galaxy Motions within 3000 Kilometers per Second. *ApJ* , 454:15.

Sheth, J. V., Sahni, V., Shandarin, S. F., and Sathyaprakash, B. S. (2003). Measuring the geometry and topology of large-scale structure using SURFGEN: methodology and preliminary results. *MNRAS* , 343(1):22–46.

Shim, J. and Lee, J. (2013). Dark Sector Coupling Bends the Superclusters. *ApJ* , 777(1):74.

Silva, D. R., Kuntschner, H., and Lyubenova, M. (2008). A New Approach to the Study of Stellar Populations in Early-Type Galaxies: K-Band Spectral Indices and an Application to the Fornax Cluster. *ApJ* , 674(1):194–208.

Skelton, R. E., Woudt, P. A., and Kraan-Korteweg, R. C. (2009). The Norma cluster (ACO3627) - II. The near-infrared K_s-band luminosity function. *MNRAS* , 396(4):2367–2378.

Skrutskie, M. F., Cutri, R. M., Stiening, R., Weinberg, M. D., Schneider, S., Carpenter, J. M., Beichman, C., Capps, R., Chester, T., Elias, J., Huchra, J., Liebert, J., Lonsdale, C., Monet, D. G., Price, S., Seitzer, P., Jarrett, T., Kirkpatrick, J. D., Gizis, J. E., Howard, E., Evans, T., Fowler, J., Fullmer, L., Hurt, R., Light, R., Kopan, E. L., Marsh, K. A., McCallon, H. L., Tam, R., Van Dyk, S., and Wheelock, S. (2006). The Two Micron All Sky Survey (2MASS). *AJ* , 131:1163–1183.

Smail, I., Edge, A. C., Ellis, R. S., and Blandford, R. D. (1998). A statistical analysis of the galaxy populations of distant luminous X-ray clusters. *MNRAS* , 293(2):124–144.

Smith, G. P., Kneib, J.-P., Smail, I., Mazzotta, P., Ebeling, H., and Czoske, O. (2005). A Hubble Space Telescope lensing survey of X-ray luminous galaxy clusters - IV. Mass, structure and thermodynamics of cluster cores at z= 0.2. *MNRAS* , 359(2):417–446.

Smith, S. (1935). Some Notes on the Structure of Elliptical Nebulae. *ApJ* , 82:192.

Smoot, G. F., Gorenstein, M. V., and Muller, R. A. (1977). Detection of Anisotropy in the Cosmic Blackbody Radiation. *PRL* , 39(14):898–901.

Solanes, J. M., Manrique, A., García-Gómez, C., González-Casado, G., Giovanelli, R., and Haynes, M. P. (2001). The H I Content of Spirals. II. Gas Deficiency in Cluster Galaxies. *ApJ* , 548(1):97–113.

Solanes, J. M., Salvador-Solé, E., and González-Casado, G. (1999). Substructure in the ENACS clusters. *A&A* , 343:733–739.

Sorce, J. G., Colless, M., Kraan-Korteweg, R. C., and Gottlöber, S. (2017). Predicting structures in the Zone of Avoidance. *MNRAS* , 471(3):3087–3097.

Springel, V., White, S. D. M., Jenkins, A., Frenk, C. S., Yoshida, N., Gao, L., Navarro, J., Thacker, R., Croton, D., Helly, J., Peacock, J. A., Cole, S., Thomas, P., Couchman, H., Evrard, A., Colberg, J., and Pearce, F. (2005). Simulations of the formation, evolution and clustering of galaxies and quasars. *Nature* , 435(7042):629–636.

Springob, C. M., Hong, T., Staveley-Smith, L., Masters, K. L., Macri, L. M., Koribalski, B. S., Jones, D. H., Jarrett, T. H., Magoulas, C., and Erdoğdu, P. (2016). 2MTF - V. Cosmography, β, and the residual bulk flow. *MNRAS* , 456(2):1886–1900.

Springob, C. M., Magoulas, C., Colless, M., Mould, J., Erdoğdu, P., Jones, D. H., Lucey, J. R., Campbell, L., and Fluke, C. J. (2014). The 6dF Galaxy Survey: peculiar velocity field and cosmography. *MNRAS* , 445:2677–2697.

Springob, C. M., Masters, K. L., Haynes, M. P., Giovanelli, R., and Marinoni, C. (2007). SFI++. II. A New I-Band Tully-Fisher Catalog, Derivation of Peculiar Velocities, and Data Set Properties. *ApJS* , 172:599–614.

Stanford, S. A., Eisenhardt, P. R., and Dickinson, M. (1998). The Evolution of Early-Type Galaxies in Distant Clusters. *ApJ* , 492(2):461–479.

Stanford, S. A., Eisenhardt, P. R. M., and Dickinson, M. (1995). Evolution of Infrared-selected Galaxies in Z approximately 0.4 Clusters. *ApJ* , 450:512.

Staveley-Smith, L., Kraan-Korteweg, R. C., Schröder, A. C., Henning, P. A., Koribalski, B. S., Stewart, I. M., and Heald, G. (2016). The Parkes H I Zone of Avoidance Survey. *AJ* , 151(3):52.

Stott, J. P., Pimbblet, K. A., Edge, A. C., Smith, G. P., and Wardlow, J. L. (2009). The evolution of the red sequence slope in massive galaxy clusters. *MNRAS* , 394:2098–2108.

Stott, J. P., Smail, I., Edge, A. C., Ebeling, H., Smith, G. P., Kneib, J.-P., and Pimbblet, K. A. (2007). An Increase in the Faint Red Galaxy Population in Massive Clusters since z ˜ 0.5. *ApJ* , 661:95–101.

Strateva, I., Ivezić, Ž., Knapp, G. R., Narayanan, V. K., Strauss, M. A., Gunn, J. E., Lupton, R. H., Schlegel, D., Bahcall, N. A., Brinkmann, J., Brunner, R. J., Budavári, T., Csabai, I., Castander, F. J., Doi, M., Fukugita, M., Győry, Z., Hamabe, M., Hennessy, G., Ichikawa, T., Kunszt, P. Z., Lamb, D. Q., McKay, T. A., Okamura, S., Racusin, J., Sekiguchi, M., Schneider, D. P., Shimasaku, K., and York, D. (2001). Color Separation of Galaxy Types in the Sloan Digital Sky Survey Imaging Data. *AJ* , 122(4):1861–1874.

Struble, M. F. and Rood, H. J. (1991). A Compilation of Redshifts and Velocity Dispersions for Abell Clusters (Epoch 1991.2). *ApJS* , 77:363.

Tabur, V. (2007). Fast Algorithms for Matching CCD Images to a Stellar Catalogue. *PASA* , 24:189–198.

Tammann, G. A. and Kraan, R. (1978). The Galactic Neighbourhood. In Longair, M. S. and Einasto, J., editors, *Large Scale Structures in the Universe*, volume 79, page 71.

Tamura, T., Fukazawa, Y., Kaneda, H., Makishima, K., Tashiro, M., Tanaka, Y., and Bohringer, H. (1998). ASCA Observations of a Nearby and Massive Galaxy Cluster Abell 3627. *PASJ* , 50:195–201.

Tanaka, M., Kodama, T., Arimoto, N., Okamura, S., Umetsu, K., Shimasaku, K., Tanaka, I., and Yamada, T. (2005). The build-up of the colour-magnitude relation as a function of environment. *MNRAS* , 362(1):268–288.

Tempel, E., Saar, E., Liivamägi, L. J., Tamm, A., Einasto, J., Einasto, M., and Müller, V. (2011). Galaxy morphology, luminosity, and environment in the SDSS DR7. *A&A* , 529:A53.

Thompson, L. A. and Gregory, S. A. (1980). The luminosity function of Coma cluster galaxies. *ApJ* , 242:1–7.

Tully, R. B., Courtois, H., Hoffman, Y., and Pomarède, D. (2014). The Laniakea supercluster of galaxies. *Nature* , 513:71–73.

Tully, R. B., Courtois, H. M., and Sorce, J. G. (2016). Cosmicflows-3. *AJ* , 152(2):50.

Tully, R. B., Shaya, E. J., Karachentsev, I. D., Courtois, H. M., Kocevski, D. D., Rizzi, L., and Peel, A. (2008). Our Peculiar Motion Away from the Local Void. *ApJ* , 676:184–205.

Valluri, M. (1993). Compressive Tidal Heating of a Disk Galaxy in a Rich Cluster. *ApJ* , 408:57.

van Driel, W., Schneider, S. E., Kraan-Korteweg, R. C., and Monnier Ragaigne, D. (2009). H I line observations of 2MASS galaxies in the zone of avoidance. *A&A* , 505:29–44.

van Haarlem, M. P., Frenk, C. S., and White, S. D. M. (1997). Projection effects in cluster catalogues. *MNRAS* , 287(4):817–832.

Visvanathan, N. and Sandage, A. (1977). The color - absolute magnitude relation for E and S0 galaxies. I. Calibration and tests for universality using Virgo and eight other nearby clusters. *ApJ* , 216:214–226.

Vogt, N. P., Haynes, M. P., Giovanelli, R., and Herter, T. (2004). M/L, Hα Rotation Curves, and H I Gas Measurements for 329 Nearby Cluster and Field Spirals. II. Evidence for Galaxy Infall. *AJ* , 127(6):3300–3324.

Vulcani, B., Poggianti, B. M., Aragón-Salamanca, A., Fasano, G., Rudnick, G., Valentinuzzi, T., Dressler, A., Bettoni, D., Cava, A., D'Onofrio, M., Fritz, J., Moretti, A., Omizzolo, A., and Varela, J. (2011). Galaxy stellar mass functions of different morphological types in clusters, and their evolution between z= 0.8 and 0. *MNRAS* , 412(1):246–268.

Wang, S., Jiang, B. W., Zhao, H., Chen, X., and de Grijs, R. (2017). The Optical-Mid-infrared Extinction Law of the l = 165° Sightline in the Galactic Plane: Diversity of the Extinction Law in the Diffuse Interstellar Medium. *ApJ* , 848(2):106.

Watkins, R., Feldman, H. A., and Hudson, M. J. (2009). Consistently large cosmic flows on scales of 100h^{-1}Mpc: a challenge for the standard ΛCDM cosmology. *MNRAS* , 392(2):743–756.

Wegner, G., Colless, M., Saglia, R. P., McMahan, R. K., Davies, R. L., Burstein, D., and Baggley, G. (1999). The peculiar motions of early-type galaxies in two distant regions - II. The spectroscopic data. *MNRAS* , 305(2):259–296.

White, S. D. M. and Rees, M. J. (1978). Core condensation in heavy halos: a two-stage theory for galaxy formation and clustering. *MNRAS* , 183:341–358.

Williams, W. L. (2011). A Near Infrared Tully-Fisher Survey Behind the Galactic Plane. Master's thesis, Univ. Cape Town.

Willick, J. A., Courteau, S., Faber, S. M., Burstein, D., Dekel, A., and Strauss, M. A. (1997). Homogeneous Velocity-Distance Data for Peculiar Velocity Analysis. III. The Mark III Catalog of Galaxy Peculiar Velocities. *ApJS* , 109(2):333–366.

Wirth, A. and Gallagher, J. S., I. (1984). The families of elliptical-like galaxies. *ApJ* , 282:85–94.

Wolf, C., Gray, M. E., and Meisenheimer, K. (2005). Red-sequence galaxies with young stars and dust: the cluster Abell 901/902 seen with COMBO-17. *A&A* , 443(2):435–449.

Woudt, P. A. (1998). PhD thesis, , Univ. of Cape Town, South Africa, (1998).

Woudt, P. A., Fairall, A., Kraan-Korteweg, R. C., Lucey, J., Schröder, A., Burstein, D., and McCall, M. L. (2005). Peculiar Velocities in the Zone of Avoidance: Determining the Distance to the Norma cluster. In Fairall, A. P. and Woudt, P. A., editors, *Nearby Large-Scale Structures and the Zone of Avoidance*, volume 329 of *Astronomical Society of the Pacific Conference Series*, page 147.

Woudt, P. A., Kraan-Korteweg, R. C., Lucey, J., Fairall, A. P., and Moore, S. A. W. (2008). The Norma cluster (ACO 3627) - I. A dynamical analysis of the most massive cluster in the Great Attractor. *MNRAS* , 383(2):445–457.

Wray, J. J., Bahcall, N. A., Bode, P., Boettiger, C., and Hopkins, P. F. (2006). The Shape, Multiplicity, and Evolution of Superclusters in ΛCDM Cosmology. *ApJ* , 652(2):907–916.

Yagi, M., Kashikawa, N., Sekiguchi, M., Doi, M., Yasuda, N., Shimasaku, K., and Okamura, S. (2002). Luminosity Functions of 10 Nearby Clusters of Galaxies. II. Analysis of the Luminosity Function. *AJ* , 123(1):87–99.

Yahil, A. and Vidal, N. V. (1977). The Velocity Distribution of Galaxies in Clusters. *ApJ* , 214:347–350.

Yamanoi, H., Komiyama, Y., Yagi, M., Okamura, S., Iye, M., Kashikawa, N., Takata, T., Furusawa, H., and Yoshida, M. (2012). The Galaxy Luminosity Functions down to M_R = -10 in the Coma Cluster. *AJ* , 144(2):40.

Yee, H. K. C., Gladders, M. D., and López-Cruz, O. (1999). The Color-Magnitude Relation of Early-Type Galaxies: A Tool for Cluster Finding and Redshift Determination. In Weymann, R., Storrie-Lombardi, L., Sawicki, M., and Brunner, R., editors, *Photometric Redshifts and the Detection of High Redshift Galaxies*, volume 191 of *Astronomical Society of the Pacific Conference Series*, page 166.

Yoon, H., Chung, A., Smith, R., and Jaffé, Y. L. (2017). A History of H I Stripping in Virgo: A Phase-space View of VIVA Galaxies. *ApJ* , 838(2):81.

York, D. G., Adelman, J., Anderson, Jr., J. E., Anderson, S. F., Annis, J., Bahcall, N. A., Bakken, J. A., Barkhouser, R., Bastian, S., Berman, E., Boroski, W. N., Bracker, S., Briegel, C., Briggs, J. W., Brinkmann, J., Brunner, R., Burles, S., Carey, L., Carr, M. A., Castander, F. J., Chen, B., Colestock, P. L., Connolly, A. J., Crocker, J. H., Csabai, I., Czarapata, P. C., Davis, J. E., Doi, M., Dombeck, T., Eisenstein, D., Ellman, N., Elms, B. R., Evans, M. L., Fan, X., Federwitz, G. R., Fiscelli, L., Friedman, S.,

Frieman, J. A., Fukugita, M., Gillespie, B., Gunn, J. E., Gurbani, V. K., de Haas, E., Haldeman, M., Harris, F. H., Hayes, J., Heckman, T. M., Hennessy, G. S., Hindsley, R. B., Holm, S., Holmgren, D. J., Huang, C.-h., Hull, C., Husby, D., Ichikawa, S.-I., Ichikawa, T., Ivezić, Ž., Kent, S., Kim, R. S. J., Kinney, E., Klaene, M., Kleinman, A. N., Kleinman, S., Knapp, G. R., Korienek, J., Kron, R. G., Kunszt, P. Z., Lamb, D. Q., Lee, B., Leger, R. F., Limmongkol, S., Lindenmeyer, C., Long, D. C., Loomis, C., Loveday, J., Lucinio, R., Lupton, R. H., MacKinnon, B., Mannery, E. J., Mantsch, P. M., Margon, B., McGehee, P., McKay, T. A., Meiksin, A., Merelli, A., Monet, D. G., Munn, J. A., Narayanan, V. K., Nash, T., Neilsen, E., Neswold, R., Newberg, H. J., Nichol, R. C., Nicinski, T., Nonino, M., Okada, N., Okamura, S., Ostriker, J. P., Owen, R., Pauls, A. G., Peoples, J., Peterson, R. L., Petravick, D., Pier, J. R., Pope, A., Pordes, R., Prosapio, A., Rechenmacher, R., Quinn, T. R., Richards, G. T., Richmond, M. W., Rivetta, C. H., Rockosi, C. M., Ruthmansdorfer, K., Sandford, D., Schlegel, D. J., Schneider, D. P., Sekiguchi, M., Sergey, G., Shimasaku, K., Siegmund, W. A., Smee, S., Smith, J. A., Snedden, S., Stone, R., Stoughton, C., Strauss, M. A., Stubbs, C., SubbaRao, M., Szalay, A. S., Szapudi, I., Szokoly, G. P., Thakar, A. R., Tremonti, C., Tucker, D. L., Uomoto, A., Vanden Berk, D., Vogeley, M. S., Waddell, P., Wang, S.-i., Watanabe, M., Weinberg, D. H., Yanny, B., Yasuda, N., and SDSS Collaboration (2000). The Sloan Digital Sky Survey: Technical Summary. *AJ* , 120:1579–1587.

Zenteno, A., Mohr, J. J., Desai, S., Stalder, B., Saro, A., Dietrich, J. P., Bayliss, M., Bocquet, S., Chiu, I., Gonzalez, A. H., Gangkofner, C., Gupta, N., Hlavacek-Larrondo, J., McDonald, M., Reichardt, C., and Rest, A. (2016). Galaxy populations in the 26 most massive galaxy clusters in the South Pole Telescope SPT-SZ survey. *MNRAS* , 462(1):830–843.

Zwicky, F. (1933). Die Rotverschiebung von extragalaktischen Nebeln. *Helvetica Physica Acta*, 6:110–127.

Zwicky, F. (1937). On the Masses of Nebulae and of Clusters of Nebulae. *ApJ* , 86:217.

Zwicky, F. (1957). *Morphological astronomy.*

Zwicky, F. (1964). The Luminosity Function of Galaxies. *ApJ* , 140:1626–1628.

Zwicky, F., Herzog, E., and Wild, P. (1968). *Catalogue of galaxies and of clusters of galaxies.*

Zwicky, F., Herzog, E., Wild, P., Karpowicz, M., and Kowal, C. T. (1961). *Catalogue of galaxies and of clusters of galaxies, Vol. I.*

Zwicky, I. F. (1942). On the Clustering of Nebulae. *ApJ* , 95:555.

Appendix A

Galaxy catalogues of the VSCL clusters

Table A.0.1: VC02 catalogue of galaxies

Designation	ℓ (deg)	b (deg)	e_J	ϕ_J (deg)	r_{k20fe} (arcsec)	J_{k20fe} (mag)	H_{k20fe} (mag)	$K_{s_{k20fe}}$ (mag)	J_{tot} (mag)	H_{tot} (mag)	$K_{s_{tot}}$ (mag)	μ_J	μ_H (mag arcsec^{-2})	μ_{Ks}	$E(B-V)$ (mag)
$ZOA081230.433-493116.48$	264.934	−8.436	0.23	53.73	3.41	16.55 ± 0.05	15.84 ± 0.04	15.31 ± 0.05	–	15.45 ± 0.06	14.78 ± 0.10	19.57	18.95	18.49	0.31
$ZOA081238.669-493340.38$	264.980	−8.439	0.04	35.78	4.22	15.61 ± 0.03	14.91 ± 0.03	14.22 ± 0.03	15.44 ± 0.07	–	14.13 ± 0.03	18.97	18.28	17.63	0.31
$ZOA081230.932-493327.72$	264.966	−8.455	0.12	−50.27	2.28	17.83 ± 0.09	16.81 ± 0.06	15.96 ± 0.06	–	–	14.85 ± 0.23	21.05	19.78	18.86	0.31
$ZOA081231.738-493702.28$	265.018	−8.485	0.36	−12.94	10.78	13.08 ± 0.02	12.30 ± 0.02	11.95 ± 0.02	12.09 ± 0.31	12.14 ± 0.04	11.82 ± 0.03	16.85	16.07	15.70	0.31
$ZOA081220.493-493542.14$	264.982	−8.499	0.26	69.96	3.30	16.52 ± 0.05	15.79 ± 0.04	15.22 ± 0.04	–	14.63 ± 0.36	14.55 ± 0.15	19.70	19.03	18.46	0.31
$ZOA081258.729-493454.23$	265.027	−8.404	0.29	−5.52	2.35	17.41 ± 0.07	16.39 ± 0.04	15.91 ± 0.06	–	–	–	20.25	19.27	18.96	0.31
$ZOA081253.467-493724.81$	265.055	−8.439	0.30	56.39	2.90	17.45 ± 0.08	16.68 ± 0.06	15.86 ± 0.06	–	–	–	20.34	19.66	18.87	0.31
$ZOA081257.124-493208.45$	264.985	−8.383	0.01	−54.51	1.91	18.13 ± 0.11	17.16 ± 0.07	16.30 ± 0.07	–	17.16 ± 0.07	16.10 ± 0.09	22.50	21.00	19.85	0.31
$ZOA081236.707-493209.33$	264.956	−8.430	0.10	14.22	2.49	17.04 ± 0.06	16.25 ± 0.04	15.78 ± 0.05	–	–	14.09 ± 0.51	20.07	19.36	19.01	0.31
$ZOA081252.596-493450.27$	265.017	−8.418	0.29	−89.73	2.45	16.84 ± 0.05	16.09 ± 0.04	15.63 ± 0.05	12.82 ± 1.22	15.11 ± 0.24	–	19.77	19.08	18.65	0.31
$ZOA081251.848-493506.34$	265.020	−8.422	0.17	−58.12	1.49	18.73 ± 0.17	17.57 ± 0.09	16.66 ± 0.09	–	–	15.82 ± 0.28	21.55	21.54	19.86	0.31
$ZOA081252.255-493518.46$	265.023	−8.423	0.18	−6.52	2.37	18.29 ± 0.12	17.48 ± 0.08	16.44 ± 0.08	–	–	–	20.85	20.47	19.38	0.31
$ZOA081234.026-493728.42$	265.027	−8.483	0.14	12.44	2.15	18.32 ± 0.12	17.30 ± 0.08	16.50 ± 0.08	–	–	–	22.32	20.60	19.60	0.31
$ZOA081232.248-493457.38$	264.989	−8.465	0.41	57.79	2.57	17.98 ± 0.10	17.12 ± 0.07	16.28 ± 0.07	–	–	12.48 ± 1.04	20.71	20.13	19.15	0.31
$ZOA081012.441-494001.20$	264.858	−8.829	0.48	−5.22	2.25	17.61 ± 0.06	16.95 ± 0.05	16.05 ± 0.06	–	–	15.19 ± 0.26	21.32	20.36	19.70	0.25
$ZOA080954.612-494053.77$	264.844	−8.878	0.39	−36.06	3.07	17.16 ± 0.05	16.48 ± 0.04	15.56 ± 0.06	–	–	–	20.22	19.65	18.71	0.25
$ZOA081018.202-493755.26$	264.836	−8.798	0.45	0.86	1.72	18.16 ± 0.09	17.43 ± 0.08	16.37 ± 0.10	–	–	16.36 ± 0.10	21.17	22.03	21.16	0.25
$ZOA081018.164-493741.37$	264.833	−8.796	0.26	−48.87	3.24	17.28 ± 0.06	16.88 ± 0.06	15.73 ± 0.07	–	15.29 ± 0.44	14.47 ± 0.32	20.20	19.76	18.93	0.25
$ZOA081040.628-493812.99$	264.873	−8.749	0.38	−8.96	2.30	17.79 ± 0.07	16.87 ± 0.06	16.58 ± 0.10	–	–	16.27 ± 0.11	20.69	19.74	19.64	0.27
$ZOA081032.647-493306.65$	264.788	−8.722	0.33	−28.14	2.61	17.62 ± 0.07	16.93 ± 0.05	16.09 ± 0.07	–	–	15.07 ± 0.30	20.80	20.42	19.37	0.27
$ZOA081029.820-493332.01$	264.790	−8.732	0.34	66.73	3.54	15.97 ± 0.03	15.21 ± 0.03	14.85 ± 0.04	15.61 ± 0.10	14.84 ± 0.05	–	19.19	18.41	18.14	0.27
$ZOA081049.437-493659.55$	264.868	−8.718	0.34	36.85	3.43	16.87 ± 0.05	16.01 ± 0.04	15.20 ± 0.05	16.75 ± 0.07	15.85 ± 0.04	15.03 ± 0.06	20.27	19.32	18.51	0.27
$ZOA081026.136-493659.60$	264.834	−8.771	0.14	−25.19	2.80	16.30 ± 0.04	15.58 ± 0.03	14.86 ± 0.04	–	14.33 ± 0.36	14.83 ± 0.04	19.56	18.78	18.32	0.27
$ZOA081008.570-493235.98$	264.746	−8.773	0.58	−73.22	5.54	15.91 ± 0.03	15.11 ± 0.03	14.72 ± 0.04	15.44 ± 0.19	14.92 ± 0.05	14.01 ± 0.18	19.32	18.54	18.10	0.27
$ZOA081034.268-493136.73$	264.769	−8.705	0.32	−51.66	2.10	18.46 ± 0.10	17.35 ± 0.07	16.66 ± 0.09	–	–	14.12 ± 0.73	21.40	20.60	19.66	0.27
$ZOA081031.037-493147.73$	264.767	−8.714	0.78	23.66	5.30	14.33 ± 0.02	13.41 ± 0.02	12.85 ± 0.02	13.80 ± 0.17	13.21 ± 0.06	–	17.79	16.87	16.33	0.27
$ZOA081044.937-492343.94$	264.672	−8.611	0.11	32.96	3.16	16.09 ± 0.04	15.46 ± 0.03	14.91 ± 0.06	15.84 ± 0.08	15.38 ± 0.10	14.50 ± 0.13	19.32	18.66	17.97	0.30
$ZOA081037.527-491807.04$	264.581	−8.578	0.25	−69.81	2.44	17.00 ± 0.05	16.33 ± 0.04	15.94 ± 0.06	–	15.98 ± 0.06	15.44 ± 0.11	20.05	19.41	19.09	0.30
$ZOA081056.719-491939.73$	264.631	−8.548	0.15	29.68	7.81	15.10 ± 0.03	14.47 ± 0.03	13.98 ± 0.03	12.07 ± 0.94	12.46 ± 0.20	12.78 ± 0.30	18.59	17.96	17.49	0.30
$ZOA081052.781-492037.25$	264.639	−8.565	0.31	81.85	2.70	16.64 ± 0.04	15.96 ± 0.03	15.49 ± 0.04	–	15.46 ± 0.14	15.39 ± 0.05	19.83	19.11	18.70	0.30
$ZOA081101.808-492055.29$	264.657	−8.547	0.35	−6.10	3.17	17.28 ± 0.06	16.46 ± 0.04	15.90 ± 0.07	–	15.43 ± 0.29	15.37 ± 0.09	20.16	19.34	19.01	0.30
$ZOA081054.117-492244.54$	264.671	−8.581	0.32	78.92	2.75	18.07 ± 0.08	17.13 ± 0.06	16.22 ± 0.07	–	–	16.02 ± 0.07	21.05	20.23	19.36	0.30
$ZOA081049.132-491757.11$	264.596	−8.550	0.21	−20.74	2.16	17.14 ± 0.05	16.42 ± 0.04	15.76 ± 0.05	–	–	15.32 ± 0.11	20.15	19.40	18.94	0.30
$ZOA081046.742-491701.41$	264.579	−8.547	0.16	28.41	1.94	17.35 ± 0.06	16.59 ± 0.04	15.87 ± 0.06	–	–	15.48 ± 0.13	20.45	19.75	19.15	0.30
$ZOA081038.048-491745.13$	264.577	−8.574	0.19	13.50	7.09	14.87 ± 0.03	14.13 ± 0.02	13.82 ± 0.03	–	13.48 ± 0.12	13.29 ± 0.07	18.49	17.75	17.42	0.30
$ZOA081217.975-492300.08$	264.798	−8.391	0.16	17.08	2.90	16.77 ± 0.05	16.19 ± 0.05	15.34 ± 0.05	–	15.39 ± 0.25	15.14 ± 0.07	19.92	19.49	18.76	0.30
$ZOA081240.263-491642.56$	264.741	−8.284	0.09	−14.53	4.30	15.91 ± 0.04	15.15 ± 0.03	14.67 ± 0.04	15.58 ± 0.14	14.76 ± 0.11	14.20 ± 0.09	19.21	18.50	17.97	0.30
$ZOA081233.070-491932.64$	264.771	−8.325	0.09	−47.70	4.25	16.60 ± 0.05	15.83 ± 0.04	15.44 ± 0.06	15.13 ± 0.56	–	14.58 ± 0.11	19.63	18.84	18.45	0.30
$ZOA081217.959-492225.14$	264.790	−8.386	0.26	−57.57	3.60	17.07 ± 0.06	16.24 ± 0.05	15.38 ± 0.05	–	14.66 ± 0.52	–	20.11	19.50	18.51	0.30
$ZOA081249.271-491828.02$	264.780	−8.279	0.23	62.12	2.58	17.43 ± 0.07	16.78 ± 0.06	16.05 ± 0.06	–	–	15.64 ± 0.08	20.61	19.86	19.15	0.30
$ZOA081226.415-491641.01$	264.720	−8.315	0.05	83.69	2.31	18.06 ± 0.12	17.10 ± 0.07	16.26 ± 0.07	–	–	–	20.70	20.02	19.07	0.30
$ZOA081218.002-491759.56$	264.727	−8.346	0.53	69.64	6.32	14.23 ± 0.02	14.09 ± 0.02	13.75 ± 0.03	13.94 ± 0.08	13.30 ± 0.23	12.83 ± 0.25	17.67	17.52	17.19	0.30
$ZOA081145.719-490942.53$	264.561	−8.346	0.15	−64.64	2.04	17.84 ± 0.07	17.09 ± 0.05	16.34 ± 0.07	–	–	15.22 ± 0.29	20.81	20.11	19.48	0.26
$ZOA081205.546-491018.23$	264.599	−8.306	0.23	19.64	9.22	13.51 ± 0.02	12.74 ± 0.02	12.39 ± 0.02	12.86 ± 0.21	12.39 ± 0.09	12.07 ± 0.06	17.23	16.45	16.09	0.26
$ZOA081210.478-491032.38$	264.610	−8.297	0.34	23.71	4.83	15.32 ± 0.03	14.58 ± 0.03	14.21 ± 0.03	14.66 ± 0.21	13.67 ± 0.20	13.45 ± 0.22	18.72	17.92	17.61	0.26
$ZOA081159.570-491450.20$	264.655	−8.360	0.61	−18.40	11.03	13.98 ± 0.02	13.19 ± 0.02	12.77 ± 0.02	13.63 ± 0.12	–	12.49 ± 0.07	17.68	16.90	16.48	0.26
$ZOA081218.357-491610.04$	264.701	−8.329	0.83	−50.55	4.74	16.18 ± 0.04	15.24 ± 0.03	14.81 ± 0.05	15.75 ± 0.31	14.52 ± 0.21	14.48 ± 0.06	19.56	18.62	18.20	0.26
$ZOA081210.202-491606.49$	264.688	−8.347	0.27	−76.41	3.22	17.52 ± 0.06	16.64 ± 0.05	15.91 ± 0.07	–	–	14.75 ± 0.30	20.46	19.75	18.92	0.26
$ZOA081209.934-491144.91$	264.626	−8.309	0.39	11.33	2.92	16.96 ± 0.05	16.25 ± 0.04	15.76 ± 0.05	–	15.14 ± 0.29	14.59 ± 0.32	19.95	19.26	19.00	0.26
$ZOA081210.640-491109.56$	264.619	−8.302	0.43	0.90	2.22	17.23 ± 0.05	16.52 ± 0.04	16.17 ± 0.07	–	–	15.00 ± 0.31	20.30	19.57	19.26	0.26
$ZOA081218.457-491402.50$	264.671	−8.310	0.05	8.55	2.22	17.33 ± 0.07	16.58 ± 0.05	15.99 ± 0.06	–	–	15.86 ± 0.07	20.56	19.85	19.14	0.31
$ZOA081248.308-491537.36$	264.738	−8.255	0.15	−77.90	2.25	17.77 ± 0.08	16.93 ± 0.07	15.92 ± 0.06	–	–	–	21.44	21.04	19.17	0.31
$ZOA081232.207-491047.37$	264.645	−8.249	0.17	−68.54	3.25	16.56 ± 0.05	15.64 ± 0.03	14.91 ± 0.04	–	15.06 ± 0.15	14.65 ± 0.05	19.75	18.85	18.14	0.31
$ZOA081227.729-490938.51$	264.622	−8.249	0.19	−60.39	3.29	16.51 ± 0.05	15.63 ± 0.04	15.29 ± 0.05	–	15.44 ± 0.04	15.20 ± 0.05	19.82	18.92	18.59	0.31
$ZOA081140.039-491634.05$	264.651	−8.420	0.29	−78.09	3.21	16.38 ± 0.04	15.76 ± 0.04	15.03 ± 0.04	–	–	–	19.68	18.85	18.20	0.27
$ZOA081146.435-491551.01$	264.650	−8.399	0.12	15.74	2.68	17.36 ± 0.06	16.57 ± 0.04	15.67 ± 0.05	–	–	15.38 ± 0.07	20.35	19.57	18.90	0.27

ZOA081124.229 − 491132.44	264.556	−8.412	0.53	−69.66	4.77	15.83 ± 0.03	14.96 ± 0.03	14.40 ± 0.03	14.88 ± 0.32	14.70 ± 0.07	13.96 ± 0.12	19.21	18.34	17.78	0.27
ZOA081145.567 − 491212.38	264.597	−8.369	0.54	−33.17	3.89	15.91 ± 0.03	15.21 ± 0.03	14.87 ± 0.04	14.54 ± 0.42	13.32 ± 0.56	14.68 ± 0.05	19.10	18.48	18.22	0.27
ZOA081139.320 − 491248.27	264.596	−8.389	0.23	−4.03	1.92	18.33 ± 0.09	17.42 ± 0.07	16.55 ± 0.09	–	–	16.54 ± 0.09	21.50	20.42	19.84	0.27
ZOA081134.761 − 491435.02	264.615	−8.415	0.29	−48.47	4.08	16.38 ± 0.04	15.72 ± 0.03	15.10 ± 0.05	–	15.35 ± 0.12	14.54 ± 0.12	19.63	19.11	18.36	0.27
ZOA081136.194 − 491520.80	264.628	−8.418	0.10	−42.67	3.38	16.95 ± 0.05	16.24 ± 0.04	15.71 ± 0.06	–	15.99 ± 0.05	14.80 ± 0.19	20.06	19.41	18.86	0.27
ZOA081130.908 − 490924.37	264.535	−8.378	0.14	66.20	2.71	17.61 ± 0.07	16.66 ± 0.05	15.71 ± 0.06	–	–	15.45 ± 0.07	20.67	19.72	18.92	0.27
ZOA081126.922 − 491141.14	264.562	−8.407	0.29	51.52	2.48	18.37 ± 0.10	17.60 ± 0.08	16.64 ± 0.09	–	–	15.62 ± 0.17	21.40	20.54	19.54	0.27
ZOA081117.227 − 490940.84	264.519	−8.412	0.33	−89.92	2.59	17.24 ± 0.06	16.59 ± 0.05	15.74 ± 0.05	–	16.15 ± 0.08	15.35 ± 0.08	19.90	19.61	18.98	0.27
ZOA080903.639 − 493824.21	264.735	−8.973	0.09	11.06	2.13	17.46 ± 0.07	17.31 ± 0.09	15.94 ± 0.07	–	–	15.64 ± 0.09	20.63	19.76	19.21	0.28
ZOA080907.506 − 493733.88	264.729	−8.956	0.36	−11.02	3.63	16.57 ± 0.04	15.86 ± 0.04	15.38 ± 0.04	–	–	–	19.58	18.86	18.42	0.28
ZOA080913.784 − 493736.98	264.738	−8.942	0.30	51.63	4.89	15.63 ± 0.03	14.84 ± 0.03	14.36 ± 0.03	13.95 ± 0.56	13.88 ± 0.27	12.16 ± 0.65	18.98	18.18	17.73	0.28
ZOA080856.857 − 493259.06	264.648	−8.941	0.39	72.15	4.00	15.80 ± 0.03	14.98 ± 0.03	14.54 ± 0.03	14.81 ± 0.32	14.50 ± 0.09	14.36 ± 0.04	19.11	18.26	17.91	0.28
ZOA080859.268 − 493657.03	264.708	−8.970	0.50	−54.45	4.11	16.45 ± 0.04	15.63 ± 0.03	15.01 ± 0.04	15.72 ± 0.26	15.24 ± 0.09	14.83 ± 0.04	19.72	18.88	18.38	0.28
ZOA080836.714 − 493201.49	264.605	−8.978	0.19	29.02	3.27	16.99 ± 0.07	16.05 ± 0.05	15.28 ± 0.05	–	15.22 ± 0.25	14.47 ± 0.22	20.18	19.23	18.54	0.28
ZOA080843.637 − 493245.95	264.625	−8.969	0.05	−70.51	3.50	16.67 ± 0.05	15.75 ± 0.04	15.06 ± 0.04	–	15.38 ± 0.07	14.65 ± 0.07	19.82	18.90	18.29	0.28
ZOA080857.726 − 493412.56	264.666	−8.949	0.76	−7.02	6.00	17.82 ± 0.09	16.80 ± 0.06	16.26 ± 0.08	–	16.06 ± 0.20	15.78 ± 0.11	20.74	19.79	19.54	0.28
ZOA080853.359 − 493129.03	264.621	−8.935	0.12	−56.31	2.49	17.51 ± 0.08	17.59 ± 0.12	15.97 ± 0.07	–	15.52 ± 0.41	14.45 ± 0.44	20.90	19.76	19.27	0.28
ZOA080912.547 − 492419.01	264.546	−8.828	0.30	−82.24	2.11	17.88 ± 0.09	17.18 ± 0.07	16.61 ± 0.09	–	–	15.86 ± 0.12	20.74	20.22	19.55	0.28
ZOA080902.615 − 492424.21	264.533	−8.852	0.14	−35.47	2.74	17.09 ± 0.06	16.21 ± 0.04	15.81 ± 0.05	–	11.79 ± 1.36	–	20.27	19.40	18.92	0.28
ZOA080846.886 − 492436.10	264.513	−8.890	0.49	62.52	4.46	15.59 ± 0.03	14.77 ± 0.03	14.45 ± 0.03	15.43 ± 0.06	14.60 ± 0.03	13.62 ± 0.23	18.99	18.17	17.82	0.28
ZOA080854.454 − 492822.35	264.578	−8.906	0.22	67.42	2.75	17.24 ± 0.06	16.48 ± 0.05	15.75 ± 0.05	–	–	15.56 ± 0.05	20.54	19.88	18.94	0.28
ZOA080858.506 − 492930.25	264.600	−8.906	0.35	49.08	3.04	16.93 ± 0.05	16.08 ± 0.04	15.52 ± 0.04	16.63 ± 0.14	15.85 ± 0.06	14.82 ± 0.12	19.96	19.29	18.58	0.28
ZOA080912.384 − 492900.69	264.613	−8.870	0.19	5.67	2.53	17.97 ± 0.09	16.93 ± 0.06	15.96 ± 0.05	–	–	14.74 ± 0.32	20.81	20.15	19.10	0.28
ZOA080837.214 − 492458.64	264.504	−8.915	0.09	−2.80	4.67	16.15 ± 0.04	15.29 ± 0.03	14.71 ± 0.04	–	14.38 ± 0.27	14.21 ± 0.10	19.44	18.61	18.00	0.28
ZOA080838.484 − 492521.58	264.512	−8.916	0.52	47.45	3.49	18.16 ± 0.10	17.14 ± 0.07	16.79 ± 0.09	–	–	–	20.31	19.54	19.42	0.28
ZOA080859.369 − 492358.02	264.522	−8.856	0.26	−50.93	3.37	15.81 ± 0.03	15.22 ± 0.03	14.96 ± 0.04	13.15 ± 0.75	14.07 ± 0.18	9.66 ± 1.66	18.88	18.34	18.23	0.28
ZOA080856.463 − 492738.60	264.570	−8.895	0.08	47.88	3.11	18.00 ± 0.09	17.15 ± 0.07	16.62 ± 0.08	–	–	14.89 ± 0.42	20.73	19.91	19.18	0.28
ZOA081043.109 − 494235.60	264.939	−8.782	0.19	−50.33	2.11	17.54 ± 0.06	16.77 ± 0.04	16.19 ± 0.07	–	–	15.14 ± 0.31	20.97	20.07	19.49	0.26
ZOA081036.207 − 494258.52	264.934	−8.801	0.08	18.19	1.94	17.86 ± 0.07	16.98 ± 0.05	16.22 ± 0.07	–	–	15.32 ± 0.25	21.03	19.98	19.49	0.26
ZOA081042.421 − 493939.11	264.896	−8.758	0.33	−6.90	1.84	18.05 ± 0.08	17.21 ± 0.06	16.18 ± 0.07	–	16.95 ± 0.10	11.72 ± 1.41	21.54	20.99	19.21	0.26
ZOA081018.237 − 493913.95	264.855	−8.809	0.04	4.86	2.42	16.77 ± 0.04	16.04 ± 0.03	15.72 ± 0.05	–	15.50 ± 0.09	15.61 ± 0.05	19.78	19.09	18.88	0.26
ZOA081018.532 − 493848.44	264.849	−8.805	0.25	−24.85	2.48	16.68 ± 0.04	15.98 ± 0.03	15.37 ± 0.04	–	15.54 ± 0.11	15.13 ± 0.06	19.92	19.16	18.64	0.26
ZOA080917.798 − 491959.44	264.492	−8.778	0.17	29.13	2.00	17.71 ± 0.08	16.88 ± 0.06	16.18 ± 0.07	–	–	15.73 ± 0.10	20.71	19.81	19.30	0.26
ZOA080914.818 − 492109.12	264.504	−8.795	0.21	−34.22	1.79	17.81 ± 0.08	17.02 ± 0.06	16.58 ± 0.09	–	–	16.51 ± 0.09	20.93	20.15	20.12	0.26
ZOA080919.802 − 492303.61	264.539	−8.801	0.16	−72.58	2.04	17.73 ± 0.08	16.78 ± 0.06	16.09 ± 0.07	–	–	12.43 ± 1.02	20.33	19.55	18.97	0.26
ZOA080835.379 − 491919.70	264.421	−8.870	0.57	−26.68	3.60	16.80 ± 0.06	16.11 ± 0.05	15.36 ± 0.06	15.85 ± 0.27	15.03 ± 0.29	14.95 ± 0.07	19.81	19.23	18.52	0.26
ZOA080848.206 − 491947.59	264.446	−8.845	0.15	−63.23	2.75	16.78 ± 0.05	16.02 ± 0.04	15.35 ± 0.04	–	–	14.98 ± 0.06	19.85	19.16	18.51	0.26
ZOA080844.909 − 492036.59	264.453	−8.859	0.14	44.32	2.69	16.93 ± 0.05	16.16 ± 0.04	15.43 ± 0.04	–	–	15.22 ± 0.05	20.09	19.48	18.63	0.26
ZOA080848.006 − 492109.07	264.465	−8.857	0.14	−11.17	2.54	17.32 ± 0.06	16.41 ± 0.04	15.65 ± 0.05	–	–	14.61 ± 0.27	20.24	19.39	18.71	0.26
ZOA080900.236 − 492150.26	264.493	−8.835	0.53	−77.83	4.83	15.99 ± 0.04	15.23 ± 0.03	14.81 ± 0.04	14.27 ± 0.56	14.30 ± 0.15	14.60 ± 0.04	19.26	18.39	18.13	0.26
ZOA080842.110 − 491645.30	264.394	−8.832	0.12	−64.00	3.11	17.35 ± 0.08	16.41 ± 0.05	15.93 ± 0.07	11.86 ± 1.82	16.31 ± 0.05	15.64 ± 0.08	20.35	19.83	19.06	0.26
ZOA080909.686 − 491830.72	264.459	−8.784	0.05	−45.18	2.45	17.92 ± 0.08	16.79 ± 0.05	15.96 ± 0.06	–	–	14.41 ± 0.37	20.97	19.91	18.96	0.26
ZOA080855.755 − 491915.00	264.449	−8.822	0.16	−61.28	2.79	17.58 ± 0.07	16.68 ± 0.05	15.94 ± 0.06	–	15.89 ± 0.20	14.75 ± 0.27	20.51	19.55	18.88	0.26
ZOA080844.106 − 492007.42	264.445	−8.857	0.32	−6.49	3.52	17.36 ± 0.06	16.80 ± 0.06	16.34 ± 0.08	–	15.60 ± 0.23	12.65 ± 1.10	19.93	19.33	18.89	0.26
ZOA081146.589 − 490503.36	264.496	−8.303	0.12	55.57	2.24	17.43 ± 0.06	16.79 ± 0.06	16.02 ± 0.07	–	–	15.89 ± 0.07	20.53	19.94	19.19	0.27
ZOA081139.697 − 490636.22	264.508	−8.332	0.72	76.56	4.15	16.41 ± 0.04	15.47 ± 0.03	15.08 ± 0.04	15.67 ± 0.12	14.62 ± 0.09	–	19.41	18.52	18.36	0.27
ZOA081135.138 − 490751.24	264.519	−8.354	0.16	3.25	2.25	17.44 ± 0.06	16.52 ± 0.05	15.93 ± 0.07	–	–	15.61 ± 0.07	20.52	19.60	18.93	0.27
ZOA081129.708 − 490259.47	264.442	−8.323	0.33	56.77	3.24	16.63 ± 0.05	15.72 ± 0.04	15.07 ± 0.05	–	14.47 ± 0.39	14.74 ± 0.09	19.79	18.93	18.33	0.27
ZOA081130.158 − 490614.73	264.489	−8.351	0.34	69.95	1.97	17.95 ± 0.08	17.22 ± 0.08	16.22 ± 0.09	–	–	–	21.29	20.54	19.35	0.27
ZOA080853.196 − 491629.45	264.406	−8.804	0.20	34.14	2.17	18.50 ± 0.13	17.38 ± 0.08	16.51 ± 0.08	–	–	16.33 ± 0.08	21.63	20.48	19.67	0.23
ZOA080912.229 − 491119.49	264.360	−8.715	0.35	30.45	4.11	15.35 ± 0.03	14.58 ± 0.03	14.14 ± 0.03	14.82 ± 0.15	14.04 ± 0.12	13.61 ± 0.10	18.63	17.92	17.48	0.23
ZOA080916.476 − 491133.63	264.369	−8.707	0.06	65.27	2.01	18.34 ± 0.11	17.52 ± 0.08	16.75 ± 0.10	–	–	–	21.47	20.50	19.93	0.23
ZOA080923.043 − 491213.42	264.388	−8.698	0.07	58.17	3.61	16.90 ± 0.06	16.13 ± 0.05	15.54 ± 0.07	–	–	15.18 ± 0.10	19.97	19.16	18.83	0.23
ZOA080916.218 − 491454.24	264.417	−8.737	0.18	−77.94	2.25	18.10 ± 0.09	17.32 ± 0.07	16.82 ± 0.09	–	–	–	21.07	20.18	19.81	0.23
ZOA080916.250 − 491011.66	264.349	−8.695	0.24	78.95	2.37	17.62 ± 0.07	16.85 ± 0.06	16.43 ± 0.08	–	16.41 ± 0.10	15.90 ± 0.08	20.45	19.88	19.29	0.23
ZOA080840.273 − 491043.64	264.305	−8.783	0.23	18.37	5.41	14.64 ± 0.03	13.85 ± 0.02	13.43 ± 0.02	–	13.16 ± 0.20	12.50 ± 0.26	18.11	17.31	16.91	0.23
ZOA080853.341 − 491105.23	264.329	−8.756	0.51	−64.41	4.55	16.07 ± 0.04	15.16 ± 0.03	14.44 ± 0.03	15.90 ± 0.09	14.95 ± 0.04	14.31 ± 0.04	19.42	18.46	17.85	0.23
ZOA080901.329 − 491240.28	264.363	−8.752	0.35	−27.96	3.75	16.76 ± 0.05	15.80 ± 0.04	15.29 ± 0.04	–	15.55 ± 0.04	14.25 ± 0.29	19.89	19.05	18.54	0.23
ZOA080846.971 − 491518.68	264.380	−8.808	0.37	82.01	3.55	15.82 ± 0.03	15.13 ± 0.03	14.76 ± 0.03	–	12.91 ± 0.65	–	19.07	18.39	18.01	0.23
ZOA080900.145 − 491550.53	264.407	−8.782	0.14	−26.09	4.29	15.22 ± 0.03	14.49 ± 0.03	14.10 ± 0.03	13.86 ± 0.44	–	13.66 ± 0.10	18.61	17.87	17.48	0.23
ZOA080900.871 − 491347.42	264.378	−8.763	0.26	−16.70	3.09	16.54 ± 0.04	15.88 ± 0.04	15.44 ± 0.05	–	15.04 ± 0.20	12.86 ± 0.71	19.61	18.95	18.54	0.23
ZOA080919.537 − 491023.50	264.357	−8.690	0.30	86.86	4.55	14.89 ± 0.03	14.26 ± 0.02	13.88 ± 0.03	14.41 ± 0.16	14.18 ± 0.03	13.05 ± 0.25	18.31	17.69	17.31	0.23

ZOA080907.150 − 491229.92	264.369	−8.737	0.23	13.94	3.40	16.75 ± 0.05	15.96 ± 0.04	15.52 ± 0.05	–	15.37 ± 0.17	15.21 ± 0.07	20.03	19.18	18.77	0.23
ZOA080910.143 − 491201.00	264.366	−8.726	0.07	−40.00	2.53	17.41 ± 0.06	16.61 ± 0.05	16.11 ± 0.06	–	–	15.02 ± 0.30	20.44	19.79	19.41	0.23
ZOA080859.625 − 491149.11	264.348	−8.748	0.11	−26.50	2.09	17.97 ± 0.08	17.17 ± 0.06	16.35 ± 0.07	–	–	–	20.77	20.01	19.33	0.23
ZOA080846.293 − 491007.83	264.305	−8.764	0.16	60.56	3.22	16.82 ± 0.05	16.10 ± 0.04	15.57 ± 0.05	–	13.81 ± 0.63	–	19.70	19.00	18.53	0.23
ZOA080857.147 − 491052.96	264.331	−8.746	0.17	−20.18	2.14	18.33 ± 0.11	17.26 ± 0.07	16.39 ± 0.07	–	–	15.32 ± 0.29	21.37	20.53	19.59	0.23
ZOA080844.726 − 491023.83	264.306	−8.770	0.33	−6.17	2.42	17.47 ± 0.07	16.70 ± 0.05	16.08 ± 0.06	–	13.71 ± 0.32	–	19.70	18.98	18.81	0.23
ZOA080856.271 − 491103.20	264.332	−8.749	0.12	−60.48	1.96	18.38 ± 0.11	17.48 ± 0.08	16.68 ± 0.09	–	–	–	22.32	20.70	19.83	0.23
ZOA080858.813 − 491025.76	264.327	−8.738	0.15	88.68	2.26	18.16 ± 0.10	17.16 ± 0.07	16.52 ± 0.08	–	16.97 ± 0.08	–	21.42	20.43	19.69	0.23
ZOA080856.171 − 491531.89	264.396	−8.789	0.18	−84.44	2.03	17.93 ± 0.09	16.99 ± 0.06	16.28 ± 0.07	–	–	–	21.03	19.99	19.47	0.23
ZOA080916.994 − 491343.08	264.401	−8.725	0.77	87.98	2.51	17.57 ± 0.07	16.65 ± 0.05	16.00 ± 0.06	15.94 ± 0.43	15.47 ± 0.16	–	20.03	19.21	18.72	0.23
ZOA081030.599 − 493028.22	264.747	−8.703	0.17	47.45	2.72	17.30 ± 0.06	16.56 ± 0.05	15.97 ± 0.07	–	15.90 ± 0.14	–	20.10	19.49	18.96	0.31
ZOA081018.060 − 492606.36	264.667	−8.693	0.39	79.84	4.62	16.12 ± 0.04	15.39 ± 0.03	15.09 ± 0.05	15.68 ± 0.14	14.86 ± 0.14	–	19.40	18.71	18.47	0.31
ZOA081029.954 − 492753.67	264.710	−8.682	0.22	5.29	2.19	17.07 ± 0.05	16.33 ± 0.04	15.63 ± 0.05	–	15.74 ± 0.09	–	20.03	19.30	18.52	0.31
ZOA081035.751 − 492917.74	264.738	−8.681	0.46	24.71	4.96	15.62 ± 0.03	14.83 ± 0.03	14.41 ± 0.04	15.08 ± 0.19	14.68 ± 0.04	14.04 ± 0.08	19.00	18.24	17.74	0.31
ZOA081032.475 − 492930.10	264.736	−8.690	0.38	73.57	6.68	14.29 ± 0.02	13.50 ± 0.02	13.04 ± 0.02	13.72 ± 0.18	12.89 ± 0.17	12.13 ± 0.25	17.82	17.02	16.56	0.31
ZOA081033.269 − 492509.93	264.675	−8.650	0.31	34.96	2.42	17.55 ± 0.07	16.77 ± 0.06	16.20 ± 0.08	–	16.13 ± 0.16	16.09 ± 0.08	20.55	19.81	19.51	0.31
ZOA081025.953 − 492903.76	264.721	−8.701	0.10	−48.23	2.73	17.32 ± 0.06	16.42 ± 0.05	16.18 ± 0.10	–	15.59 ± 0.17	15.57 ± 0.10	20.19	19.42	19.21	0.31
ZOA081113.245 − 491122.04	264.537	−8.436	0.18	11.12	2.58	16.62 ± 0.05	15.94 ± 0.04	15.46 ± 0.07	–	15.59 ± 0.05	15.14 ± 0.09	19.74	19.03	18.80	0.28
ZOA081119.717 − 491155.67	264.555	−8.426	0.47	−15.13	4.95	16.45 ± 0.05	15.67 ± 0.04	15.27 ± 0.09	16.16 ± 0.13	15.08 ± 0.09	14.87 ± 0.10	19.67	18.83	18.50	0.28
ZOA081108.368 − 491453.49	264.580	−8.478	0.08	−5.24	3.52	15.31 ± 0.03	14.56 ± 0.03	14.10 ± 0.04	–	12.55 ± 0.61	14.04 ± 0.04	18.62	17.89	17.47	0.28
ZOA081129.798 − 491501.36	264.614	−8.430	0.22	−48.65	3.40	15.51 ± 0.04	14.71 ± 0.03	14.33 ± 0.05	15.28 ± 0.08	14.50 ± 0.06	13.57 ± 0.24	18.84	18.05	17.74	0.28
ZOA081111.325 − 491520.15	264.591	−8.476	0.62	−24.12	10.65	13.72 ± 0.02	12.97 ± 0.02	12.55 ± 0.02	13.55 ± 0.06	12.86 ± 0.03	12.47 ± 0.03	17.40	16.65	16.23	0.28
ZOA081050.570 − 491010.72	264.487	−8.477	0.41	−12.87	9.09	13.79 ± 0.02	12.97 ± 0.02	12.44 ± 0.03	13.61 ± 0.07	12.83 ± 0.04	11.71 ± 0.20	17.61	16.80	16.32	0.28
ZOA081048.476 − 491507.46	264.554	−8.526	0.24	−13.14	5.37	14.72 ± 0.03	13.97 ± 0.03	13.60 ± 0.03	14.02 ± 0.23	13.34 ± 0.17	13.17 ± 0.08	18.18	17.41	17.07	0.28
ZOA081057.671 − 491522.16	264.571	−8.507	0.63	−57.25	9.59	14.05 ± 0.02	13.33 ± 0.02	12.90 ± 0.03	13.81 ± 0.08	13.15 ± 0.04	12.77 ± 0.04	17.70	16.98	16.60	0.28
ZOA081054.529 − 491459.94	264.561	−8.511	0.11	27.48	2.96	16.19 ± 0.04	15.35 ± 0.04	14.87 ± 0.05	–	15.27 ± 0.04	14.24 ± 0.19	19.55	18.77	18.18	0.28
ZOA081002.876 − 491942.85	264.553	−8.672	0.21	−5.99	2.29	17.53 ± 0.06	16.73 ± 0.05	15.98 ± 0.06	–	–	–	20.46	19.61	19.14	0.30
ZOA081005.860 − 491827.80	264.540	−8.654	0.35	−81.39	4.78	15.46 ± 0.03	14.70 ± 0.03	14.36 ± 0.03	14.90 ± 0.18	13.49 ± 0.34	–	18.81	18.07	17.68	0.30
ZOA080937.997 − 491952.80	264.519	−8.731	0.36	−58.53	1.37	18.58 ± 0.12	17.59 ± 0.09	17.39 ± 0.26	–	–	15.38 ± 0.24	20.43	19.90	19.31	0.30
ZOA081117.859 − 490842.99	264.506	−8.402	0.27	−30.69	4.37	15.55 ± 0.03	14.85 ± 0.03	14.51 ± 0.05	14.90 ± 0.17	13.87 ± 0.21	12.83 ± 0.45	18.77	18.09	17.76	0.28
ZOA081129.860 − 490431.28	264.464	−8.337	0.14	−38.84	12.19	13.54 ± 0.02	12.77 ± 0.02	12.42 ± 0.03	13.29 ± 0.08	12.55 ± 0.05	12.27 ± 0.04	17.18	16.42	16.10	0.28
ZOA081126.933 − 490439.14	264.462	−8.344	0.16	−31.36	1.92	17.88 ± 0.11	17.04 ± 0.09	16.42 ± 0.15	–	–	16.27 ± 0.15	21.94	20.81	20.15	0.28
ZOA081108.267 − 490534.62	264.447	−8.396	0.34	30.00	7.02	15.08 ± 0.03	14.35 ± 0.03	13.85 ± 0.04	14.97 ± 0.07	13.63 ± 0.24	13.55 ± 0.10	18.57	17.86	17.36	0.28
ZOA081125.968 − 490706.85	264.495	−8.369	0.05	−28.44	2.93	16.58 ± 0.05	15.81 ± 0.04	15.27 ± 0.07	–	–	–	19.67	18.89	18.42	0.28
ZOA081116.134 − 490826.30	264.500	−8.403	0.15	−48.72	2.23	17.76 ± 0.09	16.80 ± 0.06	15.93 ± 0.09	–	–	15.84 ± 0.10	20.76	20.11	19.19	0.28
ZOA081115.094 − 490359.32	264.435	−8.366	0.57	89.70	2.46	18.21 ± 0.12	17.23 ± 0.08	16.25 ± 0.10	–	–	–	21.35	20.20	19.65	0.28
ZOA081102.481 − 490226.97	264.394	−8.381	0.10	−42.94	2.48	17.52 ± 0.09	16.58 ± 0.07	15.60 ± 0.08	–	12.58 ± 1.30	15.31 ± 0.11	20.63	19.81	18.79	0.28
ZOA081051.374 − 490439.92	264.409	−8.427	0.18	−51.95	3.15	16.32 ± 0.05	15.48 ± 0.04	14.87 ± 0.05	15.34 ± 0.33	–	14.21 ± 0.11	19.45	18.71	18.09	0.28
ZOA081020.209 − 492227.33	264.618	−8.656	0.31	−35.84	5.22	15.30 ± 0.03	14.54 ± 0.03	14.15 ± 0.04	15.08 ± 0.07	14.14 ± 0.12	13.78 ± 0.09	18.67	17.97	17.61	0.31
ZOA081021.790 − 491625.11	264.534	−8.599	0.55	1.13	10.78	14.32 ± 0.02	13.47 ± 0.02	13.16 ± 0.03	13.81 ± 0.18	13.10 ± 0.08	12.37 ± 0.18	18.06	17.21	16.86	0.31
ZOA081038.878 − 491954.64	264.609	−8.591	0.34	−9.54	4.23	15.30 ± 0.03	15.15 ± 0.03	14.78 ± 0.04	15.12 ± 0.17	–	14.61 ± 0.04	18.68	18.59	18.10	0.31
ZOA081042.627 − 492353.94	264.671	−8.617	0.14	−11.56	15.04	12.62 ± 0.02	11.77 ± 0.02	11.46 ± 0.02	12.40 ± 0.09	11.07 ± 0.18	11.18 ± 0.06	16.68	15.89	15.60	0.31
ZOA081040.594 − 492237.72	264.650	−8.611	0.21	19.83	2.33	17.02 ± 0.05	16.20 ± 0.04	16.00 ± 0.06	–	–	15.17 ± 0.16	20.22	19.32	18.96	0.31
ZOA081024.035 − 492037.81	264.597	−8.631	0.64	−61.80	2.81	17.80 ± 0.07	16.91 ± 0.06	16.66 ± 0.11	15.71 ± 0.68	–	15.11 ± 0.12	19.90	19.23	18.78	0.31
ZOA080950.988 − 494410.11	264.886	−8.915	0.14	−56.44	3.19	16.29 ± 0.07	15.69 ± 0.07	14.78 ± 0.10	–	–	–	19.45	19.08	18.30	0.25
ZOA081002.334 − 494352.04	264.898	−8.886	0.27	−30.45	6.99	15.37 ± 0.05	14.50 ± 0.04	14.33 ± 0.14	13.33 ± 0.46	12.50 ± 0.75	13.94 ± 0.18	18.54	17.77	17.48	0.25
ZOA081222.132 − 492623.14	264.852	−8.412	0.33	62.20	2.59	17.66 ± 0.07	16.83 ± 0.06	16.08 ± 0.07	–	–	15.46 ± 0.12	20.64	19.82	19.17	0.30
ZOA081235.638 − 492647.19	264.878	−8.384	0.10	43.93	3.34	16.96 ± 0.06	16.05 ± 0.05	15.52 ± 0.08	–	15.88 ± 0.07	11.76 ± 0.93	20.22	19.20	18.39	0.30
ZOA081225.376 − 492927.86	264.901	−8.432	0.40	−68.79	3.44	16.13 ± 0.04	15.37 ± 0.03	14.80 ± 0.04	–	14.61 ± 0.19	13.95 ± 0.24	19.34	18.61	18.16	0.30
ZOA081219.984 − 492339.99	264.810	−8.392	0.61	−33.70	14.46	13.64 ± 0.02	12.83 ± 0.02	12.45 ± 0.02	13.31 ± 0.12	12.45 ± 0.11	11.64 ± 0.24	17.54	16.73	16.35	0.30
ZOA081225.568 − 492529.15	264.844	−8.396	0.10	81.36	2.01	17.33 ± 0.06	16.66 ± 0.05	16.00 ± 0.06	–	–	–	20.29	19.61	19.19	0.30
ZOA080947.620 − 493404.27	264.737	−8.834	0.08	18.90	2.62	17.51 ± 0.06	16.71 ± 0.04	16.11 ± 0.07	–	16.31 ± 0.06	12.48 ± 1.00	20.41	19.70	18.89	0.27
ZOA081021.163 − 493530.63	264.806	−8.769	0.19	−16.37	3.19	16.99 ± 0.05	16.22 ± 0.04	15.72 ± 0.06	–	15.70 ± 0.11	14.61 ± 0.30	20.08	19.29	18.91	0.27
ZOA081022.210 − 493603.81	264.815	−8.772	0.33	55.08	4.22	16.27 ± 0.04	15.55 ± 0.03	15.13 ± 0.05	14.96 ± 0.43	14.44 ± 0.29	13.23 ± 0.45	19.47	18.75	18.42	0.27
ZOA081239.746 − 492345.95	264.841	−8.348	0.06	38.61	2.19	17.43 ± 0.06	16.53 ± 0.05	15.80 ± 0.07	16.42 ± 0.32	–	–	20.67	19.69	19.00	0.31
ZOA081246.053 − 492633.29	264.890	−8.358	0.44	−20.48	3.81	17.03 ± 0.05	16.00 ± 0.04	15.18 ± 0.04	–	15.82 ± 0.06	14.98 ± 0.06	20.29	19.42	18.45	0.31
ZOA080953.597 − 493032.94	264.695	−8.789	0.36	−21.06	8.49	14.82 ± 0.03	14.10 ± 0.03	13.60 ± 0.04	14.20 ± 0.25	13.77 ± 0.11	12.47 ± 0.28	18.44	17.72	17.27	0.33
ZOA080915.115 − 492642.85	264.584	−8.843	0.38	53.74	4.83	16.59 ± 0.07	15.84 ± 0.06	15.34 ± 0.11	–	13.27 ± 0.78	14.99 ± 0.17	19.66	18.91	18.52	0.33
ZOA081000.151 − 492743.15	264.664	−8.749	0.20	−19.40	6.31	15.17 ± 0.04	14.48 ± 0.03	14.09 ± 0.06	14.69 ± 0.17	13.99 ± 0.08	13.49 ± 0.16	18.73	18.03	17.65	0.33
ZOA080952.626 − 492931.06	264.679	−8.782	0.60	0.52	5.47	15.46 ± 0.03	14.59 ± 0.03	14.25 ± 0.04	15.19 ± 0.09	14.15 ± 0.12	14.04 ± 0.06	18.87	18.05	17.73	0.33
ZOA080918.418 − 492559.68	264.579	−8.830	0.46	0.78	2.08	17.22 ± 0.07	16.65 ± 0.07	16.17 ± 0.12	16.73 ± 0.15	16.06 ± 0.09	15.64 ± 0.18	20.31	19.58	19.94	0.33
ZOA080956.269 − 492547.78	264.631	−8.741	0.47	70.99	4.54	15.46 ± 0.04	14.74 ± 0.03	14.42 ± 0.05	15.18 ± 0.08	13.62 ± 0.32	13.57 ± 0.25	18.82	18.11	17.87	0.33

ZOA080916.521 − 492758.22	264.604	−8.851	0.11	52.78	5.88	14.97 ± 0.03	14.13 ± 0.03	13.78 ± 0.04	13.88 ± 0.31	13.76 ± 0.08	13.49 ± 0.07	18.34	17.54	17.20	0.33
ZOA081019.257 − 491106.39	264.454	−8.558	0.28	18.55	2.62	16.56 ± 0.04	15.90 ± 0.03	15.38 ± 0.05	16.14 ± 0.13	–	15.31 ± 0.05	19.83	19.13	18.73	0.31
ZOA081018.427 − 491118.44	264.456	−8.562	0.36	−79.81	1.47	19.42 ± 0.20	17.88 ± 0.10	17.14 ± 0.15	–	–	–	24.20	22.88	20.74	0.31
ZOA081013.114 − 491127.11	264.450	−8.575	0.23	53.20	2.21	17.73 ± 0.07	17.07 ± 0.06	16.57 ± 0.09	–	16.66 ± 0.08	16.43 ± 0.09	20.79	20.15	19.89	0.31
ZOA081007.943 − 491251.03	264.463	−8.599	0.79	23.46	8.73	15.62 ± 0.03	14.53 ± 0.03	13.91 ± 0.03	15.44 ± 0.09	13.73 ± 0.23	13.05 ± 0.25	19.27	18.17	17.55	0.31
ZOA080959.065 − 490907.94	264.397	−8.587	0.67	8.07	4.31	15.94 ± 0.04	15.09 ± 0.03	14.59 ± 0.04	15.63 ± 0.09	14.82 ± 0.06	14.40 ± 0.06	19.24	18.41	18.05	0.31
ZOA081011.515 − 491003.74	264.428	−8.567	0.05	−13.44	4.57	15.31 ± 0.03	14.56 ± 0.03	14.24 ± 0.03	14.56 ± 0.21	13.52 ± 0.26	13.11 ± 0.24	18.62	17.90	17.61	0.31
ZOA080928.866 − 493441.18	264.718	−8.882	0.64	−34.33	3.77	17.06 ± 0.06	16.05 ± 0.04	15.25 ± 0.05	–	15.00 ± 0.32	14.49 ± 0.21	20.21	19.23	18.52	0.29
ZOA080926.378 − 493203.42	264.677	−8.865	0.34	−27.78	3.85	16.04 ± 0.04	15.21 ± 0.03	14.77 ± 0.05	–	14.60 ± 0.20	14.55 ± 0.07	19.46	18.62	18.16	0.29
ZOA080949.376 − 492104.40	264.553	−8.715	0.23	24.11	11.97	13.06 ± 0.02	12.29 ± 0.02	11.87 ± 0.02	12.56 ± 0.17	11.61 ± 0.20	11.35 ± 0.14	16.90	16.13	15.72	0.26
ZOA080923.297 − 492107.77	264.516	−8.775	0.48	23.91	0.35	17.97 ± 0.10	17.05 ± 0.07	16.54 ± 0.14	–	16.33 ± 0.12	–	20.64	19.99	19.52	0.26
ZOA080937.681 − 492252.35	264.562	−8.758	0.13	−25.02	2.67	17.31 ± 0.07	16.46 ± 0.06	15.54 ± 0.07	–	–	14.48 ± 0.26	20.33	19.52	18.85	0.26
ZOA080916.826 − 491824.69	264.468	−8.766	0.30	67.47	4.24	15.46 ± 0.04	14.83 ± 0.03	14.50 ± 0.06	14.53 ± 0.32	14.13 ± 0.21	13.84 ± 0.21	18.81	18.23	17.86	0.26
ZOA080958.618 − 491815.32	264.526	−8.669	0.41	−63.39	2.57	17.73 ± 0.10	16.83 ± 0.08	16.23 ± 0.14	–	–	15.36 ± 0.24	20.49	19.97	19.24	0.26
ZOA080916.298 − 492131.35	264.512	−8.795	0.29	3.56	7.00	14.15 ± 0.03	13.36 ± 0.02	12.94 ± 0.03	13.68 ± 0.15	12.91 ± 0.12	12.64 ± 0.11	17.68	16.91	16.48	0.26
ZOA080914.371 − 492129.39	264.508	−8.799	0.30	−21.10	4.31	16.30 ± 0.06	15.41 ± 0.04	14.95 ± 0.10	12.07 ± 1.40	14.85 ± 0.17	14.18 ± 0.44	19.71	18.71	18.36	0.26
ZOA081020.306 − 491229.91	264.476	−8.568	0.28	−71.23	4.67	15.49 ± 0.03	14.73 ± 0.03	14.42 ± 0.04	14.11 ± 0.43	14.17 ± 0.14	13.84 ± 0.17	18.82	18.09	17.81	0.30
ZOA081006.182 − 491004.76	264.420	−8.579	0.13	−24.99	1.91	17.57 ± 0.07	16.74 ± 0.05	16.14 ± 0.07	–	–	16.02 ± 0.08	20.88	20.06	19.66	0.30
ZOA081004.444 − 491005.97	264.418	−8.583	0.28	13.55	2.53	17.07 ± 0.06	16.33 ± 0.04	15.84 ± 0.06	–	15.56 ± 0.16	13.90 ± 0.52	19.95	19.27	18.76	0.30
ZOA081033.204 − 491001.10	264.459	−8.516	0.27	−31.43	6.08	14.29 ± 0.02	13.49 ± 0.02	13.03 ± 0.02	12.85 ± 0.47	12.71 ± 0.21	12.30 ± 0.17	17.79	16.99	16.52	0.30
ZOA080936.289 − 493521.12	264.738	−8.871	0.30	−84.09	2.29	18.81 ± 0.13	17.56 ± 0.07	16.03 ± 0.10	–	–	15.82 ± 0.11	21.73	20.47	19.23	0.32
ZOA080950.925 − 493054.65	264.696	−8.798	0.17	−4.22	3.60	17.03 ± 0.05	16.31 ± 0.04	15.86 ± 0.08	–	15.82 ± 0.10	15.40 ± 0.13	20.11	19.46	18.93	0.32
ZOA080920.106 − 493207.50	264.669	−8.880	0.41	−79.92	2.00	18.23 ± 0.09	17.25 ± 0.06	16.32 ± 0.09	–	–	16.27 ± 0.09	21.32	20.34	19.40	0.32
ZOA080925.641 − 493054.89	264.660	−8.856	0.43	44.24	4.63	15.86 ± 0.03	15.14 ± 0.03	14.68 ± 0.04	15.13 ± 0.24	14.86 ± 0.05	14.43 ± 0.06	19.09	18.42	18.00	0.32
ZOA080956.134 − 493750.91	264.803	−8.847	0.42	32.97	3.08	17.41 ± 0.06	16.87 ± 0.06	16.54 ± 0.13	13.79 ± 1.10	16.68 ± 0.07	16.05 ± 0.14	20.09	20.42	19.52	0.32
ZOA080938.478 − 491644.52	264.475	−8.702	0.51	−58.81	5.90	15.63 ± 0.04	14.84 ± 0.04	14.49 ± 0.07	14.96 ± 0.20	14.32 ± 0.10	13.97 ± 0.16	19.02	18.27	17.90	0.28
ZOA080950.323 − 491623.49	264.488	−8.671	0.14	−20.43	2.61	17.69 ± 0.10	16.83 ± 0.08	15.97 ± 0.11	–	–	15.74 ± 0.13	20.58	19.79	19.50	0.28
ZOA080917.273 − 491104.58	264.363	−8.701	0.34	−30.42	2.23	17.32 ± 0.08	16.34 ± 0.06	15.85 ± 0.10	–	15.82 ± 0.09	14.71 ± 0.32	20.39	19.36	18.80	0.28
ZOA080935.876 − 491432.65	264.440	−8.688	0.24	22.14	3.33	16.55 ± 0.05	15.80 ± 0.04	15.27 ± 0.07	15.89 ± 0.22	15.54 ± 0.06	15.11 ± 0.08	19.69	19.01	18.68	0.28
ZOA080958.828 − 491549.17	264.492	−8.647	0.32	−56.32	5.75	15.18 ± 0.04	14.73 ± 0.03	14.56 ± 0.07	12.99 ± 0.24	12.65 ± 0.29	14.15 ± 0.12	18.43	18.00	17.87	0.28
ZOA080948.746 − 491544.41	264.476	−8.669	0.93	−33.83	3.58	17.10 ± 0.07	16.03 ± 0.05	15.66 ± 0.10	16.33 ± 0.26	15.24 ± 0.21	15.26 ± 0.12	20.26	19.18	18.86	0.28
ZOA081018.898 − 490907.90	264.426	−8.541	0.13	88.10	1.86	18.12 ± 0.09	17.20 ± 0.07	16.71 ± 0.12	–	–	–	21.10	20.10	19.46	0.31
ZOA081023.124 − 490416.13	264.362	−8.488	0.09	−9.82	8.16	13.68 ± 0.02	12.95 ± 0.02	12.57 ± 0.02	13.23 ± 0.15	12.48 ± 0.13	11.93 ± 0.13	17.39	16.67	16.30	0.31
ZOA080950.335 − 490437.87	264.319	−8.567	0.56	−86.72	3.06	17.29 ± 0.06	16.57 ± 0.04	15.93 ± 0.07	16.84 ± 0.13	–	15.61 ± 0.09	20.26	19.48	19.12	0.31
ZOA081016.673 − 490442.66	264.359	−8.507	0.24	88.52	2.19	18.24 ± 0.09	17.34 ± 0.06	16.53 ± 0.09	–	–	–	21.19	20.39	19.28	0.31
ZOA081008.148 − 490536.35	264.359	−8.535	0.37	35.48	4.94	15.13 ± 0.03	14.35 ± 0.02	13.98 ± 0.03	14.96 ± 0.05	14.16 ± 0.04	13.27 ± 0.19	18.55	17.77	17.41	0.31
ZOA081009.057 − 490657.91	264.380	−8.545	0.38	25.87	2.07	17.93 ± 0.07	17.05 ± 0.06	16.34 ± 0.08	–	–	16.27 ± 0.09	20.92	20.17	19.61	0.31
ZOA081000.415 − 490708.57	264.370	−8.566	0.44	−3.54	6.31	14.47 ± 0.02	13.72 ± 0.02	13.37 ± 0.03	13.89 ± 0.18	13.06 ± 0.18	12.96 ± 0.08	17.96	17.20	16.84	0.31
ZOA081005.451 − 490804.42	264.391	−8.563	0.14	−74.67	2.02	18.05 ± 0.08	17.29 ± 0.07	16.43 ± 0.09	–	–	–	21.13	20.27	19.40	0.31
ZOA081018.310 − 490334.23	264.345	−8.493	0.09	59.81	2.48	16.93 ± 0.05	16.27 ± 0.04	15.62 ± 0.06	11.97 ± 1.60	14.94 ± 0.37	15.51 ± 0.06	19.74	19.24	18.97	0.31
ZOA080948.928 − 490221.63	264.285	−8.551	0.01	−86.95	2.27	17.39 ± 0.06	16.62 ± 0.05	15.91 ± 0.07	–	11.61 ± 1.52	–	20.11	19.46	19.08	0.31
ZOA080944.334 − 490205.18	264.274	−8.559	0.26	−46.03	3.94	15.80 ± 0.03	15.06 ± 0.03	14.51 ± 0.04	15.47 ± 0.13	–	14.43 ± 0.04	19.26	18.43	17.88	0.31
ZOA080954.844 − 490259.81	264.303	−8.543	0.13	−87.11	2.46	17.53 ± 0.09	16.50 ± 0.06	15.79 ± 0.09	11.29 ± 2.00	–	−14.20 ± 9.31	20.33	19.42	18.65	0.31
ZOA080930.409 − 490426.19	264.288	−8.612	0.20	25.80	3.71	16.35 ± 0.05	15.59 ± 0.04	14.91 ± 0.06	–	15.36 ± 0.08	14.57 ± 0.09	19.57	18.92	18.21	0.31
ZOA081010.287 − 490442.75	264.350	−8.522	0.41	−37.77	2.87	18.31 ± 0.09	17.64 ± 0.08	16.58 ± 0.10	–	–	16.19 ± 0.12	20.91	20.44	19.57	0.29
ZOA081008.320 − 490558.75	264.365	−8.538	0.23	35.18	1.92	17.69 ± 0.06	16.84 ± 0.05	16.52 ± 0.14	–	–	15.36 ± 0.32	20.63	19.78	19.73	0.29
ZOA081044.243 − 490627.99	264.425	−8.459	0.26	44.06	4.72	15.04 ± 0.03	14.29 ± 0.02	13.96 ± 0.03	13.79 ± 0.38	13.45 ± 0.20	12.37 ± 0.40	18.44	17.69	17.36	0.29
ZOA081022.325 − 490741.24	264.410	−8.521	0.11	64.87	2.91	17.81 ± 0.07	17.00 ± 0.06	16.07 ± 0.10	17.52 ± 0.12	–	13.90 ± 0.55	21.36	20.40	18.91	0.29
ZOA081024.801 − 490323.88	264.352	−8.477	0.27	−14.86	3.13	16.44 ± 0.04	15.64 ± 0.03	15.12 ± 0.04	–	14.76 ± 0.25	14.48 ± 0.14	19.61	18.84	18.35	0.29
ZOA081042.417 − 490805.53	264.445	−8.478	0.71	66.20	2.91	18.20 ± 0.09	17.27 ± 0.06	16.84 ± 0.12	17.28 ± 0.29	15.72 ± 0.34	16.20 ± 0.15	20.77	19.75	19.47	0.29
ZOA081023.699 − 494146.47	264.899	−8.819	0.23	11.42	2.15	16.78 ± 0.04	16.02 ± 0.04	15.44 ± 0.07	–	–	15.43 ± 0.07	19.94	19.12	19.26	0.26
ZOA081056.463 − 494148.66	264.947	−8.745	0.20	−58.80	2.10	17.96 ± 0.08	16.98 ± 0.06	16.01 ± 0.06	–	–	15.98 ± 0.06	21.26	20.53	19.40	0.26
ZOA081058.653 − 494234.46	264.961	−8.746	0.26	−0.45	6.39	15.02 ± 0.03	14.25 ± 0.02	13.86 ± 0.03	14.89 ± 0.05	14.08 ± 0.04	13.66 ± 0.05	18.49	17.73	17.33	0.26
ZOA081057.363 − 494344.25	264.976	−8.760	0.22	−47.38	2.95	17.08 ± 0.05	16.27 ± 0.04	15.57 ± 0.05	–	–	15.46 ± 0.05	20.46	19.69	18.98	0.26
ZOA081052.871 − 493903.20	264.902	−8.728	0.26	−57.37	2.93	17.83 ± 0.07	17.00 ± 0.06	15.99 ± 0.07	–	–	14.86 ± 0.28	20.77	20.12	18.97	0.26
ZOA081147.719 − 493229.42	264.889	−8.545	0.07	−72.95	3.23	16.39 ± 0.05	15.59 ± 0.04	14.95 ± 0.06	–	–	–	19.46	18.65	18.05	0.28
ZOA081146.050 − 493342.74	264.904	−8.559	0.41	14.02	3.62	16.63 ± 0.06	15.72 ± 0.04	15.04 ± 0.06	16.75 ± 0.06	14.94 ± 0.24	14.76 ± 0.08	19.89	19.11	18.31	0.28
ZOA081143.395 − 493417.46	264.908	−8.571	0.35	−41.84	4.68	15.91 ± 0.04	15.02 ± 0.03	14.41 ± 0.04	–	14.90 ± 0.04	–	19.19	18.41	17.68	0.28
ZOA081149.432 − 493423.74	264.918	−8.558	0.08	27.74	3.57	16.32 ± 0.05	15.54 ± 0.04	14.91 ± 0.06	–	15.00 ± 0.17	14.59 ± 0.09	19.63	18.85	18.25	0.28
ZOA081151.603 − 493420.32	264.921	−8.552	0.37	−87.35	2.94	16.55 ± 0.05	15.80 ± 0.04	15.23 ± 0.07	16.13 ± 0.09	–	14.67 ± 0.12	19.63	18.88	18.47	0.28
ZOA081153.859 − 493425.86	264.925	−8.548	0.17	66.26	5.34	14.38 ± 0.03	13.62 ± 0.02	13.30 ± 0.03	–	13.26 ± 0.05	12.44 ± 0.22	17.85	17.10	16.78	0.28
ZOA081146.142 − 493444.10	264.918	−8.568	0.16	−38.58	2.64	17.09 ± 0.07	16.23 ± 0.05	15.47 ± 0.07	–	–	15.29 ± 0.09	20.15	19.32	18.66	0.28

ZOA081145.628 − 493452.57	264.920	−8.571	0.38	−14.48	6.06	15.34 ± 0.03	14.59 ± 0.03	14.15 ± 0.04	–	13.75 ± 0.21	13.48 ± 0.14	18.79	18.03	17.58	0.28
ZOA081144.423 − 493459.19	264.919	−8.574	0.14	−82.41	6.20	15.10 ± 0.03	14.31 ± 0.03	13.64 ± 0.04	–	13.53 ± 0.25	–	18.63	17.84	17.19	0.28
ZOA081138.854 − 493540.85	264.921	−8.593	0.18	18.33	3.41	16.26 ± 0.05	15.52 ± 0.04	14.91 ± 0.05	–	13.99 ± 0.46	14.04 ± 0.23	19.38	18.74	18.24	0.28
ZOA081143.793 − 493539.00	264.928	−8.582	0.18	−66.37	3.47	16.91 ± 0.06	16.14 ± 0.05	15.43 ± 0.07	–	–	14.54 ± 0.23	20.09	19.25	18.66	0.28
ZOA081148.608 − 493619.23	264.944	−8.577	0.43	−34.14	3.10	16.70 ± 0.06	15.95 ± 0.05	15.39 ± 0.08	16.03 ± 0.23	15.28 ± 0.16	14.26 ± 0.30	19.79	19.07	18.58	0.28
ZOA081127.268 − 493730.06	264.930	−8.636	0.31	−26.56	10.72	15.18 ± 0.04	14.42 ± 0.04	13.96 ± 0.06	14.04 ± 0.53	13.11 ± 0.43	12.65 ± 0.42	18.94	18.23	17.61	0.28
ZOA081135.676 − 493147.27	264.861	−8.566	0.41	1.96	3.18	17.01 ± 0.07	16.19 ± 0.05	15.52 ± 0.07	–	–	13.30 ± 0.66	20.22	19.38	18.81	0.28
ZOA081137.582 − 493127.27	264.859	−8.559	0.58	23.65	3.10	17.83 ± 0.11	16.79 ± 0.07	16.07 ± 0.11	–	16.63 ± 0.07	–	20.94	20.08	19.25	0.28
ZOA081128.949 − 493145.36	264.851	−8.581	0.01	−56.33	2.22	17.78 ± 0.16	17.01 ± 0.10	15.82 ± 0.09	–	16.84 ± 0.11	15.79 ± 0.10	22.36	20.52	19.88	0.28
ZOA081208.356 − 493517.90	264.959	−8.523	0.00	−20.70	3.91	17.07 ± 0.07	16.22 ± 0.06	15.33 ± 0.08	–	15.80 ± 0.15	15.11 ± 0.09	20.15	19.50	18.59	0.28
ZOA081048.823 − 493913.49	264.899	−8.739	0.41	74.93	2.02	18.66 ± 0.12	17.58 ± 0.08	16.67 ± 0.10	–	–	16.58 ± 0.10	21.78	20.31	19.62	0.27
ZOA081213.684 − 492803.75	264.864	−8.446	0.12	−65.62	3.74	16.19 ± 0.05	15.40 ± 0.04	14.89 ± 0.08	–	15.10 ± 0.07	–	19.48	18.64	18.12	0.30
ZOA081159.062 − 492852.47	264.854	−8.487	0.34	26.90	3.04	16.32 ± 0.05	15.54 ± 0.04	14.91 ± 0.06	12.69 ± 1.09	12.55 ± 0.86	13.46 ± 0.38	19.36	18.66	18.15	0.30
ZOA081137.264 − 492637.32	264.790	−8.516	0.11	28.80	3.38	16.78 ± 0.06	16.13 ± 0.05	15.45 ± 0.09	–	15.95 ± 0.09	13.43 ± 0.62	20.23	19.58	18.93	0.30
ZOA081149.082 − 490130.65	264.450	−8.265	0.20	−72.12	7.12	14.56 ± 0.03	13.77 ± 0.02	13.46 ± 0.03	13.68 ± 0.28	12.30 ± 0.33	12.93 ± 0.10	18.09	17.31	16.98	0.29
ZOA081153.397 − 490427.80	264.498	−8.282	0.21	−49.43	2.81	17.30 ± 0.05	16.61 ± 0.04	16.14 ± 0.07	–	14.93 ± 0.44	14.00 ± 0.58	20.25	19.45	19.03	0.29
ZOA081133.990 − 492325.20	264.739	−8.495	0.34	−32.93	3.43	17.10 ± 0.08	16.36 ± 0.07	15.45 ± 0.10	–	12.62 ± 1.23	–	20.30	19.65	18.62	0.29
ZOA081210.526 − 491716.69	264.706	−8.357	0.70	−29.61	5.45	15.75 ± 0.04	14.92 ± 0.03	14.54 ± 0.06	14.97 ± 0.23	14.38 ± 0.10	13.59 ± 0.28	19.10	18.26	17.96	0.29
ZOA081206.698 − 491750.03	264.708	−8.371	0.05	−41.36	6.80	13.65 ± 0.02	12.90 ± 0.02	12.57 ± 0.03	12.76 ± 0.27	12.47 ± 0.09	–	17.23	16.48	16.13	0.29
ZOA081201.652 − 491858.20	264.717	−8.392	0.15	33.37	2.88	16.28 ± 0.05	15.50 ± 0.04	14.98 ± 0.06	–	15.09 ± 0.07	14.78 ± 0.07	19.47	18.66	18.29	0.29
ZOA081159.820 − 491959.42	264.728	−8.406	0.15	2.83	3.54	16.50 ± 0.06	15.79 ± 0.05	15.26 ± 0.08	–	15.21 ± 0.10	13.98 ± 0.27	19.52	18.86	18.34	0.29
ZOA081140.468 − 491746.27	264.668	−8.430	0.31	78.27	4.61	15.84 ± 0.04	15.13 ± 0.04	14.68 ± 0.06	–	–	14.44 ± 0.08	19.11	18.44	18.04	0.29
ZOA081135.263 − 492340.53	264.745	−8.495	0.04	−10.40	3.65	17.89 ± 0.14	16.68 ± 0.09	15.74 ± 0.12	–	–	15.64 ± 0.13	20.74	19.83	19.21	0.29
ZOA081111.815 − 493719.36	264.905	−8.670	0.19	−53.62	3.62	16.00 ± 0.03	15.27 ± 0.03	14.57 ± 0.04	–	14.43 ± 0.24	11.26 ± 0.94	19.27	18.54	17.86	0.27
ZOA081109.188 − 493329.02	264.847	−8.642	0.34	72.65	2.65	17.28 ± 0.05	16.47 ± 0.04	15.81 ± 0.06	–	–	14.64 ± 0.26	20.35	19.60	18.93	0.27
ZOA081056.837 − 493328.71	264.828	−8.670	0.71	54.65	3.09	17.82 ± 0.07	17.01 ± 0.05	16.29 ± 0.08	–	–	15.62 ± 0.11	20.59	20.13	19.30	0.27
ZOA081132.464 − 493634.73	264.925	−8.616	0.29	23.48	3.83	16.93 ± 0.06	16.16 ± 0.05	15.24 ± 0.06	–	15.14 ± 0.30	14.19 ± 0.30	20.22	19.30	18.57	0.27
ZOA081101.063 − 493129.41	264.806	−8.643	0.61	43.20	9.33	14.35 ± 0.02	13.56 ± 0.02	13.15 ± 0.02	14.22 ± 0.06	13.43 ± 0.04	12.98 ± 0.04	17.99	17.20	16.77	0.27
ZOA081050.503 − 492530.50	264.706	−8.614	0.08	20.77	3.46	15.67 ± 0.03	14.89 ± 0.03	14.56 ± 0.03	–	13.88 ± 0.29	14.17 ± 0.09	19.03	18.21	17.86	0.31
ZOA081127.524 − 492615.89	264.770	−8.536	0.03	28.50	2.88	17.63 ± 0.07	16.67 ± 0.04	16.05 ± 0.07	–	–	15.09 ± 0.20	20.90	19.98	19.03	0.31
ZOA081105.862 − 492626.22	264.741	−8.587	0.18	−80.48	4.53	15.58 ± 0.03	14.84 ± 0.03	14.54 ± 0.04	14.21 ± 0.43	13.72 ± 0.25	13.70 ± 0.17	18.86	18.12	17.81	0.31
ZOA081057.574 − 492641.78	264.733	−8.608	0.22	8.81	7.24	14.01 ± 0.02	13.23 ± 0.02	12.83 ± 0.02	13.72 ± 0.10	13.02 ± 0.05	12.59 ± 0.05	17.57	16.80	16.39	0.31
ZOA081124.868 − 492834.58	264.799	−8.562	0.52	39.79	5.26	15.14 ± 0.03	14.40 ± 0.02	14.06 ± 0.03	14.87 ± 0.08	13.81 ± 0.15	–	18.54	17.79	17.48	0.31
ZOA081046.258 − 492453.46	264.690	−8.618	0.09	−43.42	5.59	14.79 ± 0.03	14.03 ± 0.02	13.61 ± 0.03	14.02 ± 0.25	13.47 ± 0.14	12.73 ± 0.21	18.27	17.52	17.09	0.31
ZOA081107.530 − 492354.97	264.708	−8.560	0.46	−37.07	3.60	16.47 ± 0.04	15.65 ± 0.03	15.01 ± 0.04	15.56 ± 0.31	14.93 ± 0.18	14.42 ± 0.14	19.64	18.82	18.28	0.31
ZOA081102.555 − 492413.89	264.705	−8.575	0.10	−6.43	6.82	14.10 ± 0.02	13.28 ± 0.02	12.84 ± 0.02	13.79 ± 0.11	12.87 ± 0.12	12.56 ± 0.06	17.66	16.85	16.40	0.31
ZOA081047.176 − 492357.55	264.679	−8.608	0.23	−43.24	7.10	14.25 ± 0.02	13.46 ± 0.02	13.09 ± 0.02	13.76 ± 0.15	12.87 ± 0.13	12.67 ± 0.08	17.75	16.97	16.59	0.31
ZOA081121.125 − 492515.52	264.747	−8.541	0.22	−82.47	3.11	16.47 ± 0.04	15.70 ± 0.03	15.38 ± 0.04	15.12 ± 0.42	15.02 ± 0.13	14.54 ± 0.18	19.55	18.76	18.51	0.31
ZOA081113.599 − 492717.78	264.765	−8.577	0.07	−50.87	4.37	15.18 ± 0.03	14.40 ± 0.02	13.98 ± 0.03	14.29 ± 0.28	13.56 ± 0.23	13.48 ± 0.11	18.56	17.78	17.38	0.31
ZOA081119.261 − 492823.06	264.788	−8.573	0.42	−7.94	3.14	16.45 ± 0.04	15.71 ± 0.03	15.30 ± 0.04	–	–	13.72 ± 0.37	19.62	18.93	18.34	0.31
ZOA081115.870 − 492913.01	264.795	−8.588	0.10	77.48	3.22	18.44 ± 0.10	17.00 ± 0.05	15.65 ± 0.05	–	16.50 ± 0.20	15.36 ± 0.06	21.46	20.22	18.89	0.31
ZOA081028.930 − 493126.90	264.759	−8.716	0.62	65.65	5.63	15.87 ± 0.03	15.10 ± 0.03	14.47 ± 0.03	15.03 ± 0.28	14.75 ± 0.09	14.16 ± 0.06	19.25	18.52	17.92	0.30
ZOA081057.266 − 493455.63	264.850	−8.682	0.11	−85.65	4.37	16.41 ± 0.04	15.71 ± 0.03	15.24 ± 0.05	15.56 ± 0.28	14.71 ± 0.17	14.47 ± 0.12	19.45	18.75	18.34	0.30
ZOA081112.795 − 492348.48	264.714	−8.547	0.28	34.06	6.22	14.37 ± 0.02	13.59 ± 0.02	13.15 ± 0.03	14.11 ± 0.09	13.01 ± 0.14	12.93 ± 0.05	17.87	17.08	16.65	0.29
ZOA081133.201 − 491910.09	264.678	−8.459	0.20	−14.10	1.63	17.10 ± 0.05	16.60 ± 0.05	17.51 ± 0.27	10.22 ± 2.18	–	13.06 ± 0.67	19.99	19.38	18.72	0.29
ZOA081110.337 − 491946.42	264.653	−8.517	0.31	−36.97	2.52	16.77 ± 0.04	16.03 ± 0.03	15.73 ± 0.06	–	14.60 ± 0.39	15.26 ± 0.11	19.81	19.11	19.12	0.29
ZOA081129.672 − 492029.65	264.691	−8.479	0.53	32.48	5.55	15.34 ± 0.03	14.59 ± 0.02	13.94 ± 0.03	–	11.78 ± 0.87	12.94 ± 0.30	18.73	17.97	17.38	0.29
ZOA081112.882 − 492133.64	264.682	−8.527	0.49	8.77	4.31	15.87 ± 0.03	15.15 ± 0.03	14.69 ± 0.04	15.15 ± 0.24	14.78 ± 0.10	14.50 ± 0.05	19.24	18.51	18.10	0.29
ZOA081127.700 − 491743.79	264.649	−8.459	0.20	28.71	2.52	17.06 ± 0.05	16.39 ± 0.04	15.99 ± 0.06	–	–	15.86 ± 0.06	20.17	19.47	19.11	0.29
ZOA081131.292 − 491714.41	264.647	−8.447	0.21	33.64	2.47	17.52 ± 0.06	16.73 ± 0.05	16.03 ± 0.07	–	–	15.95 ± 0.08	21.02	20.05	19.08	0.29
ZOA081119.579 − 491911.14	264.658	−8.491	0.40	−68.49	5.29	15.89 ± 0.03	15.08 ± 0.03	14.48 ± 0.03	–	–	13.83 ± 0.18	19.18	18.38	17.80	0.29
ZOA081119.252 − 492151.05	264.695	−8.515	0.10	11.70	6.16	14.73 ± 0.03	14.00 ± 0.02	13.73 ± 0.03	14.35 ± 0.10	13.16 ± 0.25	–	18.31	17.57	17.31	0.29
ZOA081106.417 − 492016.18	264.654	−8.531	0.05	−57.16	2.83	17.19 ± 0.05	16.43 ± 0.04	16.27 ± 0.12	–	–	–	20.10	19.33	19.59	0.29
ZOA081133.605 − 492053.59	264.703	−8.474	0.35	8.34	3.00	17.61 ± 0.08	16.72 ± 0.06	15.74 ± 0.08	–	16.40 ± 0.12	15.52 ± 0.09	20.57	20.02	19.20	0.29
ZOA081122.878 − 491917.15	264.664	−8.484	0.46	−62.19	2.30	18.43 ± 0.09	17.33 ± 0.06	16.39 ± 0.07	–	–	–	21.08	20.08	19.11	0.29
ZOA081041.740 − 492617.48	264.704	−8.641	0.12	−78.16	1.77	18.65 ± 0.11	17.84 ± 0.08	16.66 ± 0.09	17.87 ± 0.26	–	16.30 ± 0.15	22.15	21.11	20.13	0.31
ZOA081026.678 − 492654.46	264.691	−8.681	0.50	84.91	4.41	17.91 ± 0.08	17.19 ± 0.06	16.15 ± 0.10	–	–	15.54 ± 0.18	20.79	20.06	19.30	0.31
ZOA081043.029 − 492718.93	264.720	−8.647	0.53	62.69	3.73	16.12 ± 0.04	15.32 ± 0.03	15.07 ± 0.05	15.24 ± 0.28	14.48 ± 0.23	13.66 ± 0.35	19.38	18.55	18.27	0.31
ZOA081045.558 − 492719.55	264.724	−8.641	0.19	−7.15	1.75	18.72 ± 0.12	17.75 ± 0.08	16.79 ± 0.12	–	–	16.62 ± 0.13	21.99	20.95	20.20	0.31
ZOA081045.150 − 492816.85	264.737	−8.651	0.10	10.85	3.54	16.43 ± 0.04	15.65 ± 0.03	14.82 ± 0.04	–	14.93 ± 0.15	14.73 ± 0.05	19.66	18.75	18.22	0.31
ZOA081054.126 − 492917.44	264.765	−8.639	0.42	−73.81	4.40	15.65 ± 0.03	14.93 ± 0.03	14.36 ± 0.03	14.83 ± 0.27	–	14.21 ± 0.04	19.05	18.29	17.78	0.31
ZOA081057.365 − 492358.30	264.694	−8.584	0.15	−52.08	1.99	17.78 ± 0.07	17.04 ± 0.05	16.76 ± 0.09	–	–	16.64 ± 0.10	20.91	20.12	20.35	0.31

$ZOA081042.158-492404.04$	264.673	−8.620	0.23	4.33	14.81	13.78 ± 0.02	13.01 ± 0.02	12.66 ± 0.03	12.98 ± 0.23	12.05 ± 0.10	10.47 ± 0.50	18.91	18.12	17.80	0.31
$ZOA081103.480-492348.80$	264.700	−8.569	0.22	38.94	5.67	14.40 ± 0.02	13.59 ± 0.02	13.20 ± 0.02	13.69 ± 0.21	12.76 ± 0.20	13.00 ± 0.05	17.86	17.05	16.68	0.31
$ZOA081038.912-492445.02$	264.678	−8.634	0.19	83.55	2.59	16.28 ± 0.04	15.52 ± 0.03	15.11 ± 0.04	–	–	14.60 ± 0.12	19.58	18.80	18.40	0.31
$ZOA081057.981-492442.68$	264.705	−8.589	0.42	−14.28	2.70	17.14 ± 0.05	16.46 ± 0.04	16.07 ± 0.06	–	–	15.78 ± 0.08	20.38	19.66	19.37	0.31
$ZOA081038.557-492427.53$	264.673	−8.632	0.46	−55.96	6.15	15.00 ± 0.03	14.21 ± 0.02	13.85 ± 0.03	14.75 ± 0.09	13.91 ± 0.06	12.97 ± 0.24	18.46	17.66	17.32	0.31
$ZOA081051.876-492651.74$	264.727	−8.623	0.21	−72.41	4.20	16.13 ± 0.04	15.39 ± 0.03	15.08 ± 0.04	15.26 ± 0.29	14.38 ± 0.29	14.55 ± 0.13	19.39	18.66	18.31	0.31
$ZOA081054.753-492722.37$	264.738	−8.620	0.27	10.12	4.20	18.95 ± 0.12	18.28 ± 0.10	17.42 ± 0.14	–	16.15 ± 0.22	16.31 ± 0.26	20.51	19.86	19.45	0.31
$ZOA081027.345-492430.73$	264.658	−8.658	0.27	−51.69	3.10	18.15 ± 0.09	17.29 ± 0.06	16.56 ± 0.09	–	–	15.00 ± 0.44	21.19	19.96	19.70	0.31
$ZOA081042.003-492323.72$	264.663	−8.614	0.51	−56.09	3.36	16.33 ± 0.04	15.54 ± 0.03	15.12 ± 0.05	16.11 ± 0.07	15.35 ± 0.04	15.03 ± 0.05	19.65	18.83	18.63	0.31
$ZOA081038.191-492323.45$	264.657	−8.623	0.13	−3.96	1.82	17.28 ± 0.06	16.39 ± 0.04	16.17 ± 0.09	–	15.31 ± 0.31	14.28 ± 0.58	20.90	19.69	19.17	0.31
$ZOA081101.085-492745.15$	264.753	−8.609	0.08	−4.91	1.71	17.68 ± 0.07	16.89 ± 0.05	16.69 ± 0.10	–	–	15.70 ± 0.25	20.49	19.80	19.67	0.31

Table A.0.2: VC04 catalogue of galaxies

Designation	ℓ (deg)	b (deg)	e_J	ϕ_J (deg)	r_{k20fe} (arcsec)	J_{k20fe} (mag)	H_{k20fe} (mag)	$K_{s\,k20fe}$ (mag)	J_{tot} (mag)	H_{tot} (mag)	$K_{s\,tot}$ (mag)	μ_J	μ_H (mag arcsec^{-2})	μ_{Ks}	$E(B-V)$ (mag)
$ZOA083616.126-553947.07$	272.118	−8.907	0.18	−49.67	2.90	17.08 ± 0.06	16.12 ± 0.04	15.79 ± 0.07	–	–	14.29 ± 0.31	19.85	18.77	18.57	0.21
$ZOA083619.857-553458.32$	272.058	−8.852	0.35	88.01	2.19	17.59 ± 0.07	16.68 ± 0.05	15.87 ± 0.06	12.89 ± 1.51	–	15.26 ± 0.18	20.04	19.28	18.98	0.21
$ZOA083548.415-553524.89$	272.020	−8.916	0.39	−59.00	1.94	18.04 ± 0.09	17.08 ± 0.06	16.30 ± 0.08	–	–	15.47 ± 0.17	21.15	20.11	19.21	0.21
$ZOA083642.994-555523.67$	272.368	−9.009	0.34	−11.02	2.35	17.40 ± 0.05	16.62 ± 0.04	15.96 ± 0.05	16.95 ± 0.18	–	15.77 ± 0.05	20.68	19.88	19.24	0.17
$ZOA083627.959-555031.35$	272.281	−8.990	0.32	−85.51	3.15	15.66 ± 0.03	14.93 ± 0.03	14.61 ± 0.03	14.12 ± 0.47	12.99 ± 0.54	10.20 ± 1.36	18.84	18.07	17.91	0.17
$ZOA083703.459-555059.83$	272.337	−8.927	0.32	−11.99	3.79	16.19 ± 0.04	15.49 ± 0.03	15.17 ± 0.05	15.38 ± 0.30	15.21 ± 0.10	14.80 ± 0.10	19.63	18.88	18.60	0.17
$ZOA083658.248-555225.32$	272.349	−8.951	0.72	9.66	11.28	13.74 ± 0.02	13.01 ± 0.02	12.72 ± 0.02	9.26 ± 1.40	10.62 ± 0.70	12.57 ± 0.04	17.55	16.78	16.46	0.17
$ZOA083646.011-555152.41$	272.325	−8.969	0.20	15.60	4.47	15.02 ± 0.03	14.27 ± 0.02	13.89 ± 0.03	14.32 ± 0.23	13.71 ± 0.16	–	18.41	17.66	17.29	0.17
$ZOA083644.915-555400.90$	272.352	−8.992	0.26	64.06	3.51	16.76 ± 0.04	15.96 ± 0.03	15.18 ± 0.04	–	–	14.21 ± 0.24	19.97	19.12	18.35	0.17
$ZOA083652.168-555359.43$	272.362	−8.978	0.21	−5.19	1.92	17.51 ± 0.06	16.67 ± 0.04	16.01 ± 0.05	–	–	–	20.64	19.61	19.22	0.17
$ZOA083702.777-555403.43$	272.378	−8.959	0.03	−51.71	2.30	17.14 ± 0.05	16.63 ± 0.04	16.28 ± 0.08	–	16.10 ± 0.08	15.75 ± 0.13	20.03	19.57	19.33	0.17
$ZOA083638.830-555410.91$	272.346	−9.005	0.05	19.04	2.21	17.89 ± 0.07	17.16 ± 0.05	16.28 ± 0.06	–	11.88 ± 1.61	15.80 ± 0.11	20.93	20.07	19.41	0.17
$ZOA083617.964-555013.31$	272.263	−9.005	0.32	−37.01	2.37	17.93 ± 0.07	17.21 ± 0.05	16.44 ± 0.06	–	–	16.20 ± 0.07	20.95	20.32	19.76	0.17
$ZOA083659.119-555009.06$	272.320	−8.927	0.13	−68.94	1.94	18.19 ± 0.08	17.21 ± 0.05	16.42 ± 0.07	–	–	–	20.96	20.04	19.05	0.17
$ZOA083624.922-554926.24$	272.262	−8.985	0.45	−55.94	3.87	15.39 ± 0.03	14.67 ± 0.02	14.30 ± 0.03	14.81 ± 0.18	14.37 ± 0.06	13.83 ± 0.12	18.73	18.01	17.66	0.17
$ZOA083649.122-554951.18$	272.302	−8.943	0.10	−42.51	4.63	15.41 ± 0.03	14.69 ± 0.02	14.26 ± 0.03	13.47 ± 0.56	14.91 ± 0.32	13.26 ± 0.60	18.66	18.14	17.47	0.17
$ZOA083728.306-560725.04$	272.595	−9.042	0.26	29.25	5.42	15.89 ± 0.03	15.18 ± 0.03	14.69 ± 0.05	–	14.11 ± 0.28	14.25 ± 0.12	19.20	18.50	18.00	0.18
$ZOA083750.752-560813.54$	272.638	−9.008	0.30	5.79	2.11	17.81 ± 0.07	16.91 ± 0.05	16.45 ± 0.12	–	–	16.16 ± 0.14	20.59	19.94	19.70	0.18
$ZOA083553.387-553657.32$	272.048	−8.922	0.48	47.12	1.64	18.63 ± 0.12	17.44 ± 0.07	16.63 ± 0.10	–	–	10.57 ± 1.92	22.21	20.61	19.76	0.21
$ZOA083559.522-553546.84$	272.040	−8.899	0.10	−89.49	2.22	17.82 ± 0.08	17.03 ± 0.06	16.20 ± 0.07	–	16.65 ± 0.13	15.28 ± 0.28	20.93	20.44	19.48	0.21
$ZOA083549.487-553900.30$	272.070	−8.950	0.46	−29.94	2.17	17.67 ± 0.07	17.05 ± 0.06	17.05 ± 0.16	15.74 ± 0.48	15.46 ± 0.33	13.81 ± 0.67	20.01	19.43	19.33	0.21
$ZOA083721.578-555454.50$	272.416	−8.931	0.43	−17.99	8.43	13.72 ± 0.02	13.00 ± 0.02	12.60 ± 0.02	13.02 ± 0.22	12.70 ± 0.06	12.36 ± 0.05	17.35	16.64	16.23	0.18
$ZOA083717.924-555225.25$	272.377	−8.914	0.30	−21.27	2.16	17.40 ± 0.06	16.72 ± 0.04	16.48 ± 0.09	–	–	15.73 ± 0.18	20.40	19.71	19.78	0.18
$ZOA083723.563-555243.81$	272.389	−8.906	0.41	12.72	5.72	15.34 ± 0.03	14.70 ± 0.03	14.29 ± 0.04	14.91 ± 0.12	14.18 ± 0.11	13.46 ± 0.23	18.70	18.03	17.66	0.18
$ZOA083712.837-555307.59$	272.379	−8.930	0.25	36.73	2.44	17.71 ± 0.07	16.97 ± 0.05	16.19 ± 0.07	–	–	15.98 ± 0.08	20.64	19.78	19.16	0.18
$ZOA083702.059-555324.58$	272.368	−8.954	0.07	−43.29	8.88	13.47 ± 0.02	12.73 ± 0.02	12.31 ± 0.02	12.69 ± 0.25	12.34 ± 0.11	11.77 ± 0.14	17.12	16.38	15.97	0.18
$ZOA083709.760-555414.18$	272.390	−8.947	0.42	85.81	5.81	15.61 ± 0.03	14.77 ± 0.03	14.15 ± 0.03	15.38 ± 0.10	14.21 ± 0.18	14.01 ± 0.04	19.04	18.18	17.61	0.18
$ZOA083659.032-555427.58$	272.378	−8.970	0.27	65.45	2.84	16.81 ± 0.04	16.02 ± 0.04	15.19 ± 0.06	–	15.60 ± 0.11	14.29 ± 0.28	19.88	19.25	18.55	0.18
$ZOA083716.510-555454.75$	272.409	−8.941	0.09	−20.81	2.27	17.09 ± 0.05	16.46 ± 0.04	16.18 ± 0.07	–	16.10 ± 0.05	15.75 ± 0.09	20.30	19.48	19.21	0.18
$ZOA083653.136-555009.80$	272.311	−8.938	0.41	37.09	2.51	18.03 ± 0.08	17.38 ± 0.06	16.63 ± 0.09	–	16.97 ± 0.08	16.02 ± 0.15	21.09	20.51	19.85	0.18
$ZOA083655.220-554958.27$	272.312	−8.933	0.28	−68.49	2.41	18.28 ± 0.09	17.45 ± 0.07	16.81 ± 0.11	–	–	16.24 ± 0.14	21.04	20.34	20.08	0.18
$ZOA083653.021-554907.11$	272.297	−8.928	0.52	12.11	3.56	16.49 ± 0.04	15.77 ± 0.03	15.32 ± 0.05	15.81 ± 0.21	15.09 ± 0.15	14.53 ± 0.16	19.61	18.93	18.50	0.18
$ZOA083656.418-554919.37$	272.305	−8.924	0.53	34.25	4.82	15.56 ± 0.03	14.85 ± 0.03	14.47 ± 0.03	15.11 ± 0.16	14.38 ± 0.14	13.89 ± 0.16	18.96	18.23	17.88	0.18
$ZOA083703.010-554929.53$	272.316	−8.913	0.44	−31.31	2.69	17.05 ± 0.05	16.28 ± 0.04	15.73 ± 0.05	12.14 ± 1.57	–	13.62 ± 0.53	19.77	19.00	18.57	0.18
$ZOA083754.541-560320.48$	272.576	−8.953	0.18	16.14	4.22	16.06 ± 0.06	15.39 ± 0.05	14.74 ± 0.13	15.76 ± 0.07	–	–	19.23	18.58	18.20	0.18
$ZOA083818.434-560304.53$	272.606	−8.905	0.40	−4.99	5.08	14.91 ± 0.04	14.19 ± 0.03	13.86 ± 0.06	14.68 ± 0.06	14.00 ± 0.05	13.25 ± 0.18	18.34	17.63	17.29	0.18
$ZOA083810.515-560254.81$	272.593	−8.919	0.44	9.49	5.17	15.49 ± 0.04	14.88 ± 0.04	14.43 ± 0.07	15.46 ± 0.05	14.55 ± 0.10	13.88 ± 0.18	18.89	18.24	17.85	0.18
$ZOA083725.627-555730.03$	272.457	−8.949	0.05	−0.52	1.81	16.91 ± 0.09	16.32 ± 0.07	15.91 ± 0.16	–	–	15.90 ± 0.16	19.86	19.17	19.72	0.18
$ZOA083726.319-555732.76$	272.458	−8.949	0.41	−14.39	2.16	17.16 ± 0.10	16.40 ± 0.07	16.05 ± 0.15	–	15.49 ± 0.09	15.94 ± 0.15	19.68	19.00	18.97	0.18
$ZOA083739.990-560603.35$	272.593	−9.007	0.38	24.84	2.00	17.35 ± 0.06	16.50 ± 0.04	15.74 ± 0.07	–	15.79 ± 0.14	14.76 ± 0.32	20.55	19.46	18.80	0.18
$ZOA083754.100-560819.81$	272.644	−9.003	0.20	−76.91	2.14	18.60 ± 0.11	17.55 ± 0.07	16.71 ± 0.13	–	–	16.61 ± 0.13	21.65	20.63	20.12	0.18
$ZOA083812.947-560447.44$	272.622	−8.933	0.25	53.74	2.69	16.81 ± 0.05	16.12 ± 0.04	15.64 ± 0.07	–	15.79 ± 0.07	–	19.91	19.35	18.86	0.18
$ZOA083758.159-560847.78$	272.656	−9.000	0.64	75.25	4.39	16.37 ± 0.04	15.64 ± 0.03	15.32 ± 0.06	15.58 ± 0.17	14.72 ± 0.12	14.45 ± 0.17	19.43	18.68	18.42	0.18
$ZOA083805.602-560915.89$	272.672	−8.991	0.43	52.37	3.63	16.70 ± 0.04	16.04 ± 0.04	15.70 ± 0.07	16.18 ± 0.17	15.58 ± 0.10	14.71 ± 0.21	19.84	19.26	19.01	0.18
$ZOA083612.583-552927.85$	271.973	−8.812	0.35	58.09	2.12	17.98 ± 0.08	17.04 ± 0.06	16.12 ± 0.07	–	–	16.10 ± 0.07	21.87	20.70	21.14	0.23
$ZOA083627.724-553244.69$	272.038	−8.815	0.26	0.97	3.84	15.35 ± 0.03	14.60 ± 0.02	14.25 ± 0.03	–	13.97 ± 0.18	–	18.70	17.97	17.61	0.23
$ZOA083546.280-552846.97$	271.926	−8.855	0.11	−14.47	2.21	17.84 ± 0.08	16.98 ± 0.06	16.25 ± 0.08	–	–	16.05 ± 0.08	20.95	20.09	19.88	0.23
$ZOA083550.564-552835.59$	271.930	−8.845	0.36	43.78	2.49	18.14 ± 0.09	17.24 ± 0.06	16.32 ± 0.07	–	–	–	21.04	19.91	19.14	0.23
$ZOA083550.778-552831.57$	271.929	−8.844	0.20	71.05	2.66	17.54 ± 0.07	16.68 ± 0.05	15.99 ± 0.07	–	–	–	20.24	19.26	18.49	0.23
$ZOA083505.517-560250.47$	272.335	−9.266	0.29	73.78	3.86	15.13 ± 0.03	14.37 ± 0.02	14.01 ± 0.03	–	13.40 ± 0.26	13.71 ± 0.07	18.50	17.71	17.40	0.19
$ZOA083507.656-560252.80$	272.339	−9.262	0.24	60.94	3.06	16.16 ± 0.04	15.38 ± 0.03	14.98 ± 0.05	–	–	14.56 ± 0.09	19.47	18.66	18.20	0.19
$ZOA083510.983-555746.22$	272.273	−9.206	0.25	−41.61	2.71	16.08 ± 0.03	15.25 ± 0.03	14.66 ± 0.03	14.43 ± 0.49	14.52 ± 0.13	–	19.11	18.32	17.92	0.19
$ZOA083458.787-555816.15$	272.263	−9.234	0.27	−40.51	2.51	17.78 ± 0.07	17.02 ± 0.05	16.61 ± 0.10	–	16.05 ± 0.23	–	20.59	19.79	19.61	0.19
$ZOA083438.306-555629.00$	272.210	−9.255	0.12	82.68	2.66	17.41 ± 0.06	16.46 ± 0.04	15.64 ± 0.05	16.72 ± 0.23	15.41 ± 0.32	15.54 ± 0.06	20.75	19.74	18.91	0.19
$ZOA083505.625-555815.55$	272.272	−9.221	0.29	69.35	2.24	17.86 ± 0.07	17.04 ± 0.05	16.15 ± 0.07	–	15.17 ± 0.56	16.03 ± 0.07	18.45	18.25	19.38	0.19
$ZOA083453.444-560334.26$	272.328	−9.296	0.54	−4.63	12.94	13.16 ± 0.02	12.49 ± 0.02	12.05 ± 0.03	12.53 ± 0.21	12.36 ± 0.04	11.84 ± 0.06	17.32	16.56	16.13	0.19

ZOA083415.840 − 560230.05	272.262	−9.356	0.21	−62.59	2.01	17.68 ± 0.07	16.76 ± 0.05	15.97 ± 0.07	–	–	15.90 ± 0.08	20.66	19.82	18.97	0.20
ZOA083411.272 − 555748.59	272.191	−9.319	0.21	−84.53	3.49	17.19 ± 0.06	16.44 ± 0.05	15.86 ± 0.08	16.82 ± 0.19	16.35 ± 0.06	14.65 ± 0.32	20.74	19.87	19.38	0.20
ZOA083419.807 − 555803.32	272.206	−9.306	0.22	−20.51	2.57	17.11 ± 0.05	16.37 ± 0.04	15.58 ± 0.06	–	–	15.43 ± 0.07	20.18	19.46	18.76	0.20
ZOA083422.151 − 555939.71	272.232	−9.317	0.17	−56.85	3.76	15.82 ± 0.03	15.13 ± 0.03	14.60 ± 0.04	–	–	13.73 ± 0.26	19.16	18.53	17.97	0.20
ZOA083419.851 − 555944.08	272.230	−9.322	0.45	11.76	2.93	17.42 ± 0.06	16.53 ± 0.05	15.94 ± 0.08	–	16.41 ± 0.06	–	20.75	19.83	19.14	0.20
ZOA083421.598 − 555549.49	272.178	−9.281	0.30	−43.73	2.92	16.90 ± 0.06	16.08 ± 0.04	15.49 ± 0.07	–	14.88 ± 0.32	14.76 ± 0.17	20.02	19.14	18.65	0.20
ZOA083355.793 − 555846.00	272.183	−9.358	0.22	−22.60	4.54	16.57 ± 0.04	15.90 ± 0.04	15.37 ± 0.07	15.35 ± 0.34	14.24 ± 0.16	14.85 ± 0.10	18.66	18.19	18.41	0.20
ZOA083423.969 − 560237.57	272.275	−9.342	0.21	56.01	3.84	16.31 ± 0.04	15.69 ± 0.04	15.19 ± 0.07	–	13.95 ± 0.46	13.86 ± 0.18	19.37	18.83	18.23	0.20
ZOA083833.781 − 554822.18	272.428	−8.731	0.16	−23.06	3.35	16.24 ± 0.04	15.48 ± 0.04	15.21 ± 0.07	–	–	14.65 ± 0.14	19.44	18.67	18.39	0.18
ZOA083817.065 − 554603.04	272.373	−8.739	0.35	4.79	3.85	16.18 ± 0.04	15.43 ± 0.04	14.62 ± 0.07	–	–	–	19.50	18.79	18.07	0.18
ZOA083611.590 − 553010.41	271.981	−8.821	0.32	88.40	1.75	18.39 ± 0.10	17.71 ± 0.08	16.88 ± 0.12	18.12 ± 0.14	–	16.84 ± 0.12	21.66	20.92	21.27	0.23
ZOA083606.569 − 553019.61	271.976	−8.832	0.13	31.86	2.00	17.95 ± 0.07	17.28 ± 0.06	16.51 ± 0.07	–	–	16.30 ± 0.08	20.60	19.90	19.52	0.23
ZOA083547.941 − 553228.18	271.979	−8.888	0.18	−59.60	2.13	18.08 ± 0.08	17.39 ± 0.06	16.72 ± 0.09	–	–	–	20.85	20.05	19.51	0.23
ZOA083553.965 − 552835.57	271.934	−8.839	0.29	15.11	5.88	14.83 ± 0.03	14.09 ± 0.02	13.72 ± 0.03	13.99 ± 0.28	13.28 ± 0.21	13.16 ± 0.12	18.29	17.56	17.19	0.23
ZOA083614.881 − 553258.05	272.023	−8.842	0.40	−30.99	2.46	17.49 ± 0.07	17.04 ± 0.06	16.66 ± 0.11	–	16.02 ± 0.29	16.34 ± 0.10	20.95	20.33	20.16	0.23
ZOA083455.311 − 555806.58	272.256	−9.239	0.41	85.13	3.45	16.35 ± 0.04	15.61 ± 0.03	15.24 ± 0.04	15.93 ± 0.14	–	14.99 ± 0.07	19.62	18.86	18.64	0.18
ZOA083500.518 − 555838.69	272.271	−9.234	0.44	1.92	3.00	18.10 ± 0.08	17.27 ± 0.06	16.87 ± 0.12	–	–	16.36 ± 0.13	20.68	19.98	19.36	0.18
ZOA083543.243 − 560059.20	272.362	−9.176	0.60	−22.77	9.02	14.56 ± 0.03	13.80 ± 0.02	13.37 ± 0.03	13.83 ± 0.26	13.59 ± 0.07	–	18.17	17.36	16.97	0.18
ZOA083523.886 − 560206.40	272.350	−9.224	0.22	−47.23	4.33	15.71 ± 0.03	15.02 ± 0.03	14.46 ± 0.04	15.03 ± 0.23	14.27 ± 0.18	13.43 ± 0.21	18.99	18.31	17.75	0.18
ZOA083524.472 − 560210.91	272.352	−9.224	0.24	−27.00	2.47	16.66 ± 0.04	15.79 ± 0.03	15.36 ± 0.04	–	14.24 ± 0.40	–	19.88	18.81	18.47	0.18
ZOA083443.169 − 555845.09	272.248	−9.268	0.48	5.04	3.31	17.18 ± 0.05	16.32 ± 0.04	15.51 ± 0.06	17.03 ± 0.11	16.13 ± 0.07	14.42 ± 0.30	20.54	19.68	18.66	0.19
ZOA083435.447 − 555925.05	272.247	−9.289	0.44	36.99	3.27	16.71 ± 0.04	16.04 ± 0.04	15.47 ± 0.06	–	15.79 ± 0.07	14.76 ± 0.16	19.92	19.36	18.71	0.19
ZOA083426.017 − 560111.18	272.258	−9.324	0.26	59.74	4.24	15.29 ± 0.03	14.53 ± 0.02	14.03 ± 0.04	14.93 ± 0.14	14.29 ± 0.07	13.81 ± 0.06	18.69	17.95	17.43	0.19
ZOA083647.182 − 554928.62	272.294	−8.943	0.09	58.76	4.98	14.99 ± 0.03	14.43 ± 0.03	13.98 ± 0.04	14.47 ± 0.15	14.27 ± 0.05	13.38 ± 0.14	18.38	17.89	17.36	0.18
ZOA083636.920 − 554907.55	272.275	−8.959	0.31	−41.18	5.09	14.98 ± 0.03	14.23 ± 0.03	13.90 ± 0.04	14.31 ± 0.23	13.28 ± 0.24	12.80 ± 0.24	18.45	17.69	17.36	0.18
ZOA083637.871 − 554918.76	272.278	−8.959	0.23	−25.93	2.36	16.80 ± 0.05	16.70 ± 0.07	15.82 ± 0.09	–	16.51 ± 0.08	15.77 ± 0.09	19.75	19.63	19.12	0.18
ZOA083644.134 − 554823.55	272.275	−8.938	0.07	−26.08	8.84	13.53 ± 0.02	12.77 ± 0.02	12.40 ± 0.02	12.84 ± 0.23	12.28 ± 0.13	11.81 ± 0.15	17.27	16.50	16.12	0.18
ZOA083645.668 − 554839.75	272.281	−8.938	0.18	23.32	2.46	17.34 ± 0.06	16.67 ± 0.06	15.87 ± 0.07	–	–	15.81 ± 0.08	20.38	19.57	19.12	0.18
ZOA083650.533 − 554458.28	272.237	−8.892	0.26	52.77	3.13	16.03 ± 0.04	15.27 ± 0.03	15.02 ± 0.04	14.49 ± 0.48	13.93 ± 0.37	13.61 ± 0.38	19.21	18.46	18.25	0.18
ZOA083650.683 − 554513.96	272.241	−8.895	0.35	−84.56	3.56	16.18 ± 0.04	15.37 ± 0.03	14.86 ± 0.04	–	–	14.66 ± 0.06	19.47	18.71	18.23	0.18
ZOA083643.486 − 554714.11	272.258	−8.928	0.33	−12.64	4.00	15.75 ± 0.03	14.92 ± 0.03	14.56 ± 0.04	15.66 ± 0.05	–	14.32 ± 0.06	19.14	18.34	18.01	0.18
ZOA083646.125 − 554747.37	272.269	−8.928	0.12	37.44	3.81	15.51 ± 0.03	14.75 ± 0.03	14.36 ± 0.03	14.53 ± 0.30	12.89 ± 0.54	12.73 ± 0.47	18.80	18.06	17.71	0.18
ZOA083644.951 − 554753.59	272.269	−8.932	0.21	35.87	4.65	14.84 ± 0.03	14.10 ± 0.02	13.73 ± 0.03	13.29 ± 0.47	12.79 ± 0.36	13.26 ± 0.12	18.23	17.49	17.16	0.18
ZOA083655.382 − 554749.09	272.283	−8.911	0.21	4.59	6.25	14.43 ± 0.03	13.78 ± 0.02	13.31 ± 0.03	13.47 ± 0.29	12.78 ± 0.28	12.64 ± 0.18	17.96	17.32	16.83	0.18
ZOA083644.094 − 554802.95	272.270	−8.935	0.09	23.84	4.76	15.11 ± 0.03	14.41 ± 0.03	14.04 ± 0.03	–	–	13.21 ± 0.23	18.52	17.82	17.47	0.18
ZOA083626.165 − 554206.95	272.164	−8.910	0.34	−81.75	3.85	16.21 ± 0.04	15.51 ± 0.04	15.29 ± 0.07	–	13.69 ± 0.45	14.82 ± 0.10	19.25	18.55	18.45	0.18
ZOA083607.177 − 554252.42	272.148	−8.954	0.33	63.34	7.06	14.57 ± 0.03	13.72 ± 0.02	13.22 ± 0.03	13.87 ± 0.26	13.26 ± 0.12	12.42 ± 0.22	18.16	17.31	16.80	0.18
ZOA083443.350 − 555026.79	272.135	−9.187	0.21	55.79	6.72	14.14 ± 0.02	13.39 ± 0.02	13.00 ± 0.02	13.57 ± 0.18	13.02 ± 0.09	12.50 ± 0.12	17.70	16.94	16.55	0.19
ZOA083512.847 − 555035.40	272.178	−9.132	0.39	46.90	2.62	17.02 ± 0.05	16.34 ± 0.04	15.55 ± 0.05	–	15.66 ± 0.20	14.73 ± 0.20	20.04	19.39	18.65	0.19
ZOA083517.144 − 555103.79	272.190	−9.129	0.27	55.16	5.21	15.60 ± 0.03	14.87 ± 0.03	14.38 ± 0.04	15.26 ± 0.13	14.13 ± 0.17	13.67 ± 0.18	19.00	18.25	17.79	0.19
ZOA083427.803 − 555123.62	272.126	−9.226	0.28	−22.30	1.77	18.11 ± 0.08	17.39 ± 0.06	16.70 ± 0.10	–	15.75 ± 0.51	–	20.89	19.91	19.53	0.19
ZOA083450.692 − 555146.90	272.163	−9.186	0.70	−33.44	2.48	18.61 ± 0.10	17.39 ± 0.06	17.27 ± 0.13	–	15.88 ± 0.43	–	20.88	20.12	19.76	0.19
ZOA083458.678 − 555156.71	272.176	−9.172	0.12	60.81	1.91	17.40 ± 0.06	16.64 ± 0.04	15.84 ± 0.06	–	–	15.83 ± 0.06	20.60	19.88	19.11	0.19
ZOA083502.992 − 555321.56	272.202	−9.178	0.35	−84.22	2.49	17.14 ± 0.05	16.30 ± 0.04	15.58 ± 0.05	–	–	15.12 ± 0.10	19.99	19.02	18.69	0.19
ZOA083455.565 − 555343.60	272.197	−9.196	0.38	−82.15	2.62	17.73 ± 0.07	16.91 ± 0.05	16.02 ± 0.07	–	–	15.86 ± 0.07	20.55	19.76	19.04	0.19
ZOA083518.434 − 555358.05	272.231	−9.155	0.52	53.40	2.39	18.02 ± 0.08	17.17 ± 0.06	16.56 ± 0.09	17.94 ± 0.10	16.72 ± 0.12	16.37 ± 0.09	21.66	20.66	19.92	0.19
ZOA083435.632 − 554920.05	272.109	−9.191	0.13	−18.67	7.82	13.71 ± 0.02	12.98 ± 0.02	12.64 ± 0.02	13.07 ± 0.19	12.49 ± 0.12	12.39 ± 0.04	17.38	16.64	16.29	0.19
ZOA083444.398 − 555156.41	272.157	−9.200	0.36	−15.08	5.12	15.82 ± 0.03	15.15 ± 0.03	14.76 ± 0.04	15.51 ± 0.10	14.75 ± 0.07	14.27 ± 0.09	19.07	18.40	18.03	0.19
ZOA083511.877 − 555223.74	272.201	−9.152	0.08	−35.51	3.12	16.59 ± 0.04	15.75 ± 0.03	15.03 ± 0.04	–	–	14.48 ± 0.12	19.74	18.93	18.24	0.19
ZOA083512.542 − 555140.77	272.192	−9.144	0.10	58.15	1.42	18.65 ± 0.12	17.62 ± 0.08	17.05 ± 0.13	–	17.47 ± 0.10	–	22.11	21.28	21.61	0.19
ZOA083407.299 − 555125.02	272.098	−9.265	0.42	−75.36	2.46	17.83 ± 0.08	17.06 ± 0.06	16.23 ± 0.09	–	–	14.69 ± 0.40	20.80	20.04	19.03	0.19
ZOA083412.197 − 555515.51	272.158	−9.293	0.36	−30.09	2.34	17.63 ± 0.07	16.95 ± 0.06	16.06 ± 0.08	–	–	15.63 ± 0.12	20.70	20.28	19.32	0.19
ZOA083357.242 − 555008.32	272.067	−9.272	0.12	−58.04	3.60	15.72 ± 0.03	14.95 ± 0.03	14.56 ± 0.04	–	14.33 ± 0.14	13.71 ± 0.21	19.00	18.21	17.83	0.19
ZOA083349.630 − 554907.40	272.042	−9.276	0.49	−83.65	5.00	15.84 ± 0.04	15.08 ± 0.03	14.58 ± 0.04	–	–	13.92 ± 0.17	19.20	18.47	17.91	0.19
ZOA083340.160 − 554907.25	272.029	−9.294	0.39	−38.83	3.37	16.87 ± 0.06	16.06 ± 0.04	15.86 ± 0.08	–	15.06 ± 0.27	–	19.98	19.18	18.79	0.19
ZOA083337.973 − 555009.37	272.040	−9.308	0.31	37.17	4.64	15.30 ± 0.03	14.62 ± 0.03	14.16 ± 0.04	14.75 ± 0.18	13.85 ± 0.23	–	18.68	18.01	17.55	0.19
ZOA083356.751 − 555023.52	272.070	−9.275	0.34	51.19	5.06	15.78 ± 0.03	15.04 ± 0.03	14.33 ± 0.04	14.23 ± 0.54	13.53 ± 0.44	13.52 ± 0.21	19.10	18.37	17.70	0.19
ZOA083431.397 − 554903.68	272.099	−9.196	0.05	−40.87	5.62	16.52 ± 0.07	15.60 ± 0.04	15.29 ± 0.08	15.90 ± 0.22	12.15 ± 1.04	14.28 ± 0.16	20.28	18.72	18.41	0.19
ZOA083405.023 − 555439.75	272.140	−9.301	0.57	12.45	6.18	15.43 ± 0.03	14.65 ± 0.03	13.92 ± 0.03	15.23 ± 0.09	14.56 ± 0.04	13.74 ± 0.04	18.89	18.18	17.41	0.19
ZOA083419.055 − 555430.14	272.157	−9.273	0.40	86.75	2.46	17.49 ± 0.07	16.86 ± 0.06	16.38 ± 0.10	–	–	15.31 ± 0.29	20.09	19.55	19.23	0.19
ZOA083400.198 − 554612.49	272.017	−9.228	0.62	−55.03	5.70	14.48 ± 0.03	13.72 ± 0.02	13.33 ± 0.03	14.31 ± 0.04	13.05 ± 0.18	12.47 ± 0.26	17.98	17.21	16.86	0.19
ZOA083425.386 − 554621.96	272.054	−9.181	0.69	17.64	4.37	16.55 ± 0.05	15.72 ± 0.04	15.51 ± 0.10	16.02 ± 0.17	14.63 ± 0.28	14.95 ± 0.13	19.89	18.90	18.58	0.19

ZOA083400.583 − 554137.05	271.954	−9.183	0.30	−58.99	4.00	15.88 ± 0.04	15.04 ± 0.03	14.69 ± 0.05	15.15 ± 0.24	14.44 ± 0.12	14.48 ± 0.08	19.17	18.27	18.02	0.19
ZOA083403.004 − 554208.51	271.965	−9.183	0.24	−62.51	3.10	17.98 ± 0.09	17.18 ± 0.07	16.36 ± 0.10	–	16.48 ± 0.17	15.37 ± 0.16	21.21	20.10	19.35	0.19
ZOA083339.941 − 554142.28	271.927	−9.223	0.29	90.00	3.01	16.34 ± 0.04	15.77 ± 0.04	15.31 ± 0.06	–	14.84 ± 0.18	–	*nan*	18.74	18.36	0.19
ZOA083347.320 − 554135.51	271.936	−9.208	0.28	80.80	6.62	14.38 ± 0.03	13.64 ± 0.02	13.26 ± 0.03	–	12.89 ± 0.21	12.35 ± 0.23	17.89	17.15	16.75	0.19
ZOA083350.178 − 554146.86	271.942	−9.204	0.19	−38.54	4.31	15.96 ± 0.04	15.17 ± 0.03	14.76 ± 0.05	–	14.23 ± 0.29	14.61 ± 0.06	19.48	18.56	18.18	0.19
ZOA083354.386 − 554240.81	271.960	−9.205	0.24	42.31	7.07	14.18 ± 0.02	13.43 ± 0.02	12.94 ± 0.02	13.51 ± 0.21	13.03 ± 0.10	11.59 ± 0.48	17.79	17.04	16.54	0.19
ZOA083355.849 − 554316.26	271.971	−9.208	0.46	31.62	2.93	16.04 ± 0.04	15.32 ± 0.03	14.92 ± 0.04	15.32 ± 0.18	14.72 ± 0.14	14.85 ± 0.04	19.17	18.52	18.28	0.19
ZOA083426.879 − 554819.35	272.083	−9.198	0.31	−12.04	2.77	16.60 ± 0.05	15.93 ± 0.04	15.12 ± 0.06	15.32 ± 0.39	14.85 ± 0.21	15.11 ± 0.07	19.64	18.89	18.19	0.19
ZOA083428.074 − 554422.91	272.030	−9.157	0.23	86.70	4.44	15.83 ± 0.04	15.33 ± 0.04	14.98 ± 0.08	15.46 ± 0.10	14.84 ± 0.05	14.83 ± 0.10	19.08	18.42	18.25	0.19
ZOA083353.561 − 554322.42	271.969	−9.213	0.75	−6.16	4.76	17.79 ± 0.08	16.98 ± 0.06	16.20 ± 0.09	17.32 ± 0.25	16.37 ± 0.10	15.62 ± 0.16	20.91	19.81	19.40	0.19
ZOA083331.565 − 554443.64	271.957	−9.268	0.30	−72.53	5.17	15.07 ± 0.03	14.38 ± 0.03	14.03 ± 0.04	14.36 ± 0.23	13.90 ± 0.09	13.79 ± 0.06	18.51	17.80	17.47	0.19
ZOA083532.353 − 555525.67	272.271	−9.143	0.41	30.19	2.55	17.82 ± 0.07	17.08 ± 0.05	16.16 ± 0.07	–	–	15.98 ± 0.08	21.17	20.66	19.48	0.17
ZOA083515.015 − 555045.84	272.183	−9.130	0.40	34.33	2.88	17.88 ± 0.07	16.95 ± 0.05	16.15 ± 0.07	–	16.76 ± 0.07	16.00 ± 0.07	21.43	20.34	19.46	0.17
ZOA083542.281 − 555050.29	272.222	−9.079	0.56	30.65	4.10	15.85 ± 0.03	15.13 ± 0.03	14.76 ± 0.04	15.53 ± 0.11	15.01 ± 0.04	14.45 ± 0.06	19.25	18.55	18.16	0.17
ZOA083520.986 − 555301.83	272.222	−9.141	0.36	−7.39	1.83	18.51 ± 0.10	17.48 ± 0.07	16.47 ± 0.09	–	–	16.34 ± 0.10	23.94	20.95	20.21	0.17
ZOA083523.527 − 555441.36	272.248	−9.152	0.25	−46.81	3.51	16.15 ± 0.04	15.36 ± 0.03	14.77 ± 0.04	14.99 ± 0.38	14.70 ± 0.17	14.04 ± 0.15	19.33	18.59	18.01	0.17
ZOA083509.239 − 554904.77	272.152	−9.124	0.48	41.51	2.19	18.13 ± 0.08	17.21 ± 0.06	16.47 ± 0.08	–	–	–	20.97	20.48	19.48	0.17
ZOA083458.627 − 554928.75	272.143	−9.149	0.19	78.22	3.24	15.89 ± 0.03	15.20 ± 0.03	14.90 ± 0.04	14.95 ± 0.29	14.69 ± 0.12	13.92 ± 0.25	19.10	18.45	18.14	0.17
ZOA083457.106 − 554904.03	272.135	−9.147	0.14	−88.09	2.54	18.33 ± 0.11	17.27 ± 0.06	16.35 ± 0.08	–	16.64 ± 0.18	16.15 ± 0.09	22.11	20.63	19.48	0.17
ZOA083433.946 − 555035.79	272.124	−9.206	0.23	26.32	5.72	14.46 ± 0.02	13.73 ± 0.02	13.36 ± 0.03	13.96 ± 0.17	13.29 ± 0.09	12.68 ± 0.20	17.92	17.17	16.84	0.19
ZOA083449.268 − 555056.26	272.150	−9.181	0.23	17.25	2.00	18.09 ± 0.09	17.48 ± 0.08	16.43 ± 0.10	–	16.96 ± 0.09	15.28 ± 0.30	21.01	20.24	19.64	0.19
ZOA083417.662 − 555125.92	272.113	−9.245	0.53	3.67	2.14	17.25 ± 0.06	16.50 ± 0.05	15.87 ± 0.07	–	14.25 ± 0.62	14.78 ± 0.28	17.53	17.48	19.16	0.19
ZOA083444.182 − 555134.54	272.151	−9.196	0.44	77.99	2.33	17.60 ± 0.07	16.73 ± 0.05	16.07 ± 0.07	–	–	15.23 ± 0.20	20.82	19.94	19.29	0.19
ZOA083452.801 − 555152.86	272.167	−9.183	0.20	37.85	2.44	17.99 ± 0.09	17.11 ± 0.07	16.48 ± 0.10	–	16.77 ± 0.07	15.97 ± 0.14	20.86	20.10	19.08	0.19
ZOA083434.414 − 555202.72	272.144	−9.219	0.25	−29.37	2.15	16.76 ± 0.04	16.07 ± 0.04	15.94 ± 0.07	–	15.63 ± 0.07	15.87 ± 0.07	19.96	19.18	19.29	0.19
ZOA083448.343 − 555247.75	272.174	−9.200	0.67	−60.33	5.94	16.35 ± 0.04	15.52 ± 0.03	15.03 ± 0.05	16.22 ± 0.09	14.55 ± 0.30	14.35 ± 0.20	19.77	18.87	18.38	0.19
ZOA083440.873 − 555259.94	272.166	−9.217	0.38	−65.45	1.90	17.84 ± 0.07	16.92 ± 0.06	16.31 ± 0.09	–	–	16.30 ± 0.09	20.60	19.86	19.63	0.19
ZOA083445.845 − 555358.41	272.186	−9.217	0.42	−73.43	2.22	17.03 ± 0.05	16.34 ± 0.04	15.76 ± 0.06	–	15.75 ± 0.14	15.25 ± 0.15	20.23	19.43	19.19	0.19
ZOA083446.509 − 555441.89	272.197	−9.222	0.30	7.40	6.85	14.55 ± 0.03	13.80 ± 0.02	13.42 ± 0.03	13.54 ± 0.31	12.84 ± 0.27	13.23 ± 0.04	18.07	17.32	16.95	0.19
ZOA083444.296 − 555519.87	272.203	−9.233	0.17	−5.25	1.64	18.74 ± 0.14	17.91 ± 0.11	16.90 ± 0.13	–	–	16.86 ± 0.13	22.50	21.16	19.93	0.19
ZOA083441.360 − 555017.36	272.130	−9.189	0.12	−16.20	4.55	14.82 ± 0.03	14.08 ± 0.02	13.55 ± 0.03	13.65 ± 0.36	13.19 ± 0.25	13.03 ± 0.11	18.21	17.46	16.96	0.19
ZOA083436.566 − 555020.25	272.124	−9.199	0.35	16.92	2.25	18.17 ± 0.09	17.49 ± 0.07	17.05 ± 0.13	–	–	16.05 ± 0.30	20.83	20.32	20.38	0.19
ZOA083425.329 − 555024.56	272.109	−9.221	0.25	16.09	3.84	15.83 ± 0.03	15.10 ± 0.03	14.60 ± 0.04	15.53 ± 0.11	14.89 ± 0.07	14.38 ± 0.06	19.15	18.48	18.00	0.19
ZOA083436.087 − 554442.31	272.046	−9.145	0.23	−11.36	3.83	15.50 ± 0.03	14.78 ± 0.03	14.46 ± 0.04	14.47 ± 0.30	13.64 ± 0.32	14.30 ± 0.05	18.77	18.11	17.90	0.19
ZOA083446.310 − 554520.98	272.069	−9.132	0.12	−11.29	4.51	15.38 ± 0.03	14.61 ± 0.03	14.15 ± 0.04	14.59 ± 0.28	13.87 ± 0.22	13.22 ± 0.23	18.80	18.03	17.52	0.19
ZOA083503.964 − 554621.91	272.107	−9.108	0.33	14.87	5.34	16.26 ± 0.04	15.61 ± 0.03	15.32 ± 0.06	15.26 ± 0.31	14.24 ± 0.22	14.02 ± 0.14	19.34	18.63	18.40	0.19
ZOA083517.517 − 554628.77	272.128	−9.083	0.36	−48.61	2.40	16.68 ± 0.04	15.94 ± 0.03	15.69 ± 0.06	–	15.65 ± 0.05	–	19.85	19.21	18.87	0.19
ZOA083446.103 − 554258.53	272.036	−9.109	0.37	−64.39	2.23	18.49 ± 0.10	17.47 ± 0.07	16.60 ± 0.09	–	–	16.53 ± 0.09	21.61	20.52	19.75	0.19
ZOA083517.961 − 554244.83	272.077	−9.046	0.33	5.65	1.59	18.35 ± 0.10	17.74 ± 0.09	16.82 ± 0.13	–	–	16.82 ± 0.13	21.23	20.78	20.09	0.19
ZOA083520.189 − 554240.89	272.080	−9.041	0.27	19.50	6.32	14.65 ± 0.03	13.94 ± 0.02	13.67 ± 0.03	13.52 ± 0.38	13.43 ± 0.12	12.80 ± 0.23	18.23	17.52	17.24	0.19
ZOA083443.737 − 554441.87	272.056	−9.130	0.25	28.82	1.97	17.79 ± 0.07	17.00 ± 0.05	16.98 ± 0.16	–	15.19 ± 0.39	–	20.22	19.43	19.52	0.19
ZOA083449.504 − 554403.22	272.056	−9.113	0.22	73.66	2.46	18.43 ± 0.09	17.70 ± 0.07	17.09 ± 0.12	–	–	16.76 ± 0.14	20.70	20.08	19.81	0.19
ZOA083639.834 − 553646.96	272.111	−8.832	0.62	−87.24	2.66	17.47 ± 0.06	16.68 ± 0.05	16.12 ± 0.08	–	15.99 ± 0.24	14.54 ± 0.43	20.54	19.70	19.17	0.22
ZOA083709.527 − 553849.75	272.180	−8.796	0.42	−69.26	6.96	14.62 ± 0.03	13.86 ± 0.02	13.43 ± 0.03	14.21 ± 0.14	13.37 ± 0.12	12.35 ± 0.30	18.15	17.39	16.97	0.22
ZOA083707.221 − 553937.58	272.188	−8.808	0.18	36.52	2.23	18.00 ± 0.08	17.20 ± 0.07	16.61 ± 0.10	–	–	16.36 ± 0.11	21.05	20.39	19.61	0.22
ZOA083702.372 − 554016.35	272.190	−8.824	0.45	82.04	2.59	16.84 ± 0.05	16.15 ± 0.04	15.84 ± 0.07	–	15.04 ± 0.20	15.24 ± 0.14	19.80	18.98	18.93	0.22
ZOA083629.998 − 553630.72	272.093	−8.848	0.31	−33.40	8.57	14.02 ± 0.02	13.21 ± 0.02	12.93 ± 0.03	13.90 ± 0.03	12.32 ± 0.23	11.97 ± 0.25	17.75	16.92	16.59	0.22
ZOA083700.239 − 553455.11	272.114	−8.775	0.09	−49.24	5.73	15.00 ± 0.03	14.30 ± 0.03	13.88 ± 0.03	14.67 ± 0.11	13.97 ± 0.07	13.55 ± 0.06	18.51	17.82	17.39	0.22
ZOA083631.907 − 553731.75	272.110	−8.854	0.27	68.38	8.59	14.52 ± 0.03	13.84 ± 0.02	13.42 ± 0.03	14.00 ± 0.17	13.06 ± 0.23	13.08 ± 0.05	18.19	17.48	17.07	0.22
ZOA083659.183 − 555101.96	272.332	−8.936	0.38	−13.52	2.63	16.49 ± 0.05	15.85 ± 0.04	15.32 ± 0.06	16.30 ± 0.06	14.80 ± 0.24	14.62 ± 0.22	19.84	18.86	18.75	0.17
ZOA083746.468 − 555107.44	272.399	−8.847	0.44	−15.98	2.21	17.90 ± 0.08	17.00 ± 0.06	16.24 ± 0.07	–	–	–	21.06	20.01	19.43	0.17
ZOA083748.300 − 555156.79	272.413	−8.852	0.38	57.05	2.68	17.66 ± 0.07	17.03 ± 0.06	16.48 ± 0.10	–	–	15.56 ± 0.29	20.68	20.17	19.61	0.17
ZOA083742.203 − 555231.44	272.412	−8.869	0.31	63.55	2.38	17.53 ± 0.06	16.87 ± 0.06	16.18 ± 0.08	–	15.73 ± 0.29	15.71 ± 0.11	20.54	19.80	19.27	0.17
ZOA083733.990 − 555240.42	272.403	−8.886	0.45	−22.98	6.89	14.19 ± 0.02	13.42 ± 0.02	13.04 ± 0.03	13.40 ± 0.25	13.05 ± 0.09	12.67 ± 0.09	17.75	16.97	16.58	0.17
ZOA083755.823 − 555432.09	272.459	−8.863	0.52	−16.06	2.63	17.15 ± 0.06	16.56 ± 0.06	15.59 ± 0.08	–	14.46 ± 0.66	14.65 ± 0.28	20.20	19.50	18.62	0.17
ZOA083748.139 − 555037.06	272.395	−8.839	0.27	−57.85	2.29	16.51 ± 0.04	15.85 ± 0.03	15.37 ± 0.05	–	15.51 ± 0.08	15.24 ± 0.05	19.80	19.18	18.72	0.17
ZOA083728.977 − 555029.81	272.366	−8.874	0.54	−55.62	3.61	16.60 ± 0.04	15.90 ± 0.04	15.37 ± 0.05	16.39 ± 0.09	15.36 ± 0.09	15.10 ± 0.06	19.83	18.99	18.48	0.17
ZOA083731.709 − 554858.60	272.349	−8.854	0.23	73.56	1.74	17.86 ± 0.08	16.96 ± 0.07	16.36 ± 0.11	–	–	16.11 ± 0.13	20.84	20.18	19.83	0.17
ZOA083727.287 − 555012.70	272.360	−8.874	0.43	29.11	4.82	14.94 ± 0.03	14.28 ± 0.02	13.85 ± 0.03	14.81 ± 0.05	14.07 ± 0.06	13.19 ± 0.17	18.38	17.70	17.27	0.17
ZOA083744.807 − 555003.31	272.382	−8.840	0.46	−81.32	2.24	18.20 ± 0.09	17.31 ± 0.06	16.50 ± 0.09	–	–	16.33 ± 0.09	21.15	20.46	19.34	0.17
ZOA083732.311 − 555314.82	272.408	−8.895	0.48	12.30	2.22	17.63 ± 0.07	16.96 ± 0.06	16.54 ± 0.11	–	15.97 ± 0.26	16.36 ± 0.12	20.75	20.13	19.70	0.17
ZOA083527.540 − 554810.22	272.165	−9.081	0.12	45.39	2.37	18.43 ± 0.09	17.84 ± 0.08	17.26 ± 0.13	–	–	16.77 ± 0.14	21.25	20.70	21.30	0.18

ZOA083545.913 − 554555.32	272.160	−9.024	0.41	41.69	8.44	14.24 ± 0.02	13.46 ± 0.02	12.98 ± 0.03	13.65 ± 0.20	13.14 ± 0.08	12.46 ± 0.12	17.92	17.14	16.74	0.18
ZOA083540.428 − 554155.46	272.097	−8.995	0.17	−36.96	2.27	17.16 ± 0.05	16.53 ± 0.04	16.11 ± 0.07	–	–	15.94 ± 0.07	20.13	19.54	19.19	0.18
ZOA083501.665 − 554328.37	272.065	−9.084	0.62	−45.38	7.08	15.04 ± 0.03	14.36 ± 0.02	13.84 ± 0.03	14.76 ± 0.09	14.08 ± 0.07	13.64 ± 0.04	18.49	17.82	17.34	0.18
ZOA083533.617 − 554751.70	272.169	−9.066	0.34	−6.43	1.67	17.69 ± 0.07	16.91 ± 0.05	16.83 ± 0.12	–	15.30 ± 0.43	–	20.37	19.66	19.21	0.18
ZOA083520.602 − 554130.77	272.064	−9.029	0.30	60.05	4.13	16.53 ± 0.04	15.82 ± 0.04	15.03 ± 0.05	–	15.26 ± 0.16	14.35 ± 0.12	19.71	19.06	18.26	0.18
ZOA083728.479 − 554351.91	272.275	−8.810	0.25	−19.87	1.76	18.40 ± 0.10	17.52 ± 0.07	16.72 ± 0.11	12.81 ± 1.78	–	16.72 ± 0.11	21.54	20.74	21.16	0.18
ZOA083751.959 − 554654.75	272.350	−8.795	0.51	−41.46	7.17	15.09 ± 0.03	14.45 ± 0.03	14.06 ± 0.04	14.88 ± 0.07	13.53 ± 0.25	13.52 ± 0.15	18.62	17.94	17.62	0.18
ZOA083740.581 − 554654.29	272.334	−8.817	0.61	−16.31	3.57	17.15 ± 0.05	16.47 ± 0.04	16.07 ± 0.08	15.63 ± 0.51	15.61 ± 0.20	15.23 ± 0.20	20.05	19.44	19.21	0.18
ZOA083735.717 − 554735.73	272.336	−8.833	0.20	60.20	2.10	17.45 ± 0.06	16.52 ± 0.04	15.92 ± 0.06	–	–	13.98 ± 0.42	20.24	19.47	18.70	0.18
ZOA083724.851 − 554759.39	272.326	−8.857	0.48	−84.63	2.85	18.06 ± 0.09	17.20 ± 0.07	16.18 ± 0.10	–	–	16.09 ± 0.10	21.21	20.31	19.90	0.18
ZOA083729.303 − 554311.19	272.267	−8.801	0.17	8.63	2.63	18.22 ± 0.09	17.42 ± 0.07	16.35 ± 0.08	–	–	–	20.86	20.42	19.21	0.18
ZOA083722.197 − 554149.77	272.239	−8.801	0.41	35.78	2.42	17.28 ± 0.06	16.60 ± 0.05	16.07 ± 0.08	–	–	14.93 ± 0.32	20.20	19.50	19.25	0.18
ZOA083736.415 − 554313.32	272.278	−8.788	0.20	−28.52	2.16	17.61 ± 0.07	16.78 ± 0.05	16.21 ± 0.08	–	–	–	20.59	19.79	18.95	0.18
ZOA083727.844 − 554232.15	272.256	−8.798	0.44	−57.87	3.02	16.51 ± 0.04	15.73 ± 0.03	15.53 ± 0.05	–	15.28 ± 0.08	14.74 ± 0.23	19.59	18.88	18.82	0.18
ZOA083714.783 − 554239.98	272.240	−8.824	0.40	73.73	2.76	16.39 ± 0.04	15.57 ± 0.03	15.22 ± 0.04	–	14.43 ± 0.32	13.61 ± 0.45	19.62	18.83	18.59	0.18
ZOA083727.492 − 554553.23	272.301	−8.831	0.40	18.54	4.46	15.55 ± 0.03	14.92 ± 0.03	14.63 ± 0.04	15.06 ± 0.14	–	14.21 ± 0.08	18.82	18.20	17.92	0.18
ZOA083748.292 − 555116.42	272.404	−8.845	0.10	−76.28	3.80	17.21 ± 0.06	16.17 ± 0.04	15.57 ± 0.06	–	15.85 ± 0.12	14.93 ± 0.14	20.42	19.49	18.69	0.17
ZOA083809.488 − 555430.88	272.477	−8.837	0.35	19.28	7.82	15.30 ± 0.03	14.54 ± 0.03	14.26 ± 0.04	14.38 ± 0.28	13.45 ± 0.27	13.13 ± 0.32	18.71	17.94	17.69	0.17
ZOA083757.995 − 555511.60	272.471	−8.866	0.44	−20.11	1.94	17.93 ± 0.08	16.98 ± 0.06	16.27 ± 0.10	–	–	15.92 ± 0.14	21.07	19.92	19.72	0.17
ZOA083731.824 − 555023.11	272.369	−8.868	0.31	−35.20	2.86	17.77 ± 0.07	16.92 ± 0.06	16.14 ± 0.08	–	15.60 ± 0.30	15.31 ± 0.16	20.54	19.66	19.11	0.17
ZOA083745.468 − 555005.05	272.384	−8.839	0.27	−30.18	1.81	18.46 ± 0.10	18.55 ± 0.15	16.59 ± 0.10	–	–	15.82 ± 0.26	21.81	22.51	19.85	0.17
ZOA083410.847 − 554340.44	271.997	−9.183	0.41	2.06	3.94	16.46 ± 0.04	15.68 ± 0.03	15.24 ± 0.05	16.35 ± 0.06	15.49 ± 0.05	15.12 ± 0.06	19.78	19.01	18.60	0.19
ZOA083428.295 − 554407.84	272.027	−9.154	0.17	35.37	2.08	16.93 ± 0.05	16.27 ± 0.04	15.78 ± 0.06	–	–	15.27 ± 0.14	20.05	19.54	19.12	0.19
ZOA083420.612 − 554453.56	272.027	−9.176	0.17	35.45	2.31	17.72 ± 0.07	16.81 ± 0.06	15.89 ± 0.07	–	–	15.18 ± 0.20	21.43	20.06	18.90	0.19
ZOA083445.686 − 554620.78	272.082	−9.143	0.64	50.26	2.01	18.44 ± 0.11	17.60 ± 0.09	16.37 ± 0.09	–	17.17 ± 0.12	16.34 ± 0.09	21.31	20.52	19.83	0.19
ZOA083447.428 − 554641.90	272.089	−9.143	0.05	30.44	2.37	17.12 ± 0.05	16.37 ± 0.04	15.63 ± 0.05	–	–	–	20.40	19.54	18.82	0.19
ZOA083429.675 − 554752.29	272.080	−9.188	0.05	−30.76	3.52	16.51 ± 0.04	15.80 ± 0.04	15.62 ± 0.09	–	14.47 ± 0.35	14.65 ± 0.19	19.55	18.81	18.49	0.19
ZOA083428.178 − 554423.06	272.031	−9.157	0.39	74.69	4.47	15.73 ± 0.03	14.98 ± 0.03	14.78 ± 0.05	14.76 ± 0.30	13.81 ± 0.31	14.08 ± 0.12	19.05	18.30	18.09	0.19
ZOA083800.952 − 554426.68	272.329	−8.754	0.25	−51.89	2.31	17.09 ± 0.05	16.35 ± 0.04	15.78 ± 0.06	–	–	–	20.25	19.66	18.98	0.18
ZOA083744.290 − 554515.13	272.316	−8.793	0.32	45.74	2.40	17.95 ± 0.08	17.07 ± 0.06	16.59 ± 0.12	12.24 ± 1.79	–	15.52 ± 0.26	20.92	19.89	19.39	0.18
ZOA083750.196 − 554735.16	272.356	−8.805	0.61	12.41	3.52	16.79 ± 0.04	15.95 ± 0.04	15.38 ± 0.06	16.66 ± 0.06	14.83 ± 0.30	15.06 ± 0.09	20.03	19.26	18.55	0.18
ZOA083759.717 − 554734.72	272.370	−8.787	0.38	−72.65	3.60	15.72 ± 0.03	15.02 ± 0.03	14.60 ± 0.04	–	14.23 ± 0.23	14.38 ± 0.06	19.03	18.34	17.98	0.18
ZOA083728.569 − 554303.90	272.264	−8.801	0.31	−22.87	2.70	16.87 ± 0.05	16.04 ± 0.04	15.34 ± 0.05	16.20 ± 0.21	15.47 ± 0.14	14.13 ± 0.25	20.25	19.30	18.43	0.18
ZOA083752.499 − 554437.48	272.319	−8.772	0.13	−63.24	4.38	16.45 ± 0.04	15.69 ± 0.03	15.38 ± 0.06	15.75 ± 0.22	14.87 ± 0.19	13.21 ± 0.59	19.50	18.81	18.50	0.18
ZOA083816.943 − 554603.62	272.373	−8.740	0.20	54.34	4.59	16.05 ± 0.04	15.46 ± 0.04	15.29 ± 0.09	–	–	13.59 ± 0.40	19.41	18.73	18.29	0.18
ZOA083512.016 − 554000.61	272.032	−9.031	0.54	9.97	3.84	16.71 ± 0.04	15.99 ± 0.04	15.23 ± 0.05	–	15.48 ± 0.16	14.42 ± 0.18	19.85	19.24	18.46	0.22
ZOA083520.219 − 554024.25	272.048	−9.019	0.24	−53.58	2.23	17.85 ± 0.07	17.07 ± 0.06	16.34 ± 0.10	–	–	16.16 ± 0.11	20.88	20.32	19.67	0.22
ZOA083518.115 − 553522.73	271.977	−8.974	0.16	36.78	2.19	17.51 ± 0.06	16.69 ± 0.04	15.93 ± 0.06	–	–	15.69 ± 0.08	20.69	19.75	19.05	0.22
ZOA083505.576 − 553403.33	271.941	−8.985	0.43	−13.80	2.58	17.63 ± 0.07	16.70 ± 0.05	15.80 ± 0.07	–	–	15.32 ± 0.13	20.63	19.87	18.83	0.22
ZOA083539.664 − 553620.31	272.020	−8.942	0.40	−25.38	2.43	17.61 ± 0.06	16.90 ± 0.05	16.48 ± 0.08	–	–	15.80 ± 0.15	20.40	19.75	19.48	0.20
ZOA083543.735 − 553629.00	272.028	−8.936	0.38	−76.45	4.54	15.21 ± 0.03	14.48 ± 0.02	14.12 ± 0.03	14.93 ± 0.08	14.16 ± 0.08	13.42 ± 0.17	18.56	17.83	17.47	0.20
ZOA083530.982 − 553739.18	272.026	−8.972	0.12	−49.99	2.21	17.59 ± 0.06	16.86 ± 0.05	16.27 ± 0.08	–	–	15.53 ± 0.14	20.41	19.75	19.27	0.20
ZOA083533.521 − 554020.57	272.066	−8.993	0.62	−63.60	15.48	13.52 ± 0.02	12.78 ± 0.02	12.33 ± 0.02	13.13 ± 0.13	12.61 ± 0.04	11.73 ± 0.17	17.66	16.96	16.47	0.20
ZOA083504.246 − 553526.88	271.958	−9.001	0.23	−35.30	2.11	17.47 ± 0.06	16.76 ± 0.05	16.13 ± 0.07	–	16.06 ± 0.19	−20.59 ± 11.58	20.34	19.84	19.16	0.20
ZOA083539.213 − 553415.78	271.991	−8.923	0.14	−82.67	2.33	17.76 ± 0.08	16.92 ± 0.06	16.27 ± 0.10	–	–	15.67 ± 0.17	20.43	19.90	19.42	0.20
ZOA083543.141 − 554110.71	272.091	−8.983	0.39	49.50	2.23	18.21 ± 0.10	17.51 ± 0.08	16.44 ± 0.10	–	–	–	21.02	20.50	19.57	0.20
ZOA083404.248 − 554154.41	271.963	−9.178	0.31	−6.87	4.18	16.14 ± 0.04	15.44 ± 0.03	14.93 ± 0.06	16.01 ± 0.07	15.28 ± 0.09	14.16 ± 0.18	19.52	18.77	18.12	0.20
ZOA083410.318 − 554117.54	271.963	−9.161	0.39	7.95	5.01	15.27 ± 0.03	14.55 ± 0.03	14.07 ± 0.03	–	14.13 ± 0.12	13.80 ± 0.07	18.69	17.97	17.49	0.20
ZOA083416.474 − 554110.19	271.970	−9.148	0.49	−74.29	3.49	15.72 ± 0.03	14.95 ± 0.03	14.49 ± 0.03	14.09 ± 0.49	–	–	18.94	18.21	17.92	0.20
ZOA083408.210 − 554055.95	271.956	−9.161	0.52	−33.57	3.29	16.58 ± 0.04	15.87 ± 0.03	15.31 ± 0.05	–	–	15.01 ± 0.07	19.73	19.02	18.57	0.20
ZOA083413.483 − 554015.88	271.954	−9.145	0.29	13.92	2.04	17.69 ± 0.07	17.04 ± 0.05	16.56 ± 0.10	–	–	16.27 ± 0.13	20.57	20.02	19.62	0.20
ZOA083425.759 − 554109.15	271.983	−9.130	0.20	36.64	2.64	17.02 ± 0.05	16.12 ± 0.04	15.72 ± 0.07	–	–	15.56 ± 0.08	20.03	19.38	18.95	0.20
ZOA083433.993 − 553754.69	271.950	−9.083	0.27	−33.15	2.41	17.38 ± 0.06	16.61 ± 0.04	15.83 ± 0.06	–	15.99 ± 0.14	15.75 ± 0.06	20.31	19.52	19.08	0.20
ZOA083444.901 − 553940.84	271.989	−9.079	0.10	−33.15	2.16	18.02 ± 0.08	17.26 ± 0.06	15.95 ± 0.07	–	–	–	21.11	20.37	18.87	0.20
ZOA083426.519 − 553642.69	271.923	−9.085	0.31	−31.05	5.14	16.24 ± 0.04	15.48 ± 0.03	15.10 ± 0.06	15.40 ± 0.29	14.36 ± 0.21	14.78 ± 0.07	19.37	18.63	18.32	0.20
ZOA083647.272 − 554152.10	272.190	−8.868	0.40	22.38	4.29	15.78 ± 0.04	15.04 ± 0.04	14.65 ± 0.06	–	14.09 ± 0.26	13.72 ± 0.22	19.16	18.35	17.93	0.20
ZOA083643.585 − 554109.84	272.175	−8.868	0.08	−31.56	4.49	14.38 ± 0.02	13.65 ± 0.02	13.22 ± 0.03	–	13.47 ± 0.05	13.07 ± 0.04	17.83	17.09	16.67	0.20
ZOA083642.019 − 553746.89	272.127	−8.838	0.19	71.65	3.32	16.20 ± 0.04	15.43 ± 0.03	15.06 ± 0.06	14.89 ± 0.41	14.89 ± 0.11	14.91 ± 0.06	19.32	18.61	18.26	0.20
ZOA083648.073 − 554017.64	272.170	−8.851	0.23	34.62	3.39	15.32 ± 0.03	14.58 ± 0.03	14.17 ± 0.03	14.61 ± 0.22	14.51 ± 0.03	14.11 ± 0.04	18.71	18.03	17.63	0.20
ZOA083644.351 − 554033.15	272.168	−8.860	0.10	4.63	9.07	13.34 ± 0.02	12.61 ± 0.02	12.21 ± 0.02	12.74 ± 0.19	12.13 ± 0.12	11.99 ± 0.04	17.11	16.37	15.96	0.20
ZOA083648.851 − 554044.99	272.177	−8.854	0.07	−56.21	2.79	15.87 ± 0.04	15.12 ± 0.03	14.81 ± 0.04	–	–	14.73 ± 0.05	19.22	18.50	18.27	0.20
ZOA083642.108 − 554057.23	272.171	−8.869	0.20	60.12	2.80	16.12 ± 0.04	15.41 ± 0.03	15.05 ± 0.05	–	15.34 ± 0.04	14.84 ± 0.07	19.40	18.82	18.44	0.20

$ZOA083620.281-553455.58$	272.058	−8.851	0.45	−2.66	3.17	16.89 ± 0.06	16.31 ± 0.06	15.62 ± 0.09	16.59 ± 0.11	16.23 ± 0.06	15.54 ± 0.10	19.96	19.60	18.97	0.20
$ZOA083653.169-554139.36$	272.196	−8.855	0.34	−1.93	3.39	16.68 ± 0.05	15.96 ± 0.05	15.56 ± 0.09	–	14.80 ± 0.29	15.41 ± 0.10	19.75	19.02	18.82	0.20
$ZOA083659.256-554825.73$	272.296	−8.910	0.50	−69.89	7.04	14.17 ± 0.02	13.36 ± 0.02	12.95 ± 0.03	13.23 ± 0.30	12.82 ± 0.14	12.11 ± 0.25	17.69	16.88	16.48	0.18
$ZOA083659.113-554532.87$	272.257	−8.882	0.12	17.18	2.61	16.63 ± 0.04	15.87 ± 0.04	15.72 ± 0.07	–	15.46 ± 0.08	14.96 ± 0.20	19.77	18.98	19.04	0.18
$ZOA083712.453-554700.82$	272.296	−8.871	0.10	−41.38	5.41	14.83 ± 0.03	14.09 ± 0.02	13.73 ± 0.03	14.06 ± 0.24	13.12 ± 0.29	13.19 ± 0.13	18.25	17.52	17.16	0.18
$ZOA083711.253-554748.68$	272.305	−8.881	0.11	−12.52	2.22	17.81 ± 0.08	16.96 ± 0.07	16.20 ± 0.08	–	–	15.86 ± 0.11	20.79	19.91	19.48	0.18
$ZOA083658.271-554749.41$	272.287	−8.906	0.15	74.45	3.45	17.14 ± 0.06	16.31 ± 0.04	15.82 ± 0.09	–	–	–	20.30	19.48	18.96	0.18
$ZOA083659.437-554756.18$	272.290	−8.905	0.31	25.46	2.86	17.62 ± 0.07	16.92 ± 0.06	15.99 ± 0.09	–	15.89 ± 0.28	–	20.37	19.94	18.93	0.18
$ZOA083701.402-554801.21$	272.294	−8.902	0.26	26.26	2.46	17.48 ± 0.06	16.76 ± 0.06	16.10 ± 0.09	–	15.76 ± 0.31	15.72 ± 0.11	20.67	20.10	19.19	0.18
$ZOA083658.085-554215.33$	272.211	−8.851	0.57	47.58	2.41	17.55 ± 0.07	16.65 ± 0.05	15.88 ± 0.07	–	15.23 ± 0.40	15.33 ± 0.11	20.52	19.70	19.04	0.18
$ZOA083707.092-554238.60$	272.229	−8.838	0.30	−14.48	1.95	17.32 ± 0.06	16.64 ± 0.05	16.18 ± 0.08	–	–	16.18 ± 0.08	20.64	19.89	19.66	0.18
$ZOA083720.729-554249.04$	272.250	−8.814	0.31	23.03	3.60	17.18 ± 0.06	16.51 ± 0.06	15.96 ± 0.09	–	16.03 ± 0.15	15.03 ± 0.27	20.29	19.58	19.08	0.18
$ZOA083710.273-553627.21$	272.149	−8.771	0.65	−60.79	4.43	16.20 ± 0.04	15.51 ± 0.03	14.86 ± 0.04	15.98 ± 0.08	13.87 ± 0.49	14.05 ± 0.24	19.57	18.70	18.31	0.20
$ZOA083729.522-553654.67$	272.182	−8.739	0.64	37.31	7.90	14.95 ± 0.03	14.18 ± 0.02	13.84 ± 0.03	14.57 ± 0.13	–	13.05 ± 0.23	18.49	17.72	17.42	0.20
$ZOA083711.680-553654.61$	272.157	−8.773	0.46	−18.02	2.52	18.01 ± 0.07	17.28 ± 0.06	16.96 ± 0.11	–	16.42 ± 0.11	16.68 ± 0.11	20.62	20.06	19.87	0.20
$ZOA083733.244-553749.93$	272.200	−8.741	0.32	42.96	2.81	16.25 ± 0.04	15.54 ± 0.03	15.19 ± 0.04	15.89 ± 0.10	15.27 ± 0.06	14.57 ± 0.16	19.50	18.84	18.47	0.20
$ZOA083709.144-553751.78$	272.166	−8.787	0.14	28.48	3.74	16.01 ± 0.03	15.30 ± 0.03	14.92 ± 0.05	–	14.51 ± 0.20	14.04 ± 0.19	19.26	18.52	18.11	0.20
$ZOA083736.147-553805.29$	272.208	−8.738	0.28	−72.73	7.38	14.67 ± 0.03	13.91 ± 0.02	13.41 ± 0.03	14.26 ± 0.14	13.53 ± 0.09	13.12 ± 0.07	18.29	17.52	17.04	0.20
$ZOA083733.643-553828.46$	272.209	−8.747	0.28	22.32	2.20	17.54 ± 0.06	16.70 ± 0.04	16.21 ± 0.07	–	–	16.10 ± 0.08	20.66	19.86	19.66	0.20
$ZOA083729.509-553831.40$	272.204	−8.755	0.16	−34.93	5.05	15.91 ± 0.03	15.09 ± 0.03	14.38 ± 0.03	–	14.53 ± 0.18	–	19.26	18.47	17.76	0.20
$ZOA083731.517-553838.21$	272.208	−8.752	0.51	21.88	2.44	18.05 ± 0.08	17.13 ± 0.06	16.43 ± 0.08	–	16.93 ± 0.07	15.34 ± 0.30	21.61	20.56	20.18	0.20
$ZOA083742.612-553931.11$	272.236	−8.740	0.22	−17.05	2.32	17.18 ± 0.05	16.40 ± 0.04	15.82 ± 0.06	–	–	15.12 ± 0.16	20.26	19.46	19.12	0.20
$ZOA083735.446-553947.36$	272.230	−8.756	0.04	−9.24	2.07	17.21 ± 0.05	16.41 ± 0.04	15.78 ± 0.06	–	–	–	20.20	19.45	18.84	0.20
$ZOA083739.205-553954.70$	272.237	−8.750	0.27	−4.18	1.90	18.87 ± 0.12	17.94 ± 0.08	16.98 ± 0.12	–	–	16.97 ± 0.12	21.30	20.85	19.72	0.20
$ZOA083729.065-553352.38$	272.140	−8.710	0.22	27.11	2.86	15.77 ± 0.03	16.73 ± 0.06	15.79 ± 0.08	11.16 ± 2.10	15.14 ± 0.52	–	16.15	19.54	18.80	0.20
$ZOA083722.595-553419.37$	272.137	−8.727	0.41	63.67	1.64	18.78 ± 0.16	21.55 ± 2.66	16.74 ± 0.14	–	$nan \pm 3.24$	16.74 ± 0.14	21.51	21.50	18.67	0.20
$ZOA083733.793-553559.79$	272.176	−8.722	0.43	−3.31	5.31	15.04 ± 0.03	14.29 ± 0.02	13.88 ± 0.03	13.90 ± 0.37	13.73 ± 0.17	13.44 ± 0.07	18.48	17.74	17.30	0.20
$ZOA083739.897-553531.41$	272.178	−8.706	0.39	83.10	2.19	18.30 ± 0.09	17.40 ± 0.06	16.52 ± 0.09	–	–	16.34 ± 0.09	21.02	20.16	19.48	0.20
$ZOA083735.838-553344.64$	272.148	−8.696	0.58	44.54	5.70	–	14.58 ± 0.03	14.17 ± 0.04	–	13.96 ± 0.20	12.64 ± 0.45	nan	18.03	17.53	0.20
$ZOA083751.358-554129.44$	272.275	−8.743	0.09	68.45	2.40	17.40 ± 0.06	16.80 ± 0.05	16.10 ± 0.10	14.68 ± 0.37	–	15.87 ± 0.11	19.71	19.48	19.37	0.20
$ZOA083800.861-554110.55$	272.284	−8.722	0.30	−44.01	3.45	15.67 ± 0.03	14.95 ± 0.03	14.55 ± 0.04	15.01 ± 0.21	13.93 ± 0.28	13.09 ± 0.41	18.95	18.24	17.86	0.20
$ZOA083751.372-554104.81$	272.270	−8.739	0.39	21.96	2.81	17.25 ± 0.06	16.49 ± 0.04	15.72 ± 0.06	–	–	15.11 ± 0.20	20.07	19.61	19.30	0.20
$ZOA083734.879-553713.00$	272.194	−8.732	0.21	−60.15	2.79	16.89 ± 0.05	16.14 ± 0.04	15.82 ± 0.07	–	15.73 ± 0.07	15.65 ± 0.08	20.04	19.25	18.96	0.20
$ZOA083812.017-553818.05$	272.261	−8.672	0.24	1.06	2.72	17.74 ± 0.08	16.75 ± 0.05	16.10 ± 0.09	–	16.11 ± 0.21	15.71 ± 0.11	20.88	19.92	19.10	0.20
$ZOA083759.192-553832.40$	272.246	−8.699	0.05	−24.14	2.11	16.95 ± 0.05	16.20 ± 0.04	15.82 ± 0.06	–	16.04 ± 0.04	–	20.19	19.40	19.02	0.20
$ZOA083755.397-553936.30$	272.255	−8.717	0.29	68.25	2.28	17.59 ± 0.06	16.89 ± 0.05	15.70 ± 0.05	–	14.50 ± 0.70	15.60 ± 0.05	20.39	19.62	18.90	0.20
$ZOA083751.144-553958.97$	272.254	−8.728	0.63	−15.43	3.46	15.86 ± 0.03	15.22 ± 0.03	14.72 ± 0.04	15.24 ± 0.21	14.80 ± 0.13	13.59 ± 0.31	19.24	18.57	18.02	0.20
$ZOA083811.389-554005.51$	272.284	−8.691	0.16	81.03	6.70	14.18 ± 0.02	13.41 ± 0.02	13.02 ± 0.02	13.39 ± 0.25	12.70 ± 0.21	12.35 ± 0.21	17.72	16.95	16.56	0.20
$ZOA083738.949-553601.09$	272.183	−8.712	0.12	−8.46	2.43	16.72 ± 0.04	15.94 ± 0.03	15.37 ± 0.05	–	–	14.84 ± 0.12	19.88	19.15	18.53	0.20
$ZOA083726.334-553520.16$	272.156	−8.729	0.26	−69.22	12.52	13.01 ± 0.02	12.23 ± 0.02	11.86 ± 0.02	12.67 ± 0.12	11.90 ± 0.08	11.63 ± 0.05	16.95	16.17	15.79	0.20
$ZOA083738.280-553532.85$	272.176	−8.709	0.42	−17.84	2.36	16.93 ± 0.05	16.16 ± 0.04	15.83 ± 0.06	16.41 ± 0.15	15.74 ± 0.09	–	20.06	19.30	19.02	0.20
$ZOA083807.718-553836.73$	272.259	−8.683	0.55	−61.12	1.95	17.29 ± 0.06	16.54 ± 0.04	16.30 ± 0.08	–	15.41 ± 0.23	14.87 ± 0.30	20.07	19.34	19.15	0.20
$ZOA083817.061-554004.33$	272.292	−8.680	0.13	−26.99	4.36	15.86 ± 0.04	15.32 ± 0.03	15.09 ± 0.07	15.39 ± 0.12	14.61 ± 0.19	14.11 ± 0.16	19.08	18.57	18.25	0.20
$ZOA083828.846-555114.60$	272.460	−8.769	0.16	21.32	2.44	17.03 ± 0.05	16.37 ± 0.05	15.58 ± 0.06	–	–	15.44 ± 0.07	20.07	19.29	18.87	0.18
$ZOA083814.567-555119.75$	272.441	−8.796	0.55	−19.84	5.62	15.35 ± 0.03	14.52 ± 0.03	14.14 ± 0.03	14.74 ± 0.19	14.24 ± 0.05	13.41 ± 0.20	18.72	17.94	17.60	0.18
$ZOA083812.609-555216.09$	272.451	−8.809	0.53	50.46	4.92	15.58 ± 0.03	14.80 ± 0.03	14.33 ± 0.04	14.58 ± 0.30	14.53 ± 0.05	14.23 ± 0.04	18.93	18.15	17.72	0.18
$ZOA083825.731-555318.53$	272.484	−8.795	0.55	−69.06	7.57	15.33 ± 0.03	14.53 ± 0.03	13.98 ± 0.03	14.53 ± 0.28	13.84 ± 0.20	13.73 ± 0.04	18.77	17.99	17.42	0.18
$ZOA083823.162-555456.50$	272.502	−8.816	0.44	−41.61	3.74	16.19 ± 0.04	15.43 ± 0.03	14.93 ± 0.05	15.97 ± 0.08	15.04 ± 0.10	14.71 ± 0.06	19.49	18.73	18.32	0.18
$ZOA083820.804-554952.72$	272.430	−8.770	0.05	−70.54	6.27	13.99 ± 0.02	13.23 ± 0.02	12.84 ± 0.03	13.05 ± 0.31	12.82 ± 0.12	11.87 ± 0.29	17.53	16.77	16.39	0.18
$ZOA083756.948-555001.30$	272.399	−8.817	0.49	49.75	3.71	16.05 ± 0.04	15.24 ± 0.03	14.83 ± 0.04	15.55 ± 0.16	14.26 ± 0.28	–	19.34	18.53	18.23	0.18
$ZOA083818.613-555004.26$	272.430	−8.776	0.41	−36.14	5.19	14.86 ± 0.03	14.10 ± 0.02	13.68 ± 0.03	14.53 ± 0.10	13.83 ± 0.06	13.54 ± 0.03	18.27	17.51	17.09	0.18
$ZOA083738.815-552902.26$	272.088	−8.644	0.20	−73.42	2.23	17.60 ± 0.06	16.83 ± 0.05	16.00 ± 0.07	–	–	14.82 ± 0.33	20.71	19.75	19.11	0.22
$ZOA083706.045-552911.30$	272.044	−8.707	0.10	−28.71	1.62	17.91 ± 0.08	17.16 ± 0.06	16.82 ± 0.12	–	–	15.82 ± 0.27	21.20	20.34	20.11	0.22
$ZOA083726.979-552929.47$	272.078	−8.671	0.27	−40.07	2.52	17.03 ± 0.05	16.22 ± 0.04	15.50 ± 0.05	–	–	14.39 ± 0.30	20.13	19.28	18.74	0.22
$ZOA083719.161-552940.71$	272.069	−8.687	0.34	−23.35	3.92	16.39 ± 0.04	15.68 ± 0.03	15.20 ± 0.05	15.98 ± 0.12	15.06 ± 0.14	14.74 ± 0.08	19.54	18.83	18.39	0.22
$ZOA083710.132-552946.47$	272.058	−8.705	0.35	25.18	2.90	17.17 ± 0.05	16.41 ± 0.04	15.73 ± 0.06	17.01 ± 0.10	15.85 ± 0.15	15.05 ± 0.15	20.37	19.50	19.01	0.22
$ZOA083723.223-553055.26$	272.092	−8.692	0.25	65.43	2.99	18.63 ± 0.13	17.35 ± 0.07	16.07 ± 0.09	–	–	15.67 ± 0.10	21.65	20.42	19.19	0.22
$ZOA083729.427-553253.36$	272.127	−8.699	0.34	10.31	4.22	16.00 ± 0.03	15.31 ± 0.03	14.86 ± 0.04	–	14.58 ± 0.21	14.42 ± 0.09	19.28	18.59	18.09	0.22
$ZOA083747.441-553304.01$	272.155	−8.667	0.36	−70.08	8.53	17.53 ± 0.07	16.84 ± 0.06	16.24 ± 0.13	–	–	15.27 ± 0.29	20.95	20.26	19.44	0.22
$ZOA083736.005-553337.11$	272.147	−8.694	0.11	13.55	2.78	16.83 ± 0.05	16.11 ± 0.04	15.72 ± 0.07	–	14.46 ± 0.32	–	19.77	18.98	18.55	0.22
$ZOA083712.404-552835.84$	272.045	−8.689	0.46	−46.19	6.29	15.01 ± 0.03	14.26 ± 0.02	13.80 ± 0.03	14.71 ± 0.10	13.68 ± 0.16	13.51 ± 0.05	18.50	17.76	17.33	0.22
$ZOA083707.386-552740.91$	272.026	−8.690	0.24	−5.08	2.11	18.02 ± 0.09	17.18 ± 0.06	16.72 ± 0.11	–	–	–	20.82	20.30	20.51	0.22

$ZOA083748.678-552730.86$	272.082	−8.610	0.39	28.55	2.41	17.87 ± 0.10	16.82 ± 0.05	16.11 ± 0.09	–	16.51 ± 0.12	15.78 ± 0.12	21.08	20.12	19.09	0.22
$ZOA083855.766-555551.35$	272.561	−8.764	0.12	−6.29	4.57	15.37 ± 0.03	14.61 ± 0.03	14.21 ± 0.04	14.64 ± 0.21	13.93 ± 0.11	14.05 ± 0.05	18.68	17.90	17.60	0.18
$ZOA083835.574-555016.45$	272.457	−8.746	0.56	−72.97	4.46	15.13 ± 0.03	14.40 ± 0.03	14.07 ± 0.03	11.87 ± 1.00	–	13.50 ± 0.14	18.45	17.74	17.46	0.18
$ZOA083818.593-555008.06$	272.431	−8.777	0.29	11.50	4.64	15.92 ± 0.04	14.95 ± 0.03	15.02 ± 0.06	15.01 ± 0.34	14.05 ± 0.22	14.56 ± 0.11	19.06	18.16	18.24	0.18
$ZOA083637.657-553422.06$	272.075	−8.812	0.09	62.56	2.91	17.37 ± 0.07	16.54 ± 0.05	15.80 ± 0.09	–	15.46 ± 0.29	15.68 ± 0.10	20.31	19.53	19.19	0.23
$ZOA083631.884-553158.49$	272.034	−8.800	0.01	−70.76	2.02	17.77 ± 0.08	16.93 ± 0.06	16.21 ± 0.13	–	–	16.15 ± 0.13	20.53	19.93	19.91	0.23
$ZOA083659.282-552914.86$	272.035	−8.721	0.36	50.31	9.45	14.08 ± 0.02	13.25 ± 0.02	12.93 ± 0.03	13.63 ± 0.18	12.61 ± 0.17	12.40 ± 0.15	17.80	17.00	16.73	0.23
$ZOA083744.229-553011.89$	272.112	−8.645	0.46	−5.84	4.00	15.77 ± 0.03	14.92 ± 0.03	14.44 ± 0.03	–	14.72 ± 0.06	13.81 ± 0.20	19.16	18.32	17.80	0.22
$ZOA083733.960-552715.80$	272.057	−8.635	0.43	22.10	3.21	17.05 ± 0.06	16.17 ± 0.04	15.48 ± 0.06	–	13.24 ± 0.91	15.01 ± 0.12	19.97	19.25	18.73	0.22
$ZOA083816.225-552802.41$	272.128	−8.563	0.47	−51.59	5.00	15.73 ± 0.03	15.14 ± 0.03	14.96 ± 0.07	15.00 ± 0.22	14.66 ± 0.10	14.28 ± 0.15	19.04	18.42	18.17	0.22
$ZOA083803.744-553225.76$	272.170	−8.630	0.30	−15.96	3.48	16.30 ± 0.04	15.59 ± 0.03	15.29 ± 0.05	16.17 ± 0.06	–	14.97 ± 0.08	19.59	18.84	18.56	0.22
$ZOA083802.319-552909.09$	272.123	−8.600	0.40	65.58	2.32	17.84 ± 0.07	17.12 ± 0.05	16.26 ± 0.08	–	–	–	21.08	20.35	19.42	0.22
$ZOA083513.350-553026.11$	271.903	−8.935	0.09	−87.64	2.51	17.96 ± 0.09	17.25 ± 0.08	16.41 ± 0.11	–	16.80 ± 0.12	13.32 ± 0.81	20.69	19.99	18.66	0.23
$ZOA083506.647-553023.12$	271.893	−8.947	0.14	81.30	1.94	17.77 ± 0.07	17.11 ± 0.06	16.45 ± 0.09	–	16.52 ± 0.09	14.46 ± 0.54	20.50	19.75	19.27	0.23
$ZOA083512.605-553037.27$	271.904	−8.938	0.11	−29.01	2.71	16.87 ± 0.05	16.01 ± 0.04	15.16 ± 0.05	–	–	14.86 ± 0.06	20.00	19.25	18.43	0.23
$ZOA083450.460-553105.30$	271.880	−8.985	0.25	8.77	2.35	18.04 ± 0.08	17.23 ± 0.07	16.45 ± 0.11	–	–	$nan \pm 0.63$	20.77	20.18	19.59	0.23
$ZOA083515.490-552806.50$	271.874	−8.908	0.21	−59.16	5.44	14.62 ± 0.03	13.97 ± 0.02	13.47 ± 0.03	13.92 ± 0.17	12.65 ± 0.28	12.63 ± 0.18	18.00	17.34	16.92	0.23
$ZOA083709.552-553137.08$	272.082	−8.725	0.53	−76.53	3.83	17.13 ± 0.06	16.65 ± 0.07	16.09 ± 0.12	15.60 ± 0.55	15.75 ± 0.14	–	19.90	19.35	18.84	0.22
$ZOA083600.166-560441.11$	272.436	−9.181	0.33	69.77	1.82	17.91 ± 0.08	17.10 ± 0.06	16.25 ± 0.08	–	–	16.23 ± 0.08	21.38	20.47	19.82	0.19
$ZOA083516.908-560611.69$	272.397	−9.277	0.36	−9.85	3.82	16.52 ± 0.04	15.87 ± 0.04	15.50 ± 0.08	–	15.17 ± 0.11	14.57 ± 0.16	19.53	18.92	18.53	0.19
$ZOA083518.046-560700.57$	272.409	−9.283	0.59	57.22	4.08	16.24 ± 0.04	15.49 ± 0.03	15.19 ± 0.09	15.01 ± 0.30	14.56 ± 0.17	–	19.29	18.59	18.36	0.19
$ZOA083552.113-560807.23$	272.472	−9.230	0.53	40.49	3.03	17.28 ± 0.06	16.48 ± 0.04	16.24 ± 0.09	–	15.82 ± 0.10	15.48 ± 0.15	20.16	19.36	19.25	0.19
$ZOA083606.205-561031.03$	272.524	−9.227	0.27	47.86	1.97	17.61 ± 0.09	17.33 ± 0.10	16.20 ± 0.13	–	–	16.09 ± 0.13	21.27	19.95	19.51	0.19
$ZOA083623.199-560453.35$	272.471	−9.139	0.38	−55.95	2.21	18.13 ± 0.08	17.39 ± 0.06	16.97 ± 0.12	–	–	15.65 ± 0.25	20.86	20.03	20.17	0.19
$ZOA083614.321-560540.31$	272.469	−9.164	0.34	−25.81	6.33	14.20 ± 0.02	13.43 ± 0.02	12.99 ± 0.02	13.01 ± 0.37	12.89 ± 0.15	12.80 ± 0.04	17.68	16.91	16.50	0.19
$ZOA083637.338-560615.12$	272.509	−9.126	0.15	31.30	2.29	17.33 ± 0.06	16.62 ± 0.05	15.96 ± 0.07	–	–	15.22 ± 0.17	20.43	19.65	19.11	0.19
$ZOA083639.018-560707.15$	272.523	−9.132	0.42	−85.92	2.08	17.39 ± 0.06	16.66 ± 0.04	16.17 ± 0.07	–	–	15.56 ± 0.20	20.45	19.76	19.55	0.19
$ZOA083617.999-560352.60$	272.449	−9.139	0.07	−11.87	2.97	17.56 ± 0.06	16.72 ± 0.05	15.86 ± 0.06	–	–	15.27 ± 0.18	20.55	19.85	19.02	0.19
$ZOA083649.687-560539.85$	272.518	−9.097	0.32	−4.05	2.32	17.20 ± 0.05	16.53 ± 0.04	15.69 ± 0.05	–	–	–	20.43	19.73	18.95	0.19
$ZOA083615.158-560604.09$	272.475	−9.166	0.36	55.96	3.14	17.04 ± 0.05	16.53 ± 0.05	16.04 ± 0.08	–	15.89 ± 0.14	15.81 ± 0.10	20.00	19.49	19.14	0.19
$ZOA083458.430-552954.36$	271.874	−8.958	0.36	23.40	1.60	18.46 ± 0.11	17.61 ± 0.10	16.69 ± 0.12	18.21 ± 0.15	17.19 ± 0.18	16.67 ± 0.12	21.84	21.90	20.50	0.23
$ZOA083513.137-553022.50$	271.901	−8.934	0.18	−65.05	2.17	17.89 ± 0.08	16.80 ± 0.05	15.80 ± 0.06	–	–	15.57 ± 0.09	21.11	19.83	19.04	0.23
$ZOA083516.582-553120.00$	271.919	−8.937	0.37	4.66	5.60	15.75 ± 0.03	15.13 ± 0.03	14.82 ± 0.06	14.77 ± 0.32	14.20 ± 0.21	13.76 ± 0.23	19.04	18.42	18.06	0.23
$ZOA083539.815-553135.38$	271.955	−8.895	0.12	35.09	2.92	16.63 ± 0.04	15.91 ± 0.04	15.49 ± 0.06	–	15.69 ± 0.07	15.29 ± 0.07	19.86	19.18	18.78	0.23
$ZOA083532.608-553342.27$	271.974	−8.930	0.46	84.85	2.25	17.81 ± 0.07	17.00 ± 0.06	16.42 ± 0.09	–	–	–	20.57	19.67	19.35	0.23
$ZOA083510.500-552908.91$	271.881	−8.927	0.31	−30.66	1.80	18.24 ± 0.09	17.45 ± 0.08	16.69 ± 0.10	–	–	15.22 ± 0.38	21.16	20.59	19.36	0.23
$ZOA083520.807-552725.09$	271.872	−8.891	0.22	72.01	1.70	17.53 ± 0.07	16.67 ± 0.06	16.40 ± 0.10	–	–	–	20.79	20.15	21.40	0.23
$ZOA083756.657-553545.08$	272.205	−8.676	0.61	−32.61	10.94	14.33 ± 0.02	13.59 ± 0.02	13.22 ± 0.03	13.81 ± 0.17	13.36 ± 0.05	12.96 ± 0.07	18.16	17.40	17.05	0.20
$ZOA083748.705-553504.69$	272.184	−8.684	0.24	−56.44	8.80	13.65 ± 0.02	12.92 ± 0.02	12.56 ± 0.03	12.67 ± 0.31	12.61 ± 0.08	12.33 ± 0.04	17.33	16.57	16.22	0.20
$ZOA083835.132-554132.31$	272.338	−8.661	0.23	−24.57	9.34	13.88 ± 0.02	12.99 ± 0.02	12.80 ± 0.03	–	11.64 ± 0.33	12.54 ± 0.08	17.60	16.87	16.52	0.20
$ZOA083607.777-560456.35$	272.450	−9.169	0.11	45.74	1.57	18.47 ± 0.11	17.57 ± 0.07	16.89 ± 0.14	–	–	16.88 ± 0.14	22.16	20.85	19.35	0.19
$ZOA083600.688-560625.98$	272.460	−9.197	0.37	32.70	5.48	15.37 ± 0.03	14.64 ± 0.03	14.22 ± 0.04	15.12 ± 0.10	14.39 ± 0.06	13.47 ± 0.13	18.84	18.11	17.68	0.19
$ZOA083630.541-560643.51$	272.506	−9.144	0.31	35.28	3.23	16.56 ± 0.04	15.77 ± 0.03	15.46 ± 0.06	–	–	14.99 ± 0.11	19.72	18.94	18.67	0.19
$ZOA083633.054-560603.43$	272.500	−9.132	0.19	41.44	2.25	17.75 ± 0.07	16.94 ± 0.05	16.19 ± 0.08	–	–	16.10 ± 0.09	20.40	19.90	19.69	0.18
$ZOA083634.321-560624.56$	272.507	−9.133	0.06	−13.06	1.76	17.73 ± 0.07	17.05 ± 0.06	16.34 ± 0.11	–	–	14.75 ± 0.48	20.94	20.43	19.70	0.18
$ZOA083716.248-560746.55$	272.583	−9.068	0.23	−47.05	2.34	18.34 ± 0.09	17.54 ± 0.07	16.73 ± 0.10	–	–	16.46 ± 0.10	21.31	20.23	20.06	0.18
$ZOA083809.461-553547.71$	272.223	−8.652	0.15	−62.62	2.82	16.26 ± 0.05	15.54 ± 0.04	14.90 ± 0.06	15.48 ± 0.26	15.53 ± 0.04	14.54 ± 0.10	19.55	19.13	18.12	0.22
$ZOA083853.626-554037.62$	272.351	−8.617	0.44	18.73	7.89	15.90 ± 0.04	15.19 ± 0.03	14.67 ± 0.05	14.09 ± 0.57	13.78 ± 0.38	14.16 ± 0.08	19.11	18.46	18.11	0.22
$ZOA083857.291-554024.76$	272.354	−8.608	0.20	−49.45	4.67	15.94 ± 0.04	15.29 ± 0.03	14.78 ± 0.06	14.83 ± 0.38	14.74 ± 0.11	14.19 ± 0.19	19.27	18.65	18.19	0.22
$ZOA083604.229-560242.75$	272.414	−9.154	0.19	−20.38	2.79	17.70 ± 0.08	16.82 ± 0.05	15.51 ± 0.06	–	–	15.34 ± 0.07	20.82	19.87	18.58	0.18
$ZOA083611.017-555806.75$	272.361	−9.096	0.05	−51.20	0.79	17.82 ± 0.09	17.57 ± 0.09	20.68 ± 5.05	–	16.88 ± 0.10	12.77 ± 5.64	20.35	20.35	20.39	0.18
$ZOA083607.396-555920.49$	272.373	−9.115	0.60	−64.04	4.52	15.80 ± 0.03	15.00 ± 0.03	14.44 ± 0.04	15.02 ± 0.27	14.78 ± 0.05	–	19.11	18.35	17.78	0.18
$ZOA083601.482-560014.87$	272.377	−9.135	0.23	−46.87	2.27	17.30 ± 0.06	16.70 ± 0.04	16.12 ± 0.07	–	–	15.96 ± 0.07	20.43	19.75	19.16	0.18
$ZOA083546.234-560029.41$	272.359	−9.166	0.36	14.91	10.71	13.65 ± 0.02	12.91 ± 0.02	12.57 ± 0.02	13.30 ± 0.11	12.79 ± 0.02	12.29 ± 0.05	17.51	16.76	16.39	0.18
$ZOA083530.711-555624.06$	272.282	−9.155	0.53	87.00	3.80	16.41 ± 0.04	15.63 ± 0.03	15.12 ± 0.05	15.78 ± 0.22	14.76 ± 0.27	14.92 ± 0.06	19.79	18.95	18.51	0.18
$ZOA083546.872-555645.98$	272.309	−9.128	0.32	−38.89	3.62	16.27 ± 0.04	15.49 ± 0.03	15.00 ± 0.04	13.48 ± 0.89	13.64 ± 0.52	14.01 ± 0.25	19.39	18.63	18.22	0.18
$ZOA083627.364-555743.58$	272.379	−9.061	0.22	−61.70	2.62	17.80 ± 0.08	16.98 ± 0.06	15.70 ± 0.06	–	–	14.31 ± 0.28	21.03	20.63	18.64	0.18
$ZOA083620.894-555750.37$	272.371	−9.075	0.46	26.53	1.31	18.77 ± 0.15	17.29 ± 0.08	16.81 ± 0.13	18.04 ± 0.22	–	10.34 ± 2.05	nan	22.83	nan	0.18
$ZOA083644.233-555757.46$	272.405	−9.032	0.31	−83.75	1.93	17.34 ± 0.05	16.72 ± 0.05	16.37 ± 0.08	–	16.36 ± 0.07	15.16 ± 0.30	20.44	19.81	19.56	0.18
$ZOA083700.461-555808.93$	272.430	−9.003	0.09	−42.99	5.71	16.88 ± 0.05	16.12 ± 0.05	16.03 ± 0.13	–	14.68 ± 0.38	14.71 ± 0.36	19.92	19.12	19.01	0.18
$ZOA083654.851-555818.54$	272.425	−9.015	0.57	−28.29	6.33	16.85 ± 0.05	16.27 ± 0.04	15.79 ± 0.07	15.87 ± 0.28	14.90 ± 0.30	14.32 ± 0.26	19.68	19.19	18.56	0.18
$ZOA083608.759-555954.10$	272.382	−9.118	0.31	21.78	2.55	16.30 ± 0.04	15.58 ± 0.03	15.23 ± 0.07	–	14.98 ± 0.15	15.03 ± 0.08	19.39	18.78	19.41	0.18

ZOA083649.173 − 560002.63	272.440	−9.043	0.33	−15.33	2.81	17.62 ± 0.06	16.96 ± 0.06	16.43 ± 0.09	–	–	14.90 ± 0.31	20.35	19.80	19.27	0.18
ZOA083645.319 − 560008.27	272.436	−9.051	0.33	−28.56	3.74	15.76 ± 0.03	15.03 ± 0.03	14.75 ± 0.04	15.02 ± 0.22	14.43 ± 0.14	–	18.99	18.28	18.09	0.18
ZOA083652.618 − 560052.04	272.456	−9.045	0.17	−18.68	2.56	16.76 ± 0.04	16.08 ± 0.04	15.62 ± 0.06	13.12 ± 1.16	14.32 ± 0.47	–	19.81	19.00	18.69	0.18
ZOA083702.929 − 560112.62	272.476	−9.029	0.48	14.70	3.27	16.16 ± 0.04	15.39 ± 0.04	15.27 ± 0.07	14.46 ± 0.55	13.87 ± 0.36	13.65 ± 0.38	19.25	18.52	18.25	0.18
ZOA083646.292 − 560113.24	272.453	−9.060	0.15	54.20	2.25	17.63 ± 0.06	16.89 ± 0.05	16.12 ± 0.07	16.93 ± 0.23	16.38 ± 0.12	15.90 ± 0.08	20.76	19.94	19.22	0.18
ZOA083642.221 − 560121.11	272.449	−9.069	0.55	86.81	3.99	16.71 ± 0.04	15.96 ± 0.04	15.75 ± 0.06	16.17 ± 0.14	15.37 ± 0.07	15.30 ± 0.09	19.75	18.91	18.76	0.18
ZOA083642.541 − 555731.85	272.397	−9.031	0.34	−34.19	2.52	17.66 ± 0.06	16.78 ± 0.05	15.93 ± 0.06	–	–	–	20.64	20.13	19.01	0.18
ZOA083651.387 − 555639.43	272.397	−9.006	0.34	−61.60	2.26	18.00 ± 0.07	17.49 ± 0.07	17.11 ± 0.13	–	11.30 ± 1.86	–	20.99	20.21	19.97	0.18
ZOA083645.617 − 555645.88	272.391	−9.017	0.14	−48.63	4.18	14.97 ± 0.03	14.20 ± 0.02	13.80 ± 0.03	14.06 ± 0.28	13.69 ± 0.12	13.20 ± 0.14	18.35	17.58	17.19	0.18
ZOA083831.906 − 560320.37	272.629	−8.883	0.35	−13.30	2.39	17.38 ± 0.06	16.93 ± 0.07	16.48 ± 0.11	–	16.33 ± 0.08	16.32 ± 0.11	20.37	19.82	19.46	0.19
ZOA083842.666 − 560144.58	272.622	−8.847	0.27	−47.48	1.90	18.15 ± 0.10	17.03 ± 0.08	16.57 ± 0.12	–	–	16.57 ± 0.12	22.06	19.93	20.01	0.19
ZOA083811.449 − 555731.52	272.521	−8.864	0.45	74.66	5.64	15.20 ± 0.03	14.42 ± 0.02	13.99 ± 0.03	14.69 ± 0.15	13.45 ± 0.25	13.18 ± 0.20	18.57	17.77	17.39	0.19
ZOA083812.333 − 555541.42	272.497	−8.844	0.17	−29.37	3.17	16.19 ± 0.04	15.32 ± 0.03	14.92 ± 0.04	–	–	14.09 ± 0.21	19.45	18.45	18.15	0.19
ZOA083757.760 − 555749.99	272.506	−8.892	0.45	62.47	2.42	18.02 ± 0.08	17.13 ± 0.06	16.41 ± 0.08	–	16.17 ± 0.28	15.60 ± 0.18	21.19	20.14	19.81	0.19
ZOA083545.508 − 555822.54	272.329	−9.147	0.04	85.12	2.04	17.29 ± 0.06	16.43 ± 0.04	15.72 ± 0.06	–	–	14.65 ± 0.33	20.51	19.69	18.99	0.17
ZOA083624.587 − 560030.42	272.413	−9.094	0.22	−85.19	10.40	13.46 ± 0.02	12.70 ± 0.02	12.31 ± 0.02	13.21 ± 0.09	12.24 ± 0.12	12.00 ± 0.08	17.40	16.66	16.25	0.17
ZOA083629.602 − 560050.78	272.424	−9.088	0.22	37.85	2.54	17.38 ± 0.06	16.68 ± 0.05	16.12 ± 0.08	–	–	15.74 ± 0.10	20.43	19.85	19.21	0.17
ZOA083608.294 − 560124.28	272.402	−9.133	0.09	−10.17	2.94	17.40 ± 0.06	16.72 ± 0.04	15.96 ± 0.09	–	16.32 ± 0.08	14.92 ± 0.32	20.33	19.73	19.07	0.17
ZOA083636.632 − 560145.67	272.446	−9.083	0.42	12.83	5.15	15.89 ± 0.03	15.09 ± 0.03	14.86 ± 0.05	14.74 ± 0.24	14.18 ± 0.18	13.88 ± 0.23	18.86	18.12	18.01	0.17
ZOA083622.988 − 560149.61	272.428	−9.110	0.41	−14.81	2.41	17.82 ± 0.07	16.94 ± 0.05	16.27 ± 0.08	–	–	15.58 ± 0.14	20.79	20.05	19.18	0.17
ZOA083629.553 − 560216.75	272.444	−9.102	0.21	−19.66	2.78	17.42 ± 0.06	16.55 ± 0.04	15.77 ± 0.06	–	–	14.85 ± 0.25	20.54	19.71	19.02	0.17
ZOA083537.875 − 555719.36	272.304	−9.151	0.17	12.65	4.58	15.89 ± 0.04	15.22 ± 0.03	14.50 ± 0.05	15.85 ± 0.06	14.16 ± 0.25	13.77 ± 0.23	19.32	18.36	17.89	0.17
ZOA083615.074 − 555626.85	272.344	−9.072	0.34	−8.91	1.62	18.16 ± 0.09	17.30 ± 0.06	16.72 ± 0.11	–	–	16.61 ± 0.11	21.19	20.61	19.58	0.17
ZOA083550.122 − 555656.85	272.316	−9.124	0.21	45.99	1.80	18.06 ± 0.09	17.21 ± 0.06	16.45 ± 0.09	–	–	15.67 ± 0.26	21.52	20.26	19.70	0.17
ZOA083635.625 − 555616.97	272.370	−9.032	0.24	−57.01	6.75	14.21 ± 0.02	13.53 ± 0.02	13.29 ± 0.03	13.72 ± 0.16	13.11 ± 0.12	12.93 ± 0.05	17.81	17.11	16.90	0.17
ZOA083627.107 − 560149.34	272.434	−9.102	0.16	−81.42	2.62	18.46 ± 0.10	17.50 ± 0.06	16.68 ± 0.10	–	–	15.24 ± 0.30	21.44	20.44	19.36	0.17
ZOA083631.444 − 560319.93	272.461	−9.109	0.29	−18.02	4.22	16.42 ± 0.04	16.23 ± 0.04	15.44 ± 0.09	–	15.03 ± 0.23	14.73 ± 0.18	19.53	19.08	18.56	0.17
ZOA083702.183 − 555836.95	272.439	−9.005	0.27	−66.77	1.91	18.52 ± 0.10	17.56 ± 0.08	16.96 ± 0.13	–	–	16.75 ± 0.15	21.73	20.74	20.09	0.18
ZOA083654.298 − 555652.67	272.404	−9.002	0.23	−44.65	2.35	17.96 ± 0.08	17.17 ± 0.06	16.45 ± 0.09	–	–	15.82 ± 0.12	20.75	20.10	19.64	0.18
ZOA083722.105 − 555709.12	272.447	−8.953	0.29	25.62	5.27	15.33 ± 0.03	14.76 ± 0.03	14.43 ± 0.04	14.64 ± 0.22	14.26 ± 0.13	14.09 ± 0.06	18.72	18.16	17.80	0.18
ZOA083722.948 − 555731.10	272.453	−8.955	0.40	−33.67	10.82	13.80 ± 0.02	13.12 ± 0.02	12.76 ± 0.03	13.38 ± 0.13	12.28 ± 0.24	11.79 ± 0.27	17.67	16.96	16.60	0.18
ZOA083722.372 − 560032.00	272.493	−8.985	0.35	−16.08	4.94	15.46 ± 0.03	14.60 ± 0.03	14.11 ± 0.03	14.73 ± 0.23	13.77 ± 0.22	13.97 ± 0.04	18.77	17.92	17.50	0.18
ZOA083717.893 − 560144.38	272.504	−9.006	0.23	28.37	3.70	16.18 ± 0.04	15.45 ± 0.03	15.15 ± 0.05	15.43 ± 0.21	14.40 ± 0.28	–	19.30	18.64	18.26	0.18
ZOA083854.570 − 555607.88	272.563	−8.769	0.28	−43.06	2.56	16.99 ± 0.05	16.47 ± 0.05	16.11 ± 0.08	–	16.08 ± 0.06	15.65 ± 0.11	20.09	19.50	19.34	0.18
ZOA083838.292 − 555716.46	272.555	−8.811	0.21	−35.55	2.11	18.18 ± 0.09	17.29 ± 0.07	16.56 ± 0.11	–	–	15.58 ± 0.32	21.99	21.11	20.76	0.18
ZOA083828.029 − 555832.89	272.558	−8.843	0.13	74.19	3.15	17.47 ± 0.06	16.65 ± 0.05	15.90 ± 0.08	–	–	14.86 ± 0.31	20.54	19.70	19.02	0.18
ZOA083851.176 − 555654.29	272.568	−8.783	0.34	59.60	2.03	17.57 ± 0.06	16.84 ± 0.05	16.27 ± 0.08	–	–	–	20.65	19.81	19.05	0.18
ZOA083856.608 − 555836.65	272.599	−8.790	0.14	30.27	2.29	17.77 ± 0.07	16.80 ± 0.05	16.17 ± 0.08	–	–	15.67 ± 0.13	20.81	19.91	19.47	0.18
ZOA083901.040 − 555839.54	272.606	−8.782	0.33	77.86	2.79	18.28 ± 0.09	17.32 ± 0.07	16.52 ± 0.10	–	–	16.04 ± 0.12	21.30	20.27	19.57	0.18
ZOA083901.794 − 555831.06	272.605	−8.779	0.33	7.96	1.89	18.44 ± 0.10	17.59 ± 0.09	16.70 ± 0.12	–	–	16.70 ± 0.12	22.00	21.03	20.40	0.18
ZOA083853.887 − 555950.41	272.612	−8.807	0.13	54.93	2.56	17.26 ± 0.06	16.31 ± 0.04	15.47 ± 0.05	11.60 ± 1.82	–	14.71 ± 0.18	20.10	19.12	18.58	0.18
ZOA083554.670 − 555028.75	272.234	−9.052	0.39	−27.61	2.53	17.84 ± 0.07	17.14 ± 0.06	16.65 ± 0.10	–	–	16.18 ± 0.12	21.00	20.11	19.29	0.18
ZOA083512.846 − 555051.83	272.181	−9.135	0.21	−40.09	4.87	16.93 ± 0.06	15.97 ± 0.04	15.17 ± 0.07	–	15.23 ± 0.17	14.73 ± 0.13	20.19	18.99	18.36	0.18
ZOA083603.010 − 555102.27	272.253	−9.042	0.32	−34.65	2.46	17.49 ± 0.06	16.55 ± 0.04	15.84 ± 0.06	–	–	15.71 ± 0.06	20.41	19.82	18.71	0.18
ZOA083544.840 − 555223.34	272.247	−9.089	0.37	59.12	2.03	18.36 ± 0.10	17.36 ± 0.07	16.53 ± 0.10	–	–	16.50 ± 0.10	21.30	20.33	19.49	0.18
ZOA083607.828 − 555321.73	272.292	−9.055	0.25	27.57	2.76	17.28 ± 0.06	16.50 ± 0.04	16.13 ± 0.08	–	–	15.61 ± 0.13	19.90	19.32	18.98	0.18
ZOA083549.951 − 555459.88	272.289	−9.105	0.38	14.67	3.61	17.00 ± 0.05	16.20 ± 0.04	15.54 ± 0.06	–	15.31 ± 0.26	15.35 ± 0.07	20.06	19.46	18.90	0.18
ZOA083612.149 − 555004.43	272.253	−9.015	0.19	−76.31	6.73	14.48 ± 0.03	13.80 ± 0.02	13.60 ± 0.03	13.55 ± 0.27	13.24 ± 0.12	13.27 ± 0.06	18.03	17.35	17.14	0.18
ZOA083533.741 − 554925.84	272.191	−9.081	0.21	−23.75	4.04	17.25 ± 0.06	16.52 ± 0.04	15.85 ± 0.06	16.79 ± 0.11	–	14.43 ± 0.35	20.37	19.52	19.06	0.18
ZOA083601.143 − 554940.69	272.232	−9.032	0.14	42.40	1.75	18.67 ± 0.12	17.93 ± 0.10	16.67 ± 0.10	–	–	–	21.59	20.97	20.77	0.18
ZOA083607.347 − 554850.80	272.230	−9.012	0.34	−40.27	3.15	16.27 ± 0.04	15.67 ± 0.04	15.31 ± 0.06	–	14.98 ± 0.17	14.53 ± 0.20	19.36	18.83	18.54	0.18
ZOA083545.356 − 554909.47	272.203	−9.057	0.27	6.63	2.01	17.61 ± 0.07	16.97 ± 0.06	16.35 ± 0.08	–	–	16.23 ± 0.09	20.75	20.07	19.56	0.18
ZOA083609.625 − 555519.13	272.321	−9.071	0.03	−66.02	2.25	18.09 ± 0.10	17.71 ± 0.11	16.55 ± 0.13	–	–	16.34 ± 0.13	20.99	20.41	19.37	0.18
ZOA083625.890 − 555512.89	272.342	−9.039	0.09	20.74	6.12	14.26 ± 0.02	13.58 ± 0.02	13.15 ± 0.02	13.48 ± 0.26	13.42 ± 0.05	12.87 ± 0.06	17.78	17.10	16.67	0.17
ZOA083628.169 − 555044.26	272.284	−8.991	0.62	−44.60	7.08	15.15 ± 0.03	14.40 ± 0.02	13.87 ± 0.03	14.64 ± 0.16	–	13.45 ± 0.12	18.63	17.86	17.38	0.17
ZOA083615.754 − 555101.21	272.271	−9.017	0.07	−79.35	1.99	18.79 ± 0.13	17.71 ± 0.08	16.95 ± 0.12	–	–	16.92 ± 0.13	21.67	20.98	19.97	0.17
ZOA083609.244 − 555120.62	272.266	−9.033	0.43	86.46	4.35	15.27 ± 0.03	14.54 ± 0.02	14.18 ± 0.03	14.97 ± 0.11	13.55 ± 0.31	13.92 ± 0.06	18.67	17.93	17.57	0.17
ZOA083610.727 − 555133.68	272.271	−9.032	0.36	85.98	2.83	17.65 ± 0.07	16.92 ± 0.05	16.76 ± 0.12	–	16.05 ± 0.14	15.41 ± 0.21	20.45	19.62	19.23	0.17
ZOA083541.422 − 555147.76	272.234	−9.090	0.36	60.65	2.17	17.90 ± 0.08	17.09 ± 0.06	16.35 ± 0.10	–	16.91 ± 0.06	–	21.22	20.39	19.58	0.17
ZOA083624.275 − 555231.59	272.303	−9.016	0.22	−34.04	2.05	18.28 ± 0.10	16.91 ± 0.05	16.22 ± 0.07	–	–	16.17 ± 0.07	21.37	20.27	19.87	0.17
ZOA083633.691 − 555300.61	272.323	−9.003	0.40	48.78	6.90	15.74 ± 0.04	15.06 ± 0.03	14.75 ± 0.05	15.25 ± 0.20	14.67 ± 0.11	13.81 ± 0.28	19.13	18.46	18.18	0.17
ZOA083616.492 − 555403.97	272.313	−9.046	0.23	80.42	1.98	17.82 ± 0.07	17.31 ± 0.06	16.73 ± 0.11	–	16.35 ± 0.25	–	20.71	20.23	19.58	0.17

$ZOA083633.425-555447.19$	272.347	−9.021	0.36	62.06	8.28	13.79 ± 0.02	13.03 ± 0.02	12.65 ± 0.02	–	12.84 ± 0.04	11.61 ± 0.28	17.42	16.66	16.26	0.17
$ZOA083622.091-554927.88$	272.259	−8.990	0.12	−19.18	4.83	15.87 ± 0.03	15.13 ± 0.03	14.80 ± 0.04	15.59 ± 0.09	14.41 ± 0.19	13.65 ± 0.30	19.13	18.41	18.06	0.17
$ZOA083614.775-555008.77$	272.258	−9.011	0.25	61.36	2.10	18.24 ± 0.09	17.54 ± 0.07	17.13 ± 0.13	–	–	16.89 ± 0.13	20.89	20.29	20.16	0.17
$ZOA083615.844-555001.21$	272.257	−9.007	0.25	70.79	2.18	17.13 ± 0.05	16.43 ± 0.04	16.19 ± 0.07	–	15.24 ± 0.31	15.97 ± 0.08	20.14	19.43	19.36	0.17
$ZOA083615.278-554930.73$	272.250	−9.004	0.17	−14.40	2.44	17.53 ± 0.06	16.84 ± 0.05	16.60 ± 0.10	–	–	–	20.71	20.02	20.79	0.17
$ZOA083618.889-554942.98$	272.257	−8.999	0.17	67.49	3.63	15.79 ± 0.03	15.03 ± 0.03	14.72 ± 0.04	12.99 ± 0.83	12.76 ± 0.58	–	18.93	18.19	17.93	0.17
$ZOA083619.681-554952.86$	272.261	−8.999	0.07	−44.69	6.90	14.01 ± 0.02	13.26 ± 0.02	12.92 ± 0.02	13.22 ± 0.23	12.68 ± 0.12	12.34 ± 0.10	17.63	16.88	16.53	0.17
$ZOA083631.040-554909.42$	272.267	−8.970	0.32	−0.24	6.49	14.49 ± 0.03	13.75 ± 0.02	13.35 ± 0.03	13.62 ± 0.27	13.12 ± 0.17	12.75 ± 0.13	17.97	17.24	16.84	0.17
$ZOA083632.135-554953.80$	272.278	−8.975	0.04	−55.62	6.87	14.67 ± 0.03	13.94 ± 0.02	13.62 ± 0.03	14.29 ± 0.11	13.50 ± 0.08	12.54 ± 0.30	18.29	17.55	17.23	0.17
$ZOA083523.858-554349.70$	272.100	−9.045	0.12	2.80	4.29	14.98 ± 0.03	14.25 ± 0.02	13.88 ± 0.03	14.89 ± 0.04	13.39 ± 0.27	12.96 ± 0.27	18.39	17.68	17.30	0.18
$ZOA083605.133-554441.63$	272.170	−8.976	0.40	−23.36	3.62	17.19 ± 0.06	16.47 ± 0.04	15.93 ± 0.07	–	16.34 ± 0.04	14.94 ± 0.29	20.17	19.61	19.06	0.18
$ZOA083602.038-554505.68$	272.171	−8.985	0.35	−40.42	2.82	17.60 ± 0.07	17.06 ± 0.06	16.02 ± 0.06	–	–	15.86 ± 0.07	21.05	20.20	19.48	0.18
$ZOA083534.840-554504.73$	272.133	−9.037	0.67	−66.53	1.79	18.37 ± 0.11	17.67 ± 0.09	17.11 ± 0.25	–	–	17.08 ± 0.25	22.75	21.48	nan	0.18
$ZOA083607.508-554507.71$	272.179	−8.975	0.35	−16.97	2.07	17.94 ± 0.08	17.19 ± 0.06	16.46 ± 0.10	–	–	16.29 ± 0.11	21.31	20.26	20.03	0.18
$ZOA083544.107-554543.77$	272.155	−9.026	0.15	36.57	4.04	16.28 ± 0.04	15.53 ± 0.03	15.16 ± 0.06	–	14.63 ± 0.24	14.14 ± 0.25	19.47	18.69	18.42	0.18
$ZOA083551.841-554617.32$	272.173	−9.016	0.32	44.12	2.32	17.76 ± 0.07	16.78 ± 0.05	16.01 ± 0.06	–	12.42 ± 1.36	–	20.69	19.89	19.24	0.18
$ZOA083608.023-554707.78$	272.207	−8.994	0.26	38.10	7.79	14.17 ± 0.02	13.43 ± 0.02	13.03 ± 0.03	13.92 ± 0.08	13.25 ± 0.04	12.82 ± 0.05	17.80	17.06	16.66	0.18
$ZOA083601.641-554709.75$	272.199	−9.006	0.23	−58.52	5.79	15.46 ± 0.03	14.69 ± 0.03	14.27 ± 0.04	15.09 ± 0.14	14.34 ± 0.08	13.98 ± 0.07	18.88	18.09	17.70	0.18
$ZOA083558.170-554732.43$	272.199	−9.017	0.58	40.70	4.33	15.82 ± 0.03	14.98 ± 0.03	14.58 ± 0.04	14.84 ± 0.32	14.72 ± 0.04	14.20 ± 0.07	19.11	18.34	17.90	0.18
$ZOA083607.535-554250.19$	272.148	−8.953	0.30	74.67	5.74	14.48 ± 0.03	13.77 ± 0.02	13.35 ± 0.03	13.48 ± 0.27	13.49 ± 0.05	13.02 ± 0.07	17.96	17.26	16.84	0.18
$ZOA083556.600-554414.36$	272.152	−8.987	0.16	−12.56	3.87	16.23 ± 0.04	15.64 ± 0.03	14.72 ± 0.04	–	15.52 ± 0.06	14.48 ± 0.06	19.59	18.99	18.02	0.18
$ZOA083556.672-554416.98$	272.152	−8.988	0.28	−89.53	3.57	16.95 ± 0.05	16.22 ± 0.04	15.97 ± 0.09	16.23 ± 0.23	15.23 ± 0.15	14.88 ± 0.12	19.77	19.00	18.57	0.18
$ZOA083623.688-554429.93$	272.193	−8.938	0.36	56.47	3.06	17.16 ± 0.06	16.53 ± 0.05	15.47 ± 0.05	–	–	–	20.29	19.82	18.77	0.18
$ZOA083624.625-554503.12$	272.202	−8.942	0.55	52.82	6.55	15.48 ± 0.03	14.65 ± 0.03	14.21 ± 0.03	–	14.47 ± 0.05	13.93 ± 0.06	18.93	18.14	17.65	0.18
$ZOA083631.891-554341.43$	272.193	−8.915	0.19	−41.03	1.92	18.24 ± 0.10	17.20 ± 0.07	16.32 ± 0.09	–	–	15.87 ± 0.14	20.79	20.09	19.11	0.18
$ZOA083613.632-554501.29$	272.186	−8.963	0.37	31.81	1.89	18.31 ± 0.10	17.45 ± 0.07	16.53 ± 0.10	–	–	–	21.76	20.85	19.73	0.18
$ZOA083605.793-554546.59$	272.185	−8.985	0.17	50.10	3.23	16.39 ± 0.04	15.67 ± 0.03	15.23 ± 0.07	–	14.47 ± 0.33	15.10 ± 0.08	19.47	18.81	18.57	0.18
$ZOA083618.641-554601.09$	272.207	−8.963	0.16	−56.70	3.48	15.62 ± 0.03	14.91 ± 0.03	14.53 ± 0.03	14.92 ± 0.19	14.38 ± 0.15	14.25 ± 0.06	18.82	18.23	17.86	0.18
$ZOA083626.927-554605.02$	272.219	−8.948	0.23	−77.70	2.57	17.66 ± 0.07	17.02 ± 0.06	16.34 ± 0.08	–	–	15.54 ± 0.12	20.28	19.71	19.08	0.18
$ZOA083616.775-554611.31$	272.206	−8.968	0.48	−85.71	6.34	14.93 ± 0.03	14.17 ± 0.02	13.71 ± 0.03	14.64 ± 0.08	13.34 ± 0.20	13.34 ± 0.06	18.55	17.77	17.31	0.18
$ZOA083629.095-554802.01$	272.249	−8.963	0.30	−71.20	3.36	16.82 ± 0.05	16.10 ± 0.04	15.70 ± 0.07	16.36 ± 0.17	15.73 ± 0.07	14.57 ± 0.32	19.86	19.23	18.91	0.18
$ZOA083614.621-554127.68$	272.139	−8.926	0.30	−43.77	2.15	16.88 ± 0.07	15.97 ± 0.05	15.40 ± 0.06	15.99 ± 0.30	15.95 ± 0.05	14.59 ± 0.26	21.73	20.35	19.66	0.18
$ZOA083607.484-554211.68$	272.139	−8.947	0.54	−45.34	3.00	17.06 ± 0.06	16.36 ± 0.05	15.78 ± 0.06	–	16.17 ± 0.05	14.77 ± 0.31	21.13	20.41	20.06	0.18
$ZOA083539.582-554310.56$	272.113	−9.009	0.54	−36.16	3.29	16.83 ± 0.06	16.12 ± 0.05	15.67 ± 0.09	16.75 ± 0.08	–	15.27 ± 0.17	20.03	19.26	19.24	0.18
$ZOA083608.848-554233.70$	272.146	−8.948	0.03	−68.58	1.82	17.76 ± 0.08	16.97 ± 0.07	16.65 ± 0.11	–	–	15.90 ± 0.19	21.13	20.36	20.81	0.18
$ZOA083559.658-554248.90$	272.136	−8.968	0.32	−5.22	2.90	16.64 ± 0.04	15.90 ± 0.03	15.55 ± 0.05	–	15.43 ± 0.08	13.94 ± 0.45	19.68	19.00	18.71	0.18
$ZOA083607.529-554106.73$	272.124	−8.936	0.33	45.81	8.78	13.69 ± 0.02	12.95 ± 0.02	12.57 ± 0.02	13.48 ± 0.07	12.14 ± 0.22	12.41 ± 0.04	17.35	16.60	16.21	0.18

Table A.0.3: VC05 catalogue of galaxies

Designation	ℓ (deg)	b (deg)	e_J	ϕ_J (deg)	r_{k20fe} (arcsec)	J_{k20fe} (mag)	H_{k20fe} (mag)	$K_{s\,k20fe}$ (mag)	J_{tot} (mag)	H_{tot} (mag)	$K_{s\,tot}$ (mag)	μ_J	μ_H (mag arcsec^{-2})	μ_{Ks}	$E(B-$ (mag)
$ZOA083941.694-572750.44$	273.872	−9.592	0.05	−29.53	2.93	17.22 ± 0.06	16.30 ± 0.04	15.46 ± 0.06	–	–	14.15 ± 0.35	20.38	19.53	18.64	0.17
$ZOA083951.061-572419.91$	273.837	−9.540	0.28	−51.45	1.98	18.09 ± 0.08	17.12 ± 0.06	16.50 ± 0.10	–	–	16.43 ± 0.10	21.19	20.09	19.81	0.17
$ZOA083947.980-572501.42$	273.842	−9.553	0.14	49.48	1.59	17.88 ± 0.07	17.11 ± 0.06	16.40 ± 0.09	–	–	15.84 ± 0.18	20.70	20.16	19.29	0.17
$ZOA083952.043-572610.13$	273.863	−9.557	0.39	−35.18	1.87	18.49 ± 0.10	17.57 ± 0.07	16.74 ± 0.10	17.49 ± 0.32	–	–	21.67	20.74	20.21	0.17
$ZOA083959.495-572727.48$	273.891	−9.556	0.19	−71.23	2.06	17.24 ± 0.05	16.51 ± 0.04	15.94 ± 0.07	–	–	15.91 ± 0.07	20.36	19.75	19.32	0.17
$ZOA083937.749-572411.22$	273.817	−9.563	0.60	75.29	3.51	17.44 ± 0.06	16.63 ± 0.04	16.30 ± 0.10	16.70 ± 0.27	15.68 ± 0.21	15.03 ± 0.28	20.32	19.53	19.14	0.17
$ZOA083752.244-571903.15$	273.604	−9.703	0.06	−65.37	2.21	17.71 ± 0.07	16.90 ± 0.05	16.30 ± 0.10	–	16.17 ± 0.15	–	20.50	19.85	19.51	0.17
$ZOA083808.112-571345.06$	273.554	−9.622	0.11	−69.98	6.03	14.69 ± 0.03	13.89 ± 0.02	13.69 ± 0.03	14.22 ± 0.14	12.70 ± 0.31	12.79 ± 0.18	18.18	17.38	17.18	0.17
$ZOA083803.966-571639.07$	273.587	−9.658	0.17	−18.72	4.41	17.14 ± 0.05	16.50 ± 0.05	16.33 ± 0.11	–	15.33 ± 0.23	15.74 ± 0.15	19.90	19.31	19.27	0.17
$ZOA083815.025-571641.30$	273.603	−9.639	0.19	−10.56	1.53	18.32 ± 0.09	17.48 ± 0.07	18.03 ± 0.32	–	16.08 ± 0.14	16.08 ± 0.26	20.25	19.60	19.85	0.17
$ZOA083801.712-571902.25$	273.617	−9.686	0.26	14.66	2.75	17.60 ± 0.07	16.68 ± 0.05	15.90 ± 0.07	–	–	14.88 ± 0.23	20.57	19.80	18.93	0.17
$ZOA083804.458-571936.40$	273.628	−9.687	0.32	87.74	2.65	17.51 ± 0.06	16.72 ± 0.05	16.04 ± 0.08	16.67 ± 0.31	-14.92 ± 9.93	14.81 ± 0.24	20.14	19.53	18.99	0.17
$ZOA083812.830-572052.86$	273.657	−9.684	0.20	−89.72	5.36	16.96 ± 0.06	15.32 ± 0.03	14.96 ± 0.06	16.38 ± 0.34	14.21 ± 0.29	14.06 ± 0.20	19.97	18.55	18.18	0.17
$ZOA083817.561-574812.07$	274.036	−9.944	0.21	86.97	2.00	18.09 ± 0.11	17.24 ± 0.08	16.55 ± 0.11	–	–	15.44 ± 0.28	20.83	20.10	20.02	0.15
$ZOA083800.962-574229.99$	273.936	−9.918	0.33	67.55	4.16	17.54 ± 0.10	16.30 ± 0.06	15.77 ± 0.08	–	15.23 ± 0.31	15.60 ± 0.09	21.02	19.32	19.07	0.15
$ZOA083743.888-574443.03$	273.944	−9.971	0.29	37.33	2.46	17.61 ± 0.07	16.86 ± 0.06	16.44 ± 0.08	–	16.37 ± 0.07	–	20.46	19.78	19.43	0.15
$ZOA083720.004-574833.58$	273.965	−10.051	0.33	−6.36	4.11	16.44 ± 0.06	15.51 ± 0.05	14.72 ± 0.05	–	15.55 ± 0.05	14.34 ± 0.11	20.00	18.85	18.09	0.15
$ZOA083729.787-575017.26$	274.001	−10.051	0.04	−8.34	4.84	17.31 ± 0.08	16.77 ± 0.08	15.90 ± 0.08	–	15.71 ± 0.27	–	20.46	19.75	19.10	0.15
$ZOA083754.420-574946.43$	274.027	−10.001	0.10	−22.10	2.42	17.44 ± 0.07	16.75 ± 0.06	16.06 ± 0.07	–	–	–	20.47	19.87	19.20	0.15
$ZOA083923.970-572854.18$	273.862	−9.635	0.11	38.58	5.95	14.97 ± 0.03	14.27 ± 0.03	13.92 ± 0.04	–	12.51 ± 0.50	13.06 ± 0.22	18.33	17.59	17.29	0.17
$ZOA083915.920-572833.67$	273.847	−9.646	0.61	82.47	8.22	15.02 ± 0.03	14.32 ± 0.03	13.79 ± 0.04	14.55 ± 0.18	14.22 ± 0.07	13.12 ± 0.18	18.60	17.91	17.27	0.17
$ZOA083927.376-572832.82$	273.862	−9.625	0.26	−16.16	7.49	15.31 ± 0.03	14.61 ± 0.03	14.27 ± 0.04	14.50 ± 0.25	14.19 ± 0.09	13.98 ± 0.07	18.62	17.94	17.55	0.17
$ZOA083920.714-572815.97$	273.849	−9.634	0.14	43.95	2.65	16.50 ± 0.04	15.73 ± 0.03	15.10 ± 0.04	–	15.36 ± 0.08	–	19.64	18.93	18.38	0.17
$ZOA083924.326-572819.26$	273.855	−9.628	0.29	−51.99	1.68	18.46 ± 0.13	17.40 ± 0.08	16.60 ± 0.12	17.72 ± 0.26	–	–	22.60	21.05	19.81	0.17
$ZOA083849.757-572457.32$	273.762	−9.657	0.24	−29.75	4.00	15.86 ± 0.03	15.07 ± 0.03	14.70 ± 0.05	15.17 ± 0.22	14.04 ± 0.28	11.65 ± 0.88	19.09	18.33	17.98	0.17
$ZOA083915.481-572547.48$	273.809	−9.619	0.30	−31.29	2.03	17.58 ± 0.07	16.80 ± 0.05	16.44 ± 0.09	–	–	–	20.69	19.92	19.50	0.17
$ZOA083910.150-572547.68$	273.801	−9.629	0.21	53.27	2.66	16.67 ± 0.04	15.96 ± 0.03	15.26 ± 0.05	–	15.46 ± 0.13	14.78 ± 0.13	19.80	19.14	18.50	0.17
$ZOA083918.240-572614.93$	273.819	−9.619	0.13	−21.34	2.93	16.96 ± 0.05	16.25 ± 0.04	15.84 ± 0.06	–	15.14 ± 0.28	14.95 ± 0.18	19.96	19.29	18.87	0.17
$ZOA083851.634-572304.11$	273.739	−9.635	0.40	84.38	2.82	18.44 ± 0.10	17.68 ± 0.07	17.24 ± 0.14	–	–	12.38 ± 1.29	20.77	19.86	19.48	0.17
$ZOA083912.277-572757.22$	273.834	−9.646	0.55	60.77	1.41	18.30 ± 0.10	17.68 ± 0.08	17.46 ± 0.28	–	–	17.41 ± 0.28	20.96	20.23	20.16	0.17
$ZOA084122.114-571954.33$	273.901	−9.332	0.14	46.29	3.25	16.63 ± 0.05	15.90 ± 0.04	15.49 ± 0.07	15.66 ± 0.28	14.45 ± 0.34	–	19.55	18.78	18.39	0.17
$ZOA084117.881-571552.76$	273.841	−9.300	0.21	7.23	4.10	15.49 ± 0.03	14.69 ± 0.03	14.29 ± 0.04	14.30 ± 0.37	13.26 ± 0.39	13.46 ± 0.20	18.80	18.00	17.65	0.17
$ZOA084117.767-571558.58$	273.842	−9.301	0.17	−7.85	3.68	16.18 ± 0.04	15.37 ± 0.03	14.92 ± 0.05	–	13.29 ± 0.56	13.57 ± 0.33	19.30	18.50	18.13	0.17
$ZOA083749.429-573244.56$	273.788	−9.843	0.12	−86.00	1.97	17.88 ± 0.08	16.96 ± 0.06	16.10 ± 0.08	–	–	–	20.88	19.96	19.14	0.16
$ZOA083737.037-573322.15$	273.780	−9.872	0.65	35.41	6.60	15.38 ± 0.03	14.60 ± 0.02	14.05 ± 0.03	15.20 ± 0.07	–	13.89 ± 0.04	18.84	18.08	17.48	0.16
$ZOA083732.688-573326.00$	273.775	−9.880	0.47	−2.00	7.43	14.71 ± 0.03	13.95 ± 0.02	13.45 ± 0.03	14.22 ± 0.17	13.83 ± 0.03	13.31 ± 0.03	18.26	17.50	17.02	0.16
$ZOA083746.009-573006.35$	273.747	−9.823	0.51	41.25	4.43	15.74 ± 0.03	14.98 ± 0.03	14.64 ± 0.04	15.41 ± 0.07	14.66 ± 0.04	14.51 ± 0.04	19.02	18.26	18.01	0.16
$ZOA083749.580-572949.02$	273.748	−9.814	0.11	−41.90	2.41	17.88 ± 0.07	17.07 ± 0.06	16.31 ± 0.10	–	–	13.70 ± 0.67	21.06	20.12	19.33	0.16
$ZOA083739.175-573418.22$	273.795	−9.877	0.24	−42.57	5.61	15.72 ± 0.03	14.96 ± 0.03	14.70 ± 0.05	–	13.89 ± 0.24	13.44 ± 0.29	19.17	18.40	18.13	0.16
$ZOA083808.870-574227.30$	273.946	−9.903	0.28	−48.24	2.85	16.52 ± 0.04	15.83 ± 0.04	15.30 ± 0.04	–	15.40 ± 0.09	15.14 ± 0.05	19.72	19.05	18.53	0.15
$ZOA083756.091-574027.08$	273.902	−9.907	0.34	85.14	5.93	14.75 ± 0.03	13.92 ± 0.02	13.47 ± 0.03	13.98 ± 0.25	13.48 ± 0.11	12.79 ± 0.18	18.21	17.39	16.95	0.15
$ZOA083800.293-574017.00$	273.905	−9.898	0.28	56.80	2.68	17.47 ± 0.07	16.50 ± 0.05	15.80 ± 0.06	–	16.22 ± 0.09	15.71 ± 0.06	20.85	19.83	19.12	0.15
$ZOA083744.397-574032.69$	273.888	−9.929	0.03	0.81	4.93	15.23 ± 0.03	14.49 ± 0.03	14.15 ± 0.03	14.37 ± 0.28	13.89 ± 0.09	–	18.64	17.89	17.55	0.15
$ZOA083743.134-574006.64$	273.880	−9.927	0.29	70.41	4.52	15.63 ± 0.03	14.95 ± 0.03	14.54 ± 0.03	14.92 ± 0.23	13.79 ± 0.31	14.24 ± 0.06	18.93	18.24	17.88	0.15
$ZOA084110.836-571723.77$	273.852	−9.328	0.41	−12.35	5.29	17.33 ± 0.07	16.63 ± 0.06	15.44 ± 0.07	16.57 ± 0.32	–	–	20.64	19.96	18.55	0.19
$ZOA084115.622-571437.89$	273.821	−9.291	0.34	−74.02	2.63	16.61 ± 0.04	15.89 ± 0.04	15.36 ± 0.05	–	15.56 ± 0.05	15.31 ± 0.05	19.80	19.04	18.97	0.19
$ZOA084135.943-571456.81$	273.853	−9.258	0.05	40.06	2.73	17.00 ± 0.06	16.26 ± 0.04	15.54 ± 0.05	–	–	–	20.16	19.43	18.78	0.19
$ZOA084142.738-571628.02$	273.883	−9.261	0.13	−30.09	2.22	17.59 ± 0.07	16.74 ± 0.05	16.00 ± 0.07	–	–	15.17 ± 0.21	20.44	19.90	19.12	0.19
$ZOA084140.766-571724.81$	273.893	−9.274	0.18	37.03	4.48	15.95 ± 0.04	15.46 ± 0.04	14.48 ± 0.04	15.25 ± 0.26	–	14.18 ± 0.07	19.23	18.80	17.85	0.19
$ZOA084137.870-571753.35$	273.895	−9.284	0.10	86.27	2.56	17.24 ± 0.06	16.54 ± 0.05	15.69 ± 0.06	–	–	15.54 ± 0.06	20.57	19.96	18.81	0.19
$ZOA084144.673-571929.47$	273.926	−9.288	0.48	48.66	3.96	16.42 ± 0.05	15.89 ± 0.04	15.04 ± 0.05	16.36 ± 0.06	–	14.98 ± 0.05	19.78	19.17	18.50	0.19
$ZOA084133.563-573437.56$	274.115	−9.459	0.29	21.91	3.11	16.12 ± 0.04	15.44 ± 0.03	14.85 ± 0.04	15.53 ± 0.18	14.96 ± 0.10	13.88 ± 0.26	19.32	18.66	18.15	0.19
$ZOA084140.960-573510.10$	274.133	−9.451	0.23	−82.71	4.46	15.19 ± 0.03	14.44 ± 0.02	14.00 ± 0.03	–	14.27 ± 0.04	13.86 ± 0.04	18.59	17.83	17.42	0.19
$ZOA083732.197-571807.39$	273.565	−9.731	0.28	−31.84	5.92	14.96 ± 0.03	14.22 ± 0.02	13.88 ± 0.03	14.38 ± 0.20	13.68 ± 0.12	12.75 ± 0.28	18.42	17.68	17.35	0.17
$ZOA083742.204-571822.17$	273.582	−9.715	0.23	72.29	5.95	14.69 ± 0.03	13.99 ± 0.02	13.62 ± 0.03	13.93 ± 0.25	13.55 ± 0.13	13.41 ± 0.06	18.13	17.44	17.08	0.17
$ZOA083740.082-571850.74$	273.585	−9.723	0.40	−48.84	1.82	18.11 ± 0.08	17.17 ± 0.06	16.43 ± 0.09	17.53 ± 0.23	–	–	21.29	20.32	20.06	0.17

ZOA083729.750 − 571823.84	273.565	−9.738	0.53	78.50	5.38	14.91 ± 0.03	14.10 ± 0.02	13.89 ± 0.03	14.59 ± 0.07	12.84 ± 0.30	13.73 ± 0.04	18.39	17.58	17.40	0.17
ZOA083935.109 − 571351.58	273.673	−9.465	0.18	−5.44	6.19	14.93 ± 0.04	14.21 ± 0.03	13.65 ± 0.07	14.15 ± 0.25	–	–	18.44	17.72	17.12	0.16
ZOA083904.737 − 570858.69	273.565	−9.472	0.04	−11.12	8.27	13.85 ± 0.03	13.10 ± 0.02	12.71 ± 0.03	13.10 ± 0.25	12.11 ± 0.29	12.24 ± 0.13	17.53	16.76	16.39	0.16
ZOA084125.434 − 572740.49	274.010	−9.404	0.38	31.43	6.45	14.81 ± 0.03	14.07 ± 0.02	13.66 ± 0.03	–	13.76 ± 0.09	13.53 ± 0.04	18.28	17.55	17.13	0.20
ZOA084109.020 − 572354.75	273.937	−9.396	0.31	−52.31	2.38	17.76 ± 0.07	16.97 ± 0.05	16.02 ± 0.07	–	–	15.93 ± 0.07	20.85	20.06	19.07	0.20
ZOA084125.465 − 572550.32	273.986	−9.386	0.19	−35.90	3.34	17.50 ± 0.07	16.60 ± 0.05	16.06 ± 0.13	16.95 ± 0.28	–	15.67 ± 0.17	20.86	20.07	19.59	0.20
ZOA084104.410 − 572301.18	273.919	−9.395	0.13	−41.28	3.02	17.22 ± 0.06	16.47 ± 0.04	15.93 ± 0.07	−20.93 ± 12.11	13.35 ± 0.97	15.73 ± 0.08	20.19	19.40	19.04	0.20
ZOA084119.075 − 572129.33	273.918	−9.354	0.89	41.14	5.98	17.05 ± 0.06	16.39 ± 0.05	15.85 ± 0.09	15.93 ± 0.45	15.91 ± 0.14	14.69 ± 0.32	20.10	19.56	18.85	0.20
ZOA084112.290 − 572154.47	273.915	−9.370	0.15	−17.93	2.95	17.51 ± 0.07	16.74 ± 0.05	15.82 ± 0.06	–	–	15.66 ± 0.07	20.75	19.94	19.20	0.20
ZOA084127.159 − 572140.95	273.932	−9.341	0.26	84.37	1.77	17.77 ± 0.07	17.10 ± 0.06	16.47 ± 0.10	–	–	–	20.66	20.19	19.53	0.20
ZOA084131.662 − 572238.95	273.951	−9.343	0.16	47.15	7.34	13.51 ± 0.02	12.74 ± 0.02	12.36 ± 0.02	13.22 ± 0.09	12.44 ± 0.07	12.25 ± 0.03	17.14	16.37	15.99	0.20
ZOA084133.310 − 572300.52	273.958	−9.343	0.24	−6.12	5.76	14.37 ± 0.02	13.66 ± 0.02	13.24 ± 0.03	13.34 ± 0.32	13.50 ± 0.03	12.51 ± 0.22	17.86	17.15	16.73	0.20
ZOA084151.913 − 572358.65	273.997	−9.320	0.30	−87.22	3.23	17.11 ± 0.06	16.31 ± 0.05	15.68 ± 0.08	–	16.16 ± 0.06	15.35 ± 0.10	20.45	19.72	19.07	0.20
ZOA084144.320 − 572635.54	274.022	−9.359	0.17	−81.99	7.19	15.05 ± 0.03	14.35 ± 0.02	13.95 ± 0.03	14.87 ± 0.06	13.48 ± 0.25	13.64 ± 0.06	18.55	17.87	17.47	0.20
ZOA084149.030 − 572826.35	274.053	−9.369	0.38	89.94	2.64	18.01 ± 0.10	17.27 ± 0.09	15.55 ± 0.07	–	13.85 ± 0.96	14.86 ± 0.17	20.12	19.43	18.50	0.20
ZOA083820.561 − 571158.88	273.546	−9.582	0.18	1.68	4.72	15.84 ± 0.04	15.12 ± 0.03	14.65 ± 0.05	15.01 ± 0.21	14.32 ± 0.13	12.27 ± 0.65	19.03	18.33	17.91	0.17
ZOA083816.395 − 570721.89	273.478	−9.544	0.19	−20.55	3.77	15.67 ± 0.03	14.90 ± 0.03	14.28 ± 0.04	14.93 ± 0.25	13.75 ± 0.35	–	19.00	18.26	17.67	0.17
ZOA083821.450 − 570902.89	273.508	−9.552	0.45	−50.40	2.55	17.42 ± 0.07	16.61 ± 0.05	16.51 ± 0.13	–	14.04 ± 0.52	12.10 ± 1.24	19.71	19.08	19.30	0.17
ZOA083827.666 − 571223.82	273.562	−9.573	0.17	9.25	3.25	16.74 ± 0.05	16.06 ± 0.04	15.21 ± 0.06	–	–	15.10 ± 0.07	20.14	19.55	18.52	0.17
ZOA083733.782 − 572318.89	273.638	−9.779	0.11	−74.59	2.12	17.60 ± 0.07	16.82 ± 0.05	16.09 ± 0.08	–	16.04 ± 0.23	16.00 ± 0.08	20.61	19.77	19.17	0.17
ZOA083734.738 − 572426.11	273.654	−9.788	0.46	−51.23	4.49	16.10 ± 0.04	15.31 ± 0.03	14.73 ± 0.04	15.74 ± 0.13	15.03 ± 0.06	13.91 ± 0.18	19.39	18.61	17.96	0.17
ZOA083746.710 − 572455.24	273.677	−9.771	0.19	18.65	3.01	16.46 ± 0.04	15.95 ± 0.04	15.68 ± 0.10	–	15.04 ± 0.25	–	19.71	19.12	18.75	0.17
ZOA083737.472 − 572532.07	273.673	−9.794	0.19	−26.71	2.54	16.49 ± 0.04	15.78 ± 0.03	15.40 ± 0.05	–	–	–	19.70	19.11	18.57	0.17
ZOA083742.241 − 572543.45	273.682	−9.787	0.08	−53.99	2.70	16.63 ± 0.04	15.91 ± 0.04	15.56 ± 0.06	–	–	15.36 ± 0.08	19.86	19.11	18.86	0.17
ZOA083748.226 − 572607.41	273.696	−9.780	0.26	74.66	17.70	13.20 ± 0.02	12.79 ± 0.02	12.39 ± 0.03	12.69 ± 0.09	11.76 ± 0.23	11.18 ± 0.29	17.39	17.03	16.70	0.17
ZOA083750.837 − 572606.15	273.699	−9.775	0.24	−29.47	4.19	15.88 ± 0.04	15.24 ± 0.04	15.02 ± 0.08	15.41 ± 0.14	13.80 ± 0.28	14.06 ± 0.30	19.09	18.41	18.35	0.17
ZOA083750.498 − 572618.24	273.701	−9.778	0.16	−83.18	10.47	14.52 ± 0.03	13.83 ± 0.03	13.47 ± 0.04	12.16 ± 0.79	11.27 ± 0.77	–	18.23	17.48	17.16	0.17
ZOA083740.504 − 572742.97	273.707	−9.810	0.17	83.94	2.00	17.68 ± 0.07	16.83 ± 0.06	16.14 ± 0.08	–	–	–	21.05	19.93	19.23	0.17
ZOA083735.876 − 572213.59	273.626	−9.764	0.23	29.38	3.38	16.03 ± 0.04	15.37 ± 0.03	14.98 ± 0.05	15.70 ± 0.12	15.03 ± 0.08	14.28 ± 0.16	19.29	18.64	18.21	0.17
ZOA083733.671 − 572445.78	273.657	−9.793	0.28	−27.85	2.59	16.57 ± 0.04	15.84 ± 0.03	15.60 ± 0.06	–	15.00 ± 0.18	14.34 ± 0.30	19.59	18.89	18.62	0.17
ZOA083724.501 − 572734.22	273.684	−9.837	0.29	48.39	3.29	16.70 ± 0.04	16.05 ± 0.04	15.67 ± 0.07	16.21 ± 0.17	15.05 ± 0.27	15.21 ± 0.10	19.79	19.11	18.81	0.17
ZOA083813.354 − 571214.20	273.540	−9.598	0.27	−42.26	3.59	16.74 ± 0.05	15.94 ± 0.04	15.26 ± 0.04	–	15.49 ± 0.11	14.23 ± 0.26	19.99	19.15	18.50	0.17
ZOA083821.095 − 570836.44	273.501	−9.548	0.67	−71.81	0.86	18.23 ± 0.13	17.57 ± 0.12	18.12 ± 0.46	–	–	10.46 ± 2.46	21.13	20.29	19.90	0.17
ZOA083803.968 − 570808.81	273.472	−9.575	0.25	−36.27	3.28	16.89 ± 0.05	15.97 ± 0.04	15.37 ± 0.04	16.19 ± 0.25	15.60 ± 0.08	14.33 ± 0.26	19.98	19.13	18.56	0.17
ZOA083735.637 − 570910.82	273.447	−9.636	0.29	29.56	4.12	16.12 ± 0.04	15.32 ± 0.03	14.73 ± 0.04	–	14.78 ± 0.14	14.04 ± 0.15	19.45	18.61	17.99	0.17
ZOA083755.604 − 571246.03	273.523	−9.635	0.42	−56.32	2.16	18.19 ± 0.10	17.03 ± 0.06	15.90 ± 0.06	–	–	15.84 ± 0.06	21.13	19.87	19.19	0.17
ZOA084108.315 − 573526.06	274.092	−9.512	0.05	30.30	1.97	18.14 ± 0.09	17.34 ± 0.07	16.56 ± 0.11	–	–	–	21.39	20.19	19.72	0.19
ZOA084114.736 − 573514.69	274.098	−9.499	0.08	7.58	4.36	15.91 ± 0.03	15.07 ± 0.03	14.35 ± 0.04	14.72 ± 0.42	–	12.94 ± 0.32	19.23	18.38	17.67	0.19
ZOA084112.229 − 573510.11	274.094	−9.503	0.22	65.14	2.80	16.74 ± 0.04	15.92 ± 0.03	15.31 ± 0.05	–	–	14.69 ± 0.13	19.83	19.08	18.47	0.19
ZOA084102.008 − 573300.20	274.051	−9.499	0.16	71.71	3.19	16.30 ± 0.04	15.49 ± 0.03	14.83 ± 0.04	–	–	14.74 ± 0.04	19.54	18.77	18.30	0.19
ZOA084104.312 − 573350.03	274.065	−9.503	0.14	−70.45	4.36	16.28 ± 0.04	15.52 ± 0.03	14.92 ± 0.05	14.89 ± 0.49	14.52 ± 0.29	14.15 ± 0.17	19.50	18.77	18.19	0.19
ZOA084105.529 − 573402.63	274.070	−9.503	0.08	−17.71	3.79	17.40 ± 0.06	16.69 ± 0.05	15.83 ± 0.07	–	15.87 ± 0.21	15.30 ± 0.09	20.37	19.72	18.90	0.19
ZOA084116.038 − 573443.39	274.093	−9.491	0.54	−43.19	3.13	16.27 ± 0.04	15.55 ± 0.03	15.09 ± 0.04	16.01 ± 0.07	–	14.15 ± 0.28	19.50	18.88	18.41	0.19
ZOA083744.875 − 572603.13	273.690	−9.785	0.43	38.35	4.95	15.00 ± 0.03	14.25 ± 0.02	13.89 ± 0.04	14.11 ± 0.27	13.97 ± 0.05	13.67 ± 0.05	18.39	17.64	17.30	0.17
ZOA083748.816 − 572606.89	273.696	−9.779	0.10	−47.74	13.37	13.28 ± 0.02	12.43 ± 0.02	12.07 ± 0.02	12.61 ± 0.23	12.05 ± 0.10	11.30 ± 0.20	17.31	16.50	16.10	0.17
ZOA083749.730 − 572651.71	273.708	−9.785	0.20	−82.61	3.29	15.94 ± 0.04	15.22 ± 0.03	14.85 ± 0.05	–	14.71 ± 0.13	14.02 ± 0.21	19.20	18.49	18.13	0.17
ZOA083734.075 − 572305.26	273.635	−9.776	0.26	81.44	4.20	15.78 ± 0.03	15.10 ± 0.03	14.72 ± 0.04	15.12 ± 0.20	13.90 ± 0.32	14.37 ± 0.08	19.02	18.32	18.02	0.17
ZOA083805.288 − 572151.41	273.660	−9.707	0.17	8.32	4.24	15.41 ± 0.03	14.41 ± 0.02	14.02 ± 0.03	14.41 ± 0.31	14.00 ± 0.11	13.76 ± 0.04	18.71	17.80	17.39	0.17
ZOA083753.891 − 572241.56	273.656	−9.736	0.36	77.58	3.13	16.09 ± 0.04	15.38 ± 0.03	15.13 ± 0.05	15.50 ± 0.18	–	–	19.25	18.61	18.25	0.17
ZOA083806.493 − 572358.63	273.691	−9.726	0.08	11.62	3.46	16.17 ± 0.04	15.43 ± 0.03	15.02 ± 0.05	–	15.18 ± 0.06	12.82 ± 0.62	19.51	18.69	18.19	0.17
ZOA083750.982 − 572606.99	273.699	−9.775	0.26	38.12	4.09	15.91 ± 0.04	15.19 ± 0.03	14.47 ± 0.04	–	9.59 ± 1.70	13.30 ± 0.28	19.08	18.42	17.73	0.17
ZOA083751.992 − 572551.36	273.697	−9.771	0.20	14.90	2.35	17.13 ± 0.05	16.40 ± 0.04	16.09 ± 0.08	–	15.92 ± 0.08	14.44 ± 0.46	20.21	19.46	18.71	0.17
ZOA083752.923 − 572610.65	273.703	−9.772	0.27	2.33	2.90	16.29 ± 0.04	15.59 ± 0.03	15.12 ± 0.05	–	15.34 ± 0.06	–	19.55	18.86	18.36	0.17
ZOA083756.482 − 572604.98	273.706	−9.765	0.18	42.25	3.09	16.12 ± 0.04	15.39 ± 0.03	15.04 ± 0.05	–	15.08 ± 0.08	14.83 ± 0.06	19.39	18.68	18.28	0.17
ZOA083756.573 − 572636.33	273.713	−9.770	0.42	−82.12	4.39	15.54 ± 0.03	14.74 ± 0.03	14.41 ± 0.04	14.88 ± 0.20	14.36 ± 0.08	13.61 ± 0.18	18.84	18.08	17.72	0.17
ZOA083757.111 − 572705.01	273.721	−9.773	0.14	19.56	3.65	15.53 ± 0.03	14.79 ± 0.03	14.32 ± 0.03	14.62 ± 0.28	14.45 ± 0.08	13.96 ± 0.08	18.83	18.12	17.63	0.17
ZOA083759.547 − 572720.34	273.727	−9.772	0.40	17.63	4.03	16.00 ± 0.04	15.29 ± 0.03	14.81 ± 0.04	15.31 ± 0.24	14.80 ± 0.14	–	19.35	18.64	18.22	0.17
ZOA083801.381 − 572719.51	273.730	−9.768	0.34	−85.26	3.91	15.15 ± 0.03	14.43 ± 0.02	14.02 ± 0.03	14.21 ± 0.29	13.90 ± 0.14	13.28 ± 0.20	18.52	17.78	17.39	0.17
ZOA083808.931 − 572735.01	273.743	−9.757	0.28	66.20	2.44	17.47 ± 0.06	16.87 ± 0.05	16.48 ± 0.12	–	14.88 ± 0.49	15.55 ± 0.17	20.16	19.50	19.28	0.17
ZOA083804.120 − 572512.88	273.705	−9.742	0.21	−35.21	2.60	17.26 ± 0.06	16.52 ± 0.04	15.86 ± 0.07	–	–	15.17 ± 0.22	20.43	19.80	19.37	0.17
ZOA084054.356 − 572353.71	273.917	−9.422	0.28	−46.49	2.23	18.10 ± 0.09	17.27 ± 0.06	16.31 ± 0.09	–	–	–	21.17	20.39	19.19	0.20
ZOA084101.728 − 572249.14	273.912	−9.398	0.12	−34.09	2.39	17.34 ± 0.06	16.66 ± 0.05	15.81 ± 0.06	12.59 ± 1.51	–	12.49 ± 0.85	20.36	19.73	18.62	0.20

ZOA084120.976 − 572559.84	273.982	−9.395	0.46	−19.69	2.98	17.06 ± 0.05	16.14 ± 0.04	15.23 ± 0.04	–	–	14.78 ± 0.08	20.24	19.40	18.47	0.20
ZOA084126.154 − 572719.74	274.007	−9.399	0.12	−26.08	5.75	17.64 ± 0.08	16.94 ± 0.07	16.22 ± 0.12	–	16.51 ± 0.09	15.63 ± 0.16	20.46	19.99	19.09	0.20
ZOA084121.507 − 572150.86	273.926	−9.353	0.08	−6.67	2.73	17.58 ± 0.07	16.63 ± 0.05	15.79 ± 0.07	–	–	15.43 ± 0.08	20.59	19.50	18.87	0.20
ZOA084133.627 − 574000.58	274.188	−9.513	0.10	−29.73	6.23	14.48 ± 0.02	13.75 ± 0.02	13.35 ± 0.03	14.23 ± 0.09	13.29 ± 0.12	12.27 ± 0.30	18.06	17.31	16.92	0.17
ZOA084144.067 − 574034.17	274.210	−9.500	0.12	41.56	3.33	15.94 ± 0.03	15.23 ± 0.03	14.74 ± 0.04	–	15.08 ± 0.03	14.03 ± 0.18	19.20	18.55	18.02	0.17
ZOA084145.186 − 574034.22	274.212	−9.498	0.15	−61.63	2.62	17.88 ± 0.07	17.34 ± 0.07	16.77 ± 0.09	–	–	16.66 ± 0.10	20.54	19.96	19.61	0.17
ZOA084152.290 − 574035.39	274.221	−9.485	0.43	−58.24	2.30	18.27 ± 0.10	17.32 ± 0.07	17.26 ± 0.16	17.03 ± 0.32	16.09 ± 0.20	–	20.73	19.82	20.06	0.17
ZOA084128.689 − 573620.01	274.132	−9.485	0.15	−53.70	2.25	17.91 ± 0.08	17.17 ± 0.07	16.46 ± 0.08	–	–	–	20.61	19.88	19.48	0.17
ZOA084134.047 − 573750.28	274.160	−9.490	0.23	−46.18	2.96	17.03 ± 0.05	16.28 ± 0.04	15.68 ± 0.05	–	13.19 ± 0.92	–	19.73	19.20	18.55	0.17
ZOA084140.851 − 573810.73	274.173	−9.481	0.32	58.91	2.69	17.48 ± 0.06	16.80 ± 0.05	16.55 ± 0.09	–	–	–	20.39	19.71	19.71	0.17
ZOA084119.528 − 574234.83	274.204	−9.563	0.55	30.31	8.73	14.04 ± 0.02	13.23 ± 0.02	12.87 ± 0.02	13.19 ± 0.27	12.98 ± 0.04	12.06 ± 0.22	17.77	16.96	16.55	0.17
ZOA084120.397 − 574310.71	274.213	−9.568	0.31	−50.95	3.37	17.06 ± 0.06	16.19 ± 0.05	14.98 ± 0.04	–	14.63 ± 0.52	13.97 ± 0.28	20.07	19.29	18.28	0.17
ZOA084136.817 − 574257.17	274.232	−9.536	0.44	−69.57	3.67	16.82 ± 0.05	16.58 ± 0.05	16.30 ± 0.08	–	–	15.24 ± 0.27	19.70	19.34	19.25	0.17
ZOA084057.437 − 573051.73	274.015	−9.486	0.40	−70.80	2.12	18.15 ± 0.09	17.34 ± 0.07	16.40 ± 0.10	–	–	14.93 ± 0.40	21.32	20.49	19.79	0.18
ZOA084055.302 − 573126.58	274.020	−9.496	0.86	6.79	3.61	16.98 ± 0.05	16.33 ± 0.04	15.56 ± 0.07	16.37 ± 0.26	15.65 ± 0.21	–	20.09	19.46	18.75	0.18
ZOA084038.433 − 573245.61	274.015	−9.539	0.62	60.22	3.15	16.09 ± 0.04	15.43 ± 0.03	15.12 ± 0.05	–	14.76 ± 0.13	14.93 ± 0.07	19.03	18.57	18.67	0.18
ZOA084101.880 − 573300.40	274.051	−9.499	0.68	35.12	2.04	16.45 ± 0.04	15.99 ± 0.04	16.03 ± 0.11	15.31 ± 0.40	14.66 ± 0.18	–	19.55	18.63	18.35	0.18
ZOA084050.672 − 573314.33	274.038	−9.522	0.07	59.54	2.18	17.86 ± 0.07	17.19 ± 0.07	16.48 ± 0.09	–	–	15.52 ± 0.30	21.96	22.58	nan	0.18
ZOA084053.026 − 573426.96	274.058	−9.530	0.05	−38.55	2.61	18.00 ± 0.08	17.09 ± 0.06	16.20 ± 0.08	–	16.70 ± 0.12	15.92 ± 0.09	21.07	20.23	19.54	0.18
ZOA083654.660 − 573915.64	273.804	−10.006	0.21	30.68	5.94	16.44 ± 0.04	15.83 ± 0.04	15.17 ± 0.08	–	14.43 ± 0.39	14.13 ± 0.29	19.58	18.95	18.32	0.16
ZOA083634.475 − 573938.18	273.782	−10.046	0.26	58.22	2.22	17.50 ± 0.06	16.76 ± 0.05	16.02 ± 0.07	–	–	14.39 ± 0.48	20.63	19.86	19.08	0.16
ZOA083652.550 − 574036.64	273.820	−10.023	0.10	−34.30	3.34	15.97 ± 0.03	15.32 ± 0.03	15.16 ± 0.06	–	14.38 ± 0.25	14.65 ± 0.16	19.23	18.56	18.66	0.16
ZOA083650.255 − 574041.93	273.818	−10.028	0.34	−28.09	3.33	16.80 ± 0.05	15.94 ± 0.04	15.31 ± 0.06	–	15.02 ± 0.26	14.85 ± 0.10	19.95	19.08	18.52	0.16
ZOA083634.581 − 574111.78	273.804	−10.061	0.04	−55.49	2.32	17.40 ± 0.06	16.52 ± 0.04	15.99 ± 0.07	–	–	14.29 ± 0.48	20.50	19.32	18.86	0.16
ZOA083602.014 − 573624.42	273.695	−10.073	0.27	−34.59	2.69	16.61 ± 0.04	15.86 ± 0.03	15.20 ± 0.04	14.50 ± 0.62	13.91 ± 0.49	–	19.45	18.75	18.43	0.16
ZOA084040.433 − 572817.01	273.957	−9.491	0.07	−68.13	2.17	16.78 ± 0.05	15.99 ± 0.04	15.63 ± 0.07	–	–	–	19.68	19.12	18.95	0.19
ZOA084033.948 − 572506.42	273.906	−9.471	0.32	68.80	2.61	17.72 ± 0.07	16.96 ± 0.05	15.93 ± 0.08	–	–	15.86 ± 0.08	20.96	19.99	19.02	0.19
ZOA084044.043 − 572523.42	273.923	−9.456	0.31	−25.55	3.90	16.92 ± 0.05	16.01 ± 0.04	15.06 ± 0.05	11.41 ± 1.86	–	14.01 ± 0.09	20.12	19.20	17.93	0.19
ZOA083639.479 − 573750.28	273.764	−10.019	0.11	16.79	2.06	17.49 ± 0.06	16.70 ± 0.05	16.02 ± 0.07	–	–	15.90 ± 0.08	20.68	19.90	19.42	0.16
ZOA083705.679 − 573739.02	273.796	−9.970	0.29	−74.92	2.66	16.99 ± 0.05	16.25 ± 0.04	15.76 ± 0.07	–	–	15.21 ± 0.12	20.07	19.36	18.89	0.16
ZOA083840.788 − 574317.56	274.000	−9.854	0.05	−60.02	2.87	16.70 ± 0.05	15.88 ± 0.04	15.11 ± 0.04	–	15.36 ± 0.13	–	19.87	19.03	18.28	0.15
ZOA083854.423 − 574401.28	274.028	−9.837	0.35	33.04	2.37	17.94 ± 0.08	16.97 ± 0.06	16.36 ± 0.07	–	–	15.59 ± 0.16	20.86	19.92	19.60	0.15
ZOA083849.996 − 574247.60	274.006	−9.833	0.36	−84.79	3.78	17.21 ± 0.07	16.40 ± 0.06	15.57 ± 0.06	–	–	14.98 ± 0.15	20.16	19.40	18.69	0.15
ZOA083859.094 − 574330.60	274.028	−9.824	0.29	−24.79	2.35	17.76 ± 0.08	16.97 ± 0.06	16.22 ± 0.07	–	16.32 ± 0.20	14.93 ± 0.35	20.85	20.08	19.29	0.15
ZOA083901.958 − 574608.40	274.067	−9.845	0.08	−66.43	2.49	17.52 ± 0.07	16.71 ± 0.05	15.97 ± 0.06	–	–	–	20.59	19.66	19.07	0.15
ZOA083841.431 − 574717.68	274.056	−9.893	0.23	41.71	4.00	16.38 ± 0.04	15.59 ± 0.04	15.07 ± 0.04	15.67 ± 0.29	12.66 ± 0.90	14.54 ± 0.09	19.62	18.87	18.30	0.15
ZOA083903.836 − 574946.17	274.119	−9.877	0.45	33.34	3.32	17.34 ± 0.06	16.57 ± 0.05	15.93 ± 0.06	17.07 ± 0.14	–	15.62 ± 0.08	20.51	19.66	19.05	0.15
ZOA083833.743 − 574925.34	274.075	−9.927	0.02	−16.68	2.36	17.69 ± 0.07	16.78 ± 0.05	16.08 ± 0.06	–	–	15.78 ± 0.07	20.84	19.96	19.18	0.15
ZOA083822.857 − 575012.60	274.071	−9.955	0.13	72.00	2.99	16.51 ± 0.05	15.83 ± 0.04	15.22 ± 0.05	–	15.51 ± 0.08	14.78 ± 0.09	19.68	19.06	18.46	0.15
ZOA083906.329 − 574743.55	274.095	−9.852	0.37	15.77	2.38	17.61 ± 0.07	16.77 ± 0.05	16.13 ± 0.06	–	–	15.35 ± 0.17	20.84	19.93	19.25	0.15
ZOA083621.842 − 572911.81	273.622	−9.967	0.33	62.52	1.54	18.97 ± 0.14	17.84 ± 0.09	16.95 ± 0.14	–	–	16.31 ± 0.25	22.87	21.34	20.23	0.16
ZOA083618.618 − 573016.12	273.633	−9.983	0.22	−37.09	2.52	18.04 ± 0.08	17.27 ± 0.06	16.40 ± 0.10	–	–	15.71 ± 0.15	21.04	20.15	19.33	0.16
ZOA083559.885 − 573146.37	273.628	−10.032	0.38	18.67	2.88	17.15 ± 0.06	16.38 ± 0.04	15.47 ± 0.07	–	15.92 ± 0.09	14.87 ± 0.20	20.11	19.39	19.07	0.16
ZOA084016.407 − 573505.10	274.017	−9.602	0.10	−65.96	1.86	17.79 ± 0.07	17.08 ± 0.06	16.27 ± 0.09	–	–	−15.21 ± 9.90	20.38	20.05	19.02	0.17
ZOA084026.156 − 573026.96	273.967	−9.538	0.19	−73.10	3.06	16.84 ± 0.05	16.08 ± 0.04	15.30 ± 0.05	–	15.68 ± 0.10	13.95 ± 0.35	19.95	19.27	18.50	0.17
ZOA083938.375 − 573056.01	273.909	−9.629	0.40	−50.70	4.25	15.89 ± 0.03	15.16 ± 0.03	14.70 ± 0.04	15.02 ± 0.28	14.87 ± 0.07	14.06 ± 0.19	19.23	18.48	18.07	0.17
ZOA084011.283 − 573330.40	273.989	−9.595	0.43	19.85	7.02	14.67 ± 0.03	13.93 ± 0.02	13.45 ± 0.03	14.49 ± 0.06	12.98 ± 0.28	13.34 ± 0.03	18.14	17.39	16.93	0.17
ZOA083938.896 − 572833.20	273.878	−9.604	0.41	10.61	2.92	17.50 ± 0.08	16.71 ± 0.05	15.98 ± 0.08	–	–	15.55 ± 0.12	20.44	19.79	18.79	0.17
ZOA083935.613 − 573131.67	273.914	−9.640	0.17	−31.64	2.73	17.68 ± 0.07	16.97 ± 0.05	16.53 ± 0.12	–	–	16.30 ± 0.13	20.18	19.52	19.49	0.17
ZOA084028.791 − 571646.30	273.786	−9.397	0.17	65.99	1.97	17.96 ± 0.07	17.17 ± 0.06	16.68 ± 0.11	–	–	16.46 ± 0.12	20.96	20.05	19.48	0.17
ZOA084032.934 − 571653.67	273.793	−9.391	0.35	−10.03	2.31	17.92 ± 0.07	17.10 ± 0.05	16.33 ± 0.09	–	–	16.24 ± 0.08	20.81	19.93	19.69	0.17
ZOA084023.254 − 571653.17	273.780	−9.408	0.03	−40.17	1.65	18.22 ± 0.09	17.21 ± 0.06	16.77 ± 0.14	–	–	–	21.16	20.13	20.07	0.17
ZOA084053.372 − 571744.29	273.832	−9.362	0.19	42.58	1.83	18.07 ± 0.09	17.14 ± 0.06	16.30 ± 0.10	–	–	–	21.90	21.01	20.06	0.17
ZOA084055.840 − 571822.90	273.844	−9.364	0.40	−11.33	3.03	17.98 ± 0.09	16.98 ± 0.07	16.30 ± 0.13	–	–	–	21.01	20.11	19.59	0.17
ZOA083840.192 − 573600.86	273.900	−9.784	0.26	−6.55	1.76	18.30 ± 0.12	17.92 ± 0.14	16.80 ± 0.12	–	–	–	21.43	20.59	19.92	0.17
ZOA083826.648 − 573538.56	273.877	−9.804	0.16	−63.10	2.52	17.58 ± 0.07	16.75 ± 0.06	16.06 ± 0.06	–	–	15.95 ± 0.07	20.79	19.95	19.58	0.17
ZOA083843.128 − 573034.17	273.830	−9.725	0.17	−26.17	3.06	16.98 ± 0.05	16.19 ± 0.04	15.48 ± 0.05	–	–	15.34 ± 0.05	20.26	19.57	18.75	0.17
ZOA083819.802 − 573029.61	273.798	−9.766	0.09	24.51	2.24	17.74 ± 0.07	17.03 ± 0.06	16.57 ± 0.09	–	15.79 ± 0.30	15.40 ± 0.32	20.68	19.89	19.58	0.17
ZOA083909.180 − 573220.22	273.889	−9.695	0.29	54.23	2.51	17.52 ± 0.06	16.88 ± 0.06	16.42 ± 0.07	–	–	–	19.96	19.85	19.25	0.17
ZOA083820.090 − 573313.51	273.835	−9.792	0.31	−47.60	2.42	18.02 ± 0.10	16.96 ± 0.06	16.30 ± 0.07	17.22 ± 0.31	16.73 ± 0.08	15.92 ± 0.11	21.58	20.39	19.75	0.17
ZOA083859.391 − 573441.26	273.908	−9.736	0.06	−71.90	2.06	18.34 ± 0.10	17.34 ± 0.07	16.57 ± 0.08	–	–	–	21.81	20.46	19.68	0.17
ZOA083836.631 − 572906.49	273.801	−9.722	0.27	−15.02	2.65	17.73 ± 0.08	16.91 ± 0.06	15.99 ± 0.06	–	13.08 ± 1.17	–	20.50	19.75	18.98	0.17

ZOA083908.739 − 572902.74	273.844	−9.663	0.39	42.44	10.79	13.53 ± 0.02	12.76 ± 0.02	12.38 ± 0.02	13.32 ± 0.08	12.32 ± 0.11	12.11 ± 0.06	17.26	16.49	16.11	0.17
ZOA083831.542 − 572935.74	273.801	−9.736	0.06	9.36	4.54	15.18 ± 0.03	14.41 ± 0.02	13.96 ± 0.03	–	13.37 ± 0.32	13.78 ± 0.04	18.59	17.83	17.36	0.17
ZOA083820.491 − 573007.27	273.793	−9.761	0.26	−88.85	6.06	15.55 ± 0.03	14.84 ± 0.03	14.49 ± 0.04	15.25 ± 0.08	14.38 ± 0.10	13.95 ± 0.09	19.00	18.30	17.97	0.17
ZOA083825.651 − 572926.41	273.791	−9.745	0.25	29.69	4.41	16.49 ± 0.04	15.82 ± 0.04	15.57 ± 0.05	15.01 ± 0.40	–	13.01 ± 0.60	19.39	18.81	18.50	0.17
ZOA083827.164 − 573117.55	273.818	−9.761	0.28	62.48	2.25	17.23 ± 0.06	16.48 ± 0.04	16.00 ± 0.06	–	–	–	20.21	19.44	18.96	0.17
ZOA083821.497 − 573300.17	273.834	−9.788	0.00	−76.54	6.20	14.94 ± 0.03	14.24 ± 0.03	13.79 ± 0.03	–	13.90 ± 0.07	13.59 ± 0.04	18.51	17.82	17.36	0.17
ZOA083823.512 − 573250.90	273.835	−9.783	0.14	−21.33	6.41	14.11 ± 0.02	13.33 ± 0.02	12.88 ± 0.02	13.58 ± 0.18	12.82 ± 0.13	–	17.67	16.89	16.42	0.17
ZOA083830.679 − 573317.32	273.850	−9.774	0.71	−51.10	4.54	17.20 ± 0.06	16.54 ± 0.05	15.86 ± 0.06	14.77 ± 0.77	14.24 ± 0.65	–	19.83	19.23	18.59	0.17
ZOA083833.074 − 573319.70	273.854	−9.770	0.38	−10.35	5.04	15.40 ± 0.03	14.65 ± 0.03	14.28 ± 0.03	15.23 ± 0.06	14.04 ± 0.16	–	18.80	18.06	17.69	0.17
ZOA083722.32 − 573314.76	273.758	−9.897	0.78	16.92	19.66	13.16 ± 0.02	12.42 ± 0.02	12.06 ± 0.02	12.42 ± 0.22	11.85 ± 0.15	11.87 ± 0.04	17.32	16.57	16.21	0.16
ZOA083712.382 − 573516.25	273.773	−9.935	0.24	49.84	2.67	17.46 ± 0.06	16.62 ± 0.05	15.69 ± 0.07	–	–	14.94 ± 0.21	20.60	19.80	18.95	0.16
ZOA083713.289 − 573257.02	273.742	−9.910	0.45	−72.46	4.03	16.11 ± 0.04	15.34 ± 0.03	14.85 ± 0.04	–	15.17 ± 0.04	14.73 ± 0.04	19.44	18.68	18.25	0.16
ZOA083635.761 − 572844.24	273.634	−9.937	0.56	20.09	4.20	15.40 ± 0.03	14.67 ± 0.03	14.28 ± 0.03	14.81 ± 0.19	14.28 ± 0.10	13.25 ± 0.31	18.77	18.06	17.68	0.16
ZOA083703.987 − 573112.36	273.706	−9.910	0.18	29.81	2.97	17.19 ± 0.05	16.49 ± 0.04	16.13 ± 0.09	–	15.25 ± 0.30	14.16 ± 0.55	20.17	19.39	19.07	0.16
ZOA083649.342 − 572951.16	273.668	−9.923	0.42	46.18	2.28	18.13 ± 0.08	17.41 ± 0.07	16.97 ± 0.14	–	–	16.55 ± 0.13	20.94	20.23	20.22	0.16
ZOA083838.298 − 572829.21	273.795	−9.713	0.35	54.10	2.52	17.81 ± 0.08	17.20 ± 0.07	16.55 ± 0.09	–	–	16.26 ± 0.09	20.84	20.36	19.53	0.18
ZOA083841.630 − 572520.42	273.757	−9.676	0.56	57.52	10.44	13.76 ± 0.02	12.88 ± 0.02	12.42 ± 0.02	13.45 ± 0.10	12.63 ± 0.06	12.25 ± 0.04	17.48	16.58	16.12	0.18
ZOA083900.077 − 572755.91	273.817	−9.668	0.27	20.14	2.35	17.08 ± 0.05	16.43 ± 0.04	16.05 ± 0.06	–	–	14.92 ± 0.30	20.15	19.49	19.09	0.18
ZOA083903.991 − 572200.53	273.742	−9.602	0.31	−64.84	1.98	18.00 ± 0.09	17.39 ± 0.07	16.86 ± 0.10	–	–	16.20 ± 0.11	20.62	20.14	19.54	0.18
ZOA083824.834 − 572633.71	273.751	−9.718	0.45	27.85	4.31	16.54 ± 0.04	15.74 ± 0.03	15.25 ± 0.04	16.33 ± 0.11	–	15.12 ± 0.05	19.87	19.06	18.64	0.18
ZOA083827.747 − 572709.28	273.763	−9.719	0.19	61.93	2.98	16.84 ± 0.05	16.09 ± 0.04	15.46 ± 0.04	–	15.81 ± 0.09	15.14 ± 0.08	20.15	19.39	18.75	0.18
ZOA083830.033 − 572702.71	273.764	−9.714	0.20	−59.26	2.19	17.09 ± 0.05	16.40 ± 0.04	16.03 ± 0.06	–	–	15.91 ± 0.06	20.47	19.79	19.29	0.18
ZOA083838.234 − 572631.43	273.768	−9.694	0.31	−81.33	2.98	16.67 ± 0.04	15.96 ± 0.03	15.48 ± 0.04	–	–	15.32 ± 0.04	19.88	19.17	18.67	0.18
ZOA083824.527 − 572800.12	273.770	−9.733	0.24	−48.03	4.17	17.45 ± 0.06	16.71 ± 0.05	16.31 ± 0.07	–	–	15.07 ± 0.32	20.40	19.76	19.28	0.18
ZOA083649.272 − 572728.26	273.635	−9.900	0.26	−18.61	1.70	18.18 ± 0.09	17.18 ± 0.06	16.43 ± 0.09	–	–	–	21.60	20.38	19.61	0.16
ZOA083655.876 − 572745.07	273.648	−9.891	0.18	44.04	3.82	16.61 ± 0.05	15.84 ± 0.04	15.51 ± 0.09	–	15.45 ± 0.09	14.72 ± 0.22	19.77	19.04	18.61	0.16
ZOA083611.867 − 572103.09	273.497	−9.905	0.42	18.91	3.98	15.53 ± 0.03	14.80 ± 0.03	14.58 ± 0.04	15.21 ± 0.11	14.60 ± 0.06	13.89 ± 0.21	18.89	18.18	17.95	0.16
ZOA083620.778 − 572117.46	273.512	−9.892	0.29	6.32	1.99	17.50 ± 0.06	16.67 ± 0.04	15.84 ± 0.06	–	–	15.78 ± 0.07	20.86	19.79	19.05	0.16
ZOA083612.756 − 572414.40	273.542	−9.935	0.52	−62.79	3.42	17.19 ± 0.05	16.44 ± 0.04	15.84 ± 0.07	16.95 ± 0.09	16.13 ± 0.09	15.35 ± 0.09	20.43	19.77	19.09	0.16
ZOA084024.576 − 572603.68	273.906	−9.497	0.13	−58.33	2.83	17.67 ± 0.07	16.81 ± 0.05	16.03 ± 0.09	–	–	–	20.94	20.07	19.30	0.17
ZOA084023.186 − 572606.77	273.905	−9.500	0.35	−9.76	2.46	17.69 ± 0.07	16.84 ± 0.05	16.12 ± 0.08	–	–	15.89 ± 0.09	20.50	19.70	19.24	0.17
ZOA083949.920 − 572134.77	273.798	−9.515	0.09	28.76	2.67	17.37 ± 0.06	16.69 ± 0.05	15.88 ± 0.07	–	–	15.70 ± 0.08	20.55	19.93	19.20	0.17
ZOA083937.862 − 572411.73	273.817	−9.563	0.44	−84.30	2.69	18.21 ± 0.09	17.34 ± 0.06	16.99 ± 0.14	16.48 ± 0.47	15.94 ± 0.19	11.93 ± 1.46	20.43	19.62	19.54	0.17
ZOA083711.423 − 572314.40	273.607	−9.819	0.18	14.02	1.97	18.26 ± 0.09	17.39 ± 0.07	16.48 ± 0.09	–	–	16.06 ± 0.13	21.71	20.71	19.55	0.17
ZOA083710.378 − 572258.24	273.602	−9.818	0.30	24.28	2.20	18.44 ± 0.09	17.54 ± 0.07	16.75 ± 0.10	–	–	16.61 ± 0.10	21.10	20.63	20.30	0.17
ZOA083652.654 − 572458.88	273.606	−9.870	0.28	−30.44	5.84	15.29 ± 0.03	14.58 ± 0.03	14.14 ± 0.04	14.42 ± 0.30	13.80 ± 0.22	13.61 ± 0.11	18.73	18.01	17.55	0.17
ZOA083707.477 − 572500.40	273.626	−9.843	0.30	60.93	1.67	18.30 ± 0.09	17.43 ± 0.07	16.68 ± 0.11	–	–	–	21.28	20.59	19.85	0.17
ZOA083701.667 − 572555.71	273.631	−9.863	0.35	−40.97	1.75	17.83 ± 0.07	16.88 ± 0.05	16.16 ± 0.07	17.13 ± 0.26	–	16.14 ± 0.08	21.13	20.09	19.47	0.17
ZOA083704.774 − 572601.21	273.636	−9.858	0.74	23.78	4.47	16.28 ± 0.04	15.65 ± 0.03	15.19 ± 0.05	–	15.28 ± 0.05	14.35 ± 0.19	19.55	18.83	18.41	0.17
ZOA083707.329 − 572254.54	273.597	−9.823	0.55	−17.34	3.03	17.25 ± 0.05	16.38 ± 0.04	15.79 ± 0.06	–	15.37 ± 0.29	15.63 ± 0.06	20.46	19.56	19.40	0.17
ZOA083721.698 − 572249.22	273.615	−9.796	0.14	−3.86	7.17	14.29 ± 0.02	13.56 ± 0.02	13.16 ± 0.03	13.91 ± 0.14	13.38 ± 0.06	12.85 ± 0.07	17.87	17.14	16.79	0.17
ZOA083712.610 − 572235.03	273.599	−9.810	0.26	53.38	2.52	17.67 ± 0.07	16.96 ± 0.05	16.25 ± 0.07	–	–	15.27 ± 0.24	20.61	19.90	19.29	0.17
ZOA083640.246 − 572204.93	273.549	−9.864	0.20	−59.54	4.50	15.08 ± 0.03	14.35 ± 0.02	13.95 ± 0.03	14.15 ± 0.29	13.62 ± 0.19	13.47 ± 0.10	18.45	17.73	17.32	0.17
ZOA083718.008 − 572158.04	273.598	−9.794	0.65	−31.92	4.14	16.65 ± 0.04	15.85 ± 0.03	15.12 ± 0.05	16.39 ± 0.11	15.44 ± 0.11	14.69 ± 0.09	19.91	19.16	18.38	0.17
ZOA083655.760 − 572745.19	273.648	−9.891	0.39	52.34	4.48	16.41 ± 0.04	15.76 ± 0.03	15.31 ± 0.07	–	14.82 ± 0.31	14.55 ± 0.20	19.80	19.12	18.59	0.17
ZOA084035.059 − 571221.23	273.734	−9.342	0.13	−44.74	2.26	17.69 ± 0.07	16.76 ± 0.05	16.04 ± 0.07	–	–	15.97 ± 0.07	21.22	19.99	19.16	0.17
ZOA084049.121 − 571247.81	273.760	−9.321	0.16	−85.22	2.47	16.95 ± 0.05	16.22 ± 0.04	15.54 ± 0.05	–	–	15.43 ± 0.06	20.24	19.49	18.92	0.17
ZOA084011.146 − 571742.52	273.774	−9.438	0.51	41.36	5.57	15.00 ± 0.03	14.21 ± 0.02	13.80 ± 0.03	14.09 ± 0.30	13.77 ± 0.12	13.69 ± 0.04	18.43	17.64	17.25	0.17
ZOA084010.508 − 571945.21	273.801	−9.460	0.41	−24.14	2.87	17.74 ± 0.07	16.80 ± 0.05	16.09 ± 0.07	–	–	15.57 ± 0.11	20.63	19.67	19.44	0.17
ZOA083936.608 − 571405.68	273.678	−9.465	0.65	3.05	4.79	15.26 ± 0.03	15.93 ± 0.04	14.30 ± 0.04	13.61 ± 0.50	14.99 ± 0.27	13.82 ± 0.12	*nan*	19.14	17.69	0.17
ZOA083948.696 − 571624.79	273.726	−9.466	0.14	39.20	2.84	16.68 ± 0.04	15.91 ± 0.03	15.33 ± 0.05	–	–	14.88 ± 0.11	19.92	19.11	18.72	0.17
ZOA083708.053 − 571632.47	273.511	−9.759	0.53	−26.92	3.19	16.46 ± 0.04	15.72 ± 0.03	15.13 ± 0.04	–	14.98 ± 0.21	14.96 ± 0.06	19.78	19.08	18.43	0.17
ZOA083718.991 − 572012.35	273.575	−9.775	0.58	−72.71	4.19	16.65 ± 0.04	15.83 ± 0.03	15.34 ± 0.05	–	15.09 ± 0.20	15.18 ± 0.06	19.95	19.15	18.71	0.17
ZOA083655.279 − 571517.54	273.476	−9.770	0.58	−23.19	7.66	14.64 ± 0.03	13.98 ± 0.02	13.45 ± 0.03	14.44 ± 0.07	13.78 ± 0.04	13.47 ± 0.04	18.18	17.52	16.98	0.17
ZOA083713.055 − 571421.45	273.488	−9.728	0.21	42.25	3.30	16.24 ± 0.04	15.68 ± 0.04	15.59 ± 0.07	15.26 ± 0.21	14.66 ± 0.14	14.75 ± 0.22	19.19	18.60	18.85	0.17
ZOA083720.155 − 571651.30	273.531	−9.740	0.62	54.01	2.84	17.51 ± 0.06	16.82 ± 0.05	16.39 ± 0.10	16.95 ± 0.15	16.28 ± 0.08	15.62 ± 0.19	20.42	19.71	19.59	0.17
ZOA083720.031 − 572034.34	273.582	−9.777	0.13	−73.73	3.31	17.55 ± 0.07	16.89 ± 0.06	16.18 ± 0.10	–	12.82 ± 1.25	14.84 ± 0.30	20.28	19.77	18.99	0.17
ZOA083818.132 − 573245.02	273.826	−9.791	0.28	25.68	9.60	13.97 ± 0.02	13.22 ± 0.02	12.84 ± 0.03	13.51 ± 0.15	12.96 ± 0.06	12.61 ± 0.06	17.59	16.84	16.47	0.17
ZOA083807.361 − 572851.24	273.759	−9.772	0.32	−87.23	3.56	15.28 ± 0.03	14.60 ± 0.02	14.32 ± 0.03	14.94 ± 0.10	14.36 ± 0.05	14.30 ± 0.03	18.62	17.96	17.84	0.17
ZOA083800.119 − 572746.88	273.734	−9.775	0.23	−80.89	4.81	15.96 ± 0.04	15.25 ± 0.03	14.70 ± 0.05	15.81 ± 0.10	14.45 ± 0.22	14.48 ± 0.08	19.58	18.58	18.15	0.17
ZOA083808.494 − 572818.14	273.753	−9.765	0.08	17.18	3.91	16.09 ± 0.04	15.34 ± 0.03	14.92 ± 0.06	15.60 ± 0.19	15.00 ± 0.08	14.61 ± 0.08	19.34	18.60	18.24	0.17
ZOA083801.862 − 573003.12	273.768	−9.794	0.34	−21.20	4.42	15.22 ± 0.03	14.50 ± 0.02	14.13 ± 0.03	14.53 ± 0.21	13.67 ± 0.22	13.10 ± 0.26	18.60	17.88	17.51	0.17

$ZOA083821.161-573259.91$	273.834	−9.788	0.05	−50.74	3.98	15.76 ± 0.04	15.17 ± 0.03	15.25 ± 0.11	15.18 ± 0.10	14.27 ± 0.05	–	18.92	18.22	18.18	0.17
$ZOA084004.985-570928.07$	273.654	−9.368	0.56	21.12	3.26	17.24 ± 0.06	16.41 ± 0.04	15.58 ± 0.06	–	15.02 ± 0.31	14.60 ± 0.11	20.15	19.25	18.40	0.16
$ZOA084015.649-571134.42$	273.697	−9.369	0.55	80.90	4.57	18.37 ± 0.11	17.19 ± 0.06	16.09 ± 0.08	–	–	14.69 ± 0.36	21.41	19.98	18.89	0.16
$ZOA084027.626-571303.61$	273.734	−9.362	0.33	0.88	2.95	16.33 ± 0.04	15.66 ± 0.03	15.26 ± 0.05	–	15.08 ± 0.11	10.94 ± 1.27	19.42	18.74	18.43	0.16
$ZOA084017.240-574929.57$	274.214	−9.743	0.11	−45.20	3.08	17.80 ± 0.08	16.96 ± 0.05	15.99 ± 0.09	–	–	14.27 ± 0.35	20.73	19.91	18.69	0.15
$ZOA084024.484-574621.31$	274.181	−9.699	0.22	55.52	6.41	14.87 ± 0.03	14.15 ± 0.02	13.76 ± 0.03	14.08 ± 0.24	13.86 ± 0.04	13.44 ± 0.07	18.39	17.68	17.29	0.15
$ZOA084023.744-574639.19$	274.184	−9.703	0.64	33.87	2.86	17.60 ± 0.06	17.14 ± 0.05	16.05 ± 0.06	–	–	15.54 ± 0.11	20.50	20.07	19.43	0.15
$ZOA084016.393-574645.61$	274.176	−9.718	0.07	−25.04	6.51	13.84 ± 0.02	13.06 ± 0.02	12.76 ± 0.02	13.33 ± 0.16	12.77 ± 0.07	–	17.40	16.62	16.32	0.15
$ZOA084018.474-574804.53$	274.196	−9.727	0.07	9.63	1.85	18.12 ± 0.08	17.16 ± 0.05	16.44 ± 0.09	–	–	16.36 ± 0.09	21.29	20.26	19.56	0.15
$ZOA084010.654-574831.51$	274.192	−9.745	0.52	−70.63	2.55	17.91 ± 0.07	17.15 ± 0.05	16.74 ± 0.09	–	–	15.48 ± 0.33	20.84	20.04	19.61	0.15
$ZOA084028.376-574857.76$	274.222	−9.718	0.48	−48.64	1.59	20.36 ± 0.42	18.17 ± 0.11	17.03 ± 0.17	13.69 ± 2.46	–	–	nan	21.35	21.19	0.15
$ZOA083949.554-574303.05$	274.089	−9.729	0.27	−24.00	2.33	18.18 ± 0.09	17.23 ± 0.05	16.50 ± 0.09	–	–	16.36 ± 0.09	21.23	20.21	19.72	0.15
$ZOA084023.601-574252.11$	274.132	−9.666	0.09	−74.79	2.28	18.29 ± 0.09	17.48 ± 0.07	16.81 ± 0.12	–	–	16.36 ± 0.12	21.32	20.55	19.42	0.15
$ZOA084005.659-574328.96$	274.117	−9.704	0.34	34.12	2.39	17.56 ± 0.06	16.85 ± 0.05	16.09 ± 0.07	–	–	14.34 ± 0.46	20.77	20.08	19.00	0.15
$ZOA083941.296-574333.03$	274.085	−9.749	0.92	39.08	3.30	18.31 ± 0.09	17.57 ± 0.07	17.03 ± 0.13	15.35 ± 0.80	16.46 ± 0.23	16.38 ± 0.16	20.10	19.76	19.78	0.15
$ZOA084010.992-574431.01$	274.138	−9.705	0.83	−47.84	4.70	14.55 ± 0.02	14.42 ± 0.02	14.48 ± 0.03	13.14 ± 0.41	13.56 ± 0.20	13.44 ± 0.24	17.84	17.70	17.82	0.15
$ZOA084022.931-574553.93$	274.173	−9.697	0.22	36.08	2.55	17.39 ± 0.06	16.78 ± 0.05	16.23 ± 0.08	–	15.63 ± 0.26	12.99 ± 0.87	20.25	19.60	19.08	0.15
$ZOA084022.083-574736.01$	274.195	−9.716	0.61	22.40	6.77	15.60 ± 0.03	14.80 ± 0.03	14.50 ± 0.04	15.04 ± 0.14	14.16 ± 0.12	13.53 ± 0.21	19.03	18.25	17.98	0.15
$ZOA084015.327-574519.86$	274.155	−9.705	0.52	−38.23	2.27	18.18 ± 0.08	17.41 ± 0.06	16.53 ± 0.09	–	16.22 ± 0.25	15.50 ± 0.26	20.88	20.30	19.53	0.15
$ZOA084015.530-574545.84$	274.161	−9.709	0.12	34.63	2.60	17.42 ± 0.06	16.68 ± 0.04	15.92 ± 0.07	16.70 ± 0.25	15.78 ± 0.28	15.08 ± 0.20	20.61	19.81	18.95	0.15
$ZOA084015.680-574352.11$	274.135	−9.690	0.23	−55.98	1.97	18.97 ± 0.14	17.50 ± 0.07	16.68 ± 0.11	–	–	16.59 ± 0.11	21.98	20.63	19.69	0.15
$ZOA084042.360-574306.77$	274.161	−9.635	0.23	−50.21	2.21	20.05 ± 0.29	18.62 ± 0.15	16.09 ± 0.07	11.61 ± 2.62	–	–	22.33	21.43	18.99	0.15
$ZOA084017.656-574331.17$	274.133	−9.683	0.24	−80.87	2.95	17.29 ± 0.05	16.53 ± 0.04	16.51 ± 0.10	–	–	16.15 ± 0.12	20.50	19.73	20.00	0.15
$ZOA084038.528-574221.39$	274.146	−9.634	0.42	−18.47	3.19	16.83 ± 0.05	16.17 ± 0.04	15.74 ± 0.09	16.24 ± 0.25	14.23 ± 0.50	14.94 ± 0.16	19.95	19.16	18.80	0.15
$ZOA084020.271-574240.70$	274.125	−9.670	0.72	85.67	5.30	19.16 ± 0.21	17.83 ± 0.12	16.14 ± 0.10	–	-14.58 ± 10.42	15.41 ± 0.19	21.69	20.54	19.37	0.15
$ZOA084056.844-574105.62$	274.153	−9.589	0.19	−44.79	2.90	16.74 ± 0.04	15.93 ± 0.03	15.15 ± 0.05	–	–	14.47 ± 0.18	20.04	19.23	18.45	0.17
$ZOA084054.527-574150.78$	274.160	−9.601	0.22	−61.32	4.35	16.53 ± 0.04	15.77 ± 0.03	15.30 ± 0.06	–	–	14.69 ± 0.17	19.72	18.99	18.44	0.17
$ZOA084014.089-573601.87$	274.027	−9.615	0.31	81.69	1.84	18.44 ± 0.10	17.59 ± 0.07	16.68 ± 0.11	–	–	16.04 ± 0.23	21.48	20.61	20.57	0.17
$ZOA084022.983-573533.66$	274.032	−9.595	0.30	−44.29	11.93	18.42 ± 0.13	17.62 ± 0.10	16.27 ± 0.13	–	–	–	21.34	20.86	19.58	0.17
$ZOA084036.921-573835.71$	274.092	−9.600	0.11	46.62	3.56	17.85 ± 0.07	17.16 ± 0.06	16.49 ± 0.10	–	16.57 ± 0.11	15.90 ± 0.12	20.72	20.12	19.59	0.17
$ZOA084038.338-574221.52$	274.145	−9.635	0.32	−87.61	3.85	17.02 ± 0.05	16.30 ± 0.04	16.04 ± 0.09	–	–	15.52 ± 0.14	20.08	19.33	19.02	0.17
$ZOA083927.725-574302.13$	274.060	−9.768	0.19	31.26	2.23	16.86 ± 0.05	16.60 ± 0.05	15.71 ± 0.07	–	13.06 ± 0.86	15.29 ± 0.13	19.36	19.02	18.97	0.15
$ZOA083922.548-574220.24$	274.043	−9.770	0.33	72.54	2.88	17.17 ± 0.05	16.28 ± 0.04	15.74 ± 0.06	–	–	15.10 ± 0.14	20.11	19.44	19.02	0.15
$ZOA083856.427-573756.85$	273.948	−9.774	0.09	−24.33	1.51	17.93 ± 0.08	17.00 ± 0.05	16.66 ± 0.11	–	–	–	20.94	19.88	19.53	0.15
$ZOA083918.890-573859.85$	273.993	−9.744	0.31	−46.71	3.25	16.43 ± 0.04	15.66 ± 0.03	15.09 ± 0.04	–	12.91 ± 0.81	12.97 ± 0.55	19.57	18.79	18.18	0.15
$ZOA083940.753-574014.22$	274.039	−9.717	0.34	−86.24	3.06	17.57 ± 0.08	16.88 ± 0.06	16.19 ± 0.12	–	–	16.09 ± 0.14	20.88	20.07	19.37	0.15
$ZOA083919.490-574037.08$	274.016	−9.759	0.33	−7.50	2.26	17.70 ± 0.07	16.70 ± 0.04	15.86 ± 0.06	–	–	15.82 ± 0.06	20.78	19.73	18.93	0.15
$ZOA083851.869-573732.84$	273.937	−9.778	0.22	−26.47	1.53	18.53 ± 0.10	17.72 ± 0.07	16.71 ± 0.11	–	–	16.30 ± 0.14	21.71	20.82	19.63	0.15
$ZOA083902.360-573741.96$	273.953	−9.760	0.16	−84.13	2.60	16.86 ± 0.04	16.11 ± 0.03	15.75 ± 0.06	–	15.71 ± 0.06	14.23 ± 0.40	19.94	19.20	18.91	0.15
$ZOA083921.588-573837.58$	273.991	−9.735	0.57	1.16	2.22	17.65 ± 0.07	16.92 ± 0.05	16.72 ± 0.11	16.31 ± 0.36	15.70 ± 0.14	12.14 ± 1.13	20.08	19.35	19.11	0.15
$ZOA083930.600-574232.69$	274.057	−9.758	0.47	84.85	3.30	17.77 ± 0.07	16.80 ± 0.05	15.92 ± 0.07	–	16.09 ± 0.19	15.74 ± 0.08	20.67	19.77	18.98	0.15
$ZOA083936.796-573745.01$	274.000	−9.699	0.25	−85.74	2.17	17.42 ± 0.06	16.76 ± 0.04	16.20 ± 0.08	–	16.03 ± 0.14	16.06 ± 0.08	20.21	19.66	19.18	0.16
$ZOA083916.823-573826.08$	273.982	−9.742	0.27	−44.56	2.28	17.80 ± 0.07	16.96 ± 0.05	16.15 ± 0.07	–	–	15.07 ± 0.29	20.80	19.94	19.09	0.16
$ZOA083941.684-574105.46$	274.052	−9.723	0.13	14.36	2.67	16.73 ± 0.04	16.00 ± 0.03	15.54 ± 0.05	–	15.76 ± 0.04	14.75 ± 0.19	19.86	19.18	18.82	0.16
$ZOA083910.903-573724.37$	273.960	−9.742	0.17	−17.20	2.51	17.82 ± 0.07	16.93 ± 0.05	16.23 ± 0.09	13.03 ± 1.51	–	14.82 ± 0.34	20.70	19.92	19.09	0.16
$ZOA083911.177-573729.77$	273.962	−9.743	0.22	−62.91	3.28	16.55 ± 0.04	15.77 ± 0.03	14.96 ± 0.04	12.52 ± 1.31	–	14.65 ± 0.08	19.79	19.02	18.30	0.16
$ZOA083944.410-573839.11$	274.022	−9.694	0.11	−7.72	2.37	17.97 ± 0.07	17.22 ± 0.06	16.32 ± 0.08	–	–	16.23 ± 0.09	21.25	20.43	19.52	0.16
$ZOA083947.877-573834.77$	274.026	−9.687	0.24	62.46	3.88	15.81 ± 0.03	15.14 ± 0.03	14.92 ± 0.04	15.41 ± 0.12	–	–	19.06	18.38	18.16	0.16
$ZOA083953.844-573853.38$	274.038	−9.680	0.32	−58.63	3.17	16.97 ± 0.05	16.10 ± 0.04	15.38 ± 0.05	16.16 ± 0.34	–	13.71 ± 0.42	19.96	19.17	18.46	0.16
$ZOA083957.065-573748.55$	274.028	−9.663	0.50	−41.94	3.47	17.12 ± 0.05	16.23 ± 0.04	15.45 ± 0.05	–	15.29 ± 0.27	15.28 ± 0.05	20.34	19.45	18.74	0.16
$ZOA083944.581-573834.19$	274.022	−9.693	0.38	39.07	2.03	18.16 ± 0.08	17.43 ± 0.06	16.63 ± 0.10	–	–	16.54 ± 0.10	21.16	20.66	19.78	0.16
$ZOA084006.277-573603.16$	274.017	−9.629	0.80	−14.81	2.13	18.25 ± 0.11	17.23 ± 0.06	17.55 ± 0.28	16.61 ± 0.51	–	14.62 ± 0.40	20.83	19.85	19.15	0.16
$ZOA083932.750-573703.61$	273.985	−9.700	0.44	22.44	3.31	16.87 ± 0.05	16.14 ± 0.04	15.63 ± 0.07	16.64 ± 0.14	15.91 ± 0.07	15.41 ± 0.07	20.26	19.47	19.02	0.16
$ZOA083952.564-574016.64$	274.055	−9.696	0.20	46.19	2.62	17.27 ± 0.05	16.49 ± 0.04	15.80 ± 0.06	–	–	15.41 ± 0.10	20.31	19.64	19.04	0.16
$ZOA083930.277-573059.61$	273.899	−9.644	0.26	21.79	2.81	17.72 ± 0.07	17.10 ± 0.06	16.36 ± 0.10	11.60 ± 2.01	–	15.96 ± 0.10	20.71	20.18	19.51	0.17
$ZOA083855.744-573118.07$	273.857	−9.709	0.25	12.34	5.67	14.55 ± 0.02	13.79 ± 0.02	13.43 ± 0.03	13.62 ± 0.28	13.43 ± 0.07	12.69 ± 0.17	18.03	17.28	16.90	0.17
$ZOA083935.714-573132.51$	273.914	−9.640	0.54	−19.26	4.01	17.19 ± 0.06	16.57 ± 0.05	16.16 ± 0.10	–	15.83 ± 0.19	14.77 ± 0.33	20.27	19.53	18.92	0.17
$ZOA083906.431-573341.08$	273.904	−9.713	0.24	−50.39	6.53	14.53 ± 0.02	13.79 ± 0.02	–	14.00 ± 0.11	13.28 ± 0.07	–	18.04	17.30	nan	0.17
$ZOA083923.115-572908.24$	273.864	−9.638	0.35	−36.50	2.98	16.08 ± 0.04	15.34 ± 0.03	14.98 ± 0.04	–	14.34 ± 0.22	14.91 ± 0.04	19.18	18.44	18.30	0.17
$ZOA083927.435-572809.75$	273.857	−9.621	0.32	−64.96	2.58	17.38 ± 0.07	16.28 ± 0.05	15.76 ± 0.08	–	14.59 ± 0.40	15.32 ± 0.11	20.53	19.05	18.91	0.17
$ZOA083934.015-573353.52$	273.944	−9.666	0.35	−7.98	8.25	14.25 ± 0.02	13.49 ± 0.02	13.14 ± 0.03	13.55 ± 0.23	13.00 ± 0.11	12.52 ± 0.16	18.01	17.25	16.90	0.17
$ZOA083926.280-572856.58$	273.866	−9.631	0.43	62.62	11.07	13.41 ± 0.02	12.69 ± 0.02	12.29 ± 0.02	12.70 ± 0.21	12.15 ± 0.13	11.93 ± 0.07	17.22	16.50	16.08	0.17

$ZOA083925.275-572901.00$	273.866	−9.633	0.10	72.28	7.48	14.55 ± 0.03	13.82 ± 0.02	13.47 ± 0.03	13.17 ± 0.43	12.69 ± 0.12	11.94 ± 0.30	18.37	17.66	17.24	0.17
$ZOA083923.484-572914.79$	273.866	−9.639	0.20	62.16	2.68	16.66 ± 0.04	15.89 ± 0.03	15.53 ± 0.05	–	14.09 ± 0.50	15.39 ± 0.06	19.71	18.86	18.66	0.17
$ZOA084003.581-573302.26$	273.972	−9.604	0.60	−6.91	2.67	17.37 ± 0.06	16.27 ± 0.04	16.02 ± 0.09	16.34 ± 0.38	–	13.58 ± 0.53	20.33	19.16	18.71	0.17
$ZOA083932.591-572821.97$	273.867	−9.614	0.28	30.59	3.10	17.16 ± 0.06	16.37 ± 0.05	15.73 ± 0.08	–	–	–	20.45	19.64	18.89	0.17
$ZOA083942.146-572834.97$	273.883	−9.599	0.29	−63.74	4.24	17.56 ± 0.07	16.37 ± 0.04	15.93 ± 0.07	–	15.91 ± 0.15	15.68 ± 0.09	20.79	19.52	19.11	0.17

Table A.0.4: VC08 catalogue of galaxies

Designation	ℓ (deg)	b (deg)	e_J	ϕ_J (deg)	r_{k20fe} (arcsec)	J_{k20fe} (mag)	H_{k20fe} (mag)	$K_{s_{k20fe}}$ (mag)	J_{tot} (mag)	H_{tot} (mag)	$K_{s_{tot}}$ (mag)	μ_J	μ_H (mag arcsec^{-2})	μ_{Ks}	$E(B-V)$ (mag)
$ZOA085648.318-575226.01$	275.628	−8.047	0.14	50.74	2.84	17.13 ± 0.07	16.66 ± 0.08	15.87 ± 0.10	16.58 ± 0.20	15.74 ± 0.29	15.80 ± 0.10	20.68	20.03	19.02	0.22
$ZOA085707.906-574718.60$	275.590	−7.959	0.23	28.81	6.35	15.35 ± 0.03	14.71 ± 0.03	14.23 ± 0.04	–	14.34 ± 0.07	13.35 ± 0.18	18.77	18.11	17.63	0.22
$ZOA085636.836-574745.78$	275.552	−8.017	0.29	−45.14	11.33	13.45 ± 0.02	12.69 ± 0.02	12.31 ± 0.03	13.18 ± 0.11	–	11.57 ± 0.20	17.50	16.76	16.38	0.22
$ZOA085700.212-574832.51$	275.595	−7.985	0.11	−39.62	2.88	17.51 ± 0.09	16.51 ± 0.07	15.59 ± 0.07	–	–	14.74 ± 0.25	20.34	19.47	18.91	0.22
$ZOA085646.873-574902.59$	275.583	−8.013	0.30	82.70	4.22	16.55 ± 0.06	15.75 ± 0.05	15.33 ± 0.07	15.60 ± 0.40	14.53 ± 0.36	–	19.57	18.96	18.47	0.22
$ZOA085656.746-575026.96$	275.615	−8.012	0.16	40.71	6.71	14.34 ± 0.03	13.60 ± 0.02	13.22 ± 0.03	13.61 ± 0.24	13.20 ± 0.09	12.91 ± 0.06	17.95	17.21	16.83	0.22
$ZOA085640.877-574550.96$	275.533	−7.990	0.12	57.58	3.67	15.33 ± 0.03	14.55 ± 0.03	14.00 ± 0.03	15.02 ± 0.09	13.24 ± 0.39	11.86 ± 0.68	18.63	17.90	17.36	0.22
$ZOA085647.800-574524.99$	275.537	−7.973	0.21	−4.19	4.84	15.33 ± 0.04	14.56 ± 0.03	14.19 ± 0.04	–	14.03 ± 0.12	–	18.69	17.92	17.55	0.22
$ZOA085633.644-574928.12$	275.569	−8.041	0.10	−85.66	3.89	17.04 ± 0.08	16.14 ± 0.06	15.27 ± 0.07	13.39 ± 1.28	14.46 ± 0.55	–	20.16	19.30	18.50	0.22
$ZOA085651.875-575753.11$	275.704	−8.099	0.38	31.61	3.38	16.59 ± 0.05	15.95 ± 0.04	15.83 ± 0.08	–	15.68 ± 0.04	–	19.64	19.09	19.20	0.23
$ZOA085638.371-580142.02$	275.734	−8.163	0.05	−32.06	2.92	16.19 ± 0.04	15.46 ± 0.03	14.84 ± 0.04	–	14.59 ± 0.27	14.43 ± 0.09	19.38	18.75	18.10	0.24
$ZOA085643.022-580324.85$	275.763	−8.173	0.35	−1.65	2.10	17.50 ± 0.08	16.60 ± 0.06	16.13 ± 0.10	–	–	–	20.38	19.70	19.56	0.24
$ZOA085710.532-580408.06$	275.811	−8.135	0.34	48.53	9.97	13.27 ± 0.02	12.49 ± 0.02	12.13 ± 0.02	–	11.94 ± 0.16	12.00 ± 0.03	16.98	16.20	15.82	0.24
$ZOA085629.176-580505.56$	275.765	−8.215	0.08	−70.08	2.92	17.21 ± 0.07	16.38 ± 0.06	15.66 ± 0.08	–	–	15.34 ± 0.09	20.18	19.47	18.81	0.24
$ZOA085703.083-580611.25$	275.827	−8.169	0.26	11.66	2.01	18.09 ± 0.13	17.17 ± 0.09	16.11 ± 0.10	–	–	15.90 ± 0.11	21.39	20.31	20.42	0.24
$ZOA085705.491-580146.31$	275.774	−8.118	0.09	76.54	2.51	17.79 ± 0.10	16.67 ± 0.06	16.12 ± 0.09	–	–	–	20.55	19.85	19.52	0.24
$ZOA085834.283-572605.83$	275.443	−7.584	0.22	50.20	3.07	16.72 ± 0.05	15.83 ± 0.04	15.30 ± 0.06	–	14.69 ± 0.33	14.96 ± 0.08	19.82	19.02	18.49	0.21
$ZOA085812.792-572637.97$	275.418	−7.627	0.28	−75.44	4.67	15.52 ± 0.04	14.71 ± 0.03	14.42 ± 0.05	15.37 ± 0.07	–	13.28 ± 0.31	18.91	18.12	17.77	0.21
$ZOA085830.956-572352.63$	275.409	−7.566	0.17	−64.48	3.72	17.32 ± 0.10	16.37 ± 0.07	15.44 ± 0.08	–	–	–	20.47	19.49	18.79	0.21
$ZOA085857.503-572746.54$	275.498	−7.562	0.06	−66.49	4.11	16.37 ± 0.05	15.63 ± 0.04	15.49 ± 0.09	14.94 ± 0.39	14.62 ± 0.15	13.01 ± 0.62	19.36	18.63	18.55	0.21
$ZOA085814.502-572651.08$	275.424	−7.626	0.68	77.28	2.59	17.83 ± 0.11	16.77 ± 0.07	16.05 ± 0.09	–	–	12.58 ± 0.98	21.20	19.72	19.03	0.21
$ZOA085813.602-572701.32$	275.424	−7.629	0.25	24.06	2.25	18.06 ± 0.12	17.04 ± 0.08	16.31 ± 0.11	–	–	16.12 ± 0.12	20.84	20.07	19.61	0.21
$ZOA085809.682-572911.78$	275.447	−7.659	0.12	36.69	3.42	17.05 ± 0.10	16.38 ± 0.08	15.66 ± 0.11	16.28 ± 0.32	–	11.31 ± 1.20	19.86	19.34	18.57	0.21
$ZOA085821.261-573250.20$	275.510	−7.679	0.21	−8.35	2.43	17.06 ± 0.06	16.16 ± 0.04	15.65 ± 0.07	11.16 ± 1.90	–	14.14 ± 0.34	20.05	19.18	18.61	0.21
$ZOA085831.042-573712.41$	275.581	−7.709	0.22	−31.29	2.97	16.72 ± 0.05	16.03 ± 0.04	15.37 ± 0.06	-11.48 ± 8.94	–	–	19.81	19.22	18.46	0.21
$ZOA085816.493-573225.22$	275.498	−7.682	0.67	−0.16	7.30	15.51 ± 0.04	14.66 ± 0.03	14.19 ± 0.04	15.15 ± 0.11	13.82 ± 0.24	13.16 ± 0.31	18.96	18.14	17.66	0.21
$ZOA085818.652-573146.87$	275.493	−7.672	0.19	45.90	2.90	16.68 ± 0.06	15.85 ± 0.04	15.23 ± 0.06	–	15.12 ± 0.21	14.49 ± 0.20	19.97	19.07	18.41	0.21
$ZOA085821.087-573256.46$	275.511	−7.680	0.05	−49.88	4.25	17.71 ± 0.10	17.01 ± 0.08	16.23 ± 0.12	–	–	15.49 ± 0.19	20.49	19.79	19.18	0.21
$ZOA085815.583-574502.92$	275.659	−7.820	0.45	33.42	6.82	14.49 ± 0.03	13.79 ± 0.02	13.38 ± 0.03	12.97 ± 0.47	12.42 ± 0.38	12.97 ± 0.04	17.96	17.26	16.87	0.22
$ZOA085902.891-574009.90$	275.665	−7.687	0.25	53.21	3.56	15.89 ± 0.04	15.14 ± 0.03	14.80 ± 0.05	–	13.31 ± 0.52	11.01 ± 1.07	19.21	18.38	17.99	0.22
$ZOA085824.933-574134.48$	275.628	−7.766	0.52	−72.60	5.50	15.10 ± 0.03	14.40 ± 0.03	13.94 ± 0.03	14.74 ± 0.13	13.86 ± 0.16	13.73 ± 0.04	18.56	17.87	17.41	0.22
$ZOA085842.568-574132.50$	275.653	−7.736	0.22	−66.53	8.02	13.90 ± 0.02	13.15 ± 0.02	12.81 ± 0.03	13.24 ± 0.22	–	12.43 ± 0.10	17.57	16.82	16.46	0.22
$ZOA085838.007-574201.32$	275.653	−7.749	0.08	−17.91	2.65	15.63 ± 0.03	15.01 ± 0.03	14.70 ± 0.04	–	14.78 ± 0.05	–	19.01	18.35	18.26	0.22
$ZOA085836.000-574252.69$	275.661	−7.762	0.22	19.23	3.03	16.78 ± 0.05	15.90 ± 0.04	15.16 ± 0.05	–	–	14.83 ± 0.09	19.95	19.12	18.39	0.22
$ZOA085852.452-574311.59$	275.689	−7.737	0.38	33.74	4.04	16.64 ± 0.05	16.02 ± 0.04	15.26 ± 0.06	–	15.79 ± 0.08	14.98 ± 0.08	20.17	19.43	18.77	0.22
$ZOA085900.120-574320.52$	275.702	−7.726	0.40	78.68	3.12	16.55 ± 0.05	15.81 ± 0.04	15.35 ± 0.06	16.20 ± 0.10	–	15.13 ± 0.08	19.70	19.03	18.62	0.22
$ZOA085821.509-574424.85$	275.659	−7.803	0.47	6.72	7.13	15.02 ± 0.03	14.27 ± 0.03	13.90 ± 0.03	14.78 ± 0.08	13.65 ± 0.17	13.70 ± 0.05	18.48	17.74	17.43	0.22
$ZOA085829.346-574338.82$	275.661	−7.781	0.04	−46.23	2.15	16.26 ± 0.04	15.61 ± 0.03	15.42 ± 0.05	–	–	15.38 ± 0.05	19.50	18.87	18.74	0.22
$ZOA085851.330-575226.84$	275.806	−7.839	0.28	−41.01	7.50	13.90 ± 0.02	13.15 ± 0.02	12.77 ± 0.03	13.31 ± 0.20	12.89 ± 0.07	12.34 ± 0.11	17.50	16.74	16.38	0.23
$ZOA085826.056-574700.67$	275.699	−7.823	0.32	−52.72	2.12	17.80 ± 0.08	16.99 ± 0.06	16.30 ± 0.09	–	–	16.14 ± 0.10	20.74	20.07	19.99	0.23
$ZOA085832.669-574710.51$	275.711	−7.814	0.09	31.85	3.74	15.91 ± 0.04	15.14 ± 0.03	14.77 ± 0.05	12.80 ± 1.03	–	–	19.07	18.30	18.00	0.23
$ZOA085832.662-574717.67$	275.713	−7.815	0.51	76.95	10.26	14.82 ± 0.03	13.89 ± 0.03	13.70 ± 0.04	12.51 ± 0.38	11.22 ± 0.36	–	18.82	17.84	17.54	0.23
$ZOA085834.963-574717.37$	275.716	−7.811	0.27	72.14	14.35	12.75 ± 0.02	11.93 ± 0.02	11.60 ± 0.02	12.31 ± 0.13	11.57 ± 0.06	10.77 ± 0.28	16.93	16.13	15.74	0.23
$ZOA085824.066-574726.50$	275.702	−7.831	0.35	3.66	2.30	17.45 ± 0.07	16.62 ± 0.05	16.32 ± 0.09	–	–	–	20.51	19.51	19.30	0.23
$ZOA085840.274-574740.08$	275.728	−7.806	0.12	28.11	2.86	15.81 ± 0.03	15.02 ± 0.03	14.65 ± 0.04	15.24 ± 0.17	14.06 ± 0.27	–	19.05	18.27	17.98	0.23
$ZOA085840.266-574749.49$	275.730	−7.808	0.25	38.80	2.24	17.03 ± 0.06	16.37 ± 0.05	15.70 ± 0.07	–	–	15.60 ± 0.07	20.33	19.58	19.22	0.23
$ZOA085820.723-574758.06$	275.704	−7.842	0.19	62.76	4.39	14.83 ± 0.03	14.03 ± 0.02	13.66 ± 0.03	14.64 ± 0.07	13.89 ± 0.04	13.44 ± 0.06	18.27	17.47	17.09	0.23
$ZOA085822.996-574922.40$	275.725	−7.854	0.27	8.12	2.27	17.52 ± 0.07	16.73 ± 0.06	16.14 ± 0.09	–	–	–	20.52	19.84	19.40	0.23
$ZOA085817.407-574948.43$	275.723	−7.868	0.08	−88.02	2.43	17.21 ± 0.07	16.30 ± 0.05	15.55 ± 0.06	–	–	14.65 ± 0.27	20.55	19.62	18.84	0.23
$ZOA085830.754-575014.86$	275.748	−7.850	0.43	−11.17	4.42	16.15 ± 0.04	15.29 ± 0.03	15.03 ± 0.06	15.39 ± 0.26	14.06 ± 0.32	14.36 ± 0.13	19.37	18.53	18.25	0.23
$ZOA085838.304-575056.53$	275.768	−7.845	0.14	−37.91	2.10	17.23 ± 0.06	16.54 ± 0.05	16.03 ± 0.08	-8.46 ± 8.13	–	14.11 ± 0.47	20.43	19.58	18.86	0.23
$ZOA085850.714-575112.93$	275.789	−7.827	0.11	−35.40	1.94	17.90 ± 0.09	17.08 ± 0.07	16.17 ± 0.10	–	16.57 ± 0.14	15.41 ± 0.17	20.52	20.03	19.09	0.23
$ZOA085902.818-574648.93$	275.750	−7.759	0.11	15.13	3.92	16.30 ± 0.04	15.43 ± 0.04	15.15 ± 0.06	15.34 ± 0.32	13.77 ± 0.44	14.93 ± 0.08	19.44	18.57	18.38	0.23
$ZOA085826.804-574641.91$	275.696	−7.818	0.14	48.12	2.58	17.05 ± 0.06	16.02 ± 0.04	15.23 ± 0.05	–	–	14.98 ± 0.08	20.26	19.25	18.54	0.23
$ZOA085857.666-574636.13$	275.740	−7.765	0.26	−15.79	2.65	17.23 ± 0.06	16.49 ± 0.05	16.10 ± 0.09	–	–	–	20.15	19.56	19.25	0.23
$ZOA085811.474-574835.90$	275.699	−7.865	0.21	−83.53	2.55	17.50 ± 0.09	16.95 ± 0.09	16.04 ± 0.11	–	-15.93 ± 10.41	–	20.68	20.23	18.95	0.23

ZOA085848.038 − 575947.43	275.895	−7.923	0.28	22.58	2.40	18.41 ± 0.15	17.48 ± 0.10	16.51 ± 0.13	–	16.13 ± 0.32	15.56 ± 0.24	21.85	20.40	19.66	0.25
ZOA085820.588 − 575904.56	275.847	−7.962	0.68	42.76	6.96	15.36 ± 0.03	14.46 ± 0.03	14.07 ± 0.03	–	13.80 ± 0.17	–	18.80	17.92	17.59	0.25
ZOA085830.801 − 575403.93	275.797	−7.891	0.13	83.58	2.31	17.65 ± 0.08	16.70 ± 0.05	15.89 ± 0.07	12.45 ± 1.65	–	15.88 ± 0.08	20.66	19.83	19.09	0.25
ZOA085842.996 − 575431.52	275.820	−7.875	0.63	−25.95	3.79	17.61 ± 0.08	16.77 ± 0.06	16.34 ± 0.11	–	16.38 ± 0.09	15.80 ± 0.13	20.52	19.82	19.59	0.25
ZOA085850.317 − 575543.11	275.846	−7.876	0.34	−59.74	4.04	16.41 ± 0.04	15.68 ± 0.04	15.25 ± 0.06	15.57 ± 0.27	14.51 ± 0.31	–	19.45	18.85	18.36	0.25
ZOA085848.837 − 575602.73	275.848	−7.882	0.45	−88.31	5.64	14.76 ± 0.03	14.00 ± 0.02	13.65 ± 0.03	14.55 ± 0.07	13.77 ± 0.06	12.72 ± 0.27	18.22	17.47	17.11	0.25
ZOA085851.251 − 575614.05	275.854	−7.880	0.24	35.20	3.04	16.39 ± 0.04	15.66 ± 0.03	15.09 ± 0.05	–	15.23 ± 0.07	15.02 ± 0.05	19.49	18.81	18.37	0.25
ZOA085847.802 − 575628.19	275.852	−7.888	0.25	23.51	7.64	15.34 ± 0.03	14.59 ± 0.03	14.22 ± 0.04	14.87 ± 0.19	14.39 ± 0.07	13.64 ± 0.15	18.96	18.19	17.83	0.25
ZOA085823.488 − 575551.35	275.809	−7.923	0.28	−41.79	2.50	18.71 ± 0.14	17.61 ± 0.09	16.43 ± 0.10	17.78 ± 0.29	–	15.66 ± 0.17	21.82	20.41	19.45	0.25
ZOA085847.908 − 580615.22	275.978	−7.993	0.44	10.86	10.82	13.50 ± 0.02	12.72 ± 0.02	12.30 ± 0.02	13.35 ± 0.06	12.43 ± 0.07	11.70 ± 0.17	17.31	16.53	16.11	0.25
ZOA085812.409 − 580151.98	275.871	−8.006	0.45	10.72	5.23	15.20 ± 0.03	14.38 ± 0.03	14.04 ± 0.03	14.27 ± 0.28	14.01 ± 0.10	13.32 ± 0.21	18.57	17.79	17.45	0.25
ZOA085826.640 − 580200.08	275.893	−7.983	0.50	79.42	5.09	16.06 ± 0.04	15.31 ± 0.03	14.51 ± 0.04	–	–	14.03 ± 0.12	19.44	18.68	17.86	0.25
ZOA085819.794 − 580304.14	275.897	−8.006	0.35	−0.67	2.73	17.29 ± 0.06	16.40 ± 0.04	15.83 ± 0.07	–	16.20 ± 0.05	14.86 ± 0.18	20.12	19.69	18.81	0.25
ZOA085856.639 − 580323.22	275.954	−7.948	0.19	−55.52	2.78	16.65 ± 0.05	15.83 ± 0.04	15.21 ± 0.05	–	15.34 ± 0.10	14.15 ± 0.30	19.85	19.00	18.48	0.25
ZOA085859.975 − 580324.27	275.959	−7.942	0.31	7.74	2.36	17.56 ± 0.07	16.72 ± 0.05	16.23 ± 0.09	–	–	–	20.21	19.45	19.06	0.25
ZOA085853.070 − 580332.90	275.951	−7.955	0.44	−37.32	3.15	17.53 ± 0.07	16.44 ± 0.05	15.79 ± 0.07	–	16.37 ± 0.05	15.60 ± 0.08	20.75	19.81	18.93	0.25
ZOA085837.556 − 580356.72	275.934	−7.986	0.09	8.24	3.22	16.29 ± 0.04	15.53 ± 0.03	15.11 ± 0.05	–	–	–	19.53	18.79	18.31	0.25
ZOA085905.959 − 580045.53	275.934	−7.904	0.03	55.44	2.73	18.15 ± 0.12	17.33 ± 0.08	16.31 ± 0.12	–	–	16.10 ± 0.13	20.93	20.02	19.29	0.25
ZOA085811.551 − 572607.64	275.410	−7.623	0.16	37.64	4.37	16.12 ± 0.04	15.30 ± 0.04	14.56 ± 0.05	15.29 ± 0.32	15.07 ± 0.08	13.90 ± 0.11	19.50	18.64	17.83	0.22
ZOA085804.486 − 572618.92	275.402	−7.637	0.20	−12.83	4.93	14.95 ± 0.03	14.26 ± 0.02	13.82 ± 0.03	14.50 ± 0.16	13.87 ± 0.10	13.30 ± 0.13	18.39	17.70	17.26	0.22
ZOA085804.125 − 572654.27	275.409	−7.644	0.22	−49.64	2.35	17.38 ± 0.07	16.34 ± 0.04	15.52 ± 0.05	–	–	15.24 ± 0.08	20.71	19.57	18.77	0.22
ZOA085800.261 − 572841.08	275.426	−7.670	0.33	−23.10	3.07	17.92 ± 0.10	16.94 ± 0.06	16.18 ± 0.09	–	–	–	20.89	20.06	19.29	0.22
ZOA085744.793 − 572843.74	275.404	−7.697	0.27	79.10	2.36	17.52 ± 0.08	16.80 ± 0.06	16.13 ± 0.08	17.19 ± 0.15	15.60 ± 0.32	15.99 ± 0.10	20.68	19.95	19.59	0.22
ZOA085722.093 − 572845.32	275.372	−7.736	0.49	13.41	3.07	17.33 ± 0.07	16.49 ± 0.05	15.84 ± 0.07	–	–	15.02 ± 0.15	20.19	19.46	18.98	0.22
ZOA085738.650 − 572908.42	275.401	−7.712	0.27	−67.40	1.86	17.92 ± 0.09	16.88 ± 0.06	16.34 ± 0.09	–	16.76 ± 0.06	–	20.69	19.90	19.43	0.22
ZOA085731.716 − 572941.98	275.398	−7.730	0.37	−72.86	2.35	17.78 ± 0.08	17.03 ± 0.06	16.19 ± 0.08	–	16.54 ± 0.10	15.53 ± 0.19	20.84	19.86	19.69	0.22
ZOA085808.106 − 572954.93	275.454	−7.670	0.37	51.96	3.22	17.07 ± 0.06	16.33 ± 0.05	15.49 ± 0.06	–	15.86 ± 0.12	14.76 ± 0.15	19.95	19.41	18.56	0.22
ZOA085734.488 − 572512.17	275.344	−7.677	0.21	−71.23	2.24	18.12 ± 0.10	17.36 ± 0.07	16.55 ± 0.10	–	–	16.10 ± 0.10	20.71	20.49	19.62	0.22
ZOA085746.438 − 573302.33	275.462	−7.740	0.19	−14.16	1.69	18.63 ± 0.13	17.69 ± 0.09	17.00 ± 0.14	–	–	12.35 ± 1.36	21.87	21.02	20.61	0.21
ZOA085754.452 − 573318.91	275.477	−7.730	0.27	−66.43	1.76	18.21 ± 0.12	17.82 ± 0.12	16.33 ± 0.10	–	–	16.19 ± 0.11	21.05	20.94	19.96	0.21
ZOA085723.182 − 573456.33	275.453	−7.801	0.32	33.04	1.72	19.98 ± 0.38	$nan \pm 1.94$	16.82 ± 0.13	11.81 ± 2.60	$nan \pm 3.40$	–	24.03	nan	19.81	0.21
ZOA085732.806 − 573526.54	275.473	−7.790	0.17	65.07	1.46	17.24 ± 0.06	16.48 ± 0.04	16.42 ± 0.10	–	14.97 ± 0.34	15.35 ± 0.27	19.80	19.12	19.33	0.21
ZOA085720.088 − 573704.17	275.476	−7.829	0.40	−45.15	2.06	17.80 ± 0.09	16.88 ± 0.06	16.04 ± 0.08	–	–	15.07 ± 0.31	21.50	20.36	19.31	0.21
ZOA085758.580 − 573053.62	275.452	−7.697	0.55	76.67	1.73	18.51 ± 0.15	17.73 ± 0.12	16.99 ± 0.18	–	–	16.73 ± 0.21	21.90	23.91	20.79	0.21
ZOA085732.443 − 573109.51	275.418	−7.744	0.15	−17.86	2.24	17.48 ± 0.07	16.66 ± 0.05	16.03 ± 0.08	–	15.66 ± 0.27	14.31 ± 0.49	20.46	19.64	19.14	0.21
ZOA085806.249 − 573744.60	275.552	−7.757	0.21	31.35	2.73	16.15 ± 0.04	15.34 ± 0.03	14.80 ± 0.04	–	14.84 ± 0.15	–	19.55	18.66	18.09	0.21
ZOA085810.192 − 573134.51	275.478	−7.684	0.30	−40.97	2.04	16.71 ± 0.05	15.96 ± 0.04	15.52 ± 0.06	–	15.81 ± 0.04	14.91 ± 0.18	19.90	19.37	18.96	0.21
ZOA090010.904 − 573737.50	275.732	−7.544	0.39	70.51	4.05	15.66 ± 0.03	14.93 ± 0.03	14.52 ± 0.04	–	14.80 ± 0.04	13.88 ± 0.19	19.01	18.31	17.90	0.22
ZOA090006.661 − 573254.60	275.665	−7.500	0.19	12.15	4.81	15.56 ± 0.03	14.73 ± 0.03	14.25 ± 0.04	14.80 ± 0.26	14.42 ± 0.06	13.58 ± 0.16	18.90	18.06	17.60	0.22
ZOA090053.968 − 573318.89	275.740	−7.424	0.52	−49.81	5.95	15.25 ± 0.03	14.53 ± 0.03	14.11 ± 0.04	15.11 ± 0.06	14.37 ± 0.04	13.44 ± 0.20	18.69	17.99	17.55	0.22
ZOA090005.332 − 573341.08	275.673	−7.511	0.28	−69.20	2.88	17.33 ± 0.07	16.43 ± 0.05	15.65 ± 0.07	–	–	14.76 ± 0.25	20.59	19.89	18.95	0.22
ZOA090022.585 − 573522.12	275.720	−7.500	0.12	54.98	1.93	17.59 ± 0.07	16.83 ± 0.06	16.07 ± 0.09	–	–	16.06 ± 0.09	20.49	19.80	19.07	0.22
ZOA090006.182 − 573615.66	275.707	−7.537	0.51	−8.08	2.96	17.73 ± 0.08	16.90 ± 0.06	16.11 ± 0.09	–	16.34 ± 0.15	15.66 ± 0.14	21.11	20.07	19.53	0.22
ZOA090040.552 − 573639.31	275.763	−7.483	0.33	79.89	4.22	16.26 ± 0.04	15.55 ± 0.04	15.18 ± 0.07	–	15.32 ± 0.07	13.83 ± 0.38	19.53	18.88	18.45	0.22
ZOA090031.420 − 573132.00	275.684	−7.443	0.35	−84.38	3.51	16.80 ± 0.05	15.94 ± 0.04	15.35 ± 0.06	–	15.36 ± 0.15	–	19.98	19.09	18.62	0.22
ZOA090004.298 − 573126.64	275.643	−7.488	0.03	83.51	2.63	17.61 ± 0.10	16.61 ± 0.06	15.95 ± 0.09	–	–	14.40 ± 0.42	20.28	19.59	19.00	0.22
ZOA085749.705 − 573954.81	275.555	−7.809	0.17	−46.38	3.40	17.27 ± 0.07	16.36 ± 0.05	15.71 ± 0.07	–	15.49 ± 0.30	14.35 ± 0.41	20.60	19.74	18.89	0.21
ZOA085739.945 − 574025.10	275.548	−7.831	0.11	86.26	1.83	18.59 ± 0.14	17.55 ± 0.09	16.57 ± 0.12	17.87 ± 0.26	–	16.45 ± 0.12	21.82	20.85	19.90	0.21
ZOA085733.773 − 574043.95	275.543	−7.845	0.36	56.32	2.02	17.79 ± 0.08	16.85 ± 0.05	16.23 ± 0.09	–	–	16.16 ± 0.09	21.15	20.00	19.42	0.21
ZOA085758.952 − 574151.33	275.594	−7.814	0.18	9.68	4.91	14.72 ± 0.03	14.00 ± 0.02	13.62 ± 0.03	13.82 ± 0.28	13.12 ± 0.21	12.01 ± 0.41	18.13	17.41	17.05	0.21
ZOA085808.401 − 574207.50	275.611	−7.801	0.24	23.19	2.67	16.08 ± 0.04	15.33 ± 0.03	14.86 ± 0.04	14.97 ± 0.32	14.55 ± 0.14	–	19.16	18.39	18.07	0.21
ZOA085737.322 − 574215.10	275.568	−7.855	0.44	74.13	1.77	17.74 ± 0.08	16.96 ± 0.06	16.11 ± 0.08	–	–	–	20.31	19.62	19.12	0.21
ZOA085738.305 − 574241.59	275.575	−7.858	0.45	−21.30	2.93	16.96 ± 0.05	16.18 ± 0.04	15.59 ± 0.06	–	15.99 ± 0.06	15.23 ± 0.12	20.28	19.53	19.02	0.21
ZOA085753.525 − 574255.96	275.600	−7.835	0.08	23.24	4.73	14.93 ± 0.03	14.21 ± 0.02	13.83 ± 0.03	–	13.73 ± 0.15	13.22 ± 0.18	18.36	17.65	17.27	0.21
ZOA085806.237 − 574256.65	275.618	−7.813	0.17	84.89	2.29	17.86 ± 0.08	16.94 ± 0.05	16.20 ± 0.08	–	–	16.05 ± 0.09	21.07	20.25	19.65	0.21
ZOA085735.378 − 574353.95	275.586	−7.876	0.08	−61.86	1.79	17.50 ± 0.07	16.57 ± 0.05	15.77 ± 0.06	–	–	–	20.80	19.83	19.04	0.21
ZOA085745.267 − 574425.48	275.607	−7.865	0.23	−15.21	1.91	17.09 ± 0.06	16.41 ± 0.04	16.18 ± 0.09	–	–	–	20.01	19.46	19.10	0.21
ZOA085755.128 − 574429.20	275.622	−7.848	0.35	−68.22	2.95	16.38 ± 0.04	15.59 ± 0.03	15.28 ± 0.05	15.03 ± 0.41	15.03 ± 0.13	14.89 ± 0.11	19.50	18.79	18.43	0.21
ZOA085803.611 − 575212.94	275.734	−7.917	0.12	72.33	2.56	17.76 ± 0.08	16.68 ± 0.05	15.69 ± 0.07	–	–	–	20.93	19.97	18.80	0.23
ZOA085735.844 − 575156.93	275.690	−7.961	0.29	28.23	3.33	16.57 ± 0.04	15.78 ± 0.03	15.18 ± 0.06	–	–	14.93 ± 0.07	20.00	19.02	18.47	0.23
ZOA085747.421 − 574651.78	275.642	−7.887	0.20	30.20	2.08	17.75 ± 0.08	16.85 ± 0.05	15.94 ± 0.07	–	–	15.75 ± 0.09	20.59	19.94	18.94	0.23
ZOA085810.533 − 574655.31	275.676	−7.848	0.04	−17.82	1.84	17.55 ± 0.07	16.81 ± 0.06	16.12 ± 0.09	12.85 ± 1.49	–	–	20.28	19.78	19.11	0.23

ZOA085745.780 − 574911.41	275.669	−7.915	0.38	41.87	2.29	17.09 ± 0.05	16.34 ± 0.04	15.72 ± 0.06	–	15.92 ± 0.08	15.57 ± 0.07	20.23	19.42	19.04	0.23
ZOA085733.305 − 575014.19	275.665	−7.947	0.31	4.73	2.47	16.75 ± 0.05	15.92 ± 0.03	15.46 ± 0.05	–	14.82 ± 0.29	14.86 ± 0.19	19.89	19.11	18.70	0.23
ZOA085758.248 − 575020.67	275.702	−7.906	0.35	−79.91	2.56	17.46 ± 0.07	16.65 ± 0.05	15.96 ± 0.08	–	16.14 ± 0.14	–	20.50	19.66	19.28	0.23
ZOA085752.238 − 575122.14	275.707	−7.927	0.37	42.57	4.04	15.47 ± 0.03	14.70 ± 0.03	14.44 ± 0.04	14.51 ± 0.28	13.83 ± 0.17	13.56 ± 0.20	18.70	17.94	17.68	0.23
ZOA085752.168 − 574612.65	275.640	−7.872	0.54	−68.97	3.84	16.38 ± 0.04	15.55 ± 0.03	15.29 ± 0.06	16.10 ± 0.09	15.12 ± 0.09	14.94 ± 0.09	19.66	18.79	18.62	0.23
ZOA090050.992 − 574453.82	275.883	−7.555	0.23	−7.10	3.25	16.59 ± 0.05	15.73 ± 0.04	15.20 ± 0.06	–	15.55 ± 0.06	14.92 ± 0.09	19.77	19.03	18.56	0.26
ZOA090040.849 − 574455.98	275.869	−7.573	0.37	63.16	2.81	17.31 ± 0.07	16.45 ± 0.05	15.66 ± 0.08	–	14.16 ± 0.71	–	20.14	19.39	18.66	0.26
ZOA090002.972 − 574215.04	275.779	−7.607	0.12	−26.34	3.17	16.01 ± 0.04	15.30 ± 0.03	14.85 ± 0.05	–	14.99 ± 0.09	13.58 ± 0.38	19.31	18.67	18.19	0.26
ZOA090006.601 − 574224.26	275.786	−7.603	0.10	−64.78	3.93	15.72 ± 0.03	15.01 ± 0.03	14.57 ± 0.04	14.93 ± 0.26	14.60 ± 0.10	–	19.04	18.33	17.88	0.26
ZOA090005.078 − 574424.61	275.810	−7.627	0.30	48.38	2.38	17.44 ± 0.07	16.68 ± 0.06	16.02 ± 0.09	–	–	–	20.85	20.05	19.14	0.26
ZOA085731.499 − 575933.94	275.782	−8.050	0.10	41.55	2.39	16.82 ± 0.05	15.96 ± 0.04	15.20 ± 0.05	–	15.05 ± 0.23	–	19.92	19.06	18.42	0.24
ZOA085731.473 − 575805.26	275.763	−8.034	0.60	−10.29	4.79	15.66 ± 0.03	14.90 ± 0.03	14.50 ± 0.04	–	14.38 ± 0.13	13.96 ± 0.11	18.97	18.23	17.77	0.24
ZOA085722.830 − 575819.46	275.754	−8.052	0.33	−79.67	7.48	14.02 ± 0.02	13.33 ± 0.02	12.99 ± 0.03	12.71 ± 0.41	–	12.61 ± 0.11	17.60	16.92	16.57	0.24
ZOA085742.362 − 575901.92	275.791	−8.026	0.34	−79.74	3.59	15.81 ± 0.03	15.10 ± 0.03	14.61 ± 0.04	14.77 ± 0.32	14.48 ± 0.15	13.95 ± 0.17	18.97	18.35	17.94	0.24
ZOA085721.135 − 575358.23	275.695	−8.008	0.25	62.24	1.85	17.87 ± 0.09	17.05 ± 0.07	16.28 ± 0.11	–	–	16.27 ± 0.11	21.19	20.39	20.49	0.24
ZOA085730.291 − 575319.89	275.700	−7.986	0.16	62.07	2.50	16.50 ± 0.04	15.80 ± 0.03	15.25 ± 0.05	–	–	–	19.63	19.11	18.44	0.24
ZOA085733.492 − 575325.93	275.706	−7.981	0.15	44.69	2.56	17.05 ± 0.06	16.25 ± 0.04	15.45 ± 0.06	–	14.85 ± 0.39	12.77 ± 0.70	19.91	19.24	18.45	0.24
ZOA090018.884 − 574655.84	275.862	−7.631	0.28	13.06	4.28	16.57 ± 0.05	15.84 ± 0.04	15.05 ± 0.05	–	15.41 ± 0.12	14.25 ± 0.21	19.82	19.13	18.29	0.24
ZOA090038.116 − 574705.10	275.892	−7.600	0.47	9.24	4.71	15.70 ± 0.03	14.94 ± 0.03	14.34 ± 0.04	15.62 ± 0.06	–	14.10 ± 0.06	19.12	18.32	17.70	0.24
ZOA090003.250 − 574732.81	275.847	−7.664	0.20	18.97	1.96	17.02 ± 0.06	16.21 ± 0.04	15.61 ± 0.06	–	15.83 ± 0.12	–	20.16	19.38	18.75	0.24
ZOA090013.946 − 574753.29	275.867	−7.650	0.38	−40.79	2.24	17.85 ± 0.08	17.07 ± 0.07	16.30 ± 0.09	–	–	–	20.50	20.20	18.92	0.24
ZOA090022.992 − 574839.59	275.890	−7.643	0.66	−85.33	3.03	17.65 ± 0.07	17.09 ± 0.07	16.32 ± 0.10	17.22 ± 0.13	15.73 ± 0.33	16.08 ± 0.11	20.73	19.97	19.80	0.24
ZOA090034.356 − 574915.68	275.915	−7.630	0.05	−2.45	4.53	15.08 ± 0.03	14.28 ± 0.02	13.70 ± 0.03	14.61 ± 0.17	13.75 ± 0.14	12.82 ± 0.22	18.49	17.68	17.11	0.24
ZOA090016.714 − 574926.66	275.891	−7.662	0.49	79.75	3.17	16.79 ± 0.05	15.91 ± 0.04	15.19 ± 0.05	–	14.71 ± 0.35	–	20.11	19.06	18.37	0.24
ZOA090037.993 − 574931.57	275.923	−7.627	0.05	33.05	2.95	17.28 ± 0.06	16.26 ± 0.04	15.62 ± 0.06	16.40 ± 0.30	15.08 ± 0.31	–	20.25	19.32	18.72	0.24
ZOA090015.703 − 575117.23	275.913	−7.684	0.41	26.06	4.24	16.00 ± 0.04	15.20 ± 0.03	14.72 ± 0.04	15.84 ± 0.08	15.05 ± 0.04	14.32 ± 0.12	19.35	18.55	18.10	0.24
ZOA090031.066 − 574541.36	275.864	−7.597	0.33	−71.62	2.84	17.62 ± 0.08	16.83 ± 0.07	16.01 ± 0.09	–	15.96 ± 0.24	–	20.39	19.71	19.01	0.24
ZOA085726.384 − 580117.95	275.797	−8.077	0.18	12.87	2.42	17.75 ± 0.08	16.93 ± 0.06	15.99 ± 0.07	–	16.49 ± 0.12	–	21.00	20.23	19.30	0.25
ZOA085725.349 − 580136.69	275.800	−8.083	0.41	−59.54	2.92	17.84 ± 0.08	16.89 ± 0.06	15.90 ± 0.07	17.50 ± 0.16	–	15.65 ± 0.09	21.43	20.32	19.14	0.25
ZOA085723.762 − 580141.51	275.799	−8.086	0.21	33.14	2.43	17.25 ± 0.06	16.40 ± 0.04	15.64 ± 0.06	–	–	14.59 ± 0.26	20.52	19.60	18.84	0.25
ZOA085729.184 − 580142.77	275.807	−8.077	0.15	−80.02	2.95	16.76 ± 0.05	15.91 ± 0.04	15.11 ± 0.05	–	–	–	20.02	19.16	18.34	0.25
ZOA085743.146 − 580444.58	275.866	−8.086	0.59	−3.04	5.78	15.79 ± 0.03	14.96 ± 0.03	14.52 ± 0.04	15.19 ± 0.21	14.84 ± 0.03	14.16 ± 0.10	19.17	18.38	17.99	0.25
ZOA085723.105 − 580555.84	275.853	−8.133	0.17	−71.67	2.00	17.76 ± 0.08	17.00 ± 0.06	16.12 ± 0.09	16.96 ± 0.27	–	12.55 ± 1.08	21.14	20.11	19.32	0.25
ZOA085801.072 − 580100.75	275.844	−8.016	0.34	48.05	2.82	17.38 ± 0.07	16.72 ± 0.05	16.15 ± 0.09	–	15.65 ± 0.30	–	20.15	19.56	18.89	0.25
ZOA085735.953 − 575950.80	275.792	−8.046	0.46	78.82	6.36	14.58 ± 0.03	13.79 ± 0.02	13.40 ± 0.03	14.12 ± 0.15	13.41 ± 0.10	13.29 ± 0.04	18.06	17.28	16.92	0.25
ZOA085721.903 − 580326.17	275.819	−8.108	0.10	−81.06	2.79	17.37 ± 0.07	16.48 ± 0.05	15.62 ± 0.07	–	16.07 ± 0.13	14.91 ± 0.15	20.46	19.82	18.78	0.25
ZOA090004.192 − 575408.44	275.933	−7.734	0.38	−58.02	2.02	17.51 ± 0.07	16.85 ± 0.07	16.26 ± 0.11	–	–	–	20.63	19.82	19.45	0.26
ZOA090024.206 − 575435.74	275.968	−7.705	0.19	−25.62	2.60	16.56 ± 0.05	15.91 ± 0.04	15.33 ± 0.06	–	–	14.95 ± 0.09	19.66	19.15	18.61	0.26
ZOA090015.232 − 575558.94	275.973	−7.735	0.29	−73.49	3.25	16.88 ± 0.05	16.12 ± 0.04	15.43 ± 0.06	15.85 ± 0.29	15.00 ± 0.27	12.90 ± 0.61	19.77	19.11	18.44	0.26
ZOA090025.909 − 575630.08	275.995	−7.723	0.26	−54.02	3.86	15.28 ± 0.03	14.50 ± 0.03	14.07 ± 0.03	13.90 ± 0.44	13.85 ± 0.19	13.91 ± 0.05	18.65	17.89	17.53	0.26
ZOA090051.126 − 575709.97	276.040	−7.688	0.07	−54.11	3.37	16.03 ± 0.04	15.19 ± 0.03	14.59 ± 0.04	–	13.69 ± 0.42	–	19.37	18.41	17.83	0.26
ZOA090050.714 − 575736.38	276.045	−7.694	0.22	−63.85	3.29	16.55 ± 0.05	15.92 ± 0.04	15.21 ± 0.06	–	–	–	19.73	19.26	18.22	0.26
ZOA090054.241 − 575813.28	276.058	−7.694	0.23	−2.05	3.44	15.99 ± 0.04	15.22 ± 0.03	14.70 ± 0.05	–	14.43 ± 0.12	14.41 ± 0.09	19.18	18.31	18.03	0.26
ZOA090037.127 − 575358.87	275.979	−7.677	0.50	−58.10	7.39	15.04 ± 0.03	14.32 ± 0.03	13.92 ± 0.04	14.71 ± 0.10	13.71 ± 0.15	13.43 ± 0.08	18.59	17.87	17.42	0.26
ZOA090019.604 − 575724.79	275.997	−7.744	0.42	−34.20	2.52	18.02 ± 0.10	17.10 ± 0.07	16.26 ± 0.09	–	–	15.98 ± 0.11	21.47	20.28	19.31	0.26
ZOA085534.004 − 573246.71	275.267	−7.965	0.07	−32.93	3.32	17.01 ± 0.06	15.98 ± 0.04	15.25 ± 0.06	–	–	13.18 ± 0.49	19.80	18.89	18.24	0.23
ZOA085615.721 − 573324.77	275.336	−7.900	0.29	54.10	3.16	16.53 ± 0.05	15.77 ± 0.04	15.22 ± 0.06	–	14.70 ± 0.31	14.75 ± 0.10	19.71	18.98	18.49	0.23
ZOA085544.695 − 573352.86	275.297	−7.958	0.42	−14.26	4.12	16.70 ± 0.05	15.86 ± 0.04	15.34 ± 0.06	–	15.20 ± 0.21	14.99 ± 0.09	20.00	19.10	18.60	0.23
ZOA085617.591 − 573358.45	275.346	−7.903	0.05	4.00	2.27	17.01 ± 0.06	16.11 ± 0.04	15.34 ± 0.05	16.94 ± 0.06	–	15.28 ± 0.06	20.39	19.49	18.82	0.23
ZOA085549.977 − 573408.00	275.308	−7.952	0.23	32.34	2.24	17.42 ± 0.07	16.63 ± 0.05	16.03 ± 0.08	–	–	15.66 ± 0.11	20.81	19.80	19.13	0.23
ZOA085536.621 − 573433.48	275.294	−7.979	0.51	−49.18	3.58	16.95 ± 0.06	16.19 ± 0.04	15.49 ± 0.07	–	15.26 ± 0.24	15.47 ± 0.07	19.95	19.26	18.62	0.23
ZOA085555.174 − 573457.59	275.326	−7.952	0.48	−73.59	4.21	16.17 ± 0.04	15.40 ± 0.03	14.86 ± 0.04	15.43 ± 0.24	15.14 ± 0.06	14.25 ± 0.14	19.44	18.72	18.13	0.23
ZOA085546.538 − 573636.88	275.335	−7.984	0.29	−56.37	2.74	17.23 ± 0.06	16.58 ± 0.05	15.99 ± 0.09	–	15.93 ± 0.14	14.55 ± 0.35	20.15	19.50	19.18	0.23
ZOA085542.650 − 573711.09	275.337	−7.997	0.07	19.98	3.00	16.36 ± 0.04	15.59 ± 0.03	14.98 ± 0.05	–	14.96 ± 0.16	14.91 ± 0.05	19.53	18.86	18.51	0.23
ZOA085611.406 − 573718.72	275.380	−7.949	0.25	60.43	6.80	14.82 ± 0.03	14.11 ± 0.03	13.69 ± 0.03	14.27 ± 0.18	13.45 ± 0.17	13.15 ± 0.10	18.37	17.66	17.26	0.23
ZOA085552.990 − 574508.83	275.455	−8.064	0.30	32.67	2.19	17.25 ± 0.06	16.31 ± 0.04	15.56 ± 0.07	–	15.29 ± 0.30	–	20.62	19.46	18.92	0.21
ZOA085616.142 − 574010.55	275.424	−7.971	0.34	−47.20	2.94	16.82 ± 0.05	16.08 ± 0.04	15.67 ± 0.08	–	–	–	19.82	19.24	18.69	0.21
ZOA085551.872 − 574008.22	275.388	−8.013	0.09	−84.08	2.08	17.16 ± 0.06	16.42 ± 0.04	15.82 ± 0.07	–	–	12.33 ± 1.04	20.35	19.60	18.80	0.21
ZOA085551.453 − 574136.43	275.407	−8.029	0.64	−0.28	5.97	15.34 ± 0.03	14.68 ± 0.03	14.46 ± 0.04	–	14.59 ± 0.03	14.25 ± 0.05	18.70	18.07	17.86	0.21
ZOA085550.852 − 574220.28	275.415	−8.038	0.17	−85.91	3.04	18.08 ± 0.09	17.48 ± 0.07	16.38 ± 0.09	–	–	16.09 ± 0.11	21.49	20.45	19.50	0.21
ZOA085532.042 − 574220.31	275.388	−8.070	0.47	−34.18	2.08	17.93 ± 0.11	17.24 ± 0.08	16.45 ± 0.14	–	16.22 ± 0.31	–	21.11	20.92	19.86	0.21
ZOA085536.379 − 574433.21	275.423	−8.086	0.30	−40.01	1.87	17.04 ± 0.06	16.30 ± 0.04	15.81 ± 0.07	11.95 ± 1.64	–	15.80 ± 0.07	20.16	19.41	18.90	0.21

ZOA085609.133 − 573923.59	275.404	−7.975	0.20	−18.75	2.48	17.28 ± 0.06	16.64 ± 0.05	16.21 ± 0.11	16.62 ± 0.20	–	15.50 ± 0.19	20.22	19.52	19.10	0.21
ZOA085546.865 − 574918.26	275.500	−8.119	0.34	−83.47	2.71	17.07 ± 0.05	16.19 ± 0.04	15.60 ± 0.06	–	15.17 ± 0.26	15.48 ± 0.07	20.23	19.26	18.84	0.21
ZOA085533.716 − 575015.96	275.494	−8.151	0.15	77.72	1.94	17.01 ± 0.06	16.36 ± 0.04	15.67 ± 0.07	–	14.45 ± 0.58	–	19.97	19.35	18.90	0.21
ZOA085546.672 − 575035.72	275.516	−8.133	0.32	−21.42	1.94	17.79 ± 0.08	17.35 ± 0.08	16.65 ± 0.14	–	–	16.42 ± 0.14	20.90	20.52	19.66	0.21
ZOA085549.740 − 575151.62	275.537	−8.141	0.70	−49.00	2.81	18.50 ± 0.13	17.38 ± 0.08	16.63 ± 0.13	–	17.16 ± 0.10	15.98 ± 0.14	22.60	21.53	19.89	0.21
ZOA085601.192 − 574607.54	275.479	−8.060	0.30	4.91	2.97	17.31 ± 0.06	16.74 ± 0.05	16.73 ± 0.15	–	16.13 ± 0.07	15.25 ± 0.30	19.98	19.54	19.41	0.21
ZOA085611.924 − 575930.33	275.668	−8.185	0.30	10.64	2.23	17.81 ± 0.09	17.05 ± 0.07	16.25 ± 0.10	–	–	15.24 ± 0.29	20.83	20.14	19.56	0.23
ZOA085610.203 − 575414.97	275.597	−8.131	0.24	−29.93	9.76	13.74 ± 0.02	13.04 ± 0.02	12.64 ± 0.02	13.16 ± 0.19	12.73 ± 0.09	12.38 ± 0.06	17.51	16.79	16.40	0.23
ZOA085534.763 − 575451.67	275.555	−8.198	0.28	3.79	2.34	17.86 ± 0.08	16.88 ± 0.06	15.96 ± 0.08	–	–	15.81 ± 0.08	21.05	20.04	19.29	0.23
ZOA085542.494 − 575529.39	275.574	−8.192	0.29	44.05	4.44	15.64 ± 0.03	14.96 ± 0.03	14.37 ± 0.04	15.24 ± 0.15	14.35 ± 0.19	13.73 ± 0.17	19.01	18.32	17.73	0.23
ZOA085606.467 − 575656.42	275.627	−8.166	0.26	−42.18	2.69	17.74 ± 0.08	16.87 ± 0.06	16.06 ± 0.08	–	12.21 ± 1.45	15.72 ± 0.09	20.51	19.75	19.07	0.23
ZOA085602.159 − 575725.73	275.627	−8.179	0.18	−51.83	2.53	17.50 ± 0.07	16.62 ± 0.05	15.81 ± 0.07	–	–	15.53 ± 0.09	20.52	19.81	18.87	0.23
ZOA085536.037 − 575843.29	275.607	−8.237	0.23	−66.48	2.09	17.13 ± 0.06	16.42 ± 0.04	15.89 ± 0.07	–	–	13.83 ± 0.61	20.55	19.63	19.25	0.23
ZOA085531.010 − 575849.64	275.601	−8.247	0.14	−7.21	2.88	16.32 ± 0.04	15.52 ± 0.03	15.01 ± 0.05	–	13.84 ± 0.41	14.39 ± 0.16	19.43	18.54	18.21	0.23
ZOA085530.553 − 575854.98	275.601	−8.249	0.16	−33.79	3.23	16.86 ± 0.06	16.15 ± 0.05	15.46 ± 0.08	–	14.78 ± 0.40	15.27 ± 0.09	19.90	19.12	18.61	0.23
ZOA085558.275 − 575307.55	275.566	−8.140	0.33	3.85	1.88	17.42 ± 0.06	16.66 ± 0.05	16.04 ± 0.07	–	15.95 ± 0.20	15.21 ± 0.27	20.61	19.73	19.45	0.23
ZOA085608.440 − 575914.02	275.659	−8.188	0.58	−17.29	1.93	18.17 ± 0.10	17.19 ± 0.07	16.79 ± 0.15	–	–	16.75 ± 0.16	20.92	20.21	19.75	0.23
ZOA085939.673 − 572748.91	275.561	−7.491	0.16	−89.33	2.29	18.07 ± 0.09	17.15 ± 0.07	16.44 ± 0.11	–	–	16.21 ± 0.11	20.80	20.26	19.29	0.22
ZOA085931.138 − 572428.64	275.505	−7.469	0.27	−65.25	2.28	18.05 ± 0.10	17.10 ± 0.07	16.19 ± 0.09	–	12.74 ± 1.36	15.61 ± 0.13	20.65	19.79	19.09	0.22
ZOA085930.751 − 572426.82	275.504	−7.470	0.27	−42.97	1.90	17.59 ± 0.07	16.86 ± 0.06	16.07 ± 0.09	–	15.48 ± 0.44	–	20.30	19.50	18.57	0.22
ZOA085936.881 − 573108.27	275.599	−7.531	0.30	−58.73	2.64	18.22 ± 0.11	17.08 ± 0.07	16.31 ± 0.10	–	–	–	22.15	20.23	19.70	0.21
ZOA085921.490 − 574007.02	275.691	−7.655	0.16	−8.12	2.26	17.70 ± 0.08	16.80 ± 0.06	16.05 ± 0.08	–	–	–	20.79	19.92	19.07	0.23
ZOA085926.260 − 574330.68	275.742	−7.683	0.45	−54.02	9.43	13.64 ± 0.02	12.92 ± 0.02	12.56 ± 0.02	13.09 ± 0.18	12.71 ± 0.04	12.33 ± 0.06	17.37	16.65	16.28	0.23
ZOA085911.351 − 574342.59	275.723	−7.711	0.12	26.20	5.85	14.74 ± 0.03	14.03 ± 0.02	13.64 ± 0.03	14.31 ± 0.15	13.04 ± 0.27	13.41 ± 0.06	18.27	17.56	17.18	0.23
ZOA085939.156 − 573907.74	275.705	−7.614	0.07	−58.65	3.65	15.55 ± 0.03	14.87 ± 0.03	14.54 ± 0.04	–	14.68 ± 0.04	14.35 ± 0.05	18.88	18.19	17.87	0.23
ZOA085906.975 − 574723.68	275.764	−7.758	0.30	61.07	3.77	16.22 ± 0.05	15.52 ± 0.04	14.81 ± 0.07	–	14.35 ± 0.38	–	19.57	18.87	18.22	0.22
ZOA085944.265 − 574856.18	275.837	−7.711	0.27	−19.07	6.08	14.83 ± 0.03	14.11 ± 0.03	13.79 ± 0.04	–	–	13.43 ± 0.09	18.33	17.62	17.30	0.22
ZOA085914.546 − 574632.72	275.764	−7.736	0.13	54.96	2.59	16.80 ± 0.05	16.00 ± 0.04	15.71 ± 0.08	–	–	15.65 ± 0.08	20.01	19.13	19.26	0.22
ZOA085944.113 − 574508.63	275.789	−7.671	0.09	−5.96	4.41	15.29 ± 0.03	14.53 ± 0.03	14.18 ± 0.04	15.05 ± 0.08	14.02 ± 0.11	13.84 ± 0.10	18.64	17.88	17.61	0.22
ZOA085922.790 − 575215.95	275.849	−7.784	0.15	−88.72	3.26	17.51 ± 0.09	16.93 ± 0.08	16.04 ± 0.13	–	–	15.92 ± 0.14	20.31	19.85	19.16	0.22
ZOA085945.126 − 575925.65	275.973	−7.823	0.28	−17.54	2.06	17.23 ± 0.06	16.49 ± 0.05	16.17 ± 0.11	–	16.24 ± 0.07	9.43 ± 2.12	20.77	19.80	20.01	0.25
ZOA085948.419 − 575900.31	275.972	−7.813	0.19	−6.67	4.41	15.02 ± 0.03	14.24 ± 0.02	13.93 ± 0.03	–	13.84 ± 0.11	–	18.42	17.66	17.32	0.25
ZOA085950.527 − 575505.28	275.925	−7.767	0.39	20.32	11.40	13.52 ± 0.02	12.72 ± 0.02	12.35 ± 0.02	12.97 ± 0.18	12.16 ± 0.15	11.61 ± 0.20	17.38	16.57	16.18	0.25
ZOA085931.442 − 575504.09	275.897	−7.799	0.29	−33.90	3.31	16.06 ± 0.04	15.33 ± 0.03	14.72 ± 0.04	–	13.71 ± 0.49	13.63 ± 0.28	19.34	18.59	18.00	0.25
ZOA085935.762 − 575520.95	275.907	−7.795	0.10	8.31	4.39	15.75 ± 0.03	14.93 ± 0.03	14.40 ± 0.04	15.35 ± 0.14	14.77 ± 0.03	13.92 ± 0.11	19.05	18.28	17.72	0.25
ZOA085949.372 − 575540.60	275.931	−7.776	0.19	0.73	1.78	18.92 ± 0.18	17.73 ± 0.11	16.75 ± 0.15	–	–	–	22.84	21.23	20.15	0.25
ZOA085919.375 − 575614.47	275.895	−7.832	0.43	71.74	3.25	16.78 ± 0.05	16.05 ± 0.04	15.49 ± 0.06	–	15.82 ± 0.05	15.20 ± 0.10	19.95	19.26	18.58	0.25
ZOA085927.628 − 575642.83	275.913	−7.824	0.28	73.49	2.45	17.21 ± 0.06	16.53 ± 0.05	16.00 ± 0.08	–	–	–	20.07	19.41	18.77	0.25
ZOA085917.081 − 575746.13	275.911	−7.853	0.13	10.04	4.02	15.44 ± 0.03	14.76 ± 0.03	14.30 ± 0.04	14.62 ± 0.24	14.37 ± 0.08	–	18.74	18.07	17.69	0.25
ZOA085940.040 − 575522.57	275.914	−7.788	0.14	50.51	3.10	17.07 ± 0.06	16.27 ± 0.05	15.93 ± 0.10	–	14.71 ± 0.18	–	19.65	18.82	18.64	0.25
ZOA085942.109 − 580623.25	276.058	−7.904	0.15	53.56	2.08	17.61 ± 0.08	16.59 ± 0.06	15.88 ± 0.09	–	–	15.87 ± 0.09	20.66	19.77	19.29	0.26
ZOA085906.721 − 580121.81	275.942	−7.909	0.02	87.19	3.26	16.74 ± 0.07	15.99 ± 0.06	15.31 ± 0.09	–	–	–	19.93	19.37	18.49	0.26
ZOA085943.718 − 580219.26	276.008	−7.857	0.12	16.89	3.88	15.78 ± 0.04	15.05 ± 0.03	14.57 ± 0.04	13.17 ± 0.83	13.21 ± 0.40	13.54 ± 0.24	18.98	18.20	17.80	0.26
ZOA085947.776 − 580230.67	276.016	−7.852	0.33	−74.45	2.76	17.57 ± 0.08	16.77 ± 0.06	15.70 ± 0.07	–	–	15.47 ± 0.08	21.41	20.28	18.77	0.26
ZOA085949.291 − 580359.87	276.038	−7.866	0.36	−42.43	4.88	15.39 ± 0.03	14.63 ± 0.03	14.03 ± 0.03	14.84 ± 0.18	–	–	18.76	18.05	17.46	0.26
ZOA085911.300 − 580358.89	275.983	−7.929	0.17	3.12	3.33	17.11 ± 0.07	16.40 ± 0.06	15.45 ± 0.08	–	–	–	20.18	19.44	18.44	0.26
ZOA085916.637 − 580432.85	275.998	−7.927	0.47	−64.41	2.62	16.83 ± 0.05	15.97 ± 0.04	15.36 ± 0.06	–	15.70 ± 0.07	15.28 ± 0.06	19.93	19.16	18.86	0.26
ZOA085951.795 − 580455.09	276.053	−7.872	0.09	−63.71	2.52	17.14 ± 0.06	16.36 ± 0.05	15.76 ± 0.08	–	–	–	20.12	19.36	18.78	0.26
ZOA085929.565 − 580600.57	276.035	−7.921	0.34	−30.90	3.44	16.81 ± 0.06	16.04 ± 0.04	15.12 ± 0.06	14.92 ± 0.65	14.17 ± 0.55	–	19.73	19.02	18.20	0.26
ZOA085926.986 − 580027.20	275.960	−7.865	0.49	−38.51	2.44	17.10 ± 0.06	16.34 ± 0.05	15.87 ± 0.08	–	15.71 ± 0.07	–	20.18	19.31	19.18	0.26
ZOA085910.906 − 580357.52	275.982	−7.930	0.16	−87.19	3.90	16.00 ± 0.04	15.11 ± 0.03	14.16 ± 0.04	–	14.63 ± 0.17	–	19.27	18.49	17.50	0.26
ZOA085714.203 − 572615.93	275.328	−7.723	0.18	−79.70	1.81	18.01 ± 0.20	17.06 ± 0.13	16.09 ± 0.17	–	–	16.08 ± 0.18	20.10	20.32	19.71	0.22
ZOA085711.866 − 573734.11	275.471	−7.848	0.07	17.31	2.66	17.32 ± 0.10	16.42 ± 0.06	15.71 ± 0.10	–	14.81 ± 0.42	11.95 ± 0.92	20.13	19.36	18.52	0.21
ZOA085656.857 − 573257.88	275.389	−7.825	0.26	28.30	4.35	15.43 ± 0.04	14.72 ± 0.03	14.18 ± 0.04	14.78 ± 0.23	14.51 ± 0.07	13.78 ± 0.12	18.83	18.14	17.59	0.21
ZOA085655.850 − 573617.11	275.431	−7.862	0.40	13.06	3.73	16.87 ± 0.07	16.17 ± 0.05	15.32 ± 0.07	–	15.72 ± 0.17	–	20.21	19.54	18.74	0.21
ZOA085715.934 − 573746.85	275.479	−7.843	0.10	41.77	2.97	17.62 ± 0.16	16.24 ± 0.06	15.35 ± 0.10	11.82 ± 1.88	15.42 ± 0.19	14.84 ± 0.15	22.68	19.34	18.49	0.21
ZOA085636.287 − 573920.68	275.442	−7.928	0.28	−27.96	4.94	15.95 ± 0.05	15.31 ± 0.04	14.83 ± 0.06	–	14.15 ± 0.33	14.26 ± 0.16	19.23	18.59	18.18	0.21
ZOA085703.625 − 573916.06	275.481	−7.880	0.27	−78.72	2.79	17.23 ± 0.10	16.55 ± 0.06	15.75 ± 0.08	–	–	15.50 ± 0.10	20.40	19.78	19.00	0.21
ZOA085708.658 − 573913.63	275.487	−7.871	0.44	36.77	2.38	16.81 ± 0.08	16.07 ± 0.04	15.29 ± 0.06	–	14.96 ± 0.33	–	19.88	19.26	18.42	0.21
ZOA085657.659 − 574119.80	275.499	−7.913	0.21	56.48	2.96	17.33 ± 0.12	16.37 ± 0.06	15.58 ± 0.08	–	–	–	20.24	19.47	18.59	0.21
ZOA085702.145 − 574334.86	275.534	−7.929	0.05	18.77	2.07	17.89 ± 0.16	16.84 ± 0.07	16.02 ± 0.10	–	16.41 ± 0.11	15.12 ± 0.27	20.49	19.86	19.10	0.21
ZOA085917.823 − 573826.93	275.665	−7.643	0.50	−29.97	10.27	13.82 ± 0.02	13.01 ± 0.02	12.57 ± 0.02	13.54 ± 0.10	11.97 ± 0.32	11.74 ± 0.24	17.42	16.62	16.20	0.21

$ZOA085805.215-580718.38$	275.931	−8.076	0.44	−18.17	6.67	14.87 ± 0.03	14.14 ± 0.02	13.78 ± 0.03	14.51 ± 0.12	13.06 ± 0.31	13.19 ± 0.15	18.39	17.67	17.30	0.25

Table A.0.5: VC10 catalogue of galaxies

Designation	ℓ (deg)	b (deg)	e_J	ϕ_J (deg)	r_{k20fe} (arcsec)	J_{k20fe} (mag)	H_{k20fe} (mag)	$K_{s_{k20fe}}$ (mag)	J_{tot} (mag)	H_{tot} (mag)	$K_{s_{tot}}$ (mag)	μ_J	μ_H (mag arcsec^{-2})	μ_{Ks}	$E(B-V)$ (mag)
$ZOA094747.053-433617.77$	271.274	7.694	0.12	−63.02	3.51	16.32 ± 0.05	15.60 ± 0.04	15.14 ± 0.06	16.14 ± 0.08	15.10 ± 0.10	–	19.56	18.77	18.29	0.26
$ZOA094759.044-434316.31$	271.377	7.629	0.18	−41.57	2.36	17.61 ± 0.09	16.87 ± 0.06	16.23 ± 0.11	–	–	–	22.07	20.10	19.88	0.26
$ZOA094849.085-440951.96$	271.781	7.386	0.22	−56.18	2.73	18.09 ± 0.09	17.10 ± 0.06	16.21 ± 0.09	–	–	15.70 ± 0.14	21.30	20.22	19.46	0.24
$ZOA094823.663-440859.39$	271.713	7.348	0.18	−36.74	3.40	16.35 ± 0.04	15.51 ± 0.03	15.08 ± 0.05	–	–	14.89 ± 0.07	19.63	18.79	18.49	0.24
$ZOA094829.369-441046.54$	271.745	7.337	0.08	−69.29	3.52	16.86 ± 0.05	15.99 ± 0.04	15.21 ± 0.06	–	15.46 ± 0.13	14.92 ± 0.06	19.91	19.16	18.40	0.24
$ZOA095018.168-435456.79$	271.827	7.748	0.35	−3.87	2.72	16.89 ± 0.06	15.99 ± 0.04	15.43 ± 0.06	–	15.83 ± 0.07	14.50 ± 0.23	20.16	19.33	18.65	0.22
$ZOA095020.448-435501.50$	271.833	7.751	0.66	28.63	3.11	17.20 ± 0.07	16.29 ± 0.04	15.63 ± 0.06	17.03 ± 0.07	16.15 ± 0.04	15.58 ± 0.07	21.03	19.93	19.70	0.22
$ZOA095027.598-435636.68$	271.867	7.745	0.61	50.56	5.51	15.43 ± 0.03	14.66 ± 0.03	14.25 ± 0.04	–	13.46 ± 0.30	–	18.87	18.12	17.72	0.22
$ZOA094851.403-440307.40$	271.714	7.477	0.36	−23.02	1.78	17.76 ± 0.08	16.95 ± 0.06	16.25 ± 0.10	–	–	15.82 ± 0.17	20.82	20.01	19.91	0.25
$ZOA094842.125-440409.29$	271.703	7.446	0.36	−85.38	3.00	17.16 ± 0.06	16.45 ± 0.04	15.58 ± 0.06	–	15.79 ± 0.19	15.38 ± 0.08	20.29	19.67	19.02	0.25
$ZOA094826.148-435753.03$	271.598	7.495	0.53	74.04	3.76	17.38 ± 0.07	16.68 ± 0.06	15.78 ± 0.09	–	16.18 ± 0.21	15.09 ± 0.23	20.69	19.95	19.21	0.25
$ZOA094837.839-440311.59$	271.683	7.450	0.14	12.57	2.31	16.93 ± 0.05	16.18 ± 0.04	15.59 ± 0.06	–	15.28 ± 0.21	14.04 ± 0.43	19.92	19.16	18.76	0.25
$ZOA094841.699-440224.92$	271.683	7.467	0.37	−28.79	4.81	15.31 ± 0.03	14.57 ± 0.03	14.16 ± 0.04	15.14 ± 0.06	14.30 ± 0.06	13.90 ± 0.06	18.71	17.97	17.57	0.25
$ZOA094820.163-435940.35$	271.604	7.461	0.33	−54.11	2.76	17.41 ± 0.06	16.59 ± 0.05	15.78 ± 0.07	–	–	15.45 ± 0.10	20.36	19.65	18.78	0.25
$ZOA094825.619-435831.93$	271.604	7.486	0.52	−72.14	5.54	15.74 ± 0.03	14.94 ± 0.03	14.44 ± 0.04	14.87 ± 0.24	13.92 ± 0.23	13.85 ± 0.09	19.04	18.25	17.75	0.25
$ZOA095102.137-435949.67$	271.982	7.769	0.76	62.46	3.72	17.25 ± 0.07	16.44 ± 0.05	15.80 ± 0.08	16.62 ± 0.26	16.14 ± 0.11	14.90 ± 0.25	20.14	19.46	19.09	0.21
$ZOA095111.386-440409.53$	272.050	7.731	0.20	−51.58	2.78	16.66 ± 0.05	15.98 ± 0.04	15.32 ± 0.06	–	15.26 ± 0.22	14.67 ± 0.16	19.87	19.22	18.47	0.21
$ZOA095119.518-440015.55$	272.027	7.797	0.04	−36.12	2.75	17.71 ± 0.10	16.77 ± 0.07	16.19 ± 0.11	–	–	15.84 ± 0.11	20.71	19.74	19.20	0.21
$ZOA095123.944-440237.50$	272.063	7.775	0.05	24.12	1.89	17.50 ± 0.07	17.90 ± 0.13	16.19 ± 0.09	–	14.67 ± 1.29	–	20.13	20.16	19.01	0.21
$ZOA095050.226-434439.35$	271.792	7.941	0.04	5.49	2.38	17.06 ± 0.06	16.37 ± 0.05	15.92 ± 0.09	–	–	–	20.20	19.42	19.11	0.21
$ZOA095050.508-434450.57$	271.794	7.940	0.37	50.08	2.33	18.19 ± 0.12	17.38 ± 0.09	16.38 ± 0.12	–	–	16.10 ± 0.12	21.23	20.11	19.22	0.21
$ZOA095032.562-434723.11$	271.780	7.872	0.09	17.61	3.35	15.89 ± 0.04	15.20 ± 0.03	14.68 ± 0.04	14.65 ± 0.40	14.52 ± 0.14	–	19.07	18.38	17.93	0.21
$ZOA095035.790-434826.52$	271.799	7.865	0.13	56.51	2.41	17.36 ± 0.07	16.54 ± 0.05	15.79 ± 0.07	–	–	15.58 ± 0.08	20.38	19.88	19.00	0.21
$ZOA095032.300-434840.54$	271.793	7.855	0.35	−1.98	4.14	16.56 ± 0.05	15.75 ± 0.04	14.96 ± 0.05	–	14.83 ± 0.28	–	19.89	19.07	18.26	0.21
$ZOA095044.164-434921.84$	271.828	7.869	0.25	−35.47	3.23	17.74 ± 0.09	16.87 ± 0.06	15.91 ± 0.08	–	–	15.54 ± 0.11	20.69	19.72	19.46	0.21
$ZOA095120.224-435240.16$	271.948	7.896	0.22	−27.96	4.03	15.97 ± 0.04	15.20 ± 0.03	14.63 ± 0.04	15.67 ± 0.11	–	14.48 ± 0.05	19.28	18.50	18.07	0.21
$ZOA095136.902-435338.43$	271.997	7.915	0.39	52.06	0.65	16.70 ± 0.06	16.30 ± 0.06	17.90 ± 0.54	15.34 ± 0.08	14.54 ± 0.06	9.88 ± 2.59	19.00	18.18	17.98	0.21
$ZOA095108.718-435513.73$	271.948	7.841	0.36	−58.48	2.06	17.41 ± 0.07	16.43 ± 0.05	15.75 ± 0.06	–	–	15.74 ± 0.06	20.55	19.62	19.00	0.21
$ZOA095112.506-435508.66$	271.956	7.849	0.13	−13.12	1.94	17.95 ± 0.10	17.04 ± 0.07	16.21 ± 0.09	–	–	15.21 ± 0.27	20.84	20.20	19.89	0.21
$ZOA094821.658-434534.37$	271.455	7.643	0.34	−69.32	2.75	16.87 ± 0.05	15.99 ± 0.04	15.17 ± 0.05	–	15.74 ± 0.08	14.72 ± 0.12	20.21	19.40	18.55	0.23
$ZOA094815.331-434714.50$	271.458	7.610	0.07	76.76	2.61	16.95 ± 0.05	16.05 ± 0.04	15.41 ± 0.06	–	–	14.46 ± 0.28	20.05	19.22	18.80	0.23
$ZOA094815.596-434748.11$	271.465	7.603	0.18	39.72	2.50	17.00 ± 0.06	16.13 ± 0.04	15.35 ± 0.06	–	–	–	20.09	19.38	18.59	0.23
$ZOA094827.700-434642.09$	271.481	7.641	0.31	−5.72	2.56	18.24 ± 0.10	17.41 ± 0.07	16.64 ± 0.13	–	16.53 ± 0.22	–	20.86	20.33	19.74	0.23
$ZOA094832.868-434656.43$	271.496	7.648	0.50	−32.90	2.02	18.69 ± 0.14	17.68 ± 0.09	16.72 ± 0.15	–	–	–	21.61	20.80	20.12	0.23
$ZOA094840.248-434541.85$	271.499	7.678	0.49	23.64	4.03	17.52 ± 0.07	16.67 ± 0.05	16.06 ± 0.10	–	16.24 ± 0.13	15.76 ± 0.14	20.73	19.75	19.17	0.23
$ZOA094826.714-434429.92$	271.455	7.667	0.16	−35.78	2.78	18.80 ± 0.16	16.65 ± 0.05	15.94 ± 0.08	–	–	15.57 ± 0.12	21.12	19.71	19.14	0.23
$ZOA094846.604-434508.80$	271.508	7.697	0.64	64.72	4.32	16.51 ± 0.04	15.55 ± 0.03	15.05 ± 0.05	15.38 ± 0.36	14.54 ± 0.28	–	19.76	18.85	18.41	0.23
$ZOA095055.431-434543.42$	271.815	7.938	0.18	−50.41	2.17	17.44 ± 0.07	16.75 ± 0.06	16.08 ± 0.08	16.98 ± 0.14	–	15.97 ± 0.09	20.53	19.75	19.40	0.22
$ZOA095109.262-434314.91$	271.821	7.996	0.13	−26.66	2.92	16.47 ± 0.05	15.67 ± 0.04	15.31 ± 0.07	15.06 ± 0.45	–	–	19.47	18.69	18.36	0.22
$ZOA095055.291-434440.70$	271.804	7.951	0.23	48.16	4.72	15.88 ± 0.04	15.14 ± 0.03	14.60 ± 0.05	–	14.38 ± 0.22	14.15 ± 0.12	19.17	18.48	17.87	0.22
$ZOA095100.966-434438.74$	271.817	7.962	0.56	66.12	5.67	15.65 ± 0.04	14.86 ± 0.03	14.38 ± 0.04	–	13.76 ± 0.30	13.66 ± 0.20	19.08	18.22	17.80	0.22
$ZOA095104.228-434419.71$	271.821	7.972	0.18	53.35	2.69	17.02 ± 0.06	16.15 ± 0.04	15.82 ± 0.08	–	15.71 ± 0.06	15.67 ± 0.08	20.00	19.16	19.12	0.22
$ZOA095103.490-434415.08$	271.818	7.972	0.12	0.85	2.43	16.94 ± 0.06	16.17 ± 0.04	15.77 ± 0.07	–	–	14.81 ± 0.28	20.03	19.22	19.18	0.22
$ZOA095109.539-434412.27$	271.832	7.984	0.08	25.66	3.57	15.95 ± 0.04	15.21 ± 0.03	14.62 ± 0.04	15.81 ± 0.08	13.63 ± 0.49	14.47 ± 0.05	19.29	18.55	17.97	0.22
$ZOA095111.080-434431.39$	271.839	7.983	0.04	0.92	2.66	17.27 ± 0.07	16.61 ± 0.05	15.89 ± 0.08	–	15.92 ± 0.15	15.63 ± 0.10	20.45	19.58	18.91	0.22
$ZOA095118.607-434436.02$	271.858	7.996	0.15	14.66	3.33	15.94 ± 0.04	15.20 ± 0.03	14.73 ± 0.04	14.78 ± 0.38	–	14.38 ± 0.09	19.17	18.44	18.03	0.22
$ZOA095120.617-434422.08$	271.860	8.003	0.13	−70.86	3.01	16.03 ± 0.04	15.28 ± 0.03	14.87 ± 0.04	–	14.98 ± 0.08	13.08 ± 0.49	19.33	18.58	18.08	0.22
$ZOA095101.605-434541.56$	271.829	7.950	0.08	−22.29	2.51	17.52 ± 0.08	16.59 ± 0.05	15.91 ± 0.08	–	–	–	20.59	19.75	18.98	0.22
$ZOA095114.444-434515.49$	271.855	7.980	0.23	−80.85	2.22	17.75 ± 0.09	17.08 ± 0.07	16.27 ± 0.10	–	–	16.10 ± 0.10	21.07	20.19	19.41	0.22
$ZOA095120.399-434545.77$	271.874	7.985	0.37	−41.56	10.23	13.65 ± 0.02	12.92 ± 0.02	12.47 ± 0.02	12.83 ± 0.24	12.42 ± 0.12	12.04 ± 0.08	17.55	16.79	16.33	0.22
$ZOA095119.802-434556.85$	271.875	7.981	0.15	−27.16	2.92	17.22 ± 0.07	16.36 ± 0.05	15.75 ± 0.08	–	–	–	20.17	19.31	18.57	0.22
$ZOA095122.254-434551.50$	271.880	7.987	0.15	−3.50	2.60	17.00 ± 0.06	16.28 ± 0.05	15.53 ± 0.06	–	–	14.30 ± 0.33	20.05	19.43	18.73	0.22
$ZOA095102.125-434754.65$	271.854	7.922	0.27	−52.59	3.29	16.99 ± 0.06	16.11 ± 0.04	15.67 ± 0.07	–	12.00 ± 1.25	15.35 ± 0.09	19.86	19.21	19.05	0.22
$ZOA095129.963-434919.40$	271.935	7.957	0.04	−69.04	2.97	16.57 ± 0.05	15.81 ± 0.04	15.22 ± 0.06	–	14.96 ± 0.23	14.32 ± 0.20	19.82	19.01	18.31	0.22
$ZOA095129.574-434319.78$	271.870	8.034	0.25	−52.61	3.15	18.18 ± 0.16	17.23 ± 0.10	16.40 ± 0.14	–	–	15.46 ± 0.23	21.92	20.34	19.70	0.22
$ZOA095124.875-434846.19$	271.917	7.955	0.29	−3.97	2.65	16.98 ± 0.06	16.16 ± 0.04	15.66 ± 0.07	–	15.25 ± 0.23	15.53 ± 0.07	19.93	19.23	18.86	0.22

ZOA095035.717 − 432834.39	271.585	8.120	0.48	−78.38	7.37	14.97 ± 0.03	14.31 ± 0.03	13.92 ± 0.04	14.68 ± 0.09	13.82 ± 0.14	13.03 ± 0.25	18.53	17.87	17.51	0.20
ZOA095033.058 − 432903.24	271.584	8.109	0.36	−75.41	2.09	17.11 ± 0.07	16.32 ± 0.05	15.61 ± 0.07	–	–	15.56 ± 0.07	20.32	19.45	19.16	0.20
ZOA095027.441 − 432827.76	271.564	8.105	0.31	−36.61	2.35	17.18 ± 0.08	16.38 ± 0.06	15.66 ± 0.08	16.77 ± 0.15	16.16 ± 0.08	15.47 ± 0.09	20.86	19.87	18.91	0.20
ZOA095011.815 − 433553.96	271.608	7.980	0.38	−8.65	5.09	15.47 ± 0.04	14.86 ± 0.04	14.26 ± 0.06	13.97 ± 0.48	13.66 ± 0.29	13.49 ± 0.21	18.78	18.18	17.66	0.20
ZOA095023.052 − 433453.78	271.623	8.014	0.07	−29.32	2.11	17.57 ± 0.08	16.67 ± 0.05	16.05 ± 0.08	–	15.72 ± 0.29	15.83 ± 0.09	20.97	19.98	19.41	0.20
ZOA095021.056 − 433329.84	271.604	8.029	0.22	−78.68	2.37	17.46 ± 0.08	16.42 ± 0.05	15.55 ± 0.06	–	16.32 ± 0.06	14.70 ± 0.24	20.99	19.81	18.86	0.20
ZOA095020.575 − 432951.25	271.563	8.074	0.36	−67.83	2.87	17.86 ± 0.10	16.82 ± 0.06	16.16 ± 0.09	–	–	15.27 ± 0.21	20.62	19.83	19.02	0.20
ZOA094830.723 − 434050.21	271.425	7.721	0.27	1.91	2.49	16.97 ± 0.05	16.16 ± 0.04	15.53 ± 0.06	–	–	14.22 ± 0.31	20.09	19.26	18.61	0.23
ZOA094833.510 − 434126.74	271.438	7.719	0.09	−8.98	2.42	17.00 ± 0.06	16.19 ± 0.04	15.47 ± 0.06	–	–	15.32 ± 0.07	20.04	19.30	18.77	0.23
ZOA094823.329 − 434134.73	271.416	7.698	0.17	44.37	2.61	17.09 ± 0.06	16.15 ± 0.04	15.43 ± 0.06	–	–	14.67 ± 0.23	20.46	19.41	18.91	0.23
ZOA094835.447 − 434239.91	271.456	7.707	0.20	−34.82	2.22	17.96 ± 0.09	17.09 ± 0.06	16.29 ± 0.10	–	–	14.84 ± 0.26	20.87	20.08	19.16	0.23
ZOA094837.380 − 434052.61	271.441	7.734	0.29	−29.89	1.95	17.66 ± 0.07	16.79 ± 0.05	16.29 ± 0.10	–	–	13.79 ± 0.76	20.82	19.96	19.46	0.23
ZOA094827.809 − 434018.14	271.412	7.723	0.20	−87.16	2.04	18.11 ± 0.10	17.11 ± 0.07	16.30 ± 0.10	–	–	15.34 ± 0.33	21.39	20.44	19.85	0.23
ZOA094828.189 − 434302.97	271.443	7.688	0.45	−1.45	2.69	18.84 ± 0.16	17.44 ± 0.08	17.15 ± 0.19	–	–	16.81 ± 0.19	22.87	20.80	20.18	0.23
ZOA095108.707 − 434321.21	271.821	7.994	0.15	−18.84	4.67	15.31 ± 0.03	14.60 ± 0.03	14.11 ± 0.04	14.66 ± 0.20	13.67 ± 0.24	13.65 ± 0.13	18.69	18.01	17.53	0.21
ZOA095058.116 − 434142.76	271.779	7.994	0.34	67.95	2.83	18.29 ± 0.14	17.36 ± 0.10	16.32 ± 0.11	–	–	15.06 ± 0.29	21.58	20.36	19.38	0.21
ZOA095122.680 − 434214.55	271.842	8.035	0.44	72.30	5.24	15.74 ± 0.04	14.89 ± 0.03	14.26 ± 0.04	15.38 ± 0.16	14.46 ± 0.14	13.94 ± 0.06	19.18	18.34	17.68	0.21
ZOA095126.337 − 434204.95	271.849	8.044	0.38	71.44	2.56	17.04 ± 0.06	16.26 ± 0.05	15.71 ± 0.07	16.20 ± 0.25	15.51 ± 0.11	–	19.89	19.13	18.70	0.21
ZOA095126.753 − 433953.81	271.826	8.073	0.18	35.07	3.11	16.76 ± 0.06	16.12 ± 0.05	15.63 ± 0.08	15.26 ± 0.50	14.80 ± 0.39	15.29 ± 0.10	19.79	19.25	18.84	0.21
ZOA095117.077 − 433928.64	271.799	8.059	0.41	7.85	5.07	16.84 ± 0.07	16.28 ± 0.06	15.54 ± 0.09	16.45 ± 0.26	15.47 ± 0.20	–	19.75	19.35	18.48	0.21
ZOA095102.485 − 433902.87	271.760	8.037	0.28	22.18	6.82	14.76 ± 0.03	13.99 ± 0.02	13.55 ± 0.03	14.58 ± 0.08	13.80 ± 0.05	12.88 ± 0.19	18.36	17.59	17.14	0.21
ZOA095131.088 − 433627.72	271.800	8.125	0.45	−81.19	10.19	13.81 ± 0.02	13.09 ± 0.02	12.78 ± 0.03	13.11 ± 0.21	12.46 ± 0.17	12.25 ± 0.13	17.61	16.87	16.57	0.21
ZOA095109.711 − 433615.04	271.747	8.087	0.20	−9.00	3.25	16.90 ± 0.06	16.16 ± 0.05	15.82 ± 0.09	–	11.51 ± 1.41	15.28 ± 0.17	19.87	19.18	19.08	0.21
ZOA095101.247 − 433548.23	271.723	8.076	0.28	−50.77	3.73	16.44 ± 0.06	15.63 ± 0.04	15.08 ± 0.07	–	14.92 ± 0.19	14.57 ± 0.14	19.52	18.87	18.37	0.21
ZOA095103.002 − 433802.06	271.751	8.051	0.17	−80.46	3.34	16.75 ± 0.06	16.08 ± 0.04	15.49 ± 0.07	–	15.26 ± 0.22	14.51 ± 0.20	19.71	19.11	18.55	0.21
ZOA095049.641 − 433855.26	271.729	8.014	0.41	−38.10	3.50	15.35 ± 0.04	14.55 ± 0.03	14.20 ± 0.04	14.98 ± 0.11	12.52 ± 0.60	14.15 ± 0.05	18.62	17.86	17.58	0.21
ZOA094756.182 − 440216.72	271.577	7.381	0.29	−40.92	2.32	16.84 ± 0.05	16.55 ± 0.05	15.63 ± 0.07	–	12.80 ± 1.19	15.40 ± 0.11	19.99	19.64	18.94	0.26
ZOA094748.211 − 440156.24	271.555	7.370	0.37	−28.65	2.20	18.48 ± 0.12	17.38 ± 0.07	16.40 ± 0.10	–	16.35 ± 0.30	15.79 ± 0.17	21.29	20.42	19.52	0.26
ZOA094802.662 − 435939.67	271.563	7.427	0.23	−33.69	2.72	16.98 ± 0.05	16.24 ± 0.04	15.65 ± 0.06	–	14.34 ± 0.58	14.87 ± 0.29	20.25	19.19	18.88	0.26
ZOA094738.325 − 440052.07	271.520	7.365	0.39	61.49	3.36	17.95 ± 0.10	16.89 ± 0.06	16.08 ± 0.09	–	16.75 ± 0.08	–	*nan*	20.44	19.33	0.26
ZOA094744.974 − 435916.01	271.518	7.398	0.37	50.62	2.31	20.43 ± 0.52	19.95 ± 0.58	16.40 ± 0.10	–	–	16.23 ± 0.11	21.72	21.13	20.10	0.26
ZOA094749.824 − 435840.22	271.523	7.415	0.25	−12.60	2.48	18.10 ± 0.09	17.35 ± 0.07	16.53 ± 0.10	–	–	12.44 ± 1.18	21.28	20.42	19.58	0.26
ZOA094850.920 − 433235.74	271.383	7.866	0.18	23.78	3.02	16.96 ± 0.06	16.06 ± 0.04	15.55 ± 0.09	–	–	15.39 ± 0.09	19.89	19.09	18.66	0.22
ZOA094849.197 − 433542.31	271.412	7.823	0.24	55.16	2.98	16.18 ± 0.04	15.43 ± 0.03	14.96 ± 0.06	−18.32 ± 10.91	–	14.79 ± 0.08	19.39	18.64	18.24	0.22
ZOA094849.080 − 433530.66	271.410	7.825	0.09	−20.33	7.85	13.91 ± 0.02	13.12 ± 0.02	12.64 ± 0.03	13.48 ± 0.14	12.87 ± 0.06	12.35 ± 0.09	17.58	16.79	16.28	0.22
ZOA094844.660 − 433006.11	271.341	7.885	0.50	41.36	3.56	17.09 ± 0.07	16.33 ± 0.05	15.85 ± 0.10	15.83 ± 0.48	15.54 ± 0.18	–	20.04	19.30	18.81	0.22
ZOA094848.049 − 432952.96	271.347	7.895	0.13	−38.60	2.81	17.52 ± 0.08	16.64 ± 0.06	15.98 ± 0.10	–	–	15.76 ± 0.12	20.48	19.83	19.27	0.22
ZOA094836.585 − 432851.06	271.309	7.886	0.21	1.15	5.32	15.33 ± 0.04	14.53 ± 0.03	14.03 ± 0.05	14.96 ± 0.12	14.20 ± 0.05	–	18.77	17.97	17.48	0.22
ZOA094823.723 − 432947.62	271.289	7.849	0.51	25.54	4.76	15.07 ± 0.03	14.27 ± 0.02	13.86 ± 0.03	14.88 ± 0.06	14.02 ± 0.04	13.56 ± 0.06	18.50	17.69	17.29	0.22
ZOA094816.613 − 432915.57	271.267	7.842	0.41	−16.18	6.73	14.52 ± 0.03	14.12 ± 0.03	13.76 ± 0.04	–	12.31 ± 0.40	13.49 ± 0.07	18.07	17.63	17.28	0.22
ZOA094812.852 − 433019.21	271.269	7.821	0.12	22.65	2.88	16.86 ± 0.07	16.08 ± 0.05	15.32 ± 0.07	–	–	15.11 ± 0.10	19.97	19.37	18.64	0.22
ZOA094822.959 − 433016.65	271.292	7.841	0.23	71.62	2.35	17.76 ± 0.09	16.80 ± 0.06	16.00 ± 0.09	–	16.10 ± 0.18	14.82 ± 0.34	20.92	19.86	19.27	0.22
ZOA094837.261 − 433133.22	271.340	7.853	0.24	71.49	2.76	17.54 ± 0.08	16.72 ± 0.06	16.00 ± 0.09	13.05 ± 1.45	16.45 ± 0.10	13.86 ± 0.59	20.57	19.80	19.18	0.22
ZOA094752.781 − 435812.23	271.525	7.426	0.23	−35.10	2.75	15.66 ± 0.04	15.28 ± 0.04	14.43 ± 0.05	15.58 ± 0.05	15.05 ± 0.04	14.47 ± 0.05	19.15	18.59	18.04	0.25
ZOA094800.739 − 435646.13	271.528	7.460	0.20	−62.10	2.92	17.62 ± 0.09	16.97 ± 0.08	16.15 ± 0.12	–	–	–	20.18	19.75	19.20	0.25
ZOA094742.569 − 435049.21	271.421	7.501	0.09	−30.15	3.22	16.87 ± 0.06	16.09 ± 0.05	15.19 ± 0.06	–	–	14.29 ± 0.26	20.00	19.38	18.44	0.25
ZOA095018.956 − 441015.39	271.993	7.553	0.53	83.92	0.74	19.24 ± 0.29	18.23 ± 0.18	18.17 ± 0.70	–	–	10.17 ± 2.62	20.77	19.48	20.23	0.21
ZOA095026.460 − 435907.94	271.891	7.710	0.28	31.96	2.71	17.01 ± 0.10	16.23 ± 0.06	15.40 ± 0.11	15.65 ± 0.48	14.35 ± 0.49	10.50 ± 1.47	19.89	19.08	18.56	0.21
ZOA095017.812 − 440142.62	271.899	7.660	0.17	−22.68	3.21	16.55 ± 0.08	15.74 ± 0.05	15.04 ± 0.09	15.45 ± 0.36	15.22 ± 0.13	–	19.58	18.97	18.43	0.21
ZOA094826.986 − 435337.49	271.554	7.551	0.08	73.82	2.53	18.14 ± 0.08	17.31 ± 0.06	16.58 ± 0.10	–	16.79 ± 0.09	16.28 ± 0.12	21.06	20.31	19.74	0.23
ZOA094832.366 − 435401.61	271.571	7.556	0.21	64.56	1.70	18.07 ± 0.08	17.22 ± 0.06	16.67 ± 0.10	–	–	16.59 ± 0.10	21.19	20.33	20.32	0.23
ZOA094832.420 − 435558.06	271.592	7.531	0.21	60.88	1.74	18.47 ± 0.10	17.53 ± 0.07	16.84 ± 0.12	–	–	–	21.55	20.80	20.08	0.23
ZOA094833.472 − 435059.86	271.541	7.597	0.12	6.60	1.95	17.13 ± 0.05	16.33 ± 0.04	15.85 ± 0.06	–	–	15.16 ± 0.18	20.50	19.79	19.19	0.23
ZOA094847.721 − 435401.30	271.607	7.586	0.13	−47.36	2.23	18.27 ± 0.09	17.39 ± 0.07	16.42 ± 0.08	–	–	16.35 ± 0.09	21.26	20.87	19.68	0.23
ZOA094931.286 − 440814.91	271.861	7.488	0.14	−65.35	2.26	17.49 ± 0.07	16.70 ± 0.05	16.03 ± 0.09	–	–	12.92 ± 0.90	20.65	19.97	19.30	0.22
ZOA094934.904 − 440938.48	271.885	7.477	0.07	11.00	7.71	15.56 ± 0.04	14.84 ± 0.03	14.38 ± 0.06	14.38 ± 0.37	14.07 ± 0.22	13.92 ± 0.13	18.85	18.14	17.68	0.22
ZOA094920.465 − 441207.41	271.878	7.417	0.34	−51.05	1.94	17.59 ± 0.08	16.88 ± 0.06	16.35 ± 0.12	–	14.51 ± 0.68	−18.34 ± 10.85	20.10	19.39	19.34	0.22
ZOA094913.434 − 441139.52	271.857	7.410	0.14	−26.25	2.12	17.50 ± 0.07	16.67 ± 0.05	16.05 ± 0.09	–	–	15.99 ± 0.09	20.58	19.90	19.31	0.22
ZOA094919.391 − 440945.80	271.850	7.445	0.35	−79.58	2.90	17.55 ± 0.07	16.86 ± 0.06	16.01 ± 0.08	–	–	15.77 ± 0.10	20.94	20.19	19.34	0.22
ZOA094921.290 − 440911.02	271.848	7.456	0.37	55.22	2.14	17.97 ± 0.09	17.01 ± 0.06	16.21 ± 0.09	–	–	–	21.49	20.68	19.79	0.22
ZOA094925.830 − 440915.86	271.859	7.464	0.37	43.49	3.56	16.38 ± 0.04	15.57 ± 0.03	15.21 ± 0.05	–	–	15.05 ± 0.06	19.58	18.85	18.55	0.22
ZOA094918.249 − 440805.83	271.829	7.465	0.06	−9.74	3.47	16.21 ± 0.04	15.40 ± 0.03	14.78 ± 0.04	–	14.37 ± 0.28	14.36 ± 0.10	19.40	18.64	18.10	0.22

ZOA094908.460 − 440800.08	271.806	7.447	0.34	57.74	2.55	17.96 ± 0.09	16.95 ± 0.06	15.97 ± 0.08	–	16.40 ± 0.16	15.53 ± 0.11	20.89	19.99	18.81	0.22
ZOA094918.990 − 440613.48	271.811	7.490	0.33	72.31	2.82	16.88 ± 0.05	16.08 ± 0.04	15.56 ± 0.06	–	15.82 ± 0.09	15.34 ± 0.08	20.16	19.43	18.68	0.22
ZOA094900.879 − 440852.26	271.797	7.421	0.19	−18.41	2.95	16.82 ± 0.05	16.08 ± 0.04	15.31 ± 0.06	–	–	14.80 ± 0.14	20.21	19.47	18.73	0.22
ZOA094857.675 − 441222.46	271.828	7.370	0.58	−7.98	3.92	18.29 ± 0.18	17.52 ± 0.15	16.06 ± 0.16	–	15.57 ± 1.13	15.64 ± 0.19	22.35	20.65	19.62	0.22
ZOA094907.419 − 441053.32	271.834	7.408	0.25	−61.00	2.26	18.45 ± 0.12	17.40 ± 0.07	16.48 ± 0.10	–	–	15.41 ± 0.28	21.10	20.19	19.26	0.22
ZOA094901.680 − 441223.28	271.837	7.378	0.41	−26.27	1.96	17.70 ± 0.09	17.05 ± 0.08	16.01 ± 0.11	–	15.57 ± 0.32	14.12 ± 0.59	20.70	19.69	19.70	0.22
ZOA094858.586 − 440440.96	271.747	7.470	0.27	−56.83	2.19	17.91 ± 0.09	17.01 ± 0.06	16.34 ± 0.10	–	–	16.29 ± 0.11	21.45	20.48	20.03	0.24
ZOA094930.010 − 440032.50	271.775	7.584	0.45	31.96	4.75	15.19 ± 0.03	14.46 ± 0.03	14.11 ± 0.03	14.74 ± 0.12	13.67 ± 0.15	13.63 ± 0.14	18.53	17.75	17.52	0.24
ZOA094853.629 − 440301.93	271.718	7.482	0.48	5.25	3.15	18.40 ± 0.14	17.49 ± 0.10	16.29 ± 0.11	–	–	15.88 ± 0.12	21.63	20.77	19.27	0.24
ZOA094930.257 − 435826.67	271.753	7.611	0.32	47.64	9.26	13.76 ± 0.02	13.01 ± 0.02	12.67 ± 0.03	13.14 ± 0.19	12.66 ± 0.07	12.46 ± 0.04	17.54	16.77	16.42	0.24
ZOA094914.652 − 435757.12	271.712	7.587	0.56	9.94	2.62	16.37 ± 0.04	15.48 ± 0.03	15.00 ± 0.05	–	14.61 ± 0.21	14.80 ± 0.06	19.60	18.59	18.30	0.24
ZOA094914.390 − 435913.24	271.725	7.571	0.37	−82.74	6.79	14.89 ± 0.03	14.15 ± 0.02	13.80 ± 0.03	–	13.95 ± 0.05	13.02 ± 0.23	18.34	17.61	17.27	0.24
ZOA094902.423 − 440001.39	271.706	7.537	0.30	5.44	3.90	16.53 ± 0.05	15.66 ± 0.04	15.20 ± 0.06	16.16 ± 0.17	–	14.82 ± 0.09	19.65	18.81	18.40	0.24
ZOA094910.793 − 440040.70	271.732	7.545	0.28	18.49	3.38	15.98 ± 0.04	15.20 ± 0.03	14.66 ± 0.04	–	14.12 ± 0.33	14.61 ± 0.04	19.33	18.51	18.10	0.24
ZOA094911.353 − 440402.31	271.770	7.503	0.33	−11.38	6.82	14.90 ± 0.03	14.11 ± 0.02	13.56 ± 0.03	–	13.37 ± 0.22	13.39 ± 0.04	18.43	17.62	17.11	0.24
ZOA095013.689 − 433738.42	271.631	7.961	0.11	26.47	2.83	16.63 ± 0.04	15.80 ± 0.03	15.03 ± 0.04	–	14.74 ± 0.30	14.33 ± 0.20	19.62	18.97	18.36	0.20
ZOA095051.462 − 434032.36	271.750	7.997	0.30	−31.47	5.56	15.89 ± 0.03	15.11 ± 0.03	14.65 ± 0.04	15.10 ± 0.26	14.25 ± 0.23	14.35 ± 0.08	19.16	18.33	17.95	0.20
ZOA095030.509 − 434233.08	271.723	7.931	0.26	−75.58	1.98	18.21 ± 0.09	17.42 ± 0.06	16.48 ± 0.09	–	16.91 ± 0.17	16.35 ± 0.10	21.71	20.75	19.99	0.20
ZOA095009.356 − 433734.46	271.620	7.954	0.34	−40.83	2.45	17.89 ± 0.08	17.25 ± 0.06	16.59 ± 0.09	–	–	15.40 ± 0.28	20.98	20.79	19.55	0.20
ZOA095043.504 − 433634.96	271.689	8.032	0.28	50.24	2.33	17.52 ± 0.06	16.79 ± 0.05	16.00 ± 0.07	–	–	14.25 ± 0.56	20.71	19.86	18.82	0.20
ZOA095043.336 − 433639.42	271.690	8.031	0.08	−20.65	2.37	17.78 ± 0.07	17.10 ± 0.06	16.43 ± 0.08	–	–	11.45 ± 1.32	20.44	19.68	18.98	0.20
ZOA095034.119 − 433654.42	271.671	8.010	0.49	−33.90	3.02	18.30 ± 0.09	17.47 ± 0.07	16.98 ± 0.12	–	14.83 ± 0.56	15.79 ± 0.23	20.12	19.61	19.39	0.20
ZOA095044.645 − 433659.67	271.696	8.029	0.36	31.82	2.60	17.19 ± 0.05	16.48 ± 0.04	16.04 ± 0.06	–	–	15.05 ± 0.29	20.49	19.86	19.34	0.20
ZOA095045.750 − 433716.31	271.702	8.028	0.08	−34.99	2.72	17.52 ± 0.07	16.66 ± 0.05	15.99 ± 0.07	–	–	–	20.93	19.95	19.23	0.20
ZOA095034.150 − 434126.20	271.720	7.952	0.35	57.54	3.59	16.48 ± 0.04	15.70 ± 0.03	15.19 ± 0.05	–	15.14 ± 0.15	14.96 ± 0.06	19.78	18.92	18.55	0.20
ZOA094911.764 − 435744.92	271.703	7.584	0.25	−5.84	10.45	13.49 ± 0.02	12.75 ± 0.02	12.40 ± 0.03	13.10 ± 0.11	12.25 ± 0.10	11.72 ± 0.17	17.32	16.55	16.18	0.22
ZOA094927.200 − 435714.97	271.733	7.621	0.15	−5.27	4.42	15.22 ± 0.03	14.54 ± 0.03	14.10 ± 0.03	14.20 ± 0.33	14.01 ± 0.12	13.14 ± 0.23	18.59	17.90	17.45	0.22
ZOA094931.324 − 435139.01	271.683	7.700	0.62	−59.11	5.68	15.42 ± 0.03	14.51 ± 0.03	14.10 ± 0.03	15.28 ± 0.06	14.21 ± 0.07	13.99 ± 0.04	18.89	17.95	17.60	0.22
ZOA094930.144 − 435826.42	271.753	7.611	0.27	52.73	5.59	15.49 ± 0.03	14.88 ± 0.03	14.65 ± 0.04	13.02 ± 0.22	12.88 ± 0.04	–	17.48	16.78	16.44	0.22
ZOA094913.124 − 435607.42	271.688	7.608	0.54	59.02	4.19	16.22 ± 0.04	15.25 ± 0.03	14.86 ± 0.05	14.89 ± 0.49	14.33 ± 0.20	13.51 ± 0.29	19.35	18.48	18.10	0.22
ZOA094859.019 − 435640.08	271.662	7.574	0.54	−0.64	2.30	18.32 ± 0.12	17.33 ± 0.08	16.50 ± 0.11	–	–	16.27 ± 0.11	21.32	20.37	20.03	0.22
ZOA094855.740 − 435403.90	271.626	7.601	0.27	3.64	6.86	14.77 ± 0.03	14.05 ± 0.03	13.60 ± 0.03	–	13.43 ± 0.12	–	18.34	17.59	17.17	0.22
ZOA094932.173 − 435109.07	271.679	7.708	0.16	−1.99	4.44	15.49 ± 0.03	14.70 ± 0.03	14.31 ± 0.04	15.39 ± 0.07	13.59 ± 0.31	14.01 ± 0.07	18.91	18.06	17.65	0.22
ZOA094804.024 − 435319.85	271.498	7.510	0.18	−75.56	1.60	17.95 ± 0.07	17.18 ± 0.05	16.71 ± 0.11	–	–	13.66 ± 0.79	20.62	20.04	19.46	0.23
ZOA094817.799 − 435431.65	271.543	7.522	0.20	−67.03	3.43	16.44 ± 0.04	15.67 ± 0.03	14.95 ± 0.04	–	15.47 ± 0.08	14.53 ± 0.13	19.82	19.07	18.37	0.23
ZOA094815.588 − 435702.42	271.565	7.485	0.41	−44.52	2.06	18.47 ± 0.10	17.36 ± 0.06	16.46 ± 0.09	–	17.29 ± 0.06	16.42 ± 0.09	22.10	20.80	20.05	0.23
ZOA094804.636 − 435031.06	271.469	7.547	0.32	−75.56	2.96	17.15 ± 0.06	16.31 ± 0.04	15.45 ± 0.05	16.52 ± 0.27	–	14.69 ± 0.17	20.31	19.57	18.57	0.23
ZOA094822.698 − 435540.51	271.567	7.516	0.17	22.84	4.63	17.04 ± 0.05	16.20 ± 0.04	15.63 ± 0.06	13.76 ± 1.14	13.31 ± 0.52	13.70 ± 0.39	19.61	18.81	18.39	0.23
ZOA094859.865 − 435033.47	271.598	7.654	0.52	49.94	2.48	17.52 ± 0.08	16.90 ± 0.07	16.15 ± 0.10	–	–	15.70 ± 0.13	20.41	19.69	19.19	0.22
ZOA094911.193 − 435025.64	271.623	7.677	0.45	−18.77	2.25	18.22 ± 0.12	17.09 ± 0.07	16.36 ± 0.12	–	–	16.09 ± 0.11	21.50	20.27	19.22	0.22
ZOA094936.290 − 434657.80	271.644	7.770	0.37	−45.10	3.90	15.77 ± 0.04	15.02 ± 0.03	15.30 ± 0.10	–	13.82 ± 0.25	–	18.96	18.10	17.88	0.22
ZOA094933.510 − 434704.29	271.638	7.763	0.23	−25.82	3.89	15.19 ± 0.03	14.44 ± 0.03	14.13 ± 0.04	14.98 ± 0.08	14.30 ± 0.04	–	18.62	17.86	17.48	0.22
ZOA094855.672 − 434947.79	271.580	7.655	0.39	49.75	2.21	18.45 ± 0.14	17.58 ± 0.10	16.31 ± 0.10	–	–	16.15 ± 0.10	22.26	21.50	19.68	0.22
ZOA094917.049 − 434331.41	271.562	7.777	0.16	26.55	3.13	16.85 ± 0.06	16.12 ± 0.04	15.83 ± 0.10	–	14.96 ± 0.30	15.36 ± 0.14	19.77	19.12	19.10	0.22
ZOA094916.977 − 434901.08	271.621	7.706	0.69	−51.54	9.79	14.37 ± 0.02	13.59 ± 0.02	13.16 ± 0.03	13.93 ± 0.14	13.34 ± 0.05	12.96 ± 0.04	18.03	17.25	16.80	0.22
ZOA094916.884 − 434914.95	271.623	7.703	0.74	−9.31	2.05	18.30 ± 0.11	17.31 ± 0.07	16.49 ± 0.11	–	–	15.73 ± 0.20	21.09	20.23	19.40	0.22
ZOA094858.595 − 435013.63	271.591	7.655	0.41	−80.86	2.08	18.20 ± 0.12	17.15 ± 0.07	16.29 ± 0.11	–	–	16.19 ± 0.11	21.78	20.43	19.95	0.22
ZOA094919.988 − 434825.07	271.621	7.720	0.15	−44.90	1.44	17.93 ± 0.09	17.27 ± 0.07	17.26 ± 0.22	–	–	−15.20 ± 10.12	20.48	19.89	19.68	0.22
ZOA094915.236 − 434707.14	271.596	7.727	0.54	−35.43	9.27	15.05 ± 0.03	14.17 ± 0.02	13.65 ± 0.03	14.70 ± 0.10	–	12.89 ± 0.47	18.55	17.66	17.19	0.22
ZOA094922.304 − 434632.40	271.606	7.748	0.21	48.59	4.44	15.41 ± 0.03	14.65 ± 0.03	14.28 ± 0.04	14.60 ± 0.27	13.80 ± 0.25	13.92 ± 0.09	18.77	18.02	17.65	0.22
ZOA094914.958 − 434554.55	271.583	7.742	0.28	−80.66	2.92	17.53 ± 0.07	16.51 ± 0.05	15.78 ± 0.07	–	–	15.48 ± 0.10	21.01	20.06	18.98	0.22
ZOA094919.644 − 434448.69	271.582	7.765	0.09	−12.90	4.86	15.21 ± 0.03	14.44 ± 0.03	14.19 ± 0.04	13.31 ± 0.49	12.53 ± 0.27	13.45 ± 0.14	18.56	17.81	17.61	0.22
ZOA094900.812 − 434438.36	271.536	7.731	0.36	−47.87	2.11	17.63 ± 0.07	16.82 ± 0.05	16.33 ± 0.10	–	16.39 ± 0.08	15.31 ± 0.29	20.55	19.84	19.02	0.22
ZOA094928.140 − 434153.22	271.570	7.819	0.39	6.64	4.51	17.34 ± 0.08	16.42 ± 0.05	15.57 ± 0.08	–	–	15.30 ± 0.09	20.50	19.58	18.71	0.21
ZOA094854.832 − 434201.87	271.494	7.753	0.27	−49.70	2.68	17.29 ± 0.07	16.47 ± 0.05	15.81 ± 0.08	–	–	14.96 ± 0.25	20.60	19.72	18.97	0.21
ZOA094902.576 − 434247.85	271.520	7.758	0.26	1.89	2.39	17.94 ± 0.09	17.12 ± 0.06	16.54 ± 0.11	–	–	16.44 ± 0.12	21.09	20.03	20.07	0.21
ZOA094913.219 − 433634.42	271.478	7.858	0.28	−11.97	1.68	18.20 ± 0.12	17.09 ± 0.07	16.52 ± 0.14	–	–	16.45 ± 0.14	21.69	20.13	20.07	0.21
ZOA094914.888 − 433911.32	271.510	7.828	0.36	44.34	1.99	17.57 ± 0.07	17.04 ± 0.07	16.72 ± 0.15	–	16.63 ± 0.12	16.70 ± 0.15	20.56	20.00	20.12	0.21
ZOA094923.324 − 433907.57	271.529	7.845	0.05	−47.53	2.21	18.23 ± 0.11	17.16 ± 0.07	16.42 ± 0.11	–	–	15.46 ± 0.29	20.89	19.93	19.32	0.21
ZOA094918.801 − 433830.01	271.512	7.844	0.20	18.29	2.31	17.92 ± 0.09	17.16 ± 0.07	16.67 ± 0.13	–	–	–	21.05	20.52	20.87	0.21
ZOA094910.388 − 433904.20	271.498	7.821	0.08	−71.31	2.61	16.98 ± 0.06	16.16 ± 0.04	15.78 ± 0.07	–	15.77 ± 0.11	15.55 ± 0.09	20.21	19.48	19.09	0.21
ZOA094910.343 − 433711.79	271.478	7.845	0.09	−48.67	1.50	18.12 ± 0.10	17.40 ± 0.08	16.90 ± 0.16	–	–	15.48 ± 0.32	20.92	20.27	19.61	0.21

$ZOA094925.080-434046.69$	271.551	7.827	0.25	13.16	2.75	16.67 ± 0.05	15.90 ± 0.04	15.17 ± 0.05	–	–	14.41 ± 0.20	19.80	19.07	18.41	0.21
$ZOA094857.664-434136.62$	271.496	7.764	0.36	25.43	3.88	16.80 ± 0.05	15.87 ± 0.04	15.11 ± 0.05	–	13.52 ± 0.72	13.80 ± 0.32	19.73	18.91	18.25	0.21
$ZOA094913.271-434219.72$	271.540	7.785	0.26	87.90	3.50	17.64 ± 0.08	16.86 ± 0.06	15.90 ± 0.09	–	–	15.71 ± 0.10	20.65	19.91	19.38	0.21
$ZOA094914.088-434133.67$	271.534	7.796	0.02	−31.59	2.88	17.79 ± 0.09	16.79 ± 0.06	16.16 ± 0.10	–	16.23 ± 0.15	15.65 ± 0.11	20.41	19.75	19.01	0.21
$ZOA095023.867-433843.43$	271.666	7.967	0.42	9.03	1.91	18.03 ± 0.08	17.07 ± 0.06	16.28 ± 0.07	–	–	15.87 ± 0.14	21.97	20.66	19.60	0.20
$ZOA095010.523-433942.88$	271.646	7.929	0.55	−39.03	2.31	18.15 ± 0.08	17.09 ± 0.05	16.10 ± 0.07	–	–	15.42 ± 0.19	20.99	20.04	19.28	0.20
$ZOA095016.919-433959.04$	271.664	7.937	0.39	7.22	2.83	17.35 ± 0.06	16.65 ± 0.04	16.17 ± 0.07	–	–	15.79 ± 0.10	20.57	19.80	19.65	0.20
$ZOA095018.775-434109.93$	271.681	7.926	0.26	12.67	1.50	18.28 ± 0.09	17.38 ± 0.07	16.75 ± 0.11	–	–	16.70 ± 0.11	21.18	20.47	19.85	0.20
$ZOA095012.883-433628.72$	271.616	7.975	0.13	20.69	3.19	16.39 ± 0.04	15.77 ± 0.03	15.41 ± 0.05	–	14.71 ± 0.29	15.23 ± 0.06	19.59	18.89	18.66	0.20
$ZOA094948.643-433724.00$	271.570	7.916	0.24	59.59	2.17	18.09 ± 0.09	17.35 ± 0.07	16.41 ± 0.09	–	–	16.33 ± 0.10	21.11	20.81	20.08	0.20
$ZOA094954.999-433634.41$	271.576	7.939	0.25	59.56	2.61	17.87 ± 0.08	16.98 ± 0.05	16.30 ± 0.07	–	–	11.99 ± 1.30	20.75	19.92	19.12	0.20
$ZOA095023.232-433653.67$	271.645	7.989	0.17	−42.39	1.86	17.97 ± 0.08	17.23 ± 0.06	16.71 ± 0.10	–	–	16.66 ± 0.10	21.38	20.46	20.58	0.20
$ZOA094954.042-433930.31$	271.605	7.899	0.24	−81.53	3.21	17.76 ± 0.07	16.97 ± 0.05	15.90 ± 0.08	–	–	15.61 ± 0.10	20.93	19.97	19.25	0.20
$ZOA094954.584-433924.09$	271.605	7.902	0.28	60.47	2.10	18.07 ± 0.08	17.28 ± 0.06	16.36 ± 0.09	–	15.98 ± 0.30	16.32 ± 0.10	20.92	20.01	19.43	0.20
$ZOA095008.875-434238.73$	271.673	7.888	0.03	−71.49	2.38	17.83 ± 0.07	17.43 ± 0.07	15.64 ± 0.07	–	–	15.02 ± 0.16	20.70	20.77	18.43	0.20
$ZOA094858.076-433604.90$	271.437	7.835	0.34	−43.99	2.88	17.89 ± 0.12	17.20 ± 0.09	16.01 ± 0.10	–	–	15.74 ± 0.11	21.02	21.68	19.00	0.21
$ZOA094934.863-433204.14$	271.480	7.958	0.56	−80.76	2.58	17.29 ± 0.08	17.43 ± 0.13	15.51 ± 0.09	15.88 ± 0.51	11.84 ± 2.58	14.22 ± 0.28	20.30	20.27	18.48	0.21
$ZOA094929.343-433043.53$	271.452	7.964	0.12	25.36	2.39	18.03 ± 0.10	17.10 ± 0.06	16.48 ± 0.11	–	–	16.41 ± 0.12	21.25	20.32	19.14	0.21
$ZOA094922.662-433452.85$	271.482	7.898	0.43	−63.64	4.12	17.14 ± 0.07	16.36 ± 0.05	15.59 ± 0.08	–	15.44 ± 0.26	14.28 ± 0.28	20.31	19.41	18.62	0.21
$ZOA094929.656-433322.08$	271.482	7.931	0.60	−18.18	2.75	17.82 ± 0.09	17.06 ± 0.07	16.58 ± 0.14	16.45 ± 0.39	15.60 ± 0.18	15.14 ± 0.25	20.20	19.33	19.13	0.21
$ZOA094914.717-433315.86$	271.446	7.903	0.25	−32.14	2.17	18.06 ± 0.10	16.92 ± 0.06	16.26 ± 0.09	–	–	15.42 ± 0.18	20.87	19.69	19.34	0.21
$ZOA094920.804-433248.19$	271.455	7.921	0.26	−6.28	2.44	17.13 ± 0.06	16.35 ± 0.04	15.64 ± 0.07	13.38 ± 1.20	–	–	19.84	19.25	18.79	0.21
$ZOA094856.000-433525.28$	271.425	7.839	0.46	−49.31	2.04	18.87 ± 0.20	17.39 ± 0.09	16.42 ± 0.12	–	–	–	21.94	20.23	19.95	0.21
$ZOA094904.053-433144.85$	271.404	7.902	0.19	−26.34	3.09	17.08 ± 0.06	16.25 ± 0.04	15.50 ± 0.06	–	16.25 ± 0.04	15.59 ± 0.07	20.44	19.61	18.78	0.21
$ZOA094924.169-432904.13$	271.422	7.975	0.63	60.04	2.98	17.95 ± 0.10	17.84 ± 0.13	16.61 ± 0.14	–	–	16.41 ± 0.17	20.95	20.62	19.59	0.21
$ZOA094856.435-432939.16$	271.364	7.914	0.23	23.77	2.38	18.65 ± 0.21	17.15 ± 0.07	16.60 ± 0.12	–	–	16.49 ± 0.13	21.65	19.96	19.38	0.21
$ZOA094856.880-433322.67$	271.405	7.867	0.28	27.04	2.58	18.43 ± 0.13	17.37 ± 0.08	16.69 ± 0.12	–	–	–	21.08	20.40	19.72	0.21
$ZOA095007.961-440744.32$	271.941	7.564	0.21	−9.53	2.62	17.40 ± 0.07	16.59 ± 0.05	15.79 ± 0.08	–	–	15.07 ± 0.20	20.73	19.85	19.43	0.21
$ZOA094953.628-440510.56$	271.880	7.570	0.48	16.06	3.08	17.54 ± 0.09	16.79 ± 0.07	15.86 ± 0.10	–	–	15.51 ± 0.11	20.30	19.62	18.88	0.21
$ZOA095008.642-440716.15$	271.937	7.572	0.37	−23.66	1.99	17.70 ± 0.09	16.95 ± 0.06	16.14 ± 0.10	–	–	–	20.95	20.27	19.50	0.21
$ZOA094956.060-440934.52$	271.933	7.518	0.36	4.91	6.84	14.26 ± 0.02	13.54 ± 0.02	13.14 ± 0.03	13.94 ± 0.10	12.92 ± 0.17	12.45 ± 0.19	17.80	17.08	16.68	0.21
$ZOA094954.336-441111.13$	271.946	7.494	0.51	13.37	3.30	16.52 ± 0.05	15.62 ± 0.03	15.14 ± 0.06	16.11 ± 0.16	15.44 ± 0.04	14.26 ± 0.23	19.79	18.94	18.39	0.21
$ZOA094956.214-441111.27$	271.951	7.498	0.37	−84.85	3.50	17.23 ± 0.07	16.50 ± 0.05	15.63 ± 0.08	–	16.32 ± 0.08	14.52 ± 0.27	20.46	19.76	18.81	0.21
$ZOA094943.115-441000.82$	271.908	7.488	0.22	2.00	2.71	17.44 ± 0.07	16.63 ± 0.05	15.98 ± 0.09	–	16.15 ± 0.11	15.01 ± 0.22	20.31	19.72	18.89	0.21
$ZOA095003.644-440946.27$	271.953	7.530	0.94	−36.64	5.69	18.24 ± 0.15	17.43 ± 0.10	15.99 ± 0.10	–	–	15.66 ± 0.14	21.16	20.30	19.20	0.21
$ZOA094932.429-441215.61$	271.907	7.438	0.54	−31.80	3.73	17.05 ± 0.09	16.24 ± 0.06	15.70 ± 0.14	–	15.60 ± 0.21	14.77 ± 0.31	20.26	19.45	19.11	0.21
$ZOA094933.175-441121.93$	271.899	7.451	0.26	63.58	0.78	18.47 ± 0.15	17.48 ± 0.09	17.22 ± 0.25	–	15.69 ± 0.61	–	20.86	20.13	19.98	0.21
$ZOA094940.267-440914.45$	271.893	7.492	0.56	−72.25	2.19	18.12 ± 0.10	17.51 ± 0.08	17.28 ± 0.22	–	–	15.46 ± 0.39	20.84	20.04	19.68	0.21
$ZOA095002.003-440738.52$	271.926	7.554	0.34	53.08	1.85	17.75 ± 0.08	16.95 ± 0.06	16.50 ± 0.11	–	15.30 ± 0.44	13.14 ± 0.82	20.33	19.65	18.98	0.21
$ZOA094953.548-440507.58$	271.879	7.570	0.19	51.26	2.26	17.32 ± 0.07	16.89 ± 0.07	16.30 ± 0.13	–	14.98 ± 0.50	14.95 ± 0.26	19.98	19.70	18.93	0.21
$ZOA094948.795-440220.54$	271.838	7.597	0.58	−44.73	12.09	13.33 ± 0.02	12.57 ± 0.02	12.21 ± 0.02	13.20 ± 0.04	12.45 ± 0.03	12.24 ± 0.04	17.15	16.39	16.02	0.21
$ZOA094948.437-440255.89$	271.844	7.588	0.18	37.22	6.95	14.64 ± 0.03	13.91 ± 0.02	13.56 ± 0.03	13.64 ± 0.26	13.23 ± 0.08	12.89 ± 0.09	18.33	17.60	17.23	0.21
$ZOA094954.261-440400.46$	271.869	7.586	0.24	−3.96	3.86	16.53 ± 0.05	15.81 ± 0.04	15.22 ± 0.06	–	14.95 ± 0.26	–	19.78	19.03	18.57	0.21
$ZOA094937.352-435842.67$	271.773	7.621	0.08	11.59	7.08	13.91 ± 0.02	13.15 ± 0.02	12.74 ± 0.02	13.62 ± 0.09	12.94 ± 0.04	12.26 ± 0.12	17.51	16.75	16.34	0.21
$ZOA094941.161-435903.64$	271.785	7.624	0.48	18.39	5.69	14.55 ± 0.03	13.80 ± 0.02	13.45 ± 0.03	14.11 ± 0.13	13.62 ± 0.04	–	18.00	17.27	16.92	0.21
$ZOA094953.131-440110.17$	271.836	7.620	0.57	−37.71	2.62	17.09 ± 0.06	16.37 ± 0.04	16.20 ± 0.09	–	14.22 ± 0.40	12.36 ± 1.00	18.55	18.43	18.68	0.21
$ZOA094936.297-435149.68$	271.696	7.707	0.11	−28.14	4.67	14.56 ± 0.03	13.80 ± 0.02	13.41 ± 0.03	13.56 ± 0.30	13.34 ± 0.10	12.66 ± 0.18	17.96	17.20	16.81	0.21
$ZOA094948.687-435211.54$	271.729	7.727	0.59	−49.37	7.77	14.26 ± 0.02	13.29 ± 0.02	12.78 ± 0.02	13.33 ± 0.29	12.57 ± 0.17	12.68 ± 0.03	17.86	16.89	16.36	0.21
$ZOA094952.046-435657.59$	271.788	7.672	0.23	−14.60	3.54	17.11 ± 0.07	16.05 ± 0.05	15.37 ± 0.07	–	14.93 ± 0.34	14.46 ± 0.23	20.55	19.25	18.53	0.21
$ZOA094955.170-435647.14$	271.793	7.680	0.12	−74.47	2.41	17.70 ± 0.09	16.82 ± 0.07	15.90 ± 0.08	–	–	15.70 ± 0.10	20.89	19.97	19.42	0.21
$ZOA094930.653-434630.41$	271.626	7.765	0.16	43.47	9.44	13.41 ± 0.02	12.67 ± 0.02	12.30 ± 0.03	13.02 ± 0.12	12.00 ± 0.18	11.86 ± 0.12	17.14	16.38	16.00	0.22
$ZOA094936.390-434657.44$	271.644	7.770	0.40	−43.62	4.12	15.56 ± 0.03	14.77 ± 0.03	14.36 ± 0.04	–	13.76 ± 0.28	12.55 ± 0.52	18.90	18.14	17.72	0.22
$ZOA094934.199-434742.00$	271.647	7.756	0.44	−59.95	4.46	14.97 ± 0.03	14.18 ± 0.02	13.87 ± 0.03	14.55 ± 0.13	13.13 ± 0.28	13.52 ± 0.08	18.36	17.57	17.27	0.22
$ZOA094935.251-434449.68$	271.618	7.795	0.33	83.52	3.51	17.96 ± 0.12	16.79 ± 0.07	15.93 ± 0.09	17.44 ± 0.24	16.17 ± 0.23	15.65 ± 0.10	21.71	20.11	19.23	0.22
$ZOA095000.290-434514.06$	271.681	7.838	0.30	11.64	2.36	18.67 ± 0.15	17.77 ± 0.11	17.19 ± 0.18	–	16.03 ± 0.15	–	20.54	19.69	19.66	0.22
$ZOA094955.736-434706.95$	271.691	7.805	0.23	−17.64	4.04	16.53 ± 0.05	15.75 ± 0.04	15.35 ± 0.07	–	14.64 ± 0.28	14.64 ± 0.15	19.63	18.87	18.54	0.22
$ZOA094959.749-434815.85$	271.712	7.798	0.17	13.07	3.41	16.54 ± 0.05	15.80 ± 0.04	15.05 ± 0.05	–	–	14.22 ± 0.20	19.83	19.16	18.29	0.22
$ZOA094941.169-434919.46$	271.680	7.749	0.18	34.59	4.13	16.60 ± 0.05	15.76 ± 0.04	15.08 ± 0.06	–	15.53 ± 0.06	14.78 ± 0.11	19.84	19.05	18.45	0.22
$ZOA094937.379-434940.12$	271.675	7.737	0.49	−13.03	4.49	15.88 ± 0.04	15.15 ± 0.03	15.27 ± 0.07	15.31 ± 0.18	14.32 ± 0.26	14.85 ± 0.10	19.14	18.40	18.50	0.22
$ZOA095003.244-433843.68$	271.618	7.927	0.59	−49.04	7.74	15.04 ± 0.03	14.27 ± 0.03	13.93 ± 0.04	14.08 ± 0.29	13.90 ± 0.06	13.55 ± 0.07	18.71	17.93	17.56	0.20
$ZOA094955.267-433936.68$	271.609	7.900	0.17	−79.77	3.18	16.86 ± 0.06	16.02 ± 0.04	15.38 ± 0.07	15.77 ± 0.41	15.21 ± 0.18	13.92 ± 0.28	19.77	19.09	18.28	0.20
$ZOA094958.984-434044.20$	271.630	7.893	0.12	89.00	2.50	17.70 ± 0.09	16.75 ± 0.06	15.97 ± 0.09	–	–	15.95 ± 0.09	20.86	19.86	18.99	0.20

$ZOA095002.233-434113.16$	271.642	7.893	0.18	−13.62	2.90	17.09 ± 0.07	16.31 ± 0.05	15.62 ± 0.08	–	15.62 ± 0.23	15.26 ± 0.14	20.27	19.53	18.83	0.20
$ZOA094933.159-433912.50$	271.553	7.863	0.19	56.49	3.42	17.20 ± 0.08	16.19 ± 0.05	15.48 ± 0.08	17.10 ± 0.11	–	14.62 ± 0.15	20.17	19.15	18.55	0.20
$ZOA094956.821-433903.24$	271.606	7.911	0.13	6.52	3.21	17.61 ± 0.09	16.67 ± 0.06	15.80 ± 0.08	12.87 ± 1.48	–	15.36 ± 0.12	20.65	19.86	19.06	0.20
$ZOA094934.652-433202.60$	271.479	7.958	0.45	−56.30	3.91	16.28 ± 0.05	15.61 ± 0.04	14.62 ± 0.05	15.34 ± 0.33	15.41 ± 0.07	14.38 ± 0.07	19.62	18.92	17.96	0.20
$ZOA095010.785-433239.72$	271.570	8.019	0.25	−44.09	2.90	17.45 ± 0.10	16.75 ± 0.08	16.11 ± 0.14	–	–	15.84 ± 0.14	21.01	20.15	19.60	0.20
$ZOA095009.102-433432.90$	271.587	7.992	0.41	−72.85	3.45	16.83 ± 0.06	16.20 ± 0.05	15.49 ± 0.08	–	16.18 ± 0.05	14.49 ± 0.25	20.05	19.55	18.66	0.20
$ZOA094958.780-433526.16$	271.572	7.961	0.52	−47.05	2.28	17.89 ± 0.10	16.95 ± 0.07	16.28 ± 0.11	17.77 ± 0.15	–	15.26 ± 0.24	20.93	20.22	19.36	0.20
$ZOA094951.231-433317.77$	271.531	7.974	0.50	70.75	5.73	15.55 ± 0.03	14.66 ± 0.03	14.10 ± 0.04	15.21 ± 0.14	–	13.14 ± 0.28	19.01	18.11	17.56	0.20
$ZOA095008.756-433352.11$	271.579	8.000	0.32	−48.91	3.31	17.60 ± 0.10	16.59 ± 0.07	15.80 ± 0.10	–	–	15.36 ± 0.13	20.55	19.68	19.01	0.20
$ZOA094949.711-433210.87$	271.516	7.985	0.20	−1.73	4.69	16.78 ± 0.06	15.91 ± 0.04	15.50 ± 0.07	15.84 ± 0.29	–	14.43 ± 0.25	20.06	19.13	18.80	0.20
$ZOA094947.233-433117.77$	271.501	7.991	0.44	−6.86	4.34	17.04 ± 0.07	16.04 ± 0.04	15.64 ± 0.08	16.94 ± 0.13	–	14.15 ± 0.34	20.15	19.01	18.63	0.20
$ZOA095010.915-433125.37$	271.557	8.036	0.20	−43.19	2.82	17.18 ± 0.08	16.20 ± 0.05	15.47 ± 0.08	–	–	15.07 ± 0.12	20.50	19.25	18.59	0.20
$ZOA095009.135-433135.07$	271.555	8.030	0.16	26.84	2.54	17.98 ± 0.12	17.14 ± 0.09	16.28 ± 0.12	–	–	15.33 ± 0.26	20.75	19.90	19.08	0.20

Table A.0.6: VC11 catalogue of galaxies

Designation	ℓ (deg)	b (deg)	e_J	ϕ_J (deg)	r_{k20fe} (arcsec)	J_{k20fe} (mag)	H_{k20fe} (mag)	$K_{s_{k20fe}}$ (mag)	J_{tot} (mag)	H_{tot} (mag)	$K_{s_{tot}}$ (mag)	μ_J	μ_H (mag arcsec^{-2})	μ_{Ks}	$E(B-V)$ (mag)
$ZOA095459.417-440634.78$	272.610	8.130	0.08	49.58	2.45	17.01 ± 0.07	16.23 ± 0.05	15.61 ± 0.06	–	–	15.39 ± 0.07	20.21	19.50	18.71	0.28
$ZOA095450.287-440121.39$	272.534	8.181	0.52	−23.52	2.91	17.42 ± 0.09	16.77 ± 0.07	16.01 ± 0.08	–	–	15.01 ± 0.13	19.96	19.32	18.73	0.28
$ZOA095506.206-440734.49$	272.637	8.130	0.58	74.57	3.46	17.37 ± 0.11	16.81 ± 0.11	15.86 ± 0.09	12.76 ± 1.80	–	–	20.17	19.47	18.81	0.28
$ZOA095637.013-440610.96$	272.837	8.318	0.14	−37.19	2.33	17.88 ± 0.12	17.26 ± 0.10	16.17 ± 0.09	–	–	16.10 ± 0.10	21.49	21.05	19.72	0.22
$ZOA095617.827-440648.50$	272.798	8.274	0.36	−35.62	2.60	17.39 ± 0.08	16.54 ± 0.06	15.86 ± 0.07	–	–	–	20.29	19.60	19.27	0.22
$ZOA095629.152-440809.07$	272.839	8.277	0.19	11.23	2.87	16.31 ± 0.05	16.39 ± 0.07	15.29 ± 0.06	15.87 ± 0.12	15.54 ± 0.32	14.83 ± 0.13	19.44	18.89	18.49	0.22
$ZOA095614.008-440217.69$	272.742	8.325	0.21	−75.05	8.09	17.49 ± 0.11	16.66 ± 0.08	15.96 ± 0.10	–	15.29 ± 0.42	14.90 ± 0.16	20.42	19.67	18.89	0.22
$ZOA095447.882-441109.09$	272.631	8.049	0.19	−21.40	2.40	17.70 ± 0.07	17.00 ± 0.05	16.13 ± 0.06	–	–	14.12 ± 0.60	20.84	19.96	19.29	0.31
$ZOA095446.119-441438.63$	272.664	8.001	0.37	−37.71	2.37	18.04 ± 0.09	17.13 ± 0.06	16.37 ± 0.09	–	12.31 ± 1.48	–	20.60	19.85	19.67	0.31
$ZOA095416.052-440839.49$	272.530	8.022	0.56	15.88	2.22	17.45 ± 0.08	17.02 ± 0.07	16.09 ± 0.08	–	–	15.96 ± 0.08	21.13	19.87	19.49	0.31
$ZOA095629.329-435326.31$	272.685	8.470	0.11	22.52	3.68	15.53 ± 0.04	14.88 ± 0.03	14.63 ± 0.05	–	13.72 ± 0.31	13.51 ± 0.24	18.70	18.14	17.86	0.19
$ZOA095641.698-435554.57$	272.740	8.460	0.32	−16.89	2.42	17.41 ± 0.10	16.85 ± 0.09	17.40 ± 0.32	–	15.24 ± 0.27	15.45 ± 0.26	19.98	19.46	19.04	0.19
$ZOA095612.523-435549.94$	272.670	8.407	0.64	32.18	11.35	14.13 ± 0.02	13.41 ± 0.02	12.90 ± 0.03	13.21 ± 0.28	12.80 ± 0.17	12.28 ± 0.17	17.89	17.13	16.66	0.19
$ZOA095616.810-435608.75$	272.684	8.411	0.20	45.98	4.08	15.33 ± 0.03	14.55 ± 0.03	14.11 ± 0.03	14.87 ± 0.15	14.33 ± 0.05	14.04 ± 0.04	18.71	17.94	17.52	0.19
$ZOA095624.926-435543.00$	272.698	8.432	0.12	33.43	26.20	16.11 ± 0.06	15.67 ± 0.06	15.16 ± 0.10	–	–	14.36 ± 0.18	19.21	18.61	18.09	0.19
$ZOA095604.068-435555.52$	272.651	8.390	0.32	−44.20	3.06	16.73 ± 0.05	16.02 ± 0.04	15.45 ± 0.06	–	–	–	20.03	19.34	18.86	0.19
$ZOA095632.548-435724.80$	272.734	8.424	0.60	11.09	8.96	14.60 ± 0.03	13.97 ± 0.03	13.41 ± 0.03	14.24 ± 0.11	12.93 ± 0.30	13.14 ± 0.04	18.28	17.63	17.11	0.19
$ZOA095634.809-435916.04$	272.759	8.404	0.20	−85.32	2.52	17.21 ± 0.07	16.52 ± 0.05	16.05 ± 0.08	–	10.25 ± 1.87	–	19.99	19.35	19.14	0.19
$ZOA095441.139-441056.50$	272.613	8.039	0.53	52.66	4.13	17.88 ± 0.07	16.97 ± 0.06	16.20 ± 0.08	–	15.89 ± 0.31	14.14 ± 0.49	20.79	19.87	19.08	0.32
$ZOA095459.148-441208.26$	272.668	8.057	0.30	−0.07	2.24	18.58 ± 0.11	17.57 ± 0.08	16.43 ± 0.09	–	–	16.31 ± 0.09	22.16	20.87	19.62	0.32
$ZOA095458.092-441331.49$	272.680	8.037	0.16	−39.18	2.15	17.99 ± 0.08	17.00 ± 0.06	16.30 ± 0.09	–	–	15.94 ± 0.11	21.06	20.10	19.21	0.32
$ZOA095515.951-441108.09$	272.697	8.102	0.49	−62.80	4.79	16.39 ± 0.04	15.49 ± 0.03	14.82 ± 0.04	–	14.84 ± 0.18	14.26 ± 0.13	19.71	18.79	18.10	0.32
$ZOA095510.194-441001.41$	272.672	8.106	0.32	53.51	2.63	17.80 ± 0.07	17.03 ± 0.06	16.09 ± 0.07	–	–	15.74 ± 0.08	20.70	19.96	19.21	0.32
$ZOA095502.405-435206.05$	272.465	8.324	0.33	81.68	3.72	16.37 ± 0.05	15.50 ± 0.04	14.95 ± 0.04	16.18 ± 0.10	15.25 ± 0.08	13.88 ± 0.32	19.66	18.84	18.23	0.26
$ZOA095503.278-435203.44$	272.466	8.326	0.14	−72.97	4.10	15.64 ± 0.04	14.90 ± 0.03	14.39 ± 0.04	14.62 ± 0.31	14.32 ± 0.14	14.24 ± 0.04	18.93	18.21	17.78	0.26
$ZOA095512.322-435203.31$	272.488	8.343	0.20	−12.47	3.27	17.02 ± 0.07	16.12 ± 0.05	15.29 ± 0.06	–	–	15.12 ± 0.06	20.33	19.23	18.43	0.26
$ZOA095514.108-435200.32$	272.491	8.347	0.10	−16.86	3.94	15.17 ± 0.03	14.43 ± 0.03	14.06 ± 0.03	–	13.79 ± 0.14	13.11 ± 0.23	18.49	17.76	17.39	0.26
$ZOA095501.612-434917.18$	272.433	8.359	0.42	14.56	4.29	15.27 ± 0.03	14.61 ± 0.03	14.22 ± 0.03	–	13.85 ± 0.20	13.93 ± 0.06	18.59	17.91	17.60	0.26
$ZOA095516.459-434906.79$	272.467	8.389	0.46	−54.78	16.84	13.92 ± 0.03	13.52 ± 0.03	13.10 ± 0.03	13.29 ± 0.18	13.17 ± 0.08	12.76 ± 0.07	17.76	17.48	17.00	0.26
$ZOA095521.253-434714.77$	272.458	8.423	0.12	−26.84	0.88	18.53 ± 0.15	18.19 ± 0.17	17.79 ± 0.24	13.26 ± 1.29	–	10.35 ± 2.37	20.01	19.55	18.60	0.26
$ZOA095515.774-434940.76$	272.471	8.381	0.59	−3.53	3.37	16.41 ± 0.05	15.78 ± 0.05	15.58 ± 0.07	–	15.22 ± 0.13	–	19.62	18.99	18.77	0.26
$ZOA095506.329-435130.12$	272.468	8.339	0.07	66.30	2.78	17.08 ± 0.07	16.36 ± 0.06	15.79 ± 0.07	–	–	14.89 ± 0.27	20.47	19.58	19.01	0.26
$ZOA095611.620-435258.27$	272.638	8.443	0.20	20.46	4.45	15.70 ± 0.04	15.03 ± 0.03	14.58 ± 0.04	14.23 ± 0.48	12.74 ± 0.68	14.28 ± 0.15	18.96	18.34	17.90	0.20
$ZOA095622.435-434717.55$	272.604	8.537	0.03	55.86	2.16	17.57 ± 0.08	16.91 ± 0.07	16.48 ± 0.10	–	16.41 ± 0.09	15.74 ± 0.18	20.33	19.76	19.70	0.20
$ZOA095623.882-435228.45$	272.662	8.472	0.15	−44.04	3.48	15.85 ± 0.04	15.09 ± 0.03	14.56 ± 0.04	–	–	-9.45 ± 7.53	19.12	18.33	17.88	0.20
$ZOA095621.407-435206.74$	272.652	8.472	0.12	7.29	2.51	16.28 ± 0.04	15.66 ± 0.04	15.36 ± 0.05	–	–	–	19.31	18.78	18.52	0.20
$ZOA095607.236-435238.16$	272.624	8.439	0.39	73.04	5.35	14.62 ± 0.03	13.85 ± 0.02	13.38 ± 0.03	14.34 ± 0.09	13.29 ± 0.17	13.13 ± 0.06	18.07	17.32	16.83	0.20
$ZOA095607.744-435224.33$	272.623	8.443	0.14	25.66	3.71	15.54 ± 0.03	14.81 ± 0.03	14.34 ± 0.03	–	14.48 ± 0.10	14.26 ± 0.04	18.93	18.21	17.77	0.20
$ZOA095609.556-435051.35$	272.611	8.466	0.11	−78.31	2.09	17.81 ± 0.10	17.01 ± 0.08	16.03 ± 0.07	–	–	15.76 ± 0.09	21.05	20.21	19.27	0.20
$ZOA095607.551-435205.50$	272.619	8.446	0.36	−56.35	3.13	17.43 ± 0.09	16.74 ± 0.07	15.96 ± 0.08	–	16.49 ± 0.11	15.84 ± 0.09	20.67	19.99	19.36	0.20
$ZOA095603.647-435023.93$	272.592	8.461	0.05	2.53	2.29	17.81 ± 0.10	17.01 ± 0.08	16.08 ± 0.08	–	–	14.51 ± 0.39	20.92	19.54	19.09	0.20
$ZOA095618.059-434951.67$	272.621	8.495	0.41	−59.65	3.09	18.45 ± 0.17	17.29 ± 0.11	16.30 ± 0.10	–	16.54 ± 0.28	14.83 ± 0.39	21.23	20.33	19.28	0.20
$ZOA095623.466-434723.46$	272.608	8.537	0.22	−63.41	2.35	18.20 ± 0.13	17.09 ± 0.09	16.21 ± 0.08	–	15.55 ± 0.43	–	21.35	19.98	19.24	0.20
$ZOA095633.179-434802.32$	272.638	8.547	0.49	−57.47	2.62	17.55 ± 0.09	16.63 ± 0.07	15.87 ± 0.07	-17.22 ± 11.07	15.73 ± 0.32	15.68 ± 0.07	20.52	19.87	18.96	0.20
$ZOA095435.060-435820.98$	272.466	8.191	0.32	−85.53	5.67	14.60 ± 0.03	13.84 ± 0.02	13.45 ± 0.03	14.39 ± 0.06	12.95 ± 0.26	12.67 ± 0.23	18.04	17.31	16.91	0.31
$ZOA095411.175-435519.01$	272.378	8.186	0.57	80.57	6.63	15.39 ± 0.03	14.51 ± 0.03	13.97 ± 0.03	15.26 ± 0.06	13.80 ± 0.19	13.88 ± 0.03	18.84	17.98	17.44	0.31
$ZOA095401.287-435433.31$	272.346	8.177	0.10	−29.23	3.98	16.64 ± 0.08	15.95 ± 0.07	15.57 ± 0.09	16.30 ± 0.11	14.92 ± 0.25	–	19.57	18.98	18.67	0.31
$ZOA095413.046-435514.70$	272.381	8.190	0.34	−7.74	1.92	17.52 ± 0.08	16.85 ± 0.07	16.26 ± 0.09	–	–	–	20.46	19.88	19.65	0.31
$ZOA095406.013-435819.40$	272.397	8.137	0.40	51.99	3.46	17.09 ± 0.07	16.67 ± 0.07	15.77 ± 0.08	–	–	15.67 ± 0.08	20.38	19.91	18.96	0.31
$ZOA095403.359-435812.44$	272.390	8.134	0.21	9.08	2.47	18.05 ± 0.13	17.14 ± 0.09	16.37 ± 0.11	17.15 ± 0.34	–	15.45 ± 0.21	20.90	20.20	19.50	0.31
$ZOA095605.142-441131.69$	272.817	8.188	0.04	−52.91	2.23	18.52 ± 0.10	17.49 ± 0.07	16.44 ± 0.08	–	–	15.84 ± 0.15	21.94	20.62	19.66	0.26
$ZOA095442.924-435104.08$	272.408	8.301	0.42	−32.08	7.66	14.40 ± 0.03	13.69 ± 0.03	13.30 ± 0.03	13.89 ± 0.16	13.17 ± 0.14	12.88 ± 0.09	17.98	17.25	16.91	0.26
$ZOA095437.176-435247.51$	272.412	8.268	0.28	17.95	3.29	17.64 ± 0.11	16.57 ± 0.07	15.77 ± 0.08	–	–	15.19 ± 0.17	21.06	19.83	19.06	0.26
$ZOA095436.511-435042.08$	272.389	8.294	0.12	−27.29	8.06	13.97 ± 0.02	13.19 ± 0.02	12.73 ± 0.02	13.58 ± 0.14	12.94 ± 0.07	–	17.61	16.84	16.39	0.26
$ZOA095433.871-435122.61$	272.390	8.280	0.62	8.06	2.78	17.21 ± 0.07	16.57 ± 0.07	16.17 ± 0.09	16.66 ± 0.17	16.22 ± 0.07	15.51 ± 0.11	20.19	19.65	19.21	0.26
$ZOA095410.210-435054.97$	272.329	8.241	0.26	−28.17	2.11	17.74 ± 0.08	17.12 ± 0.07	16.57 ± 0.10	–	–	–	20.83	20.02	19.61	0.26

ZOA095412.669 − 435039.54	272.332	8.249	0.42	−27.78	2.38	18.03 ± 0.11	17.24 ± 0.09	16.53 ± 0.10	–	–	–	20.79	20.19	19.66	0.26
ZOA095430.876 − 434933.55	272.363	8.298	0.03	13.90	2.93	17.23 ± 0.07	16.54 ± 0.06	15.99 ± 0.07	–	15.78 ± 0.16	15.77 ± 0.08	19.82	19.41	19.18	0.26
ZOA095420.197 − 434813.81	272.324	8.295	0.61	29.48	2.48	17.64 ± 0.08	16.98 ± 0.07	16.55 ± 0.10	–	15.83 ± 0.19	15.36 ± 0.20	20.60	19.63	19.36	0.26
ZOA095430.607 − 434659.05	272.335	8.331	0.17	−61.13	2.24	17.90 ± 0.11	17.02 ± 0.08	15.88 ± 0.07	–	–	–	21.26	20.26	18.99	0.26
ZOA095518.512 − 434257.02	272.407	8.473	0.43	81.89	3.70	16.48 ± 0.07	15.61 ± 0.05	14.89 ± 0.06	–	15.16 ± 0.12	10.41 ± 1.35	19.63	18.85	18.16	0.22
ZOA095445.337 − 434522.75	272.353	8.379	0.32	10.63	8.45	13.76 ± 0.03	13.01 ± 0.02	12.60 ± 0.03	13.32 ± 0.15	12.49 ± 0.13	11.72 ± 0.24	17.43	16.70	16.28	0.22
ZOA095454.691 − 434431.69	272.367	8.408	0.43	−1.11	4.52	15.01 ± 0.03	14.30 ± 0.03	13.93 ± 0.04	14.92 ± 0.04	13.26 ± 0.30	13.79 ± 0.05	18.43	17.68	17.35	0.22
ZOA095510.489 − 434455.04	272.408	8.433	0.32	−56.80	3.78	16.73 ± 0.08	15.93 ± 0.06	15.08 ± 0.07	–	15.93 ± 0.06	14.69 ± 0.10	20.04	19.22	18.39	0.22
ZOA095617.774 − 434118.15	272.530	8.606	0.23	−41.99	2.54	17.30 ± 0.07	16.58 ± 0.06	16.33 ± 0.10	–	15.96 ± 0.13	16.11 ± 0.10	20.04	19.49	19.82	0.20
ZOA095640.307 − 434251.73	272.600	8.628	0.14	55.37	1.88	17.14 ± 0.07	16.52 ± 0.07	16.41 ± 0.12	–	–	16.39 ± 0.13	20.32	19.71	19.70	0.20
ZOA095618.140 − 434426.72	272.564	8.566	0.16	25.95	3.66	16.16 ± 0.04	15.48 ± 0.04	15.05 ± 0.05	14.17 ± 0.61	–	–	19.29	18.65	18.27	0.20
ZOA095607.004 − 434327.97	272.527	8.558	0.16	6.89	3.30	16.28 ± 0.04	15.56 ± 0.04	14.98 ± 0.04	–	15.37 ± 0.05	14.68 ± 0.07	19.59	18.92	18.28	0.20
ZOA095626.130 − 434221.99	272.561	8.608	0.94	15.47	4.23	17.75 ± 0.10	16.80 ± 0.07	16.01 ± 0.08	15.96 ± 0.87	–	14.33 ± 0.38	20.65	19.82	18.78	0.20
ZOA095620.944 − 434342.62	272.563	8.581	0.44	56.52	3.16	17.96 ± 0.12	16.75 ± 0.07	15.97 ± 0.08	–	–	14.85 ± 0.30	19.96	18.78	18.94	0.20
ZOA095627.459 − 434007.74	272.541	8.640	0.29	−72.51	9.04	16.82 ± 0.07	16.25 ± 0.06	15.77 ± 0.09	15.78 ± 0.26	15.25 ± 0.18	14.99 ± 0.12	19.67	19.05	18.64	0.20
ZOA095616.984 − 441116.38	272.843	8.214	0.10	14.01	2.13	17.51 ± 0.06	16.77 ± 0.05	16.58 ± 0.10	–	–	–	20.48	19.77	19.39	0.24
ZOA095556.122 − 440940.15	272.777	8.196	0.40	−5.37	2.87	16.83 ± 0.05	16.20 ± 0.04	15.82 ± 0.07	–	–	15.66 ± 0.07	19.98	19.46	19.04	0.24
ZOA095629.018 − 440820.34	272.840	8.275	0.12	−11.19	5.37	14.74 ± 0.03	13.99 ± 0.02	13.61 ± 0.03	14.04 ± 0.21	12.80 ± 0.32	13.26 ± 0.07	18.18	17.43	17.07	0.24
ZOA095626.269 − 441247.09	272.880	8.211	0.37	−33.14	2.30	18.15 ± 0.09	17.15 ± 0.06	16.30 ± 0.08	–	–	16.00 ± 0.08	21.07	20.10	19.19	0.24
ZOA095633.594 − 440943.97	272.866	8.265	0.34	14.41	2.60	17.43 ± 0.06	16.51 ± 0.05	15.80 ± 0.06	–	–	14.40 ± 0.32	20.42	19.57	18.76	0.24
ZOA095430.107 − 434556.52	272.323	8.343	0.58	10.27	3.71	16.17 ± 0.04	15.51 ± 0.04	15.02 ± 0.05	15.67 ± 0.14	14.50 ± 0.22	14.28 ± 0.12	19.45	18.66	18.18	0.24
ZOA095440.687 − 434307.18	272.319	8.400	0.12	65.15	2.79	16.97 ± 0.06	16.03 ± 0.05	15.19 ± 0.05	–	14.88 ± 0.28	–	19.95	19.09	18.19	0.24
ZOA095411.553 − 434503.40	272.270	8.320	0.49	76.16	4.78	15.46 ± 0.03	14.69 ± 0.03	14.20 ± 0.03	15.30 ± 0.07	13.62 ± 0.32	14.06 ± 0.04	18.86	18.11	17.63	0.24
ZOA095453.502 − 433936.02	272.312	8.470	0.22	3.49	3.09	16.64 ± 0.08	16.50 ± 0.12	15.65 ± 0.12	16.72 ± 0.07	15.56 ± 0.14	14.01 ± 0.48	20.09	19.11	19.08	0.25
ZOA095508.978 − 433621.79	272.314	8.541	0.16	−12.59	2.78	17.09 ± 0.08	18.79 ± 0.80	15.61 ± 0.09	16.28 ± 0.27	11.59 ± 2.09	15.47 ± 0.09	22.31	*nan*	19.17	0.25
ZOA095513.190 − 433222.16	272.282	8.601	0.23	−24.08	4.46	15.50 ± 0.04	14.73 ± 0.03	14.22 ± 0.04	14.45 ± 0.35	14.21 ± 0.14	13.44 ± 0.22	18.86	18.09	17.60	0.25
ZOA095513.734 − 433814.16	272.345	8.526	0.32	−8.90	2.95	18.27 ± 0.15	17.39 ± 0.12	16.78 ± 0.15	–	15.18 ± 0.56	14.60 ± 0.38	20.64	19.69	19.13	0.25
ZOA095509.540 − 433842.44	272.340	8.512	0.32	2.34	3.08	17.46 ± 0.11	16.69 ± 0.09	15.94 ± 0.10	–	16.69 ± 0.09	15.76 ± 0.11	20.42	19.86	18.83	0.25
ZOA095501.168 − 433816.60	272.316	8.501	0.48	−19.71	2.21	18.37 ± 0.16	17.17 ± 0.10	16.42 ± 0.11	–	16.96 ± 0.10	15.98 ± 0.16	22.45	20.37	19.95	0.25
ZOA095542.346 − 440904.88	272.738	8.178	0.55	66.29	7.45	14.43 ± 0.03	13.62 ± 0.02	13.24 ± 0.03	14.17 ± 0.08	12.53 ± 0.31	12.14 ± 0.33	18.04	17.24	16.86	0.26
ZOA095534.399 − 441431.55	272.776	8.092	0.27	29.00	2.86	17.49 ± 0.08	16.66 ± 0.06	16.01 ± 0.09	–	–	14.23 ± 0.44	20.49	19.77	18.95	0.26
ZOA095542.429 − 441107.62	272.760	8.151	0.09	48.34	2.81	17.83 ± 0.10	16.70 ± 0.06	16.09 ± 0.09	–	–	16.01 ± 0.10	21.06	19.86	19.50	0.26
ZOA095540.573 − 441119.78	272.757	8.145	0.85	−30.90	3.91	17.25 ± 0.07	16.55 ± 0.06	15.81 ± 0.09	–	14.51 ± 0.61	–	19.93	19.40	18.72	0.26
ZOA095620.251 − 433354.22	272.458	8.707	0.26	−11.28	2.04	17.84 ± 0.07	17.19 ± 0.05	16.64 ± 0.10	–	–	15.05 ± 0.25	20.61	19.96	19.18	0.20
ZOA095640.799 − 433648.46	272.538	8.708	0.37	56.48	7.41	15.30 ± 0.03	14.66 ± 0.03	14.29 ± 0.04	14.87 ± 0.14	14.32 ± 0.06	13.83 ± 0.08	18.86	18.22	17.79	0.20
ZOA095653.900 − 433736.08	272.578	8.722	0.33	48.33	2.52	17.36 ± 0.06	16.53 ± 0.04	15.92 ± 0.06	–	–	–	20.05	19.35	19.00	0.20
ZOA095521.530 − 440239.37	272.621	8.223	0.50	1.58	3.01	17.36 ± 0.08	16.66 ± 0.07	15.77 ± 0.08	17.05 ± 0.14	16.22 ± 0.12	15.39 ± 0.12	20.37	19.97	19.20	0.28
ZOA095539.696 − 440403.74	272.679	8.238	0.35	75.44	3.36	16.09 ± 0.04	15.37 ± 0.03	14.75 ± 0.04	15.73 ± 0.11	14.83 ± 0.14	14.49 ± 0.07	19.33	18.64	18.15	0.28
ZOA095540.572 − 440451.39	272.689	8.230	0.23	−12.60	2.20	17.55 ± 0.07	16.74 ± 0.06	16.01 ± 0.08	–	16.41 ± 0.09	14.73 ± 0.29	20.61	19.92	19.21	0.28
ZOA095554.895 − 440516.61	272.728	8.251	0.29	−27.72	2.11	17.61 ± 0.08	16.83 ± 0.06	16.43 ± 0.11	–	15.82 ± 0.21	16.33 ± 0.12	20.61	19.73	19.59	0.28
ZOA095536.124 − 440511.99	272.682	8.217	0.46	−11.85	3.04	16.43 ± 0.04	15.88 ± 0.04	15.66 ± 0.07	16.31 ± 0.05	15.25 ± 0.17	13.64 ± 0.56	19.74	19.10	18.87	0.28
ZOA095540.776 − 440633.10	272.708	8.208	0.10	−3.62	2.64	16.56 ± 0.05	15.83 ± 0.04	15.16 ± 0.05	–	–	14.51 ± 0.18	19.87	19.16	18.51	0.28
ZOA095526.006 − 440710.39	272.679	8.172	0.16	−51.90	5.08	15.37 ± 0.03	14.64 ± 0.03	14.08 ± 0.03	14.16 ± 0.39	14.28 ± 0.09	13.61 ± 0.11	18.73	18.01	17.47	0.28
ZOA095719.973 − 440241.38	272.902	8.443	0.22	80.15	3.79	16.66 ± 0.06	16.29 ± 0.08	15.76 ± 0.11	13.52 ± 0.92	−17.43 ± 10.55	13.28 ± 0.75	19.45	19.05	18.55	0.18
ZOA095752.011 − 440050.25	272.959	8.527	0.37	52.42	2.37	18.22 ± 0.12	17.86 ± 0.16	16.81 ± 0.14	–	–	14.87 ± 0.36	20.72	20.41	19.40	0.18
ZOA095753.278 − 440320.36	272.988	8.496	0.65	50.98	0.90	19.09 ± 0.16	17.16 ± 0.06	18.75 ± 0.44	–	–	11.18 ± 2.43	20.75	19.51	19.98	0.18
ZOA095757.981 − 440319.86	272.999	8.505	0.42	−8.46	2.76	16.66 ± 0.05	15.99 ± 0.04	15.28 ± 0.05	15.73 ± 0.26	14.95 ± 0.27	–	19.67	19.04	18.23	0.18
ZOA095749.616 − 440417.81	272.989	8.477	0.02	−69.97	2.68	17.21 ± 0.06	16.56 ± 0.06	15.78 ± 0.06	–	–	–	20.15	19.69	18.77	0.18
ZOA095742.050 − 440552.50	272.988	8.442	0.51	86.09	2.74	17.02 ± 0.06	16.28 ± 0.04	15.91 ± 0.07	16.34 ± 0.16	15.69 ± 0.05	14.70 ± 0.32	20.02	19.32	19.14	0.18
ZOA095757.380 − 440549.37	273.024	8.471	0.51	−64.16	4.44	17.24 ± 0.07	16.52 ± 0.06	16.01 ± 0.08	–	–	13.35 ± 0.67	20.25	19.41	18.85	0.18
ZOA095744.941 − 440433.96	272.981	8.465	0.09	34.73	2.10	17.23 ± 0.06	16.80 ± 0.06	16.32 ± 0.08	–	15.80 ± 0.28	–	20.43	20.07	19.66	0.18
ZOA095645.405 − 433518.47	272.533	8.736	0.15	−3.80	2.19	18.45 ± 0.09	17.54 ± 0.06	16.55 ± 0.10	–	–	15.50 ± 0.30	21.26	20.61	19.29	0.20
ZOA095657.904 − 433530.71	272.565	8.757	0.39	63.88	2.32	18.11 ± 0.08	17.36 ± 0.06	16.93 ± 0.12	–	–	–	20.71	19.98	19.80	0.20
ZOA095650.139 − 433242.57	272.517	8.779	0.18	−50.93	1.95	18.54 ± 0.10	17.76 ± 0.07	16.65 ± 0.09	–	–	–	20.95	20.34	19.39	0.20
ZOA095651.701 − 433251.21	272.523	8.780	0.32	−46.28	2.68	17.04 ± 0.05	16.23 ± 0.04	15.59 ± 0.05	12.89 ± 1.33	15.90 ± 0.07	–	20.23	19.39	18.76	0.20
ZOA095712.584 − 433557.80	272.605	8.779	0.17	38.66	7.54	14.01 ± 0.02	13.26 ± 0.02	12.91 ± 0.02	13.31 ± 0.22	12.32 ± 0.26	11.87 ± 0.29	17.58	16.83	16.47	0.20
ZOA095711.976 − 433324.14	272.577	8.811	0.17	−6.50	3.21	17.05 ± 0.05	16.31 ± 0.04	15.58 ± 0.05	–	–	14.76 ± 0.18	20.21	19.51	18.67	0.20
ZOA095649.238 − 433233.99	272.514	8.779	0.20	42.38	4.47	14.80 ± 0.03	14.38 ± 0.02	14.20 ± 0.03	14.48 ± 0.10	14.07 ± 0.08	13.43 ± 0.21	18.18	17.77	17.58	0.20
ZOA095709.227 − 433153.47	272.555	8.826	0.13	−61.21	2.79	16.83 ± 0.05	16.13 ± 0.04	15.54 ± 0.05	–	–	15.16 ± 0.10	19.86	19.20	18.70	0.20
ZOA095722.883 − 435912.62	272.873	8.494	0.09	8.91	2.36	16.86 ± 0.05	16.12 ± 0.04	15.56 ± 0.06	–	15.97 ± 0.05	15.48 ± 0.06	20.04	19.24	18.92	0.17
ZOA095805.051 − 435428.47	272.924	8.634	0.59	−37.30	8.77	–	13.08 ± 0.02	12.71 ± 0.03	–	12.43 ± 0.20	*nan* ± 0.25	*nan*	16.89	16.73	0.17
ZOA095742.299 − 435333.71	272.860	8.604	0.45	42.44	2.11	17.98 ± 0.12	17.19 ± 0.10	16.64 ± 0.14	–	–	–	20.54	20.16	19.50	0.17

$ZOA095734.771-435540.63$	272.864	8.562	0.18	−41.67	2.34	16.91 ± 0.05	16.09 ± 0.04	15.49 ± 0.05	–	–	15.08 ± 0.11	20.08	19.22	18.75	0.17
$ZOA095731.101-435600.43$	272.859	8.551	0.46	56.66	4.63	15.50 ± 0.03	14.82 ± 0.03	14.44 ± 0.03	–	14.59 ± 0.06	14.31 ± 0.04	18.84	18.20	17.80	0.17
$ZOA095728.963-435716.35$	272.867	8.531	0.44	29.83	5.72	16.29 ± 0.04	15.64 ± 0.04	15.16 ± 0.06	16.07 ± 0.08	14.63 ± 0.29	–	19.55	18.89	18.35	0.17
$ZOA095727.244-435736.33$	272.866	8.523	0.13	−11.28	5.15	16.16 ± 0.04	15.54 ± 0.04	15.12 ± 0.06	–	14.23 ± 0.26	14.05 ± 0.17	19.20	18.65	18.25	0.17
$ZOA095726.697-435743.89$	272.866	8.520	0.24	78.95	6.63	14.90 ± 0.03	14.24 ± 0.03	13.83 ± 0.03	–	13.73 ± 0.11	–	18.48	17.81	17.41	0.17
$ZOA095731.090-435707.15$	272.870	8.537	0.40	−44.47	2.45	17.32 ± 0.07	16.54 ± 0.05	16.22 ± 0.08	–	16.06 ± 0.12	14.19 ± 0.49	20.17	19.65	18.95	0.17
$ZOA095756.098-435914.78$	272.952	8.555	0.18	−73.28	3.07	17.28 ± 0.08	16.63 ± 0.07	15.74 ± 0.07	–	–	14.86 ± 0.20	20.68	19.72	18.87	0.17
$ZOA095801.453-440029.56$	272.978	8.549	0.64	7.62	3.33	17.03 ± 0.08	16.44 ± 0.08	15.65 ± 0.08	–	16.36 ± 0.09	15.42 ± 0.10	20.30	19.93	18.92	0.17
$ZOA095757.962-435822.99$	272.948	8.570	0.43	41.99	2.63	18.41 ± 0.14	17.37 ± 0.10	16.71 ± 0.12	–	–	–	21.20	20.48	19.38	0.17
$ZOA095447.229-440028.87$	272.517	8.187	0.12	18.85	3.14	16.33 ± 0.04	15.55 ± 0.03	15.16 ± 0.04	–	–	15.06 ± 0.04	19.57	18.83	18.46	0.32
$ZOA095447.415-440001.56$	272.513	8.193	0.07	−40.33	1.99	18.14 ± 0.08	17.19 ± 0.05	16.33 ± 0.07	–	–	16.21 ± 0.08	21.31	20.27	19.29	0.32
$ZOA095452.643-440014.53$	272.528	8.200	0.15	−0.04	2.16	18.33 ± 0.09	17.50 ± 0.06	16.56 ± 0.09	–	–	–	21.54	20.64	19.67	0.32
$ZOA095443.196-435932.99$	272.498	8.191	0.06	−39.74	2.11	17.87 ± 0.07	18.32 ± 0.10	16.58 ± 0.09	–	–	16.13 ± 0.11	20.79	20.25	19.68	0.32
$ZOA095500.399-435833.01$	272.528	8.236	0.26	37.34	9.95	14.82 ± 0.03	14.02 ± 0.02	13.56 ± 0.03	13.87 ± 0.32	12.88 ± 0.32	12.92 ± 0.12	18.48	17.68	17.24	0.32
$ZOA095454.490-435644.61$	272.495	8.249	0.08	−31.92	2.46	17.92 ± 0.07	17.10 ± 0.05	16.20 ± 0.07	–	–	15.71 ± 0.07	21.24	20.45	19.13	0.32
$ZOA095430.211-435347.84$	272.407	8.241	0.13	84.93	2.63	18.43 ± 0.10	17.73 ± 0.07	16.72 ± 0.09	–	–	–	21.26	20.61	19.74	0.32
$ZOA095441.221-435328.67$	272.429	8.266	0.18	17.26	2.36	17.93 ± 0.07	17.17 ± 0.06	16.21 ± 0.07	–	–	16.00 ± 0.08	20.76	20.17	19.34	0.32
$ZOA095443.549-435419.48$	272.444	8.260	0.06	−3.87	2.07	18.09 ± 0.08	17.45 ± 0.06	16.93 ± 0.10	–	–	15.97 ± 0.15	20.82	20.15	19.54	0.32
$ZOA095436.706-435318.42$	272.417	8.260	0.56	76.10	2.17	18.72 ± 0.13	17.59 ± 0.07	16.81 ± 0.11	–	–	16.64 ± 0.12	21.77	20.38	19.69	0.32
$ZOA095435.390-435452.36$	272.430	8.237	0.20	−65.27	1.77	18.55 ± 0.11	17.68 ± 0.07	16.89 ± 0.11	–	–	16.89 ± 0.11	21.97	20.89	21.15	0.32
$ZOA095523.670-435202.86$	272.515	8.365	0.39	35.14	8.43	14.36 ± 0.03	13.58 ± 0.02	13.20 ± 0.03	14.23 ± 0.05	13.24 ± 0.08	13.02 ± 0.05	17.97	17.20	16.81	0.26
$ZOA095557.110-435203.54$	272.594	8.427	0.20	−20.18	2.19	17.49 ± 0.07	16.71 ± 0.05	16.49 ± 0.11	–	–	–	20.08	19.49	19.53	0.26
$ZOA095549.988-434634.69$	272.520	8.485	0.17	−47.39	3.75	15.51 ± 0.03	14.83 ± 0.03	14.53 ± 0.04	14.92 ± 0.16	14.52 ± 0.05	14.22 ± 0.08	18.78	18.12	17.88	0.26
$ZOA095551.781-434920.78$	272.553	8.453	0.24	1.35	3.47	17.50 ± 0.08	16.67 ± 0.06	15.79 ± 0.08	–	15.91 ± 0.24	15.45 ± 0.09	20.58	19.67	18.81	0.26
$ZOA095559.905-434831.34$	272.564	8.479	0.18	−2.11	1.68	17.65 ± 0.08	16.92 ± 0.07	16.11 ± 0.09	–	–	–	20.84	20.11	19.17	0.26
$ZOA095524.830-434945.60$	272.493	8.397	0.09	−24.11	3.15	15.86 ± 0.04	15.20 ± 0.03	14.74 ± 0.05	–	15.07 ± 0.04	–	19.25	18.60	18.11	0.26
$ZOA095531.499-434949.27$	272.510	8.408	0.22	87.54	2.13	17.85 ± 0.09	17.05 ± 0.07	16.45 ± 0.11	–	15.48 ± 0.39	16.43 ± 0.11	20.46	19.73	19.19	0.26
$ZOA095537.632-435015.20$	272.529	8.414	0.42	71.50	3.91	15.06 ± 0.03	14.37 ± 0.02	14.14 ± 0.03	14.76 ± 0.06	13.39 ± 0.26	13.04 ± 0.31	18.35	17.71	17.50	0.26
$ZOA095537.992-435047.08$	272.535	8.408	0.27	−60.14	11.80	13.22 ± 0.02	12.48 ± 0.02	12.14 ± 0.02	12.68 ± 0.17	11.97 ± 0.11	11.83 ± 0.06	17.09	16.34	15.99	0.26
$ZOA095528.186-434923.93$	272.497	8.408	0.13	−4.10	2.28	16.94 ± 0.05	16.25 ± 0.04	15.85 ± 0.07	–	15.79 ± 0.08	15.18 ± 0.20	19.96	19.27	19.08	0.26
$ZOA095558.119-435129.70$	272.591	8.437	0.08	49.94	2.81	17.92 ± 0.10	16.92 ± 0.07	15.94 ± 0.08	–	–	15.80 ± 0.09	21.20	20.16	19.08	0.26
$ZOA095600.945-435126.68$	272.597	8.442	0.69	−89.38	2.15	18.19 ± 0.11	17.60 ± 0.10	16.97 ± 0.17	15.44 ± 0.57	15.32 ± 0.19	12.70 ± 0.83	19.80	19.18	18.85	0.26
$ZOA095531.437-435001.35$	272.512	8.406	0.10	−17.75	1.51	18.28 ± 0.12	17.55 ± 0.10	16.87 ± 0.17	–	–	–	21.10	20.69	20.83	0.26
$ZOA095538.569-435136.92$	272.545	8.398	0.11	−73.74	5.31	15.31 ± 0.03	14.61 ± 0.03	14.26 ± 0.04	–	13.70 ± 0.14	12.89 ± 0.29	18.68	18.02	17.64	0.26
$ZOA095538.890-435143.25$	272.547	8.398	0.12	−9.07	6.33	14.72 ± 0.03	14.02 ± 0.02	13.59 ± 0.03	–	13.43 ± 0.19	12.88 ± 0.19	18.28	17.57	17.15	0.26
$ZOA095541.276-435218.69$	272.559	8.394	0.34	33.46	6.72	14.14 ± 0.02	13.36 ± 0.02	12.93 ± 0.02	13.67 ± 0.15	13.13 ± 0.06	12.28 ± 0.19	17.66	16.88	16.45	0.26
$ZOA095544.768-435214.93$	272.567	8.402	0.15	78.55	2.72	17.32 ± 0.07	16.62 ± 0.05	16.23 ± 0.10	–	16.02 ± 0.07	–	20.35	19.46	19.09	0.26
$ZOA095548.171-435214.73$	272.575	8.408	0.43	7.03	4.68	15.89 ± 0.04	15.04 ± 0.03	14.77 ± 0.05	15.50 ± 0.12	–	14.57 ± 0.06	19.15	18.32	18.11	0.26
$ZOA095529.519-435226.96$	272.533	8.370	0.42	22.61	2.74	17.00 ± 0.06	16.18 ± 0.04	15.80 ± 0.07	15.84 ± 0.34	15.67 ± 0.09	–	19.85	19.24	18.91	0.26
$ZOA095525.155-435253.79$	272.527	8.356	0.19	32.27	5.66	15.31 ± 0.03	14.61 ± 0.03	14.12 ± 0.04	14.60 ± 0.26	13.83 ± 0.24	13.76 ± 0.07	18.78	18.08	17.59	0.26
$ZOA095536.166-435246.29$	272.552	8.379	0.36	46.90	3.22	15.91 ± 0.04	15.26 ± 0.03	14.90 ± 0.04	–	15.02 ± 0.05	13.57 ± 0.35	19.13	18.54	18.11	0.26
$ZOA095556.346-435328.94$	272.607	8.407	0.54	−85.58	5.03	16.50 ± 0.05	15.80 ± 0.04	15.28 ± 0.08	13.27 ± 1.07	15.62 ± 0.06	14.98 ± 0.10	19.69	19.06	18.63	0.26
$ZOA095734.832-435310.50$	272.838	8.595	0.07	89.00	2.01	17.30 ± 0.07	16.44 ± 0.05	15.95 ± 0.07	–	–	–	20.44	19.66	19.15	0.17
$ZOA095758.119-435300.06$	272.892	8.641	0.45	−87.13	6.71	14.21 ± 0.02	13.47 ± 0.02	13.10 ± 0.03	13.68 ± 0.17	12.50 ± 0.29	13.00 ± 0.03	17.70	16.98	16.60	0.17
$ZOA095727.788-434756.31$	272.767	8.650	0.19	−58.08	4.16	15.77 ± 0.04	15.08 ± 0.03	14.60 ± 0.04	15.73 ± 0.05	14.90 ± 0.05	14.24 ± 0.06	19.14	18.42	17.90	0.17
$ZOA095748.534-434718.42$	272.810	8.697	0.18	42.67	1.83	17.61 ± 0.08	17.28 ± 0.09	16.22 ± 0.08	–	–	-14.79 ± 9.69	20.50	20.03	19.24	0.17
$ZOA095753.996-434826.98$	272.835	8.693	0.21	28.00	2.95	16.10 ± 0.04	15.38 ± 0.03	15.19 ± 0.04	–	15.12 ± 0.07	–	19.41	18.70	18.54	0.17
$ZOA095640.750-440047.52$	272.789	8.395	0.37	38.45	3.23	16.35 ± 0.06	15.91 ± 0.07	15.42 ± 0.09	15.72 ± 0.18	15.29 ± 0.17	14.59 ± 0.26	19.30	19.09	18.68	0.18
$ZOA095719.422-435954.42$	272.872	8.478	0.70	33.47	15.45	13.97 ± 0.03	13.24 ± 0.02	12.81 ± 0.03	13.79 ± 0.08	13.01 ± 0.06	12.09 ± 0.19	17.85	17.12	16.70	0.18
$ZOA095717.424-435802.29$	272.848	8.499	0.22	55.95	2.44	17.26 ± 0.07	16.52 ± 0.06	16.06 ± 0.08	–	–	15.88 ± 0.09	20.35	19.60	19.25	0.18
$ZOA095638.290-435922.62$	272.769	8.409	0.39	43.39	3.28	16.85 ± 0.08	16.07 ± 0.06	15.67 ± 0.10	16.83 ± 0.08	15.24 ± 0.24	15.46 ± 0.14	20.29	19.23	18.86	0.18
$ZOA095648.115-435413.32$	272.738	8.494	0.43	−28.02	2.97	16.00 ± 0.04	15.38 ± 0.04	14.98 ± 0.05	15.52 ± 0.15	15.05 ± 0.07	14.26 ± 0.19	19.37	18.62	18.33	0.18
$ZOA095649.319-435413.89$	272.741	8.497	0.42	−19.20	2.49	16.90 ± 0.06	16.17 ± 0.05	15.69 ± 0.07	–	15.35 ± 0.21	14.64 ± 0.27	20.10	19.35	18.87	0.18
$ZOA095652.282-435942.90$	272.805	8.430	0.19	−59.63	3.94	15.89 ± 0.04	15.21 ± 0.04	14.72 ± 0.04	15.39 ± 0.19	15.13 ± 0.04	14.47 ± 0.06	19.26	18.60	18.03	0.18
$ZOA095713.725-435956.15$	272.859	8.467	0.57	55.40	10.37	13.93 ± 0.02	13.27 ± 0.02	12.77 ± 0.02	12.33 ± 0.49	12.68 ± 0.14	12.34 ± 0.09	17.64	16.93	16.45	0.18
$ZOA095648.222-435748.74$	272.776	8.448	0.52	−4.95	4.63	16.08 ± 0.04	15.24 ± 0.04	14.72 ± 0.04	–	–	13.87 ± 0.20	19.43	18.59	18.00	0.18
$ZOA095706.801-435742.96$	272.819	8.484	0.49	−27.80	5.24	15.23 ± 0.03	14.60 ± 0.03	14.16 ± 0.03	–	–	13.80 ± 0.07	18.61	18.03	17.57	0.18
$ZOA095650.328-435714.92$	272.775	8.459	0.17	−1.01	6.18	14.33 ± 0.03	13.61 ± 0.02	13.22 ± 0.03	13.91 ± 0.14	13.36 ± 0.06	12.70 ± 0.15	17.85	17.13	16.75	0.18
$ZOA095657.114-435657.69$	272.788	8.475	0.43	−10.02	6.44	14.31 ± 0.03	13.57 ± 0.02	13.23 ± 0.03	13.61 ± 0.22	13.05 ± 0.08	12.53 ± 0.17	17.80	17.04	16.72	0.18
$ZOA095646.716-435623.94$	272.757	8.463	0.17	−62.35	13.65	12.78 ± 0.02	12.13 ± 0.02	11.76 ± 0.02	12.45 ± 0.08	11.09 ± 0.29	11.59 ± 0.03	16.95	16.25	15.87	0.18
$ZOA095645.568-435607.25$	272.752	8.465	0.28	11.81	4.17	15.35 ± 0.03	14.62 ± 0.03	14.11 ± 0.03	–	–	–	18.75	18.00	17.49	0.18
$ZOA095653.292-435607.60$	272.770	8.479	0.07	−2.49	11.04	12.88 ± 0.02	12.26 ± 0.02	11.84 ± 0.02	12.10 ± 0.23	11.87 ± 0.10	11.60 ± 0.05	16.78	16.11	15.71	0.18

ZOA095704.282 − 435629.28	272.800	8.495	0.23	−53.18	3.76	16.47 ± 0.05	15.83 ± 0.04	15.35 ± 0.06	–	13.84 ± 0.62	14.87 ± 0.10	19.74	19.03	18.61	0.18
ZOA095645.100 − 435756.02	272.770	8.440	0.26	54.88	2.12	17.72 ± 0.10	16.90 ± 0.07	16.24 ± 0.09	–	16.28 ± 0.18	14.90 ± 0.35	20.76	20.06	19.50	0.18
ZOA095644.023 − 435528.57	272.741	8.470	0.22	35.95	4.41	16.44 ± 0.06	15.83 ± 0.05	15.16 ± 0.06	16.04 ± 0.20	15.52 ± 0.09	13.98 ± 0.31	19.66	19.12	18.42	0.18
ZOA095646.396 − 435521.21	272.746	8.476	0.48	27.63	5.42	15.29 ± 0.03	14.60 ± 0.03	14.24 ± 0.04	–	13.49 ± 0.32	13.79 ± 0.12	18.75	18.03	17.63	0.18
ZOA095651.177 − 435514.54	272.756	8.487	0.15	63.24	5.26	15.17 ± 0.03	14.40 ± 0.03	13.91 ± 0.03	14.71 ± 0.15	–	13.04 ± 0.22	18.55	17.76	17.29	0.18
ZOA095651.738 − 435539.68	272.762	8.482	0.37	79.88	3.10	16.78 ± 0.06	16.12 ± 0.05	15.89 ± 0.07	–	15.75 ± 0.08	15.20 ± 0.17	20.04	19.45	19.34	0.18
ZOA095652.955 − 435523.23	272.762	8.488	0.29	26.07	3.01	16.19 ± 0.04	15.78 ± 0.04	15.16 ± 0.05	15.62 ± 0.17	15.32 ± 0.11	15.10 ± 0.05	19.57	18.92	18.64	0.18
ZOA095652.176 − 435511.96	272.758	8.489	0.18	−16.89	2.59	16.61 ± 0.05	16.00 ± 0.04	15.52 ± 0.06	–	–	15.11 ± 0.10	19.91	19.16	18.83	0.18
ZOA095649.275 − 435505.39	272.750	8.485	0.04	−89.85	2.54	17.14 ± 0.06	16.67 ± 0.06	15.93 ± 0.07	16.61 ± 0.15	–	–	20.40	19.70	19.08	0.18
ZOA095647.963 − 435446.00	272.743	8.487	0.19	15.65	7.39	13.63 ± 0.02	12.91 ± 0.02	12.50 ± 0.02	13.31 ± 0.11	12.67 ± 0.07	12.34 ± 0.05	17.21	16.48	16.07	0.18
ZOA095645.039 − 435418.82	272.732	8.487	0.39	−58.31	14.97	13.13 ± 0.02	12.32 ± 0.02	12.02 ± 0.02	13.00 ± 0.04	11.23 ± 0.30	11.85 ± 0.04	17.21	16.41	16.09	0.18
ZOA095631.144 − 433513.81	272.498	8.711	0.08	−43.08	2.43	17.47 ± 0.06	16.59 ± 0.04	15.92 ± 0.06	–	–	15.85 ± 0.07	20.52	19.74	19.17	0.20
ZOA095633.666 − 433656.91	272.522	8.693	0.16	−6.77	2.82	17.02 ± 0.05	16.39 ± 0.04	15.61 ± 0.06	16.27 ± 0.26	–	15.44 ± 0.06	20.29	19.59	18.92	0.20
ZOA095639.610 − 433712.39	272.539	8.701	0.29	−36.15	3.92	17.67 ± 0.08	16.90 ± 0.07	16.78 ± 0.17	–	16.42 ± 0.07	16.26 ± 0.20	20.62	19.95	19.53	0.20
ZOA095610.389 − 433312.75	272.428	8.698	0.49	40.44	2.00	17.73 ± 0.07	17.17 ± 0.06	16.66 ± 0.10	–	–	–	20.62	20.28	19.59	0.20
ZOA095630.304 − 433216.46	272.465	8.748	0.30	24.71	2.04	18.03 ± 0.10	17.66 ± 0.11	16.53 ± 0.12	17.41 ± 0.26	–	15.87 ± 0.20	21.45	20.50	19.39	0.20
ZOA095506.993 − 435955.87	272.558	8.231	0.13	54.88	4.37	15.06 ± 0.03	14.39 ± 0.02	14.06 ± 0.03	14.70 ± 0.11	13.36 ± 0.28	12.61 ± 0.38	18.43	17.75	17.40	0.31
ZOA095509.850 − 440010.87	272.568	8.233	0.49	−11.72	2.14	18.69 ± 0.11	17.73 ± 0.07	16.74 ± 0.10	–	17.19 ± 0.17	–	21.97	21.16	19.95	0.31
ZOA095508.666 − 435534.39	272.516	8.291	0.18	77.31	1.92	19.04 ± 0.13	18.16 ± 0.09	17.04 ± 0.12	18.55 ± 0.18	−14.13 ± 10.14	–	22.39	20.81	19.52	0.31
ZOA095501.234 − 435634.26	272.509	8.264	0.27	−0.77	2.18	18.41 ± 0.09	17.54 ± 0.06	16.59 ± 0.09	–	–	16.03 ± 0.13	21.23	20.37	19.81	0.31
ZOA095452.253 − 435649.17	272.491	8.244	0.33	6.91	4.65	15.58 ± 0.03	14.83 ± 0.03	14.44 ± 0.04	14.72 ± 0.28	14.29 ± 0.14	13.99 ± 0.09	18.93	18.21	17.79	0.31
ZOA095510.455 − 435733.24	272.541	8.268	0.10	−37.49	2.19	18.47 ± 0.10	17.52 ± 0.06	16.34 ± 0.07	–	–	–	21.29	20.27	19.34	0.31
ZOA095508.483 − 435802.20	272.542	8.258	0.06	68.65	1.64	18.34 ± 0.09	17.43 ± 0.06	16.78 ± 0.11	–	–	16.73 ± 0.11	21.78	20.59	19.98	0.31
ZOA095513.040 − 435820.92	272.556	8.263	0.39	−47.84	1.68	18.85 ± 0.13	17.68 ± 0.07	16.74 ± 0.11	–	–	16.15 ± 0.20	22.56	21.00	20.20	0.31
ZOA095517.898 − 435826.21	272.568	8.271	0.24	80.79	1.87	18.35 ± 0.09	17.76 ± 0.07	16.98 ± 0.13	–	–	16.11 ± 0.13	20.94	20.05	19.70	0.31
ZOA095500.817 − 435832.49	272.529	8.237	0.15	−81.24	6.52	15.22 ± 0.03	14.49 ± 0.02	14.16 ± 0.04	14.93 ± 0.07	14.01 ± 0.07	13.05 ± 0.23	18.71	18.00	17.63	0.31
ZOA095517.717 − 435849.05	272.572	8.265	0.52	21.46	2.35	18.29 ± 0.09	17.24 ± 0.06	16.44 ± 0.09	–	–	16.22 ± 0.09	21.36	20.23	19.41	0.31
ZOA095512.282 − 435940.15	272.568	8.244	0.18	−86.42	1.87	17.64 ± 0.06	16.88 ± 0.05	16.42 ± 0.08	–	–	15.94 ± 0.17	20.92	20.11	19.65	0.31
ZOA095503.214 − 435950.63	272.548	8.225	0.22	62.61	2.47	16.69 ± 0.04	16.15 ± 0.03	15.93 ± 0.06	–	–	15.85 ± 0.06	19.95	19.36	19.27	0.31
ZOA095446.255 − 435526.21	272.462	8.250	0.33	33.06	2.01	19.16 ± 0.13	18.34 ± 0.09	17.38 ± 0.13	–	–	–	21.97	20.98	20.82	0.31
ZOA095445.428 − 435521.65	272.459	8.250	0.21	8.49	2.83	17.37 ± 0.06	16.55 ± 0.04	15.94 ± 0.06	–	15.81 ± 0.16	15.54 ± 0.08	20.29	19.48	18.99	0.31
ZOA095516.778 − 440033.80	272.588	8.241	0.23	−35.06	2.80	17.33 ± 0.06	16.76 ± 0.05	15.93 ± 0.08	–	–	15.76 ± 0.09	20.29	20.37	18.86	0.31
ZOA095507.396 − 435811.52	272.541	8.254	0.01	53.48	2.31	19.11 ± 0.14	17.89 ± 0.07	16.79 ± 0.10	–	–	16.66 ± 0.11	22.09	21.37	20.13	0.31
ZOA095659.295 − 435343.45	272.759	8.522	0.58	30.31	7.47	14.63 ± 0.03	14.00 ± 0.03	13.63 ± 0.04	14.40 ± 0.07	12.85 ± 0.32	13.15 ± 0.12	18.26	17.60	17.23	0.19
ZOA095655.577 − 435321.58	272.747	8.520	0.26	85.69	2.07	17.25 ± 0.08	16.59 ± 0.07	16.15 ± 0.10	–	–	15.32 ± 0.27	20.57	19.78	19.38	0.19
ZOA095705.856 − 434639.13	272.701	8.626	0.34	−14.11	2.27	17.75 ± 0.11	17.25 ± 0.11	16.34 ± 0.11	–	16.02 ± 0.33	16.23 ± 0.11	20.89	19.61	19.50	0.19
ZOA095709.711 − 434917.59	272.738	8.599	0.43	−36.07	4.46	15.54 ± 0.04	14.78 ± 0.03	14.33 ± 0.04	15.15 ± 0.13	14.26 ± 0.10	–	18.88	18.07	17.69	0.19
ZOA095705.256 − 434704.60	272.704	8.620	0.73	−33.86	2.99	17.95 ± 0.12	17.23 ± 0.10	16.69 ± 0.14	–	–	16.41 ± 0.14	21.21	20.60	20.77	0.19
ZOA095649.218 − 435019.10	272.700	8.547	0.47	49.12	2.11	18.29 ± 0.14	17.82 ± 0.15	16.52 ± 0.11	–	–	16.48 ± 0.11	21.23	21.02	19.98	0.19
ZOA095649.456 − 435031.66	272.702	8.545	0.22	−85.31	2.19	17.67 ± 0.10	16.79 ± 0.07	16.14 ± 0.09	–	–	–	20.58	19.66	19.18	0.19
ZOA095534.680 − 434651.77	272.486	8.453	0.28	58.92	11.78	13.37 ± 0.02	13.17 ± 0.03	12.35 ± 0.03	13.04 ± 0.13	–	11.13 ± 0.33	17.53	16.90	16.33	0.20
ZOA095536.091 − 434034.92	272.423	8.537	0.53	−73.88	5.78	15.82 ± 0.04	15.06 ± 0.03	14.37 ± 0.04	–	13.98 ± 0.33	–	19.17	18.44	17.80	0.20
ZOA095555.558 − 434424.64	272.510	8.524	0.20	9.99	2.82	17.05 ± 0.07	16.18 ± 0.05	15.52 ± 0.07	–	–	15.43 ± 0.08	20.08	19.23	18.90	0.20
ZOA095718.310 − 434107.50	272.673	8.722	0.29	50.91	1.98	17.76 ± 0.11	16.90 ± 0.09	16.30 ± 0.12	–	16.75 ± 0.09	13.72 ± 0.63	20.75	19.43	18.87	0.20
ZOA095745.439 − 434011.99	272.728	8.785	0.03	−71.32	2.16	17.85 ± 0.09	17.21 ± 0.08	16.24 ± 0.08	–	–	15.18 ± 0.33	20.96	20.17	19.65	0.20
ZOA095732.984 − 434354.25	272.737	8.713	0.38	61.96	4.34	15.49 ± 0.03	14.72 ± 0.03	14.12 ± 0.03	–	–	13.90 ± 0.05	18.81	18.06	17.50	0.20
ZOA095750.956 − 434341.16	272.778	8.749	0.73	9.30	2.87	17.41 ± 0.07	16.60 ± 0.06	15.81 ± 0.07	17.06 ± 0.21	16.42 ± 0.10	15.53 ± 0.07	20.91	20.02	19.16	0.20
ZOA095733.216 − 434506.81	272.750	8.698	0.46	−52.38	1.93	18.34 ± 0.11	17.95 ± 0.12	17.41 ± 0.17	–	–	16.56 ± 0.16	21.24	21.19	21.00	0.20
ZOA095758.158 − 434542.24	272.816	8.736	0.25	65.27	2.31	17.98 ± 0.10	17.42 ± 0.10	16.67 ± 0.13	–	–	16.40 ± 0.13	20.67	20.14	19.83	0.20
ZOA095751.860 − 434152.43	272.761	8.775	0.19	−68.88	2.52	18.31 ± 0.11	17.66 ± 0.10	16.65 ± 0.09	17.27 ± 0.27	–	16.47 ± 0.10	21.09	20.62	19.52	0.20
ZOA095750.789 − 434046.96	272.747	8.787	0.40	20.36	2.79	18.27 ± 0.11	17.97 ± 0.13	16.76 ± 0.11	–	–	–	21.36	21.38	19.67	0.20
ZOA095732.988 − 434112.15	272.709	8.748	0.58	84.47	2.46	18.43 ± 0.12	17.75 ± 0.11	16.81 ± 0.12	–	–	16.45 ± 0.12	21.86	21.61	19.76	0.20
ZOA095340.653 − 440114.77	272.369	8.051	0.06	−55.01	3.41	17.27 ± 0.07	16.53 ± 0.05	15.81 ± 0.07	15.70 ± 0.60	15.99 ± 0.15	–	19.99	19.71	18.91	0.31
ZOA095341.401 − 440255.62	272.388	8.031	0.58	0.73	4.31	16.07 ± 0.04	15.18 ± 0.03	14.55 ± 0.04	–	–	14.25 ± 0.07	19.40	18.53	17.90	0.31
ZOA095351.317 − 440421.20	272.427	8.031	0.29	−24.77	2.50	17.36 ± 0.06	16.47 ± 0.04	15.55 ± 0.06	–	–	–	20.73	19.74	18.51	0.31
ZOA095353.624 − 440357.67	272.428	8.041	0.13	−59.90	2.22	17.63 ± 0.06	16.69 ± 0.04	16.00 ± 0.06	–	–	14.90 ± 0.32	20.65	19.78	19.25	0.31
ZOA095352.296 − 440353.97	272.424	8.039	0.34	16.76	2.79	18.17 ± 0.09	17.33 ± 0.06	16.17 ± 0.08	–	–	15.74 ± 0.09	21.33	20.53	19.31	0.31
ZOA095422.021 − 440433.16	272.501	8.086	0.40	50.90	6.18	17.21 ± 0.07	16.52 ± 0.06	15.83 ± 0.09	–	14.02 ± 0.79	14.76 ± 0.29	20.18	19.51	18.72	0.31
ZOA095423.236 − 440422.05	272.502	8.091	0.25	40.98	4.25	16.18 ± 0.04	15.46 ± 0.03	15.20 ± 0.06	–	11.52 ± 1.22	15.00 ± 0.07	19.46	18.73	18.42	0.31
ZOA095407.680 − 440606.98	272.484	8.039	0.13	76.55	2.38	18.07 ± 0.08	17.09 ± 0.05	16.25 ± 0.07	–	–	16.01 ± 0.07	21.42	20.25	19.68	0.31
ZOA095409.005 − 440717.41	272.499	8.027	0.02	7.05	2.39	17.31 ± 0.06	16.39 ± 0.04	15.64 ± 0.05	16.59 ± 0.25	–	–	20.49	19.62	18.87	0.31
ZOA095408.467 − 440613.32	272.487	8.039	0.34	−1.99	2.18	18.26 ± 0.09	17.25 ± 0.06	16.26 ± 0.07	–	–	–	21.10	20.27	19.50	0.31

ZOA095415.765 − 440800.04	272.523	8.030	0.27	−24.36	1.93	18.11 ± 0.09	17.41 ± 0.07	16.67 ± 0.12	–	16.39 ± 0.13	16.11 ± 0.12	21.29	19.75	19.51	0.31
ZOA095404.126 − 440530.85	272.469	8.040	0.35	−50.17	2.22	19.16 ± 0.15	17.97 ± 0.09	16.77 ± 0.10	–	17.00 ± 0.31	16.53 ± 0.10	21.81	20.99	19.91	0.31
ZOA095404.634 − 440518.36	272.468	8.044	0.42	26.15	1.84	18.66 ± 0.11	17.66 ± 0.07	17.06 ± 0.14	–	–	–	21.79	19.48	19.82	0.31
ZOA095541.633 − 440130.89	272.657	8.275	0.26	−24.88	2.36	17.82 ± 0.09	17.60 ± 0.11	16.15 ± 0.10	–	–	15.84 ± 0.12	20.61	19.68	19.03	0.26
ZOA095540.264 − 440125.86	272.653	8.274	0.26	−0.12	4.18	16.79 ± 0.06	15.63 ± 0.04	14.85 ± 0.06	–	15.59 ± 0.04	14.50 ± 0.11	20.29	18.94	18.29	0.26
ZOA095521.321 − 435612.64	272.553	8.306	0.26	75.12	1.64	18.82 ± 0.13	17.99 ± 0.10	17.30 ± 0.16	–	–	–	21.87	21.14	20.01	0.26
ZOA095539.010 − 435823.04	272.618	8.311	0.04	−48.69	2.35	18.13 ± 0.09	17.30 ± 0.07	16.53 ± 0.10	–	–	16.24 ± 0.10	21.38	20.30	19.43	0.26
ZOA095530.902 − 435428.63	272.557	8.347	0.45	−85.66	4.77	15.74 ± 0.03	14.95 ± 0.03	14.65 ± 0.04	15.38 ± 0.10	13.86 ± 0.32	14.14 ± 0.12	19.04	18.26	17.96	0.26
ZOA095524.667 − 435440.66	272.545	8.332	0.58	−39.31	4.19	16.22 ± 0.04	15.28 ± 0.03	14.75 ± 0.04	–	14.89 ± 0.10	14.50 ± 0.05	19.45	18.64	18.07	0.26
ZOA095523.669 − 435442.82	272.543	8.330	0.32	76.02	1.92	18.25 ± 0.10	17.26 ± 0.06	16.77 ± 0.10	–	–	–	21.23	20.26	19.81	0.26
ZOA095552.000 − 440000.71	272.665	8.314	0.08	−36.07	2.17	17.60 ± 0.07	16.61 ± 0.05	15.98 ± 0.07	16.75 ± 0.28	15.69 ± 0.27	15.37 ± 0.16	20.73	19.75	19.13	0.26
ZOA095553.281 − 435902.58	272.658	8.329	0.54	7.33	5.56	16.35 ± 0.04	15.53 ± 0.03	15.09 ± 0.05	–	14.83 ± 0.17	14.44 ± 0.12	19.64	18.84	18.38	0.26
ZOA095552.818 − 435801.64	272.647	8.341	0.16	−46.99	2.03	17.77 ± 0.07	17.02 ± 0.06	16.32 ± 0.08	–	–	16.28 ± 0.08	20.77	19.99	19.72	0.26
ZOA095542.056 − 435552.34	272.598	8.349	0.27	−31.75	4.64	15.78 ± 0.03	15.05 ± 0.03	14.68 ± 0.04	14.92 ± 0.27	14.33 ± 0.18	14.27 ± 0.08	19.04	18.31	17.99	0.26
ZOA095547.029 − 435607.48	272.613	8.355	0.47	−9.11	5.90	14.44 ± 0.02	13.61 ± 0.02	13.18 ± 0.02	14.07 ± 0.11	13.39 ± 0.05	12.61 ± 0.14	17.90	17.08	16.64	0.26
ZOA095548.383 − 435526.38	272.609	8.367	0.11	29.52	3.65	16.94 ± 0.05	16.25 ± 0.04	16.04 ± 0.09	–	13.11 ± 0.97	–	20.05	19.36	19.01	0.26
ZOA095541.689 − 435435.73	272.584	8.365	0.05	−22.84	3.00	16.34 ± 0.04	15.60 ± 0.03	15.33 ± 0.05	–	14.72 ± 0.24	14.99 ± 0.07	19.56	18.84	18.55	0.26
ZOA095550.072 − 435330.05	272.592	8.395	0.42	14.76	4.21	15.21 ± 0.03	14.49 ± 0.03	14.14 ± 0.03	14.55 ± 0.20	13.60 ± 0.20	14.01 ± 0.04	18.54	17.78	17.53	0.26
ZOA095521.591 − 435349.80	272.528	8.338	0.51	−41.26	4.83	15.64 ± 0.04	14.90 ± 0.03	14.59 ± 0.04	15.48 ± 0.05	14.11 ± 0.23	13.57 ± 0.27	18.92	18.23	17.91	0.26
ZOA095552.560 − 435815.95	272.648	8.338	0.13	−80.50	2.27	17.43 ± 0.06	16.88 ± 0.05	16.55 ± 0.09	11.90 ± 1.74	–	15.36 ± 0.28	20.48	19.88	19.43	0.26
ZOA095423.204 − 440758.56	272.540	8.044	0.21	70.98	2.40	17.71 ± 0.08	17.09 ± 0.06	16.09 ± 0.09	–	16.17 ± 0.14	15.21 ± 0.24	20.54	19.69	19.37	0.34
ZOA095412.160 − 440249.40	272.459	8.090	0.09	−52.00	1.80	18.62 ± 0.12	17.64 ± 0.07	16.76 ± 0.11	–	–	16.76 ± 0.11	23.33	21.67	20.63	0.34
ZOA095441.413 − 440642.98	272.569	8.095	0.28	53.40	7.69	14.41 ± 0.02	13.64 ± 0.02	13.20 ± 0.03	14.05 ± 0.13	12.93 ± 0.20	12.83 ± 0.07	18.02	17.24	16.80	0.34
ZOA095413.501 − 440236.09	272.460	8.096	0.24	−9.23	2.54	17.60 ± 0.07	16.80 ± 0.05	15.89 ± 0.06	–	12.22 ± 1.46	15.45 ± 0.12	20.76	19.94	19.23	0.34
ZOA095432.617 − 440458.37	272.530	8.101	0.39	62.47	4.24	15.70 ± 0.03	14.90 ± 0.03	14.50 ± 0.03	15.15 ± 0.17	14.00 ± 0.20	13.44 ± 0.28	18.98	18.18	17.81	0.34
ZOA095431.016 − 440426.89	272.521	8.105	0.11	−23.38	3.37	17.07 ± 0.05	16.34 ± 0.04	15.94 ± 0.07	–	15.69 ± 0.09	15.48 ± 0.09	20.03	19.22	18.98	0.34
ZOA095424.647 − 440431.29	272.507	8.092	0.61	−28.41	12.17	14.14 ± 0.02	13.32 ± 0.02	12.77 ± 0.02	13.73 ± 0.15	13.13 ± 0.06	12.64 ± 0.03	17.93	17.10	16.54	0.34
ZOA095428.375 − 440257.98	272.499	8.119	0.19	−73.09	2.88	17.85 ± 0.07	16.98 ± 0.05	16.17 ± 0.07	–	–	14.92 ± 0.29	20.79	19.81	19.11	0.34
ZOA095407.881 − 440151.67	272.439	8.095	0.45	57.86	2.40	18.99 ± 0.14	18.40 ± 0.11	17.03 ± 0.11	–	–	16.14 ± 0.12	21.61	21.38	19.65	0.34
ZOA095430.110 − 440115.99	272.485	8.144	0.29	−82.61	1.94	18.36 ± 0.10	17.57 ± 0.07	16.57 ± 0.09	–	–	–	21.16	20.16	19.44	0.34
ZOA095601.129 − 433216.37	272.396	8.693	0.07	−40.42	2.74	17.31 ± 0.07	16.48 ± 0.05	15.67 ± 0.06	–	14.57 ± 0.50	13.83 ± 0.38	20.14	19.30	18.55	0.20
ZOA095610.500 − 433652.41	272.466	8.650	0.47	12.58	2.28	18.52 ± 0.11	17.61 ± 0.08	16.65 ± 0.10	–	–	–	21.51	20.91	19.60	0.20
ZOA095516.952 − 433442.20	272.316	8.578	0.09	61.79	2.47	17.83 ± 0.10	16.99 ± 0.08	16.19 ± 0.10	–	–	–	20.57	20.06	19.55	0.22
ZOA095518.845 − 433451.29	272.322	8.579	0.28	5.62	3.62	16.75 ± 0.05	16.05 ± 0.04	15.91 ± 0.08	–	9.97 ± 1.80	15.46 ± 0.10	19.50	18.86	18.95	0.22
ZOA095558.439 − 433604.85	272.429	8.638	0.32	−72.26	3.50	16.19 ± 0.04	15.52 ± 0.03	14.96 ± 0.05	15.09 ± 0.36	–	14.66 ± 0.12	19.45	18.83	18.17	0.22
ZOA095545.241 − 433240.41	272.362	8.657	0.21	−13.24	3.19	17.12 ± 0.05	16.36 ± 0.04	15.80 ± 0.06	17.07 ± 0.07	–	–	20.33	19.56	18.70	0.22
ZOA095543.417 − 433259.56	272.361	8.650	0.38	−75.76	2.26	18.33 ± 0.09	17.58 ± 0.07	16.80 ± 0.10	–	–	16.25 ± 0.14	21.43	20.73	20.22	0.22
ZOA095527.720 − 433336.22	272.330	8.612	0.11	55.75	1.74	18.65 ± 0.12	17.89 ± 0.10	17.02 ± 0.14	–	17.11 ± 0.27	17.02 ± 0.14	21.74	20.89	20.85	0.22
ZOA095520.703 − 433231.26	272.302	8.613	0.20	87.04	1.94	17.99 ± 0.10	17.33 ± 0.07	16.57 ± 0.10	–	–	16.57 ± 0.10	21.76	20.60	19.45	0.22
ZOA095545.382 − 433331.02	272.371	8.647	0.52	−0.93	1.75	19.09 ± 0.15	18.09 ± 0.10	17.00 ± 0.13	–	–	16.99 ± 0.13	21.82	21.12	19.98	0.22
ZOA095527.112 − 435454.59	272.553	8.334	0.28	72.40	3.14	16.12 ± 0.04	15.35 ± 0.03	14.84 ± 0.04	15.93 ± 0.08	14.79 ± 0.16	–	19.46	18.67	18.12	0.26
ZOA095529.302 − 435512.22	272.561	8.334	0.18	−75.28	6.41	14.65 ± 0.03	13.95 ± 0.02	13.46 ± 0.03	13.97 ± 0.21	13.22 ± 0.19	12.93 ± 0.13	18.18	17.47	16.99	0.26
ZOA095508.922 − 435407.47	272.502	8.310	0.44	−59.13	2.55	17.75 ± 0.07	16.81 ± 0.05	16.14 ± 0.07	16.57 ± 0.36	15.44 ± 0.34	15.67 ± 0.12	20.22	19.53	19.42	0.26
ZOA095503.351 − 435421.34	272.491	8.297	0.84	67.76	3.57	16.21 ± 0.04	15.57 ± 0.03	15.07 ± 0.04	15.61 ± 0.20	15.12 ± 0.12	–	19.37	18.82	18.25	0.26
ZOA095523.922 − 435654.40	272.566	8.302	0.35	−13.35	2.60	17.33 ± 0.06	16.58 ± 0.04	15.86 ± 0.06	16.92 ± 0.15	–	15.55 ± 0.08	20.33	19.78	19.07	0.26
ZOA095532.443 − 435753.70	272.597	8.305	0.53	−77.25	2.55	17.32 ± 0.06	16.64 ± 0.05	15.95 ± 0.07	–	–	15.48 ± 0.10	20.42	19.69	18.93	0.26
ZOA095530.099 − 435821.30	272.596	8.295	0.31	−29.74	5.80	18.68 ± 0.13	17.54 ± 0.08	16.50 ± 0.10	–	–	15.43 ± 0.24	21.73	20.46	19.66	0.26
ZOA095508.247 − 435423.54	272.503	8.305	0.10	−59.90	2.12	18.28 ± 0.10	17.41 ± 0.07	16.67 ± 0.09	–	–	16.41 ± 0.09	21.32	20.66	20.12	0.26
ZOA095654.375 − 434607.65	272.668	8.612	0.26	−47.25	3.40	15.82 ± 0.03	15.12 ± 0.03	14.67 ± 0.04	14.62 ± 0.39	14.96 ± 0.04	13.91 ± 0.22	19.08	18.45	18.05	0.21
ZOA095638.321 − 434338.23	272.604	8.614	0.49	63.82	6.98	14.86 ± 0.03	14.06 ± 0.02	13.58 ± 0.03	14.45 ± 0.14	13.69 ± 0.10	13.37 ± 0.05	18.36	17.54	17.09	0.21
ZOA095653.356 − 434320.07	272.636	8.646	0.20	51.33	3.27	17.16 ± 0.06	16.36 ± 0.05	15.57 ± 0.06	–	16.15 ± 0.09	–	20.31	19.66	18.64	0.21
ZOA095616.308 − 434235.48	272.540	8.587	0.30	55.20	4.56	15.89 ± 0.04	15.29 ± 0.04	14.79 ± 0.06	15.58 ± 0.11	15.01 ± 0.07	14.49 ± 0.09	19.20	18.61	18.15	0.21
ZOA095649.714 − 434320.27	272.628	8.640	0.20	−30.73	2.57	18.50 ± 0.11	17.57 ± 0.09	16.58 ± 0.10	–	17.10 ± 0.12	16.26 ± 0.12	21.19	20.39	19.91	0.21
ZOA095630.396 − 434206.68	272.569	8.619	0.31	63.94	2.65	16.92 ± 0.05	16.21 ± 0.04	15.42 ± 0.05	–	15.99 ± 0.05	14.72 ± 0.22	20.01	19.35	18.92	0.21
ZOA095653.481 − 433947.79	272.600	8.693	0.11	20.50	4.59	15.21 ± 0.03	14.54 ± 0.03	14.12 ± 0.03	15.02 ± 0.06	14.29 ± 0.05	14.00 ± 0.04	18.58	17.91	17.50	0.21
ZOA095659.775 − 440641.81	272.896	8.353	0.40	−14.96	2.00	18.50 ± 0.10	17.49 ± 0.07	16.47 ± 0.10	–	–	–	21.89	20.64	19.45	0.19
ZOA095644.067 − 440153.98	272.809	8.387	0.22	34.02	4.71	15.83 ± 0.03	15.12 ± 0.03	14.80 ± 0.04	15.16 ± 0.22	14.62 ± 0.11	14.09 ± 0.17	19.10	18.40	18.06	0.19
ZOA095652.452 − 440115.68	272.822	8.411	0.30	27.39	2.48	18.01 ± 0.08	17.03 ± 0.05	16.15 ± 0.07	–	–	16.06 ± 0.08	21.15	20.23	19.41	0.19
ZOA095701.736 − 440206.53	272.853	8.417	0.40	38.12	2.86	17.67 ± 0.07	16.77 ± 0.05	15.94 ± 0.07	–	12.66 ± 1.33	15.66 ± 0.07	20.90	19.79	19.06	0.19
ZOA095714.828 − 440608.36	272.926	8.388	0.25	−15.54	3.45	17.45 ± 0.06	16.63 ± 0.05	16.01 ± 0.07	–	15.56 ± 0.34	15.79 ± 0.07	20.99	19.94	19.13	0.19
ZOA095706.991 − 440733.82	272.922	8.355	0.17	11.04	2.23	18.00 ± 0.08	17.08 ± 0.05	16.26 ± 0.07	–	16.59 ± 0.12	15.46 ± 0.21	20.80	20.24	19.26	0.19
ZOA095645.326 − 433958.06	272.582	8.675	0.11	45.37	7.12	14.14 ± 0.02	13.39 ± 0.02	12.96 ± 0.03	13.80 ± 0.12	13.06 ± 0.09	12.60 ± 0.08	17.76	17.01	16.56	0.21

$ZOA095711.692-434210.13$	272.668	8.696	0.25	59.25	3.26	16.80 ± 0.05	16.05 ± 0.04	15.90 ± 0.08	16.22 ± 0.12	15.43 ± 0.12	15.31 ± 0.11	19.70	19.04	18.93	0.21
$ZOA095713.814-434530.83$	272.708	8.656	0.10	−51.92	4.82	16.24 ± 0.04	15.59 ± 0.04	15.09 ± 0.06	–	15.08 ± 0.12	14.38 ± 0.15	19.49	18.81	18.29	0.21
$ZOA095508.882-433549.63$	272.309	8.548	0.06	−6.52	4.10	15.16 ± 0.03	14.42 ± 0.02	13.98 ± 0.03	14.79 ± 0.12	14.07 ± 0.08	13.01 ± 0.29	18.52	17.78	17.40	0.25
$ZOA095645.089-440241.76$	272.819	8.378	0.55	−20.07	5.42	15.19 ± 0.03	14.45 ± 0.02	14.09 ± 0.03	14.50 ± 0.23	13.88 ± 0.16	13.46 ± 0.19	18.63	17.88	17.56	0.19
$ZOA095651.099-440742.68$	272.886	8.324	0.17	75.25	2.26	17.80 ± 0.07	17.00 ± 0.05	16.19 ± 0.07	–	–	15.99 ± 0.08	20.75	20.01	19.51	0.19

Appendix B

Plots of the six observed VSCL clusters

B.1 The VC02 cluster

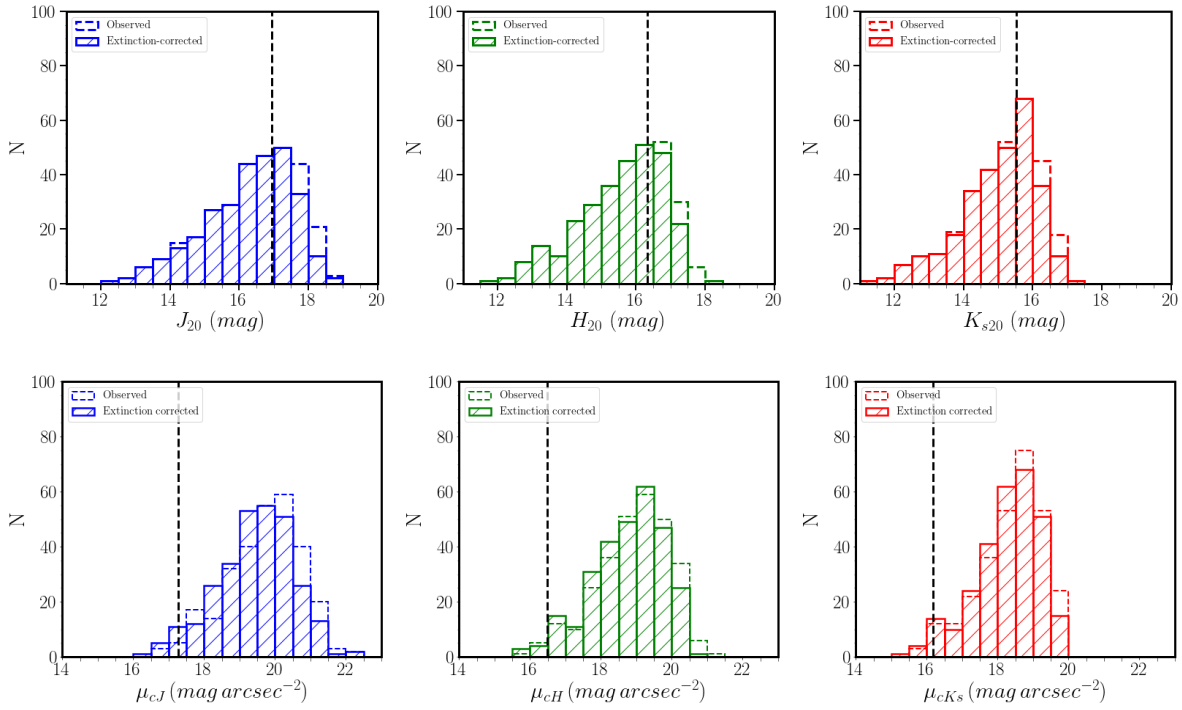

Figure B.1.1: Top: VC02 histograms of isophotal magnitudes at $K_s = 20\overset{\text{m}}{.}0$ in J, H and K_s bands. The dashed histograms show the observed magnitudes and the hatched ones are the extinction-corrected. The dashed lines are the completeness magnitude limits in each band. Bottom: Histograms of central surface brightness of VC02 galaxies in J, H and K_s bands. The dividing values of central surface brightnesses between elliptical and spiral galaxies in each band are shown by the dashed lines.

Table B.1.1: Photometric parameters of the VC02 galaxies.

Parameter	Max	Min
J^0_{20} (mag)	18.67	12.34
H^0_{20} (mag)	18.09	11.58
K^0_{s20} (mag)	17.30	11.33
μ^0_{cJ} (mag arcsec^{-2})	22.10	16.40
μ^0_{cH} (mag arcsec^{-2})	20.85	15.71
μ^0_{cKs} (mag arcsec^{-2})	19.83	15.47

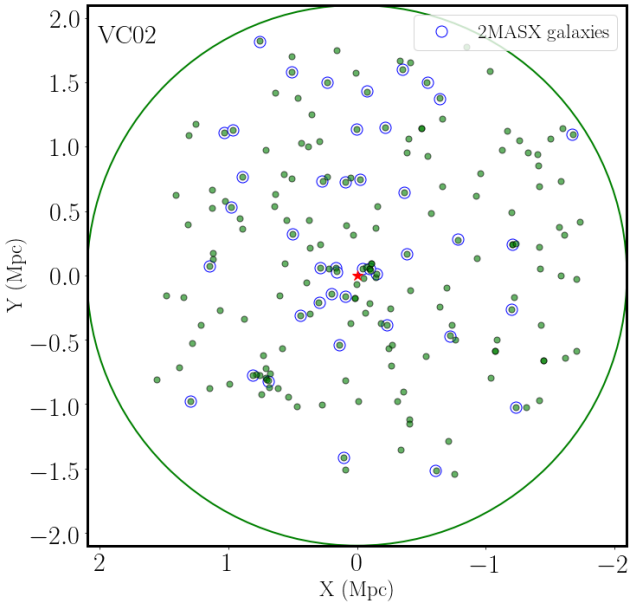

Figure B.1.2: The on-sky distribution of galaxies with $K^o_s < 15\overset{\text{m}}{.}5$ and $r > 2''$ in VC02. The IRSF galaxies are shown with filled green circles. Galaxies that have counterpart in 2MASX are encircled in blue.

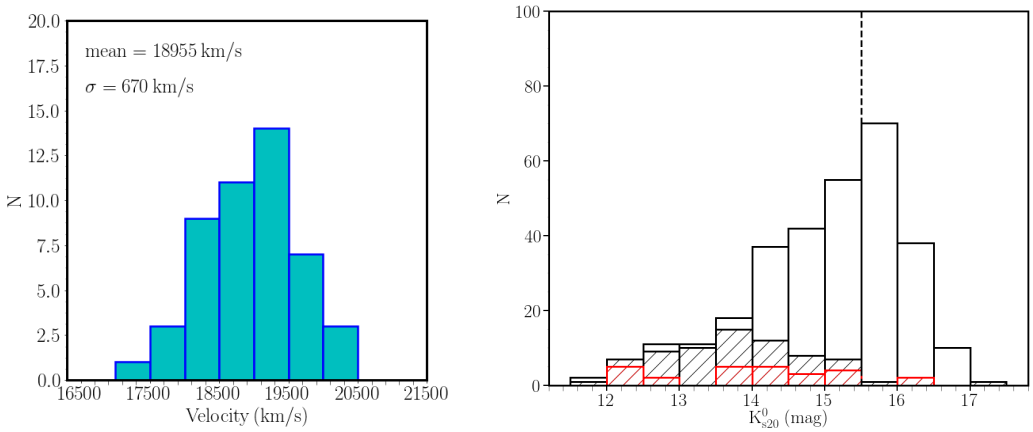

Figure B.1.3: Left: the velocity histogram of the VC02 cluster. Right: the distribution of the extinction-corrected K_s magnitude for identified galaxies in VC02 with $r > 2''$. The galaxies with redshift data are shown as black hatched areas. The red areas mark foreground and background galaxies (10 with $v < 17000$ km s^{-1} and 16 with $v > 21000$ km s^{-1} respectively).

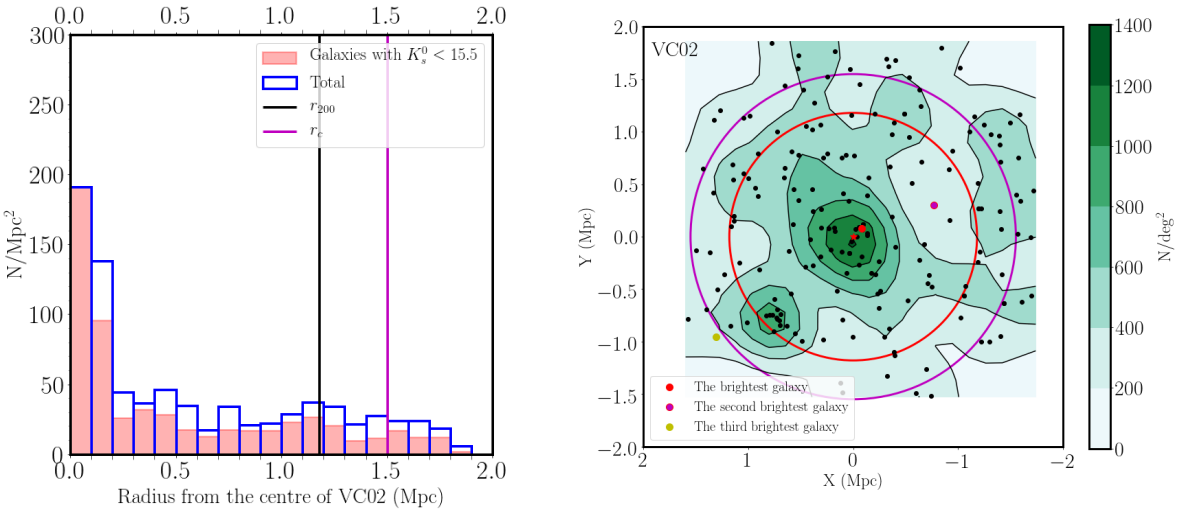

Figure B.1.4: Left: the radial density profile, N/Mpc^2, out to $r < 2$ Mpc. The total number density of galaxies is shown in blue histogram and the completeness-limited sample ($K^0_{slim} < 15\overset{m}{.}5$) in pink. Right: iso-density map of VC02 for $r < 2$ Mpc. Galaxies are shown as black dots and the centre of cluster as red star. The red and magenta circles represent the r_{200} and r_c respectively. The three brightest galaxies are shown as red, magenta and yellow dots.

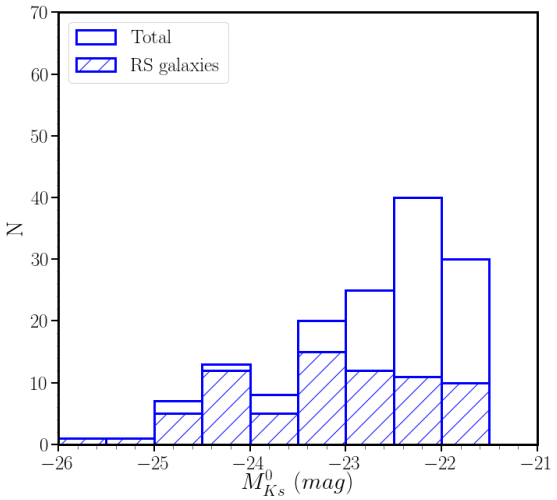

Figure B.1.5: The distribution of the extinction-corrected absolute magnitude $M^o_{K_s}$ up to $M^o_{Ks} < -21\overset{m}{.}5$ and $r_c < 1.5$ Mpc for identified galaxies in VC02. The hatched areas shows the identified Red-Sequence galaxies in VC02.

B.2 The VC04 cluster

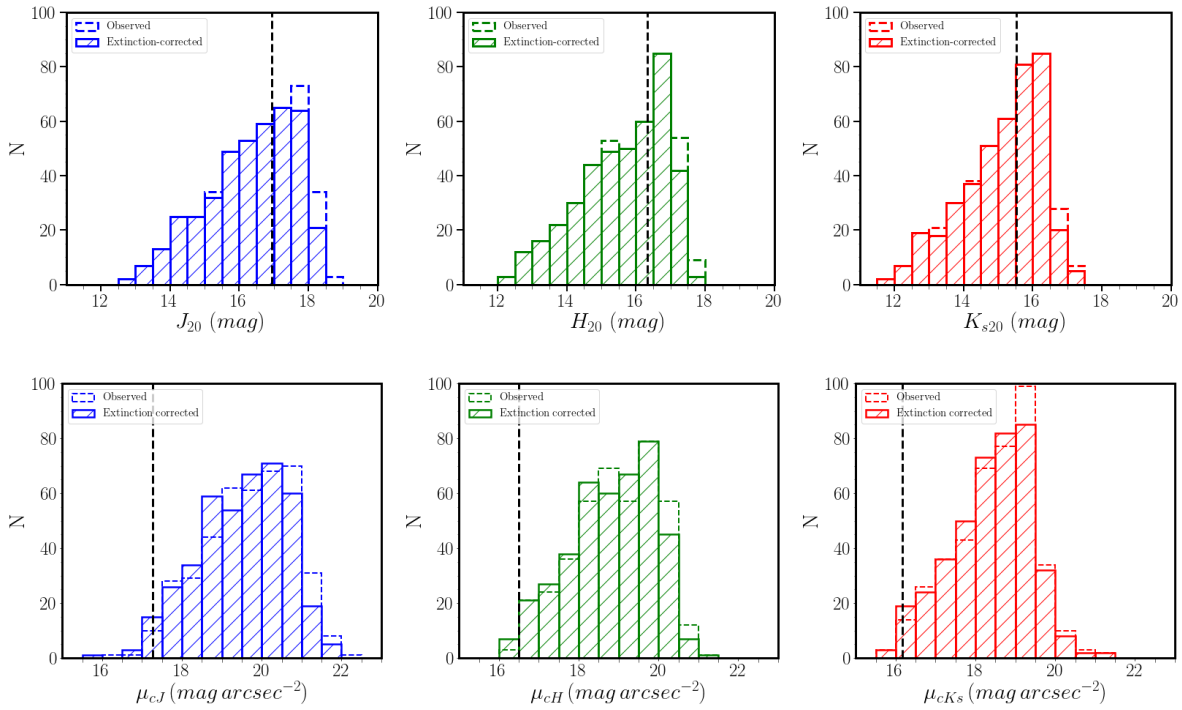

Figure B.2.1: Top: VC04 histograms of isophotal magnitudes at $K_s = 20\overset{\text{m}}{.}0$ in J, H and K_s bands. The dashed histograms show the observed magnitudes and the hatched ones are the extinction-corrected. The dashed lines are the completeness magnitude limits in each band. Bottom: Histograms of central surface brightness of VC04 galaxies in J, H and K_s bands. The dividing values of central surface brightnesses between elliptical and spiral galaxies in each band are shown by the dashed lines.

Table B.2.1: Photometric parameters of the VC04 galaxies.

Parameter	Max	Min
J^0_{20} (mag)	18.44	12.82
H^0_{20} (mag)	17.73	12.10
K^0_{s20} (mag)	17.20	11.76
μ^0_{cJ} (mag arcsec^{-2})	21.94	15.95
μ^0_{cH} (mag arcsec^{-2})	21.01	16.04
μ^0_{cKs} (mag arcsec^{-2})	21.37	15.71

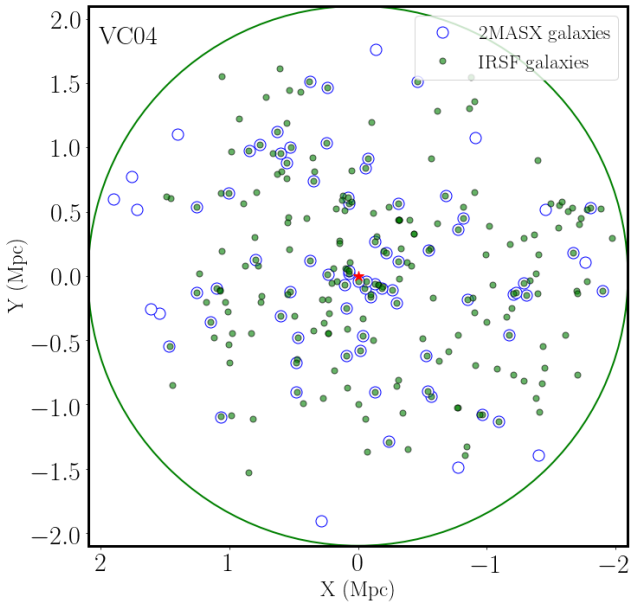

Figure B.2.2: The on-sky distribution of galaxies with $K_s^o < 15\overset{\text{m}}{.}5$ and $r > 2''$ in VC04. The IRSF galaxies are shown with filled green circles. Galaxies that have counterpart in 2MASX are encircled in blue.

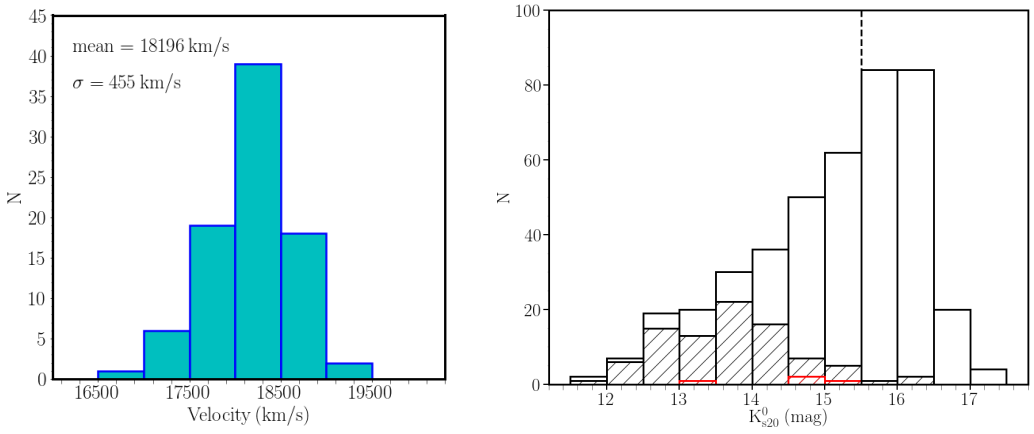

Figure B.2.3: Left: the velocity histogram of VC04. Right: the distribution of the extinction-corrected K_s magnitude for 416 identified galaxies in VC04. The 89 galaxies with redshift data are shown as black hatched areas. The red areas mark foreground and background galaxies ($v < 16000$ km s^{-1} and $v > 20000$ km s^{-1} respectively).

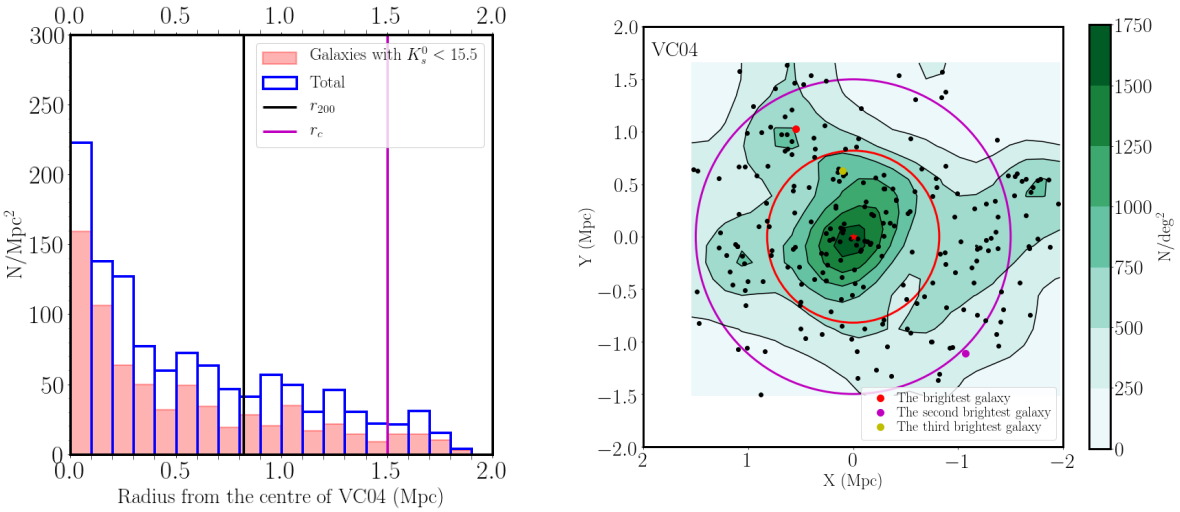

Figure B.2.4: Left: the radial density profile, N/Mpc^2, out to $r < 2$ Mpc. The total number density of galaxies is shown in blue histogram and the completeness-limited sample ($K^0_{slim} < 15\overset{\text{m}}{.}5$) in pink. Right: iso-density map of VC04 for $r < 2$ Mpc. Galaxies are shown as black dots and the centre of cluster as red star. The red and magenta circles represent the r_{200} and r_c respectively. The three brightest galaxies are shown as red, magenta and yellow dots.

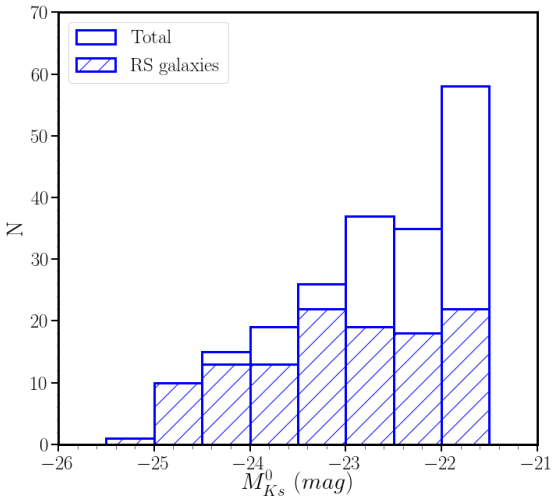

Figure B.2.5: The distribution of the extinction-corrected absolute magnitude up to $M^o_{Ks} < -21\overset{\text{m}}{.}5$ and $r_c < 1.5$ Mpc for identified galaxies in VC04. The hatched areas shows the identified Red-Sequence galaxies in VC04.

B.3 The VC05 cluster

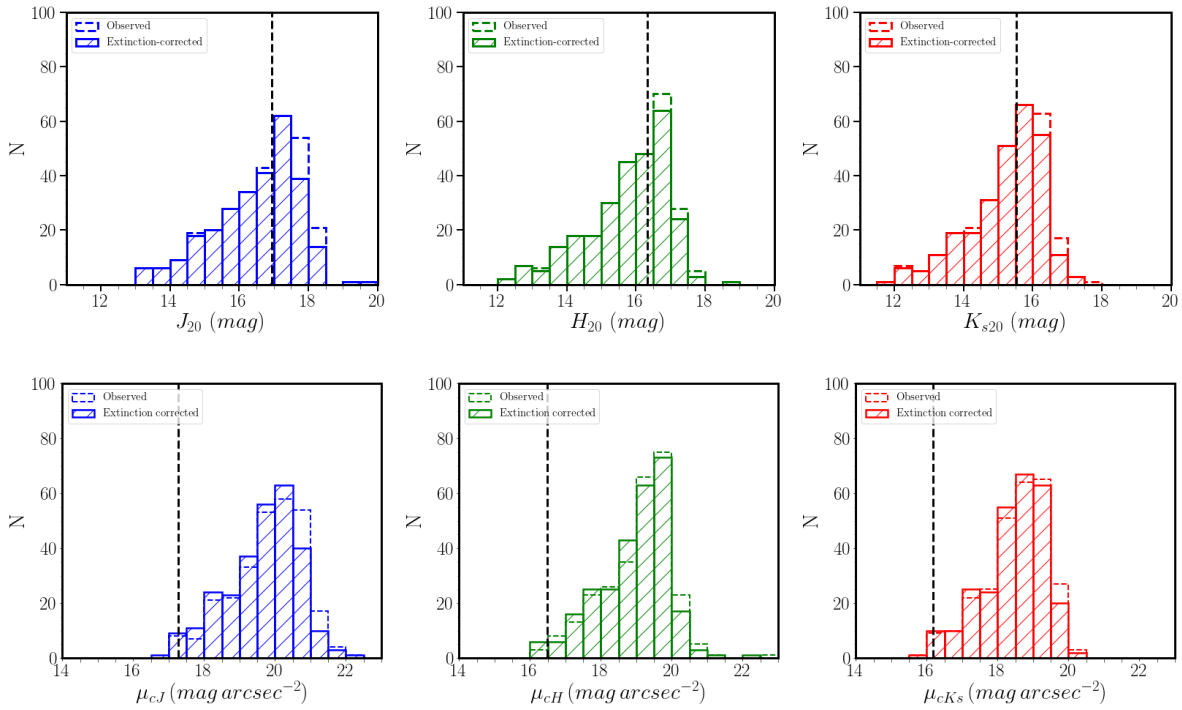

Figure B.3.1: Top: VC05 histograms of isophotal magnitudes at $K_s = 20\overset{\text{m}}{.}0$ in J, H and K_s bands. The dashed histograms show the observed magnitudes and the hatched ones are the extinction-corrected. The dashed lines are the completeness magnitude limits in each band. Bottom: Histograms of central surface brightness of VC05 galaxies in J, H and K_s bands. The dividing values of central surface brightnesses between elliptical and spiral galaxies in each band are shown by the dashed lines.

Table B.3.1: Photometric parameters of the VC05 galaxies.

Parameter	Max	Min
J^0_{20} (mag)	19.90	13.02
H^0_{20} (mag)	18.52	12.32
K^0_{s20} (mag)	17.48	11.99
μ^0_{cJ} (mag arcsec^{-2})	22.18	16.96
μ^0_{cH} (mag arcsec^{-2})	22.46	16.25
μ^0_{cKs} (mag arcsec^{-2})	20.23	15.91

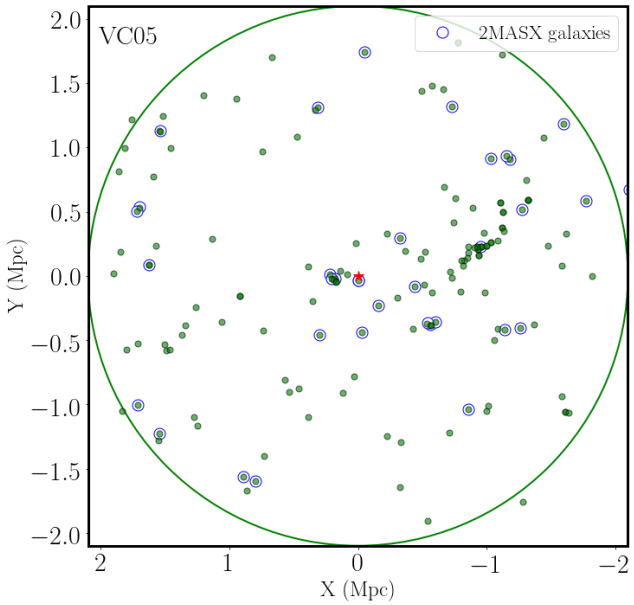

Figure B.3.2: The on-sky distribution of galaxies with $K_s^o < 15\overset{\text{m}}{.}5$ and $r > 2''$ in VC04. The IRSF galaxies are shown with filled green circles. Galaxies that have counterpart in 2MASX are encircled in blue.

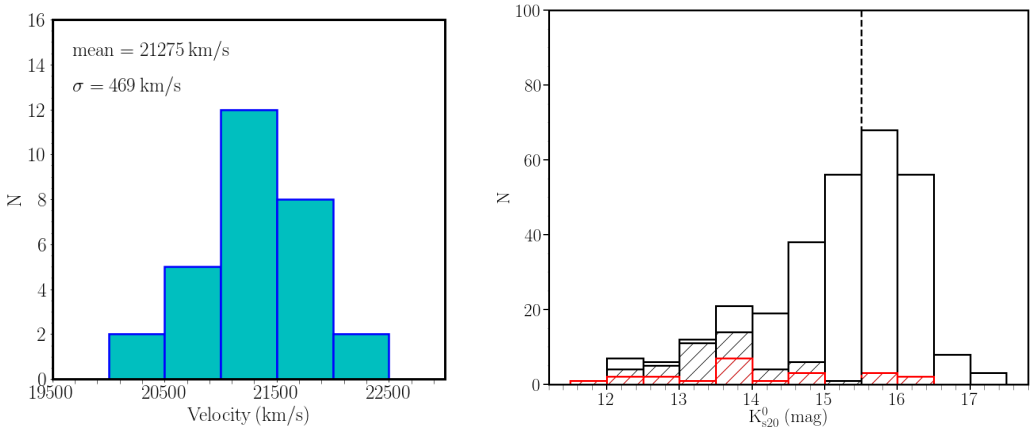

Figure B.3.3: Left: the velocity histogram of the VC05 cluster. Right: the distribution of the extinction-corrected K_s magnitude for identified galaxies in VC05 with $r > 2''$. The galaxies with redshift data are shown as black hatched areas. The red areas mark foreground galaxies (22 with $v < 19000$ km s^{-1}).

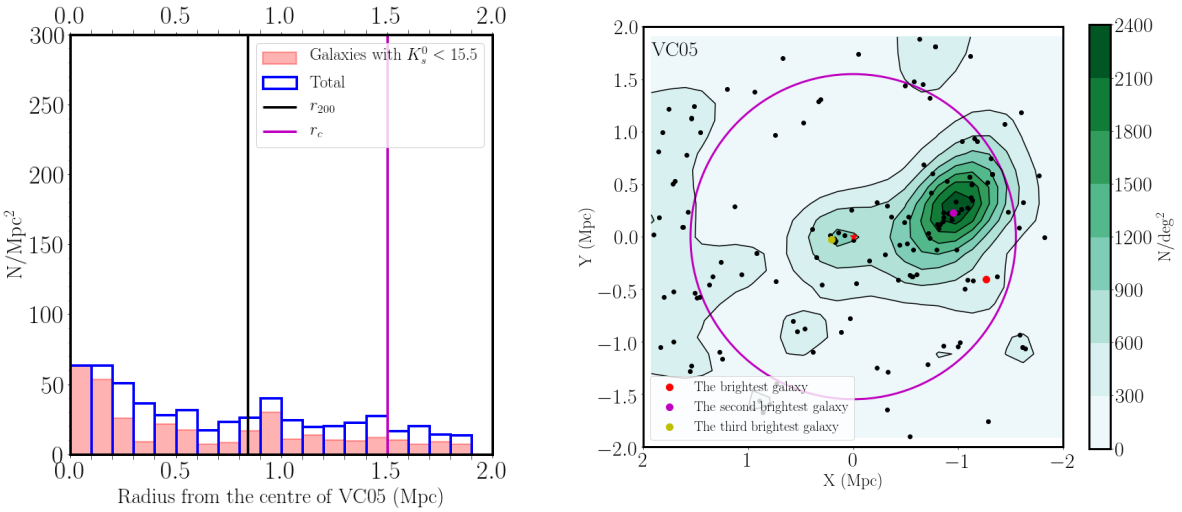

Figure B.3.4: Left: the radial density profile, N/Mpc^2, out to $r < 2$ Mpc. The total number density of galaxies is shown in blue histogram and the completeness-limited sample ($K^0_{slim} < 15\overset{m}{.}5$) in pink. Right: iso-density map of VC05 for $r < 2$ Mpc. Galaxies are shown as black dots and the centre of cluster as red star. The red circle represents the r_c. The three brightest galaxies are shown as red, magenta and yellow dots.

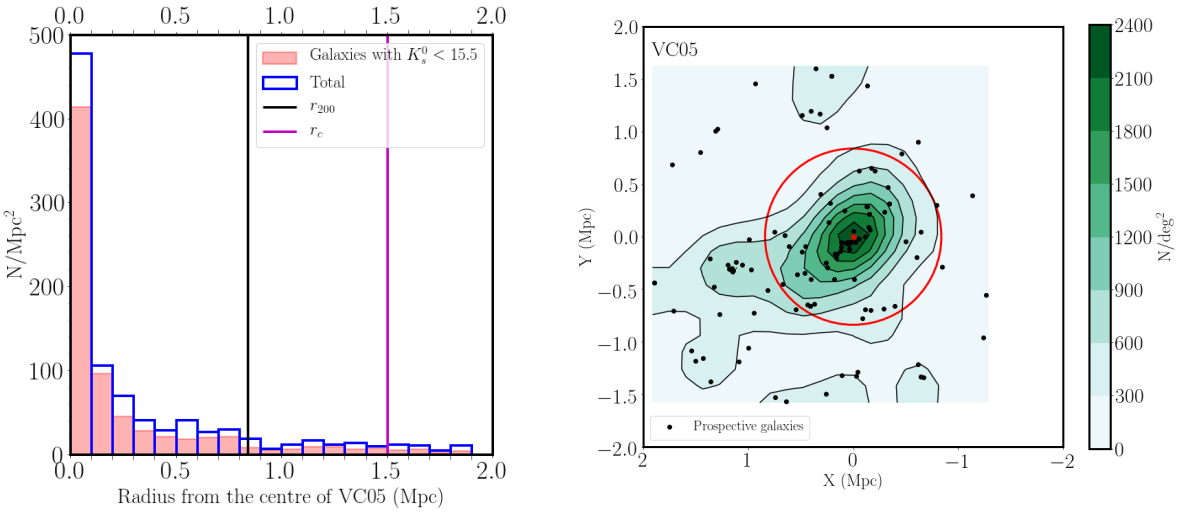

Figure B.3.5: The radial density profile, N/Mpc^2 (left) and iso-density contour map of VC05 out to $r < 2$ Mpc (right), using the adjusted centre.

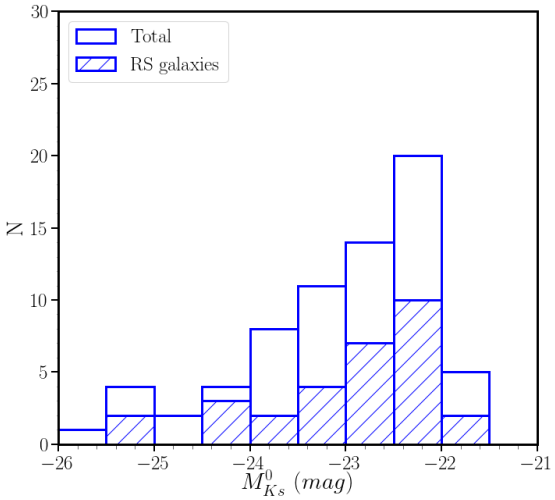

Figure B.3.6: The distribution of the extinction-corrected absolute magnitude up to $M^o_{Ks} < -21\overset{\text{m}}{.}5$ and $r_c < 0.5$ Mpc (around the adjusted centre) for identified galaxies in VC05. The hatched areas shows the identified Red-Sequence galaxies in VC05.

B.4 The VC08 cluster

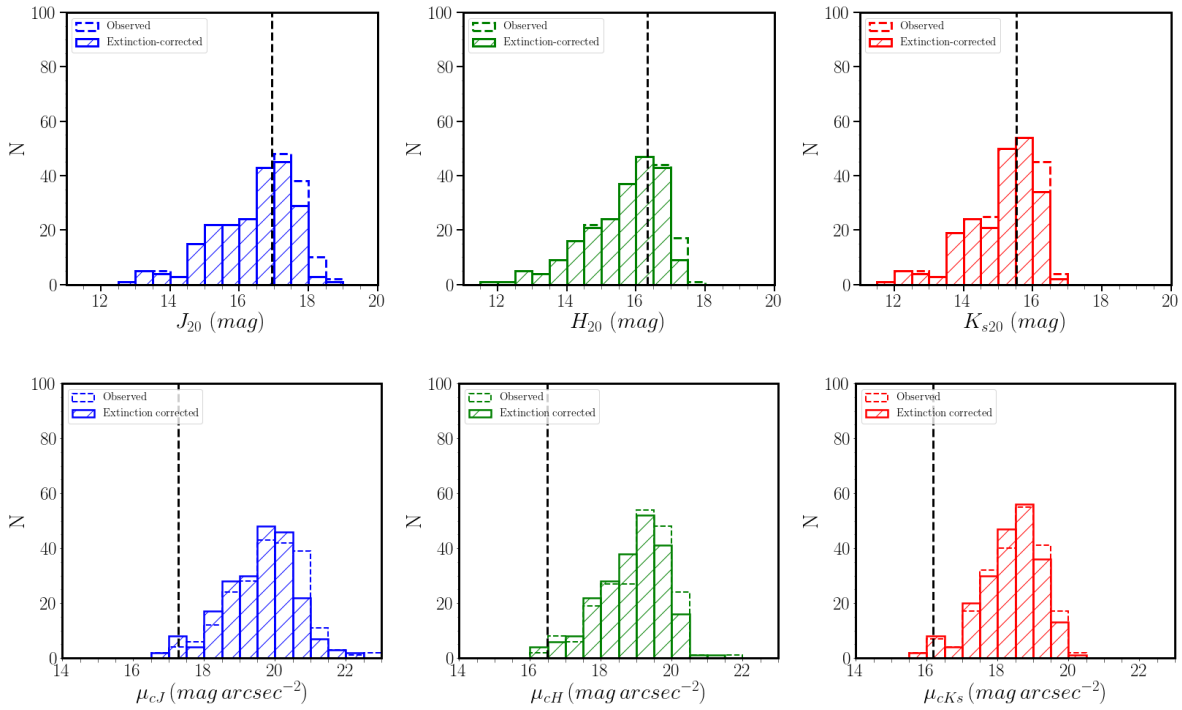

Figure B.4.1: Top: VC08 histograms of isophotal magnitudes at $K_s = 20\overset{m}{.}0$ in J, H and K_s bands. The dashed histograms show the observed magnitudes and the hatched ones are the extinction-corrected. The dashed lines are the completeness magnitude limits in each band. Bottom: Histograms of central surface brightness of VC08 galaxies in J, H and K_s bands. The dividing values of central surface brightnesses between elliptical and spiral galaxies in each band are shown by the dashed lines.

Table B.4.1: Photometric parameters of the VC08 galaxies.

Parameter	Max	Min
J^0_{20} (mag)	18.50	12.56
H^0_{20} (mag)	17.47	11.80
K^0_{s20} (mag)	16.65	11.52
μ^0_{cJ} (mag arcsec^{-2})	22.49	16.74
μ^0_{cH} (mag arcsec^{-2})	21.40	16.00
μ^0_{cKs} (mag arcsec^{-2})	20.32	15.66

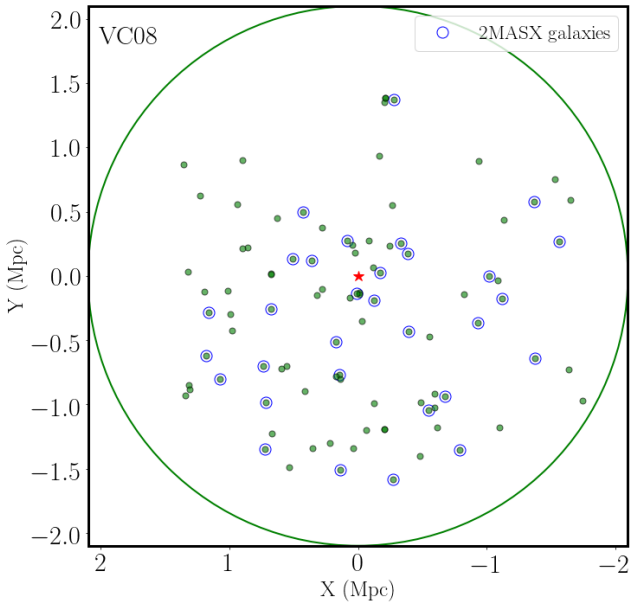

Figure B.4.2: The on-sky distribution of galaxies with $K_s^o < 15\overset{\text{m}}{.}5$ and $r > 2''$ in VC04. The IRSF galaxies are shown with filled green circles. Galaxies that have counterpart in 2MASX are encircled in blue.

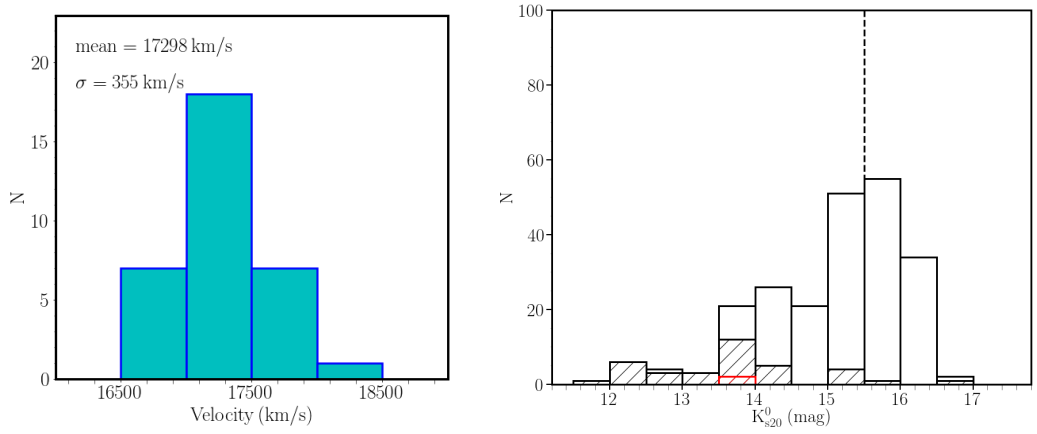

Figure B.4.3: Left: the velocity histogram of the VC08 cluster. Right: the distribution of the extinction-corrected K_s magnitude for identified galaxies in VC08 with $r > 2''$. The galaxies with redshift data are shown as black hatched areas. The red areas mark background galaxies (2 with $v > 19000$ km s^{-1}).

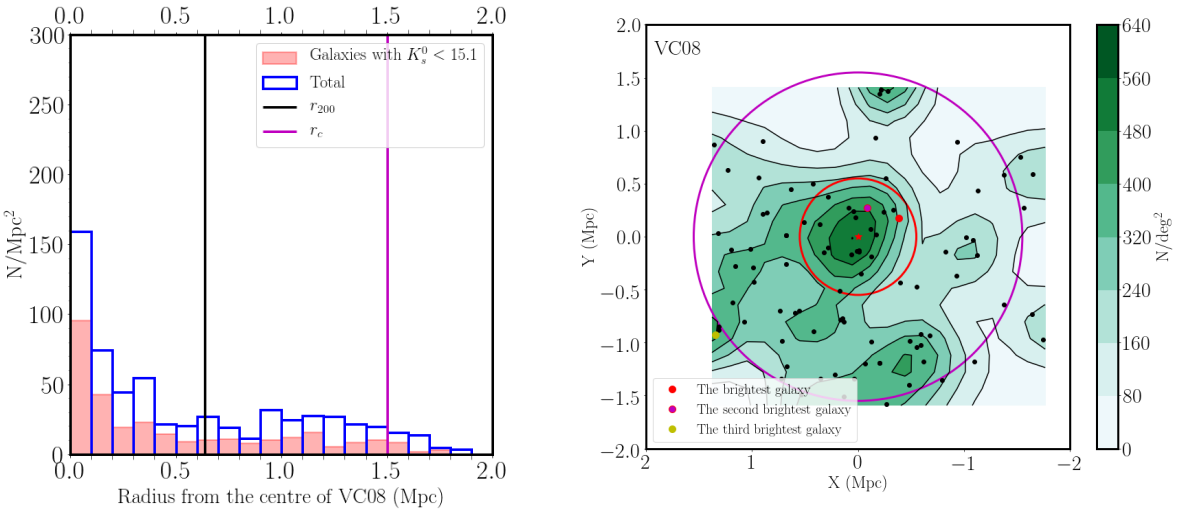

Figure B.4.4: Left: the radial density profile, N/Mpc^2, out to $r < 2$ Mpc. The total number density of galaxies is shown in blue histogram and the completeness-limited sample ($K^0_{slim} < 15\overset{m}{.}1$) in pink. Right: iso-density map of VC08 for $r < 2$ Mpc. Galaxies are shown as black dots and the centre of cluster as red star. The red and magenta circles represent the r_{200} and r_c respectively. The three brightest galaxies are shown as red, magenta and yellow dots.

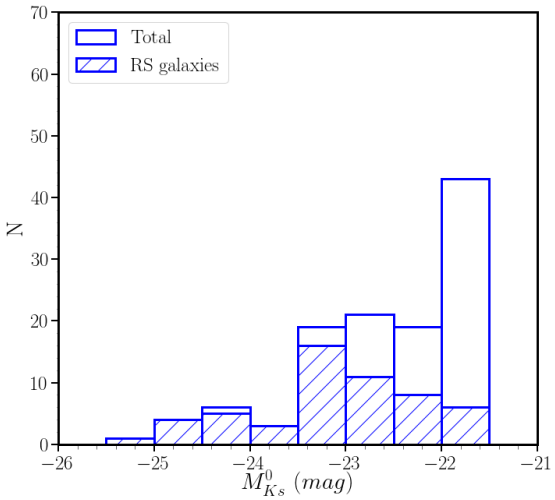

Figure B.4.5: The distribution of the extinction-corrected absolute magnitude up to $M^o_{Ks} < -21\overset{m}{.}5$ and $r_c < 1.5$ Mpc for identified galaxies in VC08. The hatched areas shows the identified Red-Sequence galaxies in VC08.

B.5 The VC10 cluster

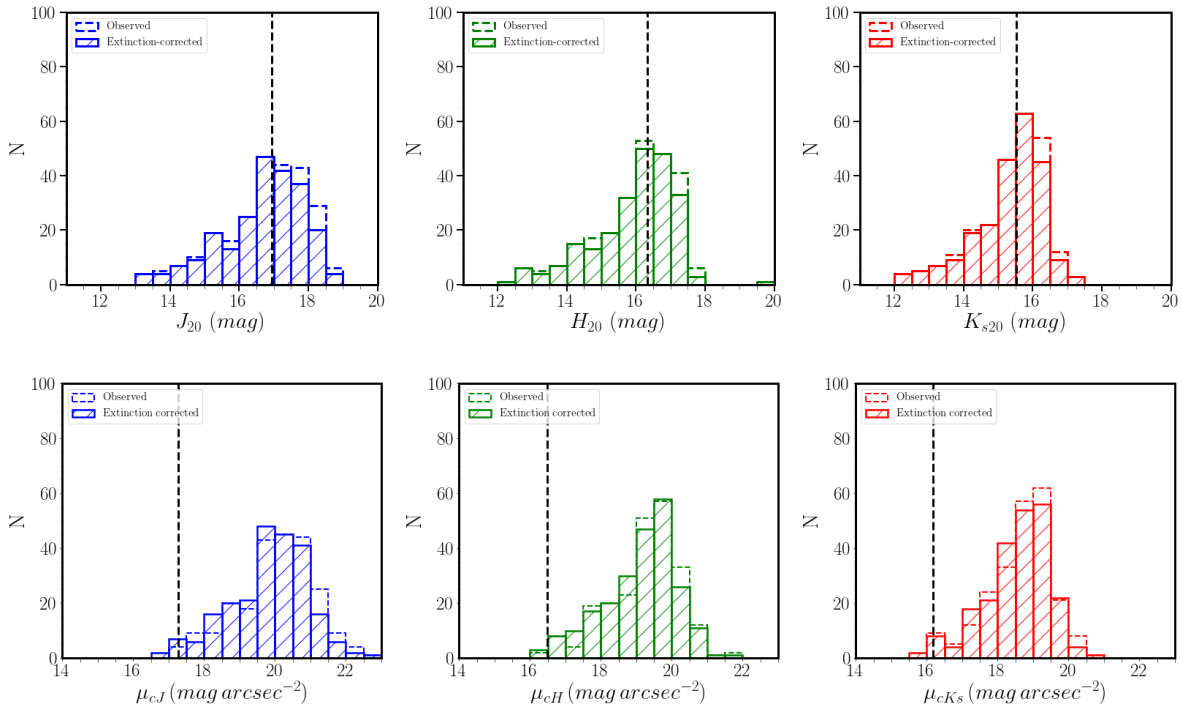

Figure B.5.1: Top: VC10 histograms of isophotal magnitudes at $K_s = 20\overset{\text{m}}{.}0$ in J, H and K_s bands. The dashed histograms show the observed magnitudes and the hatched ones are the extinction-corrected. The dashed lines are the completeness magnitude limits in each band. Bottom: Histograms of central surface brightness of VC10 galaxies in J, H and K_s bands. The dividing values of central surface brightnesses between elliptical and spiral galaxies in each band are shown by the dashed lines.

Table B.5.1: Photometric parameters of the VC10 galaxies.

Parameter	Max	Min
J^0_{20} (mag)	20.20	13.14
H^0_{20} (mag)	19.80	12.45
K^0_{s20} (mag)	17.19	12.12
μ^0_{cJ} (mag arcsec^{-2})	22.67	16.95
μ^0_{cH} (mag arcsec^{-2})	21.55	16.26
μ^0_{cKs} (mag arcsec^{-2})	20.79	15.92

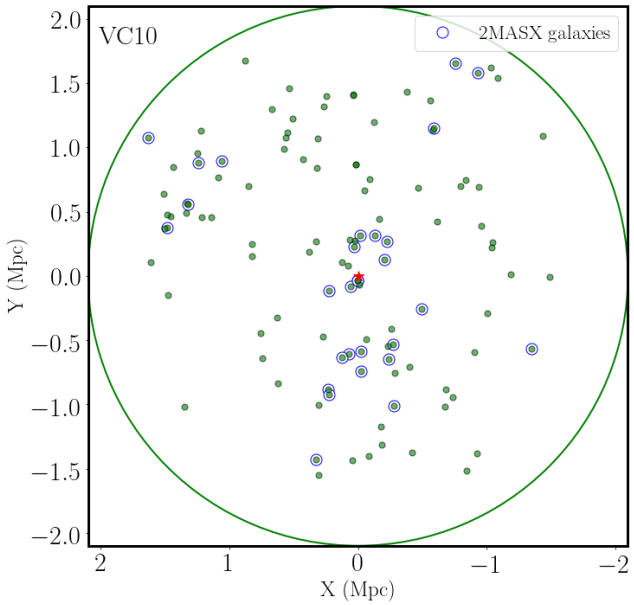

Figure B.5.2: The on-sky distribution of galaxies with $K_s^o < 15\overset{\text{m}}{.}5$ and $r > 2''$ in VC04. The IRSF galaxies are shown with filled green circles. Galaxies that have counterpart in 2MASX are encircled in blue.

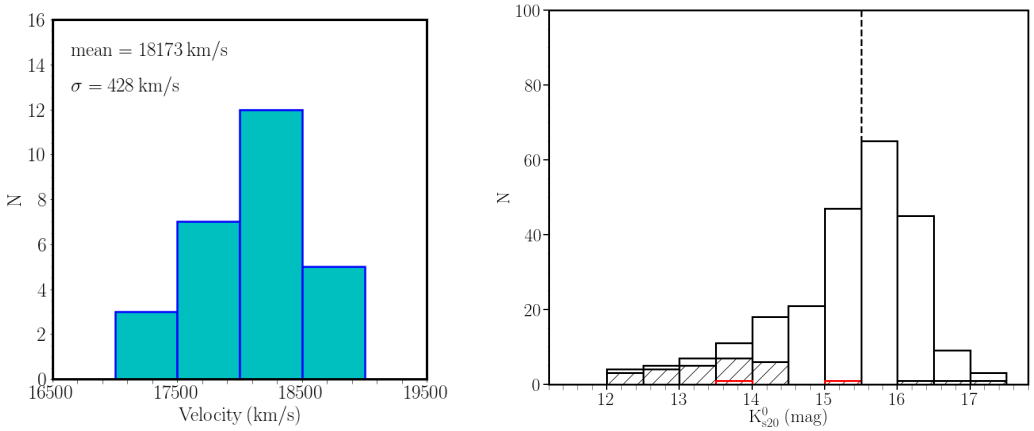

Figure B.5.3: Left: the velocity histogram of the VC10 cluster. Right: the distribution of the extinction-corrected K_s magnitude for identified galaxies in VC10 with $r > 2''$. The galaxies with redshift data are shown as black hatched areas. The red areas mark background galaxies (2 with $v > 20000$ km s^{-1}).

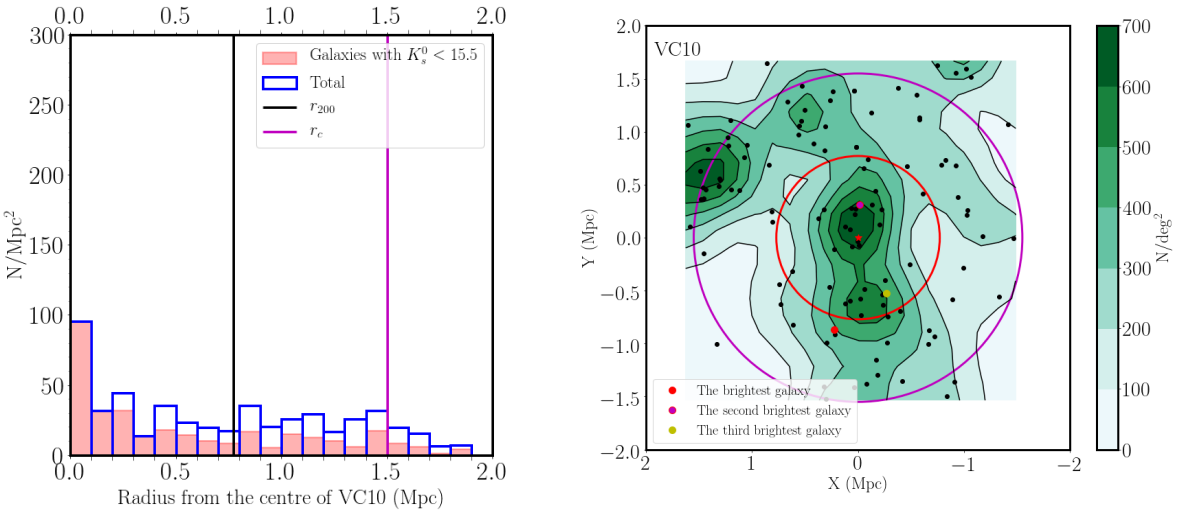

Figure B.5.4: Left: the radial density profile, N/Mpc^2, out to $r < 2$ Mpc. The total number density of galaxies is shown in blue histogram and the completeness-limited sample ($K^0_{slim} < 15\overset{\text{m}}{.}5$) in pink. Right: iso-density map of VC10 for $r < 2$ Mpc. Galaxies are shown as black dots and the centre of cluster as red star. The red and magenta circles represent the r_{200} and r_c respectively. The three brightest galaxies are shown as red, magenta and yellow dots.

B.6 The VC11 cluster

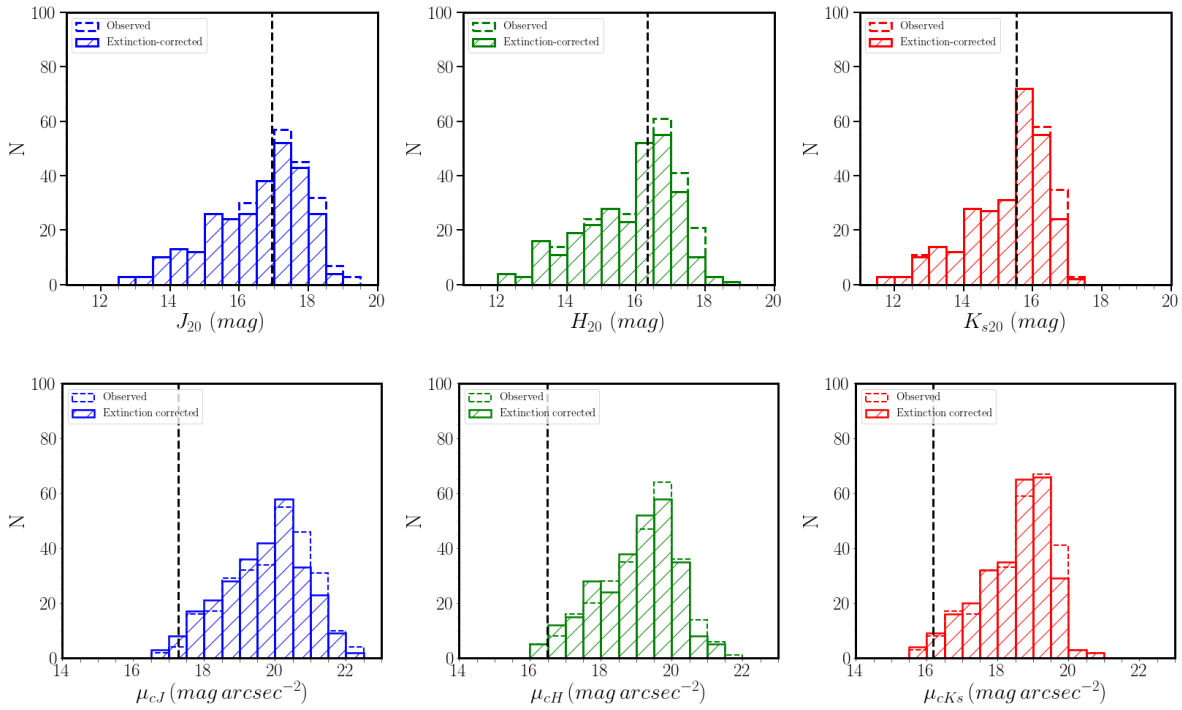

Figure B.6.1: Top: VC11 histograms of isophotal magnitudes at $K_s = 20\overset{\text{m}}{.}0$ in J, H and K_s bands. The dashed histograms show the observed magnitudes and the hatched ones are the extinction-corrected. The dashed lines are the completeness magnitude limits in each band. Bottom: Histograms of central surface brightness of VC11 galaxies in J, H and K_s bands. The dividing values of central surface brightnesses between elliptical and spiral galaxies in each band are shown by the dashed lines.

Table B.6.1: Photometric parameters of the VC11 galaxies.

Parameter	Max	Min
J_{20}^0 (mag)	18.91	12.62
H_{20}^0 (mag)	18.65	12.02
K_{s20}^0 (mag)	17.33	12.68
μ_{cJ}^0 (mag arcsec^{-2})	22.24	16.62
μ_{cH}^0 (mag arcsec^{-2})	21.48	16.00
μ_{cKs}^0 (mag arcsec^{-2})	20.72	15.63

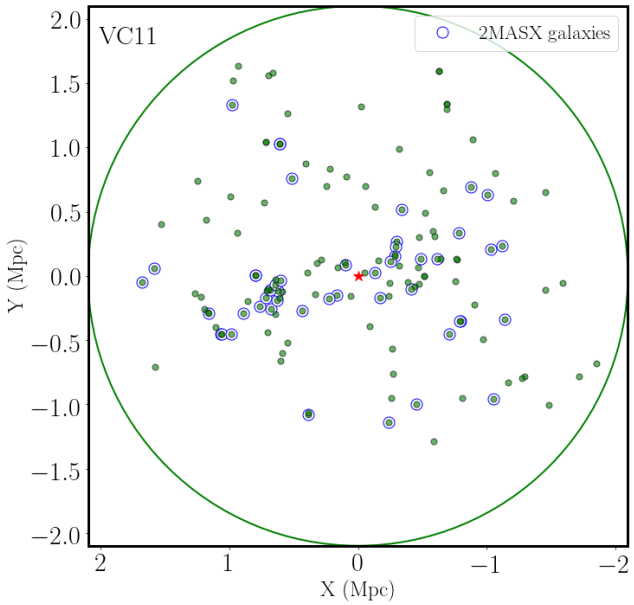

Figure B.6.2: The on-sky distribution of galaxies with $K_s^o < 15\overset{\text{m}}{.}5$ and $r > 2''$ in VC04. The IRSF galaxies are shown with filled green circles. Galaxies that have counterpart in 2MASX are encircled in blue.

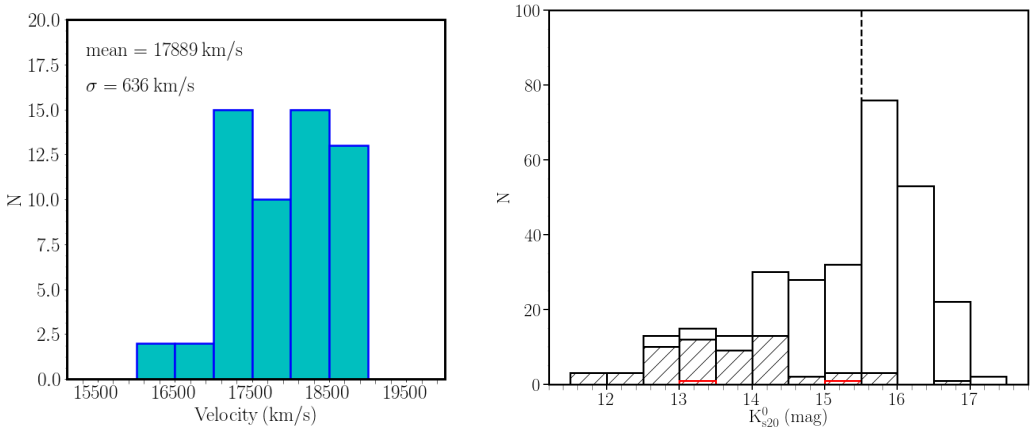

Figure B.6.3: Left: the velocity histogram of the VC11. Right: the distribution of the extinction-corrected K_s magnitude for identified galaxies in VC11 with $r > 2''$. The galaxies with redshift data are shown as black hatched areas. The red areas mark foreground and background galaxies (1 with $v < 16000$ km s^{-1} and 1 with $v > 20000$ km s^{-1} respectively).

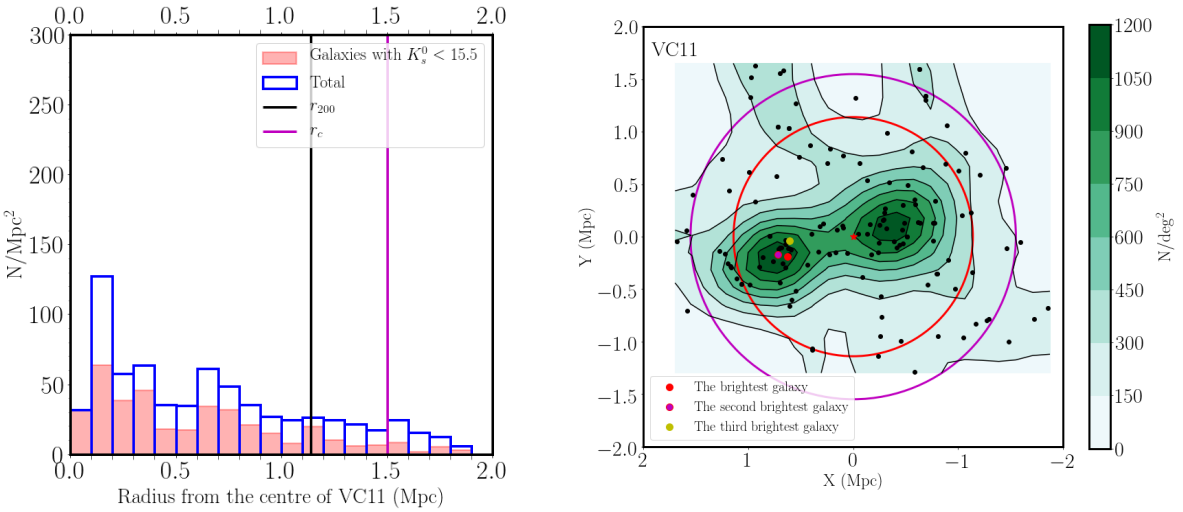

Figure B.6.4: Left: the radial density profile, N/Mpc^2, out to $r < 2$ Mpc. The total number density of galaxies is shown in blue histogram and the completeness-limited sample ($K^0_{slim} < 15\overset{\text{m}}{.}5$) in pink. Right: iso-density map of VC11 for $r < 2$ Mpc. Galaxies are shown as black dots and the centre of cluster as red star. The red and magenta circles represent the r_{200} and r_c respectively. The three brightest galaxies are shown as red, magenta and yellow dots.

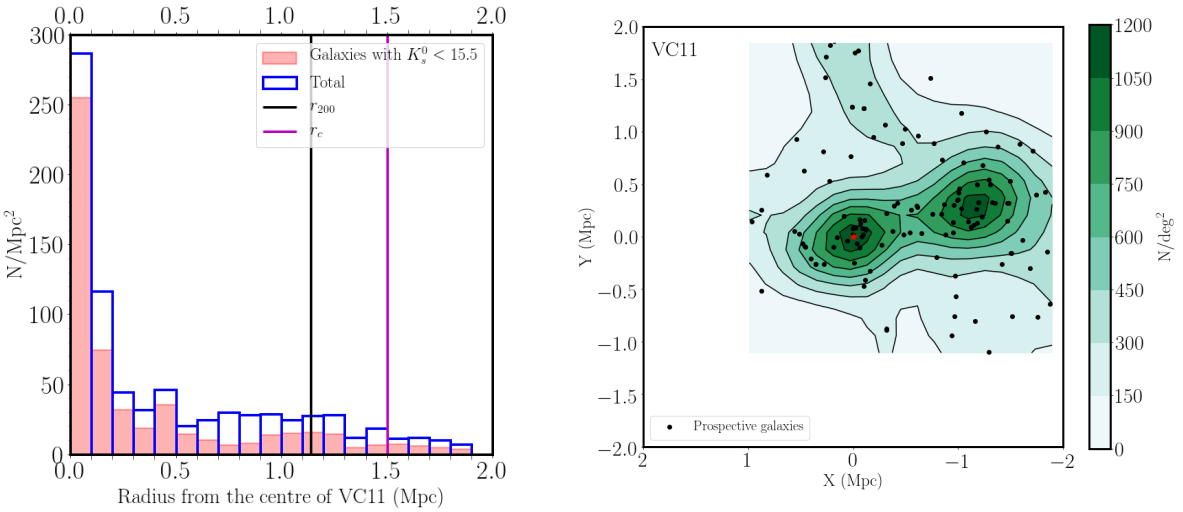

Figure B.6.5: The radial density profile, N/Mpc^2 (left) and iso-density contour map of VC11a out to $r < 2$ Mpc (right), using the centre of left clump.

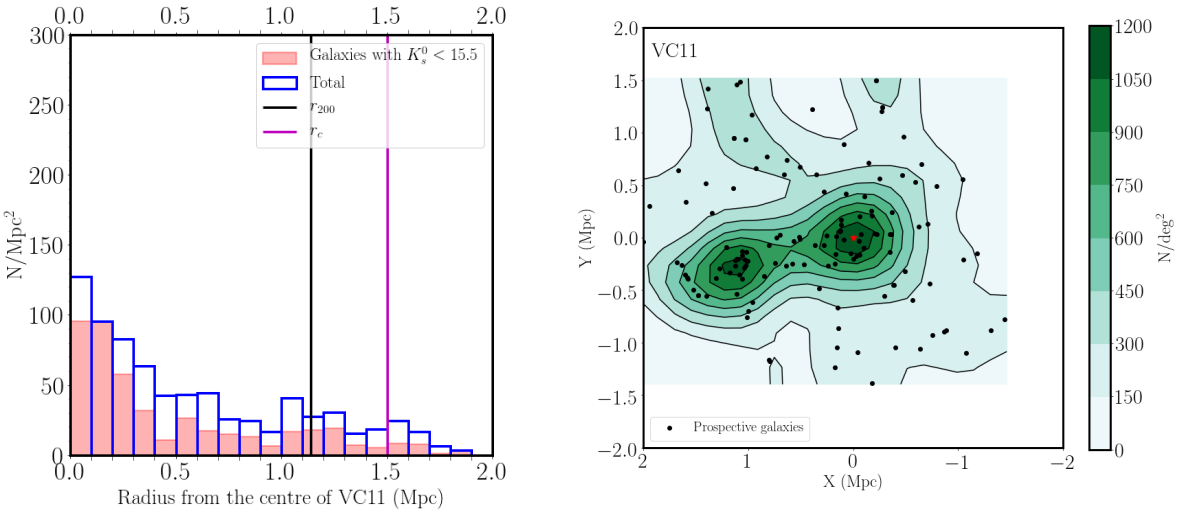

Figure B.6.6: The radial density profile, N/Mpc^2 (left) and iso-density contour map of VC11b out to $r < 2$ Mpc (right), using the centre of right clump.

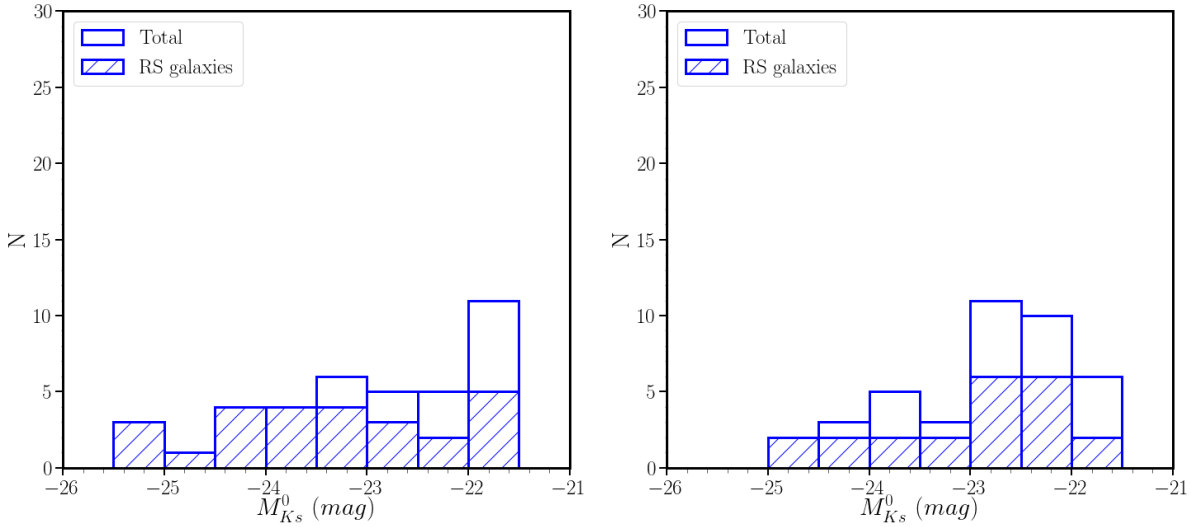

Figure B.6.7: The distribution of the extinction-corrected absolute magnitude up to $M^o_{Ks} < -21\overset{m}{.}5$ and $r_c < 0.5$ Mpc (around the adjusted centres) for identified galaxies in VC11a and VC11b (left and right panel respectively). The hatched areas shows the identified Red-Sequence galaxies in VC11a.